OBRABOTKA METALLOV

METAL WORKING & MATERIAL SCIENCE

НГТУ НЭТИ

Технологии,
которые работают.

1950 ⟶ 2025

ИНЖЕНЕРНОЕ СЕРДЦЕ СИБИРИ: НГТУ НЭТИ ОТМЕЧАЕТ 75-ЛЕТИЕ

В 2025 году один из крупнейших технических вузов страны – Новосибирский государственный технический университет НЭТИ празднует 75-летний юбилей. Вуз под названием НЭТИ (Новосибирский электротехнический институт) был создан под задачи индустриального прорыва в Сибири после окончания Великой Отечественной войны в 1950 году.

РЕКТОР НГТУ НЭТИ ДОКТОР ТЕХНИЧЕСКИХ НАУК, ПРОФЕССОР АНАТОЛИЙ АНДРЕЕВИЧ БАТАЕВ:

Спустя 75 лет НГТУ НЭТИ остается центром прикладной науки, производя новые знания в виде результатов фундаментальных исследований и технологических решений.

Университет обеспечивает подготовку инженерных кадров для важнейших отраслей, определяющих специфику промышленного развития региона, в том числе для машино-, самолето- и приборостроения, энергетики, электроники, IT-отрасли, для предприятий оборонно-промышленного комплекса страны. За 75 лет вуз выпустил более 200 тысяч профессионалов.

В настоящее время в НГТУ НЭТИ 11 факультетов дневного отделения, Институт социальных технологий, народный факультет. Общее число студентов превышает 15 тысяч человек. Сегодня в университете осуществляется подготовка по более чем 130 направлениям.

Профессорско-преподавательский состав — это коллектив выдающихся ученых и инженеров, сохраняющих традиции академических знаний и технической школы, в содружестве с молодыми преподавателями, готовыми совершать прорыв в постиндустриальной экономике вместе со студентами.

В НГТУ НЭТИ учебный процесс осуществляют более 1500 преподавателей, в их числе два академика и пять членов-корреспондентов РАН, более 200 докторов наук. Ежегодно ученые и инженеры НГТУ НЭТИ создают около 200 разработок в области новых материалов, электроники, энергетики и ИТ для предприятий России.

Ознакомиться с годовой программой празднования юбилея:
www.nstu.ru/university/university_events_people/NETI75

The journal is issued since 1999

Publication frequency – 4 numbers a year

Data on the journal are published in
«Ulrich's Periodical Directory»

Journal "Obrabotka Metallov" ("Metal Working and Material Science") has been Indexed in Clarivate Analytics Services.

Journal "Obrabotka Metallov – Metal Working and Material Science" is indexed in the world's largest abstracting bibliographic and scientometric databases Web of Science and Scopus.

Journal "Obrabotka Metallov" ("Metal Working & Material Science") has entered into an electronic licensing relationship with EBSCO Publishing, the world's leading aggregator of full text journals, magazines and eBooks. The full text of JOURNAL can be found in the EBSCOhost™ databases.

CONTENTS

Obrabotka metallov –

Metal Working and Material Science

Machining performance evaluation of eco-friendly copper oxide-based nanofluids in turning operations

Javvadi Eswara Manikanta [1, a], *Nitin Ambhore* [2, b, *], *Krishna Birudugadda Murthy* [3, c],
Gopala Rao Thellaputta [4, d], *Devendra Agrawal* [5, e]

[1] Department of Mechanical Engineering, Shri Vishnu Engineering College for Women (A), Bhimavaram, Andhra Pradesh, 534202, India

[2] Department of Mechanical Engineering, Vishwakarma Institute of Technology, SPPU, Maharashtra, Pune 411037, India

[3] Department of Mechanical Engineering, Sasi Institute of Technology and Engineering, Tadepalligudem, 534101, India

[4] Department of Mechanical Engineering, St. Ann's College of Engineering & Technology (Autonomous), Chirala, Andhra Pradesh, 523187, India

[5] Department of Mechanical Engineering, College of Engineering, Malegaon (Bk), Baramati, Maharashtra, Pune 413115, India

[a] https://orcid.org/0000-0002-0881-4899, ✉ manijem66@gmail.com; [b] https://orcid.org/0000-0001-8468-8057, ✉ nitin.ambhore@vit.edu;
[c] https://orcid.org/0009-0007-4457-0266, ✉ bkmurthy@sasi.ac.in; [d] https://orcid.org/0000-0001-5622-4140, ✉ drtgopalarao@gmail.com;
[e] https://orcid.org/0000-0002-2477-1841, ✉ dpagrawal@engg.svpm.org.in

ARTICLE INFO

ABSTRACT

Introduction. There is a growing demand for eco-friendly cutting fluids in machining due to their non-toxicity, sustainability, high performance, and ability to improve surface quality. These fluids support green manufacturing practices and promote a safe working environment. Copper oxide-based nanofluids offer the combined benefits of enhanced heat transfer, increased safety, and reduced tool wear and cutting forces. **The purpose of the work.** This research focuses on evaluating the performance of copper oxide-based cutting fluids in turning processes to support sustainable and eco-conscious manufacturing. The study investigates the turning of *SS 304* steel using varying concentrations of copper oxide nanofluids. **The methods of investigation.** In this study, the turning process was tested under various machining conditions using different concentrations of copper oxide nanoparticles (0.3 %, 0.6 %, 0.9 %, 1.2 %, and 1.5 %). Corn oil was selected as the base oil, and the copper oxide nanoparticles were dispersed in the corn oil to prepare the nanofluid. Machining trials were conducted under different lubrication environments: dry, wet, minimum quantity lubrication (*MQL*), and nano-enhanced *MQL* (*nMQL*). A comparative study was performed to assess cutting temperature and cutting forces. **Results and discussion.** The results showed that the use of 1.2 % copper oxide nanofluid led to significant reductions in cutting force and cutting temperature, by approximately 17.54 % and 29.53 %, respectively, compared to traditional dry and wet machining environments. Furthermore, the nanofluid was observed to form a protective film at the tool-workpiece interface, reducing tool wear. These findings highlight the potential of copper oxide-based green cutting fluids to improve turning operation efficiency and promote environmentally sustainable practices.

Introduction

In traditional machining operations, chemical-based cutting fluids are typically used to reduce friction and improve the efficiency of machining processes by providing cooling and lubrication [1]. However, the use of these fluids has raised substantial environmental concerns and poses health hazards to workers due to their toxicity [2]. Therefore, there is an increasing demand for sustainable manufacturing approaches that reduce or eliminate the use of conventional cutting fluids [3]. Consequently, a promising alternative

* Corresponding author
Ambhore Nitin, Ph.D. (Engineering), Assistant Professor
Vishwakarma Institute of Technology,
Pune - 411037, Maharashtra, India
Tel.: +91-2026950441, **e-mail:** nitin.ambhore@vit.edu

in this regard is *MQL*, which delivers a small, controlled amount of lubricant mixed with compressed air directly to the cutting zone, thus offering both ecological and economic benefits [4-5]. This technique not only reduces lubricant consumption but also improves machining performance [6].

Recent advancements have demonstrated that the addition of nanoparticles to biodegradable vegetable oils in *MQL* systems significantly enhances cutting performance while eliminating health and environmental risks [7]. Nanoparticles like graphene have been shown to reduce tool wear and improve surface finish during machining operations [8]. For example, studies have reported better machining outcomes with nano-SiO_2-enhanced lubrication compared to conventional systems [9-10]. Similarly, *Emami et al.* [11] observed improved grinding performance of ceramics using *MQL*. Furthermore, vegetable oil-based *MQL* fluids demonstrated enhanced tool life and surface finish when machining *Inconel* alloys [12]. Studies utilizing different vegetable oils, such as sunflower and neem, in *MQL* applications have also shown improved machining performance [13].

During metal cutting, tool tip temperatures often rise, accelerating tool wear and machine downtime. Selecting the right cutting fluid and lubrication strategy is essential to reduce such effects and prolong tool life [14]. Studies have shown that nanofluids enhance both heat dissipation and lubrication due to superior wettability and thermal conductivity [15]. *Estelle et al.* [16] studied carbon-nanotube-based water-based nanofluids and found enhanced thermal conductivity and viscosity. *Mia et al.* [17] compared dry, conventional, and *MQL* methods during hardened steel machining and observed lower cutting forces with *MQL*. Additionally, extreme pressure (*EP*) additives in vegetable-oil-based lubricants reduced cutting forces in *AISI 304L* steel machining, although higher *EP* concentrations led to increased surface roughness. Nevertheless, vegetable-based cutting fluids were still considered a viable alternative to hazardous petroleum fluids. *Srikant et al.* [18] demonstrated that copper oxide nanofluids in water-based systems significantly reduced tool tip temperatures due to enhanced heat extraction capabilities. *Padmini et al.* [19] also confirmed the tribological and thermal advantages of properly formulated nanofluids in metal cutting. *Shrivastava* and *Gangopadhyay* [20] conducted microdrilling tests under compressed air, pure vegetable oil *MQL*, and nanodiamond-enhanced vegetable oil *MQL*. The best performance was achieved with a 2.0 vol% nanodiamond mixture. *Azami et al.* [21] observed improved milling performance with 0.1 wt% graphene nanoparticle (*GnP*)-enhanced vegetable oil compared to plain oil. *Sharma et al.* [22] emphasized the application of nanofluid-based *MQL* for machining ultra-hard materials. *Manikanta et al.* [23] reported that the material removal rate and surface finish during *SS304* machining are significantly influenced by both cutting speed and nanofluid concentration. *Virdi et al.* [24] demonstrated improved surface finish and lower temperatures in *Ni-Cr* alloy grinding using *MQL* with 0.5–1 wt% *CuO* nanofluids. *Gaurav et al.* [25] evaluated jojoba-oil-based nanofluids in *MQL* machining of titanium and observed reduced cutting forces and improved machining quality due to enhanced cooling and lubrication.

A review of the literature reveals that researchers have explored the use of various nanofluids in machining. However, the application of copper oxide-based nanofluids appears to be limited in turning operations. Therefore, **the objective of this study** is to investigate the impact of varying concentrations of CuO nanofluids under dry, wet, *MQL*, and *nMQL* conditions.

Methods

A stainless steel bar served as the workpiece material for the experiments. Machining processes were performed using a *Turn Master 35* lathe. The lathe was operated under the following parameters: a speed of 900 rpm, a feed of 80 mm/min, and a depth of cut of 0.30 mm, following standard machine specifications.

The turning operation was performed under four lubrication conditions: dry, wet, *MQL*, and nano-enhanced *MQL*. For wet machining, a commercially available traditional cutting fluid was used. For the *MQL* setup, a cutting fluid was applied at a flow rate of 450 mL/hr. The *nMQL* experiments used a green cutting fluid based on corn oil, containing copper oxide nanoparticles at concentrations of 0.3%, 0.6%, 0.9%, 1.2%, and 1.5% by volume.

During the machining operation, the temperature at the tool tip was measured using a digital pyrometer. A piezoelectric dynamometer was used to measure the cutting forces produced during the turning operations.
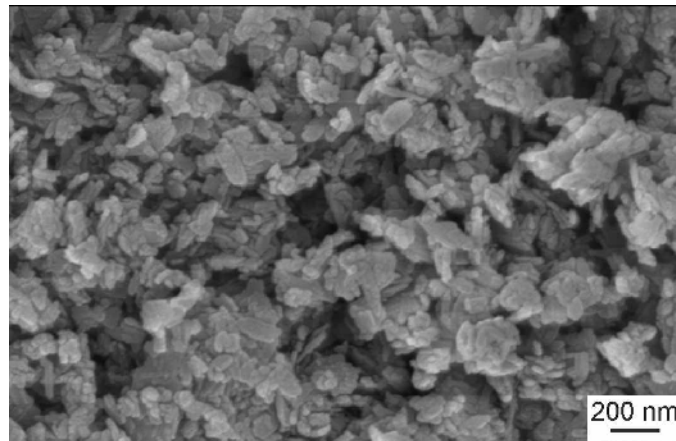
Fig. 1. SEM image of copper oxide nanoparticles

The diffusion process was carried out at different weight concentrations of *CuO*. Fig. 1 presents a field emission scanning electron microscope (*FESEM*) image of the copper oxide nanoparticles used in the study. To achieve a homogeneous blend, magnetic stirring was applied to uniformly disperse the nanoparticles throughout the base fluid. Moreover, to improve dispersion stability and inhibit nanoparticle agglomeration, *lauryl sodium sulphate* (*LSS*) was added at a quantity equal to 0.1% of the nanoparticle weight. Fig. 2 illustrates the appearance of the prepared copper-oxide-based nanofluids.

Fig. 2. Copper-oxide-based nanofluids

Experimental setup details

Parameter	Description
Machine tool	Center lathe machine, *Turn-master-35*, (*Kirloskar*)
Workpiece material	*SS 304* alloy
Workpiece size	50 mm diameter, 200 mm length
Tool holder	*PSBNR2525 M-12*
Cutting tool	*SNMG 120408 NSU* (coated carbide)

Results and Discussion

Extreme cutting forces during turning can accelerate tool wear, reduce tool life, increase the need for frequent tool changes, and degrade surface quality due to vibration and chatter. Fig. 3 shows the cutting forces recorded under various machining conditions, including dry, conventional (wet), *MQL*, and nano-enhanced *MQL* modes, using different cutting fluids such as conventional cutting fluid (*CCF*), green cutting

fluid (*GCF*), and *GCF* blended with copper oxide nanoparticles at concentrations of 0.3 wt.%, 0.6 wt.%, 0.9 wt.%, 1.2 wt.%, and 1.5 wt.%. The highest cutting force, 120.7 N, was observed under dry conditions due to the absence of lubrication. In contrast, conventional wet machining using CCF resulted in a reduced cutting force of 103.2 N. An additional decrease was noted under *MQL* conditions with *GCF*, where the cutting force measured was 99.2 N. The application of copper oxide-based nanofluids in *MQL* led to a further reduction in cutting forces, indicating improved lubrication and reduced tool-workpiece friction.
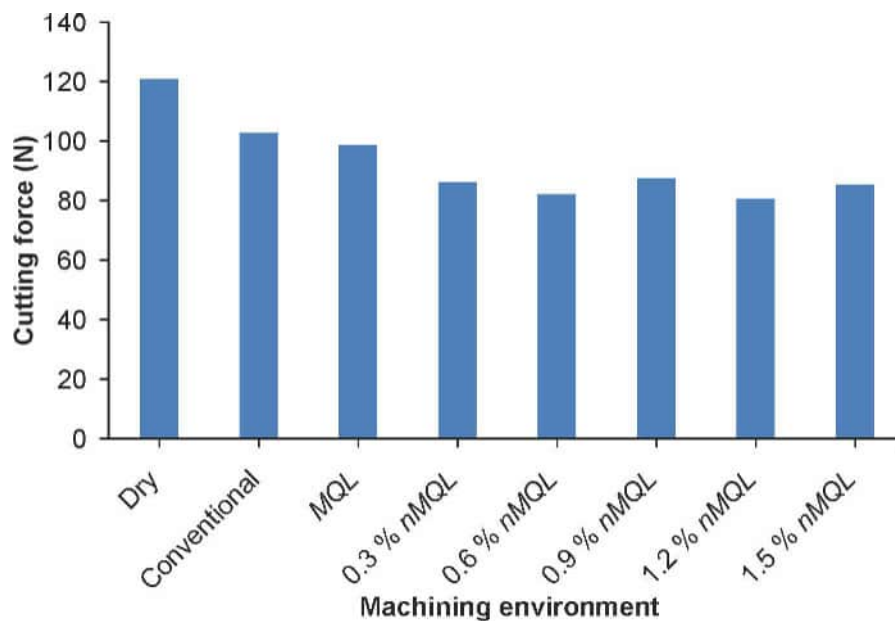
Fig. 3. Cutting forces under different machining environments

The use of 0.3 wt.% *CuO*-based nanofluid resulted in a decrease in cutting force to 86.7 N at the cutting zone. Further increases in *CuO* concentration to 0.6 wt.%, 0.9 wt.%, and 1.2 wt.% yielded cutting forces of 82.8 N, 87.7 N, and 81.3 N, respectively, compared to the 0.3 wt.% condition. This reduction was attributed to enhanced lubrication, as the nanoparticles formed a stable lubricating film on the workpiece surface, thereby promoting efficient heat dissipation. The improved thermal conductivity and lubricating properties at higher *CuO* concentrations helped diminish friction and reduce heat generation at the cutting zone. However, when the concentration reached 1.5 wt.%, the cutting force increased to 85.9 N, a value higher than that observed at 1.2 wt.%. This was due to nanoparticle agglomeration, which negatively affected the dispersion stability and diminished the overall effectiveness of the nanofluid.

Elevated cutting temperatures accelerate tool wear by softening the tool material, which contributes to rapid deterioration and a significant reduction in tool life. Moreover, high temperatures can adversely affect the surface finish due to thermally induced vibrations and instability during the turning operation. In extreme cases, the heat generated during cutting can change the microstructure of the workpiece material, potentially damaging its mechanical properties, such as hardness, tensile strength, and residual stress distribution. Fig. 4 shows the cutting temperatures recorded under various turning conditions, including dry (conventional), *MQL*, and *nMQL* modes. The tests were conducted using different cutting fluids such as conventional cutting fluid (*CCF*), green cutting fluid (*GCF*), and *GCF* blended with copper oxide nanoparticles at concentrations of 0.3 wt.%, 0.6 wt.%, 0.9 wt.%, 1.2 wt.%, and 1.5 wt.%.

Under dry machining mode, the highest cutting temperature was noted at 84 °C, primarily due to the absence of any cooling medium. When conventional cutting fluid (*CCF*) was used in wet machining, the cutting temperature decreased to 52 °C. A further decrease to 50 °C was detected with *MQL* using green cutting fluid. The use of copper oxide nanofluids under *MQL* conditions demonstrated enhanced cooling effectiveness, as evidenced by the significant temperature reductions measured during the turning operations.

With the application of 0.3 wt.% *CuO* nanofluid, the cutting temperature at the tool-chip interface was reduced notably to 45 °C. As the *CuO* concentration increased to 0.6 wt.%, 0.9 wt.%, and 1.2 wt.%, the
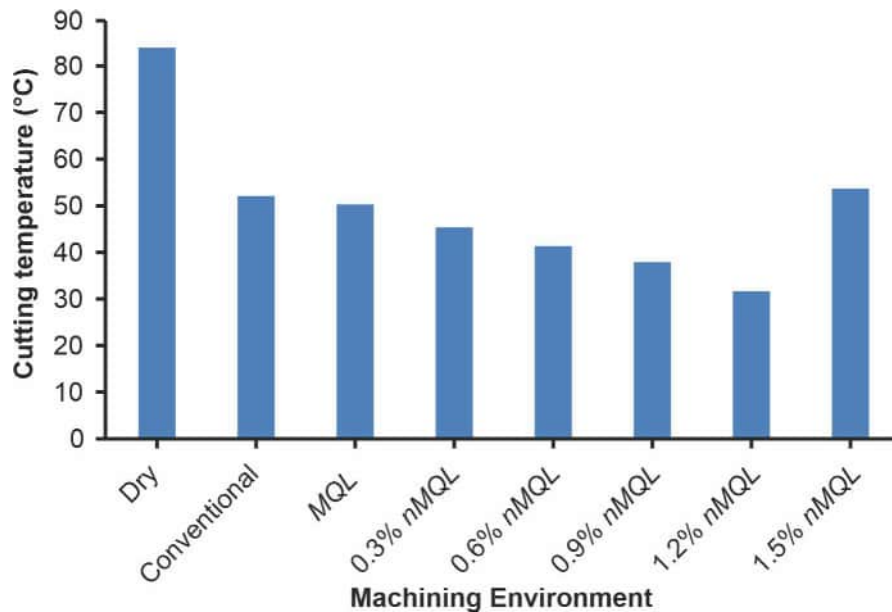
Fig. 4. Cutting temperature under different machining environments

identified temperature reductions were 41 °C, 38 °C, and 32 °C, respectively, compared to the 0.3 wt.% baseline. This consistent decline in temperature was mainly attributed to improved lubrication and higher thermal conductivity offered by the nanofluids. The dispersed nanoparticles formed a stable and sturdy lubricating film on the metal surface, while the characteristic high thermal conductivity of *CuO* facilitated fast heat dissipation. Moreover, the increased nanoparticle concentration provided additional lubrication, reducing frictional forces and consequently decreasing heat generation.

However, at 1.5 wt.% *CuO* concentration, the cutting temperature rose to 54 °C, which is higher than that observed at 1.2 wt.%. This increase was attributed to nanoparticle agglomeration, which adversely affected dispersion stability and reduced the cooling and lubricating performance of the nanofluid.

Fig. 5 shows the tool wear in different machining environments. Dry, wet, and *nMQL* metal cutting methods significantly affect tool wear during machining operations, particularly when nanofluids are used. In dry machining, the absence of lubricant leads to high cutting temperatures, accelerating tool wear due to thermal stress and poor chip removal. Wet machining, using conventional flood coolants, reduces heat and friction but raises environmental and disposal concerns. *MQL*, particularly when enhanced with biodegradable nanofluids containing nanoparticles such as copper oxide, offers a sustainable alternative. These nanofluids improve lubrication and thermal conductivity, forming a protective film at the tool-workpiece interface, which reduces abrasion, adhesion, and diffusion wear. As a result, *MQL* with nanofluids significantly reduces tool wear compared to dry and even traditional wet machining, enhancing tool life and machining performance.

a   *b*   *c*
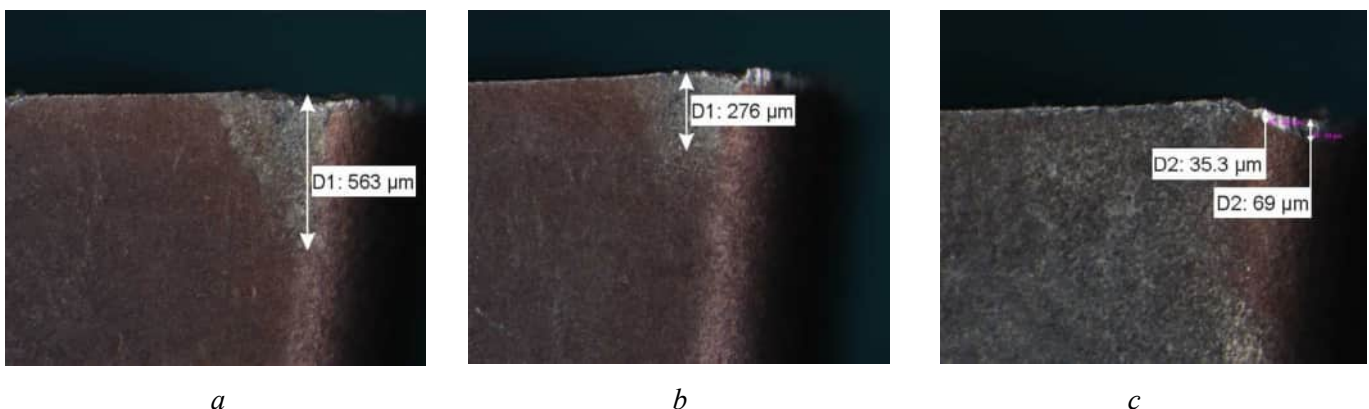
Fig. 5. Tool wear in (*a*) dry, (*b*) MQL, and (*c*) nMQL machining environments

Conclusions

In this study, an investigation was conducted on corn oil-based cutting fluid with variable concentrations of copper oxide nanoparticles. A relative evaluation has been reported for various cooling systems such as conventional dry, wet, and *MQL*. The findings reveal that the integration of copper oxide nanoparticles at concentrations of 0.3%, 0.6%, 0.9%, 1.2%, and 1.5% into the corn-based green cutting fluid significantly improved machining performance under the tested conditions. The use of *nMQL* using the copper oxide-enhanced green cutting fluid led to notable reductions in both cutting force and cutting temperature, contributing to prolonged tool life. The greatest favorable results were observed at a concentration of 1.2 wt.% *CuO*, where the lowest cutting force and temperature were recorded. The 1.2% *nMQL* is proposed as the ideal lubricant for machinability improvement and reduced tool wear. These findings will be helpful for real-time process monitoring using a simple controller to maintain force and cutting temperature within targets.

References

1. Manikanta J.E., Ambhore N., Nikhare C., Gurajala, N.K., Ch. H.K. Sustainable machining: enhancing performance with vegetable oil-based nano cutting fluids. *Discover Materials*, 2025, vol. 5, p. 63. DOI: 10.1007/s43939-025-00236-4.

2. Hiran Gabriel D.J., Parthiban M., Kantharaj I., Beemkumar N. A review on sustainable alternatives for conventional cutting fluid applications for improved machinability. *Machining Science and Technology*, 2023, vol. 27 (2), pp. 157–207. DOI: 10.1080/10910344.2023.2194966.

3. Ben Said L., Kolsi L., Ghachem K., Almeshaal M., Maatki C. Application of nanofluids as cutting fluids in machining operations: A brief review. *Applied Nanoscience*, 2023, vol. 13 (6), pp. 4247–4278. DOI: 10.1007/s13204-021-02140-8.

4. Manikanta J.E., Abdullah M., Ambhore N., Kotteda T.K. Analysis of machining performance in turning with trihybrid nanofluids and minimum quantity lubrication. *Scientific Reports*, 2025, vol. 15 (1). DOI: 10.1038/s41598-025-97039-7.

5. Khatai S., Sahoo A.K., Kumar R., Panda A. Investigation on machinability and sustainability aspects during hard turning under GO nanofluid MQL environment for precision and cleaner manufacturing. *Precision Engineering*, 2025, vol. 95, pp. 379–408. DOI: 10.1016/j.precisioneng.2025.05.006.

6. Adil A., Baig T., Jamil F., Farhan M., Shehryar M., Ali H.M., Khushnood S. Nanoparticle-based cutting fluids in drilling: A recent review. *The International Journal of Advanced Manufacturing Technology*, 2024, vol. 131 (5), pp. 2247–2264. DOI: 10.1007/s00170-023-11048-2.

7. Kuram E., Ozcelik B., Demirbas E., Şik E., Tansel I.N. Evaluation of new vegetable-based cutting fluids on thrust force and surface roughness in drilling of AISI 304 using Taguchi method. *Materials and Manufacturing Processes*, 2011, vol. 26 (9), pp. 1136–1146. DOI: 10.1080/10426914.2010.536933.

8. Baldin V., da Silva L.R., Gelamo R.V., Iglesias A.B., da Silva R.B., Khanna N., Rocha Machado A. Influence of graphene nanosheets on thermo-physical and tribological properties of sustainable cutting fluids for MQL application in machining processes. *Lubricants*, 2022, vol. 10 (8). DOI: 10.3390/lubricants10080193.

9. Syafiq A.M., Redhwan A.A., Hazim A.A., Aminullah A.R., Ariffin S.Z., Nughoro W., Arifuddin A., Hawa A.B. An experimental evaluation of SiO_2 nano cutting fluids in CNC turning of aluminium alloy AL319 via MQL technique. *IOP Conference Series: Materials Science and Engineering*, 2021, vol. 1068 (1), pp. 1–11. DOI: 10.1088/1757-899X/1068/1/012009.

10. Shuang Y., John M., Songlin D. Experimental investigation on the performance and mechanism of graphene oxide nanofluids in turning Ti-6Al-4V. *Journal of Manufacturing Processes*, 2019, vol. 43, pp. 164–174. DOI: 10.1016/j.jmapro.2019.05.005.

11. Emami M., Karimipour A. Theoretical and experimental study of the chatter vibration in wet and MQL machining conditions in turning process. *Precision Engineering*, 2021, vol. 72, pp. 41–58. DOI: 10.1016/j.precisioneng.2021.04.006.

12. Gong L., Bertolini R., Ghiotti A., He N., Bruschi S. Sustainable turning of Inconel 718 nickel alloy using MQL strategy based on graphene nanofluids. *The International Journal of Advanced Manufacturing Technology*, 2020, vol. 108 (9), pp. 3159–3174. DOI: 10.1007/s00170-020-05626-x.

13. Makhesana M.A., Patel K.M. Performance assessment of vegetable oil-based nanofluid in Minimum Quantity Lubrication (MQL) during machining of Inconel 718. *Advances in Materials and Processing Technologies*, 2022, vol. 8 (3), pp. 3182–3198.

14. Kumar M.S., Krishna V.M. An investigation on turning AISI 1018 steel with hybrid biodegradeable nanofluid/MQL incorporated with combinations of $CuO-Al_2O_3$ nanoparticles. *Materials Today: Proceedings*, 2020, vol. 24, pp. 1577–1584. DOI: 10.1016/j.matpr.2020.04.478.

15. Rapeti P., Pasam V.K., Gurram K.M., Revuru R.S. Performance evaluation of vegetable oil based nano cutting fluids in machining using grey relational analysis – A step towards sustainable manufacturing. *Journal of Cleaner Production*, 2018, vol. 172, pp. 2862–2875. DOI: 10.1016/j.jclepro.2017.11.127.

16. Estellé P., Halelfadl S., Maré T. Thermophysical properties and heat transfer performance of carbon nanotubes water-based nanofluids. *Journal of Thermal Analysis and Calorimetry*, 2017, vol. 127 (3), pp. 2075–2081. DOI: 10.1007/s10973-016-5833-8.

17. Mia M., Gupta M.K., Singh G., Królczyk G., Pimenov D.Y. An approach to cleaner production for machining hardened steel using different cooling-lubrication conditions. *Journal of Cleaner Production*, 2018, vol. 187, pp. 1069–1081. DOI: 10.1016/j.jclepro.2018.03.279.

18. Berger Bioucas F.E., Koller T.M., Fröba A.P. Effective thermal conductivity of nanofluids containing silicon dioxide, titanium dioxide, copper oxide, polystyrene, or polymethylmethacrylate nanoparticles dispersed in water, ethylene glycol, or glycerol. *International Journal of Thermophysics*, 2025, vol. 46 (2). DOI: 10.1007/s10765-024-03488-z.

19. Padmini R., Krishna P.V., Mohana Rao G.K. Experimental evaluation of nano-molybdenum disulphide and nano-boric acid suspensions in vegetable oils as prospective cutting fluids during turning of AISI 1040 steel. *Proceedings of the Institution of Mechanical Engineers, Part J: Journal of Engineering Tribology*, 2016, vol. 230 (5), pp. 493–505. DOI: 10.1177/1350650115601.

20. Shrivastava A., Gangopadhyay S. Evaluation of adequacy of lubricants in MQL micro-drilling by a developed analytical model and experiments. *Journal of Manufacturing Processes*, 2023, vol. 8 (101), pp. 1592–1604. DOI: 10.1016/j.jmapro.2023.07.017.

21. Azami A., Salahshournejad Z., Shakouri E., Sharifi A.R., Saraeian P. Influence of nano-minimum quantity lubrication with MoS2 and CuO nanoparticles on cutting forces and surface roughness during grinding of AISI D2 steel. *Journal of Manufacturing Processes*, 2023, vol. 3 (87), pp. 209–220. DOI: 10.1016/j.jmapro.2023.01.029.

22. Sharma A.K., Tiwari A.K., Dixit A.R. Effects of minimum quantity lubrication (MQL) in machining processes using conventional and nanofluid based cutting fluids: A comprehensive review. *Journal of Cleaner Production*, 2016, vol. 2 (127), pp. 1–8. DOI: 10.1016/j.jclepro.2016.03.146.

23. Manikanta J.E., Ambhore N., Thellaputta G.R. Investigation of vegetable oil-based cutting fluids enhanced with nanoparticle additions in turning operations. *Obrabotka metallov (tekhnologiya, oborudovanie, instrumenty) = Metal Working and Material Science*, 2025, vol. 27, no. 1, pp. 20–33. DOI: 10.17212/1994-6309-2025-27.1-20-33.

24. Virdi R.L., Chatha S.S., Singh H. Processing characteristics of different vegetable oil-based nanofluid MQL for grinding of Ni-Cr alloy. *Advances in Materials and Processing Technologies*, 2022, vol. 8 (1), pp. 210–223. DOI: 10.1007/s40684-018-0035-4.

25. Gaurav G., Sharma A., Dangayach G.S., Meena M.L. Assessment of jojoba as a pure and nano-fluid base oil in minimum quantity lubrication (MQL) hard-turning of Ti–6Al–4V: A step towards sustainable machining. *Journal of Cleaner Production*, 2020, vol. 272. DOI: 10.1016/j.jclepro.2020.122553.

Conflicts of Interest

The authors declare no conflict of interest.

Obrabotka metallov -
Metal Working and Material Science

Journal homepage: http://journals.nstu.ru/obrabotka_metallov

Research and analysis of electrical discharge machining in the manufacture of products from heat-resistant alloys: a literature review

Evgeniy Shlykov [a, *], Timur Ablyaz [b], Vladimir Blokhin [c], Karim Muratov [d], Ilya Osinnikov [e]

Perm National Research Polytechnic University, 29 Komsomolsky prospekt, Perm, 614990, Russian Federation

[a] https://orcid.org/0000-0001-8076-0509, Kruspert@mail.ru; [b] http://orcid.org/0000-0001-6607-4692, lowrider11-13-11@mail.ru;
[c] https://orcid.org/0009-0009-2693-6580, warkk98@mail.ru; [d] http://orcid.org/0000-0001-7612-8025, Karimur_80@mail.ru;
[e] https://orcid.org/0009-0006-4478-3803, ilyuhaosinnikov@bk.ru

ARTICLE INFO

ABSTRACT

Introduction. In modern mechanical engineering, there is a growing trend toward the development and implementation of novel heat-resistant alloys with enhanced physical and mechanical properties. Electrical discharge machining (*EDM*) is a promising method for manufacturing products from these new-generation heat-resistant alloys. This paper presents an analysis of current research in the field of *EDM* of heat-resistant alloys. The primary focus is on analyzing output qualitative and quantitative indicators in relation to input parameters – machining mode and conditions. The key factors influencing the efficiency of *EDM* are considered, including machining parameters and the composition of the working fluid and electrode material. This analysis of current research is intended for specialists in the field of heat-resistant alloy machining, developers of *EDM* technologies, and researchers working to improve manufacturing methods for aircraft engine components. **The purpose of this work** is to conduct a literature review of existing research on modern methods for ensuring and improving the efficiency and quality of electrical discharge machining (*EDM*) of heat-resistant materials. **The methods of investigation** involved a theoretical analysis of current research on electrical discharge machining of heat-resistant alloys. **Results and discussion.** A literature analysis was conducted, and it revealed that current strength and pulse duration are the main technological parameters determining the quality of the processed surface and the material removal rate. The effectiveness of using modified working fluids (with graphene and carbon nanotubes) during heat-resistant material processing to improve surface quality was confirmed. It is of particular interest to conduct experimental studies on the influence of adding various material components to the working fluid to improve surface quality indicators after complex pulse electrical discharge machining (*CPEDM*) and to assess the impact of these alloying materials on the surface layer of heat-resistant materials.

Introduction

The key driver of modern industry is the active development and implementation of novel heat-resistant materials possessing a specific set of mechanical and physical-chemical properties. These characteristics ensure the retention of strength properties in structural components of equipment and machinery throughout their service life. Numerous research teams are dedicated to investigating the effects of various processing methods on the characteristics of heat-resistant alloys, which are critical for key industries such as aerospace engine manufacturing, power generation (including nuclear power), and the automotive industry. High resistance to corrosion and oxidation, enhanced ductility, heat resistance, mechanical strength, and excellent fatigue and creep resistance even at elevated temperatures – these properties make heat-resistant

---

* Corresponding author
Shlykov Evgeniy S., Ph.D. (Engineering), Associate Professor
Perm National Research Polytechnic University,
29 Komsomolsky prospekt,
614990, Perm, Russian Federation
Tel.: +7 961 759-88-49, **e-mail:** Kruspert@mail.ru

alloys superior to other classes of materials. Most heat-resistant alloys are primarily nickel-based. Due to their excellent high-temperature mechanical and chemical properties — including high heat resistance, thermal shock resistance, enhanced fatigue strength, high fracture toughness, phase stability, superior erosion and corrosion resistance, improved ductility and toughness, and high melting point — nickel-based alloys can operate for extended periods in aggressive service environments. Active research into heat-resistant materials stems from their strategic importance for critical technological development, the continuous demand for improved material characteristics, and the expansion of their application areas in modern industry. International research primarily focuses on the nickel-based superalloy *Inconel* [1–7] and its various grades, which differ in the type and concentration of alloying elements. The properties of heat-resistant materials are tailored by specific alloying elements:

– **Nickel**, as the primary base, contributes to the alloy's ductility, toughness, and heat capacity.

– **Molybdenum** and **tungsten** enhance creep resistance and high-temperature mechanical strength.

–**Vanadium**, typically in small quantities, improves overall high-temperature properties.

– **Niobium** prevents intergranular corrosion.

– **Titanium** enhances corrosion resistance.

– **Cobalt** increases relaxation resistance.

As reported in studies [8–15], nickel-based alloys are widely used in many critical components of aerospace engines and gas turbines, particularly in parts exposed to high temperatures, such as jet turbine blades, turbocharger vanes, and combustion chambers. Nickel-based alloys can account for approximately half of the total mass of aircraft engines. Beyond the aerospace sector, nickel-based alloys are also employed in nuclear reactors, food processing, shipbuilding, environmental protection facilities, and petrochemical industries, among others. Current research on heat-resistant alloys emphasizes compositions containing refractory transition metals (molybdenum, tungsten, tantalum, rhenium, and ruthenium). Promising domestic heat-resistant alloys include

– *VV751P* (*Cr*-56 %*Ni-Co-V-Mn-Ti-Al-B*);

– *ZhS6* (*Cr*-57% *Ni-V-Co-Al-Ti-Mn-B*),

– *KhN70Yu* (*Cr*-70% *Ni-Al*)

– *KhN60VT* (*Cr*-60% *Ni-V-Ti*),

– *KhN65VMTYu* (*Cr*-65% *Ni-V-Mn-Ti-Al*),

– *KhN55VMTKYu* (*Cr*-55% *Ni-V-Mn-Ti-Co-Al*),

– *KhN78T* (*Cr*-78% *Ni-Ti*),

– *EP741NP* (ХН51КВМТЮБ *Cr*-51% *Ni-Co-B-Mn-Ti-Al-B*),

– *EI698* (*Cr*-73% *Ni-Mn-B-Ti-Al*) [16–18].

The machining of heat-resistant alloys is complicated by several inherent properties, including low thermal conductivity, high melting points, significant work hardening effects, susceptibility to burr formation, the generation of high cutting forces, chemical affinity with tool materials, and the presence of abrasive carbide particles in their microstructure. These properties are exacerbated by elevated temperatures during machining, which significantly increase the load on the cutting edge, intensify tool wear, and necessitate wear compensation in the machine's control program. Furthermore, plastic deformation of these materials is challenging due to their austenitic face-centered cubic (*FCC*) crystal structure, which exhibits low yield strength despite possessing high ultimate tensile strength. Their inherent abrasiveness, often intensified by the presence of hard carbide inclusions and other abrasive particles, leads to severe tool wear and significantly reduced tool life. Heat-resistant alloys are classified as difficult-to-machine materials. The combination of these issues severely limits the achievable precision and overall efficiency in the machining of such alloys [19–24].

Electrical discharge machining (*EDM*) has emerged as a promising method for processing heat-resistant materials, drawing significant interest from scientific communities. This paper presents a review of scientific literature focused on the electrical discharge machining (*EDM*) process of heat-resistant alloys.

The purpose of this work is to conduct a literature review of existing research on modern methods for ensuring and improving the efficiency and quality of electrical discharge machining (*EDM*) of heat-resistant materials.

To achieve this purpose, the following research ***tasks*** were undertaken:

– Classification of key *EDM* process parameters and modern methods for their optimization;

– Determination of the advantages, disadvantages, and limitations of these modern methods for enhancing the efficiency and quality of electrical discharge machining of heat-resistant materials;

– Identification of current development trends for these methods.

Research methodology

A comprehensive literature review has been conducted on research in the field of electrical discharge machining (*EDM*) of heat-resistant materials, focusing on methods for ensuring surface integrity and improving *EDM* efficiency. Various methods for increasing *EDM* efficiency and enhancing surface integrity are described, along with their limitations, advantages, and disadvantages. The main trends in the development of modern methods for ensuring and improving *EDM* efficiency during the machining of heat-resistant alloys are identified.

Results and Discussion

The main advantages of *EDM* are presented in Fig. 1.
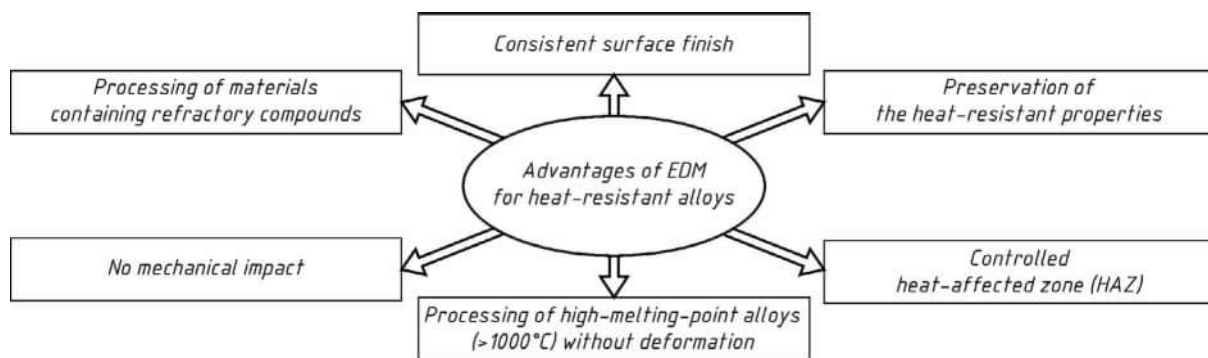
Fig. 1. Advantages of the *EDM* process

Table presents an analysis of research trends focusing on the output parameters of wire electrical discharge machining (*WEDM*) and copy-piercing electrical discharge machining (*EDM*) of heat-resistant alloys. *EDM* of heat-resistant materials often results in crack formation on the machined surfaces and the transfer of particles from the tool electrode and working fluid to the surface, thereby altering the characteristics of the surface layer. This redeposition of tool electrode particles and working fluid degradation products compromises the operational properties of the machined products. This is attributed to the non-uniform surface microstructure (including microcracks and other surface defects) and the softening of the surface layer.

Consequently, a critical review of modern solutions for ensuring surface integrity and preserving operational properties during electrical discharge machining of heat-resistant alloys is a crucial undertaking.

The main research trends concerning the *EDM* process of heat-resistant alloys are presented in Fig. 2.

A literature review on modern *EDM* studies revealed that authors' attention is primarily focused on investigating the influence of parameters such as current in the interelectrode gap (*IEG*), the duration of the electrical pulses (t_{on}), voltage (***U***), polarity, tool electrode material, tool electrode geometry, the size of the machined surface, as well as the working fluid characteristics (e.g., type, purity, feed rate, filtration system). These parameters are studied for their impact on processing quality indicators, specifically surface roughness and the modified surface layer (recast layer).

Directions of scientific papers studying the *WEDM* and *EDM* processes of heat-resistant alloys

No.	Variation parameters	Output parameters	Paper number
1	T_{on}, T_{off}, h, Working fluid	Surface roughness	25–41
2	T_{on}, I, P	Wear coefficient	32, 42–47
3	T_{on}, T_{off}, h	Cutting width for *WEDM*	48–51
4	T_{on}, T_{off}, I, U Polarity	Size of defective (white) layer	32, 39–40, 54–60
5	*ET* Material, I, T_{on}	Quality indicators (presence of cracks)	39, 43–45, 57, 69
6	Flushing of *IEG*	Surface roughness, precision of *EDM* processing, productivity	75–77

- Surface roughness
- Processing accuracy
- Wear of ET
- Modified defective (white) layer
- Surface alloying with an electrode tool
- Effect of flushing
- Influence of the working environment
- Surface quality (presence of depressions, cracks)
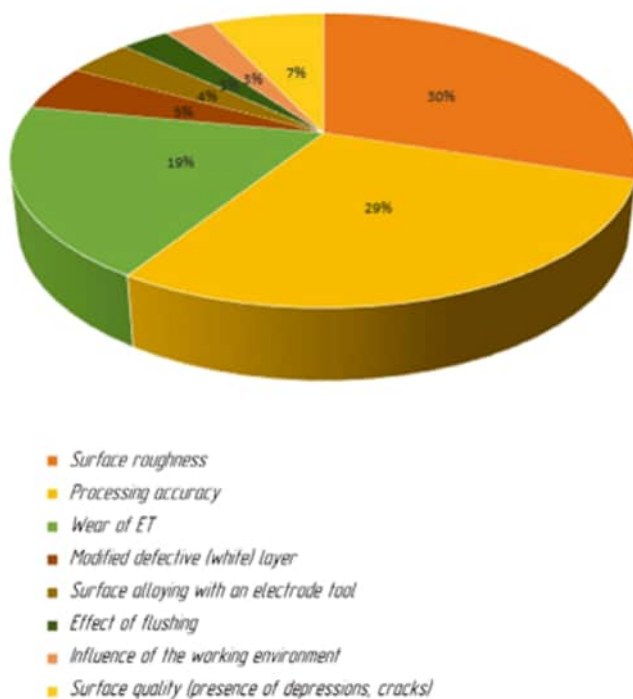
Fig. 2. Main trends in scientific research of the *EDM* process of heat-resistant alloys

Surface quality indicator after EDM: roughness (Ra)

The studies of the *WEDM* process in [25–31] investigated the processing of *Inconel 625* using an orthogonal experimental design, where various processing parameters were selected: current (I), pulse-on time (t_{on}), and pulse-off time (t_{off}). Response models were developed, and the authors found that the greatest influence on surface quality, specifically Ra roughness, is exerted by parameters such as pulse-on time (t_{on}) and current (I). In [25, 29], it was noted that a low discharge current contributes to the formation of a smoother machined surface, which is attributed to a more accurately controlled process of single discharge formation. Furthermore, adjusting the pulse-on time with a correctly selected mode promotes uniform melting of the material on the workpiece surface, evaporation, and removal from the processing zone, which has a favorable effect on surface finish. In all studies, the best roughness values were obtained with a pulse-on time of 100 to 110 μs, while the current was 7–9 A.

In [32], it was noted that to ensure the required surface roughness with minimal tool electrode wear in the *EDM* process, it is necessary to use minimal peak current and the shortest pulse duration. The authors found that the pulse duration had an insignificant effect on the surface roughness.

In [33–37], the authors investigated the influence of the input parameters of the *EDM* process on process productivity and surface roughness (*Ra*). Factorial experiments were conducted, and response functions were obtained, which showed that the pulse current had a greater influence on these parameters. With an increase in the current, process productivity increased, while the surface quality deteriorated compared to lower current settings.

In [38], experiments were conducted using the *Taguchi-Gray* analysis method for the *WEDM* of *Inconel 825*. The experiments showed that the pulse-on time and spark gap voltage had the greatest effect on surface roughness. It was found that the optimal parameters for *Inconel* processing were: pulse-on time of 105 μs, pulse-off time of 40 μs, and spark gap voltage of 30 V.

In [39], the authors investigated the effect of inclusions in the working fluid on surface roughness (*Ra*). The inclusions used were graphene and multi-walled carbon nanotubes. The studies were carried out in a

single processing mode at a pulse-on time of 35 μs, a current of 12 A, and a voltage of 40 V. The paper shows that with the addition of nanocarbon particles to the dielectric fluid, a smoother surface finish was achieved (Ra = 4.836 μm with the addition of graphene and Ra = 4.96 μm with the addition of carbon nanotubes) compared to conventional dielectric fluid (Ra = 6.2 μm). A comparative analysis of the results allows us to conclude that it is necessary to use a modified working fluid to improve the surface quality.

In [40], the authors conducted a study of the influence of the working fluid on the quality and topography of the surface (Fig. 3).
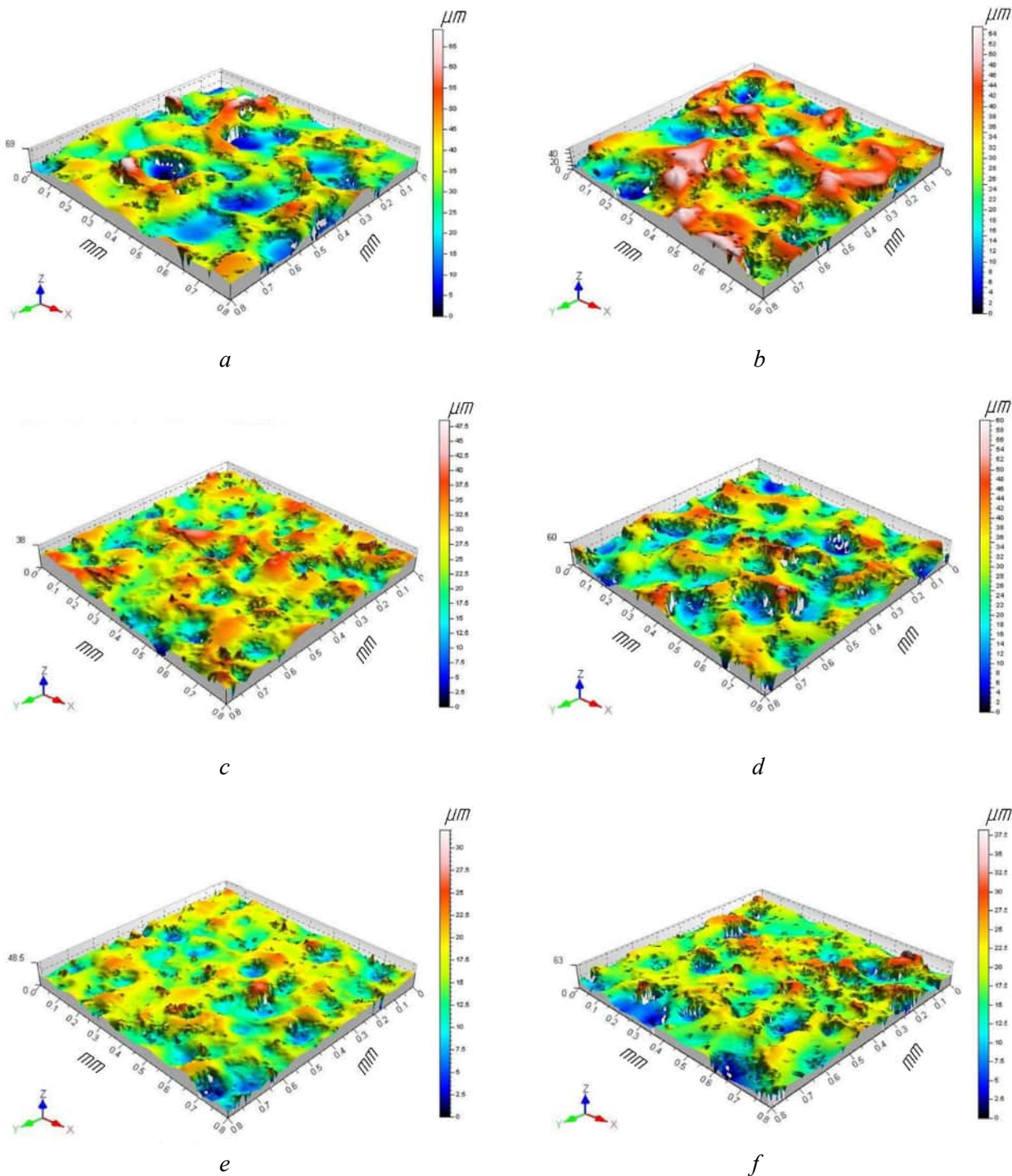
Fig. 3. Surface topography after *EDM* of *AlSi 1045* steel using deionized water as a dielectric (*a, c, e*):

a) at a current of 9 A and a pulse on-time of 100 μs, *c)* at a current of 3 A and a pulse on-time of 100 μs, *e)* at a current of 6 A and a pulse on-time of 100 μs; and using kerosene as a dielectric (*b, d, f*): *b)* at a current of 6 A and a pulse on-time of 100 μs, *d)* at a current of 9 A and a pulse on-time of 100 μs; *f)* at a current of 3 A and a pulse on-time of 100 μs [40]

The authors noted that current has the greatest impact on the formation of the surface characteristics and the incidence of surface defects. A direct correlation was observed: an increase in current resulted in a deterioration of all surface quality indicators. To achieve a smoother surface finish, minimum values of current and pulse duration should be employed.

In [41], the effect of processing parameters on surface roughness (Ra) was investigated. It was noted that an increase in pulse duration, peak current, and voltage led to increased roughness. After optimizing the processing parameters (pulse-on time: 0.5 μs, pulse-off time: 16 μs, current: 6 A) based on experimental results, the authors were able to reduce the surface roughness from 4.2 μm (Fig. 4, *a*) to 0.396 μm (Fig. 4, *d*).

a

b

c

d

e
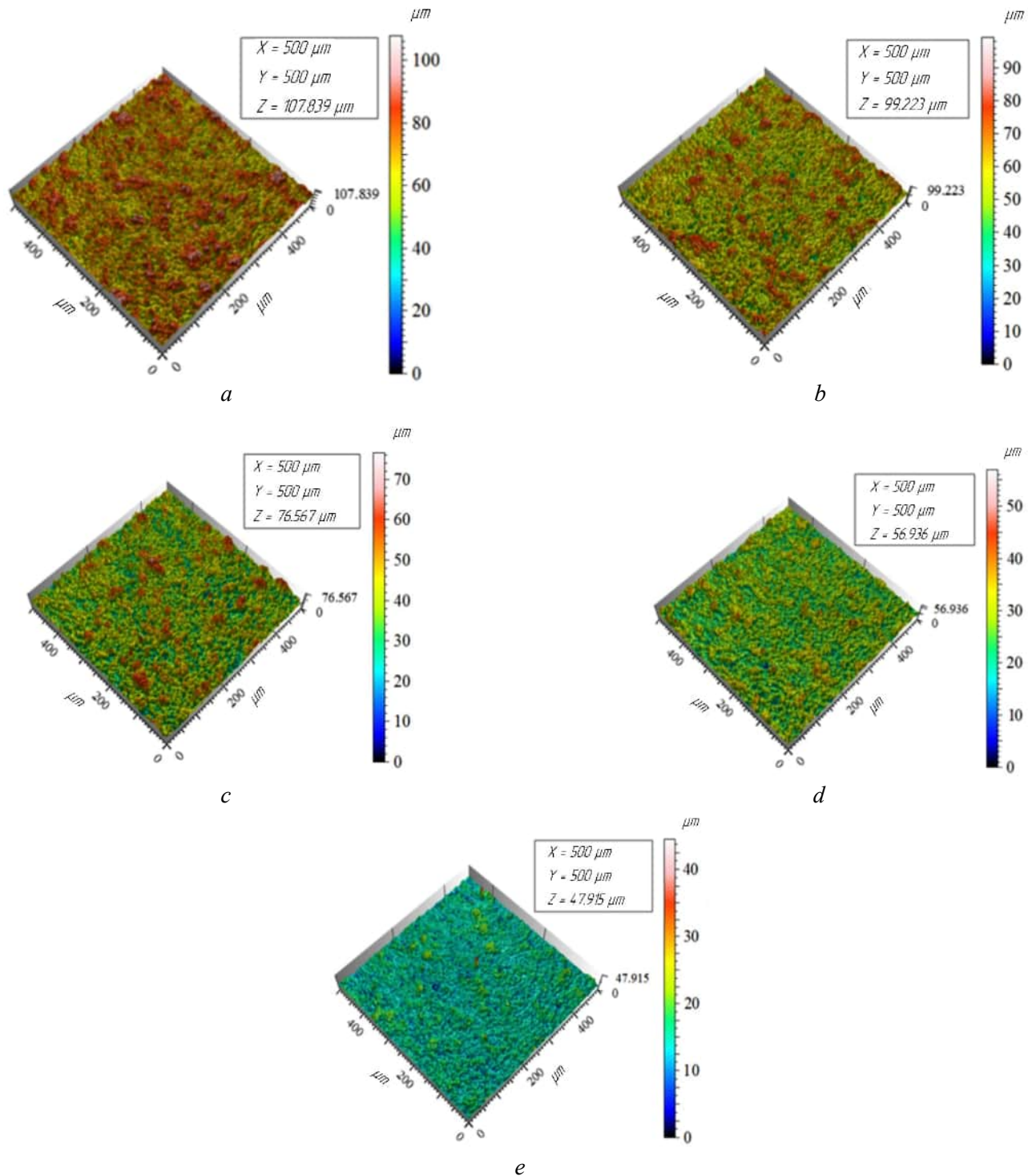
Fig. 4. Surface topography after *WEDM* of *Inconel 718* using:

a) T_{on} = 12 μs, T_{off} = 0.5 μs, I = 12 A; *b)* T_{on} = 12 μs, T_{off} = 7.5 μs, I = 15 A; c) T_{on} = 4.5 μs, T_{off} = 7.5 μs, I = 10 A; *d)* T_{on} = 2 μs, T_{off} = 7.5 μs, I = 8 A; *e)* T_{on} = 0.5 μs, T_{off} = 16 μs, I = 6 A [41]

The authors note that the improvement in roughness occurs primarily due to a significant difference between the pulse-on and pulse-off times. It is noted that, compared to other material groups, the machining of heat-resistant materials requires more careful adjustment of processing parameters due to alloying elements and a higher tendency to form intermetallic phases. When machining heat-resistant materials, a lower single pulse energy is employed than when machining other material groups (steels and stainless steels) to achieve low roughness.

EDM process performance

In [42], an experiment was conducted on the material removal rate during *EDM*. The experiments were conducted using three tool electrode materials: copper, graphite, and aluminum. It was found that the graphite electrode demonstrated the highest material removal rate (*MRR*), followed by copper and aluminum electrodes. The graphite electrode also exhibited the lowest wear rate, which is attributed to its high melting point, while the aluminum electrode yielded the best roughness in the experiments. It was noted that when processing heat-resistant materials, non-uniformity of tool electrode wear occurs. This is due to the non-uniform composition of heat-resistant materials and the presence of refractory material inclusions (tungsten, molybdenum), which lead to varying erosion resistance in the machined surface areas. Areas with molybdenum and tungsten are characterized by increased melting thresholds and different thermal conductivity compared to other areas. In contrast, when processing materials from other material groups, such as steel or stainless steel, uniform tool electrode wear and material removal are characteristic, attributed to the homogeneity of the processed material areas.

In [32], it is noted that to achieve minimal tool electrode consumption in the *EDM* process, the lowest peak current and the shortest pulse duration should be employed. In [43], it is noted that the main parameter affecting *EDM* quality is the current, which determines the material removal rate, while the pulse duration is a key indicator primarily influencing tool electrode wear. Studies have shown that an increase in the discharge current of a single pulse leads to a stronger spark and the melting of a larger amount of material per single pulse.

In [44], the authors investigated the effect of inclusions in the working fluid on process productivity. The inclusions used were graphene and multi-walled carbon nanotubes. It was observed that the addition of nanocarbon particles slowed the material removal rate from the workpiece by an average of 15–17%. This effect is associated with an increase in liquid viscosity and a deterioration in sludge removal from the processing zone.

A comparison of the effect of the environment using oil and high-carbon liquid as the working fluid is presented in [45]. The results demonstrated a significant increase in discharge energy density, leading to intensified material removal from the workpiece surface.

The tool electrode material plays an important role in *EDM* process productivity. The main tool electrode materials are presented in Fig. 5.

Recent studies have been conducted on the effect of the tool electrode material on process productivity in [46–47]. It has been established that the copper electrode exhibits a higher material removal rate (up to 10.7 mm³/min) and the lowest tool electrode wear (13–14%). Copper electrodes are used for finishing passes when processing heat-resistant alloys, ensuring high quality of the machined surface with minimal formation of surface defects. Copper tool electrodes
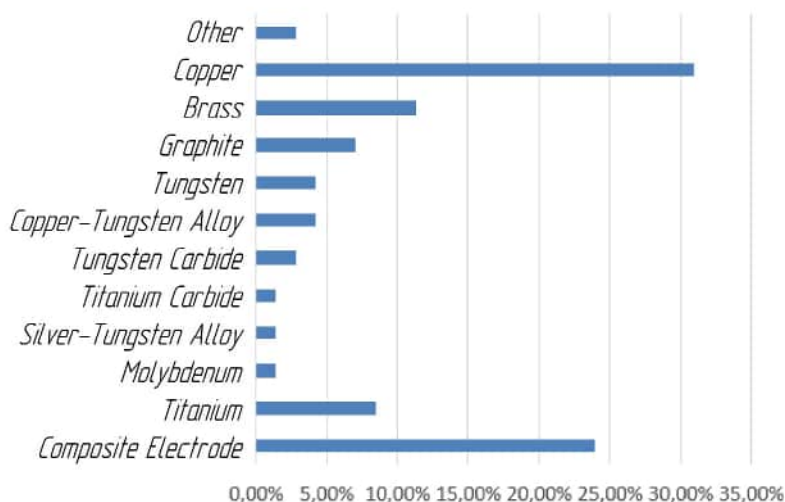
Fig. 5. Types of tool electrode materials used in the *EDM* process

are characterized by high electrical conductivity, which ensures effective electrical current flow, and excellent thermal conductivity, which facilitates rapid heat removal from the processing zone, especially when machining areas containing refractory materials.

Accuracy of the EDM process

In the case of *WEDM* of heat-resistant alloys, one of the key accuracy parameters is the interelectrode gap (*IEG*). The stability of the *WEDM* process depends on the *IEG* value – an increase in the gap leads to uneven pulse energy distribution, resulting in process instability and deviations in geometric dimensions [48].

Fig. 6 shows the results of studies on the cutting width of heat-resistant materials [49–51].

a

b

c

d
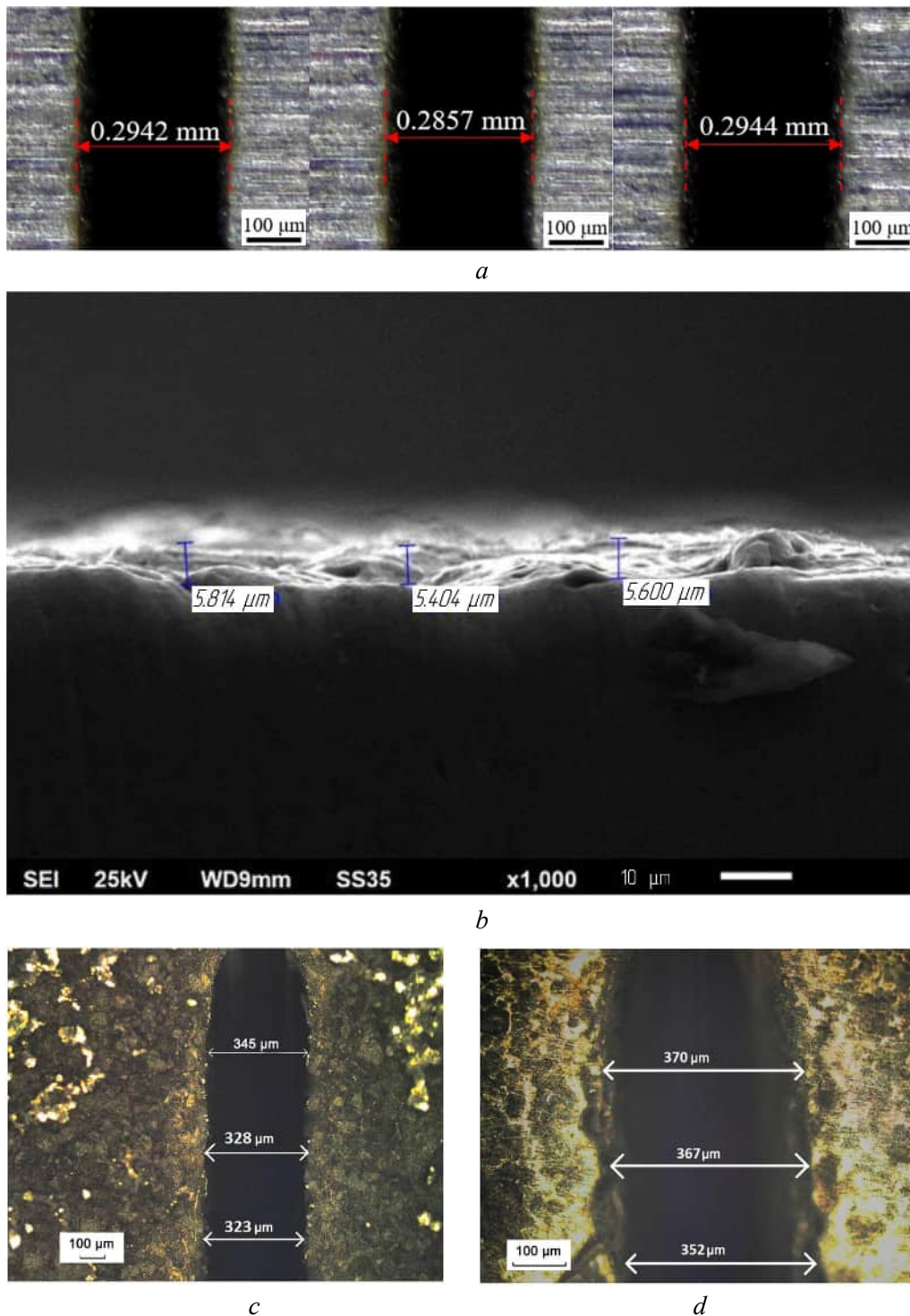
Fig. 6. Investigation of the cutting width in *WEDM*:

a) Inconel 718 [49]; *b) Inconel 617* [50]; *c) VV751P* [51]

The authors of [49–51] investigated the effect of processing parameters—current (I), pulse-on time (t_{on}), and pulse-off time (t_{off}) — on the cutting width and the interelectrode gap (IEG) size in $WEDM$, using a 0.25 mm diameter wire as the tool electrode. The developed empirical models indicate that with an increase in current and pulse-on time, single discharge intensity increases, leading to more intense material melting. In [49], the smallest cutting width was obtained at the highest processing power. The authors note that this is attributed to the fact that at higher power, the tool electrode melts the material faster and traverses the machining path more quickly, thereby transferring less thermal energy to the workpiece. The results obtained from these studies enable rationalization of processing parameters and control of the cutting width with minimal thermal impact on the workpiece, thereby minimizing surface defects. A comparative analysis of the results from three independent studies suggests that the results are consistent and demonstrate a high degree of reproducibility under identical electrical discharge machining conditions. The consistency of the output parameter – the cutting width – when machining various heat-resistant materials indicates that the machining parameters are universally applicable to heat-resistant materials, allowing their use for a wide range of such alloys.

Deformed (white) layer

It has been established that during electrical discharge machining (EDM), when removing material in the spark gap between the tool electrode and the workpiece, part of the material is flushed away by the working fluid, while the remaining molten metal re-solidifies and hardens in the presence of a dielectric fluid. This re-solidified material forms the recast layer, often referred to as the white layer. The white layer typically possesses a fine-grained, hard, and brittle microstructure due to local thermal action. As the cooling rate from the surface into the bulk material is very high, a steep thermal gradient is created, influencing the microstructure of this layer. Residual stresses, inherent to the EDM process, often lead to the formation of voids and microcracks, which adversely affect the product's operational properties. This layer must be minimized by careful selection of processing parameters due to the presence of voids, micropores, and surface microcracks that can extend deep into the base material. Each material exhibits unique characteristics of white layer formation, which are associated with its operational properties and chemical composition [52–53].

It is noted that there are few studies by research teams investigating the formation and influence of the altered (white) layer during the processing of heat-resistant alloys. This is primarily attributed to the complexity of studying and obtaining high-quality samples for research, as the layer's formation results from intricate and often difficult-to-predict thermal processes. Furthermore, the authors [32, 54] note that the formation of a recast (white) layer on the surface of heat-resistant alloys is affected by numerous factors, including the processing mode, the workpiece material, and the working fluid parameters, which complicates the research process. The authors of these works note that when a white layer forms on heat-resistant materials after processing, a more intense formation of a deformed layer with greater depth is characteristic compared to processing other material groups (e.g., steel or stainless steel). This is attributed to the high heat resistance of the material and its thermal properties. The uneven distribution of the white layer is due to the complex nature of heat-resistant materials, characterized by heterogeneity of both their chemical composition and structural components.

In [55], the authors found that the size of the recast (white) layer during $WEDM$ is affected by the processing parameters, namely, the current at constant voltage and the pulse duration. It is noted that when using minimum parameter settings, the size of the white layer is stable and continuous, which is important for post-processing and product operation. In [54], the authors drew attention to the influence of not only the duty cycle but also the polarity on the consistency of the resulting modified layer. It is noted that when using direct polarity, the modified layer is more stable, and the machined surface exhibits a smooth and uniform structure, in contrast to reverse polarity, which is characterized by cracks and craters on the machined surface.

Fig. 7 shows the results of studies by the authors [56–59] on the modified layer during $WEDM$ of various heat-resistant materials.
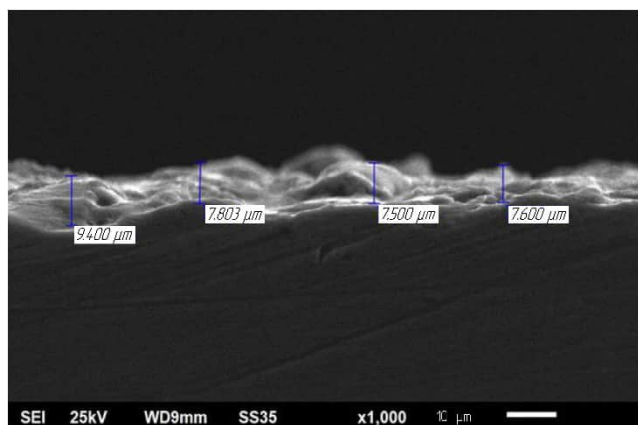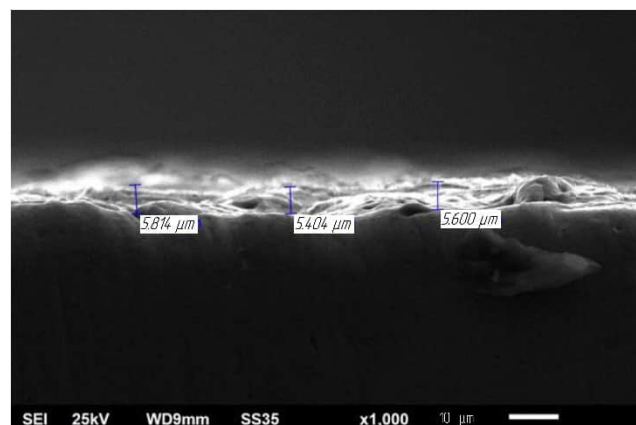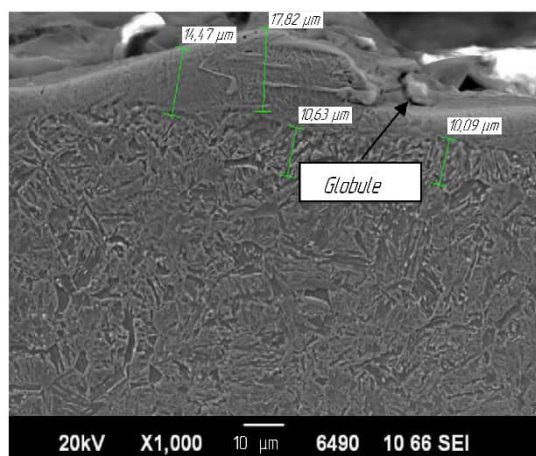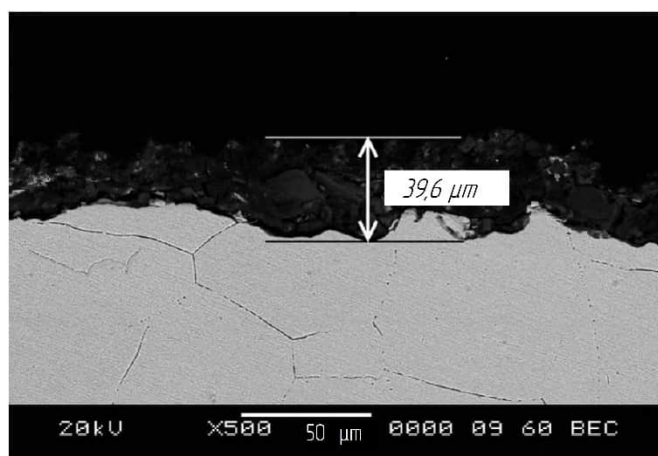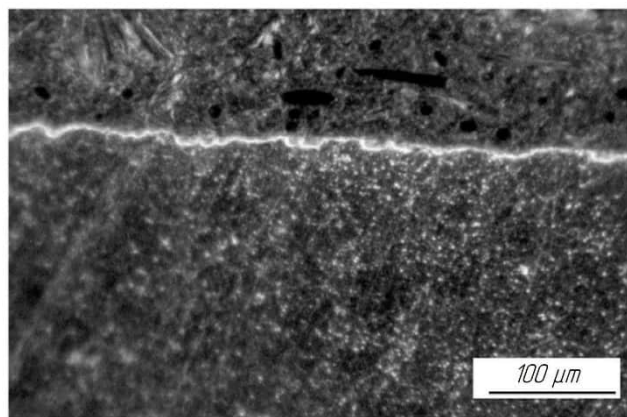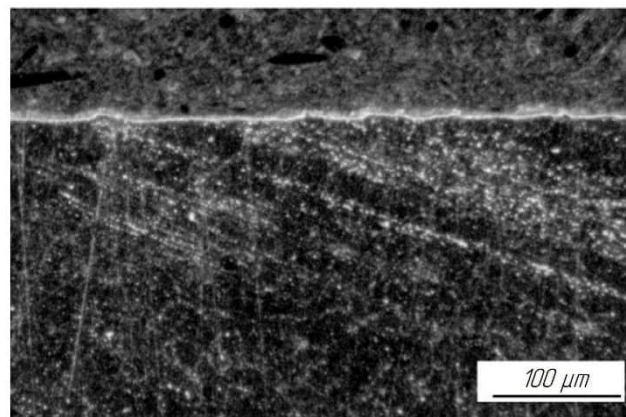
Fig. 7. Modifications of the (white) layer on different materials:

a) Monel 400 (a nickel-copper alloy) [57]; *b) Monel 400* with aluminum powder added to the working fluid [57]; *c)* high-strength low-alloy steel [56]; *d) Inconel 706* [58]; *e) VV751P* at minimum mode [59]; *f) VV751P* at maximum mode [59]

The authors of [56] conducted a factorial experiment on the recast (white) layer and found (Fig. 7, *c*) that under a specific processing mode with a pulse-on time of 96 μs, the layer thickness was unevenly formed, measuring 14–17 μm. This was attributed to unstable interelectrode gap conditions and current instability. They also suggested that this layer is formed by molten material not fully removed from the *IEG* zone during processing. In [57], a study investigated the effect of adding aluminum powder to the working fluid on the formation of a recast (white) layer. It was found that the thickness of the white layer using distilled water ranged from 7 to 9 μm (Fig. 7, *a*), and the addition of aluminum powder to the working fluid had a positive effect, reducing the layer thickness to 5 μm.

In [58], it was established that during WEDM processing of the material, the thickness of the modified layer was 39.6 μm (Fig. 7, *g*), attributed to the high energy of single pulses in the selected mode. The large thickness of the modified layer led to the formation of numerous microvoids and microcracks and resulted in lower hardness due to thermal alteration of this layer. In [59], studies investigated the influence of *WEDM* parameters, namely the current intensity and pulse timing, on the formation of the modified layer. It was established that the size of the modified layer was consistently about 10 μm over the entire area (Figs. 7, *d* and 7, *e*). In [58, 59], residual stresses in the modified layer were studied. It was established that tensile stresses were observed during the processing of *Inconel 706*, as well as *VV751P*. Residual stresses arise due to significant local thermal impact and can lead to a decrease in the hardness of the surface layer. The relationship between residual tensile stresses and microhardness is discussed in [60].

In [39], the authors investigated the influence of inclusions in the working fluid on the formation of a recast (white) layer. The inclusions used were graphene and multi-walled carbon nanotubes. The authors found that when using graphene during the processing of Inconel 825, the thickness of the modified layer was 21.5 μm, and when using multi-walled carbon nanotubes, the layer thickness was 29.5 μm, which is significantly less than that obtained with conventional processing (42.21 μm). The observed difference in recast layer formation may be attributed to an increased thermal energy transfer rate due to the improved dielectric medium. It is the presence of conductive nanocarbon particles in the dielectric medium that acts as an additional discharge channel, facilitating heat dissipation.

In [40], the authors conducted a study of the influence of the working fluid on the formation of the recast (white) layer. Deionized water was found to be the most effective dielectric, attributed to its lower viscosity and density, which favorably impact multiple discharges in the interelectrode gap and reduce the altered (recast) layer thickness (Fig. 8). This effect is most noticeable when using the maximum power mode (at a current of 9 A): in deionized water, the altered layer thickness was 16 μm, compared to 18 μm in kerosene. The altered layer structure obtained with deionized water was also noted to be smoother, lacking sharp phase transitions, whereas in kerosene, individual areas of uneven recast layer distribution were observed. In conclusion, it is worth noting that although kerosene is a common commercial dielectric, the use of deionized water has a favorable effect on surface quality.

In [61], the authors conducted experimental studies to analyze the role of the thermal conductivity of the workpiece material in the electrical discharge machining process. The workpieces used were aluminum, brass, and *Inconel 617*. Under the same machining conditions, a comparatively thicker recast (white) layer (16 μm–17.4 μm) was formed on aluminum than on brass (6.4 μm–8.5 μm), while the thinnest recast layer was formed on Inconel 617 (1.5 μm–2.1 μm). This phenomenon can be attributed to the fact that materials with lower thermal conductivity struggle to dissipate the heat generated during electrical discharge machining. This results in a localized temperature increase, which in turn contributes to the formation of thinner layers, as the heat becomes concentrated over a smaller area.

Surface quality: cracks and depressions

In [43], it was observed that an increase in the discharge current of a single pulse leads to an intensification of crack formation on the surface of samples and an increase in the thickness of the recast (white) layer.

A modern and promising method for improving surface quality and significantly increasing the productivity of the electrical discharge machining process is powder electrical discharge machining (*PEDM*). The essence of this technology is that fine particles (metal powders, carbon allotropes) are added to the working fluid. Fine particles dispersed in the liquid form conductive chains within the fluid, thereby enhancing the electrical breakdown efficiency. This enhanced breakdown efficiency leads to an increase in the material removal rate (*MRR*) from the tool-electrode (*TE*) surface. The authors of [62–63] found that, upon applying an appropriate voltage, an electric field is created that induces positive and negative charges on the powder particles. These charged particles migrate rapidly in a zigzag pattern, effectively bridging the inter-electrode gap and enhancing the localized electric field strength. This enhanced localized electric field strength, resulting from the reduced effective gap, facilitates efficient inter-electrode breakdown. When the

Fig. 8. Modified layer after *EDM* of *AlSi 1045 steel* using deionized water as a dielectric:
a) at a current of 9 A and a pulse on-time of 100 µs; *b)* at a current of 6 A and a pulse on-time of 100 µs; *c)* at a current of 3 A and a pulse on-time of 100 µs using air; *d)* at a current of 9 A and a pulse on-time of 100 µs; *e)* at a current of 6 A and a pulse on-time of 100 µs; *f)* at a current of 3 A and a pulse on-time of 100 µs [40]

critical breakdown voltage is reached in the region of minimum inter-electrode gap, an electrical discharge occurs, which leads to material removal from the workpiece.

In [64], the author investigated the effect of adding aluminum, chromium, and copper powders to the dielectric fluid on the material removal rate (*MRR*) and tool wear rate during electrical discharge machining. The authors concluded that the particle concentration, particle size, particle density, electrical resistance, and thermal conductivity of the powders play an important role in improving the efficiency of electrical

discharge machining. Proper selection of powder type and concentration can lead to an increased material removal rate and reduced tool wear. Based on the results of the research, the authors concluded that powder with a small particle size can improve both the material removal rate (*MRR*) and the surface quality. However, with a small particle size, a relatively thick recast (white) layer was found, while the thickness of the recast layer decreased as particle size increased. Additionally, silicon powder-mixed electrical discharge machining was employed, with varying powder concentration and flushing rate. It was concluded that the use of a silicon powder-mixed dielectric can significantly improve the surface morphology in terms of reducing the size of craters, obtaining a thin recast layer, and an excellent surface finish. The authors also emphasized that the powder concentration and flushing rate must be carefully selected to improve machining efficiency and surface quality. This is attributed to the significant impact of the working fluid's rheological properties on flushing efficiency in electrical discharge machining. Different types of particles have different effects on the viscosity of the fluid, which, in turn, influences the optimal flushing parameters.

For example, tungsten powder when mixed with the dielectric fluid provides an increased material removal rate and reduces tool electrode wear [65]. Silicon carbide powder dispersed in the dielectric fluid improves surface finish [66] and increases the recast (white) layer thickness [67]. The authors of [68] investigated the inclusion of silicon and chromium powder in the working fluid. The results indicate a significant improvement in the material removal rate and a reduction in tool electrode wear rate. Chromium exhibits high wear resistance and resistance to abrasion, thereby promoting high-quality surface treatment. Its high temperature resistance makes it an ideal candidate for inclusion in the working fluid. Chromium powder mixed with a dielectric fluid improves the material removal rate, reduces tool wear, and the electrode wear ratio.

In [57], the authors noted the positive effect of aluminum powder inclusions on surface morphology, leading to a smoother surface texture with fewer craters and cracks. They explained that cracks are formed due to cavitation shocks that occur when the vapor-gas bubble collapses. These shocks are attributed to significant thermal differences (at the discharge zone, the temperature reaches 10,000 °C, while the working fluid temperature is 20 °C) [43–45].

In [39], the authors investigated the effect of inclusions in the working fluid on surface quality. The inclusions used were graphene and multi-walled carbon nanotubes. They noted that the use of these materials in the working fluid reduces crack formation during processing by 20–25%.

For example, in [57], the authors provide an explanation for the reduction in crack density when adding carbon nanoparticles to the dielectric fluid. According to their research, the addition of microsilicon containing carbon nanopowders improves the thermal conductivity of the dielectric medium, which enhances the rate of heat transfer within the dielectric medium and facilitates heat removal from the *IEG* zone. Consequently, the improved heat transfer rate reduces the energy density in the channel of a single discharge, thereby reducing the crack density on the surface of the samples. Based on this analysis, it is evident that the use of conductive nanoparticles is promising for this industry and requires additional attention from research teams.

The features of the processed surface were investigated by scanning electron microscopy in [69]. It was found that samples processed in a dielectric fluid with added titanium powder had fewer cracks, depressions, and micro-holes, as well as less deposition of material from the working fluid and electrode, compared to samples treated in a medium with added graphite powder. However, this study did not include a comparison with an oil-based dielectric medium. Hydrocarbon-based dielectric fluid is recognized as the most suitable for high-energy single discharges. However, it was also found that the density of defects (cracks and micro-holes) increased with increasing discharge energy. The thickness of the recast layer also increased with increasing fluid viscosity due to inefficient removal of debris from the interelectrode gap zone, which led to re-solidification of the material in the processing zone.

In [70], a study was conducted on the effect of Al_2O_3 inclusions in the working fluid during *EDM* of *Inconel 825* alloy. The surface characteristics were compared between treatment with Al_2O_3 inclusions in the working fluid and processing in a pure working fluid. The authors note that during conventional *EDM* (i.e., with pure working fluid), many micro-holes, micro-cracks, and material redeposition are concentrated

on the surface, which arise due to uncontrolled deposition of material from the working fluid. In contrast, when Al_2O_3 was added to the working fluid during processing, these defects were largely absent.

In [40], the authors conducted a study of the effect of pulse duration and the type of working fluid on crack formation during machining. They noted that an increase in pulse duration intensifies microcrack formation. This is attributed to the fact that a longer pulse duration leads to an increased energy input into the single discharge zone, which, in turn, raises localized temperatures and the temperature gradient on the processed surface, consequently increasing crack density.

When using kerosene as a working fluid, a greater number of cracks were observed on the surface. Deionized water, due to its distinct discharge characteristics (e.g., more frequent but lower energy discharges), generates lower spark power and discharge energy. Accordingly, lower spark intensity and a reduced temperature gradient on the processed surface result in a lower probability of microcrack formation when machining with deionized water. Another reason for the higher crack density on the processed surface when using kerosene is the difference in thermal conductivity between the two dielectric types, which affects the cooling rate in the discharge zone. The high cooling rate of deionized water effectively dissipates heat from the molten material and limits microcrack formation.

Moreover, during the *EDM* process with kerosene as a dielectric, carbonization leads to carbon residues adhering to the electrode surface, which eventually results in carbide formation on the workpiece surface. This condition results in unstable machining in the discharge zone, accompanied by increased impulsive forces, which, in turn, leads to a greater tendency for crack propagation during machining with kerosene.

In [71], the authors conducted a comprehensive study of the effect of machining parameters and the addition of carbon nanotubes to the working fluid on crack formation during the machining of Inconel-718 alloy. The machining was carried out at a current of 2 to 8 A. They found that with an increase in the peak current up to 6 A, the density of surface cracks tended to increase. However, with a current ranging from 6 to 8 A, the density of cracks on the processed surface decreased sharply (fig. 9).

This phenomenon may be due to the fact that an increasing peak current removes protruding material particles from the processed surface. However, a further increase in current leads to an intensification of single-pulse discharges and a larger volume of material removal, which, in turn, reduces the flushing efficiency of the dielectric liquid in the interelectrode gap. Upon the termination of discharges, when the electrode retracts to clean the interelectrode gap, due to the large temperature difference, unremoved particles remaining on the surface re-solidify, forming a secondary layer. Subsequently, the machining process is repeated, and the molten material can potentially fill these pores and cracks. Thus, it becomes difficult to assess and detect the presence of surface cracks.

Most studies are aimed at investigating the processed surface with the addition of inclusions, but the issue of the effect of the added powder on the properties of the working medium and the relationship between the change in dielectric properties due to the addition of powder has not been fully studied, as emphasized by the authors of [72]. They compared the addition of a conductive micropowder (graphite) and a non-conductive micropowder (aluminum oxide) to the working fluid (*WF*). The dielectric breakdown voltage values measured for kerosene, a mixture of kerosene with graphite powder, and a mixture of kerosene with aluminum oxide powder were 1,521.74 V, 26 V, and 1,652.17 V, respectively. It was found that the dielectric breakdown voltage is minimal in the presence of graphite powder and maximal in the presence of aluminum oxide powder.

This may be due to the fact that graphite powders possess electrical conductivity, and therefore, when graphite powder is added to a dielectric, its insulating capacity decreases, consequently reducing the dielectric breakdown voltage. Since aluminum oxide powder is not electrically conductive, its addition to a dielectric can increase the dielectric breakdown voltage even more than in the uncontaminated state of the dielectric. It was concluded that the choice of powder additives requires a careful approach, considering not only their effect on the processed surface but also their impact on the dielectric properties of the working medium.

Inclusions in the surface layer after machining

One of the parameters that are difficult to predict is the surface alloying of heat-resistant alloys with tool electrode material particles. This difficulty arises from the fact that it is extremely difficult to develop
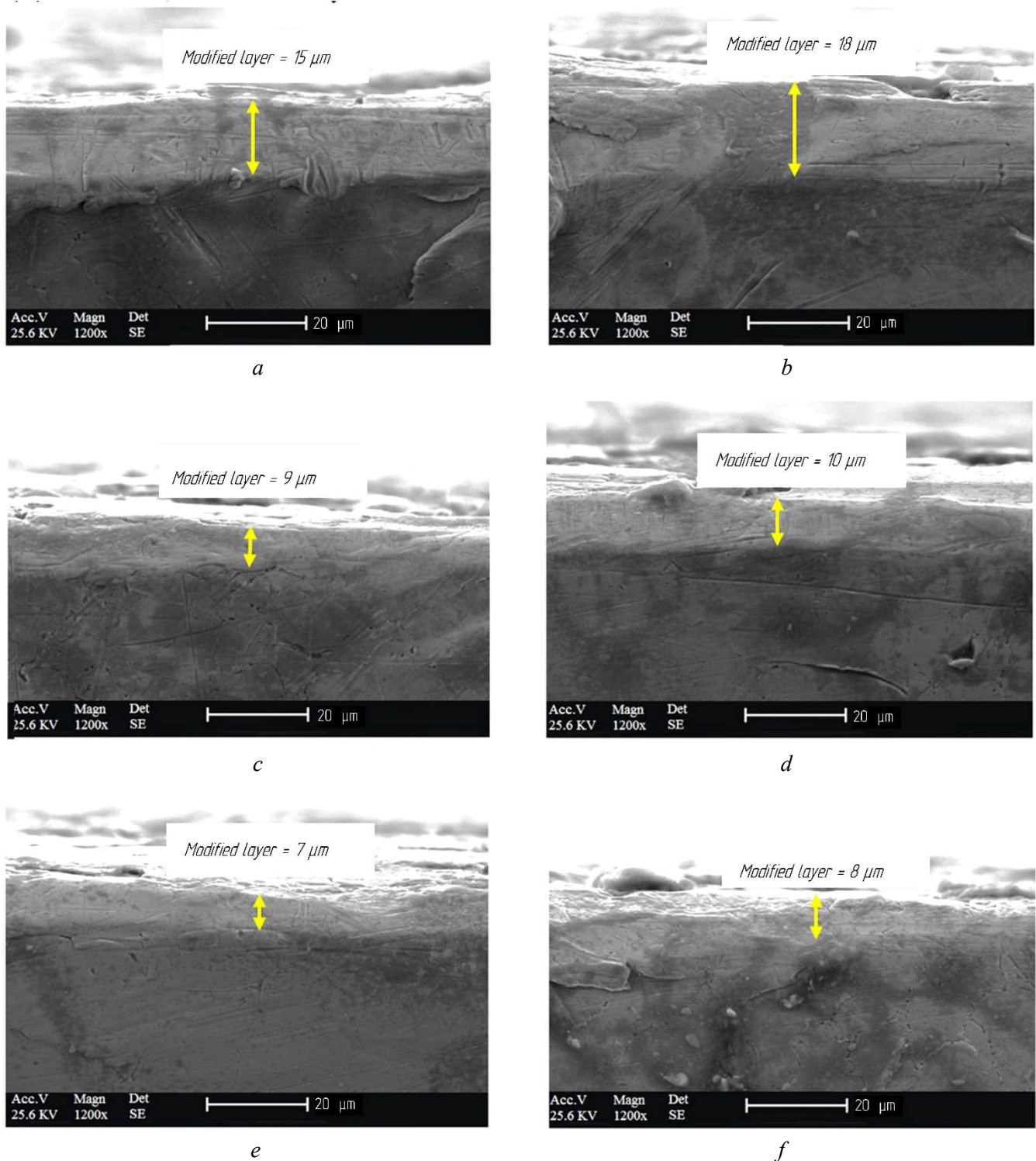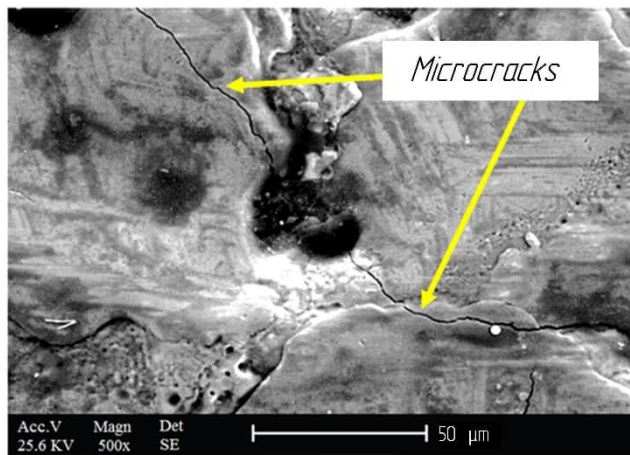
a
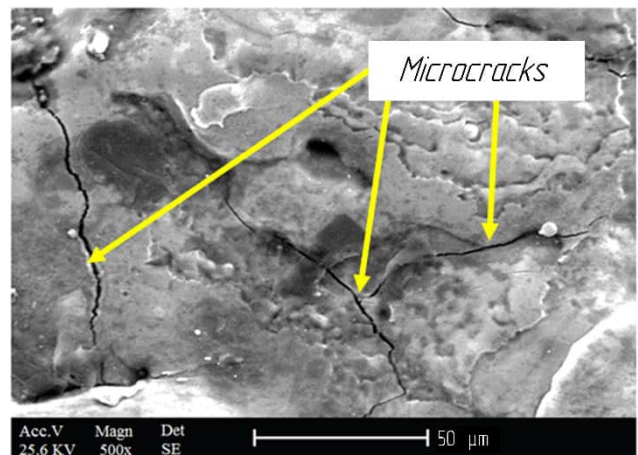
b
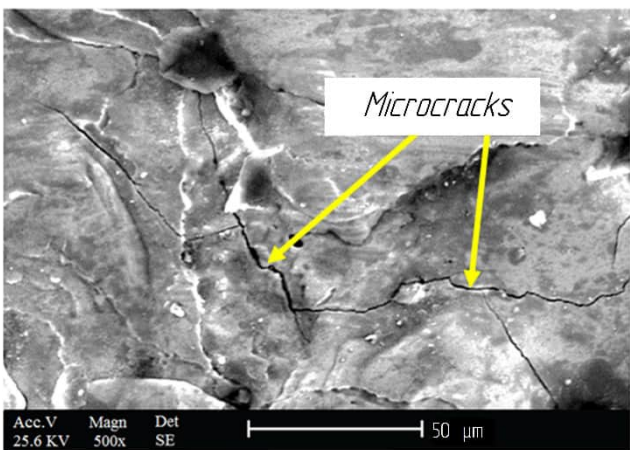
c
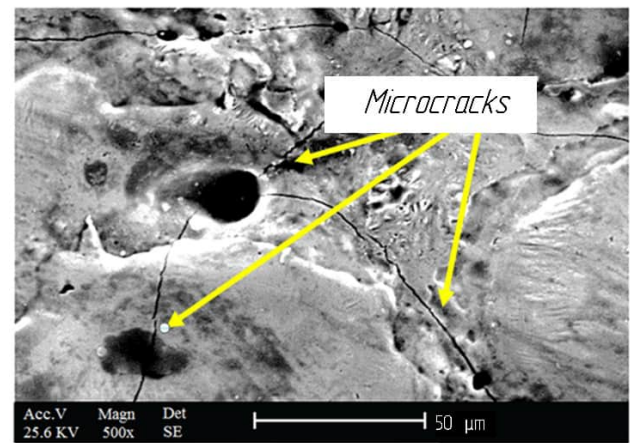
d
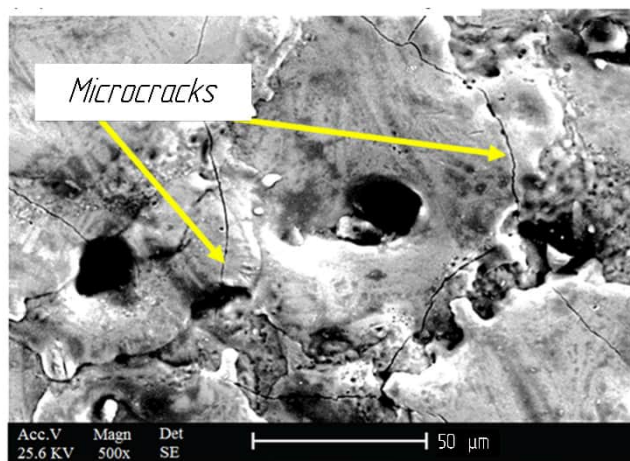
e
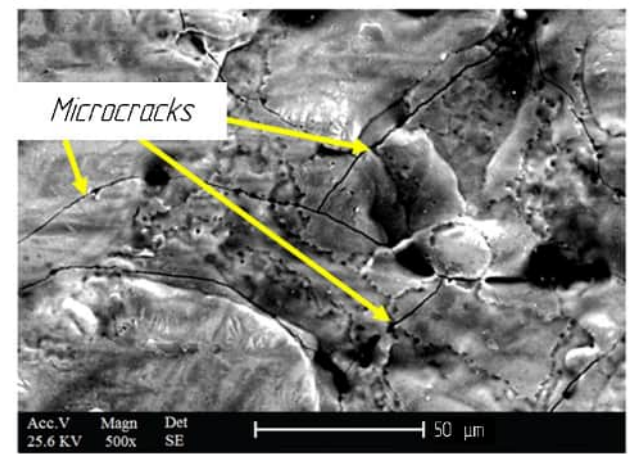
f

Fig. 9. The surface after *EDM* of *AlSi 1045* steel using deionized water as a dielectric (*a, c, e*):

a) at a current of 6 A and a pulse on-time of 150 μs, c) at a current of 6 A and a pulse on-time of 100 μs, e) at a current of 6 A and a pulse on-time of 50 μs and kerosene (*b, d, f*): *b*) at a current of 6 A and a pulse on-time of 150 μs; *d*) at a current of 6 A and a pulse on-time of 100 μs, *f*) at a current of 6 A and a pulse on-time of 50 μs [40]

a mathematical model describing the processes occurring on the machined surface, particularly considering the mass transfer of erosion products. Currently, there is no unified thermodynamic model of the process, nor have fundamental studies been conducted on the formation processes of surface modified layers.

Microstructural changes in the processed surface of heat-resistant materials after *EDM* are represented by residual electrical discharge machining debris, tool electrode material particles, erosion products, and closed pores containing the working fluid. The mechanical characteristics of the processed surface
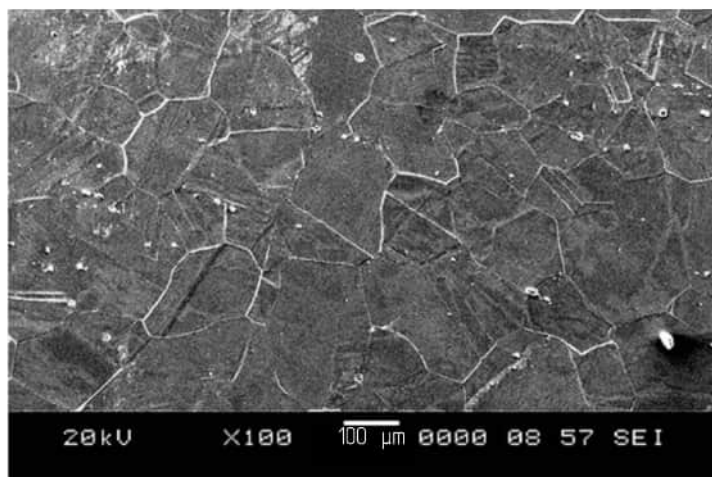
Fig. 10. Inclusions in the surface layer after *WEDM* of *Inconel 706* [44]

significantly depend on the nature and extent of inclusions. The presence of inclusions in the surface layer reduces the fatigue strength of the product.

In [58], the authors also investigated the modified layer after *WEDM* for the presence of inclusions and revealed the presence of inclusions, including oxygen (12.96 %) in the surface layer, which confirms the formation of an oxide film on the machined surface, as well as copper and zinc on the layer's surface (Fig. 10).

In [73], the authors established that in the heat-affected zone, there was a change in chemical composition relative to the base material: a 9% decrease in nickel content, a 1% decrease in the concentration of cobalt and aluminum, and the appearance of foreign elements not inherent to the original chemical composition – 9 % sodium, 4 % chlorine, and approximately 1 % potassium.

Analysis of point **2**, which was located on the recast (white) layer, revealed more significant changes in the main elemental composition of this alloy: a reduction in nickel to 50 %, a 9 % decrease in chromium content, and a 3 % decrease in aluminum. Complete removal of cobalt, molybdenum, tungsten, and vanadium from the surface layer was also observed. This layer was also characterized by the appearance of up to 47 % chlorine and up to 31 % sodium, which is attributed to the use of distilled water as the working fluid. The change in the concentration of alloying elements is associated with the high machining temperature and their solubility in the liquid phase, their migration within the crystallizing material, and the directional crystallization of the recast layer, which collectively accelerate the thermal diffusion of the elements.

In [74], the authors conducted a study of the influence of machining parameters on inclusions in the surface layer and changes in the chemical composition (Fig. 11).

The experiments were conducted across various machining operations, including rough machining, finishing, grinding, and grinding with etching. It was found that the surface after rough *WEDM* showed the

Fig. 11. Inclusions in the surface layer after *WEDM* of *Nimonik C263* material

presence of oxygen due to oxidation of various alloying elements. Finishing resulted in a slight 10–12 % decrease in oxygen content on the workpiece surface. The surface layer contained elements such as zinc and copper, which diffused from the tool electrode during machining. The surface obtained by multi-pass cutting exhibited a higher retention of the original alloy elements.

Influence of tool electrode configuration and material

Scientific studies of the efficiency of the *EDM* process less extensively investigate the influence of flushing in the interelectrode gap (*IEG*). The authors of such studies often note the influence of *IEG* flushing on increasing process productivity and improving surface quality.

In [75–76], the authors designed tool electrodes with internal channels for more efficient removal of debris from the machining zone and enhancing the cooling efficiency of the tool electrode. This resulted in a 40–45% increase in process productivity.

In [77], the authors conducted a comparison of a solid tool electrode and a porous electrode (Fig. 12).

The use of a hollow porous electrode resulted in a three-fold increase in machining efficiency compared to a solid electrode. The machining time was reduced by 47%, which is attributable to better cooling of the tool electrode and a more efficient flow of working fluid.

a   b
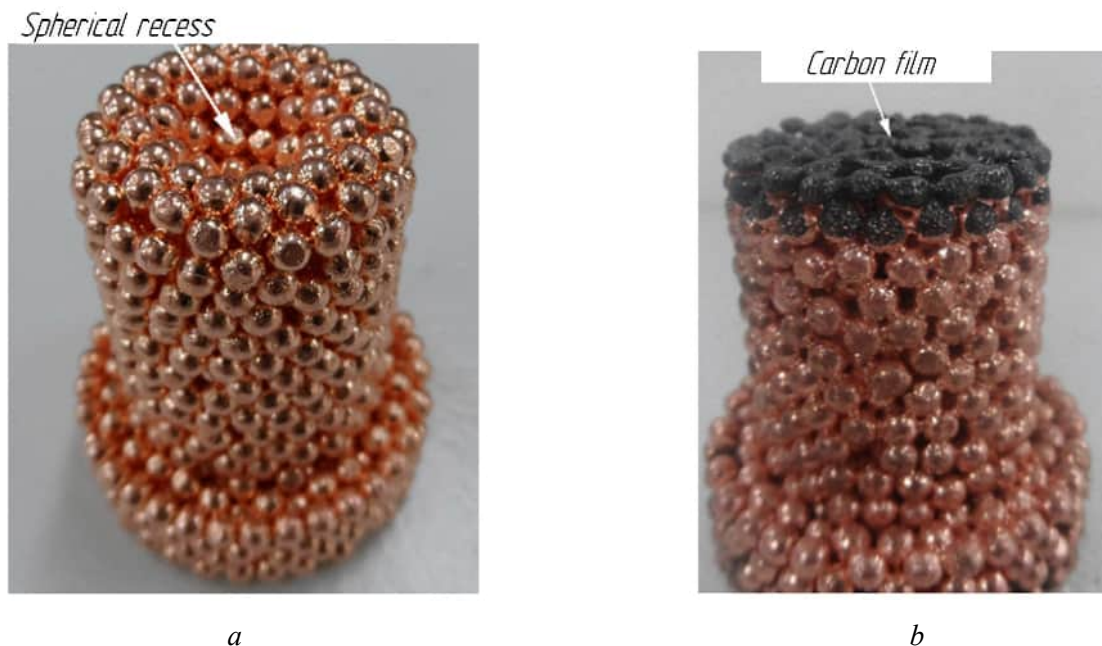
Fig. 12. Copper electrode tool used in *EDM* :

a) before processing; *b)* after processing [53]

In [78–79], the authors manufactured tool electrodes using a reinforcing matrix of graphene. The unique properties of graphene (high electrical and thermal conductivity, superior to copper's) make it a promising material for use as a tool electrode in *EDM*. However, due to the high cost of the material, it is advisable to use it as a reinforcing matrix or as inclusions in the manufacture of tool electrodes. The authors found that the use of composite tool electrodes made it possible to reduce the wear of tool electrodes during machining. This is associated with enhanced heat dissipation in the machining zone and a reduction in the tool electrode temperature experienced during machining. The use of these matrices enables a significant increase in the service life of the tool electrodes.

In [80], the authors conducted research on the use of a spiral tool electrode. The study particularly focused on the removal of debris from the processing zone and the supply of working fluid to the processing zone when machining *Inconel-718*. The electrodes used were cylindrical and spiral tool electrodes (Fig. 13), which were rotated at the same speed during machining.

The efficiency of the spiral electrode in *EDM* exceeds that of traditional cylindrical electrodes due to the higher axial speed. With an increase in the rotation speed, the maximum axial speed of the spiral electrode increases, thereby significantly increasing the circulation

a   b
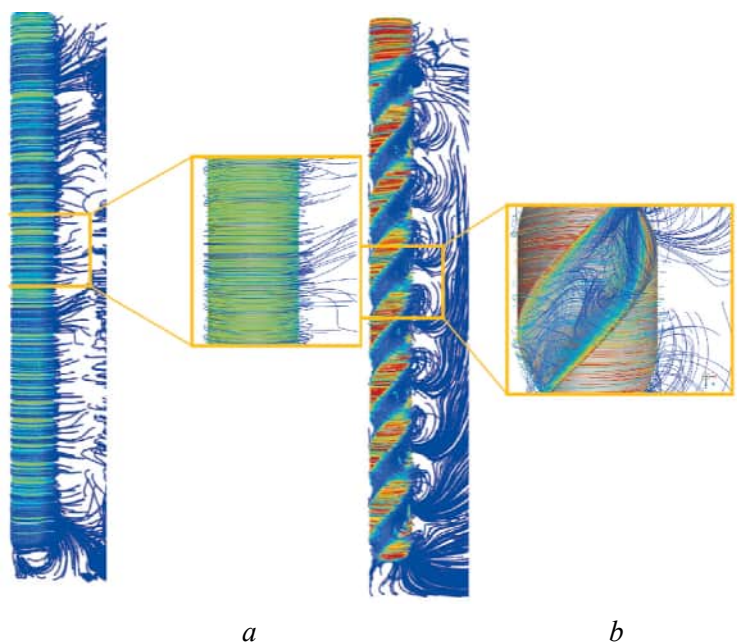
Fig. 13. Axial velocity contours of *a)* cylindrical and *b)* spiral tool electrodes [80]

of the working fluid in the machining zone. Additionally, the spiral tool electrode has a lower electrode wear rate than the cylindrical one, which positively impacts the efficiency of using these electrodes.

On the side wall of the slot, the surface roughness of the workpiece machined with the spiral electrode is only 11 μm, which is better than 28 μm of the cylindrical electrode. The spiral electrode shows superiority over the traditional cylindrical electrode in discharge stability, electrode life, slot dimensional accuracy, and surface quality.

Under the same machining conditions, the thickness of the recast layer was reduced from 107.82 μm to 44.37 μm for the spiral electrode compared to the cylindrical electrode process, while in some areas the recast layer was absent.

The analysis shows that the spiral electrode has significant advantages in the debris removal system compared to the cylindrical one. This is due to its design features, which provide more efficient movement and removal of debris particles from the machining zone. The spiral geometry of the electrode creates unique conditions, specifically: the formation of vortex flows of the working fluid, improved circulation of the working fluid in the machining zone, an optimized and ordered trajectory for the removal of debris particles, and the prevention of stagnant zones, which can lead to secondary remelting.

In [81–83], the authors conducted research on micro-electrode erosion drilling using three different electrodes: a solid tungsten carbide cylindrical electrode, a carbide-tipped drill electrode, and a brass tool electrode. After analyzing the results, the authors established that with the use of the cylindrical electrode, a cone was formed at the exit of the through-hole, attributed to inefficient debris removal from the machining zone during electrical discharge drilling. The geometry of the carbide drill, however, improved debris removal from the interelectrode gap, stabilized the temperature in the machining zone, and reduced the machining time. The choice of tool material significantly affects the productivity of electrical discharge machining: brass provides the most accurate micro-holes (with the least wear, overcut, and taper), though it requires extended machining time. Conversely, tungsten carbide provides high wear resistance but results in larger overcut and taper angles with a moderate machining time. Carbide drills provide a balance of wear resistance, machining time, and overcut/taper angles.

In [84–90], the authors investigated the effects of cryogenic treatment of the tool electrode on the quality and efficiency of electrical discharge machining. Based on the results obtained, it was found that the cryogenically treated tool electrode provides superior machining performance (maximum material removal rate and improved surface roughness) compared to a conventional tool electrode. The authors noted an increase in the electrical conductivity of the brass wire during shallow cryogenic treatment. In addition, it was found that the grains became finer.

These results are directly related to the effect of cryogenic treatment on the structural changes in the tool electrode: the formation of a more uniform structure, the elimination of pores and structural defects, and the reduction of internal stresses. Consequently, the wear resistance of the tool electrode is enhanced.

The effect of cryogenic treatment was further investigated by conducting studies of the machinability of electrical discharge machining on *Inconel 601* using cryogenically treated copper as the tool electrode. Tool wear was reduced by 33% by cryogenic treatment compared to untreated copper tools. The work focused on the influence of current, gap voltage, and pulse duration on material removal rate, electrode wear, and surface roughness. It was found that current was the most important control factor.

Conclusions

This paper reviews the current state of research in the field of electrical discharge machining of heat-resistant alloys. It presents current trends and research interests of scientific teams engaged in this area. A literature analysis of experimental studies was conducted, which revealed the lack of generalized and comprehensive research results. *EDM* is a complex process, the outcome of which is influenced by a multitude of factors, and currently, there are no comprehensive technological or recommendation databases for the machining of heat-resistant alloys.

Based on the conducted literature analysis, the following key findings were established:

1. It is relevant to conduct experimental studies on the influence of various material components added to the working fluid to improve surface quality indicators after *EDM*, and to investigate the impact of alloying the surface layer of heat-resistant materials with these materials.

2. It has been established that the current strength and pulse duration are the main technological parameters determining the quality of the treated surface and the material removal rate. However, exceeding the optimal pulse duration leads to accelerated wear of the tool electrode and excessive melting of the workpiece, which, in turn, leads to difficulty in efficiently removing debris from the interelectrode gap.

3. The efficiency of using a modified working fluid (e.g., containing graphene and carbon nanotubes) for improving surface quality in the machining of heat-resistant materials has been established.

4. It has been established that inclusions in the working fluid have a significant impact on the process parameters and quality of electrical discharge machining. Analysis shows that the correct selection of material and concentration of inclusions can significantly improve the results of the process.

5. It has been established that the geometric parameters of the tool electrode are one of the determining factors influencing the result of electrical discharge machining. Analysis of the literature shows that the correct configuration of the tool electrode can significantly improve the quality and efficiency of the process. A correctly selected tool electrode design ensures more intensive removal of erosion products from the interelectrode gap, which directly affects the quality of the machining.

References

1. Wang X., Wang G., Wang W., Liu X., Liu Y., Jin Y., Zhang Y. Enhancing corrosion resistance of nickel-based alloys: A review of alloying, surface treatments, and environmental effects. *Journal of Alloys and Compounds*, 2025, vol. 1032, pp. 181–195. DOI: 10.1016/j.jallcom.2025.181014.

2. Li H., Liu H., Li J., Yao H. High-temperature corrosion resistance of weld overlay In625 coating in aggressive environments of waste incinerators. *Corrosion Science*, 2025, vol. 249. DOI: 10.1016/j.corsci.2025.112865.

3. Madhusudan S., Epifano E., Favergeon J., Sanviemvongsak T., Marechal D., Monceau D. High temperature intergranular oxidation of nickel based superalloy Inconel 718. *High Temperature Corrosion of Materials*, 2024, vol. 101, pp. 873–884. DOI: 10.1007/s11085-024-10260-z.

4. Karmuhilan M., Kumanan S. A review on additive manufacturing processes of Inconel 625. *Journal of Materials Engineering and Performance*, 2022, vol. 31, pp. 2583–2592. DOI: 10.1007/s11665-021-06427-3.

5. Pendokhare D., Chakraborty S. A review on multi-objective optimization techniques of wire electrical discharge machining. *Archives of Computational Methods in Engineering*, 2025, vol. 32, pp. 1797–1839. DOI: 10.1007/s11831-024-10195-3.

6. Badoniya P., Srivastava M., Jain P.K., Rathee S. A state-of-the-art review on metal additive manufacturing: milestones, trends, challenges and perspectives. *Journal of the Brazilian Society of Mechanical Sciences and Engineering*, 2024, vol. 46 (6), pp. 339–351. DOI: 10.1007/s40430-024-04917-8.

7. Hasan M.M., Saleh T., Sophian A., Rahman M.A., Huang T., Ali M.S. Experimental modeling techniques in electrical discharge machining (EDM): A review. *The International Journal of Advanced Manufacturing Technology*, 2023, vol. 127, pp. 2125–2150. DOI: 10.1007/s00170-023-11603-x.

8. Ajay P., Dabhade V.V. Heat treatments of Inconel 718 nickel-based superalloy: A review. *Metals and Materials International*, 2025, vol. 31, pp. 1204–1231. DOI: 10.1007/s12540-024-01812-8.

9. Zhou N., Lv D.C., Zhang H.L., McAllister D., Zhang F., Mills M.J., Wang Y. Computer simulation of phase transformation and plastic deformation in IN718 superalloy: Microstructural evolution during precipitation. *Acta Materialia*, 2014, vol. 65, pp. 270–286. DOI: 10.1016/j.actamat.2013.10.069.

10. Lv D.C., McAllister D., Mills M.J., Wang Y. Deformation mechanisms of D022 ordered intermetallic phase in superalloys. *Acta Materialia*, 2016, vol. 118 (1), pp. 350–361. DOI: 10.1016/j.actamat.2016.07.055.

11. Sonar T., Balasubramanian V., Malarvizhi S., Venkateswaran T., Sivakumar D. An overview on welding of Inconel 718 alloy – Effect of welding processes on microstructural evolution and mechanical properties of joints. *Materials Characterization*, 2021, vol. 174, pp. 1–22. DOI: 10.1016/j.matchar2021.110997.

12. Erdoğan N.N., Başyiğit A.B. Investigating thermal shock and corrosion resistance of Inconel 601 super alloy after thermal barrier coating with %8 YSZ powder. *Materials Today Communications*, 2023, vol. 36, pp. 1–14. DOI: 10.1016/j.mtcomm.2023.106516.

13. Kang H.S., Kim H., Yoon E.Y., Lee Y.S., Kim S., Kim J.G. Re-heat treatment effect on the microstructure and mechanical properties of the Inconel 706 alloy for repair. *Journal of Materials Research and Technology*, 2024, vol. 31, pp. 2193–2201. DOI: 10.1016/j.jmrt.2024.07.011.

14. Mao J., Li X., Bao S., Ge R., Yan L. The experimental and numerical studies on multiaxial creep behavior of Inconel 783 at 700 °C. *International Journal of Pressure Vessels and Piping*, 2019, vol. 173, pp. 133–146. DOI: 10.1016/j.ijpvp.2019.05.005.

15. Jiang R., Mostafaei A., Pauza J., Kantzos C., Rollett A.D. Varied heat treatments and properties of laser powder bed printed Inconel 718. *Materials Science and Engineering: A*, 2019, vol. 755, pp. 170–180. DOI: 10.1016/J.MSEA.2019.03.103.

16. Jamil M.F., Sahto M.P., Mehmood A. Comprehensive study on high-performance machining (HPM) of Inconel-718: a review. *The International Journal of Advanced Manufacturing Technology*, 2025, vol. 139 (11–12), pp. 5305–5337. DOI: 10.1007/s00170-025-16225-z.

17. Bazyleva O.A., Arginbaeva E.G., Shestakov A.V. Zharoprochnye intermetallidnye nikelevye splavy dlya dvigatelei letatel'nykh apparatov [High-temperature intermetallic nicel alloys for aircraft engines]. *Idei i novatsii = Ideas and Innovations*, 2020, vol. 8, no. 3–4, pp. 138–146. DOI: 10.48023/2411-7943_2020_8_3_4_138.

18. Gromov V.I., Yakusheva N.A., Vostrikov A.V., Cherkashneva N.N. Vysokoprochnye konstruktsionnye stali dlya valov gazoturbinnykh dvigatelei (obzor) [High strength structural steels for gas turbine engine shafts (review)]. *Aviatsionnye materialy i tekhnologii = Aviation Materials and Technologies*, 2021, vol. 62, iss. 1, pp. 3–12. DOI: 10.18577/2713-0193-2021-0-1-3-12.

19. Kuznetsov V.P., Lesnikov V.P., Popov N.A. *Struktura i svoistva zharoprochnykh nikelevykh splavov* [Structure and properties of heat-resistant nickel alloys]. Yekaterinburg, Ural University Publ., 2016. 164 p.

20. Sudhir, Sehgal A.K., Nain S.S. Machine learning algorithms evaluation and optimization of WEDM of nickel based super alloy: A review. *Materials Today: Proceedings*, 2022, vol. 50 (5), pp. 1793–1798. DOI: 10.1016/j.matpr.2021.09.202.

21. Abhilash P.M., Chakradhar D. Prediction and analysis of process failures by ANN classification during wire-EDM of Inconel 718. *Advanced Manufacturing*, 2020, vol. 8, pp. 519–536. DOI: 10.1007/s40436-020-00327-w.

22. Paturi U.M.R., Cheruku S., Pasunuri V.P.K., Salike S., Reddy N.S., Cheruku S. Machine learning and statistical approach in modeling and optimization of surface roughness in wire electrical discharge machining. *Machine Learning with Applications*, 2021, vol. 6. DOI: 10.1016/j.mlwa.2021.100099.

23. Manikandan N., Raju R., Narasimhamu K.L., Damodaram A.K. Optimization of wire electrical discharge machining of Monel 400 using Taguchi-Grey approach. *Materials Today: Proceedings*, 2022, vol. 68 (5), pp. 1690–1696. DOI: 10.1016/j.matpr.2022.08.215.

24. Manikandan N., Binoj J.S., Thejasree P., Abhishek H., Goud B.K. Multi aspects optimization on spark erosion machining of Incoloy 800 by Taguchi Grey approach. *Materials Today: Proceedings*, 2021, vol. 39 (1), pp. 148–154. DOI: 10.1016/j.matpr.2020.06.403.

25. Goyal A. Investigation of material removal rate and surface roughness during wire electrical discharge machining (WEDM) of Inconel 625 super alloy by cryogenic treated tool electrode. *Journal of King Saud University – Science*, 2017, vol. 29, pp. 528–535. DOI: 10.1016/j.jksus.2017.06.005.

26. Archana G., Dharma K.D., Venkataramaiah P. Study on machining response in wire EDM of Inconel 625. *International Journal of Applied Engineering Research*, 2018, vol. 13 (21), pp. 15270–15277.

27. Tata N., Pacharu R.K., Devarakonda S.K. Multi response optimization of process parameters in wire-cut EDM on INCONEL 625. *Materials Today: Proceedings*, 2021, vol. 47 (19), pp. 6960–6964. DOI: 10.1016/j.matpr.2021.05.214.

28. Tonday H.R., Tigga A.M. Empirical assessment and modeling of MRR and surface roughness acquired from wire electrical discharge machining of Inconel 718. *International Journal of Mechanical Engineering and Technology*, 2017, vol. 8 (1), pp. 152–159.

29. Sinha A., Majumder A., Gupta K. A RSM based MOGOA for process optimization during WEDM of Inconel 625. *Proceedings of the Institution of Mechanical Engineers, Part E: Journal of Process Mechanical Engineering*, 2022, vol. 236 (5), pp. 1824–1832. DOI: 10.1177/09544089221074837.

30. Biswas S., Paul A.R., Dhar A.R., Singh Y., Mukherjee M. Multi-material modeling for wire electro-discharge machining of Ni-based superalloys using hybrid neural network and stochastic optimization techniques. *CIRP Journal of Manufacturing Science and Technology*, 2023, vol. 41, pp. 350–364. DOI: 10.1016/j.cirpj.2022.12.005.

31. Shlykov E.S., Ablyaz T.R., Blokhin V.B., Osinnikov I.V., Muratov K.R. Povyshenie effektivnosti elektroerozionnoi obrabotki izdelii, vypolnennykh iz granulirovannogo zharoprochnogo nikelevogo splava VV751P [Increasing the efficiency of electrical discharge machining of products made of granulated heat-resistant nickel alloy

VV751P]. *Konstruktsii iz kompozitsionnykh materialov = Composite Materials Constructions*, 2025, no. 1 (177), pp. 27–30. DOI: 10.52190/2073-2562_2025_1_27.

32. Said A., Lajis M.A. An electrical discharge machining (EDM) of Inconel 718 by using copper electrode at higher peak current and pulse duration. *Conference Series: Materials Science and Engineering*, 2016, vol. 15 (5), pp. 1–7.

33. Tsai H.C., Yan B.H., Huang F.Y. The properties and characteristics of the new electrodes based on Cr-Cu for EDM machines. *International Journal of Machine Tools & Manufacture*, 2003, vol. 43 (3), pp. 245–252.

34. Zhang J.J., Jiang K.Y., Yan J., Wang F., Wang X.W. Performance and microstructure of TiN/Cu EDM electrodes. *Applied Mechanics and Materials*, 2012, vol. 268, pp. 82–86. DOI: 10.4028/www.scientific.net/AMM.268-270.82.

35. Rajyalakshmi G. Optimization of process parameters of wire electrical discharge machining on Inconel825 using grey relational analysis coupled with principle component analysis. *International Journal of Applied Engineering Research*, 2013, vol. 8 (11), pp. 1294–1314.

36. Jay M., Çaydas U., Hasçalık A. Optimization of micro-EDM drilling of Inconel 718 superalloy. *International Journal of Advanced Manufacturing Technology*, 2013, vol. 66 (5), pp. 1015–1023. DOI: 10.1007/s00170-012-4385-8.

37. Baldin V., Baldin C.R.B., Machado A.R., Amorim F.L. Machining of Inconel 718 with a defined geometry tool or by electrical discharge machining. *Journal of the Brazilian Society of Mechanical Sciences and Engineering*, 2020, vol. 42 (5), pp. 1–14. DOI: 10.1007/s40430-020-02358-7.

38. Mohanty A., Talla G., Gangopadhyay S. Experimental investigation and analysis of EDM characteristics of Inconel 825. *Materials and Manufacturing Processes*, 2014, vol. 29, pp. 540–459. DOI: 10.1080/10426914.2014.901536.

39. Chen N., Kong L., Lei W., Qiu R. Experimental study on EDM of CFRP based on graphene aqueous solution. *Materials and Manufacturing Processes*, 2023, vol. 38 (9), pp. 1180–1189. DOI: 10.1080/10426914.2023.2165674.

40. Rahimi H., Masoudi S., Tolouei-Rad M. Experimental investigation of the effect of EDM parameters and dielectric type on the surface integrity and topography. *The International Journal of Advanced Manufacturing Technology*, 2022, vol. 118, pp. 1767–1778. DOI: 10.1007/s00170-021-08040-z.

41. Sun L., Shi S., Li X., Hou Y., Chu Z., Chen B. Surface microstructure evolution and mechanical property investigation of Inconel 718 alloy using multiple trimmings and WEDM. *Experimental Techniques*, 2025, vol. 49, pp. 299–312. DOI: 10.1007/s40799-024-00749-2.

42. Hascalık A., Caydas U. Electrical discharge machining of titanium alloy (Ti–6Al–4V). *Applied Surface Science*, 2007, vol. 253, pp. 9007–9016. DOI: 10.1016/j.apsusc.2007.05.031.

43. Mohanty C.P., Mahapatra S.S., Singh M.R. An experimental investigation of machinability of Inconel 718 in electrical discharge machining. *Procedia Materials Science*, 2014, vol. 6, pp. 605–611. DOI: 10.1016/j.mspro.2014.07.075.

44. Talla G., Gangopadhyay S., Biswas C.K. Influence of graphite powder mixed EDM on the surface integrity characteristics of Inconel 625. *Particulate Science and Technology*, 2016, vol. 35 (2), pp. 219–226. DOI: 10.1080/02726351.2016.1150371.

45. Paswan K., Pramanik A., Chattopadhyaya S., Khan A.M., Singh S. An analysis of machining response parameters, crystalline structures, and surface topography during EDM of die-steel using EDM oil and liquid based viscous dielectrics: a comparative analysis of machining performance. *Arabian Journal for Science and Engineering*, 2023, vol. 48 (1), pp. 1–17. DOI: 10.1007/s13369-023-07626-x.

46. Sonker P.K., Nahak B., Singh T.J. Comparative study of copper and graphite electrodes performance in Electrical Discharge Machining (EDM) of die steel. *Materials Today: Proceedings*, 2022, vol. 68, pp. 167–170. DOI: 10.1016/j.matpr.2022.07.182.

47. Singh G., Mahajan A., Devgan S., Sidhu S.S. Comparison of copper and tungsten electrodes for the electric discharge machined SUS-316L. *Sustainable Machining Strategies for Better Performance: Select Proceedings of SMSBP 2020*. Springer, 2022, pp. 197–206. DOI: 10.1007/978-981-16-2278-6_17.

48. Khayrulin V.T., Ablyaz T.R., Shlykov E.S., Blokhin V.B., Muratov K.R. Issledovanie vliyaniya rezhimov protsessa provolochno-vyreznoi elektroerozionnoi obrabotki na formirovanie znacheniya shiriny reza pri obrabotke zharoprochnogo nikelevogo splava VV751P [Study of the influence of wire-cut electrical discharge machining process modes on the formation of the cut width value when processing heat-resistant nickel alloy VV751P]. *STIN = Russian Engineering Research*, 2024, no. 6, pp. 27–30. (In Russian).

49. Sun L., Chu Z., Hou Y., Rajurkar K., Li X., Shi S. Utilizing wire electrical discharge machining for surface quality and precise profile control of Inconel 718 fir-tree slot. *The International Journal of Advanced Manufacturing Technology*, 2024, vol. 133, pp. 1271–1283. DOI: 10.1007/s00170-024-13826-y.

50. Dzionk S., Siemiatkowski M.S. Studying the effect of working conditions on WEDM machining performance of super alloy Inconel 617. *Machines*, 2020, vol. 8 (3), pp. 1–18. DOI: 10.3390/machines8030054.

51. Khairulin V.T., Ablyaz T.R., Shlykov E.S., Blokhin V.B., Muratov K.R. Factors affecting the cut width in the wire-cut electrical discharge machining of VV751P heat-resistant nickel alloy. *Russian Engineering Research*, 2024, vol. 44 (7), pp. 1014–1016. DOI: 10.3103/S1068798X24701387.

52. Padhi P.C., Routara B.C. Effect of recast layer thickness of high-carbon alloy (EN-31) in wire EDM process by varying operating parameters. *Recent Advances in Thermofluids and Manufacturing Engineering*: *Select Proceedings of ICTMS 2022*. Springer, 2022, pp. 505–517. DOI: 10.1007/978-981-19-4388-1_43.

53. Walder G., Richard J. Removal of the heat affect zone created by EDM with pico-second LASER machining. *Procedia CIRP*, 2016, vol. 42, pp. 475–480. DOI: 10.1016/j.procir.2016.02.235.

54. Ji R., Liu Y., Diao R., Xu C., Li X., Cai B., Zhang Y. Influence of electrical resistivity and machining parameters on electrical discharge machining performance of engineering ceramics. *PLoS ONE*, 2017, vol. 9 (11), pp. 1–9. DOI: 10.1371/journal.pone.0110775.

55. Ablyaz T.R., Shlykov E.S., Osinnikov I.V., Muratov K.R., Khayrullin V.T. Issledovanie mikrostruktury poverkhnostnogo sloya zharoprochnykh materialov, obrabotannykh metodom elektroerozionnoi obrabotki [Study of the microstructure of the surface layer of heat-resistant materials processed by electrical discharge machining]. *STIN = Russian Engineering Research*, 2024, no. 6, pp. 33–35. (In Russian).

56. Azam M., Jahanzaib M., Abbasi J.A., Abbas M., Wasim A., Hussain S. Parametric analysis of recast layer formation in wire-cut EDM of HSLA steel. *The International Journal of Advanced Manufacturing Technology*, 2016, vol. 87, pp. 713–722. DOI: 10.1007/s00170-016-8518-3.

57. Rohilla V.K., Goyal R., Kumar A., Singla Y.K., Sharma N. Surface integrity analysis of surfaces of nickel-based alloys machined with distilled water and aluminium powder-mixed dielectric fluid after WEDM. *The International Journal of Advanced Manufacturing Technology*, 2021, vol. 116, pp. 2467–2472. DOI: 10.1007/s00170-021-07610-5.

58. Sharma P., Chakradhar D., Narendranath S. Analysis and optimization of WEDM performance characteristics of Inconel 706 for aerospace application. *Silicon*, 2018, vol. 10, pp. 921–930. DOI: 10.1007/s12633-017-9549-6.

59. Ablyaz T.R., Shlykov E.S., Blokhin V.B., Osinnikov I.V., Khayrulin V.T., Muratov K.R. Issledovanie vliyaniya rezhimov elektroerozionnoi obrabotki na ekspluatatsionnye svoistva izdelii, vypolnennykh iz granulirovannogo zharoprochnogo nikelevogo splava VV751P [Investigation of the influence of electrical discharge machining modes on operational properties of products made of granulated heat-resistant nickel alloy VV751P]. *Konstruktsii iz kompozitsionnykh materialov = Composite Materials Constructions*, 2024, vol. 2 (174), pp. 22–27. DOI: 10.52190/2073-2562_2024_2_22.

60. Sharma R.K., Singh J. Determination of multi-performance characteristics for powder mixed electric discharge machining of tungsten carbide alloy. *Proceedings of the Institution of Mechanical Engineers, Part B: Journal of Engineering Manufacture*, 2016, vol. 230 (2), pp. 303–315. DOI: 10.1177/0954405414554017.

61. Paswan K., Sharma S., Li C., Mohammed K.A., Kumar A., Abbas M., Tag-Eldin E.M. Unravelling the analysis of electrical discharge machining process parameters, microstructural morphology, surface integrity, recast layer formation, and material properties: A comparative study of aluminum, brass, and Inconel 617 materials. *Journal of Materials Research and Technology*, 2023, vol. 27, pp. 7713–7729. DOI: 10.1016/j.jmrt.2023.11.186.

62. Bui V.D., Mwangi J.W., Schubert A. Powder mixed electrical discharge machining for antibacterial coating on titanium implant surfaces. *Journal of Manufacturing Processes*, 2019, vol. 44, pp. 261–270. DOI: 10.1016/j.jmapro.2019.05.032.

63. Besinis A., Hadi S.D., Le H.R., Tredwin C., Handy R.D. Antibacterial activity and biofilm inhibition by surface modified titanium alloy medical implants following application of silver, titanium dioxide and hydroxyapatite nanocoatings. *Nanotoxicology*, 2017, vol. 11 (3), pp. 327–338. DOI: 10.1080/17435390.2017.1299890.

64. Kumar S., Dhingra A.K., Kumar S. Parametric optimization of powder mixed electrical discharge machining for nickel-based superalloy inconel-800 using response surface methodology. *Mechanics of advanced materials and modern processes*, 2017, vol. 7 (3). DOI: 10.1186/s40759-017-0022-4.

65. Kumar N., Ahsan R. Study of PMEDM efficiency on EN-31 steel using tungsten powder in dielectric fluid. *International Journal of Emerging Technologies in Engineering Research*, 2017, vol. 5 (5), pp. 17–24.

66. Bhaumik M., Maity K. Effect of machining parameter on the surface roughness of AISI 304 in silicon carbide powder mixed EDM. *Decision Science Letters*, 2017, vol. 6 (3), pp. 261–268. DOI: 10.5267/j.dsl.2016.12.004.

67. Al-Khazraji A.N., Amin S.A., Ali S.M. The effect of SiC powder mixing electrical discharge machining on white layer thickness, heat flux and fatigue life of AISI D2 die steel. *Engineering Science and Technology, an International Journal*, 2016, vol. 19 (3), pp. 1400–1415. DOI: 10.1016/j.jestch.2016.01.014.

68. Kazi F., Waghmare C.A., Sohani M.S. Multi-objective optimization of machining parameters in hybrid powder-mixed EDM process by response surface methodology and normalized fuzzy logic algorithm. *The International Journal on Interactive Design and Manufacturing*, 2021, vol. 15, pp. 695–706. DOI: 10.1007/s12008-021-00788-8.

69. Bhowmick S., Paul A., Biswas N., Sarkar S., Majumdar G. Synthesis and characterization of titanium and graphite powder mixed electric discharge machining on Inconel 718. *Advances in Transdisciplinary Engineering*, 2022, vol. 27, pp. 58–63. DOI: 10.3233/ATDE220722.

70. Kumar A., Mandal A., Dixit A.R., Kumar A., Kumar S., Ranjan R. Comparison in the performance of EDM and NPMEDM using Al_2O_3 nanopowder as an impurity in DI water dielectric. *The International Journal of Advanced Manufacturing Technology*, 2019, vol. 100, pp. 1327–1339. DOI: 10.1007/s00170-018-3126-z.

71. Kumar S.B., Saurav D., Mahapatra S.S. On electro-discharge machining of Inconel 718 super alloys: An experimental investigation. *Materials Today: Proceedings*, 2018, vol. 5, pp. 4861–4869. DOI: 10.1016/j.matpr.2017.12.062.

72. Sahu D.R., Kumar V., Mandal A. Surface integrity analysis in powder mixed EDM of Nimonic 263. *Materials Today: Proceedings*, 2022, vol. 62 (1), pp. 353–359. DOI: 10.1016/j.matpr.2022.03.467.

73. Ablyaz T.R., Shlykov E.S., Osinnikov I.V., Blokhin V.B., Muratov K.R. Elektronno-mikroskopicheskii analiz poverkhnostnogo sloya izdelii iz zharoprochnykh nikelevykh splavov posle elektroerozionnoi obrabotki [Electron-microscopic analysis of the surface layer of products made of heat-resistant nickel alloys after electrical discharge machining]. *STIN = Russian Engineering Research*, 2025, no. 5, pp. 55–58. (In Russian).

74. Mandal A., Dixit A.R., Chattopadhyaya S., Paramanik A., Hloch S., Królczyk G. Improvement of surface integrity of Nimonic C 263 super alloy produced by WEDM through various post-processing techniques. *The International Journal of Advanced Manufacturing Technology*, 2017, vol. 93, pp. 433–443. DOI: 10.1007/s00170-017-9993-x.

75. Nguyen H.P., Ngo N.V., Nguyen C.T. Study on multi-objects optimization in EDM with nickel coated electrode using Taguchi-AHP-Topsis. *International Journal of Engineering*, 2022, vol. 35 (2), pp. 276–282. DOI: 10.5829/ije.2022.35.02b.02.

76. Bozdana A.T., Alkarkhi N.K. Comparative experimental investigation and gap flow simulation in electrical discharge drilling using new electrode geometry. *International Journal of Mechanical Sciences*, 2017, vol. 8 (2), pp. 289–298. DOI: 10.5194/ms-8-289-2017.

77. Jiang Y., Kong L., Yu J., Hua C., Zhao W. Experimental research on preparation and machining performance of porous electrode in electrical discharge machining. *Journal of Mechanical Science and Technology*, 2022, vol. 36 (12), pp. 6201–6215. DOI: 10.1007/s12206-022-1134-2.

78. Mondal S., Paul G., Mondal S.C., Mondal K., Seikh Z., Sekh M. Fabrication of graphene reinforced aluminium metal matrix composites for advanced tool materials. *Journal of the Institution of Engineers (India): Series D*, 2024. DOI: 10.1007/s40033-024-00847-w.

79. Mondal S., Paul G., Mondol K., Mondal S.C. Electric discharge machining with graphene reinforced aluminium metal matrix composite (Gr Al MMC) tool for EN 31 die steel work piece. *The Journal of the Institution of Engineers (India): Series C*, 2025, vol. 106, pp. 541–551. DOI: 10.1007/s40032-025-01163-2.

80. Chen X., Ma N., Liu H., Chen Y., Nie R., Zhang Z., Zhou J., Zhou Z. Study on immersion rotary helical electrode electrochemical discharge machining of Inconel 718 alloy. *Journal of Materials Research and Technology*, 2025, vol. 38, pp. 288–305. DOI: 10.1016/j.jmrt.2025.07.191.

81. Korgal A., Karanth P.N., Shettigar A.K., Madhavi J.B. A novel application of the micro-wire-electro-discharge-grinding (μ-WEDG) method for the generation of tantalum and brass nanoparticles. *Micro and Nano Systems Letters*, 2024, vol. 12 (1), pp. 1–19. DOI: 10.1186/s40486-024-00210-4.

82. Sharma A., Sharma N., Singh R.P., Arora R., Gill R.S., Singh G. Micro-drill on Al/SiC composite by EDD process: An RSM-MOGOA based hybrid approach. *International Journal of Lightweight Materials and Manufacture*, 2022, vol. 5 (4), pp. 564–575. DOI: 10.1016/j.ijlmm.2022.07.002.

83. Korgal A., Shettigar A.K., Karanth N.P., Kumar N., Bindu M.J. Electro-discharge machining of microholes on 3d printed Hastelloy using the novel tool-feeding approach. *International Journal of Lightweight Materials and Manufacture*, 2025, vol. 8 (2), pp. 157–164. DOI: 10.1016/j.ijlmm.2024.10.005.

84. Goyal A. Investigation of material removal rate and surface roughness during wire electrical discharge machining (WEDM) of Inconel 625 super alloy by cryogenic treated tool electrode. *Journal of King Saud University – Science*, 2017, vol. 29 (4), pp. 528–535. DOI: 10.1016/j.jksus.2017.06.005.

85. Pandey A., Kumar R. Some studies using cryogenically treated rotary Cu-tool electrode electrical discharge machining. *Materials Today: Proceedings*, 2018, vol. 5 (2), pp. 7635–7639. DOI: 10.1016/j.matpr.2017.11.438.

86. Torres A., Puertas I., Luis C.J. Modelling of surface finish, electrode wear and material removal rate in electrical discharge machining of hard-to-machine alloys. *Precision Engineering*, 2015, vol. 40, pp. 33–45. DOI: 10.1016/j.precisioneng.2014.10.001.

87. Kumar S.V., Kumar M.P. Optimization of cryogenic cooled EDM process parameters using grey relational analysis. *Journal of Mechanical Science and Technology*, 2018, vol. 28, pp. 3777–3784. DOI: 10.1007/s12206-014-0840-9.

88. Tharian B.K., Dhanish P.B., Manu R. Enhancement of material removal rate in electric discharge machining of Inconel 718 using cryo-treated graphite electrodes. *Materials Today: Proceedings*, 2021, vol. 47, pp. 5172–5176. DOI: 10.1016/j.matpr.2021.05.506.

89. Datta R.S., Biswal B.B. Experimental studies on electro-discharge machining of Inconel 825 super alloy using cryogenically treated tool/workpiece. *Measurement*, 2019, vol. 145, pp. 611–630. DOI: 10.1016/j.measurement.2019.06.006.

90. Singh N., Routara B.C., Nayak R.K. Study of machining characteristics of Inconel 601 with cryogenic cooled electrode in EDM using RSM. *Materials Today: Proceedings*, 2018, vol. 5 (11), pp. 24277–24286. DOI: 10.1016/j.matpr.2018.10.223.

Conflicts of Interest

The authors declare no conflict of interest.

Obrabotka metallov –
Metal Working and Material Science
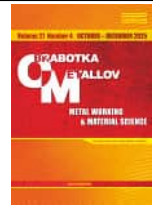
ANFIS modeling of turning Al7075 hybrid nanocomposites under compressed air cooling

Satish Chinchanikar [1, a, *], Suhas Patil [2, b], Paresh Kulkarni [3, c]

[1] Department of Mechanical Engineering, Vishwakarma Institute of Technology, Affiliated to Savitribai Phule Pune University, Pune- 411037, India

[2] Department of Mechanical Engineering, Vishwakarma Institute of Information Technology, Affiliated to Savitribai Phule Pune University, Pune– 411048, India

[3] Department of Mechanical Engineering, D.Y. Patil International University, Akurdi, Pune, Maharashtra, 411044, India

[a] https://orcid.org/0000-0002-4175-3098, satish.chinchanikar@vit.edu; [b] https://orcid.org/0000-0002-2965-1531, suhas.221p0007@viit.ac.in; [c] https://orcid.org/0000-0002-2761-8754, paresh2410@gmail.com

ARTICLE INFO

ABSTRACT

Introduction. Hybrid metal matrix composites (*HMMCs*) are increasingly used in the aviation and automotive industries due to their low density, high stiffness, and exceptional specific strength. Among aluminum *MMCs*, *Al7075*-based composites are gaining wider acceptance. Continuous research and development in this field focuses on improving the durability and performance of these advanced materials. **Purpose of the work.** Machinability of *Al7075* is a significant challenge because the abrasive reinforcement phase causes rapid tool deterioration, increased machining forces, and a poor surface finish. Moreover, the industrial focus on green manufacturing has led to a shift from traditional coolant-based machining to sustainable alternatives. In this context, researchers have optimized machining performance using advanced technological advancements and techniques. However, limited work is reported on modeling the machining performance of *Al7075* nanocomposites during turning under compressed air cooling. **Methods of investigation.** Manufacturers can gain a better understanding of increasing the effectiveness of turning processes for *Al7075* nanocomposites by creating a comprehensive model. Therefore, this work models the machining performance of hybrid *Al7075* nanocomposites during turning under compressed air-cooling conditions with an artificial neuro-fuzzy inference system (*ANFIS*) to predict tool wear (*TW*), surface roughness (*Ra*), and cutting force (*Fc*) as a function of process parameters. **Results and discussion.** In this work, an *ANFIS* model was developed to predict the machining performance considering the effect of process parameters such as cutting speed, feed rate, and depth of cut for different *Al7075*-based nanocomposites. These nanocomposites were prepared using silicon carbide (30–50 nm) and graphene (5–10 nm) nanoparticles as reinforcements by the stir casting process. Reinforcement materials affect the mechanical and physical properties of composites. For engineering applications, *SiC* and graphene are preferred reinforcements with distinctive features. *ANFIS* models were developed to predict *Ra*, *F_c*, and *TW* based on the experimental results. The *Sugino* method was used to represent fuzzy rules and membership functions, as it utilizes weighted averages in the defuzzification process and offers better processing efficiency. The *MATLAB ANFIS* toolbox was used to design and tune fuzzy inference systems. The developed *ANFIS* model predicts machining responses effectively and offers a practical approach for optimizing process parameters with high reliability. The results of this research show good agreement between the experimental results and the predicted *ANFIS* outcomes, with an average prediction error below 8%. Specifically, the *ANFIS* model yielded errors of 5.1% for *Ra*, 13.45% for *F_c*, and 7.92% for *TW*. The model exhibited excellent agreement with experimental data, demonstrating high prediction accuracy and generalization capability. 3-D graphs are plotted for a better understanding of the effect of process parameters on *F_c*, *Ra*, and *TW* for different nanocomposites. The findings affirm the efficacy of compressed air cooling in improving machinability while minimizing environmental impact. Furthermore, the developed ANFIS model serves as a reliable tool for optimizing turning parameters for Al7075 composites, supporting the advancement of green manufacturing strategies. This research warrants further investigation into the application of *ANFIS* in machining processes, specifically exploring various metal matrix composite types and rigorously assessing the long-term effects of compressed air cooling on both environmental sustainability and tool life.

* Corresponding author
Satish Chinchanikar, Ph.D. (Engineering), Professor
Department of Mechanical Engineering,
Vishwakarma Institute of Information Technology,
Affiliated to Savitribai Phule Pune University, Pune – 411048, India
Tel.: 91-2026950401, **e-mail:** satish.chinchanikar@vit.edu

Introduction

Hybrid metal matrix composites (*HMMCs*) are increasingly found in the aviation and automotive industries because of their extraordinary properties, including low density, high stiffness, outstanding specific strength, and a low coefficient of thermal expansion. The growing demand for advanced materials in the aerospace, automotive, and defense sectors has driven the widespread adoption of aluminum metal matrix composites (*MMCs*), particularly *Al7075*, due to its excellent specific strength and corrosion resistance [1].

However, the machinability of *Al7075* composites presents a significant challenge due to their abrasive reinforcement phase, which accelerates tool wear, increases cutting forces, and degrades surface finish. Concurrently, the industrial shift towards green manufacturing has emphasized a move away from traditional coolant-based machining to sustainable alternatives. One such method is compressed air cooling, which not only reduces the environmental impact but also improves chip removal and provides localized cooling at the tool-workpiece interface.

Intelligent modeling techniques have proven highly effective in addressing the nonlinear and multi-parametric nature of the turning process under compressed air cooling. Traditional flood cooling relies heavily on mineral-based fluids, which have adverse effects on the environment, operator health, and operational costs due to fluid disposal. Consequently, alternative methods such as minimum quantity lubrication (*MQL*), nanofluids, cryogenic cooling, and compressed air techniques have gained significant demand in machining. These sustainable alternatives address not only environmental concerns but also key machinability aspects, including tool wear, cutting force, and surface finish [2, 3].

Studies have shown that turning *Al7075* under *MQL* with a coolant chilled to −20°C significantly improves surface finish and reduces cutting force compared to other cutting environments [4]. Furthermore, research indicates that tool nose radius has a more substantial influence on surface finish than most other process parameters. In recent decades, manufacturing has heavily relied on empirical data from previous studies. To achieve superior machining outcomes, the application of advanced cutting techniques combined with scientifically validated approaches, such as artificial intelligence (*AI*), is essential. Precise modeling is critical for obtaining desired results in machining processes. Owing to their fuzzy logic rules, self-learning capability, and ability to process complex, non-linear data, soft computing techniques are now extensively employed for modeling [5].

The literature suggests that the adaptive neuro-fuzzy inference system (*ANFIS*) often outperforms other computational methods in estimating machining responses [6, 7]. Comparative studies indicate that while gene expression programming (*GEP*) may surpass artificial neural networks (*ANN*) in specific applications, *ANFIS* frequently yields more accurate predictions. Furthermore, both *ANN* and *ANFIS* have been demonstrated to provide superior results compared to response surface methodology (*RSM*) in several investigations [8–12]. The application of optimization approaches is crucial for enhancing surface quality and advancing machining technology [13]. For instance, genetic algorithms (*GA*) have been successfully applied to optimize the milling of *Al7075-T6*, with the developed models proving adequate for predicting cutting forces [14]. Similarly, studies utilizing ANN to forecast the tribological properties of *Al7075-Al₂O₃* composites have reported close agreement between experimental data and model predictions [15].

Researchers have also modeled machining responses using nanofluids under minimum quantity lubrication (*NFMQL*) [16, 17]. Among various modeling techniques, *ANFIS* has been widely adopted in most studies due to its superior capability in capturing the complex, non-linear dependencies among machining parameters [18–21]. However, a significant research gap remains: few investigations have considered the effect of varying the weight percentage of nanoparticles within the *Al7075* matrix on machinability. Furthermore, *ANFIS* modeling of the machining performance for hybrid *Al7075* nanocomposites under compressed air cooling conditions is virtually unreported. To address this gap, the present work develops an *ANFIS* model to predict the machining performance of hybrid *Al7075* nanocomposites, with a specific focus on quantifying the influence of nanoparticle weight percentage and cutting parameters on key output responses.

Accordingly, in the present study, nine distinct *Al7075*-based nanocomposites were fabricated with varying weight percentages of silicon carbide (*SiC*) and graphene reinforcements. For each nanocomposite

specimen, nine turning experiments were conducted under compressed air cooling. An adaptive neuro-fuzzy inference system (*ANFIS*) model was developed to predict cutting force, flank wear, and surface roughness, accounting for the influences of both turning parameters and nanocomposite composition. Finally, additional validation trials were performed to verify the predictive accuracy of the developed *ANFIS* model.

Methods

This section details the experimental methodology employed to develop adaptive neuro-fuzzy inference system (*ANFIS*) models for predicting surface roughness (***Ra***), cutting force (***F_c***), and tool wear (***TW***) during the turning of *Al7075* nanocomposites. The experimental setup, including the machining configuration and conditions, is described, followed by a comprehensive explanation of the *ANFIS* model development process.

The workpieces were cylindrical bars (300 mm in length and 30 mm in diameter) made from *Al7075*-based nanocomposites. Turning was performed using a *CNMG120408MS* carbide insert mounted on a *PCBNR2525M12 ISO*-coded tool holder. All cutting experiments were conducted on a precision *CNC* lathe to ensure consistent tool positioning and geometry throughout the operation. The machining setup is illustrated in Fig. 1. The chemical composition of the base *Al7075* alloy is provided in Fig. 2, while Table 1 summarizes the specifications of the different composite specimens fabricated via the stir casting process.
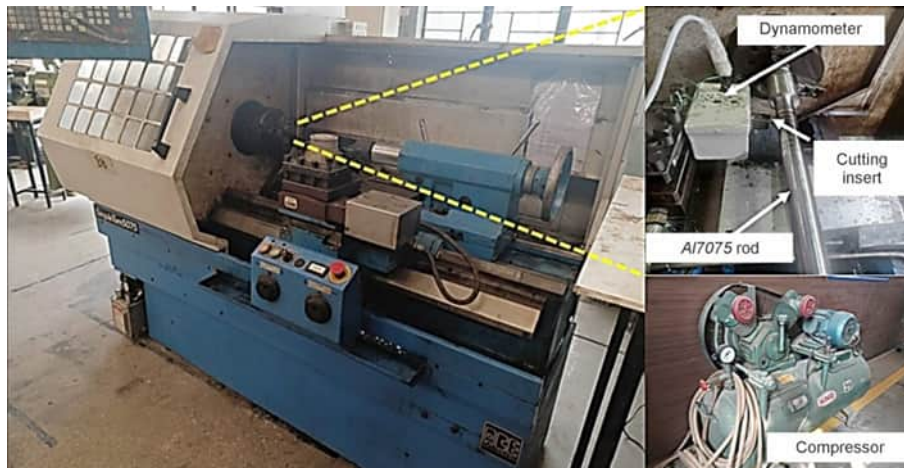
Fig. 1. Appearance and components of the lathe setup

Fig. 2. Elemental composition of *Al7075* alloy

The input parameters were selected based on a comprehensive analysis of the literature, preliminary experimental trials, the operational limits of the machine tool, and technical specifications from the tooling manufacturer. The finalized parameter ranges were chosen to optimize machining performance and extend tool life. A full factorial design of experiments was employed, resulting in a total of 81 turning trials conducted across the nine distinct composite specimens, as summarized in Fig. 3.

The trials involved varying the cutting speed (***V***) from 100 to 200 m/min, the feed rate (***f***) from 0.1 to 0.3 mm/rev, and the depth of cut (***d***) from 0.2 to 0.8 mm. For each machining experiment, the output responses – surface roughness (***Ra***), cutting force (***F_c***), and tool wear (***TW***) – were recorded. The cutting force (***F_c***) was measured using a pre-calibrated dynamometer. Tool wear (***TW***), specifically flank wear (***FW***), was measured after each pass using a *Dino-Lite* digital microscope. Surface roughness (***Ra***) was measured using

_Al7075_ aluminum alloy nanocomposites with different types of reinforcement

Specimen	Types of reinforcement
S1	Unreinforced _Al7075_
S2	_Al7075_ + 0.5 % _SiC_ + 0.1 % graphene
S3	_Al7075_ + 0.5 % _SiC_ + 0.2 % graphene
S4	_Al7075_ + 0.5 % _SiC_ + 0.3 % graphene
S5	_Al7075_ + 0.5 % graphene + 1 % _SiC_
S6	_Al7075_ + 0.5 % graphene + 2 % _SiC_
S7	_Al7075_ + 0.5 % graphene + 3 % _SiC_
S8	_Al7075_ + 1 % graphene + 2 % _SiC_
S9	_Al7075_ + 1 % graphene + 4 % _SiC_

Fig. 3. Nine samples of various composite materials

a surface profilometer. Tool wear was monitored in accordance with _ISO 3685:1993_ standards, with the tool life failure criterion defined as either 0.2 mm of average flank wear or the occurrence of catastrophic tool failure.

Adaptive neuro-fuzzy inference system (ANFIS)

The adaptive neuro-fuzzy inference system (_ANFIS_) is ideally suited for modeling complex systems characterized by uncertainty and imprecise information, while maintaining model transparency and interpretability. This machine learning technique synergistically combines the intuitive reasoning of fuzzy logic with the learning capabilities of artificial neural networks. The _ANFIS_ approach constructs an adaptive network that maps inputs to outputs by integrating fuzzy inference mechanisms with neural learning rules. The _ANFIS_ architecture comprises five distinct layers, each consisting of interconnected nodes, as illustrated in Fig. 4 [8]. Input data is processed sequentially through these layers, with each stage executing a specific function within the overall inference mechanism.

The first layer, the fuzzification layer, converts crisp input values into fuzzy membership grades using predefined membership functions. In the subsequent product layer, the firing strength of each fuzzy rule is computed by multiplying the incoming membership grades. The third layer, the normalization layer, calculates the relative contribution of each rule by dividing its firing strength by the sum of all firing strengths, thereby ensuring that the total influence of all rules is unity. The normalized firing strengths are then processed in the defuzzification layer, where each is used to weight a linear function to generate
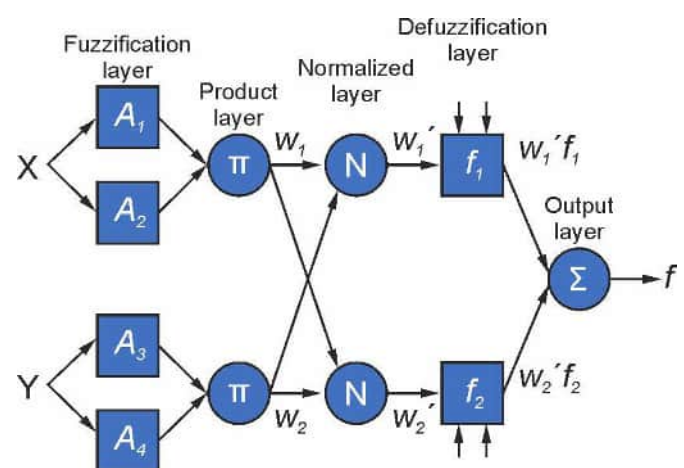
Fig. 4. General structure of _ANFIS_

the output of individual rules. Finally, the output layer aggregates all the weighted rule outputs to produce a single, crisp value representing the system's final prediction.

Results and Discussion

This section presents the development and analysis of adaptive neuro-fuzzy inference system (*ANFIS*) models for predicting the turning performance of *Al7075*-based nanocomposites under compressed air cooling. The models were constructed to evaluate the influence of key process parameters and varying nanocomposite compositions on surface roughness (*Ra*), cutting force (*F$_c$*), and tool wear (*TW*). Experimental data were gathered, and distinct *ANFIS* models were established for each output response. The model's decision-making logic is encapsulated in its fuzzy rules and membership functions, the parameters of which were optimized through a data-driven learning process.

The *Sugeno* fuzzy inference method was selected for this study due to its computational efficiency and straightforward implementation, as it utilizes weighted averages during the defuzzification process. A principal advantage of the *Sugeno* method is its ability to represent complex nonlinear systems through a set of linear equations. The *ANFIS* modeling was conducted using the *MATLAB* environment, which provides a dedicated toolbox offering a user-friendly interface for designing, training, and tuning fuzzy inference systems, making it accessible for researchers in artificial intelligence.

The procedure for creating the *ANFIS* models in *MATLAB* is illustrated in Fig. 5. Since the *ANFIS* architecture is designed for single-output systems, three separate models were developed and analyzed independently to predict surface roughness (*Ra*), cutting force (*F$_c$*), and tool wear (*TW*). Each model utilized cutting speed (*V*), feed rate (*f*), and depth of cut (*d*) as input variables. The initial step in constructing each *ANFIS* model involved defining the input-output variables, their respective value ranges, and partitioning the relevant experimental data for model training and testing.
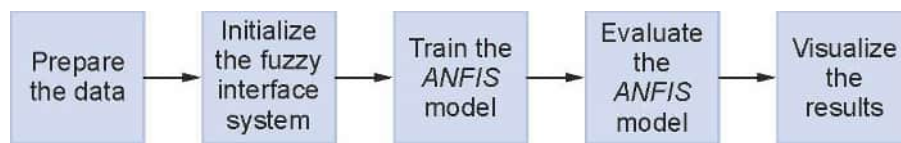
Fig. 5. Stages of *ANFIS* modeling

The initial fuzzy inference system (*FIS*) was generated using the grid partitioning method available in the *MATLAB ANFIS* toolbox. Grid partitioning was selected as it simplifies the rule base and enhances the interpretability of the resulting *FIS* model. Triangular membership functions were chosen for the input variables, while constant membership functions were assigned to the outputs. The model was then trained using a hybrid optimization algorithm to fine-tune its parameters, including the membership function shapes and rule weights. The training was conducted over 10 epochs. The specific hyperparameters configured for the *ANFIS* models predicting *Ra*, *F$_c$*, and *TW* are detailed in Fig. 6.
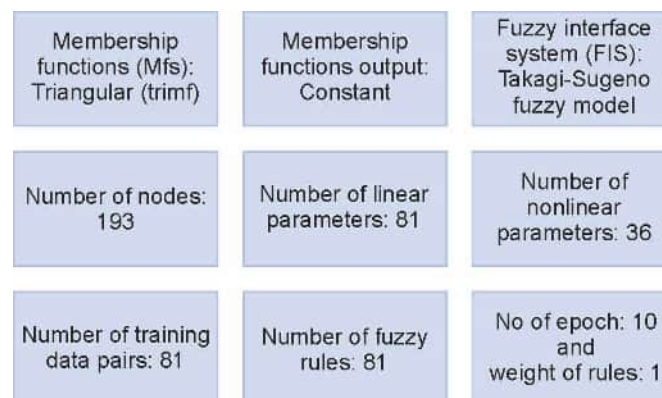
Fig. 6. ANFIS model parameters

Fuzzy inference system *(FIS)* training was terminated once the predefined target epoch was reached and the minimum root mean squared error (*RMSE*) for the developed model was achieved. Specifically, the *RMSE* values for the *ANFIS* models predicting *Ra*, *Fc* and *TW* were found to be 1.56637, 1.56637, and 3.31021, respectively, when utilizing triangular membership functions (*MFs*). In this study, a total of eighty-one fuzzy rules were employed for each model. The *ANFIS* structures developed for predicting *Ra*, *Fc* and *TW* are illustrated in Fig. 7.
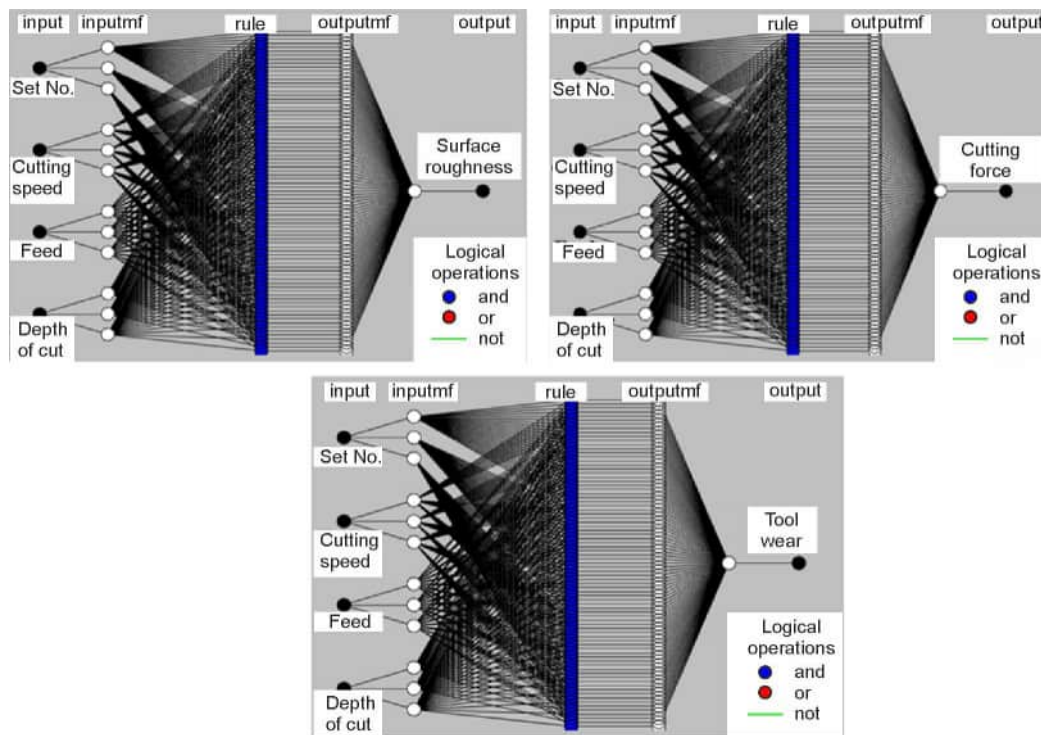
Fig. 7. Developed *ANFIS* model structure

Following model development, the prediction errors for both the training and testing datasets were evaluated for *Ra*, *Fc* and *TW*. Fig. 8 illustrates the correlation between the *FIS* outputs and the experimental data for training and testing, achieved using the triangular membership function configuration. The resulting training and testing errors were 0.057 and 0.086 for surface roughness (*Ra*), 1.55 and 0.82 for cutting force (*Fc*), and 3.310 and 4.15 for tool wear (*TW*), respectively.

To better understand the concurrent influence of process parameters on the responses, three-dimensional surface plots for *Ra*, *Fc* and *TW* were generated, as shown in Figs. 9–11. These plots facilitate a more intuitive analysis of machining performance by providing visual clarity on the effects of input parameters. Each plot illustrates the variation of an output response with two input parameters, while the third parameter was held constant at its central value ($V_c = 150$ m/min, $f = 0.2$ mm/rev, $d = 0.5$ mm).

Analysis of the surface plots in Figs. 9–11 indicates that a lower surface roughness (*Ra*) is achieved by employing a higher cutting speed (*V*) in combination with moderate to low feed rate (*f*) and depth of cut (*d*) settings. Similarly, cutting force (*Fc*) is minimized by using a higher cutting speed with lower feed and depth of cut. Tool wear (*TW*) is also reduced at higher cutting speeds, even when maintaining feed rate and depth of cut settings.

To validate the *ANFIS*-predicted results, additional turning experiments were conducted using parameter combinations not included in the original training dataset. A comparison between the experimental results and the *ANFIS* predictions is presented in Table 2. These validation trials allowed for a detailed assessment of model performance across an expanded range of input variables. The experimental values for *Ra*, *Fc* and *TW* represent averages from three separate trials to minimize the influence of outliers.

The *ANFIS* model demonstrated reliable predictive accuracy, with an average prediction error below 8 % across all responses, showing strong agreement with the experimental data. Specifically, the model
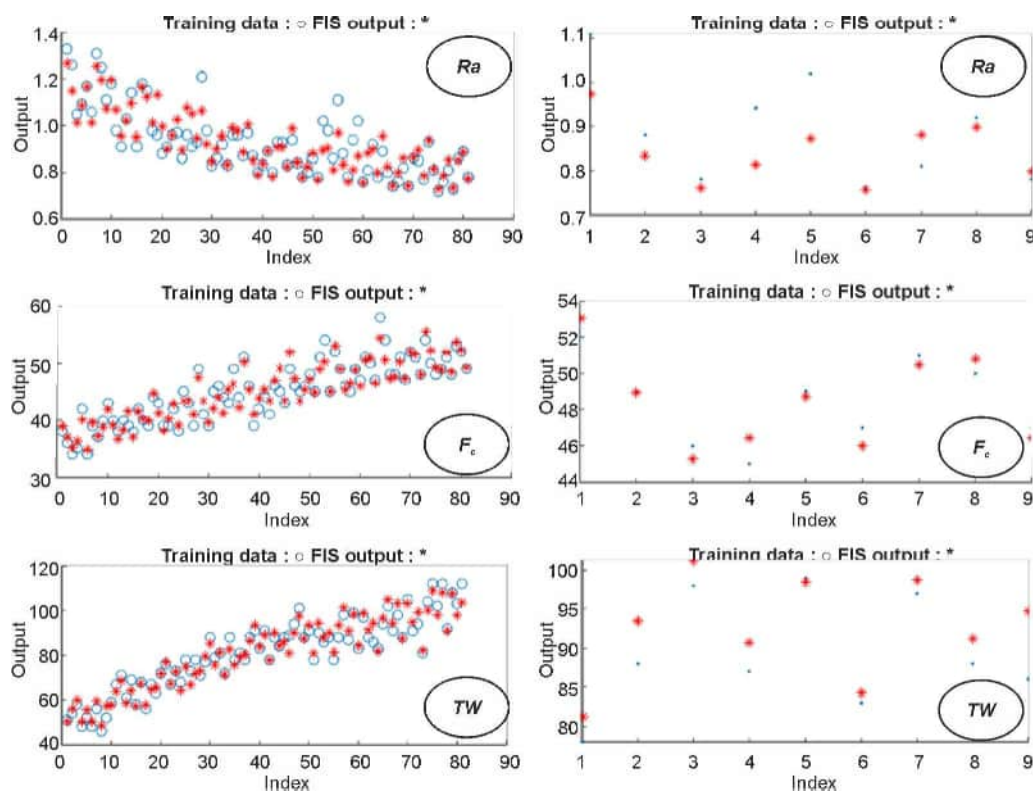
Puc. 8. Mapping test and training data using *FIS* output
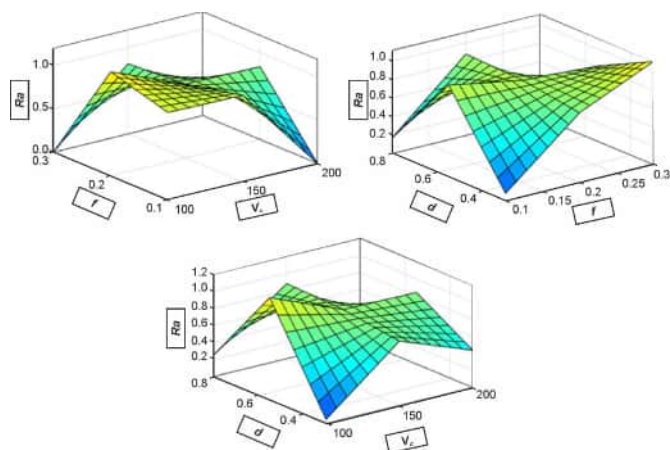
Fig. 9. Dependence of **Ra** on process parameters
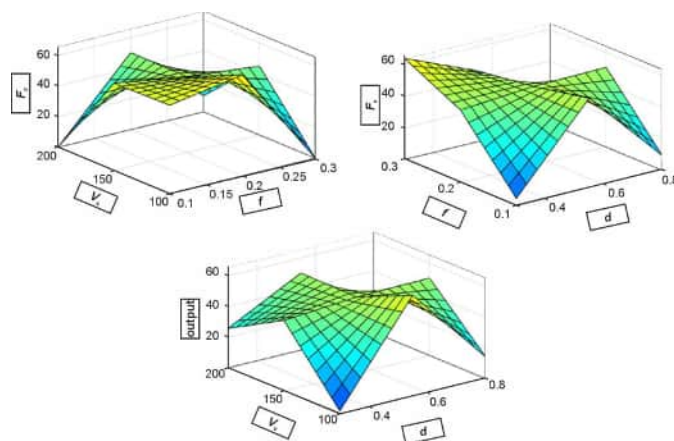
Fig. 10. Dependence of F_c on process parameters
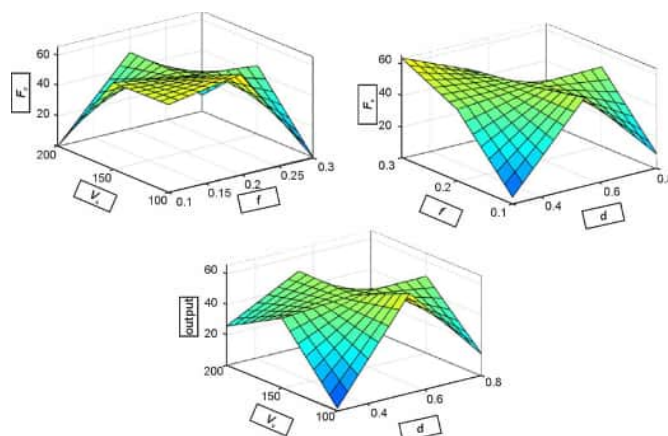
Fig. 11. Dependence *of **TW*** on process parameters

Validation experiments

V (m/min), f (mm/rev), d (mm)	Ra (µm)		Fc (N)		TW (µm)	
	Expt.	ANFIS	Expt.	ANFIS	Expt.	ANFIS
110; 0.12; 0.4	0.854	0.843	51.39	55.7	83.47	87.5
130; 0.17; 0.45	0.875	0.835	55.92	63.1	86.19	91.7
165; 0.23; 0.65	0.836	0.841	58.38	49.7	94.88	103.7
180; 0.27; 0.75	0.812	0.896	48.33	57.7	112.32	122.7
200; 0.15; 0.35	0.701	0.759	39.89	44.6	94.95	104.3

yielded errors of 5.1% for surface roughness (**Ra**), 13.45% for cutting force (**F_c**), and 7.92% for tool wear (**TW**). These results confirm the potential of *ANFIS* as a robust and effective tool for predicting machining performance in the turning of *Al7075* metal matrix composites.

Conclusion

This study successfully demonstrates the application of an adaptive neuro-fuzzy inference system (*ANFIS*) for modeling the turning performance of *Al7075* hybrid nanocomposites under compressed air cooling. The key findings are summarized as follows:

– Compressed air cooling is confirmed as a viable and environmentally sustainable alternative to conventional flood cooling, effectively enhancing machinability in the turning of *Al7075* nanocomposites.

– The developed *ANFIS* model provides a highly reliable and practical methodology for predicting key machining outputs enabling the optimization of process parameters.

– The ANFIS model exhibited strong predictive accuracy with the average prediction error remaining below 9%, with errors of 5.1% for **Ra**, 13.45% for **F_c**, and 7.92% for **TW**, demonstrating a high degree of alignment with experimental validation data.

– This research establishes a framework that integrates sustainable cooling technology with intelligent modeling, presenting a significant advancement for green machining strategies in the manufacturing of metal matrix composites.

Furthermore, the study underscores that the specific composition of the nanocomposite (i.e., reinforcement percentage and type) is a critical input variable for accurately modeling machining performance, a key insight for industrial application.

References

1. Mohammed S.M.A.K., Nisar A., John D., Sukumaran A.K., Fu Y., Paul T., Hernandez A.F., Seal S., Agarwal A. Boron nitride nanotubes induced strengthening in aluminium 7075 composite via cryomilling and spark plasma sintering. *Advanced Composites and Hybrid Materials*, 2025, vol. 8 (1), art. 155. DOI: 10.1007/s42114-024-01173-1.

2. Devitte C., Souza A.J., Amorim H.J. Impact of cooled compressed air and high-speed cutting on the drilling of hybrid composite-metal stacks. *The International Journal of Advanced Manufacturing Technology*, 2023, vol. 125 (11), pp. 5445–5461. DOI: 10.1007/s00170-023-11083-z.

3. Kulkarni P., Chinchanikar S. Machinability of Inconel 718 using unitary and hybrid nanofluids under minimum quantity lubrication. *Advances in Materials and Processing Technologies*, 2025, vol. 11 (1), pp. 421–449. DOI: 10.1 080/2374068X.2024.2307103.

4. Bagheri A., Abedini V., Hajialimohamadi A. Impact of machining parameters on surface roughness and machining forces in Al7075 turning with minimum quantity lubrication and cold fluid. *Proceedings of the Institution of Mechanical Engineers, Part E: Journal of Process Mechanical Engineering*, 2025. DOI: 10.1177/09544089241 308052.

5. Kulkarni P., Chinchanikar S. Modelling turning performance of Inconel 718 with hybrid nanofluid under MQL using ANN and ANFIS. *Fracture and Structural Integrity*, 2024, vol. 18 (70), pp. 71–90. DOI: 10.3221/ IGF-ESIS.70.04.

6. Prabhu S., Vinayagam B.K. Adaptive neuro fuzzy inference system modelling of multi-objective optimisation of electrical discharge machining process using single-wall carbon nanotubes. *Australian Journal of Mechanical Engineering*, 2015, vol. 13 (2), pp. 97–117. DOI: 10.7158/M13-074.2015.13.2.

7. Sharma D., Bhowmick A., Goyal A. Enhancing EDM performance characteristics of Inconel 625 superalloy using response surface methodology and ANFIS integrated approach. *CIRP Journal of Manufacturing Science and Technology*, 2022, vol. 37, pp. 155–173. DOI: 10.1016/j.cirpj.2022.01.005.

8. Hewidy M., Salem O. Integrating experimental modelling techniques with the Pareto search algorithm for multiobjective optimization in the WEDM of Inconel 718. *The International Journal of Advanced Manufacturing Technology*, 2023, vol. 129 (1–2), pp. 299–319. DOI: 10.1007/s00170-023-12200-8.

9. Sen B., Mia M., Mandal U.K., Mondal S.P. GEP-and ANN-based tool wear monitoring: a virtually sensing predictive platform for MQL-assisted milling of Inconel 690. *The International Journal of Advanced Manufacturing Technology*, 2019, vol. 105, pp. 395–410. DOI: 10.1007/s00170-019-04187-y.

10. Kumar A., Pradhan M.K. An ANFIS modelling and genetic algorithm-based optimization of through-hole electrical discharge drilling of Inconel-825 alloy. *Journal of Materials Research*, 2023, vol. 38 (2), pp. 312–327. DOI: 10.1557/s43578-022-00728-6.

11. Premnath A.A., Alwarsamy T., Sugapriya K. A comparative analysis of tool wear prediction using response surface methodology and artificial neural networks. *Australian Journal of Mechanical Engineering*, 2014, vol. 12 (1), pp. 38–48. DOI: 10.7158/M12-075.2014.12.1.

12. Babu K.N., Karthikeyan R., Punitha A. An integrated ANN–PSO approach to optimize the material removal rate and surface roughness of wire cut EDM on INCONEL 750. *Materials Today: Proceedings*, 2019, vol. 19, pp. 501–505. DOI: 10.1016/j.matpr.2019.07.643.

13. Imran M., Shuangfu S., Yuzhu B., Yuming W., Raheel N. Optimising subsurface integrity and surface quality in mild steel turning: A multi-objective approach to tool wear and machining parameters. *Journal of Materials Research and Technology*, 2025, vol. 35, pp. 3440–3462. DOI: 10.1016/j.jmrt.2025.01.246.

14. Subramanian M., Sakthivel M., Sooryaprakash K., Sudhakaran R. Optimization of cutting parameters for cutting force in shoulder milling of Al7075-T6 using response surface methodology and genetic algorithm. *Procedia Engineering*, 2013, vol. 64, pp. 690–700. DOI: 10.1016/j.proeng.2013.09.144.

15. Pramod R., Kumar G.V., Gouda P.S., Mathew A.T. A study on the Al_2O_3 reinforced Al7075 metal matrix composites wear behavior using artificial neural networks. *Materials Today: Proceedings*, 2018, vol. 5 (5), pp. 11376–11385. DOI: 10.1016/j.matpr.2018.02.105.

16. Kulkarni P., Chinchanikar S. Cutting force modeling during turning Inconel 718 using unitary Al_2O_3 and hybrid MWCNT + Al_2O_3 nanofluids under minimum quantity lubrication. *International Journal on Interactive Design and Manufacturing (IJIDeM)*, 2025, vol. 19 (7), pp. 5185–5202. DOI: 10.1007/s12008-024-02120-6.

17. Chinchanikar S., Kulkarni P. Machining effects and multi-objective optimization in Inconel 718 turning with unitary and hybrid nanofluids under MQL. *Fracture and Structural Integrity*, 2024, vol. 18 (68), pp. 222–241. DOI: 10.3221/IGF-ESIS.68.15.

18. Zare Chavoshi S. Tool flank wear prediction in CNC turning of 7075 AL alloy SiC composite. *Production Engineering*, 2011, vol. 5 (1), pp. 37–47. DOI: 10.1007/s11740-010-0282-x.

19. Veluchamy B., Karthikeyan N., Krishnan B.R., Sundaram C.M. Surface roughness accuracy prediction in turning of Al7075 by adaptive neuro-fuzzy inference system. *Materials Today: Proceedings*, 2021, vol. 37, pp. 1356–1358. DOI: 10.1016/j.matpr.2020.06.560.

20. Guvenc M.A., Bilgic H.H., Cakir M., Mistikoglu S. The prediction of surface roughness and tool vibration by using metaheuristic-based ANFIS during dry turning of Al alloy (AA6013). *Journal of the Brazilian Society of Mechanical Sciences and Engineering*, 2022, vol. 44 (10), p. 474. DOI: 10.1007/s40430-022-03798-z.

21. Ramakrishnan H., Balasundaram R., Selvaganapathy P., Santhakumari M., Sivasankaran P., Vignesh P. Experimental investigation of turning Al 7075 using Al_2O_3 nano-cutting fluid: ANOVA and TOPSIS approach. *SN Applied Sciences*, 2019, vol. 1 (12), p. 1639. DOI: 10.1007/s42452-019-1664-0.

Conflicts of Interest

The authors declare no conflict of interest.

Obrabotka metallov –
Metal Working and Material Science

Journal homepage: http://journals.nstu.ru/obrabotka_metallov

Milling of a blank from austenitic stainless steel AISI 321, deposited using wire-arc additive manufacturing (WAAM)

Qingrong Zhang [1, c], Vasiliy Klimenov [1, b, *], Viktor Kozlov [1, c], Dmitry Chinakhov [2, d],
Zeli Han [1, e], Mengxu Qi [1, f], Zeru Ding [1, g], Menghua Pan [1, h]

[1] National Research Tomsk Polytechnic University, 30 Lenin Avenue, Tomsk, 634050, Russian Federation
[2] Novosibirsk State Technical University, 20 Prospekt K. Marksa, Novosibirsk, 630073, Russian Federation

[a] https://orcid.org/0009-0002-7820-1227, ✉ cinzhun1@tpu.ru; [b] https://orcid.org/0000-0001-7583-0170, ✉ klimenov@tpu.ru;
[c] https://orcid.org/0000-0001-9351-5713, ✉ kozlov-viktor@bk.ru; [d] https://orcid.org/0000-0002-4319-7945, ✉ chinakhov@corp.nstu.ru;
[e] https://orcid.org/0000-0001-6502-6541, ✉ hanzelizy@gmail.com; [f] https://orcid.org/0000-0003-3738-0193, ✉ mensyuy1@tpu.ru;
[g] https://orcid.org/0009-0009-6303-7453, ✉ czezhu1@tpu.ru; [h] https://orcid.org/0009-0004-1128-9935, ✉ menhua1@tpu.ru

ARTICLE INFO

ABSTRACT

Introduction. Wire arc additive manufacturing (*WAAM*), due to its "design as manufacturing" characteristic, is gradually becoming one of the most promising technologies. However, at present, there are no comprehensive comparative studies on the microstructure and mechanical properties of deposited samples made from austenitic stainless steel at different locations of the sample. In addition, their machinability remains insufficiently investigated. **The purpose of this study** is to compare the microstructure and mechanical properties of samples made of austenitic stainless steel ER321 (analogues – *AISI 321*, 0.08% *C*-18% *Cr*-10% *Ni-Ti*) obtained by the *WAAM* method at different locations within the sample and to assess their machinability by the magnitude of the components of the cutting force during end milling and the roughness of the machined surface. The properties and microstructure of samples obtained by wire-arc additive technology are investigated, and milling forces **are investigated**. The effect of the feed on the components of the cutting force and the roughness of the machined surfaces during conventional milling of *ER321* steel workpieces using 12 mm diameter cemented carbide end mills with a wear-resistant *AlTiN* coating applied by physical vapor deposition (*PVD*) is determined. **Research methods.** The content of elements and the solidification pattern in various parts of the workpieces were determined using X-ray microanalysis. The microstructure of the samples was studied by a metallographic method. Stress-strain diagrams were obtained by tensile tests, and the microhardness of the samples was also measured. In comparison with the pattern of conventional milling of rolled workpieces, a pattern of changes in cutting forces and surface roughness was established depending on the feed rate during milling of deposited workpieces. **Results and discussion.** During deposition, ferrite with a vermicular morphology is primarily formed in the lower region of the sample, whereas austenite with a dendritic ferrite structure is observed in other regions. The microhardness values of the deposited and rolled samples are close, averaging around 230 HV0.1. The ultimate tensile strength of the rolled samples is 666 MPa, which is approximately 40 MPa higher than that of the deposited samples. During milling of the deposited workpieces, the lateral cutting force acting perpendicular to the feed direction is greater, and the surface quality is poorer. During milling of deposited workpieces, the lateral cutting force acting perpendicular to the feed direction is greater, and the surface quality is poorer. During milling of deposited workpieces, the feed force acting in the feed direction is greater under high feed rates.

* Corresponding author
Klimenov Vasily A., D.Sc. (Engineering), Professor
National Research Tomsk Polytechnic University,
30 Lenin Avenue,
634050, Tomsk, Russian Federation
Tel.: +7 913 850-44-51, **e-mail:** klimenov@tpu.ru

Introduction

Wire arc additive manufacturing (*WAAM*) offers high deposition rates (up to 800 g/min), low production costs (approximately an order of magnitude lower than powder-based additive methods), and significant advantages for the 3D prototyping of complex structures and the on-demand fabrication of functional materials. These benefits position *WAAM* as a leading direction in the development of additive manufacturing (*AM*) [1–7]. Among welding techniques, cold metal transfer (*CMT*) is particularly notable due to its controlled short-circuiting process. This method significantly reduces heat input, promotes grain refinement, and is widely used in *WAAM* when dimensional accuracy and surface roughness requirements are moderate [6, 7].

Austenitic stainless steel, valued for its high ductility, excellent strength, and good corrosion resistance, has become a primary material for additive manufacturing in engineering and medical applications [8]. However, the complexity of *AM* thermal cycles complicates the prediction of microstructure and mechanical properties in fabricated parts. For instance, *AISI 308LSi* stainless steel specimens produced by electric-arc deposition using graphite sliders in an argon atmosphere exhibit more uniform structural growth and an average 12% increase in hardness due to a more intensive δ-ferrite to austenite transformation [9]. Variations in cooling conditions can lead to a 10% difference in ultimate tensile strength between the upper and lower sections of *AISI 304* stainless steel specimens [10]. Similarly, a direct heat transfer in *AISI 316L* steel results in a 10% anisotropy in tensile strength [11].

Furthermore, the surface quality of *AM*-produced parts, particularly those made by *WAAM*, is often low. High heat input causes instability and spreading of the weld pool, accompanied by spatter adhesion to the specimen surface. According to [12], the lateral surface roughness of *WAAM* products, defined by weld bead geometry, can reach 1.06 mm. Consequently, mechanical post-processing is typically required to improve surface finish [13]. The machining of stainless steel is complicated by its high ductility, which promotes significant work hardening, chip adhesion to the tool, built-up edge formation, and micro-voids on the machined surface. While *Dabwan* et al. [14] investigated cutting forces and surface quality in additively manufactured *316L* stainless steel under different printing parameters, and *Guo* et al. [15] studied these parameters for high-power direct laser deposition at various milling rates, neither study compared additively manufactured specimens with conventionally rolled counterparts. Given the prevalent use of wire from the People's Republic of China (*PRC*) in wire-feed electron beam additive manufacturing, it is crucial to compare products fabricated in Russia and the *PRC*, considering differences in synthesis processes and the chemical composition of the feedstock wire.

Current research predominantly focuses on the machinability of refractory nickel and titanium alloys produced by *AM*, while the machinability of austenitic stainless steels remains largely unexplored [16]. Therefore, investigating the machinability of austenitic stainless steel specimens, especially those fabricated by *WAAM*, and comparing them with rolled specimens is necessary.

The purpose of this work is to determine the microstructure and mechanical properties of a *WAAM*-fabricated specimen in different regions and to compare its machinability with that of a rolled specimen. The following investigations were conducted:

– Determination of the solidification mechanism based on the chemical composition in different regions of the *WAAM*-fabricated specimen.

– Analysis of the relationship between mechanical properties (hardness, ultimate tensile strength, ultimate elongation) and microstructure in different regions of the fabricated specimen.

– Comparison of changes in cutting forces and surface roughness as a function of feed rate during the milling of *WAAM*-fabricated and rolled specimens.

Notation

λ – thermal conductivity, W/(m·ºC)

C – heat capacity, J/(kg·K)

γ – austenite

δ – ferrite

L – liquid

γ_{cut} – face angle of a cutter, deg.

α_{cut} – back angle of a cutter, deg.

z – number of teeth of a cutter, pcs.

B – milling width, mm

t – milling depth, mm

s_m – feed rate, mm/min

s_t – feed per tooth, mm/min

n – rotational speed of a cutter, rpm

v – cutter speed, mm/min

ψ – engagement angle, deg. It indicates the angular location of the cutting edge of the cutter tooth tip from the pierce point to its location at opposed milling

$P_h(F_x)$ – feed force, N. It is oriented along the feed per minute direction. In opposed milling, the feed force is directed to the specimen in the opposite direction of the feed per minute. In cutdown milling, this force is directed to the specimen and coincides with the direction of the feed per minute

$P_v(F_y)$ – lateral force, N. It is directed normal to the direction of the feed per minute

$P_x(F_z)$ – axial force, N. It is directed along the cutter axis

P_y – radial force, N. It is directed normal to the cutter speed vector and from the axis of rotation to the point considered on the cutting edge

P_z – tangential force, N. This force coincides with the direction of the cutter speed vector

N – normal force. This force is directed from the cut surface to the back surface of the cutting edge

P_{hv} – total force P_h and P_v, N. $P_{hv} = (P_h^2 + P_v^2)^{1/2}$

P_{yz} – total force P_y and P_z, N. $P_{yzv} = (P_y^2 + P_z^2)^{1/2}$

T – temperature, °C

R_a – surface roughness, μm. It means arithmetic mean from absolute values of the surface profile deviation within the specimen length

P_{tot} – total milling force, N. $P_{tot} = (Ph^2 + Pv^2 + Px^2)^{1/2}$

h_p – height of protrusion not removed by a cutter, μm

Methods

A specimen measuring 194×80×34 mm was fabricated using *WAAM* with *CMT*, employing a *KUKA R1810* robot and a *Fronius TPS 400i* power source. To minimize specimen distortion during *WAAM*, the substrate was made of *Q235B* steel (analogous to rimmed low-carbon steel *St3*), selected for its lower cost. The potential influence of the substrate on the deposited metal's structure and properties is governed primarily by differences in thermal conductivity λ and, to a lesser extent, specific heat capacity **C** [17]. While the specific heat capacities are nearly identical (C_{Q235B} = 498 J/(kg·K), $C_{ER321(AISI\ 321)}$ = 494 J/(kg·K)), there is a significant difference in thermal conductivity (λ_{Q235B} = 54 W/(m·°C), $\lambda_{ER321(AISI\ 321)}$ = 18 W/(m·°C) at 200°C. This difference significantly affects heat transfer only for the initial 2–3 deposited layers. Afterwards, this difference dissapeared due to the high temperature and thickness of deposited layers that served as a heat barrier, thus making insufficient thermal conductivity of the substrate with increasing distance from it [10, 18]. This aligns with standard *WAAM* practice, where a substrate of common, low-cost steel like rimmed low-carbon steel *St3* is typically used. The substrate thickness was 10 mm to ensure sufficient strength and prevent deformation during the printing process.

A shielding gas mixture of 98% *Ar* and 2 % CO_2 was used. The feedstock was 1.2 mm diameter *ER321* austenitic stainless steel welding wire. The same grade was used for the rolled specimen to ensure scientific consistency and comparability of the obtained data. The chemical compositions of the wire, substrate, and rolled specimen are provided in Table 1.

Table 2 summarizes *WAAM + CMT* process parameters, and Fig. 1 presents a photograph and a process chart of the *WAAM + CMT* system.

The specimens were etched in a mixture of 67 wt.% HNO_3 and 33 wt.% *HCl*, and their microstructure was examined using an *Axio Observer A1m* inverted microscope (*Carl Zeiss*, Germany). The ferrite

T a b l e 1

Chemical composition of the wire, substrate, and rolled product

Materials	Elemental composition, wt.%									
	C	Si	Mn	P	S	Cr	Ni	Mo	Cu	Ti
Wire	0.06	0.49	1.52	0.021	0.002	18.9	9.08	0.08	0.13	0.17
Substrate	0.18	0.16	0.45	0.019	0.019	/	/	/	/	/
Rolled product	0.08	0.45	1.51	0,023	0.002	18.2	9.12	0.05	/	0.16

T a b l e 2

WAAM + CMT process parameters

Wire feed speed, m/min	4.5	Shielding gas rate, L/min	20
Printing speed, m/min	0.6	Voltage, V	19.1
Temperature, °C	200	Current, A	121
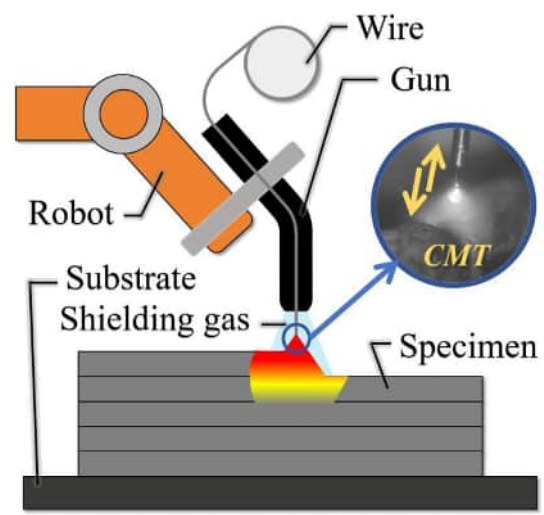
Fig. 1. WAAM + CMT system:
full view (*a*), process chart (*b*)

content was determined from micrographs using the *ImageJ* image analysis software. Scanning electron microscopy with energy-dispersive X-ray spectroscopy (*SEM/EDS*) was performed on different regions of the *WAAM*-fabricated specimen using a *Quanta 200 3D SEM* (*FEI Company*, USA) equipped with an energy-dispersive X-ray analyzer.

The schematic in Fig. 2, *b* illustrates the specimen sections and their orientation. The *OX* axis is aligned with the scanning direction, the *OY* axis is aligned with the transverse direction, and the *OZ* axis is aligned with the layer-building direction (normal to the deposition plane). Microhardness was measured using a *DuraScan-10* hardness tester (*EMCO TEST*, Austria) with a 0.1 kgf load and a 10 s dwell time.

Tensile tests were performed at room temperature on an *MIM 4* testing machine at a crosshead speed of 2 mm/min. The dimensions of the 2 mm thick dog-bone specimens are shown in Fig. 2, *c*. Although milling involves high-strain-rate deformation, stress-strain curves obtained at room temperature provide relevant insight into the material's mechanical properties [19]; therefore, high-temperature tensile testing was not conducted in this study.
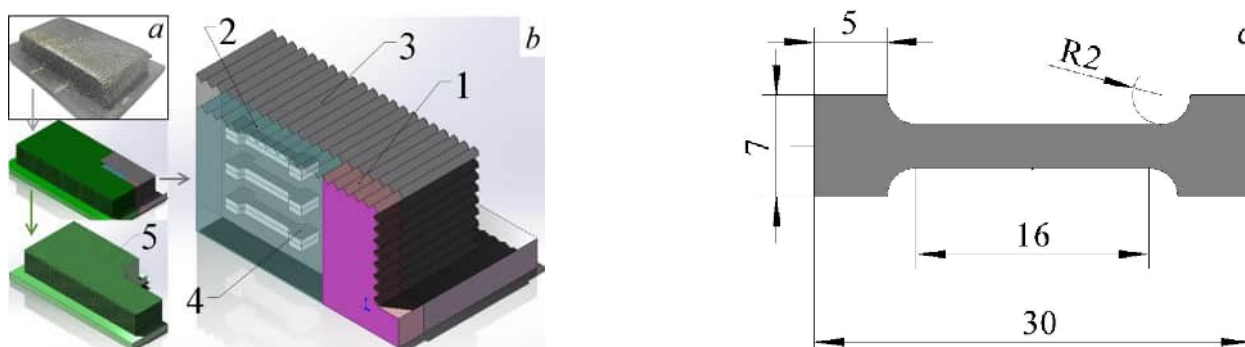
Fig. 2. Photograph of the *WAAM*-fabricated specimen (*a*), samples cut from the specimen (*b*), dimensions of 2 mm thick dog bone specimens, mm (*c*):

1 – for metallographic analysis, 2 – for tensile strength testing, 3 – for milling, 4 – dog bone specimens, 5 – for other analyses

The locations for metallographic observation, tensile test specimen selection, and hardness measurements were in the lower part of the *WAAM*-fabricated specimen (approximately 3 mm from the substrate) and in the upper part (approximately 3 mm from the top surface).

The specimen was milled on a *Concept Mill 155 CNC* milling machine (*EMCO*, Austria). A photograph of the milling setup is shown in Fig. 3, *a*. As illustrated in Fig. 3, *b*, a *Kistler 9257BA* (Switzerland) three-component dynamometer (**1**) was used to measure the three components of the milling force: the feed force **Fx = Ph**, acting along the feed direction s_m; lateral force **Fy = Pv**, acting normal to the s_m direction; axial force **Fz = Px**, acting along the cutter axis. In the *Kistler 9257BA* software, the directions of the **Fx**, **Fy** and **Fz** axes were aligned with the direction of forces acting during the axial turn process. Within the measured range, the dynamometer's sensitivity was 7.5 N, with a measurement error of ±0.005%.
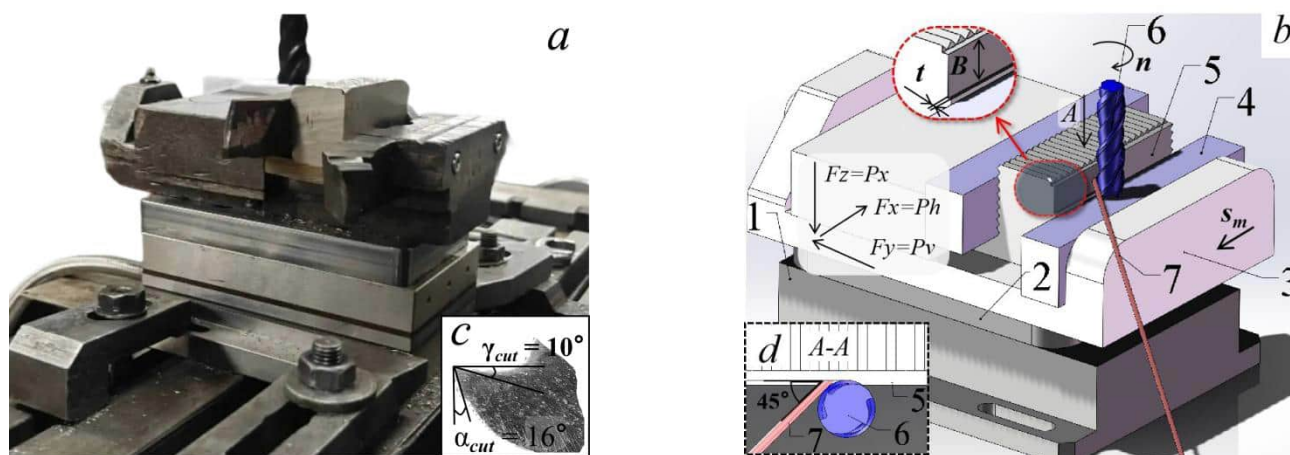
Fig. 3. Photograph (*a*), three-dimensional model (*b*) of dynamometer, cutter, specimen, cutter tooth geometry installed in the main section plane (*c*), and position of the infrared thermometer beam, specimen and cutter along *A* arrow. **B** – milling width, *t* – milling depth, *n* – rotational speed of a cutter, s_m – feed per minute (*d*)

A mounting plate (**2**) is used to secure the machine vice (**3**) to the dynamometer (**1**). A fixture (**4**), attached to the vice jaw (**3**), features a shallow longitudinal groove into which the specimen is inserted to prevent displacement of the 80×35×34 mm *WAAM*-fabricated or rolled specimen (**5**) relative to the vice jaws. The rolling direction of the specimen was aligned parallel to the feed direction s_m.

The end mill (**6**), with a 12 mm diameter, four teeth, and a 35° lead angle, was made of *VK10* hard alloy coated with an *AlTiN* layer applied by physical vapor deposition (*PVD*). The tool's face angle (γ_{cut}) and back angle (α_{cut}) are indicated in Fig. 3, *c*. The infrared beam path (**7**) from a *YCR-D2080AR* single-beam *IR* thermometer (*Wuxi Youtian Environmental Technology*, China) was oriented tangentially to the cutter,

forming a 45° angle with the machined surface (Fig. 3, *d*). The temperature measurement point *T* was set at the average height of the machined surface. The thermometer's emissivity was set to 0.39.

Surface roughness *Ra* was measured using a *TR200* profilometer (*JITA*, China) at the average height of the vertical machined surface (i.e., at the center of the milling width *B*). A *GP-304K* microscope (*KSGAOPIN*, China) was used to examine the machined surface. The reported values for the *Ph*, *Pv* and *Px* forces, the cutting temperature *T*, and the surface roughness *Ra* represent the average of three measurements.

The milling parameters are given in Table 3. These parameters, commonly used for conventional (non-CNC) milling machines, were selected to ensure practical relevance. In this work, conventional (up) milling was employed, a technique often used for machining rough surfaces with uneven topography, such as those typical of *WAAM*-fabricated specimens after deposition. The cutter overhang was maintained at 35 mm.

Ta b l e 3

Milling parameters

Parameters	Feed per minute s_m, mm/min	Rotational speed n, rpm	Milling width B, mm	Milling depth t, mm
Values	25, 50, 80, 125, 160, 200	315	7	1

Results and Discussion

The chemical composition of different regions in the *WAAM*-fabricated specimen is presented in Table 4. The carbon content in both the upper and lower regions is comparable to that of the initial wire. A slightly higher carbon content in the lower region is attributed to carbon diffusion from the substrate into the first (lower) deposited layer. The diffusion of iron (*Fe*), present in high concentration in the substrate, into the deposited layer also reduces the *Cr* and *Ni* content in the lower region of the specimen.

Ta b l e 4

X-ray microanalysis results for different regions of *WAAM*-fabricated specimen

Regions	Chemical composition, wt.%						
	Cr	*Ni*	*C*	*Si*	*Mn*	*Fe*	Other elements
Lower	17.86	8.02	0.18	0.31	1.3	70.21	2.12
Central	18.75	9.18	0.05	0.51	1.61	68.33	1.57
Upper	18.97	9.12	0.06	0.53	1.62	68.14	1.56

Based on the elemental composition of the austenitic stainless steel, Eqs. (1) and (2) [22] can be used to calculate the chromium (Cr_{eq}) and nickel (Ni_{eq}) equivalents, and Eq. (3) is used to determine the solidification mechanism in different regions of the *WAAM*-fabricated specimen. The different solidification mechanisms result in a different sequence of γ-ferrite and δ-austenite formation:

$$Cr_{eq} = \text{wt.\% } Cr + \text{wt.\% } Mo + 1.5 \times \text{wt.\% } Si + 0.5 \times \text{wt.\% } Nb \tag{1}$$

$$Ni_{eq} = \text{wt.\% } Ni + 0.5 \times \text{wt.\% } Mn + 30 \times \text{wt.\% } C + 30 \times \text{wt.\% } N \tag{2}$$

$$\text{Order } A \ (Cr_{eq}/Ni_{eq} < 1.25): L \rightarrow (L + \gamma) \rightarrow \gamma,$$

$$\text{Order } AF \ (1.25 < Cr_{eq}/Ni_{eq} < 1.48): L \rightarrow (L + \gamma) \rightarrow (L + \gamma + \delta) \rightarrow (\gamma + \delta),$$

$$\text{Order } FA \ (1.48 < Cr_{eq}/Ni_{eq} < 1.95): L \rightarrow (L + \delta) \rightarrow (L + \delta + \gamma) \rightarrow (\delta + \gamma),$$

$$\text{Order } F \ (Cr_{eq}/Ni_{eq} > 1.95): L \to (L + \delta) \to \delta \tag{3}$$

where Cr_{eq}/Ni_{eq} is the ratio of chromium to nickel equivalents.

Although Eq. (3) does not account for the cooling rate effect, it provides a reliable approximation [23]. The calculated Cr_{eq}/Ni_{eq} ratios for different regions of the *WAAM*-fabricated specimen are presented in Table 5.

Table 5

Cr_{eq}/Ni_{eq} ratio for different parts of *WAAM*-fabricated specimen

Regions	Cr_{eq}	Ni_{eq}	Cr_{eq}/Ni_{eq} ratio
Lower	18.32	14.07	1.30
Middle	19.51	11.49	1.70
Upper	19.77	11.73	1.69

The low *Ti* content was omitted from the calculations due to its negligible influence on the solidification mechanism. As shown in Table 5 and Eq. (2), solidification in the upper and central regions corresponds to order *AF*, while in the lower region it corresponds to order *FA*. This shift in solidification order in the lower region is caused by carbon diffusion from the substrate into the deposited layer, which stabilizes austenite.

The microstructure of the lower region of the *WAAM*-fabricated specimen is shown in Fig. 4, *a*. Vermicular ferrite is observed, which is typical for solidification order *AF* [22]. The initial ferrite content is low. Furthermore, carbon diffusion within the deposited layer is limited during the eutectic reaction due to the high cooling rate inherent to the deposition process, which is particularly rapid near the substrate. This further suppresses ferrite formation and reduces its content. Carbon atoms diffusing from the substrate into the deposited layer increase the carbon content in the lower region, thereby enhancing its hardness.

As seen in Fig. 4, *b*, the central region of the *WAAM*-fabricated specimen consists of ferrite with a dendritic morphology. Multiple thermal cycles in this region promote elemental diffusion that favors ferrite formation, resulting in increased ferrite thickness and the highest ferrite content [23].

Fig. 4, *c* shows the microstructure of the upper region. The limited number of thermal cycles provides insufficient diffusion of ferrite-promoting elements, leading to the formation of fine ferrite precipitates. Nevertheless, the overall ferrite content remains high. The fine and closely spaced ferrite impedes dislocation slip at phase interfaces, enhancing the hardness of this region. Concurrently, the limited thermal cycling results in insufficient remelting in the upper region, generating numerous pores that reduce hardness but increase ultimate elongation.

At the specimen periphery (Fig. 4, *d*), the microstructure is similar to that of the upper region. Both the ferrite content and hardness are comparable to the upper region and remain high. This microstructure is primarily attributed to a higher cooling rate. Furthermore, the peripheral area with distinct microstructural properties was of insufficient size to cut off standard-sized tensile specimens. Therefore, tensile testing was not performed on the peripheral material.

For the rolled specimen (Fig. 4, *e*), the ferrite is finer and its content is lower compared to the *WAAM*-fabricated specimen. The ferrite morphology is elongated along the rolling direction. The hardness of the rolled specimen is similar to that of the upper region and periphery of the *WAAM*-fabricated specimen. However, both the hardness and ultimate elongation of the rolled specimen are higher.

As shown in Table 6 and Fig. 5, the microstructure and mechanical properties of regions within the *WAAM*-fabricated specimen – excluding the lower region – exhibit certain variations. These variations are comparable to data reported for wire-feed electron beam additive manufacturing [10]. However, the differences are minor and do not significantly affect milling machinability. Consequently, the milling machinability of different specimen regions was not investigated separately. The lower region of the

a

b

c

d

e
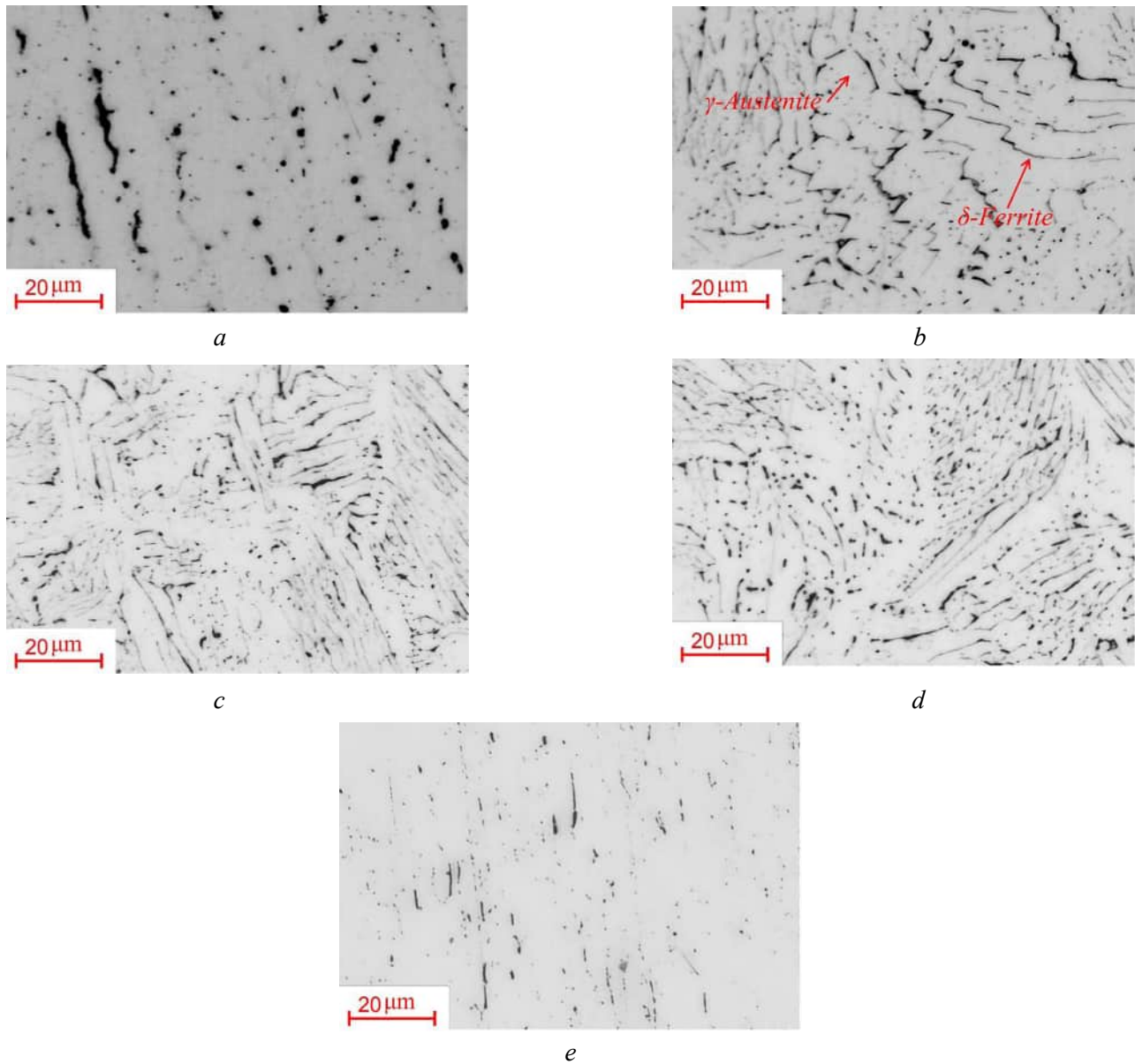
Fig. 4. Microstructure at lower (*a*), central (*b*), upper (*c*) and periphery (*d*) parts of *WAAM*-fabricated specimen and rolled specimen (*e*)

Table 6

Hardness and ferrite content in *WAAM*-fabricated and rolled specimens

	WAAM-fabricated				Rolled
	Lower region	Central region	Upper region	Peripheral region	
Hardness HV$_{0.1}$	226.7 ± 4.6	227.6 ± 5.3	231.4 ± 9.2	230.1 ± 4.1	230 ± 3.1
Ferrite content φ_δ, %	5.8 ± 1.4	17.56 ± 5.2	16.21 ± 4.8	15.89 ± 6.3	3.2 ± 1.2

specimen, along with the substrate, was removed by wire electrical discharge machining (*EDM*). As *EDM* falls outside the scope of this paper, the milling machinability of the lower region is not included in this study.

Fig. 6 shows the key parameters in a cross-sectional view of the cutter and workpiece (specimen) during conventional (up) milling. The values for s_m, n, *Ph* and *Pv* correspond to those defined in Fig. 3.
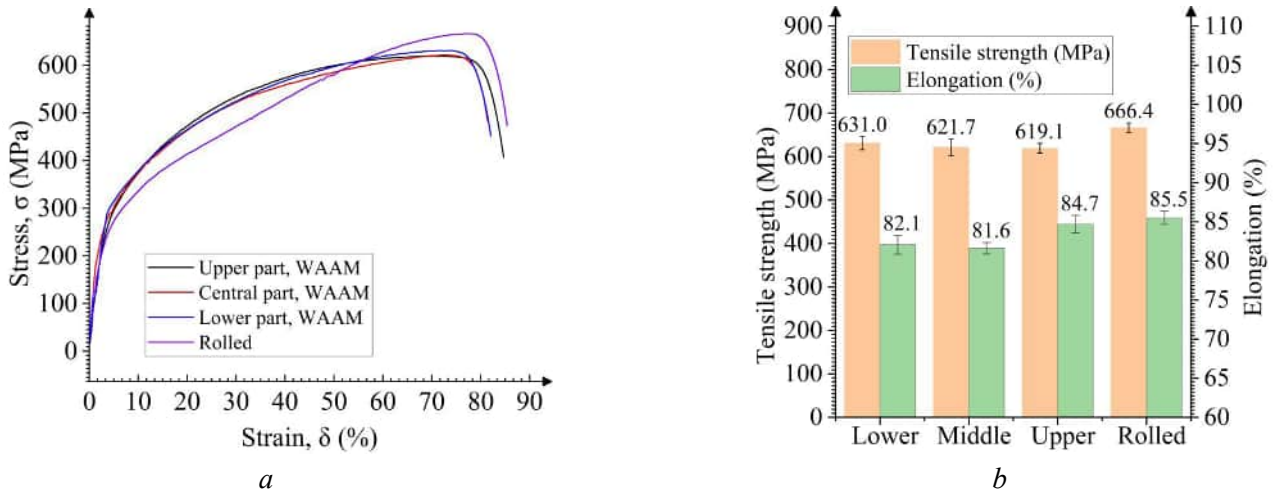
Fig. 5. Tensile stress-strain diagrams, ultimate tensile strength, and ultimate elongation of *WAAM*-fabricated and rolled specimens
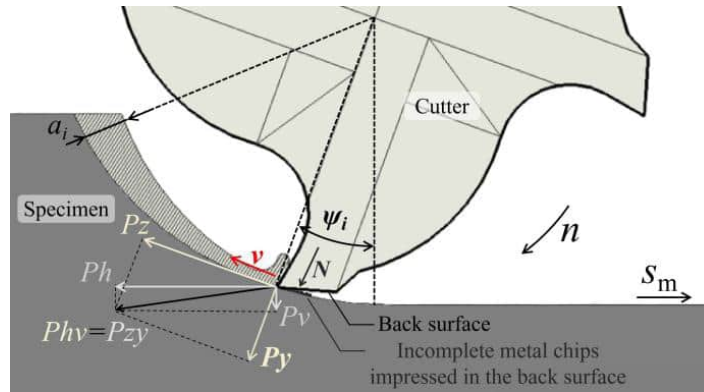
Fig. 6. Direction of forces P_h, P_v, P_z, and P_y in conventional milling

The engagement angle (ψ) indicates the angular position of the cutter tooth tip relative to its point of entry into the workpiece (specimen). The cutting speed is denoted by *v*, and the instantaneous thickness of cut by a_i. The tangential force (P_z) acts along the direction of the cutting speed, while the radial force (P_y) acts perpendicular to the cutter axis. P_z and P_y are derived from Eqs. (4) and (5) with minor simplification based on geometrical relations. The normal force (*N*), acting on the tool back surface, arises from the interference of uncut material with this surface and is a component of the radial force P_y.

$$P_z = P_h \times \cos \psi - P_v \times \sin \psi \qquad (4)$$

$$P_y = P_h \times \sin \psi + P_v \times \cos \psi \qquad (5)$$

The cutting speed *v*, thickness of cut a_i, tangential force P_z, and radial force P_y vary with the engagement angle ψ. The resultant force P_{hv} is derived from P_h and P_v, while P_{zy} is derived from P_z and P_y. These resultant forces are calculated as:

$$P_{hv} = \sqrt{\left(P_h^2 + P_v^2 \right)}, \qquad (6)$$

$$P_{zy} = \sqrt{\left(P_z^2 + P_y^2 \right)}. \qquad (7)$$

The total cutting force P_{tot} is calculated from:

$$P_{tot} = \sqrt{\left(P_h^2 + P_v^2 + P_x^2\right)}. \tag{8}$$

Fig. 7 shows the variation of these parameters with feed rate s_m. The feed per tooth s_t is obtained from:

$$s_t = s_m / (n \times z). \tag{9}$$

where $z = 4$ is the number of cutter teeth.

a

b
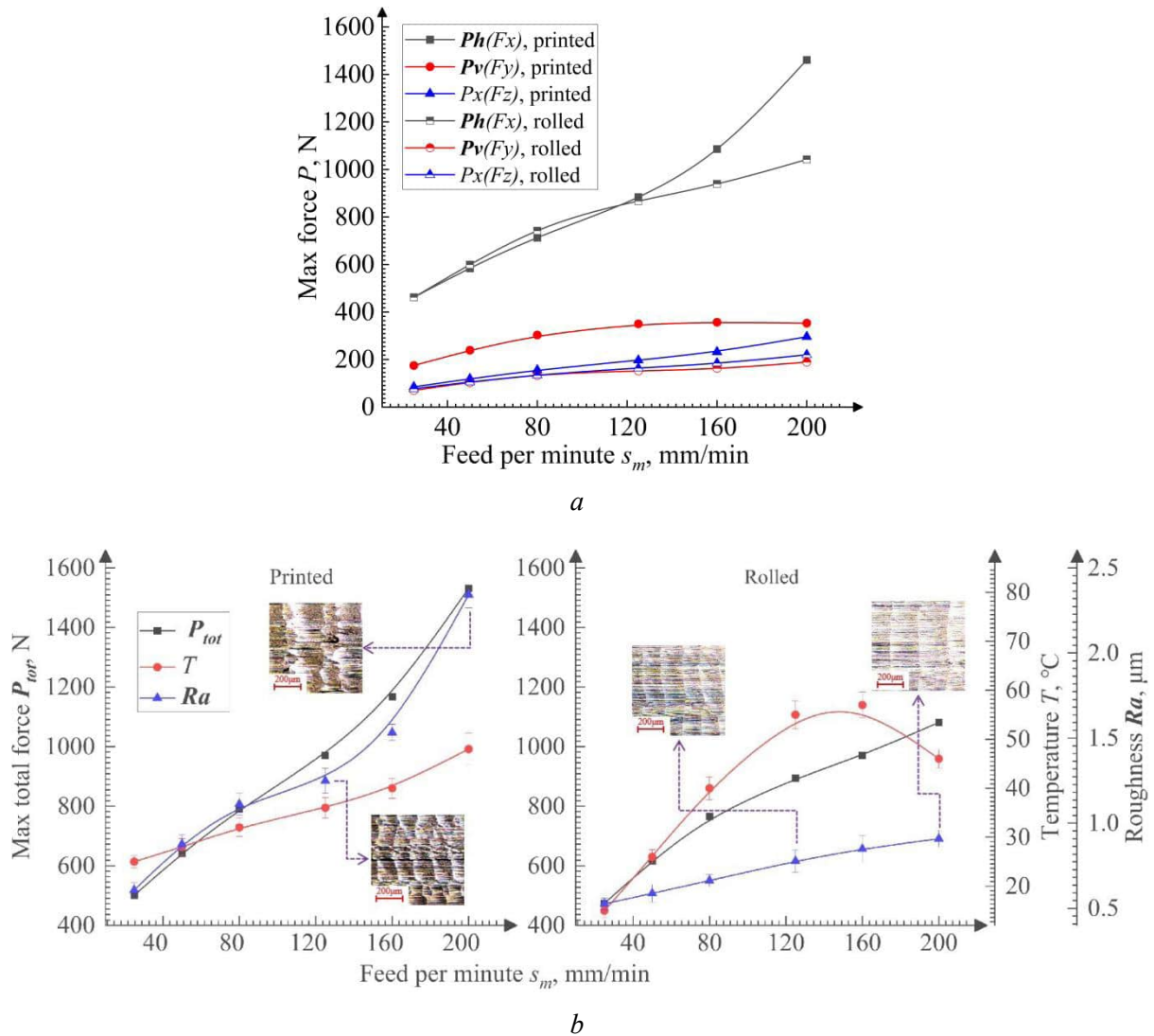
Fig. 7. Dependences of the feed rate s_m on the feed force Ph, lateral force Pv and axial force Px (*a*) and maximum resultant force P_{tot}, temperature T, and surface roughness Ra (*b*) during milling of fabricated and rolled specimens

Fig. 7, *a* shows the dependence of the feed force components P_h, P_v, and P_x on the feed rate s_m during milling of the *WAAM*-fabricated and rolled specimens. All force components increase with s_m due to the greater thickness of cut a_i. The feed force P_h is the largest and most sensitive to changes in s_m. This behavior is attributed to the use of conventional milling in this experiment, combined with a low depth of cut t (only 8.3% of the cutter diameter). In conventional milling, when the cutter tooth engages the workpiece, the resultant force P_{zy} acts primarily in the feed direction. The low depth of cut prevents significant changes in the direction of P_{zy} before the tooth exits the cut. Consequently, P_{zy} has the greatest influence on the feed force P_h [24], making P_h the largest and most sensitive component to variations in s_m. As a result, the total force P_{tot} follows a trend similar to P_h, albeit slightly exceeding it (Fig. 7, *b*).

The lateral force P_v is lower for the rolled specimen than for the *WAAM*-fabricated one. This is because less material is displaced beneath the cutting edge due to the higher tensile strength of the rolled material (see Fig. 5, *b*). This phenomenon is examined in greater detail in [25]. The cutting edge radius of a fresh tool ranges from 1 to 5 µm, depending on the hard alloy grain size and the face and back angles [26].

At high s_m values, the growth of P_h with further increases in s_m slows during milling of the rolled specimen, whereas this effect is not observed for the *WAAM*-fabricated specimen. The differences in P_v and P_h between the two materials can be explained by their distinct properties (Table 6, Fig. 5) and the effect of s_m on cutting temperature T (Fig. 7, *a*).

The lower hardness of the *WAAM*-fabricated specimen allows more material to be displaced beneath the rounded cutting edge. In the cutting and indentation zone, this material undergoes work hardening due to plastic deformation, increasing its yield strength. During elastic recovery of the machined surface, this hardened material contacts the tool back surface, generating a high normal force N and, consequently, a higher passive force P_v (Fig. 6) [27]. These two factors account for the elevated P_v during milling of the *WAAM*-fabricated specimen.

At low s_m, the cut thickness a_i is also small, promoting greater material displacement beneath the cutting edge and, as noted, leading to increased P_v and temperature.

At high s_m, the increased cut thickness facilitates material removal over the back surface and reduces indentation beneath the cutting edge, lowering the temperature. The significantly lower ductility of the *WAAM*-fabricated specimen also promotes chip fracture and removal, reducing the radial force on the face surface. This diminishes the elastic strain in the primary deformation zone and the subsequent elastic recovery against the back surface. According to *Das* and *Ghosh* [28], reduced contact lengths on both the face surface and back surface enhance heat dissipation and lower cutting temperatures. The absence of a slowdown in the increase of P_h at higher feed rates is due to the larger volume of material removed and the lower temperatures [13].

As shown in Fig. 8, *b*, surface roughness increases with feed rate (s_m). This relationship is explained in Figs. 8, *a* and 8, *b*: the higher feed per tooth (s_t) resulting from an increased s_m (see Eq. 9) leads to a greater height of the residual material protrusion (h_p, red areas in Fig. 8, *a*, *b*), which consequently increases surface roughness. Furthermore, surface roughness is higher for the *WAAM*-fabricated specimen than for the rolled specimen, with the difference becoming significant at higher s_m values. This difference is attributed to the lower hardness but higher yield strength of the *WAAM*-fabricated specimen, meaning it offers greater resistance to plastic deformation. Fig. 8, *c* shows the machined surface of the *WAAM*-fabricated specimen.
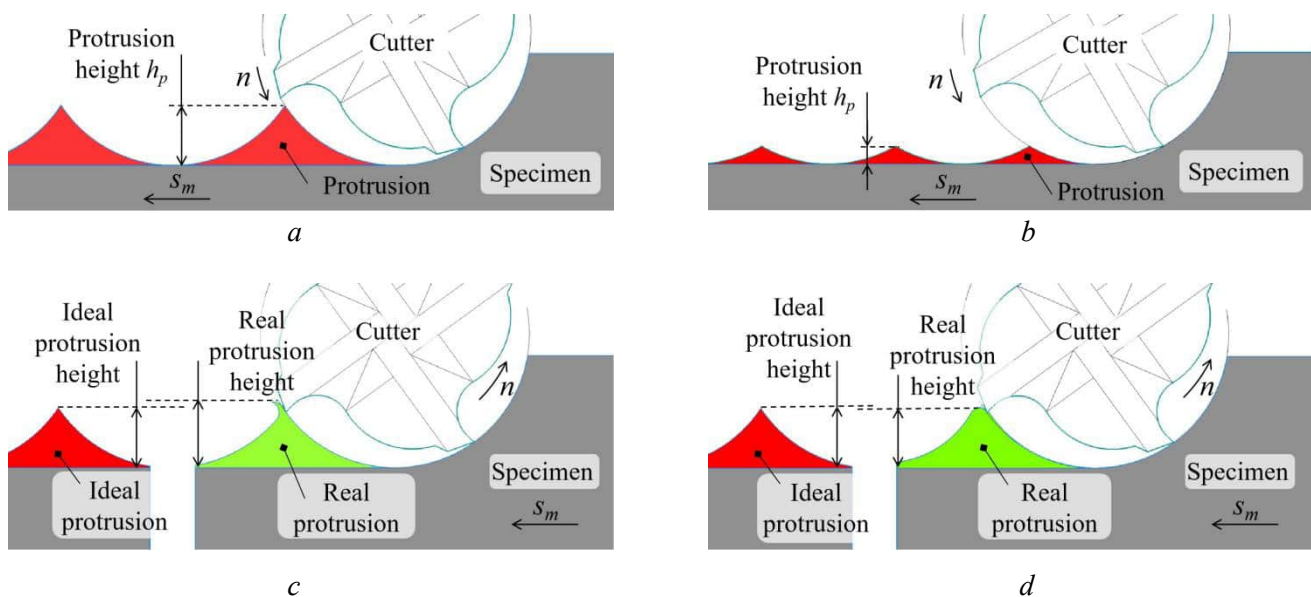
Fig. 8. Profiles of the machined surface at low (*a*) and high (*b*) feed per minute s_m and machined surface during opposing milling of *WAAM*-deposited (*c*) and rolled (*d*) specimens

The upper region of the protrusion is forced against the tool back surface due to the material's low hardness, undergoing severe plastic deformation. The lower region deforms less due to the higher yield strength. Consequently, in milling the *WAAM*-fabricated specimen, the protrusion height (h_p) is greater, resulting in higher surface roughness.

Conversely, the rolled specimen has higher hardness and lower yield strength, offering less resistance to plastic deformation. Its machined surface is shown in Fig. 8, *e*. The protrusion deforms more readily due to the lower yield strength, while less material is displaced beneath the tool back surface due to the higher hardness. Thus, in milling the rolled specimen, the protrusion height is smaller, leading to lower surface roughness.

The difference in protrusion height between the two materials becomes more pronounced with increasing feed rate, which correspondingly amplifies the difference in their surface roughness.

Conclusion

1. The lower region of the *WAAM*-fabricated *ER321* austenitic stainless steel specimen solidified according to order *FA*, influenced by the *Q235B* steel substrate.

2. A vermicular ferrite microstructure was observed in the lower region, while dendritic ferrite characterized the central and upper regions. The hardness (~230 HV0.1) was similar in all regions and comparable to that of the rolled specimen.

3. The ultimate tensile strength was below 631 MPa in all regions of the *WAAM*-fabricated specimen, compared to 666 MPa for the rolled specimen.

4. At low feed rates, the feed force was similar for both specimens. However, as the feed rate increased, the feed force became lower for the rolled specimen than for the *WAAM*-fabricated specimen due to thermal effects.

5. During milling, the surface roughness of the *WAAM*-fabricated specimen was higher than that of the rolled specimen, due to the former's combination of higher yield strength and lower hardness. This difference became more significant at higher feed rates, reaching approximately 1 μm.

References

1. Ahuja B., Karg M., Schmidt M. Additive manufacturing in production: Challenges and opportunities. *Proceedings of SPIE*, 2015, vol. 9353, pp. 11–20. DOI: 10.1117/12.2082521.

2. Altaf K., Abdul Rani A.M., Raghavan V.R. Prototype production and experimental analysis for circular and profiled conformal cooling channels in aluminium filled epoxy injection mould tools. *Rapid Prototyping Journal*, 2013, vol. 19 (4), pp. 220–229. DOI: 10.1108/13552541311323236.

3. Rozvany G.I. A critical review of established methods of structural topology optimization. *Structural and Multidisciplinary Optimization*, 2009, vol. 37, pp. 217–237. DOI: 10.1007/s00158-007-0217-0.

4. Sobczak J.J., Drenchev L. Metallic functionally graded materials: A specific class of advanced composites. *Journal of Materials Science & Technology*, 2013, vol. 29 (4), pp. 297–316. DOI: 10.1016/j.jmst.2013.02.006.

5. Klimenov V.A., Kolubaev E.A., Han Z, Chumaevskii A.V., Dvilis E.S., Strelkova I.L., Drobyaz E.A., Yaremenko O.B., Kuranov A.E. Modul' uprugosti i tverdost' titanovogo splava, sformirovavshegosya v usloviyakh elektronnogo luchevogo splavleniya pri EB-pechati provolokoi [Modulus of elasticity and hardness of titanium alloy formed under conditions of electron beam melting in EB wire printing]. *Obrabotka metallov (tekhnologiya, oborudovanie, instrumenty) = Metal Working and Material Science*, 2023, vol. 25, no. 4, pp. 180–201. DOI: 10.17212/1994-6309-2023-25.4-180-201.

6. Chen J., Wei H., Zhang X., Peng Y., Kong J., Wang K. Flow behavior and microstructure evolution during dynamic deformation of 316 L stainless steel fabricated by wire and arc additive manufacturing. *Materials & Design*, 2021, vol. 198, p. 109325. DOI: 10.1016/j.matdes.2020.109325.

7. Long P., Wen D., Min J., Zheng Z., Li J., Liu Y. Microstructure evolution and mechanical properties of a wire-arc additive manufactured austenitic stainless steel: Effect of processing parameter. *Materials*, 2021, vol. 14 (7), p. 1681. DOI: 10.3390/ma14071681.

8. Prakash K.S., Kannan A.R., Pramod R., Kumar N.P., Shanmugam N.S. Microstructure, mechanical properties and fracture toughness of SS 321 stainless steel manufactured using wire arc additive manufacturing. *Transactions of the Indian Institute of Metals*, 2023, vol. 76 (2), pp. 537–544. DOI: 10.1007/s12666-022-02713-3.

9. Chinakhov D.A., Akimov K.O. Formation of the structure and properties of deposited multilayer specimens from austenitic steel under various heat removal conditions. *Metals*, 2022, vol. 12 (9), p. 1527. DOI: 10.3390/met12091527.

10. Astafurova E.G., Panchenko M.Y., Moskvina V.A., Maier G.G., Astafurov S.V., Melnikov E.V., Kolubaev E.A. Microstructure and grain growth inhomogeneity in austenitic steel produced by wire-feed electron beam melting: The effect of post-building solid-solution treatment. *Journal of Materials Science*, 2020, vol. 55 (22), pp. 9211–9224. DOI: 10.1007/s10853-020-04424-w.

11. Khodabakhshi F., Farshidianfar M.H., Gerlich A.P., Nosko M., Trembošová V., Khajepour A. Effects of laser additive manufacturing on microstructure and crystallographic texture of austenitic and martensitic stainless steels. *Additive Manufacturing*, 2020, vol. 31, p. 100915. DOI: 10.1016/j.addma.2019.100915.

12. Thompson M.K., Moroni G., Vaneker T., Fadel G., Campbell R.I., Gibson I., Martina F. Design for additive manufacturing: Trends, opportunities, considerations, and constraints. *CIRP Annals*, 2016, vol. 65 (2), pp. 737–760. DOI: 10.1016/j.cirp.2016.05.004.

13. Babaev A.S., Kozlov V.N., Semenov A.R., Shevchuk A.S., Ovcharenko V.A., Sudarev E.A. Issledovanie sil rezaniya i obrabatyvaemosti pri frezerovanii poroshkovoi korrozionno-stoikoi stali, poluchennoi po tekhnologii pryamogo lazernogo vyrashchivaniya [Investigation of cutting forces and machinability during milling of corrosion-resistant powder steel produced by laser metal deposition]. *Obrabotka metallov (tekhnologiya, oborudovanie, instrumenty) = Metal Working and Material Science*, 2024, vol. 26, no. 2, pp. 38–56. DOI: 10.17212/1994-6309-2024-26.2-38-56.

14. Dabwan A., Anwar S., Al-Samhan A.M., AlFaify A., Nasr M.M. Investigations on the effect of layers' thickness and orientations in the machining of additively manufactured stainless steel 316L. *Materials*, 2021, vol. 14 (7), p. 1797. DOI: 10.3390/ma14071797.

15. Guo P., Zou B., Huang C., Gao H. Study on microstructure, mechanical properties and machinability of efficiently additive manufactured AISI 316L stainless steel by high-power direct laser deposition. *Journal of Materials Processing Technology*, 2017, vol. 240, pp. 12–22. DOI: 10.1016/j.jmatprotec.2016.09.005.

16. Milton S., Duchosal A., Chalon F., Leroy R., Morandeau A. Thermal study during milling of Ti6Al4V produced by Electron Beam Melting (EBM) process. *Journal of Manufacturing Processes*, 2019, vol. 38, pp. 256–265. DOI: 10.1016/j.jmapro.2018.12.027.

17. Kok Y., Tan X.P., Wang P., Nai M.L.S., Loh N.H., Liu E., Tor S.B. Anisotropy and heterogeneity of microstructure and mechanical properties in metal additive manufacturing: A critical review. *Materials & Design*, 2018, vol. 139, pp. 565–586. DOI: 10.1016/j.matdes.2017.11.021.

18. *Marochnik stali i splavov* [Database of Steels and Alloys]. Website, 2003–2025. Available at: https://www.splav-kharkov.com (accessed 17.10.2025).

19. Chen J., Wei H., Zhang X., Peng Y., Kong J., Wang K. Flow behavior and microstructure evolution during dynamic deformation of 316 L stainless steel fabricated by wire and arc additive manufacturing. *Materials & Design*, 2021, vol. 198, p. 109325. DOI: 10.1016/j.matdes.2020.109325.

20. Astafurov S., Astafurova E. Phase composition of austenitic stainless steels in additive manufacturing: A review. *Metals*, 2021, vol. 11 (7), p. 1052. DOI: 10.3390/met11071052.

21. Bajaj P., Hariharan A., Kini A., Kürnsteiner P., Raabe D., Jägle E.A. Steels in additive manufacturing: A review of their microstructure and properties. *Materials Science and Engineering: A*, 2020, vol. 772, p. 138633. DOI: 10.1016/j.msea.2019.138633.

22. Elmer J.W., Allen S.M., Eagar T.W. Microstructural development during solidification of stainless steel alloys. *Metallurgical Transactions A*, 1989, vol. 20, pp. 2117–2131. DOI: 10.1007/BF02650298.

23. Zheng B., Zhou Y., Smugeresky J.E., Schoenung J.M., Lavernia E.J. Thermal behavior and microstructural evolution during laser deposition with laser-engineered net shaping: Part I. Numerical calculations. *Metallurgical and Materials Transactions A*, 2008, vol. 39, pp. 2228–2236. DOI: 10.1007/s11661-008-9557-7.

24. Martyushev N.V., Kozlov V.N., Qi M., Tynchenko V.S., Kononenko R.V., Konyukhov V.Y., Valuev D.V. Production of workpieces from martensitic stainless steel using electron-beam surfacing and investigation of cutting forces when milling workpieces. *Materials*, 2023, vol. 16 (13), p. 4529. DOI: 10.3390/ma16134529.

25. Zhang Q., She L., Guo T., Kozlov V.N. [Calculation of stresses in the cutting tool at the beginning of cutting]. *Nauchnaya initsiativa inostrannykh studentov i aspirantov* [Scientific initiative of foreign students and postgraduates]. Collection of reports of the III International scientific and practical conference, Tomsk, 2023, pp. 450–456. (In Russian).

26. Kozlov V.N., Babaev A.S., Shults N.A., Semenov A.S., Shevchuk A.S. Study of a methodology for calculating contact stresses during blade processing of structural steel. *Metals*, 2023, vol. 13 (12), p. 2009. DOI: 10.3390/met13122009.

27. Gusarov A.V., Yadroitsev I., Bertrand P., Smurov I. Heat transfer modelling and stability analysis of selective laser melting. *Applied Surface Science*, 2007, vol. 254 (4), pp. 975–979. DOI: 10.1016/j.apsusc.2007.08.074.

28. Das C.R., Ghosh A. Performance of carbide end mills coated with new generation nano-composite TiAlSiN in machining of austenitic stainless steel under near-dry (MQL) and flood cooling conditions. *Journal of Manufacturing Processes*, 2023, vol. 104, pp. 418–442. DOI: 10.1016/j.jmapro.2023.09.020.

Conflicts of Interest

The authors declare no conflict of interest.

Obrabotka metallov –
Metal Working and Material Science

Mathematical analysis of the titanium alloy surface profile under various modes of electromechanical treatment

Mikhail Romanenko [1, a, *], Igor Zakharov [1, b], Vyacheslav Bagmutov [1, c], Vladislav Barinov [1, d], Minh Tuong Nguyen [2, e]

[1] Volgograd State Technical University, 28 Lenin Avenue, Volgograd, 400005, Russian Federation
[2] Russian Technological University MIREA, 78 Vernadsky Avenue, Moscow, 119454, Russian Federation

[a] https://orcid.org/0000-0002-4800-7151, romanenko.mihail2009@yandex.ru; [b] https://orcid.org/0000-0001-7177-7245, 4zaxap@gmail.com;
[c] https://orcid.org/0000-0003-3648-8450, sopromat@vstu.ru; [d] https://orcid.org/0000-0001-9400-7366, barinov@vstu.ru;
[e] https://orcid.org/0009-0004-7484-7009, nguen_m@mirea.ru

ARTICLE INFO

ABSTRACT

Introduction. Currently, many mathematical approaches exist for approximating surface profile curves. Most employ volumetric mathematical expressions to describe surface profile parameters after various types of processing. **Purpose of the work** is to select a mathematical apparatus that is simple enough from an engineering perspective to approximate the surface profile of *VT22* titanium alloy samples after surface plastic deformation (*SPD*) and various electromechanical processing (*EMP*) modes, with the possibility of eliminating random technological errors. **The paper investigates** the effect of *EMP* modes using alternating and direct current at densities of 100, 300, and 600 A/mm^2, considering both the application of force by the deforming tool-electrode (150 N) and its absence (10 N), on the surface geometry of *VT22* titanium alloy samples. The electromechanical processing of metal alloys used in this work can significantly change the geometric profile, structure, and operational properties of the surface. Its distinctive feature is the creation of both microdeviations (roughness) and macrodeviations and relief (waviness, "oil pockets", build-ups from metal surfacing to the repair size) on the surface. **Research methods.** Profilometric analysis was performed using a *PM-7* device, followed by processing of the roughness measurement results using the fast *Fourier* transform (*FFT*) on the surface of a cylindrical sample made of *VT22* titanium alloy with a diameter of 16 mm after electromechanical rolling with a tool-electrode, previously subjected to semi-finish turning. The error of the model curves of the surface profile was estimated using the *Pearson* correlation coefficient (*R*). **Results and discussion.** The use of high-density direct current helps to obtain a surface with a high relative support length of the profile (98.8%), a low arithmetic mean deviation of the profile (1.9 μm), and an average step of profile irregularities (56 μm). Based on the *FFT*, the considered modes of electromechanical processing contribute to the formation of profile waviness with different pitch and height. The greatest correlation is observed for modes 2, 4, and 9 (*R* > 0.7), while the lowest correlation coefficient was noted for *EMP* with a direct current density of 100 and 300 A/mm^2 (modes 5 and 6, *R* < 0.25).

Introduction

The ability to control the macro- and microgeometry of metal alloy surfaces following various processing methods is a critical objective throughout the entire lifecycle of machine components in mechanical engineering – from manufacturing and assembly to operation, such as ensuring durable contact interaction between surfaces.

---

* Corresponding author
Romanenko Mikhail D., Ph.D. (Engineering), Senior Lecturer
Volgograd State Technical University,
28 Lenin Avenue,
400005, Volgograd, Russian Federation
Tel.: +7 977 064-06-19, **e-mail:** romanenko.mihail2009@yandex.ru

The theory of technological inheritance plays a significant role in mechanical engineering in forming the required quality of a part's surface layer. In manufacturing, to achieve a specified set of surface properties, all operations and their respective technological stages are taken into account. Quantitative assessment typically employs empirical coefficients of inheritance, which include factors for their mutual influence [1–3].

High-energy surface treatment of metal alloys induces significant restructuring of the crystal lattice and microstructure, alters the stress-strain state, and modifies surface geometry [4–6]. For instance, electromechanical processing (*EMP*) using alternating current on steel alloys can reduce the arithmetic mean deviation of the profile (***R_a***) to 0.2–0.63 μm in a smoothing mode with a moving tool (roller). Using direct current can reduce Ra by a factor of 2–3 compared to the preceding value [7]. Direct current application, compared to alternating current, enables a higher degree of micro-roughness smoothing (eliminating "noise") [8]. According to [9–14], several surface hardening technologies can substantially improve surface micro-geometry parameters, for example, through high-speed plastic deformation (ultrasonic treatment [12–13]), local melting (laser treatment [13–14]), and positively impact the static and fatigue strength of metal alloys.

Applying mathematical models and methods allows for a detailed analysis of component surface profiles, identifying patterns in their geometry formation, and assessing the contribution of each technological operation to the final quality [15–22].

Most publications utilize combined models based on contact mechanics and fractal theory [15, 16], the geometry of hardening/cutting tools and *Hertz* theory [17, 18], regression and statistical models (linear and stepwise regression, pairwise correlation matrix, particle swarm optimization), discrete *Fourier* transform, and machine learning [19–22].

The purpose of this work is to determine the principal components of the surface profile geometry and to identify the patterns of microgeometry formation on a *VT22* alloy sample subjected to various electromechanical processing (*EMP*) modes using mathematical processing of discrete signal data (fast *Fourier* transform).

To achieve this purpose, the following ***research tasks*** were defined:

1) Prepare a sample from *VT22* titanium alloy and strengthen it according to specified processing modes.

2) Obtain surface profiles and key roughness parameters using an "*ABRIS PM7*" profilograph-profilometer.

3) Perform *FFT* analysis to obtain the main harmonics of the surface profile for each processing mode.

4) Construct model curves of the surface profile for each mode.

5) Classify the model curves and their harmonics according to the type of longitudinal surface profile deviation.

6) Use the correlation coefficient to identify the electromechanical processing (*EMP*) and surface plastic deformation (*SPD*) modes that most accurately represent the surface profile of the sample.

Methods

Cylindrical sample preparation through turning (final diameter 16 mm) and subsequent electromechanical processing (*EMP*) was performed on a *16K20* lathe (Fig. 1). Machining was conducted at a minimum feed rate of 0.125 mm/rev, with two sequential passes removing a 0.2 mm layer from the diameter.

The process of setting up and adjusting the devices for electromechanical treatment is described as follows.

The titanium sample (**1**) is secured in the chuck jaws (**2**). The tailstock quill (**3**) with the current collection unit (**4**) and a centering cone is advanced toward the sample (**1**).

The spring-loaded *EMP* device (**6**) is clamped with the bolts of the tool holder (5) through current-insulating gaskets. The tool-electrode (**7**) is manually brought into contact with the sample with the required force (calibrated via the device's spring).

The coolant supply tube (**8**) is attached to the tool holder (**5**), and power cables with terminals (**9**) are connected to the current collection unit (**4**) and the *EMP* device (**6**). A coolant collection container (**10**) is positioned beneath the processing zone.
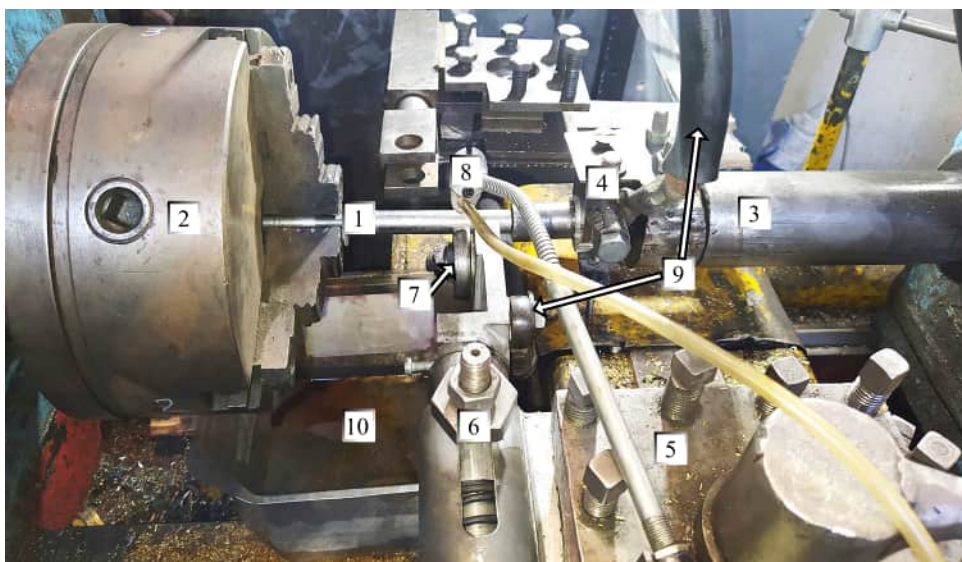
Fig. 1. Schematic of the experimental device for conducting *EMP* on a *16K20* lathe. Key components:

1 – titanium workpiece; 2 – chuck; 3 – tailstock quill; 4 – current collection device; 5 – toolholder; 6 – device for *EMP*; 7 – tool-electrode (roller); 8 – coolant supply tube; 9 – power cables with tips; 10 – container

Electromechanical processing involves passing a high-density electric current through the small contact area between the working tool and the part surface (Fig. 2), with continuous coolant (technical water) supply. This process is characterized by: high local heating and cooling rates (10^5–10^6 $^{\circ}$C/c), high current density (up to 1,500 A/mm²), and low voltage (2–6 V). Coolants used include machine oil, specialized emulsions (as in turning/milling), and technical water for achieving hardened microstructures [23].
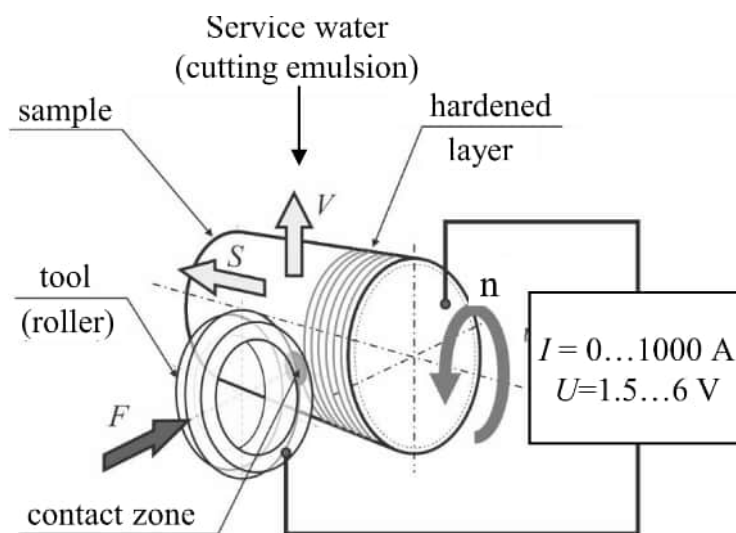
Fig. 2. Schematic of electromechanical processing

Constant parameters for both alternating current (*AC*) and direct current (*DC*) *EMP* were: Longitudinal feed (0.4 mm/rev), rotating frequency (13 rpm).

The tool-electrode was a toroidal roller made of *VK6C* hard alloy (94% *WC*, 6% *Co*) with a 60 mm diameter and a 5–6 mm profile radius. Variable mode parameters are summarized in Table 1.

For all modes, the initial surface was the semi-finish turned surface. Higher initial roughness does not qualitatively improve with additional *EMP* passes [23]. Current densities exceeding 600 A/mm² (regardless of type) were excluded as they caused surface burning and cavity formation. Low current density *EMP*

T a b l e   1

Electromechanical treatment modes with alternating and direct current

Mode No.	1	2	3	4	5	6	7	8	9	10
Parameters of *EMP*										
Current density, A/mm²	–	–	$\overline{600}$	$\widetilde{600}$	$\widetilde{100}$	$\widetilde{300}$	$\widetilde{600}$	$\widetilde{100}$	$\widetilde{300}$	$\widetilde{600}$
Tool pressing force, N	–	150	10	10	150	150	150	150	150	150

Note: mode 1 represents the initial state after turning. The symbol "~" denotes alternating current, "–" denotes direct current.

(100 A/mm²) is recommended for surface smoothing without altering microstructure or hardness [23]. Tool-electrode forces below 10 N were deemed impractical, as they prevented reliable contact and led to micro-arcing.

Surface roughness parameters were measured five times per processing mode using an *ABRIS PM-7* profilometer-profilograph.

The fast *Fourier* transform (*FFT*) was employed to determine the duration of periods and amplitude-phase characteristics of height and step irregularities. This method decomposes the original discrete profile signal into a series of harmonic (spectral) components – sinusoids defined by amplitude, phase, and frequency, ordered by magnitude [24].

For constructing predictive models, a general equation (1) describes the dynamics of the studied parameter.

When constructing predictive models of various quantities, a general equation (1) is used to determine the dynamics of the studied quantity: $D(t)$

$$D(t) = T(t) + C(t) + R(t),\tag{1}$$

where $T(t)$ is the main trend; $C(t)$ is the cyclical component; $R(t)$ is the random component ("noise").

The primary equation (2) for constructing the time series y_t, incorporating harmonics identified via *FFT*, is:

$$S(t) = \frac{a_0}{2} + \sum_{i=1}^{n}\left(a_i \cos\frac{2\pi}{T_i}t + b_i \sin\frac{2\pi}{T_i}t \right) = \frac{a_0}{2} + \sum_{i=1}^{n} c_i \sin\left(\frac{2\pi}{T_i}t + \varphi_i \right),\tag{2}$$

where a_0 is the constant component (zero harmonic); $c_i = \sqrt{a_i^2 + b_i^2}$ is the amplitude of the *i*-type harmonic; $T_i = N / i$ is the period of the *i*-type harmonic oscillation; N is the number of original data in the time series; a_i, b_i are the *Fourier* time series coefficients [24].

FFT and graph construction were performed in *Microsoft Excel*. The analyzed data series was limited to 2,048 points due to the *FFT* requirement for data length to be a power of two (2^{11} = 2,048). Subharmonics were selected based on *Pearson's* correlation coefficient, maximizing its value for each specific case – a method aligned with prior work [25]. A maximum of five harmonics were used in the equations describing the time series.

Following established literature [26], macro- and micro-deviations of a part's longitudinal surface profile are classified by the ratio of the step length to the height of the protrusion (*l/H*):

Macro-deviation: *l/H* ≥ 1,000

Waviness: 50 ≤ *l/H* ≤ 1,000

Roughness: 0 ≤ *l/H* ≤ 50

A diagram illustrating these scale levels of longitudinal profile deviations is shown in Fig. 3. These ratios were used to classify the model curves by their deviation scale.

A diagram explaining the difference in scale levels of profile deviations of longitudinal sections is presented in Fig. 3.
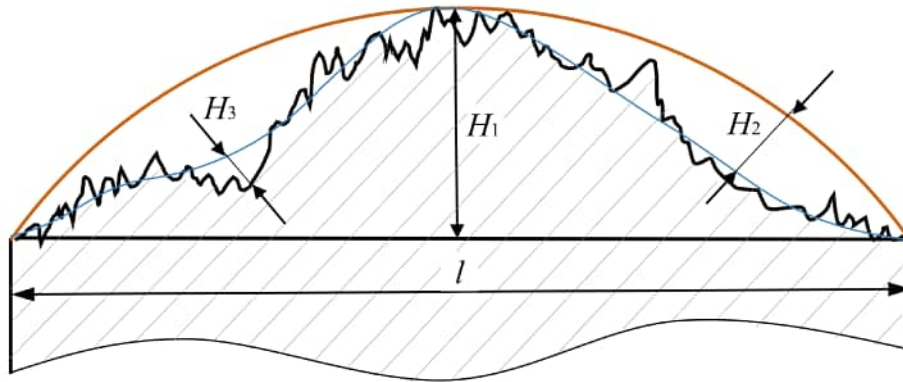
Fig. 3. Scheme of differentiation of surface quality parameters of parts:

H_1 – shape deviation (barrel shape), H_2 – surface waviness (second-order shape deviation), H_3 – surface roughness (third-order shape deviation, microroughness), l – base length

These ratios were used to classify the model curves by their deviation scale.

Results and Discussion

Electromechanical processing (*EMP*) of a *VT22* titanium alloy sample under eight distinct modes yielded surfaces with varied macro- and micro-geometric parameters and discoloration (Fig. 4).
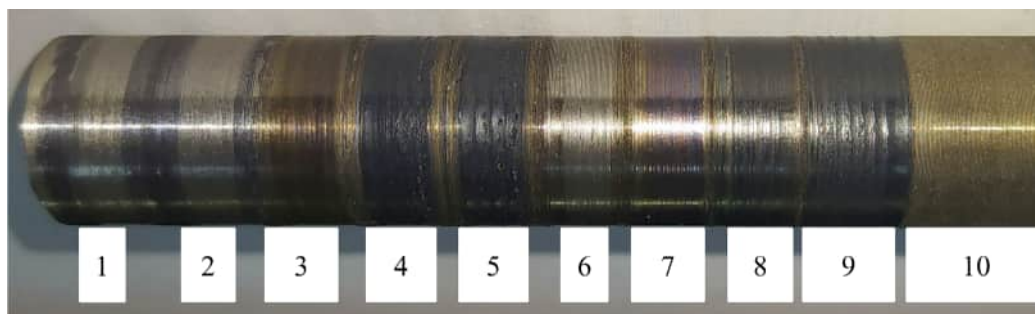
Fig. 4. Micrographs showing the surface morphology of *VT22* titanium alloy sample following different electromechanical processing (*EMP*) modes. Modes:

1 – 150 N; 2 – $\widetilde{100}$ A/mm², 150 N; 3 – $\widetilde{300}$ A/mm², 150 N; 4 – $\widetilde{600}$ A/mm², 10 N; 5 – $\widetilde{600}$ A/mm², 150 N; 6 – $\overline{100}$ A/mm², 150 N; 7 – $\overline{300}$ A/mm², 150 N; 8 – $\overline{600}$ A/mm², 10 N; 9 – $\overline{600}$ A/mm², 150 N; 10 – initial (conventional turning, feed: 0.125 mm/rev)

The reference state was the initial surface after semi-finish turning, with the following roughness parameters: R_a = 12.42 μm; S_m = 128 μm; t_{60} (60%) = 44.7%. The section level of the profile's support length was chosen to be 60%. The arithmetic mean deviation of the profile (R_a) was used as the primary height parameter due to its informativeness. Surface processing analysis revealed that modes No. 3, 7, and 9 were optimal in terms of height, step, and structural surface layer parameters (Fig. 5).

The mode of electromechanical smoothing (*EMS*) with high-density direct current (600 A/mm², **Mode 3**) reduced the indicators: R_a by a factor of 6.52, S_m by a factor of 1.27, and t_{60} increased by a factor of 2.21.

EMP with direct current of the same density with a pressing force of 150 N (**Mode 7**) reduced R_a, S_m by factors of 4.43 and 2.28, respectively, and practically doubled the t_{60}.

Alternating current with a density of 600 A/mm² during *EMP* (**Mode 10**) resulted in the appearance of secondary roughness due to the higher amplitude of AC compared to **Mode 9** [8], while the step parameter (S_m) for these modes decreased by 6%, and the t_{60} parameter increased by 1.58 times (Fig. 5).

Rolling without current (**Mode 2**) and *EMS* with low current density (100 A/mm²) using either *AC* (**Mode 5**) or *DC* (**Mode 8**) did not qualitatively alter the surface profile (Fig. 5).

Despite the low processing speed and low deformation force (10 N) in **Modes 3** and **4**, R_a decreased significantly (to 1.9 µm) and t_{60} increased to 98.8% (Figs. 5 and 6, **Mode 3**), a similar effect was observed in the prior research [27].
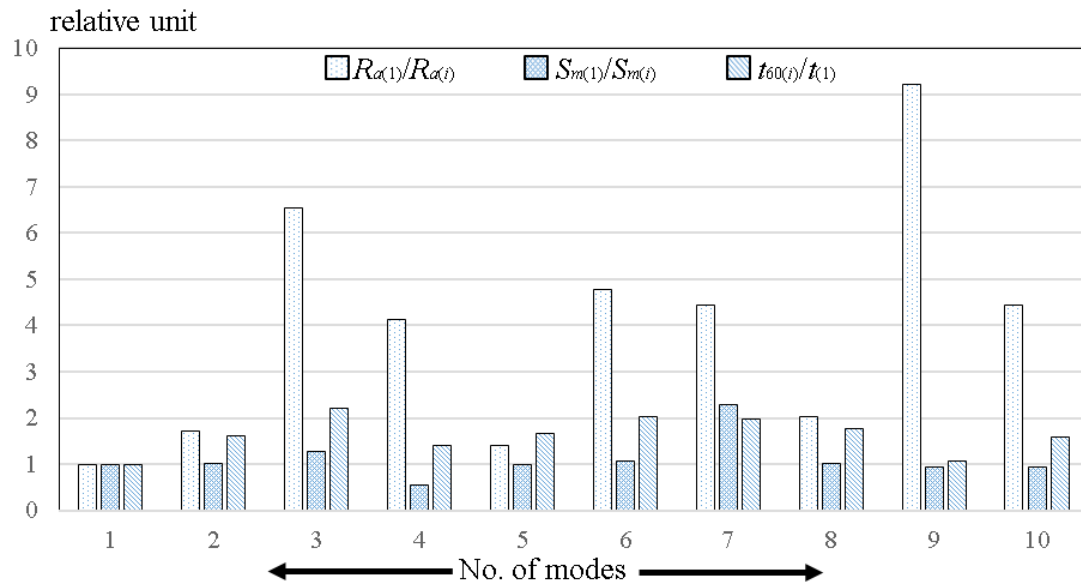
Fig. 5. Comparison of different processing modes (1–10) for three types of roughness parameters (R_a, S_m, t_{60})
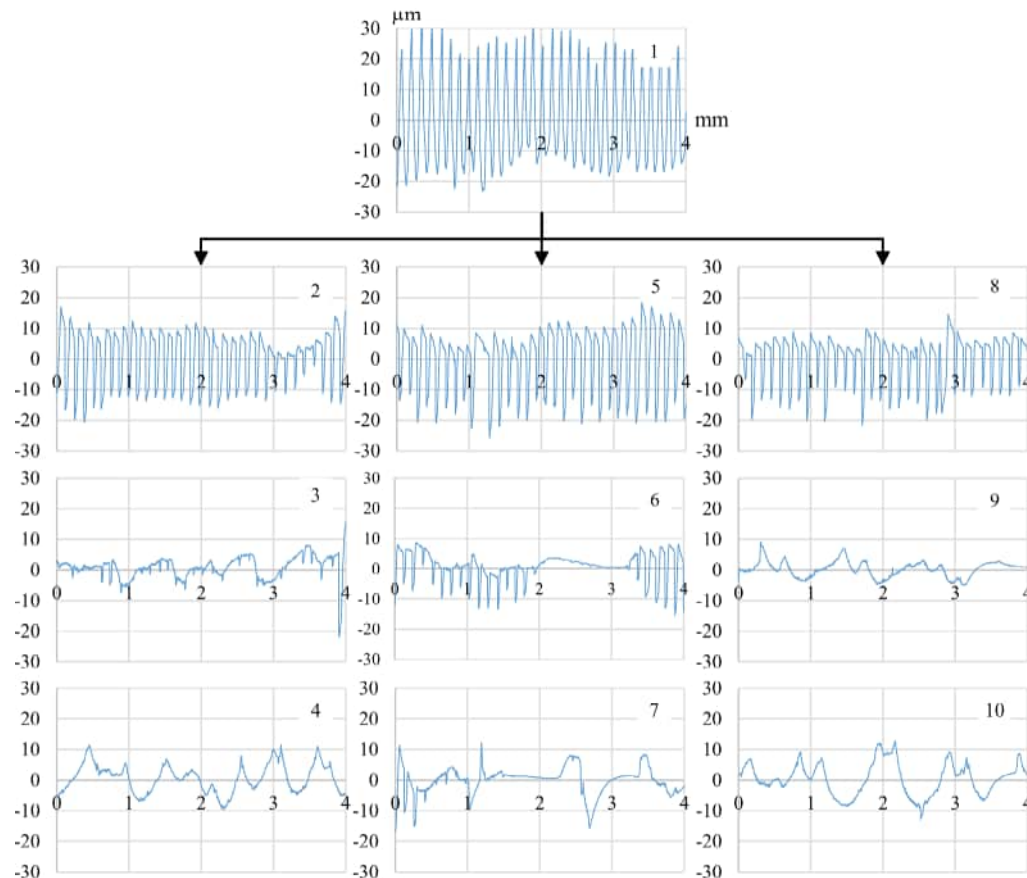
Fig. 6. The surface layer profilograms of titanium alloy after different processing modes (1–10)

Profilogram analysis (Fig. 6) indicated that *AC*-based processing promotes pronounced waviness and a high-rigidity profile (Fig. 6, **Mode 10**). *DC* causes greater heating of the initial micro-protrusions from turning, reducing their deformation resistance and minimizing vibration during smoothing (Fig. 6, **Mode 7**) [8]. *EMP* with *DC* of 300 A/mm² showed partial technological inheritance of the semi-finish turning profile (Fig. 6, **Mode 6**).

Profiles from **Modes 4** and **7**, despite their concave shape and lower rigidity, and load-bearing capacity, possess adequate oil retention and can be suitable for specific friction pair applications [7, 8].

Applying the fast Fourier transform (*FFT*) yielded characteristic profilograms representing the main amplitude-frequency components of the discrete signal, excluding subharmonic "noise" (Fig. 7, **Modes 1–10**).
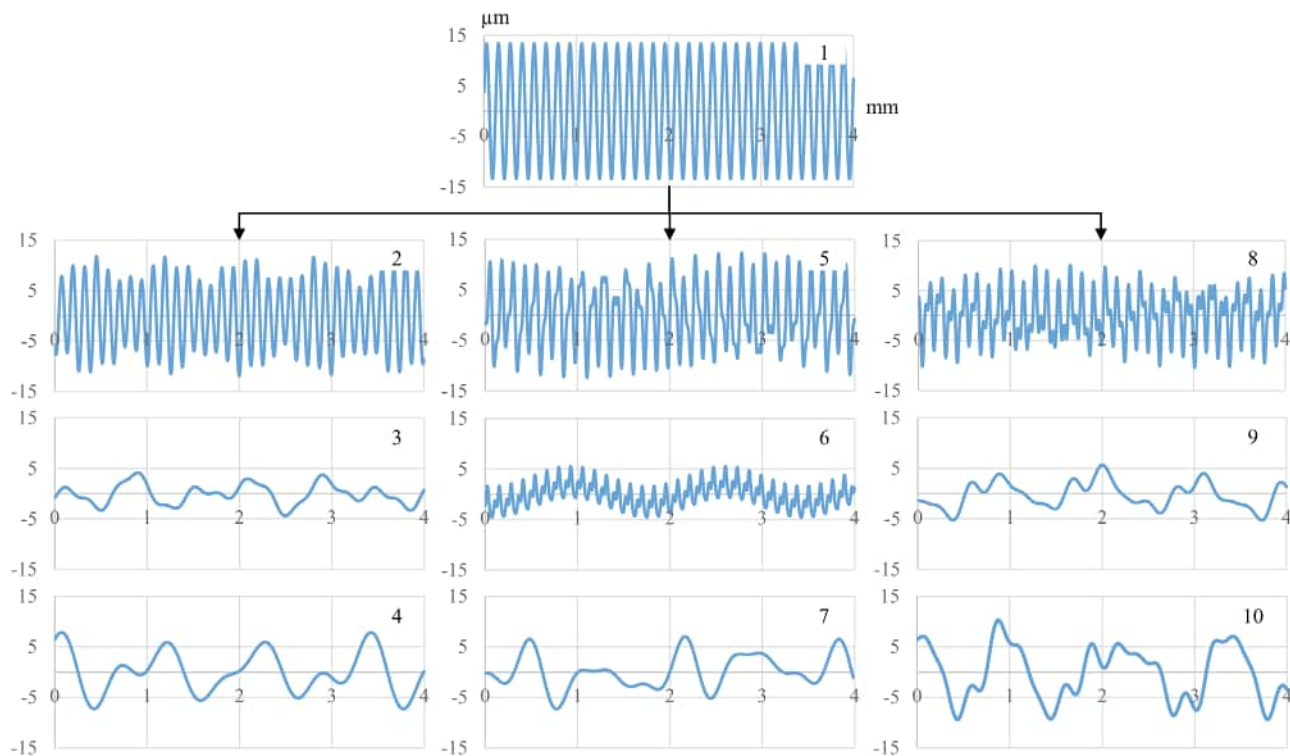
Fig. 7. The surface model profilograms of titanium alloy *VT22* after *FFT* by fundamental harmonics

For the initial state and modes involving simple running-in or low-current-density processing (100 A/mm²), the dominant harmonic corresponds to the semi-finish turning (Fig. 7, **Modes 1, 2, 5, 8**).

EMP with high current density (**Modes 3-4, 6-7, 9-10**) generated profiles with a prominent low-frequency component and smoother irregularities (reducing R_a by up to 9.2 times and S_m by 2.28 times). Fig. 7 shows that increasing current density during *EMP* suppresses high-frequency profile components, giving rise to a dominant ("carrier") frequency.

Fig. 8 presents the curves of relative bearing surfaces for different levels of *P* **Modes 1–10**. Based on these curves, microprofiles are classified as:

Low-rigidity: **Modes 1–6**

Medium-rigidity: **Modes 8** and **9**

High- rigidity: **Modes 7** and **10.**

For applications requiring reliable interference fits (resistant to premature loosening from asperity crushing) and low wear in friction pairs, *DC EMP* at 300 or 600 A/mm² – in either smoothing (10 N) or deformation (150 N) modes – is recommended. The improvement stems from increased actual contact area [26].

The strength of the interference fit and the tightness of the connections are achieved due to larger actual contact support areas [26].
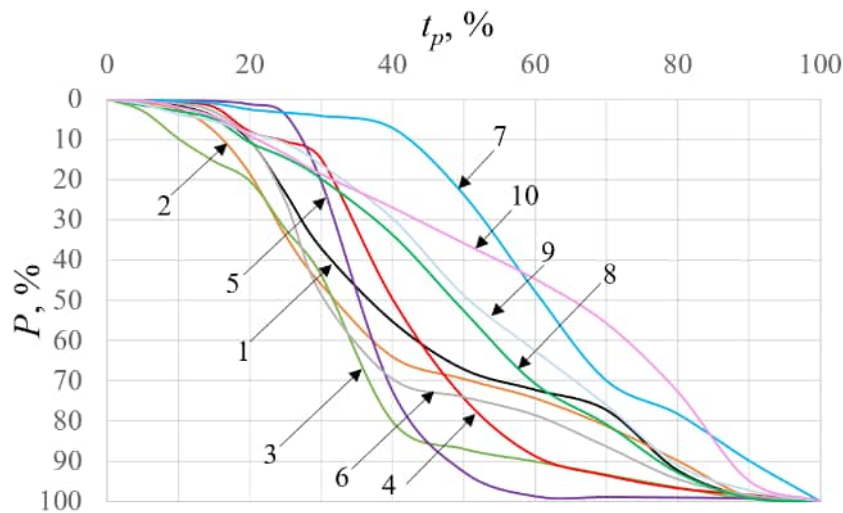
Fig. 8. Profile reference line curves for modes 1–10

For example, model surface profile curves for **Modes 2**, **4**, and **5** are decomposed into their constituent harmonics (Figs. 9, *a–f*).

As shown in Fig. 9, *d*, it is evident that despite the plastic deformation of the surface by the roller, the prevailing period remained the feed rate of the cutter during semi-finishing, i.e., 0.125 mm.

For *DC EMP* with a current density of 600 A/mm² (Fig. 9, *e,* Fig. 6, 9*,* **Mode 7**), the main harmonic shifts toward longer periods, indicating profile waviness. The large roller radius caused overlapping processing tracks, which broadened (blurred) the main peak in the spectrogram (Fig. 9, *e*). A similar effect is observed for **Mode 10** (Fig. 9, *f*), where a minimum of five harmonics were required to achieve a visually accurate fit to the original profilogram and the highest correlation coefficient (Fig. 9, *c*).

To classify the scale of longitudinal profile deviations for the model curves, the ratio of the step length to the height of the protrusion (*l*/*H*) was calculated for each mode and harmonic (Fig. 10).
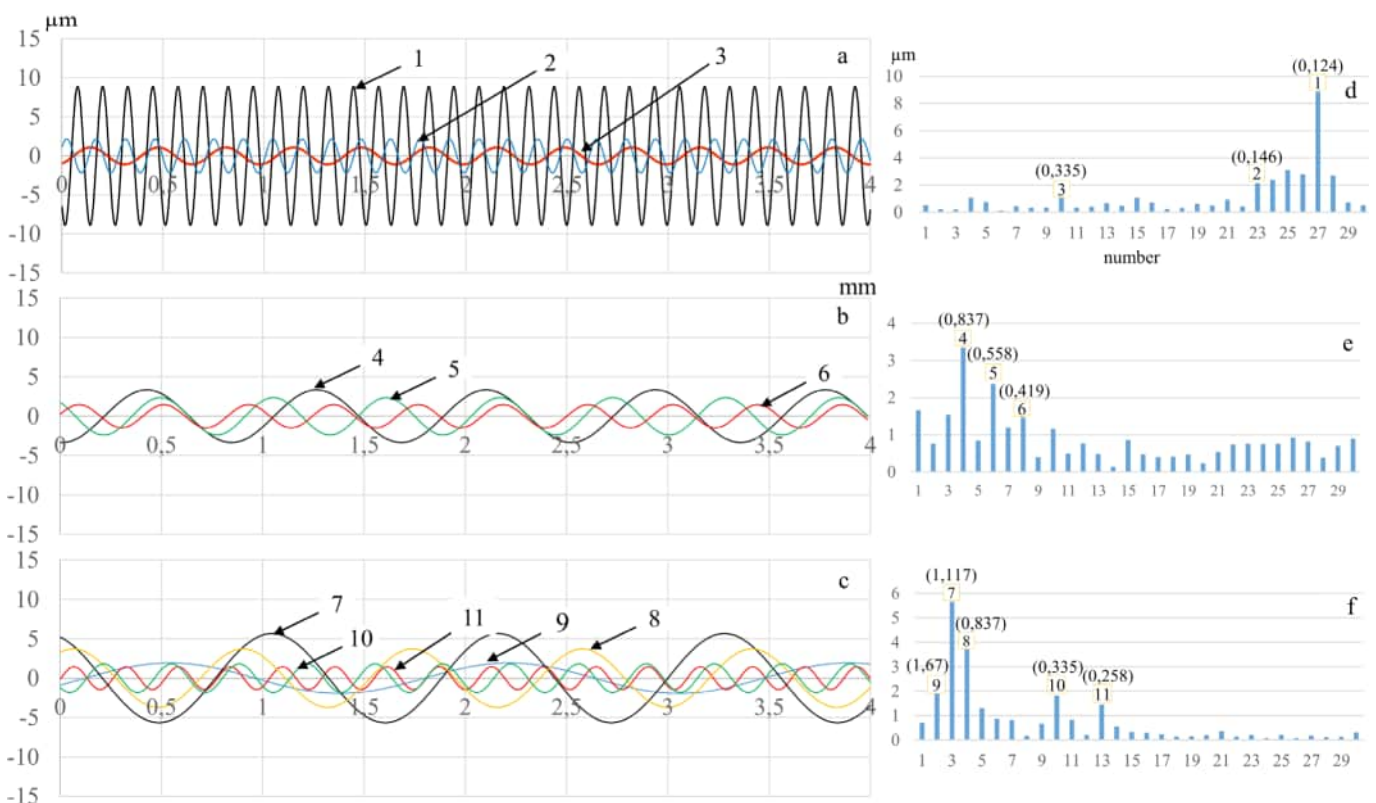
Fig. 9. Example of harmonic decomposition of model surface profile curves for modes 2, 7, and 10 (*a–c*). Numbers in *a–c* indicate harmonics (in order of decreasing amplitudes), *d–e* – spectrograms (periods are indicated in brackets)
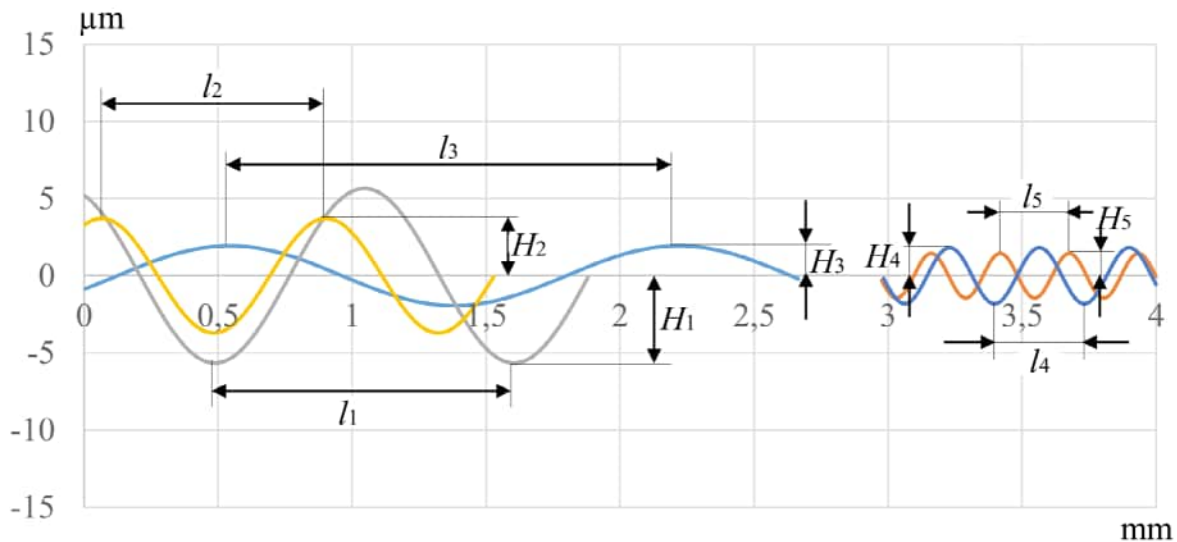
Fig. 10. Example of a diagram for determining the type of deviation of the longitudinal profile

Fig. 10 illustrates the determination of the *l/H* ratio and the corresponding deviation scale using five harmonics from **Mode 10** as an example.

The *l/H* ratios calculated for all processing modes of the *VT22* titanium alloy sample are presented in Fig. 11.

Harmonics corresponding to surface roughness are evident in **Modes 1**, **2**, **5**, **6**, and **8** (Fig. 11). These are inherited from the preceding semi-finish turning operation (0.125 mm/rev feed rate) and persist on the profilograms (Fig. 6) due to the weak thermomechanical impact of the working tool under these conditions. In contrast, these roughness-related harmonics are entirely absent in modes processed with higher current densities (**Modes 3**, **4**, **7**, **9**, and **10**), regardless of current type (Fig. 11). The lowest *l/H* ratios were recorded for **Modes 5** and **8**.

As noted in prior studies [7, 8, 28], surface engineering technologies such as vibro-rolling and electromechanical processing can create specific micro-reliefs designed to enhance lubrication. This is achieved by forming artificial micro-wedges between friction pairs, which can initiate a hydrodynamic lubrication effect. For instance, electromechanical processing was shown to increase the wear resistance of Steel 45 (0.45% *C*) and *VT22* titanium alloy by factors of 5 and 100, respectively, compared to their initial states. This significant improvement is attributed to the formation of oil-retaining pockets and a high-strength surface layer [29, 30].
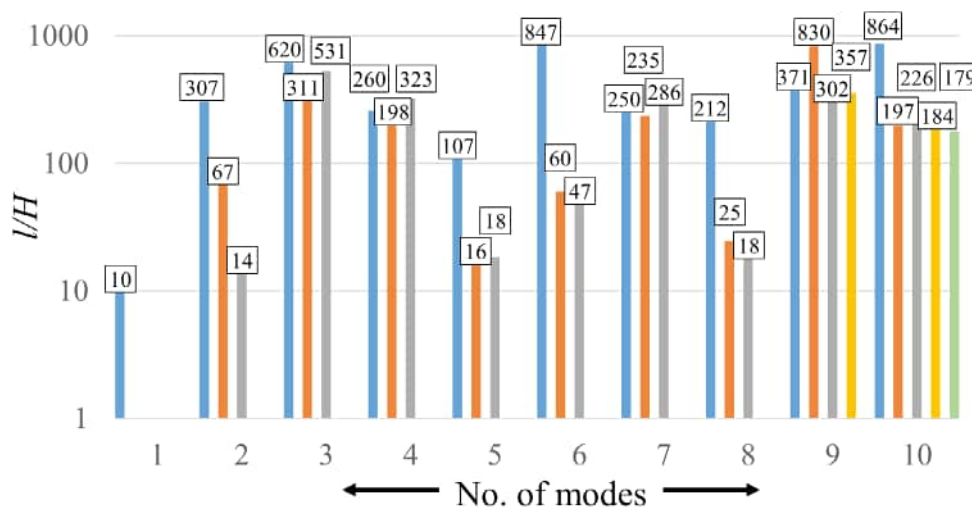
Fig. 11. Diagrams of the *l/H* ratio of modes 1–10 (the numbers above the columns are the *l/H* harmonic values). Note: the ordinate axis is given on a logarithmic scale

Analysis of the correlation coefficients (Table 2) reveals a strong correlation ($R \geq 0.7$) for the surface layer hardened by roller tool processing (**Mode 2**) and for electromechanical smoothing/processing with alternating current (**Modes 4** and **9**). A moderate correlation ($0.5 \leq R \leq 0.7$) is observed for **Modes 1** and **3**.

T a b l e   2

Correlation coefficients between experimental data and model profile curves

Mode No.	1	2	3	4	5	6	7	8	9	10
Correlation coefficient $|R|$	0.57	0.71	0.51	0.73	0.20	0.23	0.37	0.26	0.74	0.40

In contrast, a weak correlation between the model curves and experimental data is found for *EMP* using direct current with a 150 N force at densities of 100, 300, and 600 A/mm² (**Modes 5**, **6**, **7**), as well as for alternating current *EMP* at 100 and 600 A/mm² with the same force (**Modes 8** and **10**).

The low correlation coefficient for **Mode 5** may result from spectral amplitudes falling into adjacent frequencies, which can distort or mask lower-amplitude peaks [31]. The authors attribute the small R-value for **Mode 6** to the absence of a distinct cyclic component over more than one-third of the profile length, indicating the limited sensitivity of this mathematical approach to localized signal variations.

Optimum interference fits for movable joints require surfaces with low height parameters. High-profile asperities promote premature loosening and wear via plastic deformation, compromising joint sealing and accelerating corrosion [32]. Furthermore, increasing the bearing length ratio (t_p) and mean spacing of profile irregularities (S_m) reduces the friction coefficient and enhances wear resistance. A high S_m combined with a low R_a significantly mitigates the stress-concentrating effect of surface irregularities, thereby improving fatigue strength and durability [33].

Proper selection of *EMP* and *SPD* modes, coupled with precise process control and analytical techniques like *FFT*, enables the production of high-quality surface profiles. This approach minimizes artifacts from sample vibration, fluctuating contact pressure against the current collector, and other experimental variabilities.

Conclusion

1. Analysis of surface profilograms for the *VT22* titanium alloy demonstrated that all applied processing modes reduced height parameters (achieving R_a as low as 1.35 μm) and improved the surface finish grade from 3 to 6. Electromechanical processing (*EMP*) with high-density direct current was particularly effective in qualitatively suppressing profile "chatter" inherited from the preceding semi-finish turning.

2. Electromechanical processing and smoothing (**Modes 3, 6, 7**) significantly reduce the profile step parameter by up to a factor of 2.28 and increase the relative bearing length to 98.8%, producing "oil-pockets" profiles with varying rigidity levels and waviness characterized by different step and height parameters.

3. The application of the fast *Fourier* transform (*FFT*) enabled the identification of principal components resulting from the complex multi-stage processing, isolation of the profile's cyclic component, generation of profile irregularity distribution graphs based on approximation models, and filtering of random artifacts from the process (e.g., potential vibration, low system rigidity, and sample flapping in the chuck) for correct interpretation of the results obtained. The highest correlation coefficient ($R > 0.7$) was observed for surface plastic deformation (*SPD*) and alternating current electromechanical processing (*EMP*), attributable to the combined dominance of the trend from the preceding semi-finish turning and the waviness induced by *EMP* (**Modes 2, 4, 9**).

4. Fast *Fourier* transform (*FFT*) can be used as an express assessment and classification by the scale factor of longitudinal deviations of the machine parts' surface profile after various types of processing.

5. As the most optimal processing mode in terms of surface microgeometry parameters for a mechanical engineering technologist, **Mode 3** is recommended. It effectively reduces height and step parameters and significantly increases the structural parameter responsible for the load-bearing capacity of mating parts.

References

1. Heifetz M.L., Gretsky N.L., Prement G.B. Technological inheritance of operational quality parameters in the life cycle of internal combustion engine parts. *Naukoemkie tekhnologii v mashinostroenii = Science Intensive Technologies in Mechanical Engineering*, 2019, no. 7 (97), pp. 35–42. DOI: 10.30987/article_5cf7bd2fec7 7a9.13115279. (In Russian).

2. Averchenkov V.I., Vasiliev A.S., Heifetz M.L. Technological heredity in the formation of the quality of manufactured parts. *Naukoemkie tekhnologii v mashinostroenii = Science Intensive Technologies in Mechanical Engineering*, 2018, no. 10 (88), pp. 27–32. (In Russian).

3. Grzesik W., Żak K., Chudy R., Prażmowski M., Małecka J. Optimization of subtractive-transformative hybrid processes supported by the technological heredity concept. *CIRP Annals*, 2019, vol. 68 (1), pp. 101–104. DOI: 10.1016/j.cirp.2019.03.005.

4. Fedorov A.A., Zhdanova Yu.E., Linovskii A.V., Bobkov N.V., Bredgauer Yu.O. Vliyanie fazovogo sostava titanovykh splavov na parametry sherokhovatosti, poluchaemye v protsesse provolochnoi elektroerozionnoi obrabotki [Influence of the phase composition of titanium alloys on the roughness parameters obtained during wire electrical discharge machining]. *Omskii nauchnyi vestnik = Omsk Scientific Bulletin*, 2021, no. 4 (178), pp. 18–24. DOI: 10.25206/1813-8225-2021-178-18-24. (In Russian).

5. Muratkin G.V., Sarafanova V.A. Vliyanie tekhnologicheskoi nasledstvennosti napryazhenno-deformirovanno-go sostoyaniya na tochnost' nezhestkikh detalei [Influence of technological heredity of the stress-strain state on the accuracy of non-rigid parts]. *Problemy mashinostroeniya i nadezhnosti mashin = Problems of Mechanical Engineering and Machine Reliability*, 2020, no. 1, pp. 56–64. DOI: 10.31857/S0235711920010095.

6. Zhang H., Ren Z., Liu J., Zhao J., Liu Z., Lin D., Zhang R., Graber M.J., Thomas N.K., Kerek Z. D., Wang G.-X., Dong Y., Ye C. Microstructure evolution and electroplasticity in Ti64 subjected to electropulsing-assisted laser shock peening. *Journal of Alloys and Compounds*, 2019, vol. 802, pp. 573–582. DOI: 10.1016/j.jallcom.2019.06.156.

7. Bagmutov V.P., Parshev S.N., Dudkina N.G., Zakharov I.N., Savkin A.N., Denisevich D.S. *Elektromekhanicheskoe uprochnenie metallov i splavov* [Electromechanical hardening of metals and alloys]. Volgograd, VolgSTU Publ., 2016. 460 p.

8. Askinazi B.M. *Uprochnenie i vosstanovlenie detalei mashin elektromekhanicheskoi obrabotkoi* [Strengthening and restoration of machine parts by electromechanical treatment]. 3rd ed., rev. Moscow, Mashinostroenie Publ., 1989. 200 p.

9. Sneddon S., Xu Y., Dixon M., Rugg D., Li P., Mulvihill D.M. Sensitivity of material failure to surface roughness: A study on titanium alloys Ti64 and Ti407. *Materials & Design*, 2021, vol. 200, p. 109438. DOI: 10.1016/j.matdes.2020.109438.

10. Gao K., Zhang Y., Yi J., Dong F., Chen P. Overview of surface modification techniques for titanium alloys in modern material science: A comprehensive analysis. *Coatings*, 2024, vol. 14 (1), p. 148. DOI: 10.3390/coatings14010148.

11. Ojo S.A., Manigandan K., Morscher G.N., Gyekenyesi A.L. Enhancement of the microstructure and fatigue crack growth performance of additive manufactured titanium alloy parts by laser-assisted ultrasonic vibration processing. *Journal of Materials Engineering and Performance*, 2024, vol. 33, pp. 10345–10359. DOI: 10.1007/s11665-024-09323-8.

12. Amanov A., Yeo I.K., Jeong S.H. Advanced post-processing of Ti6Al4V alloy fabricated by selective laser melting: A study of laser shock peening and ultrasonic nanocrystal surface modification. *Journal of Materials Research and Technology*, 2025, vol. 35, pp. 4020–4031. DOI: 10.1016/j.jmrt.2025.02.038.

13. Liu R., Yuan S., Lin N., Zeng Q., Wang Z., Wu Y. Application of ultrasonic nanocrystal surface modification (UNSM) technique for surface strengthening of titanium and titanium alloys: A mini review. *Journal of Materials Research and Technology*, 2021, vol. 11, pp. 351–377. DOI: 10.1016/j.jmrt.2021.01.013.

14. Nakatani M., Masuo H., Tanaka Y., Murakami Y. Effect of surface roughness on fatigue strength of Ti-6Al-4V alloy manufactured by additive manufacturing. *Procedia Structural Integrity*, 2019, vol. 19, pp. 294–301. DOI: 10.1016/j.prostr.2019.12.032.

15. Civiero R., Perez-Rafols F., Nicola L. Modeling contact deformation of bare and coated rough metal bodies. *Mechanics of Materials*, 2023, vol. 179, p. 104583. DOI: 10.1016/j.mechmat.2023.104583.

16. Han T., Fan J. Ultrasonic measurement of contact stress at metal-to-metal interface based on a real rough profile through modeling and experiment. *Measurement*, 2023, vol. 217, p. 113046. DOI: 10.1016/j.measurement.2023.113046.

17. Qi B., Huang X., Guo W., Ren X., Chen H., Chen X. A novel comprehensive framework for surface roughness prediction of integrated robotic belt grinding and burnishing of Inconel 718. *Tribology International*, 2024, vol. 195, p. 109574. DOI: 10.1016/j.triboint.2024.109574.

18. Xue Z., Lai M., Xu F., Fang F. Influence factors and prediction model of surface roughness in single-point diamond turning of polycrystalline soft metal. *Journal of Materials Processing Technology*, 2024, vol. 324, p. 118256. DOI: 10.1016/j.jmatprotec.2023.118256.

19. Stampfer B., Bachmann J., Gauder D., Böttger D., Gerstenmeyer M., Lanza G., Wolter B., Schulze V. Modeling of surface hardening and roughness induced by turning AISI 4140 QT under different machining conditions. *Procedia CIRP*, 2022, vol. 108, pp. 293–298. DOI: 10.1016/j.procir.2022.03.050.

20. Li S., Li S., Liu Z., Petrov A.V. Roughness prediction model of milling noise-vibration-surface texture multidimensional feature fusion for N6 nickel metal. *Journal of Manufacturing Processes*, 2022, vol. 79, pp. 166–176. DOI: 10.1016/j.jmapro.2022.04.055.

21. Sakthivel N.R., Cherian J., Nair B.B., Sahasransu A., Aratipamula L.N.V.P., Gupta S.A. An acoustic dataset for surface roughness estimation in milling process. *Data in Brief*, 2024, vol. 57, p. 111108. DOI: 10.1016/j.dib.2024.111108.

22. Wang J., Wu X., Huang Q., Mu Q., Yang W., Yang H., Li Z. Surface roughness prediction based on fusion of dynamic-static data. *Measurement*, 2025, vol. 243, p. 116351. DOI: 10.1016/j.measurement.2024.116351.

23. Bagmutov V.P., Vodopyanov V.I., Zakharov I.N., Ivannikov A.Y., Bogdanov A.I., Romanenko M.D., Barinov V.V. Features of changes in the surface structure and phase composition of the of α + β titanium alloy after electromechanical and thermal treatment. *Metals*, 2022, vol. 12 (9), p. 1535. DOI: 10.3390/met12091535.

24. He J., Li B., Sun Q., Li Y., Lyu H., Wang W., Xie Z. The improved fault location method based on natural frequency in MMC-HVDC grid by combining FFT and MUSIC algorithms. *International Journal of Electrical Power & Energy Systems*, 2022, vol. 137, p. 107816. DOI: 10.1016/j.ijepes.2021.107816.

25. Fedorov V.L. Kriterii opredeleniya chisla garmonik ryadov Fur'e, approksimiruyushchikh napryazheniya i toki transformatora [Criterion for determining the number of harmonics of Fourier series approximating transformer voltages and currents]. *Omskii nauchnyi vestnik = Omsk Scientific Bulletin*, 2018, no. 5 (161), pp. 82–89. DOI: 10.25206/1813-8225-2018-161-82-89.

26. Muratkin G.V., comp. *Konspekt lektsii po distsipline «Osnovy vosstanovleniya detalei i remont avtomobilei»* [Lecture notes on the discipline "Fundamentals of Parts Restoration and Car Repair"]. Tolyatti, TSU Publ., 2008. 120 p.

27. Malyshko S.B., Tarasov V.V. [The influence of the technological parameters of the electromechanical treatment on the surface roughness]. *Problemy transporta Dal'nego Vostoka* [Problems of Transport in the Far East]. Proceedings from 13th Scientific and Practical Conference. Vladivostok, 2019, pp. 63–65. (In Russian).

28. Uchkin P.G. Primenenie vibronakatyvaniya gil'z tsilindrov dvigatelya vnutrennego sgoraniya s tsel'yu uvelicheniya ikh resursa [The use of vibration rolling of cylinder liners of an internal combustion engine in order to increase their resource]. *Izvestiya Orenburgskogo gosudarstvennogo agrarnogo universiteta = Izvestia Orenburg State Agrarian University*, 2023, no. 2 (100), pp. 99–105. DOI: 10.37670/2073-0853-2023-100-2-99-105.

29. Parshev S.N., Serov I.M., Zubkov A.V., Korobov A.V. Vliyanie impul'snogo elektromekhanicheskogo uprochneniya na iznosostoikost' podvizhnykh sopryazhenii [Influence of pulsed electromechanical hardening on the wear resistance of movable joints]. *Molodoi uchenyi = Young Scientist*, 2015, no. 23 (103), pt. 2, pp. 200–204.

30. Bagmutov V.P., Zakharov I.N., Romanenko M.D., Barinov V.V., Tikhaeva V.V. Influence of technological modes of combined high-energy treatment on wear resistance of transition class titanium alloy. *Russian Physics Journal*, 2024, vol. 67 (10), pp. 1647–1653. DOI: 10.1007/s11182-024-03294-y.

31. Manus H. An ultra-precise fast Fourier transform. *Science Talks*, 2022, vol. 4, p. 100097. DOI: 10.1016/j.sctalk.2022.100097.

32. Leonov O.A., Vergazova Yu.G. Otnositel'naya opornaya dlina profilya poverkhnosti i dolgovechnost' detalei [Relative bearing length of the surface profile and durability of parts]. *Innovatsionnaya nauka = Innovative Science*, 2016, no. 1-2 (13), pp. 81–83.

33. Aliev A.A., Bulgakov V.P., Prikhod'ko B.S. Kachestvo poverkhnosti i svoistva detalei mashin [Surface quality and properties of machine parts]. *Vestnik Astrakhanskogo gosudarstvennogo tekhnicheskogo universiteta = Vestnik of Astrakhan State Technical University*, 2004, no. 1 (20), pp. 8–12.

Conflicts of Interest

The authors declare no conflict of interest.

Obrabotka metallov –
Metal Working and Material Science

Journal homepage: http://journals.nstu.ru/obrabotka_metallov

Evaluation of the melting ability of oxide fluxes in A-TIG welding of carbon and low-alloy steels

Antonina Karlina [1, a*], Viktor Kondratiev [2, 3, b], Vitaly Gladkikh [1, c], Galina Vitkina [3, d], Roman Kononenko [4, e]

[1] National Research Moscow State University of Civil Engineering, 26 Yaroslavskoe Shosse, Moscow, 129337, Russian Federation

[2] A.P. Vinogradov Institute of Geochemistry of the Siberian Branch of the Russian Academy of Sciences, 1A Favorsky str., Irkutsk, 664033, Russian Federation

[3] Cherepovets State University, 5 Lunacharsky pr., Cherepovets, 162600, Russian Federation

[4] Irkutsk National Research Technical University, 83 Lermontova str., Irkutsk, 664074, Russian Federation

[a] https://orcid.org/0000-0003-3287-3298, ✉ karlinat@mail.com; [b] https://orcid.org/0000-0002-7437-2291, ✉ imz@mail.ru;
[c] https://orcid.org/0000-0003-1953-1584, ✉ gladkich_87@mail.ru; [d] https://orcid.org/0000-0002-1076-2709, ✉ 20procents@mail.ru;
[e] https://orcid.org/0009-0001-5900-065X, ✉ istu_politeh@mail.ru

ARTICLE INFO

ABSTRACT

Introduction. Tungsten inert gas (*TIG*) welding has gained widespread popularity due to its advantages, including effective shielding, a stable arc, easy heat input adjustment, reduced metal spatter, and an attractive weld appearance. However, relatively shallow penetration and low efficiency limit its application. To improve welding efficiency and expand its scope of application, researchers both domestically and internationally have conducted significant studies aimed at increasing the energy density of the traditional TIG arc. This includes activating *TIG* (*A-TIG*) arc welding, which utilizes a flux applied to the weld surface. Further investigation of the mechanism for increasing arc energy density in *A-TIG* welding will allow us to propose new ideas and methods for highly efficient *TIG* welding technology. **The purpose** of this study is to evaluate the technological potential of using oxide activators TiO_2 and SiO_2 to improve penetration efficiency and weld quality of carbon and low-alloy steels. **Methods.** This work involved comparative *A-TIG* welding tests. The tests included the use of 3.5 mm and 8 mm thick plates (300 mm × 300 mm) made of unalloyed (carbon) steel *St3* and low-alloy steel *0.09 C-2Mn-Si*. Welding tests included the use of single-component fluxes in the form of oxides (TiO_2, SiO_2). All experimental welds were performed under the same conditions, without the use of filler metal (*TIG* welding), with a current in the range of 10–200 A and a welding speed of 150 mm/min. Arc voltage was maintained in the range of 10.4 V to 12.8 V; heat input was in the range of 0.499 kJ/mm to 0.614 kJ/mm. All welds were subjected to visual inspection of the surface condition and macrostructural studies to determine their dimensions. **Results and discussion.** Most tests observed significant differences in arc shape compared to traditional *TIG* and *A-TIG* processes. Results of *A-TIG* welding tests on unalloyed and low-alloy steels showed that penetration depth increased slightly in steels characterized by a higher degree of deoxidation and metallurgical purity. Evidently, not every activator was responsible for the increased penetration depth, but the use of TiO_2 and SiO_2 oxides was undoubtedly beneficial. An arc constriction mechanism is proposed, which is widely applicable to *A-TIG* welding of steel with various types of fluxes studied. Arc constriction occurs due to the formation of negative ions in the outer region of the arc or due to the flux coating on the surface. Thus, arc constriction increases the current density and heat intensity at the root of the anode. This increases the force and pressure of magnetic constriction, resulting in a strong downward convection flow. The use of silicon and titanium oxides (TiO_2 and SiO_2) increases penetration depth during *A-TIG* welding, regardless of steel type and grade. The degree of penetration increase was limited to a range of 40% to 200%.

Introduction

Welding is the preferred method for joining different grades of steel, allowing for strong, continuous joints with superior corrosion resistance compared to bolt or rivet joints. *TIG* (tungsten inert gas) or *GTA* (gas tungsten arc) welding is often used due to its precision and excellent weld quality. It uses an electric arc

* Corresponding author
Karlina Antonina I., Ph.D. (Engineering), Research Associate
National Research Moscow State University of Civil Engineering,
26 Yaroslavskoe Shosse,
129337, Moscow, Russian Federation
Tel: +7 950 120-19-50, **e-mail:** karlinat@mail.ru

and an inert gas (such as argon) to protect the weld pool from contamination. This method is highly effective for thin or fragile materials, providing low deformation, excellent control, and a polished surface, making it suitable for applications in machine parts and mechanisms that require both strength and precision.

Despite its advantages, *TIG* welding has limitations, especially in terms of weld penetration depth. Typically, *TIG* welding of stainless steels in argon environments limits full weld penetration to seams no thicker than 3 mm and relatively low welding speeds. Although welding speeds can be significantly increased (up to 160%) by using helium or helium-argon mixtures with hydrogen additions as shielding gas, the weld penetration depth increases only slightly (1–2 mm) [1–3]. The ability to improve penetration by selecting a protective mixture is further limited by the need to use inert or weakly reducing gases, which limits the choice to argon and helium and their mixtures.

As mentioned above, a single pass of butt joints with square edges provides a penetration of about 3 mm, which leads to the need for additional passes for thicker materials, increasing the welding time and cost. Additional passes generate even more heat, expanding the heat-affected zone (*HAZ*) and potentially altering both the metallurgical and microstructural characteristics of the weld. Thicker components require wider root gaps and more filler material, resulting in increased material consumption and welding time [1–3].

Preparing the edges for *TIG* welding, especially for thick materials, is a time-consuming and laborious process. The *ISO 9692-1:2013* standard requires beveling or grooving the edges to reduce the thickness of the weld at the root, ensuring sufficient penetration. However, this procedure increases the labor intensity, welding time, and overall costs [1–5].

To eliminate these limitations, the technology of activated *TIG* welding (*A-TIG*) was developed, which involves applying a thin layer of activating flux (usually oxides or halides in combination with solvents such as acetone or ethanol) to the base material before welding [1, 2]. *A-TIG* welding (*A-GTAW*) with activated flux is a welding method that was first used at the E. O. Paton Institute of Electric Welding, Ukraine, in the late 1950s and early 1960s [1–3]. Initially, the *A-TIG* method was used for welding titanium, then for welding high-strength martensitic steels ($R_m \approx 1{,}500$ MPa), and finally for welding stainless steels [3–10].

The free-burning argon arc is compressed into a plasma arc through mechanical, thermal, and magnetic compression. The energy density of the plasma arc is 1–2 orders of magnitude higher than that of a conventional free-burning arc, making plasma arc welding *(PAW)* one of the three high-energy-density welding methods. The arc compression mechanism provides a new method for increasing the energy density of the TIG arc. Based on this mechanism, many methods have been developed to increase the energy density of the TIG arc. These include activating *TIG* arc welding (*A-TIG*), double-electrode *TIG* welding (*DE-TIG*), keyhole *TIG* welding (*K-TIG*), high-frequency pulse *TIG* welding (*H-TIG*), hybrid *TIG* arc welding with ultrasound (*U-TIG*), magnetic field controlled *TIG* welding (*M-TIG*), and hollow tungsten electrode negative pressure arc welding (*HWP-TIG)*.

In recent years, researchers [3–19] have paid great attention to the *A-TIG* welding technology of various metals and alloys. Many research articles by domestic and foreign authors have been published on TIG welding of steel with various activated fluxes and their combinations [8–25].

Many authors [8–16] have investigated the effect of five different oxide fluxes, MnO_2, TiO_2, MoO_3, SiO_2, and Al_2O_3, on weld geometry changes, microstructural behavior, and hardness changes during *TIG* welding of 6–8 mm thick stainless steel. All fluxes, with the exception of Al_2O_3, increase weld penetration due to a combined effect of the reverse *Marangoni* effect and arc constriction, thereby reducing the angular deformation of the welded joints. In addition, the SiO_2 flux facilitated the penetration of the root pass. The difficulty in dissolving aluminum oxide leads to a lack of arc constriction, resulting in a shallow weld in the case of Al_2O_3. Another study was conducted [16] on stainless steel using SiO_2, TiO_2, Cr_2O_3, and *CaO* fluxes. They also noted that the SiO_2 flux had the most significant impact on penetration and proposed a mechanism for arc constriction for deeper penetration.

The authors of [16–22] analyzed the microstructure, mechanical properties, and corrosion resistance of *A-TIG* welds, which revealed the mechanism for improving the microstructure of *A-TIG* welds.

In [5–9, 18–22], the composition of a composite nanoparticle-based activator was developed and optimized, further clarifying the relationship between the activator and the formation and quality of the weld. Many studies [4–16] have shown that most activators can significantly compress the arc, increase the penetration depth, and reduce the width of the weld bead.

According to studies [17–22], it is not clear whether the *Marangoni* effect in the molten pool is the main reason for increased penetration, but arc compression is not an inevitable phenomenon in *A-TIG*. Some activators can compress the arc, while others do not affect the arc state. However, arc compression will inevitably lead to increased arc energy density.

The effect of activating fluxes Cr_2O_3, TiO_2, SiO_2, Fe_2O_3, NaF, and AlF_3, both individually and as binary fluxes such as SiO_2-TiO_2, has been studied in many articles [5–29], where the depth of penetration was used as a criterion for evaluation. In some cases, activating fluxes (especially oxides) have a positive effect on the depth of penetration, increasing it by 40–50% [15–25], while in other cases, they have a negligible effect [4, 5, 30–38]. This is due to the fact that most of the studies [15–39] have been conducted under various conditions of the welding process (current value, arc voltage, welding speed, coating thickness, type of binder used in the preparation of the flux, particle size of the flux, etc.). According to the authors [1, 2], all of these factors will affect the penetration capability of the welding arc and, as a result, the effectiveness and application of the activating flux.

The purpose of the work is to evaluate the penetration capability of *A-TIG* welding using TiO_2 and SiO_2 oxide fluxes on carbon and low-alloy steels. To achieve this purpose, the following ***tasks*** were solved during the research:

– determination of technological parameters of the *A-TIG* welding process using TiO_2 and SiO_2 oxide fluxes (current value, coating thickness, welding speed) affecting the penetration capability;

– conducting metallographic studies of welds during *A-TIG* welding using TiO_2 and SiO_2 oxide fluxes;

– conducting visualized studies of the process using photo documentation of individual stages of the process.

Research methods and materials

For the experiments, plates of dead-melted steel *St3* (*ASTM A283* Grade C**)** with dimensions of 5500 mm × 100 mm and thicknesses of 3, 5, 8, 10, 12, and 25 mm, as well as low-alloy steel 0.9% *C*-2% *Mn*-1% *Si*, were used. The welding tests included the use of single-component fluxes in the form of oxide powders (*TiO₂*, *SiO₂*), with particle sizes of 40 and 80 micrometers, produced by *Real-Dzerzhinsk LLC*, Russia. The components were ground in a ceramic mortar and then sieved through a laboratory sieve with a mesh size of 0.056 mm. Before application, the powder was mixed with a fast-evaporating liquid (acetone) to create a paste-like suspension. The prepared flux was then applied to the surface of the plates using a brush. This method of applying the activating flux is currently used in most studies related to the *A-TIG* process. A bonding varnish and double-sided conductive tape were also used. To achieve consistent flux thickness and minimize the impact of this factor on the test results, the paste consistency was kept constant. The coating thickness was monitored using a *TP-34* thickness gauge based on an eddy current transducer. The methodology adopted for the experimental work is presented in Fig. 1.

All experimental welds were performed under the same conditions, without the use of filler metal (autogenous *TIG* welding), with a current range of 10–200 A and a welding speed of 150 mm/min. The arc voltage was in the range of 10.4 V to 12.8 V, and the linear energy input was in the range of 0.499 kJ/mm to 0.614 kJ/mm. The welding experiments were conducted using a *TIG 250P AC/DC* welding machine, which consists of a *TIG* welding power supply, a welding fixture, a *TIG* torch, and an argon cylinder. The *TIG* welding equipment has a current range of 10 to 200 A, an open-circuit voltage of 75 to 85 V, a frequency of 50/60 Hz, and forced air cooling. The **arc** length (distance between the tungsten electrode and the workpiece), the welding speed, and the welding current are the most influential variables that require optimal control to obtain accurate and repeatable experimental results. The welding fixture was developed in-house to securely hold the torch and workpiece and accurately control the welding speed and the arc
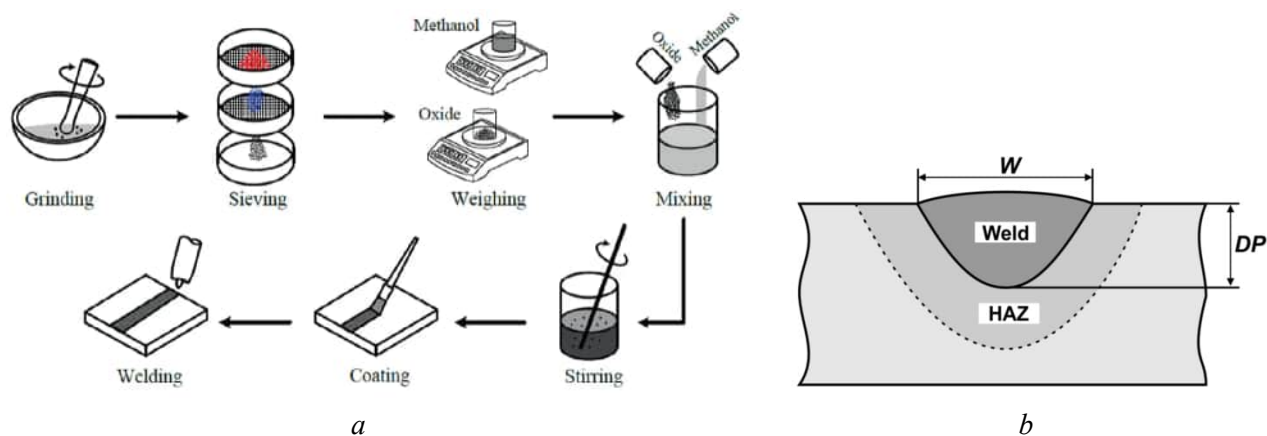
Fig. 1. Methodology [29] for the preparation of activating fluxes:

a – weld parameters; *b* – (***W*** – weld width; ***DP*** – penetration depth; ***HAZ*** – heat-affected zone; ***Weld*** – weld)

length during welding. It holds the base plate for welding and sets the desired welding speed between 40 and 200 mm/min. The flow rate of the shielding argon was maintained between 10 L/min and 15 L/min. A tungsten electrode (ø 2.4 mm) doped with thorium oxide (grade *WT20* according to *EN ISO 6848*) was used. All welds were subjected to visual inspection of the surface condition and macro-structural studies to determine their dimensions. Samples for macrostructural studies were cut, mounted, ground, polished and etched with a 4% *Nital* reagent. The width of the welds was measured every 10 mm along the entire length of the welds. For statistical processing of the results, 3 experiments were carried out for each welding condition, then the results were averaged.

Samples for macrostructural studies were selected from the central part of the weld. The arc burning process was recorded by a digital *SLR* camera *-á SONY 350* and a high-speed camera *PCO.1200s* according to the method described in [15]. A *Tektronix TDS-1012B* digital oscilloscope was used to measure current and voltage.

Research results

The results of macrostructural tests of welds performed on the respective steel grades using various activated fluxes (*TiO₂, SiO₂*) are presented in Figs. 2–4, and the results of measurements of the penetration depth and weld width are presented in Table 1.

Macroscopic images of weld geometry at 50× magnification are shown in Fig. 2 with calibrated measurements of weld penetration and weld width. The weld penetration depth, weld bead width, and weld depth-to-width (***D/W***) ratio are three key metrics that describe the geometric characteristics of welds.

The geometric characteristics of the *A-TIG* welds obtained with the selected combinations of current, speed, and flux are shown in Table 1 and Figs. 2 and 3. The penetration depth and bead width of the *A-TIG* weld varied significantly depending on the flux and application method parameters. Different combinations of flux and application method resulted in variations in penetration depth and bead width compared to the conventional *TIG* process. The effect of increasing the penetration depth for a given welding current is clearly visible when an activated flux is used during the welding process (Table 1, Figs. 2–4).

The experiments showed that the maximum penetration depth is achieved at high welding currents during *A-TIG* welding, but the increase in penetration depth is limited for conventional *TIG* welding, as shown in Fig. 4.

An increase in current also leads to a wider weld bead (Fig. 4). The flux layer thickness has a strong effect on the weld penetration, as a thicker flux layer can increase the weld penetration. The weld penetration depends on the welding current, but the optimal flux layer thickness is crucial for a high-quality weld. Fig. 5 shows the weld penetration as a function of coating thickness, and Fig. 6 shows the weld penetration as a function of steel chemical composition.
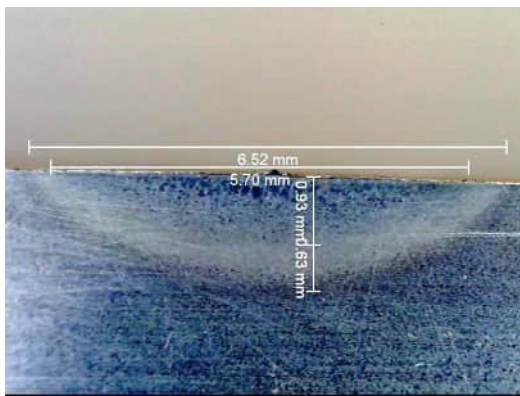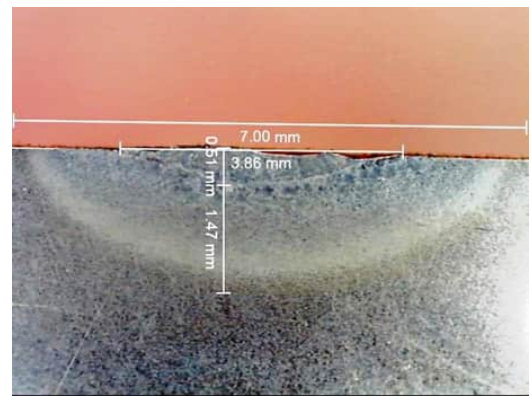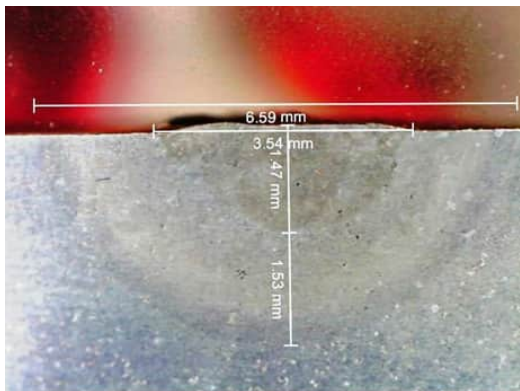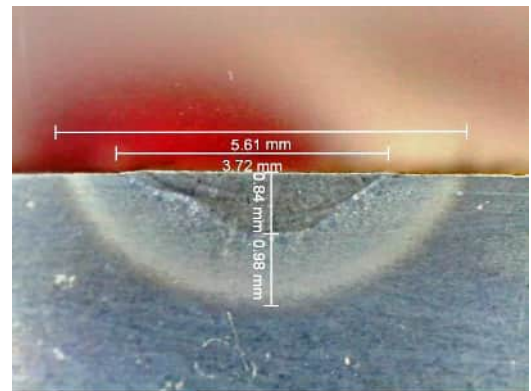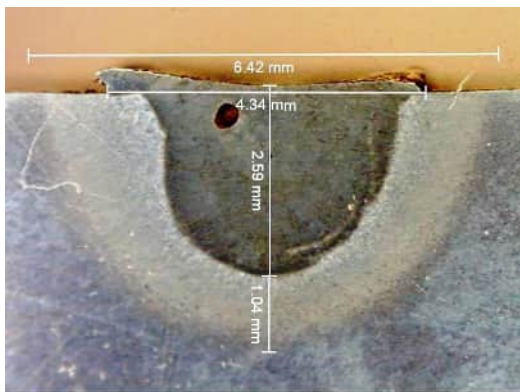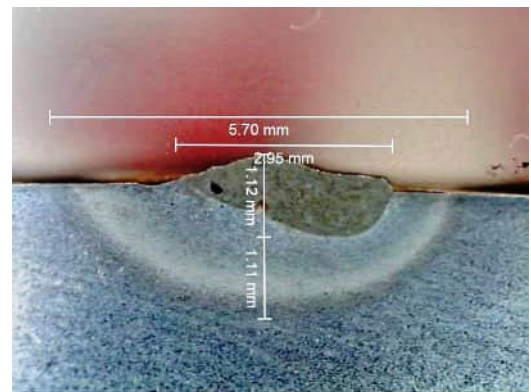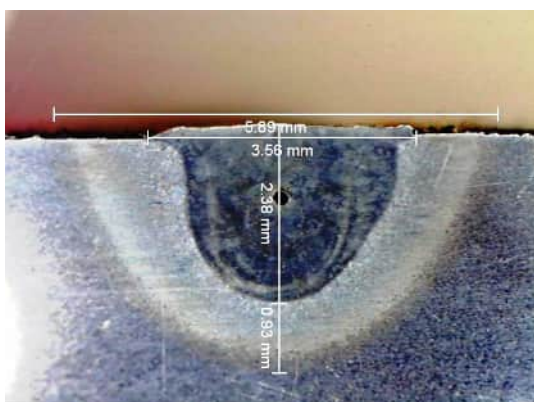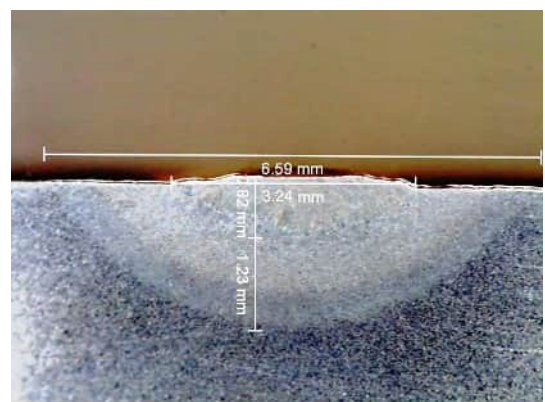
Fig. 2. Cross sections of steel:
a – without flux and without surface melting (current 100 A); *b* – without flux and with surface melting (current 120 A); *c* – silicon oxide (current 120 A); *d* – titanium oxide (current 120 A); *e* – silicon oxide (current 150 A); *f* – titanium oxide (current 150 A); *g* – silicon oxide (current 160 A); *h* – titanium oxide (current 160 A)

The influence of the composition of activating fluxes of different particle size on the width and depth of penetration

Current, A	Flux applied to *St3* steel	Depth of penetration, mm	Penetration width, mm
100	Without flux	1.15	5.3
100	SiO_2 0.04 mm particle size (double-sided conductive tape, bonding varnish)	1.64	5.37
100	SiO_2 0.08 mm particle size (bonding varnish)	2.66	5.35
100	SiO_2 0.04 mm particle size (bonding varnish)	2.52	4.98
100	SiO_2 0.08 mm particle size (double-sided conductive tape and bonding varnish)	1.2	4.3
100	**Aerosil®** (bonding varnish)	1.96	1.96
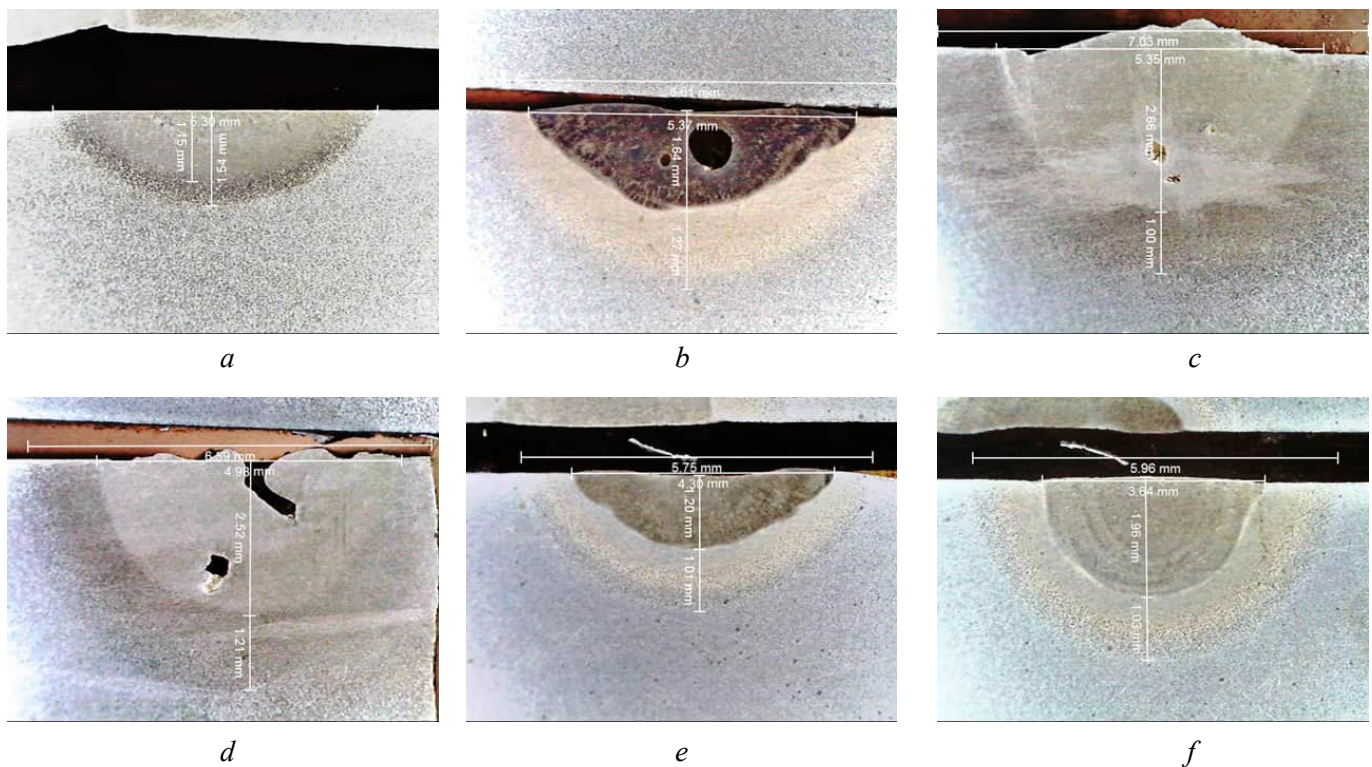
Fig. 3. Cross sections (current 100A):
a – without flux; *b* – SiO_2 0.04 (double-sided conductive tape, bonding varnish); *c* – SiO_2 0.08 (bonding varnish); *d* – SiO_2 0.04 (bonding varnish); *e* – SiO_2 0.08 (double-sided conductive tape, bonding varnish); *f* – *Aerosil* (bonding varnish)

Figs. 7–10 below show photographs of the melting process of different types of activating fluxes on the surface of *St3* steel during conventional *TIG* and *A-TIG* welding. The welding process without flux is visualized in Fig. 7. A diffuse combustion mode of the welding arc without distinct anode and cathode spots is visible. The arc column has a conical (bell-shaped) form.

Fig. 8 shows the welding process with a 0.08 mm layer of SiO_2 flux applied using acetone as a carrier. It can be seen that the intense vaporization of the activating flux causes the arc column to constrict, resulting in a more concentrated anode region directed towards the cathode. The electric arc enters a constricted (or focused) attachment mode, forming a concentrated anode spot.

The heating time of the surface with the activated flux applied was increased compared to the heating of the surface without the activated flux. This leads to a constriction of the arc column and a deviation of
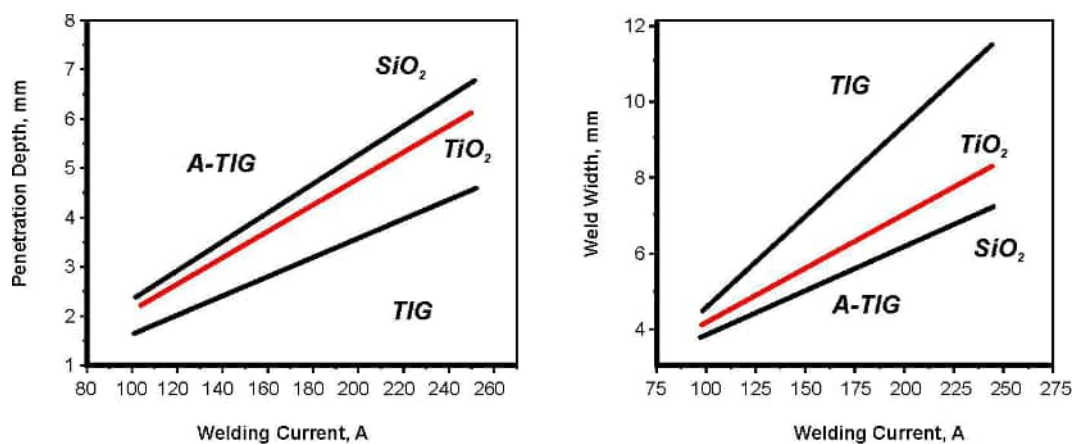
Fig. 4. Change in the geometric dimensions of the melting zone on a steel *St3* plate, 20 mm thick (penetration depth and weld width) with changing current during *TIG* and *A-TIG* welding
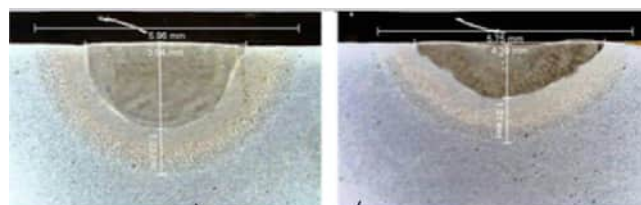
Fig. 5. Effect of changing coating thickness on penetration depth
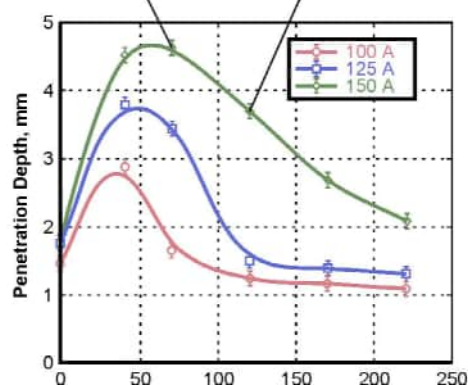
Fig. 6. Dependence of penetration depth on chemical composition of steel (plate thickness 10 mm, current 200 A)
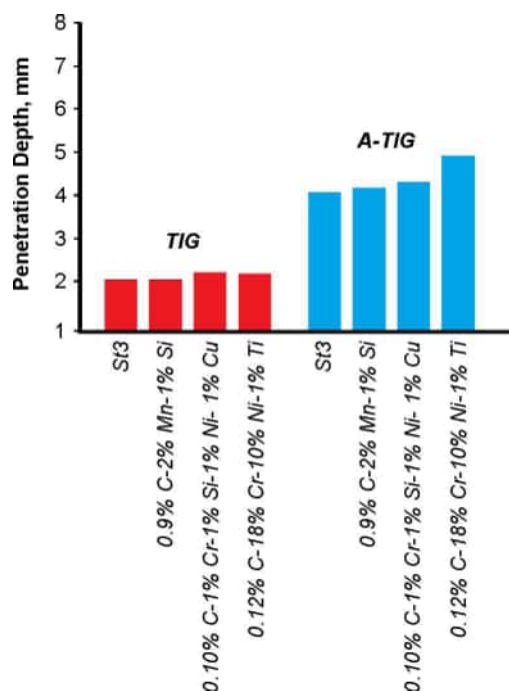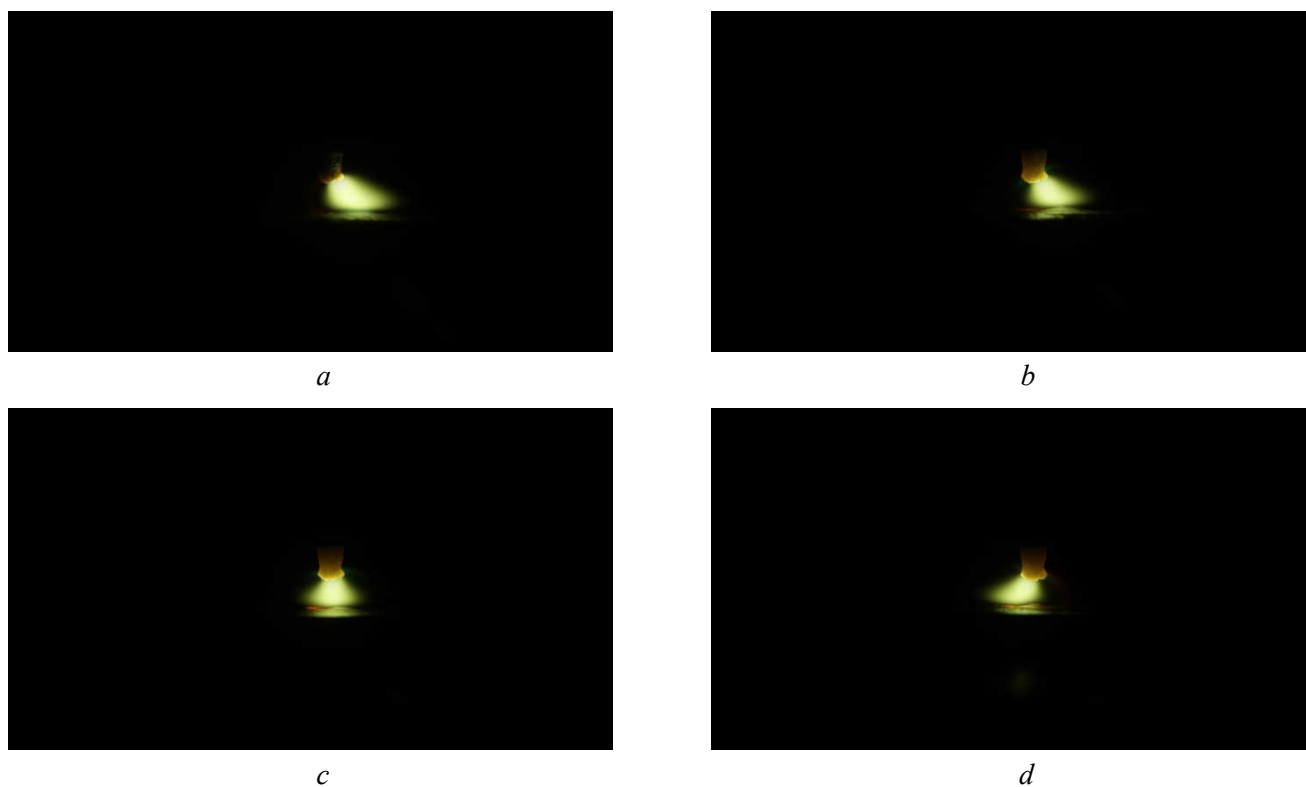
Fig. 7. The process of welding steel-3 without flux:
a, *b*, *c*, *d* – stages of movement of the welding arc along the sample
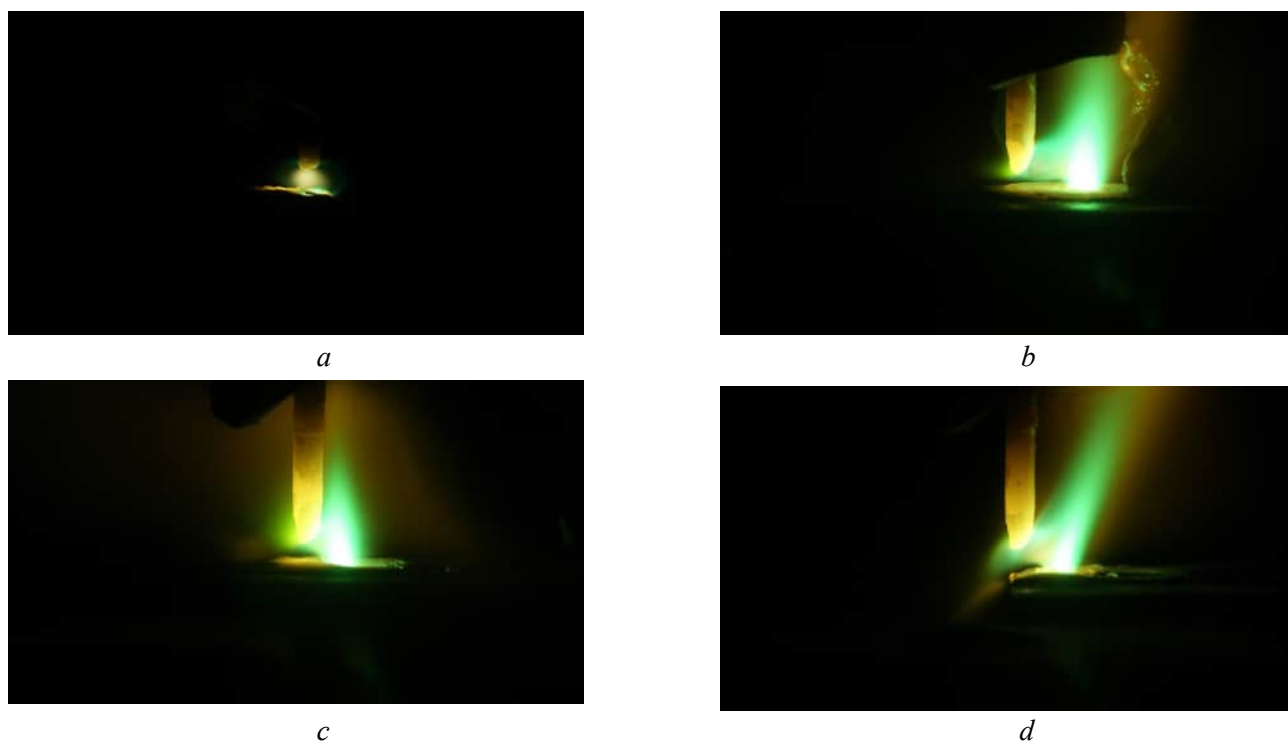
Fig. 8. The process of welding steel *St3* with applied flux *SiO₂*, particle size 0.08 mm, using acetone as a binder:

a, *b*, *c*, *d* – stages of movement of the welding arc along the sample

the anode spot from the arc axis. This causes an increase in the arc length and, as a result, an increase in the arc voltage, which is accompanied by an increase in the effective arc power ($P=U{\times}I$). The same situation is presented in Fig. 9, which shows photographs of the melting process of the activated flux SiO_2 with a particle size of 0.08 mm using a bonding varnish.

a

b

c

d
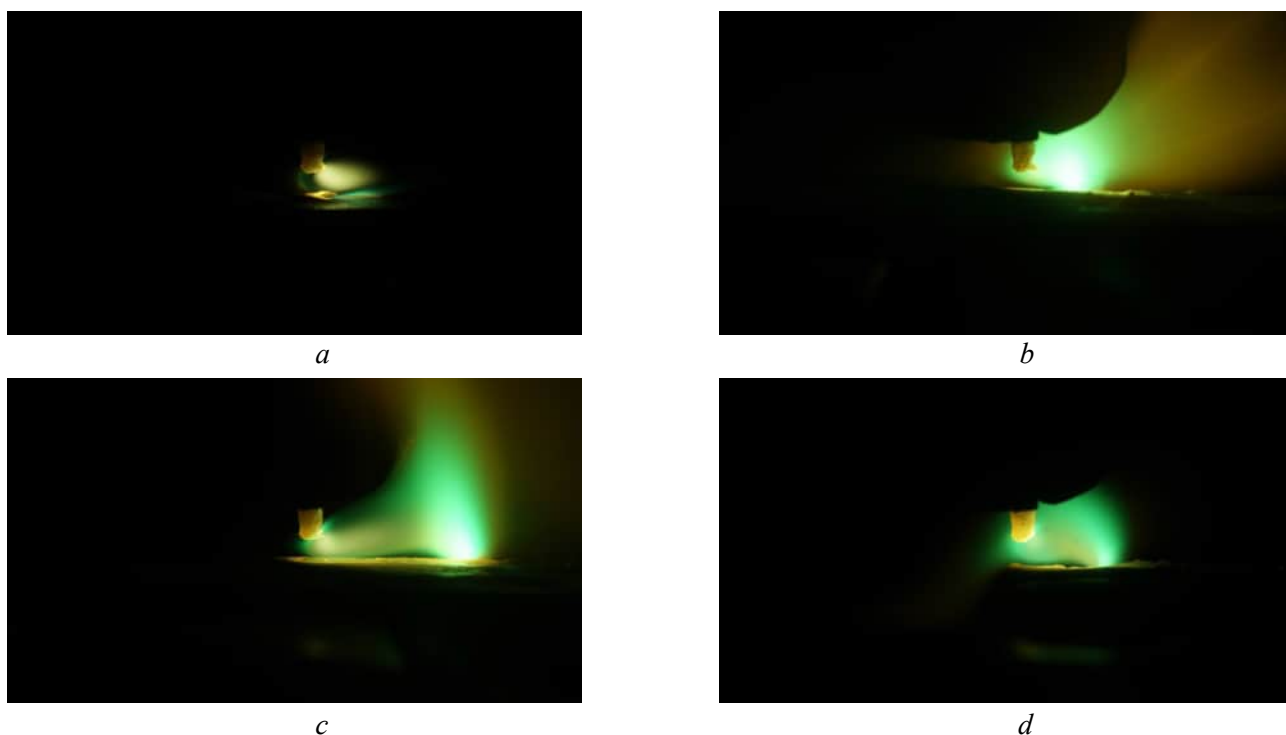
Fig. 9. The process of welding steel *St3* with applied flux *SiO$_2$* particle size 0.08 mm using a bonding varnish:

a, *b*, *c*, *d* – stages of movement of the welding arc along the sample

Fig. 10 shows photographs of the process of melting the *SiO$_2$* activating flux with a particle size of 0.04 mm using a bonding varnish. Similarly to the 0.08 mm fraction, the heating time of the surface with the activated flux applied compared to the heating of the surface without the activated flux increased,

a

b

c

d
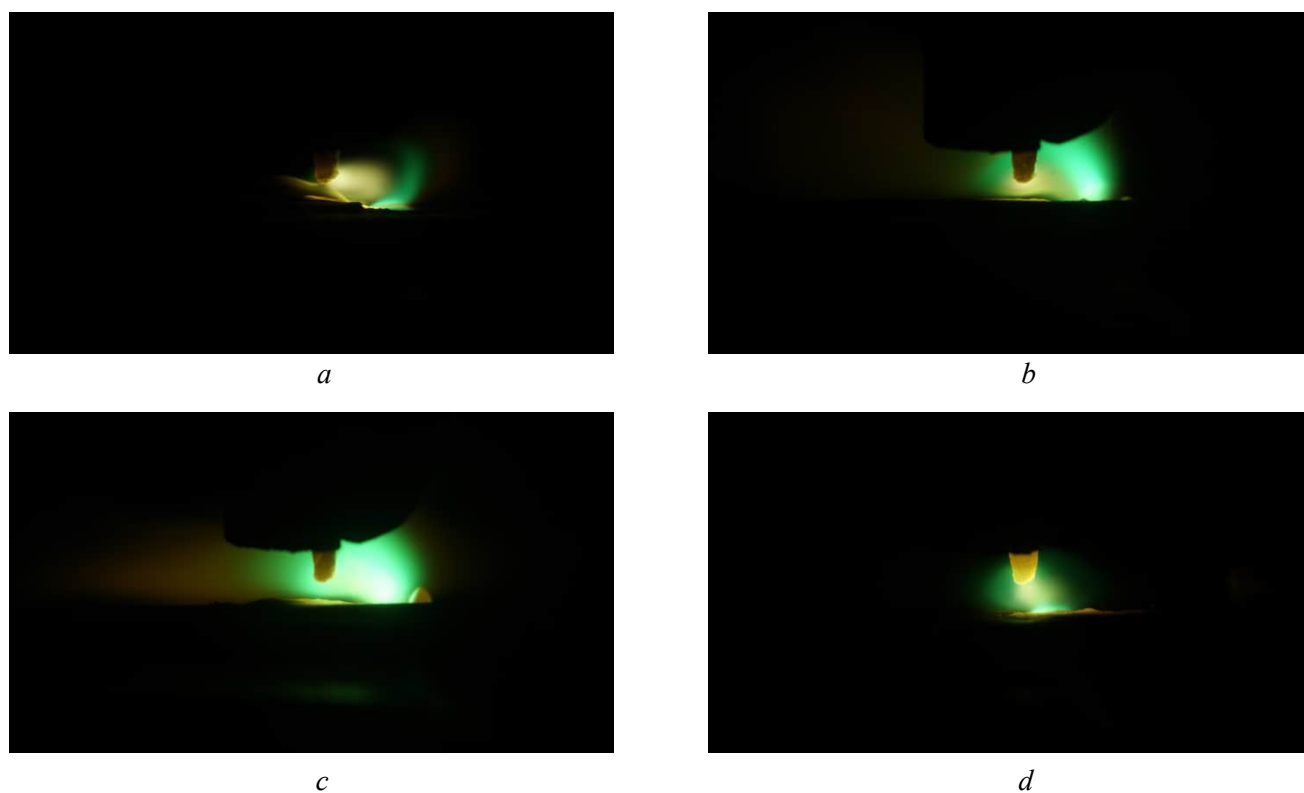
Fig. 10. The process of welding steel *St3* with applied flux with *TiO$_2$* particle size of 0.04 mm using a bonding varnish:

a, *b*, *c*, *d* – stages of movement of the welding arc along the sample

which led to the arc column constriction and the anode spot deviating from the axis of the column moving at a speed of 3.3 mm/sec. At the initial moment of arc ignition, the column has a typical spatial position; after 0.24 seconds, intensive vaporization of the activating flux begins and the arc column constricts, a more concentrated anode region appears, directed towards the cathode. The anode region length is 20–30 % greater than for the 0.08 mm fraction. The noted features of vaporization **o**f activating fluxes and the behavior of the arc column in Fig. 8–10 are also observed for other flux compositions.

Fig. 11 shows the oscillograms of the arc burning process without flux and with flux. It can be seen that the arc burning over the flux layer has higher voltage values due to the constricted mode of arc attachment.

Fig. 12 shows the welding process of *St3* steel samples with *TiO₂* flux, which is applied in a 1.5 mm thick layer using a bonding varnish, and a 0.5 mm thick layer in Fig. 13.
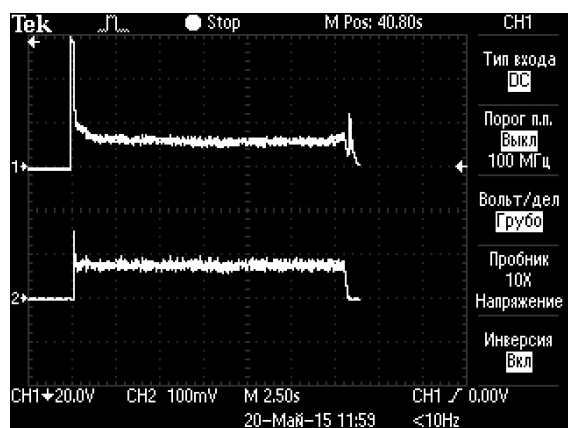
a
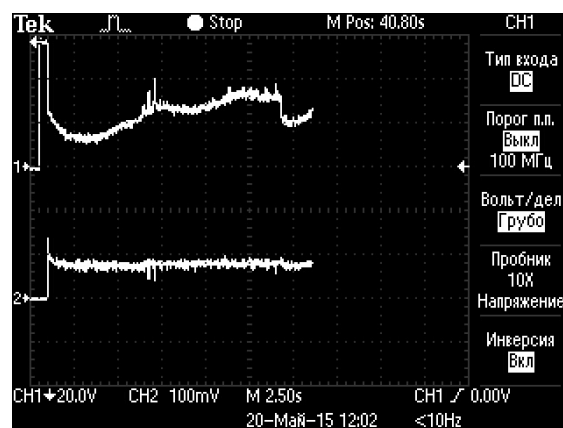
b

Fig. 11. Oscillograms of current and voltage of the welding arc:

a – without flux; *b* – with flux
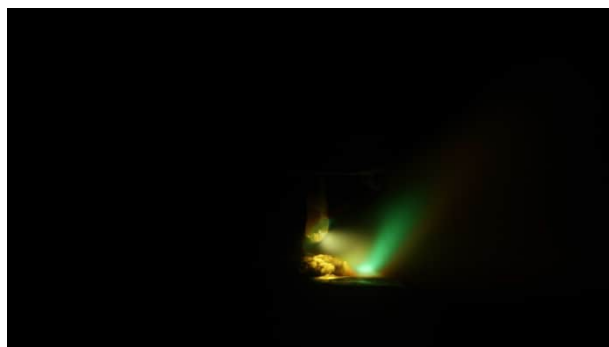
a
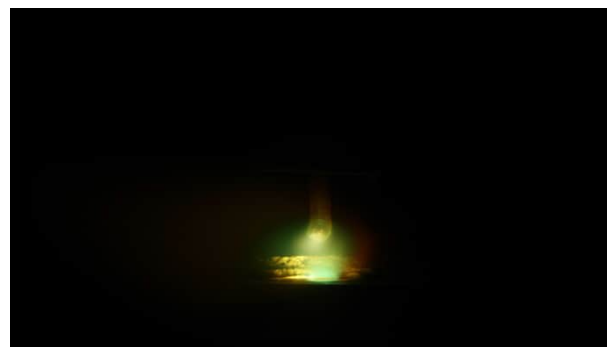
b

c

d

Fig. 12. The process of welding steel *St3* with *TiO₂* applied in a 1.5 mm layer using a bonding varnish:

a, *b*, *c*, *d* – stages of movement of the welding arc along the sample
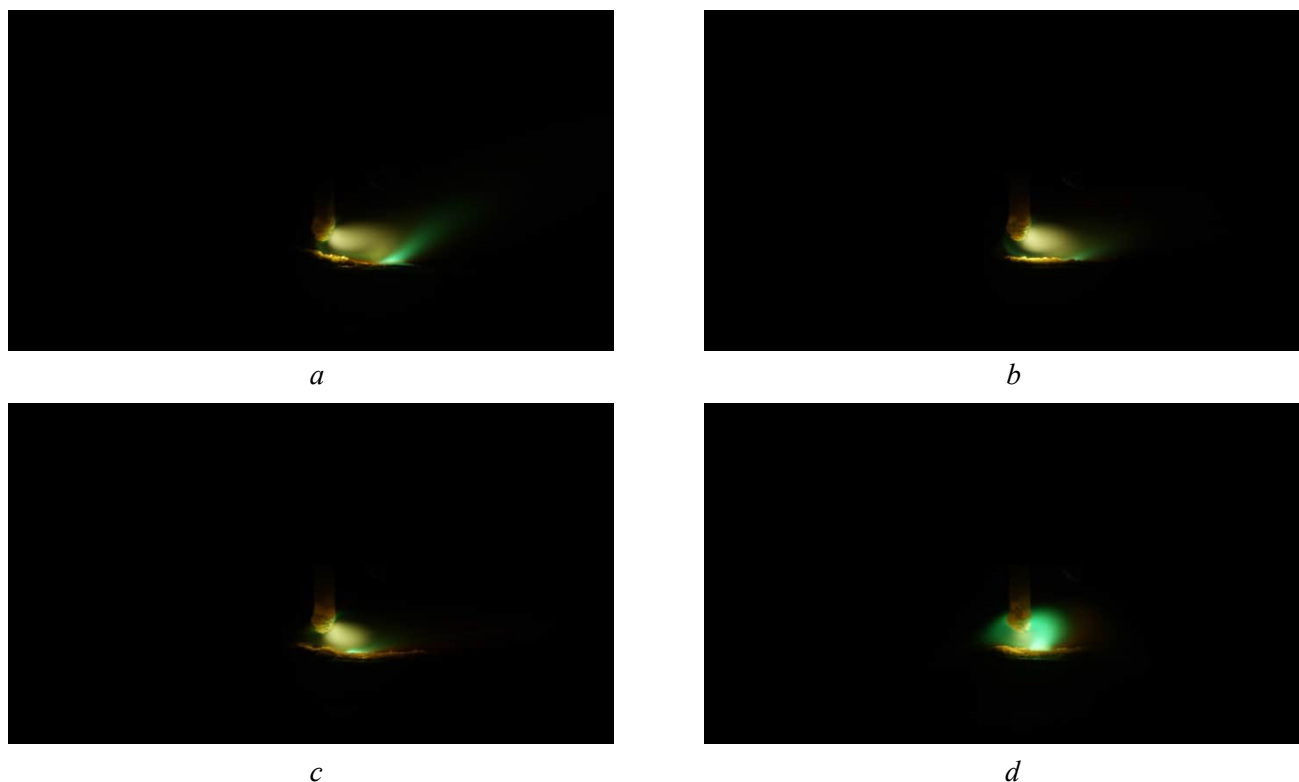
Fig. 13. The process of welding steel *St3* with TiO_2 C flux applied in a 0.05 mm layer using a bonding varnish:

a, *b*, *c*, *d* – stages of movement of the welding arc along the sample

The results of the experiments show that the penetration depth increased in almost all cases where activating flux was applied. A comparison of the effect of activated fluxes on the penetration depth during *A-TIG* welding of low-alloy steels and stainless steel revealed a similar effect of TiO_2 and SiO_2 oxides on both groups of steels. The effect of oxides, or rather the oxygen supplied by the oxides to the weld pool, can be explained by Marangoni convection, as has been reported in many scientific publications [3–29].

Arc images obtained during some tests are presented. In most tests, there were no significant differences in the arc shape compared to the conventional *TIG* process. In some tests using SiO_2 flux, the electric arc exhibited a tendency to deviate forward. This type of flux also caused the most significant changes in arc voltage, which were at least twice as high as those observed with other fluxes.

It is observed that the flux layer thickness has a very strong effect on the weld penetration (Fig. 5). The weld penetration initially increases linearly with the flux layer thickness up to 50–70 μm, and then shows a downward trend (Fig. 5). The Conventional *TIG* weld penetration corresponds to zero coating thickness and ranges from 1.4 to 1.9 mm for the investigated welding currents of 100 to 150 A. Depending on the welding current, the maximum penetration in *A-TIG* is achieved for a flux layer thickness of 40 to 70 μm. The observed maximum weld penetration values are 4.8 mm, 3.9 mm, and 2.9 mm, respectively, for welding currents of 150, 125, and 100 A. The optimal thickness appears to increase with increasing welding current. For example, the maximum penetration depth is achieved at about 40 μm at 100 A and about 70 μm at 150 A. Thus, the optimization of flux layer thickness depends on the heat input of the welding arc.

When the flux layer thickness exceeds the optimal value, the penetration is significantly reduced. This rapid decrease can be explained by the higher energy consumption required to overcome the flux barrier. Silicon dioxide is essentially a non-conductive material, providing high electrical resistance to the arc. A stable arc can only be established once the flux becomes liquid or is completely removed through vaporization. As the energy consumption for this effect increases with the flux layer thickness, the proportion of the incident energy that is effectively utilized for creating the weld pool decreases significantly.

In addition, as the flux layer thickness increases, the electric arc becomes unstable due to the unmelted flux, which provides higher electrical resistance on the advancing side. This causes a change in the arc pro-

file, which then stretches back towards the molten pool (Fig. 7–9). This lagging effect becomes increasingly important as the flux layer thickness increases for a given current or as the welding current decreases for a given thickness. Even with an optimal flux layer thickness of about 50 μm (Fig. 7–9), the lagging effect is observed when comparing TIG and A-TIG video frames. The lagging effect is associated with the higher electrical resistance of silicon oxide, which decreases with increasing temperature, especially when it enters the liquid phase. Since melting occurs at a higher temperature on the advancing side, the arc tends to lag behind the tip of the tungsten electrode. This arc lag increases the effective arc length and partially contributes to the increased arc voltage, as described later in this paper.

In the *A-TIG* process, there is an improvement in **the depth-to-width (*D/W*)** ratio, which is achieved through the combined effect of arc constriction and "reverse" *Marangoni* convection, also known as surface tension-induced convection or thermocapillary convection. In Marangoni convection, when the activating flux is applied to the workpiece, it delivers surface-active elements (e.g., oxygen) to the weld pool. This changes the surface tension gradient to become positive ($d\gamma/dT > 0$), and the oxygen content therefore affects the flow of the liquid in the weld pool [5].

The relationship between surface tension and temperature has been studied in [6–21]. It has been found that when welding low-sulfur and low-oxygen steel, the surface tension decreases with increasing temperature, resulting in a negative surface tension gradient. This leads to a radially outward flow in the weld pool. This phenomenon is discussed in detail in [22]. The authors believe that concentrations of surfactants above 50 ppm affect the direction and magnitude of thermocapillary forces [22], which changes the surface tension gradient in the weld pool from negative to positive [6–12].

The flow in the weld pool occurs from a region of higher surface tension (cooler liquid weld pool) to a region of lower surface tension (warmer liquid weld pool), causing the molten metal on the upper surface to flow outwards. However, in the presence of surface-active elements like oxygen, this gradient reverses, causing an inward flow towards the center. This internal flow results in deeper penetration and a narrower weld bead. This change in the direction of the surface tension gradient explains the change in the direction of the Marangoni flow.

In the arc constriction mechanism, the electron affinity (electronegativity) of the flux plays an important role [6, 7]. The arc, which exists on the surface of the flux-coated workpiece, produces a large number of positive ions at the temperature of the arc column [4]. It can be concluded that electrons are absorbed by the flux vapors around the weld pool, resulting in a decrease in the number of charged particles present in the arc. The highly electronegative vapor pushes the arc column inward in a radial direction. The resulting ions attract the free electrons present in the arc column, creating a constriction of the arc, and the base metal melts, promoting deeper penetration [5–22].

The electromagnetic *Lorentz* force also contributes to increasing the *D/W* ratio in the A-*TIG* mechanism. As the welding current increases, the magnitude of the *Lorentz* force increases. The smaller the radius of the arc root, the higher the *Lorentz* force [18–20]. The greater *Lorentz* force acts vertically downward in the center of the molten weld pool and increases the penetration. The electromagnetic *Lorentz* force and Marangoni force control the convection of the weld pool and increase the *D/W* ratio. The weld pool experiences driving forces such as buoyancy, aerodynamic shear stress, and plasma-induced reaction forces on the surface. All of them effectively improve the penetration in the *A-TIG* process, but their role is minimal compared to the *Marangoni* force, and therefore they can be neglected in the micro-scale analysis.

The research conducted has shown that the geometry of the weld is certainly influenced by variable parameters that must be precisely controlled to achieve the best weld quality. Some of these parameters that affect the *A-TIG* process are discussed below.

Many studies have shown [5–26] that the vaporization/decomposition of flux depends on the rate of its reaction, which in turn depends on the specific surface area of the particles. Therefore, it has been experimentally established [5–22] that flux particles with a size of 0.8 to 4 μm improve the penetration of the weld. However, this effect is not observed when using larger particles (25 μm) because they have a lower vaporization rate. Smaller flux particles have a higher specific surface area compared to larger particles, which results in better vaporization [12]. As the flux layer thickness increases, so does the heat required to

overcome the flux barrier, which reduces the depth of penetration at a given current value. Although it is known that penetration depends on the welding current, the optimal flux layer thickness is still important for achieving a high-quality weld [4–16].

It is important to understand that before applying a flux layer, it is converted into a paste by mixing the powdered flux with a suitable solvent, which must be evaporated before the welding process begins. Acetone and alcohol are the most commonly used carriers. Experiments have shown that acetone is the solvent that provides the best results, resulting in maximum penetration [10–14]. However, many studies do not pay close attention to the influence of the solvent type, which may affect the results obtained.

The welding current directly affects the geometric characteristics of the weld, such as the cross-sectional area, width, and depth of penetration. When comparing conventional *TIG* and *A-TIG* welding, there is almost a twofold difference in the depth of penetration when the current is increased. For conventional *TIG* welding with higher current values, the increase in weld width is very slight, while it increases significantly for *A-TIG* welding.

Increasing the welding speed leads to a decrease in the heat input to the weld and results in a shallower weld. The depth of penetration is inversely proportional to the welding speed at a given welding current.

The arc energy density is directly dependent on the arc length, which is a critical factor in *A-TIG* welding [3–9]. Generally, shorter arcs are preferred to prevent the dissipation of arc heat into the environment and to ensure that the maximum arc heat is transferred to the workpiece. However, a minimum distance must be maintained to ensure arc stability and minimize electrode contamination [5–12]. For *A-TIG* welding of stainless steel, a 2-4 mm arc length is typically used [4–6].

When maintaining a constant travel speed and welding current and using an activating flux, there is a slight increase in arc voltage. It is known that the flux vapors attract electrons during vaporization, which leads to a constriction of the arc and an increase in voltage. The degree of increase depends primarily on the composition of the oxide flux. Experiments have clearly shown that there is an obvious correlation between the measured arc voltage and the resulting arc constriction, so higher voltage values will result in a more pronounced arc constriction, as confirmed by other authors [16–29].

Experiments by various authors [1–8] show that the depth of penetration depends on the oxygen content in the weld pool during welding, as it contributes to the development of reverse *Marangoni* convection. The oxygen content can be precisely controlled by using a suitable flux composition and optimizing the welding parameters [1, 2].

Research by various authors shows [5–7] that the addition of nitrogen to the shielding gas increases arc energy and has a positive effect on the geometry and properties of the weld [22–29]. For example, the depth of penetration and cross-sectional area of the weld increase when nitrogen is added to an argon environment [26–31]. Angular deformation is also minimized when nitrogen is added, as it is directly related to the width of the weld, and nitrogen promotes complete penetration, which reduces angular deformation [24–28]. It has been found that hardness, tensile strength, and resistance to hot cracking can increase significantly when nitrogen is added [27–29].

It is known [1–6] that hydrogen-based shielding gas has high thermal conductivity at temperatures close to the dissociation of hydrogen molecules. Therefore, the addition of hydrogen has a significant impact on the volume of molten material in the weld pool [26–29]. An increase in arc voltage, penetration depth, melting efficiency, heat input, and cross-sectional area has been observed, while oxide formation tends to be reduced when hydrogen is added [5–7, 10–16].

Conclusions

The main results can be summarized as follows:

1. The use of silicon and titanium oxides (TiO_2 and SiO_2) increased the weld penetration depth during *A-TIG* welding, regardless of the type and grade of steel. The increase in weld penetration depth ranged from 30% to more than 200%.

2. The flux layer thickness is an important parameter in *A-TIG* welding. This study shows significant variations in the weld penetration for a thickness range of 0–200 μm. It has been found that the optimized

thickness in the *A-TIG* process ranges from 40 to 70 μm, depending on the welding current, and results in a twofold increase in weld penetration at a given current level.

3.. The welding current directly affects the geometric characteristics of the weld when using *TiO₂* and *SiO₂* fluxes, such as the cross-sectional area, width, and depth of the weld. When comparing conventional *TIG* and *A-TIG* welding, there is almost a twofold difference in the depth of penetration for the same increase in current.

4. The effect of the type and grade of steel on the penetration capability when using activating fluxes has not been clearly identified. Only minor changes in the depth of penetration have been recorded between low-alloy and stainless steels.

References

1. Paton B.E., Zamkov V.N., Prilutsky V.P., Poritsky P.V. Kontraktsiya dugi flyusom pri svarke vol'framovym elektrodom v argone [Arc contraction by flux during tungsten electrode welding in argon]. *Avtomaticheskaya svarka = Automatic Welding*, 2000, no. 1, pp. 3–9.

2. Savitsky M.M., Kushnirenko B.N., Oleynik O.N. Osobennosti svarki stalei vol'framovym elektrodom s aktiviruyushchimi flyusami [Features of welding steels with a tungsten electrode with activating fluxes]. *Avtomaticheskaya svarka = Automatic Welding*, 1999, no. 12, pp. 18–22.

3. Acharya S., Patra S., Das S. Predicting A-TIG weld bead geometry of 304 stainless steel using artificial neural networks. *Discover Mechanical Engineering*, 2025, vol. 4 (1), p. 12. DOI: 10.1007/s44245-025-00096-5.

4. Modenesi P.J. The chemistry of TIG weld bead formation. *Welding International*, 2015, vol. 29 (10), pp. 771–782. DOI: 10.1080/09507116.2014.932990.

5. Mohsein Z.H., Abdulwahhab A.B., Abbas A.M. Study effect of active flux on mechanical properties of TIG welding process. *Results in Engineering*, 2025, vol. 26, p. 104681. DOI: 10.1016/j.rineng.2025.104681.

6. Görgün E. Advancing welding quality through intelligent TIG welding: A hybrid deep learning approach for defect detection and quality monitoring. *Dicle Üniversitesi Mühendislik Fakültesi Mühendislik Dergisi*, 2025, vol. 16 (3), pp. 677–685. DOI: 10.24012/dumf.1642978.

7. Morisada Y., Fujii H., Xukun N. Development of simplified active flux tungsten inert gas welding for deep penetration. *Materials & Design*, 2014, vol. 54, pp. 526–530. DOI: 10.1016/j.matdes.2013.08.081.

8. Dhandha K.H., Badheka V.J. Effect of activating fluxes on weld bead morphology of P91 steel bead-on-plate welds by flux assisted tungsten inert gas welding process. *Journal of Manufacturing Processes*, 2015, vol. 17, pp. 48–57. DOI: 10.1016/j.jmapro.2014.10.004.

9. Nayee S.G., Badheka V.J. Effect of oxide-based fluxes on mechanical and metallurgical properties of dissimilar activating flux assisted-tungsten inert gas welds. *Journal of Manufacturing Processes*, 2014, vol. 16 (1), pp. 137–143. DOI: 10.1016/j.jmapro.2013.11.001.

10. Shravan C., Radhika N., Deepak Kumar N.H., Sivasailam B. A review on welding techniques: properties, characterisations and engineering applications. *Advances in Materials and Processing Technologies*, 2023, vol. 10, pp. 1126–1181. DOI: 10.1080/2374068X.2023.2186638.

11. Mi H., Ma J., Feng L., Guo W., He B. A critical review on advanced welding technologies to fabricate test blanket modules and irradiation damage behaviour of the welded joints in nuclear fusion applications. *Journal of Manufacturing Processes*, 2025, vol. 141, pp. 829–864. DOI: 10.1016/j.jmapro.2025.03.025.

12. Fande A.W., Taiwade R.V., Raut L. Development of activated tungsten inert gas welding and its current status: A review. *Materials and Manufacturing Processes*, 2022, vol. 37 (8), pp. 841–876. DOI: 10.1080/10426914.2022.2039695.

13. Tanaka M., Shimizu T., Terasaki T., Ushio M., Koshiishi F., Yang C.-L. Effects of activating flux on arc phenomena in gas tungsten arc welding. *Science and Technology of Welding and Joining*, 2000, vol. 5 (6), pp. 397–402. DOI: 10.1179/136217100101538461.

14. Babkin A.S., Kotov N.S., Terekhov V.V. Vliyanie aktiviruyushchikh flyusov na kharakteristiki elektricheskoi dugi i kachestvo shvov pri svarke austenitnykh stalei [The influence of activating fluxes on the characteristics of the electric arc and the quality of seams in welding austenitic steels]. *Izvestiya TulGU. Tekhnicheskie nauki = Bulletin of Tula State University. Technical Sciences*, 2022, no. 10, pp. 507–514. DOI: 10.24412/2071-6168-2022-10-507-514.

15. Ivanchik N.N., Balanovsky A.E., Kondratyev V.V., Tyutrin A.A. Issledovaniya produktov pererabotki otkhodov kremniya v kachestve ul'tradispersnykh aktiviruyushchikh flyusov dlya dugovoi svarki [Research of silicon waste processing products as ultradispersed activating fluxes for arc welding]. *Zhurnal Sibirskogo federal'nogo*

universiteta. Tekhnika i tekhnologii = Journal of Siberian Federal University. Engineering and Technologies, 2018, no. 11 (2), pp. 155–167. DOI: 10.17516/1999-494X-0019.

16. Parshin S.G. *Nanostrukturirovannye i aktiviruyushchie materialy dlya dugovoi svarki* [Nanostructured and activating materials for arc welding]. St. Petersburg, Polytechnic University Publ., 2020. DOI: 10.18720/SPBPU/2/si20-888.

17. Jayakrishnan S., Chakravarthy P. Flux bounded tungsten inert gas welding for enhanced weld performance – A review. *Journal of Manufacturing Processes*, 2017, vol. 28, pp. 116–130. DOI: 10.1016/j.jmapro.2017.05.023.

18. Bhanu V., Gupta A., Pandey C. Role of A-TIG process in joining of martensitic and austenitic steels for ultra-supercritical power plants-a state of the art review. *Nuclear Engineering and Technology*, 2022, vol. 54 (8), pp. 2755–2770. DOI: 10.1016/j.net.2022.03.003.

19. Pandya D., Badgujar A., Ghetiya N. A novel perception toward welding of stainless steel by activated TIG welding: a review. *Materials and Manufacturing Processes*, 2021, vol. 36 (8), pp. 877–903. DOI: 10.1080/10426914.2020.1854467.

20. Kumar N., Pandey C., Kumar P. Dissimilar welding of Inconel alloys with austenitic stainless-steel: a review. *Journal of Pressure Vessel Technology*, 2023, vol. 145 (1), p. 011506. DOI: 10.1115/1.4055329.

21. Martyushev N.V., Skeeba V.Yu. The method of quantitative automatic metallographic analysis. *Journal of Physics: Conference Series*, 2017, vol. 803 (1), p. 012094. DOI: 10.1088/1742-6596/803/1/012094.

22. Kavishwar S., Bhaiswar V., Kochhar S., Fande A. Comprehensive studies on conventional and novel weld cladding techniques and their variants for enhanced structural integrity: an overview. *Welding International*, 2024, vol. 38 (9), pp. 618–638. DOI: 10.1080/09507116.2024.2402285.

23. Sharma P., Dwivedi D.K. A-TIG welding of dissimilar P92 steel and 304H austenitic stainless steel: Mechanisms, microstructure and mechanical properties. *Journal of Manufacturing Processes*, 2019, vol. 44, pp. 166–178. DOI: 10.1016/j.jmapro.2019.06.003.

24. Efremenkov E.A., Martyushev N.V., Skeeba V.Yu., Grechneva M.V., Olisov A.V., Ens A.D. Research on the possibility of lowering the manufacturing accuracy of cycloid transmission wheels with intermediate rolling elements and a free cage. *Applied Sciences*, 2022, vol. 12 (1), p. 5. DOI: 10.3390/app12010005.

25. Vidyarthy R.S., Dwivedi D.K., Vasudevan M. Influence of M-TIG and A-TIG welding process on microstructure and mechanical behavior of 409 ferritic stainless steel. *Journal of Materials Engineering and Performance*, 2017, vol. 26 (3), pp. 1391–1403. DOI: 10.1007/s11665-017-2538-5.

26. Zhang R.H., Pan J.L., Katayama S. The mechanism of penetration increase in A-TIG welding. *Frontiers of Materials Science*, 2011, vol. 5, pp. 109–118. DOI: 10.1007/s11706-011-0125-5.

27. Singh S.R., Khanna P. A-TIG (activated flux tungsten inert gas) welding: – A review. *Materials Today: Proceedings*, 2021, vol. 44, pp. 808–820. DOI: 10.1016/j.matpr.2020.10.712.

28. Wu H., Chang Y., Mei Q., Liu D. Research advances in high-energy TIG arc welding. *The International Journal of Advanced Manufacturing Technology*, 2019, vol. 104 (1), pp. 391–410. DOI: 10.1007/s00170-019-03918-5.

29. Tseng K.H., Lin P.Y. UNS S31603 stainless steel tungsten inert gas welds made with microparticle and nanoparticle oxides. *Materials*, 2014, vol. 7 (6), pp. 4755–4772. DOI: 10.3390/ma7064755.

30. Mamadaliev R.A., Bakhmatov P.V., Martyushev N.V., Skeeba V.Yu., Karlina A.I. Influence of welding regimes on structure and properties of steel 12KH18N10T weld metal in different spatial positions. *Metallurgist*, 2022, vol. 65 (11–12), pp. 1255–1264. DOI: 10.1007/s11015-022-01271-9.

31. Balanovskiy A.E., Astafyeva N.A., Kondratyev V.V., Karlina A.I. Study of mechanical properties of C-Mn-Si composition metal after wire-arc additive manufacturing (WAAM). *CIS Iron and Steel Review*, 2021, vol. 22, pp. 66–71. DOI: 10.17580/cisisr.2021.02.12.

32. Karlina A.I., Karlina Y.I., Kondratiev V.V., Kononenko R.V., Breki A.D. Study of wear of an alloyed layer with chromium carbide particles after plasma melting. *Crystals*, 2023, vol. 13 (12), p. 1696. DOI: 10.3390/cryst13121696.

33. Kolosov A.D., Gozbenko V.E., Shtayger M.G., Kargapoltsev S.K., Balanovskiy A.E., Karlina A.I., Sivtsov A.V., Nebogin S.A. Comparative evaluation of austenite grain in high-strength rail steel during welding, thermal processing and plasma surface hardening. *IOP Conference Series: Materials Science and Engineering*, 2019, vol. 560, p. 012185. DOI: 10.1088/1757-899X/560/1/012185.

34. Malushin N.N., Gizatulin R.A., Martyushev N.V., Valuev D.V., Karlina A.I., Kovalev A.P. Strengthening of metallurgical equipment parts by plasma surfacing in nitrogen atmosphere. *Metallurgist*, 2022, vol. 65 (11–12), pp. 1468–1475. DOI: 10.1007/s11015-022-01292-4.

35. Nokhrina O.I., Gizatulin R.A., Golodova M.A., Proshunin I.E., Valuev D.V., Martyushev N.V., Karlina A.I. Alloying and modification of iron-carbon melts with natural and man-made materials. *Metallurgist*, 2022, vol. 65 (11–12), pp. 1429–1448. DOI: 10.1007/s11015-022-01289-z.

36. Yelemessov K., Baskanbayeva D., Martyushev N.V., Skeeba V.Y., Gozbenko V.E., Karlina A.I. Change in the properties of rail steels during operation and reutilization of rails. *Metals*, 2023, vol. 13, p. 1043. DOI: 10.3390/met13061043.

37. Skeeba V.Yu., Ivancivsky V.V., Kutyshkin A.V., Parts K.A. Hybrid processing: the impact of mechanical and surface thermal treatment integration onto the machine parts quality. *IOP Conference Series: Materials Science and Engineering*, 2016, vol. 126 (1), p. 012016. DOI: 10.1088/1757-899x/126/1/012016.

Conflicts of Interest

The authors declare no conflict of interest.

Obrabotka metallov –
Metal Working and Material Science

Journal homepage: http://journals.nstu.ru/obrabotka_metallov

Optimal milling parameters of 0.12 C-18 Cr-10Ni-Ti stainless steel fabricated by electron beam additive manufacturing

*Mengxu Qi [1, a], Sergey Panin[2, b, *], Dmitry Stepanov [2, c], Mikhail Burkov [2, d], Qingrong Zhang[1, e]*

[1] National Research Tomsk Polytechnic University, 30 Lenin Avenue, Tomsk, 634050, Russian Federation

[2] Institute of Strength Physics and Materials Sciences SB RAS, 2/4 per. Academicheskii, Tomsk, 634055, Russian Federation

[a] https://orcid.org/0000-0003-3738-0193, ✉ mensyuy1@tpu.ru; [b] https://orcid.org/0000-0001-7623-7360, ✉ svp@ispms.ru;
[c] https://orcid.org/0000-0003-2558-7613, ✉ sdu@ispms.ru; [d] https://orcid.org/0000-0002-3337-6579, ✉ burkovispms@mail.ru;
[e] https://orcid.org/0009-0002-7820-1227, ✉ cinzhun1@tpu.ru

ARTICLE INFO

ABSTRACT

Introduction. Unlike traditional manufacturing processes, additive manufacturing (*AM*) offers improved efficiency while being environmentally friendly. A significant limitation hindering the adoption of wire-based electron beam additive manufacturing (*EBAM*) technology is the relatively low quality and high surface roughness of 3D-printed parts. **The purpose of this study** is to establish the optimal values of milling process parameters (rotational speed, feed rate, and milling width) based on the simultaneous evaluation of the surface roughness of the machined surface and the material removal rate. **Methods and materials.** This study investigated specimens fabricated using *EBAM* technology. Uniaxial tensile tests were conducted on an electromechanical testing machine. Cutting forces were determined with a *Kistler 9257B* dynamometer. Milling studies of *EBAM* 321 steel workpieces were performed on a semi-industrial *CNC* milling machine. **Results and discussion.** It was shown that in order to increase the material removal rate and reduce the cutting force on a milling machine without the use of coolant, it is recommended to increase the milling speed, but not to increase the feed rate. To investigate the relationship between material removal rate and surface roughness relative to milling parameters on a semi-industrial machine (with an average stiffness of the portal frame), multiple linear regression models and nonlinear models based on feedforward neural networks were employed. It was demonstrated that linear regression models are sufficient for predicting optimal milling parameters. However, it should be noted that the study was conducted within a narrow range of gentle machining conditions, with short processing times and without accounting for tool wear. Under these constraints, the optimal milling parameters for *EBAM 321* steel were predicted as follows: spindle speed of 4,500 rpm, feed rate S = 404 mm/min, and cutting depth B = 0.43 mm, resulting in a predicted surface roughness (Ra) of 0.648 μm and a material removal rate of 695 mm³/min.

* Corresponding author
Panin Sergey V., D.Sc. (Engineering), Professor
Institute of Strength Physics and Materials Sciences SB RAS,
2/4 per. Academicheskii,
634055, Tomsk, Russian Federation
Tel.: +7 3822 286-904, **e-mail:** svp@ispms.ru

Introduction

Traditionally, stainless steels are classified into five categories: (*I*) austenitic, (*II*) ferritic, *III*) martensitic, (*IV*) duplex, and (*V*) precipitation-hardened. Among them, the austenitic steels are the most widely used in terms of fabricated metal products [1]. *AISI 321* steel possesses excellent resistance to intercrystalline corrosion and maintains stable functional properties at elevated temperatures. Therefore, it is often used under severe conditions, such as high pressures, radiation exposure, and corrosive environments [2–3].

Unlike traditional subtractive manufacturing technologies, additive manufacturing (*AM*) offers several advantages: reduced production time, increased material utilization rate, and the ability to create complex internal structures within components. When applied to metallic materials, *AM* includes various methods: Selective Laser Melting (*SLM*), Electron Beam Selective Melting (*EBSM*), Wire Laser AM (*WLAM*), Wire Arc AM (*WAAM*), and Electron Beam Wire-Feed AM (*EBWAM*) [3–16]. Compared with *WLAM* and *WAAM*, electron beam wire-feed *AM* (*EBWAM*) is characterized by a higher production rate (up to 12 kg/h [7]), as well as reduced atmospheric contamination [8] and spatter of molten material [9, 10].

In recent years, additive manufacturing (*AM*) has rapidly expanded its application scope due to a range of advantages. This production method enables the fabrication of complex-shaped parts with high precision using various materials, from plastics to metals, while significantly reducing time and costs compared to traditional manufacturing technologies [1–4]. Depending on the requirements for the final product, different *AM* technologies are employed. Active development of *AM* leads to a reduction in product cost. It makes rapid production possible for parts and workpieces with not only complex geometries but also simpler shapes made of expensive materials [5–6]. Flanges made of heat-resistant materials are an example of such parts. When using *AM*, there is no need to create holes through drilling; moreover, the volume of material removed through subtractive processing is reduced. This economically justifies the application of *AM*. The use of *AM* for manufacturing flanges allows them to be tailored to specific sizes, resulting in even greater time and cost savings compared to the production of similar parts from wrought stock [7–9].

A specific limitation hindering the adoption of wire-based additive manufacturing technology is the low dimensional (shape) accuracy and high surface roughness of as-built parts [14]. Powder-based additive manufacturing technologies (specifically SLM) enable the production of parts with high dimensional accuracy and low surface roughness. However, even they cannot match the surface roughness achieved by finish turning and/or finish milling [16], necessitating post-process machining.

On the other hand, compared to powder-based processes, the wire-based *AM* methods, particularly the *EBWAM* method, offer higher production rates and are better suited for manufacturing large-sized products [6–10]. Consequently, parts produced by wire-based *AM* inevitably require subsequent machining. Thus, the development of hybrid technologies that combine additive and subtractive manufacturing processes is receiving significant attention in scientific and technical literature [16].

Additive manufacturing also offers advantages in customization, prototyping, and the fabrication of complex geometries; however, it is generally unsuitable for large-scale mass production, which often requires the use of expensive, dedicated multi-axis machining equipment. In contrast, semi-industrial (light-duty, universal) milling machines are cheaper and more flexible to reconfigure compared to traditional industrial equipment. They are typically used for small-batch, custom production or can be effective during the stage of optimizing process parameters for post-additive machining.

Given the demand for wire-based *AM* technologies, the use of semi-industrial (light-duty, universal) *CNC* milling machines within a unified technological cycle alongside *3D*-printing systems appears promising. This approach would not only allow for the adaptive selection of machining parameters for the printed workpiece, primarily based on criteria for improving accuracy and reducing surface roughness, but also enable the establishment of a correlation between the process parameters of *AM* and the resulting machinability. The latter could also minimize the scope of required metallurgical investigations.

In this context, it is relevant to study the machinability of wire-feed electron beam additively manufactured (*EBAM*) austenitic stainless steel *AISI 321* and to determine the optimal cutting parameters when machining on both industrial (including dry machining) and semi-industrial (universal, easily reconfigurable) *CNC*

machines, for which the corresponding recommendations from cutting tool manufacturers cannot always be directly applied.

The purpose of this study was to select the optimal values for the process parameters of finish milling (spindle speed, feed rate, and depth of cut / cutting width) based on a simultaneous evaluation of the machined surface roughness and material removal rate (*MRR*) during the machining of workpieces made of *EBAM AISI 321* austenitic stainless steel. To address the aim, the following ***objectives*** were set:

– assessment of mechanical properties of *EBAM AISI 321* stainless steel;

– establishing a correlation between cutting speed and feed rate and the cutting force during dry machining on a conventional (industrial) machine;

– establishing the relationship between the *MRR* and surface roughness and milling parameters during machining on a semi-industrial large-format *CNC* milling machine with coolant, employing both multiple linear regression models and non-linear models based on feedforward neural networks (*FFNN*).

Methods

AISI 321 steel wire with a diameter of 1.2 mm was used as the feedstock. In all cases, *AISI 321* steel plates, 5 mm thick, were used as substrates, which were initially ground and cleaned with acetone.

Samples were fabricated using an electron beam wire-feed additive manufacturing (*EBWAM*) facility with a vacuum chamber volume of 8 m³, developed by the Institute of Strength Physics and Materials Science *SB RAS* [17]. A thick wall with dimensions of 85 mm × 20 mm × 25 mm (Fig. 1) was built from the 1.2 mm diameter wire at an accelerating voltage of 30 kV, a chamber pressure of 5×10^{-3} Pa, a beam travel speed of 400 mm/min, and a wire feed rate of 1,768 mm/min. A circular beam oscillation pattern was applied with a beam diameter of 4 mm at a frequency of 1 kHz. The beam current was 75 mA for the first layer and 50 mA for all subsequent layers, with a layer height of 1 mm. The chemical composition of the wire is shown in Table 1.
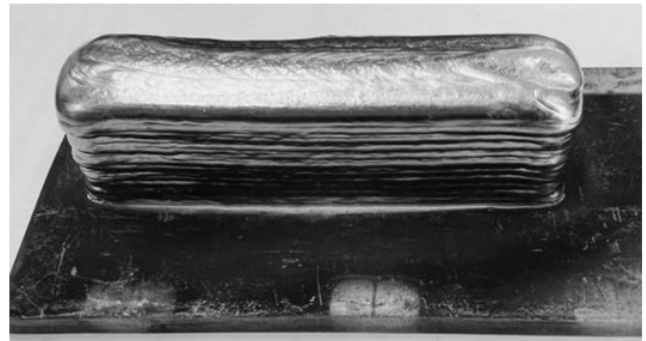
Fig. 1. Photographs of the 3D-built *EBAM 0.12C-18Cr-10Ni-Ti sample*

Table 1

Chemical composition of the *0.12C-18Cr-10Ni-Ti* stainless steel wire

Chemical composition, wt%								
Fe	*Cr*	*Ni*	*Mn*	*Ti*	*Si*	*Cu*	*Mo*	*Co*
65.3	19.6	11.5	0.8	0.7	0.7	0.5	0.32	0.7

Microhardness was measured using an automated system based on an *EMCO-TEST DuraScan-10* microhardness tester. Measurements were conducted according to the *Vickers* method under a load of 1 kgf with a dwell time of 10 seconds. Uniaxial tensile tests were performed on a *UTS-110M-100* electromechanical testing machine. The *crosshead* speed was 2 mm/min.

Milling of the additively manufactured blanks under dry conditions was performed on a *FU-251* (Russia) milling machine. The cutting force was measured using a *Kistler 9257B* (Switzerland) dynamometer (Fig. 2, *a*). Data analysis was conducted using *DynoWare* software. The dynamometer's resolution is 7.5 N, with a linearity error of ±0.005 %. Across multiple experimental runs (involving workpiece or tool repositioning) under identical parameters, the measured force variation did not exceed 15%. In machining processes, this represents acceptable repeatability, considering the complexity of the cutting process and potential inhomogeneity of the workpiece material.

a

b
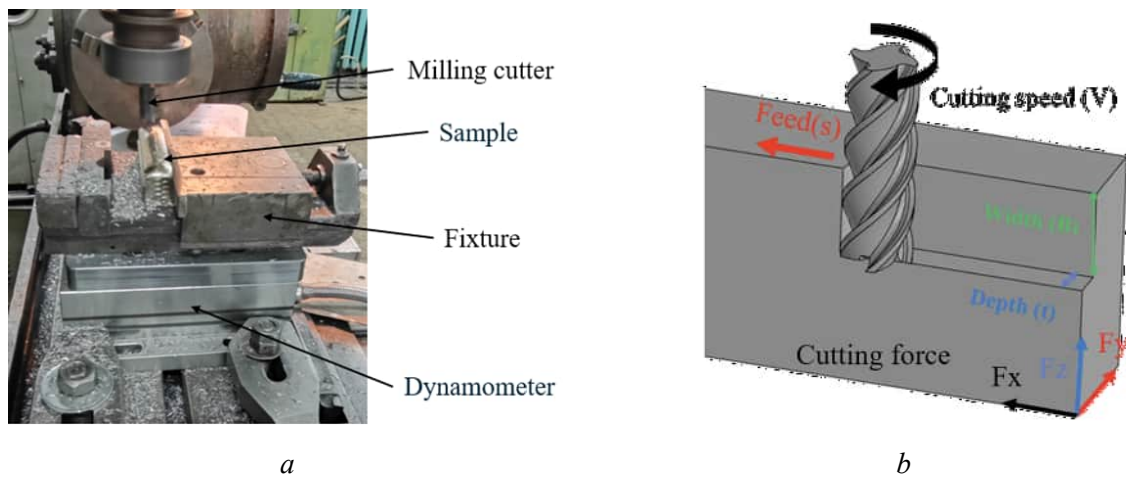
Fig. 2. General view of the setup fixed on the milling machine (*a*); milling scheme (*b*)

Fig. 2, *b* shows the milling parameters, including feed per tooth (f_z), cutting speed (v_c), depth of cut (a_p), width of cut (**B**), and the resultant cutting force (**F**). Solid carbide end mills (*GESAC UP210-S4-12030*) with a diameter of 12 mm were used. The helix angle was $\omega = 35°$, the flute length was 30 mm, the overall length was 75 mm, the rake angle (γ) was 7°, and the clearance angle (α) was 5°.

Research on milling workpieces made of *EBAM AISI 321* stainless steel with coolant was conducted on a large-format *PureLogic RM0813 CNC* milling machine (Russia) (Fig. 3, *a*). This machine is designed for milling, drilling, engraving, and cutting parts from non-ferrous metals and plastics, with the following specifications: spindle power of 2.2 kW, working volume ($X \times Y \times Z$) of 1,300 × 800 × 200 mm, and a positioning accuracy of 0.1 mm over 100 mm. Solid carbide end mills (**ZC-CCT VSM-4E-D8.0**) with a diameter of 8 mm were utilized. The variable helix angle was $\omega = 38°/41°$, the flute length was 20 mm, the overall length was 60 mm, the rake angle (γ) was 7°, and the clearance angle (α) was 10°. The surface roughness (R_a) of the milled side faces of the workpieces was measured using a **TR200** (China) stylus profilometer (Fig. 3, *b*). To enhance productivity and reduce cutting force when using coolant, higher values of cutting speed and feed rate were employed.

The *Taguchi* method was used for designing the machining experiments. This method employs the signal-to-noise ratio (**S/N** ratio) as an optimization criterion to evaluate the robustness and reliability of output parameters (primarily surface roughness) and utilizes orthogonal arrays to minimize the number of experimental runs [18, 19]. The Taguchi method is widely used to analyze the influence of various process parameters on output quality characteristics [20]. An L_9 orthogonal array was selected. The milling

a

b
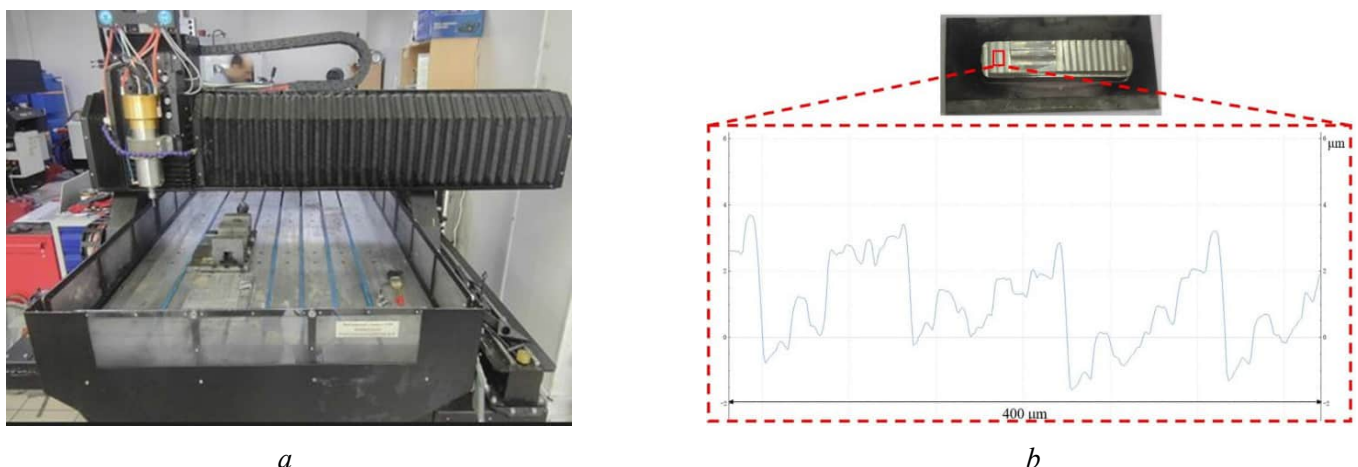
Fig. 3. The *RM0813-01S2 CNC* machine (a); an example of the surface profile after milling (*b*)

process parameters (factors: spindle speed **n**, feed rate **S**, and width of cut **B**) and their levels are presented in Table 2. Three levels were chosen for each factor, which also determine the material removal rate (*MRR*). The key output response was surface roughness (**R**$_a$).

Table 2

Mechanical properties of the *EBAM 0.12C-18Cr-10Ni-Ti* sample

Samples	Tensile strength, MPa	Yield strength, MPa	Elongation, %	Hardness, HV
EBAM 0.12C-18Cr-10Ni-Ti	570±10	208±10	70±2	191±5
Wrought 0.12C-18Cr-10Ni-Ti	700 ± 10	250 ± 10	63 ±3	230 ±5

Results and Discussion

The hardness and other key mechanical properties of the investigated samples are presented in Table 2. The *EBAM AISI 321* stainless steel exhibited high ductility (70 %), tensile strength (570 MPa), and hardness (191 HV). The strength properties of the wrought *AISI 321* steel were higher than those of the additively manufactured sample, which is attributed to the wrought condition, characterized by higher ferrite content, finer grain, and a higher dislocation density [21]. For the *EBAM* sample, the layer-by-layer deposition process involved multiple thermal cycles, leading to the formation of columnar grains. However, the corrosion rate of the wrought *AISI 321* steel was approximately twice as high as that of the additively manufactured steel.

Machinability Studies on a Stationary Milling Machine. As shown in Table 3, nine milling modes were used to investigate the variation in cutting force for the *EBAM AISI 321* stainless steel workpieces. These modes included combinations of low speed with high feed, high speed with low feed, and medium speed with medium feed.

The selection of milling parameters was based on the tool manufacturer's recommendations. It should be noted that using a high-performance milling regime (a high width-to-depth ratio, see Table 3) helps reduce rapid tool wear.

Fig. 4, *a* shows the influence of different milling regimes on the cutting force for the *EBAM AISI 321* stainless steel workpiece. The resultant cutting force (**F**$_{xyz}$), calculated as the vector sum, was used for evaluation according to Equation (1):

$$F_{xyz} = \sqrt{\left(F_X^{\max}\right)^2 + \left(F_Y^{\max}\right)^2 + \left(F_Z^{\max}\right)^2} , \qquad (1)$$

where $F_{\max}$ is the maximum force value within the analysis interval.

Table 3

Parameters applied for studying the cutting forces during milling using the industrial machine

Number	Cutting speed **V**, m/min	Feed rate **S**, mm/min	Width **B**, mm	Depth **t**, mm
1	25	50		
2	25	160		
3	25	250		
4	50	50		
5	50	160	8	0,5
6	50	250		
7	75	50		
8	75	160		
9	75	250		
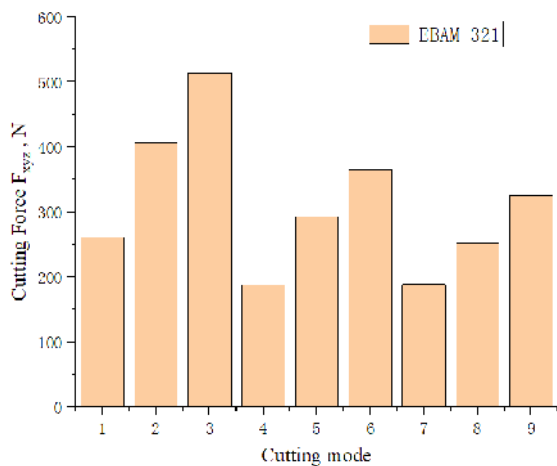
a
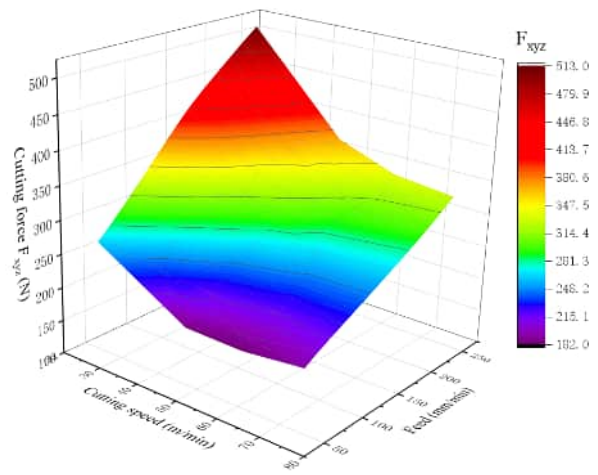
b

Fig. 4. The effect of different cutting modes on the cutting force (*a*); the effect of cutting speed and feed rate on the cutting force during machining (*b*)

It was found that Mode No. 4 resulted in the smallest cutting force (F_{xyz} = 188 N).

Fig. 4, *b* shows the influence of cutting speed (v_c) and feed per tooth (f_z) on the cutting force during machining of the *EBAM* workpiece. It is evident that the strength and hardness of the additively manufactured steel significantly affected the cutting force. Low cutting speed combined with high feed rate led to an increase in cutting force, while high cutting speed with low feed rate reduced it.

Overall, two trends were observed: the cutting force decreased with increasing cutting speed and increased with increasing feed rate. When the depth (a_p) and width (*B*) of cut remain constant, a higher feed rate increases productivity. Therefore, to machine *EBAM AISI 321* steel with increased productivity and reduced cutting force, a higher cutting speed should be used, while the feed rate should not be increased excessively.

Machinability studies on the large-format *RM0813 CNC* milling machine. It is known that surface roughness depends on numerous parameters, including cutting speed, feed rate, depth of cut, and tool wear [22]. Table 4 shows the milling parameters used to investigate surface roughness (R_a) and *MRR*, including spindle speed (*n*), feed rate (*S*), and width of cut (*B*).

As noted earlier, machining on large-format *CNC* milling machines may be performed using regimes that differ from the cutting tool manufacturers' recommendations. Therefore, developing approaches to

T a b l e 4

Milling parameters for the semi-industrial machine, determined using the *Taguchi* method and machinability assessment results

Number	Spindle speed *N*, rpm	Feed rate *S*, mm/min	Width *B*, mm	Depth *t*, mm	Surface roughness *Ra*, μm	*MRR*, mm^3/min
1	1,000	200	0.1		0.46±0.02	80
2	1,000	400	0.3		1.29±0.04	480
3	1,000	600	0.5		2.57±0.23	1200
4	2,500	200	0.3		0.59±0.03	240
5	2,500	400	0.5	4	1.01±0.04	800
6	2,500	600	0.1		0.88±0.04	240
7	4,000	200	0.5		0.63±0.03	400
8	4,000	400	0.1		0.40±0.01	160
9	4,000	600	0.3		0.75±0.03	720

determine optimal milling parameters with minimal time and cost is highly relevant. Determining optimal cutting parameters can be considered a task of finding milling regimes that satisfy an optimality condition.

The optimality criterion should provide a comprehensive assessment of both the milling process efficiency and the finished product quality. Among the process characteristics, the material removal rate (*MRR*) was analyzed, while product quality was characterized by the post-processing surface roughness (**R_a**). Tool wear, another critical characteristic, was excluded from these experiments as the selected regimes were conservative and the testing duration was short. Consequently, the optimality criterion can be formulated as a system of boundary expressions:

$$\begin{cases} Ra(S, B, N) \to \min, \\ MRR(S, B) \to \max. \end{cases} \quad (2)$$

Based on expression (2), a more formal suboptimality criterion can be derived as a system of inequalities:

$$\begin{cases} Ra(S, B, N) \le \overline{R_a}, \\ MRR(S, B) \ge \overline{MRR}. \end{cases} \quad (3)$$

where $\overline{R_a}$ and $\overline{MRR}$ are the maximum allowable roughness and minimum required *MRR*, respectively.

The range of parameters (**S, B, n**) satisfying the system of inequalities (3) defines the region of suboptimal parameters (*SOP*) [23].

The results of the acceptable milling parameters analysis are presented in Table 5. The used linear regression ("Regress") model had the following statistics: coefficient of determination **R^2** = 0.884, normalized mean square error **NMSE** = 0.214, and significance level **p** = 0.0089. Based on this model, predicted roughness values were calculated within the allowable parameter range, the *SOP* satisfying condition (3) was identified, and a response surface graph for this region was plotted (Fig. 5, *a*, *c*). Despite the obtained high-quality metrics of the regression model, the hypothesis of a non-linear relationship between roughness and milling parameters was subsequently tested.

Based on the data from the *L₉ Taguchi* design experiments (see Table 4), the coefficients for the multiple linear regression were calculated using the least squares method [24–26]. The resulting roughness equation is:

$$R_a = 0.2014 - 0.00028N + 0.0021S + 2.059B. \quad (4)$$

As a non-linear modeling approach capable of generalizing experimental results, feedforward neural network (*FFNN*) modeling was chosen [27–28]. The network architecture was selected following the principle "from simple to complex". The training dataset was formed from experimental data (Table 4) with normalization of input and output values within the limits specified in Table 5. The best convergence

Table 5

**Limiting ranges and suboptimality boundaries for the milling parameters
and analyzed characteristics**

	Permissible limits		Suboptimality boundaries	
	Min	Max	Min	Max
Parameter				
Spindle speed **N**, rpm	500	5,000		
Feed rate **S**, mm/min	100	800		
Width **B**, mm	0.1	1		
Characteristics				
Surface roughness **Ra**, μm	0	4	–	0.8
MRR, mm³/min	0	2,000	300	–
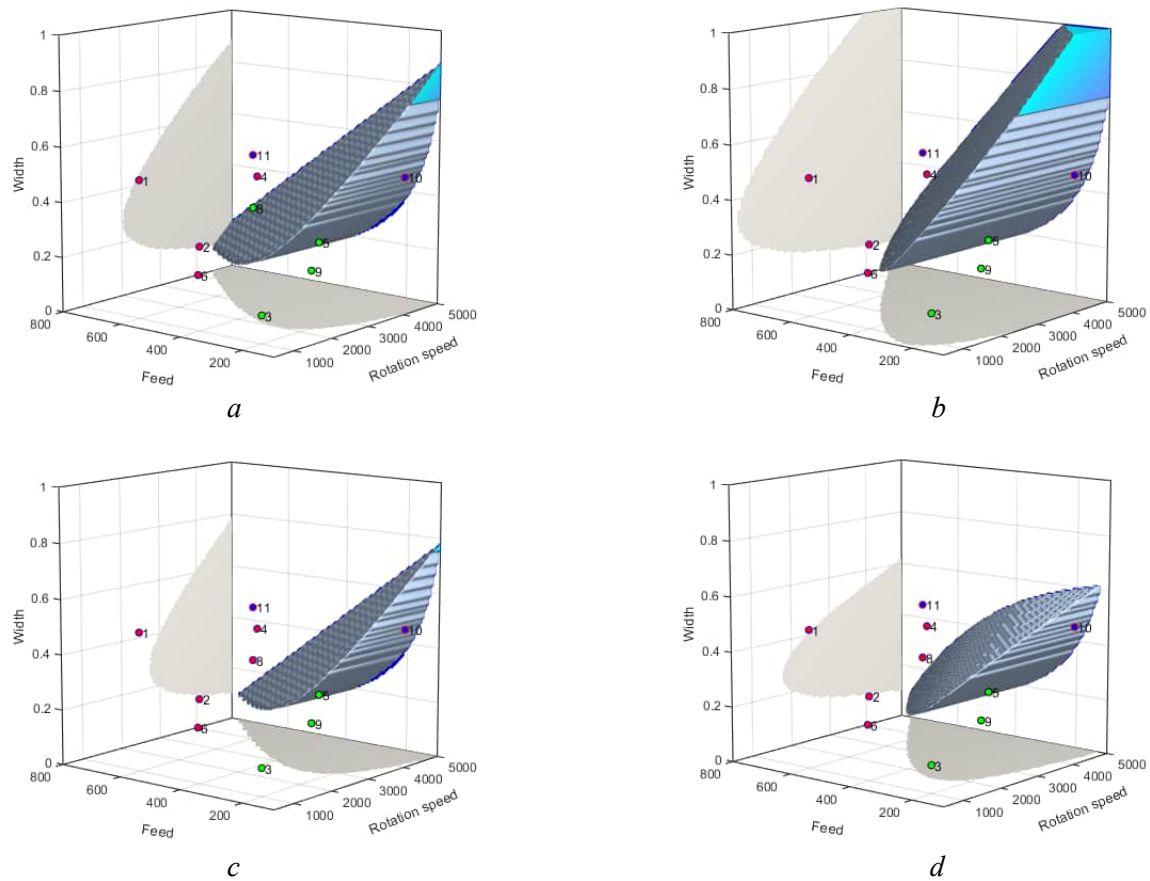
Fig. 5. Milling parameters and the *SOP* regions plotted using the linear regression model (*a, c*) and the *FFNN* model (*b, d*) at $\overline{p}$ = 300 mm³/min; $\overline{Ra}$ = 0.8 μm (*a, b*) and $\overline{Ra}$ = 0.6 μm (*c, d*)

rate during training was achieved using the logarithmic tangent activation function and the *Levenberg-Marquardt* optimization algorithm. The number of layers and neurons per layer was chosen based on the analysis of the resulting model's *SOP*.

Among all considered variants, a network with one hidden layer containing three neurons was selected, as it demonstrated the simplest and most plausible *SOP* (Fig. 5, *b, d*). This model showed better agreement with the training dataset compared to the regression model: $\boldsymbol{MSE}$ = 0.00049061, $\boldsymbol{R^2}$ = 0.99504.

Comparing the obtained results, it was concluded that the *FFNN* model constrained the *SOP* region from above with a surface that was close to linear but had a steeper slope for high roughness values ($\overline{Ra}$ > 0.65 μm). In other words, the *FFNN* model included milling parameters with higher width of cut and *MRR* values in the low-feed *SOP* region. For low roughness values ($\overline{Ra}$ < 0.65 μm), this non-linear surface had the opposite effect: parameters with high width of cut and spindle speed were excluded from the *SOP*.

To verify the identified discrepancies, the developed models were validated through physical experiments by comparing predicted and actual surface roughness measurements. The experimental parameters were selected according to the following conditions: values outside the predicted *SOP* (No. 10, Table 6), boundary values of the *SOP* (No. 11, Table 6), and an internal point within the *SOP* (No. 12, Table 6). Table 6 also includes the predicted and experimental roughness values.

It was established that both models provided errors within an acceptable range, but the linear regression model demonstrated higher accuracy in terms of mean deviations. Its prediction for the optimal milling parameters is: spindle speed $\boldsymbol{n}$ = 4500 rpm, feed rate $\boldsymbol{S}$ = 404 mm/min, and width of cut $\boldsymbol{B}$ = 0.43 mm, with a predicted roughness $\boldsymbol{R_a}$ = 0.648 μm and a material removal rate MRR = 695 mm³/min.

Holkar, H., et al. [29] selected optimal cutting parameters for milling *AISI 321* stainless steel using the Taguchi method. The study considered the effect of spindle speed, feed rate, and depth of cut on surface roughness, tool wear, and *MRR*. *Arlyapov, A.*, et al. [30] compared various tool geometries, cutting speeds,

T a b l e 6

Milling parameters for model verification, along with experimental and predicted results

No.	Milling parameters			Characteristics			
	Spindle speed N, rpm	Feed rate S, mm/min	Width B, mm	MRR, mm³/min	Surface roughness Ra, μm		
					Experiment	Regress	*FFNN*
10	4,000	100	0.5	200	0.333	0.3117	0.6115
11	4,000	600	0.5	1200	1.193	1.3617	1.0429
12	4,500	400	0.3	480	0.425	0.3889	0.5224
Average deviation						0.0753	0.1753

feed rates, and depth-to-width of cut ratios to evaluate tool wear and cutting force. It was shown that selecting milling parameters is a complex multi-criteria problem requiring extensive experimentation. A promising direction of the present research is the evaluation of factors affecting the surface roughness of *EBAM AISI 321* samples while ensuring a high *MRR*.

In summary, comparing the machinability assessment data for the industrial (dry) and the semi-industrial large-format *CNC* (with coolant) milling machines during finish milling of *EBAM AISI 321* stainless steel indicates that to achieve a higher *MRR*, reduced roughness, and lower cutting force, the cutting speed should be increased, while the feed rate should not be raised proportionally.

Furthermore, the developed regression and *FFNN* models for the semi-industrial machine enable the prediction of optimal process parameters, which is highly relevant for optimizing 3D-printing parameters that influence the microstructure and mechanical properties of layer-by-layer fabricated workpieces. Tool wear remains an important factor in assessing material machinability, as surface roughness increases with machining time due to cutting tool wear.

Future research plans include using the linear regression model to determine the optimal parameter range, followed by investigating the influence of machining time on tool wear and surface roughness.

Conclusion

1. Additively manufactured (*EBAM*) *AISI 321* stainless steel, fabricated with the utilized process parameters, exhibited high ductility (70 %), tensile strength (570 MPa), and hardness (191 HV).

2. It was established that to increase the material removal rate and reduce the cutting force during dry milling on a conventional milling machine, it is recommended to increase the cutting speed, while avoiding a proportional increase in the feed rate.

3. To investigate the relationship between material removal rate, surface roughness, and milling parameters on a semi-industrial large-format *CNC* milling machine (with a portal frame of moderate stiffness) under coolant supply, both multiple linear regression and non-linear feedforward neural network (*FFNN*) models were employed. It was shown that a linear regression model provided sufficient accuracy for predicting optimal milling parameters under the given conditions. However, the study was conducted within a narrow range of conservative regimes, with short machining times and without accounting for tool wear. Within these constraints, the following optimal milling parameters for the *EBAM AISI 321* were identified: spindle speed of 4,500 rpm, feed rate $S = 404$ mm/min, and width of cut $B = 0.43$ mm, yielding a predicted surface roughness of $R_a = 0.648$ μm and a material removal rate of 695 mm³/min.

References

1. Lippold J.C., Kotecki D.J. *Welding metallurgy and weldability of stainless steels*. Hoboken, John Wiley & Sons, 2005. 357 p. ISBN 978-0-471-47379-4.

2. Huang Z., Zhang J., Ma Z., Yuan S., Yang H. Research progress on the relationship between microstructure and properties of AISI 321 stainless steel. *Applied Sciences*, 2024, vol. 14 (22), p. 10196. DOI: 10.3390/app142210196.

3. Yin Q., Chen G., Cao H., Zhang G., Zhang B., Wei S. Transformation law of microstructure evolution and mechanical properties of electron beam freeform fabricated 321 austenitic stainless steel. *Vacuum*, 2021, vol. 194, p. 110594. DOI: 10.1016/j.vacuum.2021.110594.

4. Ma M., Wang Z., Gao M., Zeng X. Layer thickness dependence of performance in high-power selective laser melting of 1Cr18Ni9Ti stainless steel. *Journal of Materials Processing Technology*, 2014, vol. 215, pp. 142–150. DOI: 10.1016/j.jmatprotec.2014.07.034.

5. Kameneva A.L., Minkova A.A., Cherkashneva N.N., Karmanov V.V. Correlation between heat treatment process parameters, phase composition, texture, and mechanical properties of 12H18N10T stainless steel processed by selective laser melting. *IOP Conference Series: Materials Science and Engineering*, 2018, vol. 447 (1), p. 012043. DOI: 10.1088/1757-899X/447/1/012043.

6. Wang X., Hu Q., Liu W., Yuan W., Shen X., Gao F., Tang D., Hu Z. Microstructure and corrosion properties of wire arc additively manufactured multi-trace and multilayer stainless steel 321. *Metals*, 2022, vol. 12, p. 1039. DOI: 10.3390/met12061039.

7. Zhong C., Gasser A., Backes G., Fu J., Schleifenbaum J.H. Laser additive manufacturing of Inconel 718 at increased deposition rates. *Materials Science and Engineering: A*, 2022, vol. 844, p. 143196. DOI: 10.1016/j.msea.2022.143196.

8. Sciaky Inc. *Benefits of Wire vs. Powder Metal 3D Printing. Comparing Sciaky's wirefeed 3D printing process, a.k.a. Electron Beam Additive Manufacturing, to powder-based feedstock 3D printing processes*. Available at: https://www.sciaky.com/additive-manufacturing/wire-vs-powder (accessed 30.10.2025).

9. Chen Y., Chen X., Jiang M., Lei Z., Wang Z., Liang J., Wu S., Ma S., Jiang N., Chen Y. Coaxial laser metal wire deposition of Ti6Al4V alloy: process, microstructure and mechanical properties. *Journal of Materials Research and Technology*, 2022, vol. 20, pp. 2578–2590. DOI: 10.1016/j.jmrt.2022.08.068.

10. Caballero A., Ding J., Ganguly S., Williams S. Wire + arc additive manufacture of 17-4 PH stainless steel: Effect of different processing conditions on microstructure, hardness, and tensile strength. *Journal of Materials Processing Technology*, 2019, vol. 268, pp. 54–62. DOI: 10.1016/j.jmatprotec.2019.01.007.

11. Węglowski M.S., Błacha S., Phillips A. Electron beam welding – Techniques and trends – Review. *Vacuum*, 2016, vol. 130, pp. 72–92. DOI: 10.1016/j.vacuum.2016.05.004.

12. Wang D., Liu Z., Liu W. Experimental measurement of vacuum evaporation of aluminum in Ti-Al, V-Al, Ti6Al4V alloys by electron beam. *Metals*, 2021, vol. 11 (11), p. 1688. DOI: 10.3390/met11111688.

13. Lyu Z., Sato Y.S., Tokita S., Zhao Y., Jia J., Wu A. Microstructural evolution in a thin wall of 2Cr13 martensitic stainless steel during wire arc additive manufacturing. *Materials Characterization*, 2021, vol. 182, p. 111520. DOI: 10.1016/j.matchar.2021.111520.

14. Martyushev N.V., Kozlov V.N., Qi M., Tynchenko V.S., Kononenko R.V., Konyukhov V.Yu., Valuev D.V. Production of workpieces from martensitic stainless steel using electron-beam surfacing and investigation of cutting forces when milling workpieces. *Materials*, 2023, vol. 16, p. 4529. DOI: 10.3390/ma16134529.

15. Ravi G.A., Hao X., Wain N., Wu X., Attallah M.M. Direct laser fabrication of three dimensional components using SC420 stainless steel. *Materials & Design*, 2013, vol. 47, pp. 731–736. DOI: 10.1016/j.matdes.2012.12.062.

16. Grzesik W. Hybrid additive and subtractive manufacturing processes and systems: A review. *Journal of Machine Engineering*, 2018, vol. 18, pp. 5–24. DOI: 10.5604/01.3001.0012.7629.

17. Klimenov V.A., Kolubaev E.A., Han Z., Chumaevskii A.V., Klopotov A.A., Ustinov A.M., Kovalevskaya Z.G, Moskvichev E., Pan M. Influence of anisotropy properties and structural inhomogeneity on elasticity and fracture of titanium alloys produced by electron-beam melting. *The International Journal of Advanced Manufacturing Technology*, 2024, vol. 135, pp. 5575–5594. DOI: 10.1007/s00170-024-14843-7.

18. Park S.H. *Robust design and analysis for quality engineering*. London, Chapman & Hall, 1996. 256 p.

19. Phadke M.S. *Quality engineering using robust design*. Englewood Cliffs, NJ, Prentice-Hall, 1989. 320 p.

20. Nalbant M., Gökkaya H., Sur G. Application of Taguchi method in the optimization of cutting parameters for surface roughness in turning. *Materials & Design*, 2007, vol. 28 (4), pp. 1379–1385. DOI: 10.1016/j.matdes.2006.01.008.

21. Panin S.V., Qi M., Stepanov D.Y., Burkov M.V., Rubtsov V.E., Kushnarev Y.V., Litovchenko I.Yu. Comprehensive analysis of microstructure and mechanical, operational, and technological properties of AISI 321 austenitic stainless steel at electron beam freeform fabrication. *Construction Materials*, 2025, vol. 5 (3), p. 62. DOI: 10.3390/constrmater5030062.

22. Zhang J.Z., Chen J.C., Kirby E.D. Surface roughness optimization in an end-milling operation using the Taguchi design method. *Journal of Materials Processing Technology*, 2007, vol. 184 (1–3), pp. 233–239. DOI: 10.1016/j.jmatprotec.2006.11.029.

23. Stepanov D.Y., Tian D., Alexenko V.O., Panin S.V., Buslovich D.G. Application of neural network models with ultra-small samples to optimize the ultrasonic consolidation parameters for 'PEI Adherend/Prepreg (CF-PEI Fabric)/PEI Adherend' lap joints. *Polymers*, 2024, vol. 16, p. 451. DOI: 10.3390/polym16040451.

24. Draper N.R., Harry S. *Applied regression analysis*. 3rd ed. Wiley-Interscience, 1998. 736 p. ISBN 0471170828. ISBN 9780471170822.

25. Kuprienko N.V., Ponomareva O.A., Tikhonov D.V. *Statisticheskie metody izucheniya svyazei: Korrelyatsionno-regressionnyi analiz* [Statistical methods for studying relationships]. St. Petersburg, SPbPU Publ., 2009. 118 p.

26. Yan X., Su X. *Linear regression analysis: Theory and computing*. Singapore, World Scientific Publishing, 2009. 328 p. ISBN 9812834109. ISBN 9789812834102.

27. Haykin S.S. *Neural networks and learning machines*. 3rd ed. Upper Saddle River, NJ, Pearson Education, 2009. ISBN 978-0131471399.

28. Swingler K. *Applying neural networks: A practical guide*. San Francisco, CA, Morgan Kaufman Publishers, 1996. 303 p. ISBN 0126791708. ISBN 9780126791709.

29. Holkar H., Sadaiah M. Optimization of end milling machining parameters of AISI 321stainless steel using Taguchi method. *International Journal on Recent and Innovation Trends in Computing and Communication*, 2016, vol. 4, pp. 20–23.

30. Arlyapov A., Volkov S., Promakhov V., Matveev A., Babaev A., Vorozhtsov A., Zhukov A. Study of the machinability of an Inconel 625 composite with added NiTi-TiB$_2$ fabricated by direct laser deposition. *Metals*, 2022, vol. 12 (11), p. 1956. DOI: 10.3390/met12111956.

Conflicts of Interest

The authors declare no conflict of interest.

Obrabotka metallov –
Metal Working and Material Science

Journal homepage: http://journals.nstu.ru/obrabotka_metallov

Investigation of the thermal loading during turning of a metal–composite system as a function of cutting speed, feed rate, and depth when machining a thin-walled 2 mm metal shell

Nikolay Lubimyi [a], Boris Chetverikov [b, *], Sergey Klyuyev [c], Nikolay Zagorodniy [d],
Andrey Polshin [e], Ardalion Mal'tsev [f], Mikhail Bytsenko [g]

Belgorod State Technological University named after V.G. Shukhov, 46 Kostyukova St., Belgorod, 308012, Russian Federation

[a] https://orcid.org/0000-0002-6131-3217, ✉ nslubim@bk.ru; [b] https://orcid.org/0000-0003-1801-6767, ✉ await_rescue@mail.ru;
[c] https://orcid.org/0000-0002-1995-6139, ✉ klyuyev@yandex.ru; [d] https://orcid.org/0000-0002-2997-3282, ✉ n.zagorodnij@yandex.ru;
[e] https://orcid.org/0000-0001-5809-4458, ✉ info@polshin.ru; [f] https://orcid.org/0000-0002-0878-3658, ✉ ardalion_bgtu@mail.ru;
[g] https://orcid.org/0009-0004-2133-885X, ✉ b.michutka2005@gmail.com

ARTICLE INFO

ABSTRACT

Introduction. This paper is devoted to the study of the thermal loading of the turning process for metal–composite systems (*MCS*) consisting of a thin-walled, additively manufactured metal shell and a metal-polymer filler. **The purpose of this study** is to investigate the influence of technological turning parameters on the temperature in the cutting zone of metal-composite systems (*MCS*) with a 2 mm thick metal shell and to determine the permissible machining conditions that prevent thermal degradation of the metal-polymer filler. **Methodology.** For experimental modeling of the *MCS*, a hardware-software complex was developed, including a replaceable metal sleeve made of *0.12C18Cr-10Ni-Ti* steel, ferrochrome metal–polymer (*TU 2257-002-48460567-00*), three thermocouples with *MAX6675* analog-to-digital converters, and a wireless data transmission module based on an *ESP32*. The temperature at the metal-metal-polymer interface was recorded in real time. The results were verified using a non-contact method with a *FLUKE Ti400* thermal imager (error of 3–5 °C). The experiment was conducted according to a full factorial design $2^3 + n_0$ with variation of cutting speed V (m/min), feed rate S (mm/rev), and depth of cut t (mm), including central points for assessing the curvature of the response surface. **Results and discussion.** Based on the experimental data obtained for the 2 mm shell, a second-order regression model (*2T3*) was constructed, demonstrating high adequacy. Analysis of the model coefficients showed that the depth of cut t has the greatest influence on the temperature increase, followed by the feed rate S, while the cutting speed V has the least effect within the studied range. Using the model, response surfaces and contour maps were constructed, allowing visualization of *safe* machining regions that satisfy the constraint T ≤ 170 °C — the heat resistance limit of the metal-polymer. The obtained dependencies provide a basis for standardizing finishing turning parameters for tooling components with additively formed shells and metal-polymer fillers.

Introduction

Manufacturing of components with intensive heat exchange, such as injection-molding dies for thermoplastics and solid-body cutting tools, has increasingly relied in recent years on metal-composite systems (*MCS*) [1], which combine a thin-walled metallic shell with a filler made of metal-polymer

---

composite material (*MPCM*). This approach allows integrating the high strength and stiffness of the metallic framework with the damping properties and processing advantages of *MPCM*, while simultaneously reducing the overall weight and production cost.

The key enabler behind the development of metal–composite systems (*MCS*) is the capability of additive manufacturing (*AM*) [2], particularly selective laser melting (*SLM*), to produce curvilinear (conformal) cooling channels within metallic shells [3]. For molding dies, this enables directed heat extraction from zones of maximum thermal load, uniform temperature distribution, a reduction in the molding or stamping cycle time, and improved dimensional stability.

From a technological standpoint, the process can be described as follows: a pocket is machined in the metallic base plate of the die to accommodate a replaceable forming insert; the forming insert itself is produced as a thin-walled metallic shell with integrated curvilinear cooling channels; after assembly, the cavity between the shell and the base plate is filled with a metal-polymer composite material (*MPCM*), which secures the insert, enhances thermal contact, and ensures load transfer during die operation.

A similar design and technological concept can be implemented in cutting tools [3], for example, in a composite drill: the metallic *SLM*-manufactured shell of the drill body, featuring specially designed internal cooling channels, delivers the cutting fluid (*CF*) directly to the cutting zone, while the internal cavity formed as a result of topology optimization (*TO*) [4] is filled with metal-polymer composite material (*MPCM*). The filler absorbs volumetric loads and enhances the vibration damping of the tool. This configuration increases the durability of the carbide cutting head by improving heat removal from the cutting area.

In recent years, additive manufacturing (*AM*) has become a powerful technological solution for producing complex thin-walled shells and hollow components with integrated cooling channels. For example, the review [5] emphasizes that during the machining of *AM*-produced parts, post-processing operations such as turning play a crucial role, since the layered structure, residual stresses, and altered thermal conductivity of the material significantly affect chip formation, dimensional accuracy, and thermal loads. For a thin-walled metallic shell filled with *MPCM*, this means that turning requires consideration not only of the cutting parameters but also of the shell geometry, specific features of the additively manufactured structure, and the thermal behavior at the metal-polymer interface.

Fig. 1, *a* shows a digital model of the drill body after topology optimization (*TO*), which allowed for a 40 % reduction in metal consumption – an essential factor for ensuring the economic feasibility of applying *SLM*-based additive manufacturing (*AM*) technology in industrial production [6]. Fig. 1, *b* presents a physical sample of the topology-optimized metal-composite drill body with its internal cavities filled with *MPCM*, forming a complete metal-composite system (*MCS*).

A critical technological stage in manufacturing *MCS* is the mechanical finishing (including turning) of the outer and seating surfaces after the internal cavities have been filled with *MPCM*. Unlike homogeneous metallic workpieces, the heat flux in this case is constrained by the metal-*MPCM* interfacial boundary, while the *MPCM* itself exhibits lower thermal conductivity and limited heat resistance. Overheating during turning can lead to local thermal degradation of the polymer matrix, loss of strength, and weakened adhesion at the interface, which in turn causes deterioration of dimensional accuracy and reduced service life of the product. Meanwhile, engineering recommendations for selecting turning parameters for such hybrid shells with composite fillers remain scarce [7]. Most available data [8, 9] refer either to monolithic metallic parts or to polymer-based composites without a metallic shell.

One of the key challenges in machining thin-walled and metal-composite systems is the increase in temperature in the cutting zone and the resulting thermal loading, which leads to thermal deformations, deterioration of surface quality, and reduced dimensional accuracy of the workpiece. For instance, the study [10] demonstrated that during dry turning of aluminum-based composites reinforced with dispersed phases, thermal loading increases significantly compared to monolithic alloys: higher cutting speeds and feeds cause temperature spikes in the cutting zone. In the context of machining metallic shells with fillers – especially thin-walled ones (with thicknesses of about 2 mm or less) – the effect of thermal loading is further aggravated by reduced structural stiffness and limited heat dissipation through the workpiece.

a   *b*
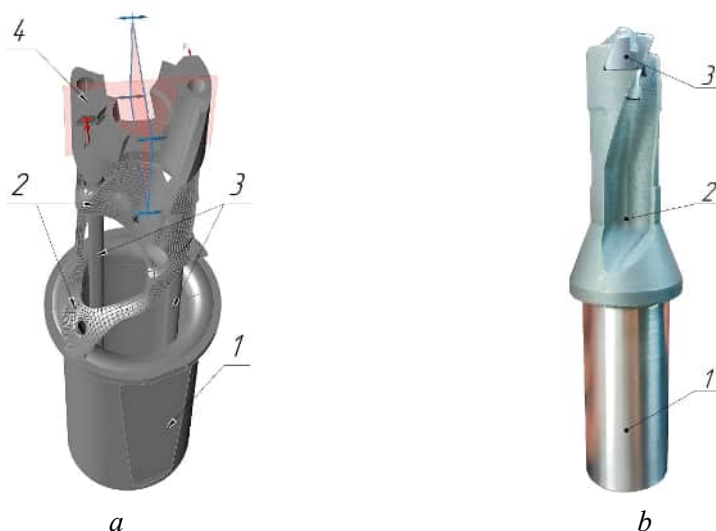
Fig. 1. (*a*) Digital model of the drill body with topology optimization applied (the middle part of the chip grooves is conventionally omitted):

1 – shank area (metal); 2 – load-bearing structural elements formed by topology optimization (metal); 3 – cooling channels (metal); 4 – mounting seat for a replaceable carbide cutting head (*b*) Physical sample of the topology-optimized metal–composite drill body manufactured using *SLM* technology: 1 – turned metal–composite shank; 2 – chip grooves; 3 – cutting head of the drill body

The design features of thin-walled shells and their interaction with the metal–polymer filler are important aspects of the design of metal-composite systems (*MCS*). The review [11] emphasizes that thin-walled components possess low stiffness and unstable thermal-mechanical characteristics, which impose significant constraints on cutting parameters as well as on the requirements for tooling and fixturing. When a metal-polymer filler is introduced inside the shell, an additional thermal and phase interface – metal–*MPCM* – is formed. This interface requires detailed analysis of the temperature distribution precisely at this boundary to prevent thermal degradation of the filler and to ensure that surface quality requirements are maintained.

Studies have also focused on the influence of cutting tool design and machining technology on thermal load and cutting quality. For example, the work [12] demonstrates how variations in the material and coating of the cutting insert can reduce both tool and workpiece temperatures during the turning process. It is increasingly recognized that not only the cutting parameters (speed, feed, and depth of cut), but also the tool geometry, insert material, and the applied cooling or lubrication system play a crucial role in controlling thermal loading during machining.

In recent years, cooling and lubrication strategies have been considered among the key factors determining the thermal state of the tool-workpiece system. The review [13] notes that the choice of coolant and its delivery strategy – whether conventional emulsion supply, minimum quantity lubrication (*MQL*), or the use of nanofluids – has a significant impact on cutting temperature, chip formation stability, and tool wear. For the machining of thin-walled structures and composites, where the heat flux is limited due to the low thermal conductivity and small mass of the workpiece, cooling efficiency becomes critically important. Therefore, the correct selection of coolant composition, supply pressure, and flow rate is an essential condition for obtaining reliable temperature measurements and provides an objective basis for constructing regression models of thermal loading for the turning process of metal-composite systems (*MCS*).

It is also worth noting the studies devoted to the influence of protective and anti-friction coatings of cutting tools on heat distribution and cutting temperature. For example, the paper [14] shows that the use of *PVD* coatings significantly reduces both tool and workpiece temperatures, improves surface quality, and decreases wear when machining thin-walled components. This confirms the necessity of considering not only cutting speed, feed rate, and depth of cut in the study, but also the tool properties (insert material and coating) as well as the cooling conditions.

Therefore, for the reliable implementation of metal–composite systems (*MCS*) in industrial production, a quantitative assessment of the thermal loading during the turning process is required, taking into account the actual geometry and thickness of the metallic shell, the properties of the *MPCM*, and the cutting parameters — cutting speed (*V*), feed rate (*S*), and depth of cut (*t*). Such an assessment should lead to engineering-applicable models and allowable parameter domains that ensure the required surface quality and preservation of the *MPCM* structure [15, 16].

The purpose of this study was to quantitatively assess the thermal loading during the turning of metal-composite systems (*MCS*) consisting of a thin-walled additively manufactured metallic shell and a metal-polymer composite filler, to develop a model describing the dependence of temperature at the metal-*MPCM* interface on the cutting parameters (*V, S, t*), and to justify the acceptable operating range of cutting conditions that ensure the required surface quality and prevent thermal degradation of the *MPCM* in practical applications. To achieve this goal, the following ***research objectives*** were formulated:

– Development of a hardware-software setup simulating a metal-composite system (metallic shell + metal-polymer filler), enabling temperature measurement at the metal-*MPCM* interfacial boundary during external turning of a thin-walled metallic shell with a thickness of 2 mm;

– Execution of an experimental study on the turning of the simulated metal–composite model according to a full factorial experimental design of type $2^3 + n_0$;

– Construction of a regression model based on the experimental data, with evaluation of the statistical significance of the coefficients and the adequacy of the model;

– Development of graphical representations of the regression model in the form of response surface plots and contour maps, illustrating the dependence of interfacial temperature on cutting parameters for analyzing the thermal state of the cutting process.

Methods
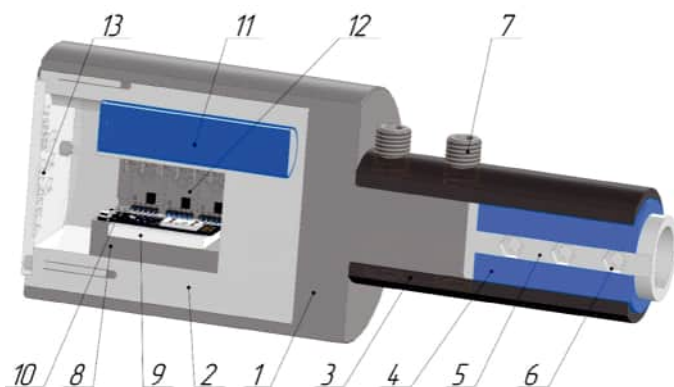
Fig. 2. 3D model of the hardware–software device for measuring temperature during turning of the metal–composite system (*MCS*), simulating a metal shell filled with *MPCM*:

1 – housing (*0.4C* steel); 2 – plastic holder for fastening electrical components inside the housing; 3 – replaceable sleeve (*0.12C18Cr-10Ni-Ti*); 4 – *MPCM* insert; 5 – plastic holder for mounting thermocouples; 6 – holes for M8 nuts; 7 – fastening screws for securing the replaceable sleeve; 8 – microprocessor enclosure; 9 – prototyping board; 10 – *ESP32* microcontroller; 11 – 2,600 mAh rechargeable battery; 12 – *MAX6675* thermocouples; 13 – cover

To study the thermal loading during the turning process, a specially developed hardware-software device was used, simulating a metal–composite system (metallic shell + metal-polymer filler). The assembly consists of a steel housing with a battery unit, a replaceable metallic sleeve, a metal-polymer insert, and three measurement channels based on *MAX6675* modules (thermocouple-to-digital converters) that transmit real-time data via Wi-Fi (*ESP32* microcontroller → *PC*). The digital model of the experimental device is shown in Fig. 2.

The design allows for quick replacement of sleeves to vary the thickness of the metallic wall and enables mounting of the workpiece in the chuck of a *16K20* lathe. The consistency of readings from the contact sensors was verified using a *FLUKE Ti400* thermal imager, with discrepancies not exceeding 3–5 °C. To ensure proper thermal contact, *KPT-8* thermal paste was applied at the sensor mounting points.

Fig. 3 shows the physical model of the developed hardware–software device used for the experimental study.

The replaceable metallic sleeves (Fig. 4) were manufactured from *0.12% C-12% Cr-18% Ni-1% Ti* (*AISI 304*) steel tubing, selected as an accessible material analog for high-alloy steel with low thermal conductivity [17].
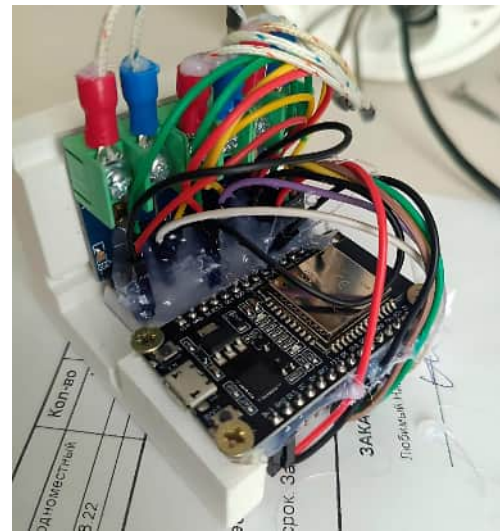
a   *b*

Fig. 3. Physical model of a device for measuring temperature data during turning Physical model
of a device for measuring temperature data during turning:

(*a*) assembled device body; (*b*) assembly of the microprocessor unit

Fig. 4. Replacement sleeves processed during the experiment

The thermal conductivity of *0.12% C-12% Cr-18% Ni-1% Ti* steel is approximately 15–16 W/(m·K), which is close to that of the *EP648* heat-resistant alloy (12–15 W/(m·K)) commonly used in additive manufacturing. This ensured comparable heating conditions during the turning of the *MCS*.

The metal–polymer composite material (*MPCM*) "Ferro-Chrome" (*TU 2257-002-48460567-00*) [18] was used as the filler. This material has lower thermal conductivity than steel and limited heat resistance, necessitating temperature control during finish machining. The insert was formed by casting the compound into a mold, followed by turning to match the inner diameter of the metallic sleeve.

For the experiments aimed at developing a temperature model at the *MCS* interface, Tungaloy *DNMG150408-TF AH6225* turning inserts designed for finishing operations were used. The dimensional layout of the insert is shown in Fig. 5, and its geometric characteristics are listed in Table 1. The cutting tool material was cemented carbide *AH6225* (*WC–Co–TiC–Al$_2$O$_3$*) with a *TiAlN + TiN PVD* coating, providing high heat and wear resistance when machining steels.
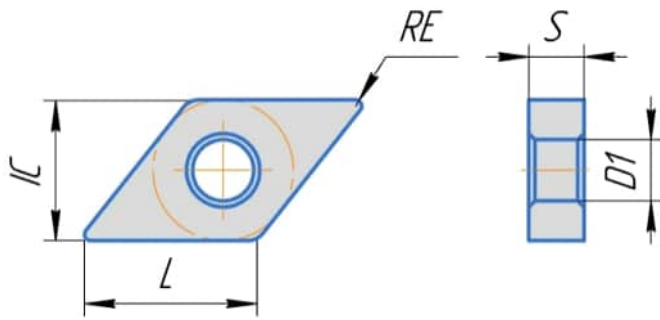
Fig. 5. Tungaloy *DNMG150408-TF AH6225* cutting
insert geometry diagram

The tool holder used was *DCLNR 2020K12 – M* (medium type, with a negative rake angle).

The summarized maximum temperature values obtained for each experimental run are presented in Table 1.

The machining was carried out on a *16K20* universal lathe using a coolant and lubrication supply system (*CLSS*). The working fluid was a mineral-based water–oil emulsion of type *I-20A* with the addition of 5 % *Emulsol ED-20*, providing effective cooling and friction reduction in the tool-workpiece contact zone. The emulsion was supplied as a continuous jet under a pressure of 0.25 ± 0.05 MPa directly into the cutting zone, with an average flow rate of 2–3 L/min. The selected coolant composition and delivery parameters correspond to the standard recommendations for finish turning of structural steels.

Table 1

Geometrical and operational parameters of the cutting insert *Tungaloy DNMG150408-TF AH6225*

Designation	*Параметр / Parameter*	*Meaning*
RE	Radius at the apex	0.80 mm
IC	Inscribed circle	12.7 mm
S	Plate thickness	4.76 mm
D1	Hole in the center	5.16 mm
–	Angle of the shape	55° (rhombic)
–	Cutting edge type	*TF* (thin, finishing)
–	Class	*M* (medium negative rake angle)

The measurement setup involved positioning three sensors near the metal–*MPCM* interfacial boundary along the sample axis. A sampling rate of 200 ms ensured recording of the temperature response during steady-state cutting. Data transmission was carried out via **UDP** protocol to a personal computer, while visualization and data logging were performed using a custom *Python* application (Fig. 6).

Verification of the surface temperature distribution was performed using thermographic method [19], and the analysis was based on the maximum cutting temperature values [20]. Fig. 7 shows the verification of temperature measurement data obtained using the thermal imager.

The experiment was carried out according to a full factorial design of type $2^3 + n_0$. The varying factors were cutting speed V (m/min), feed per revolution S (mm/rev), and depth of cut t (mm) [21]. The experimental matrix included eight factorial points (levels −1 / +1 in coded form) and $n_0 = 5$ central runs (0, 0, 0) to estimate the reproducibility variance and to test the curvature of the response surface.

The selected range of variation for the depth of cut (t = 0.5–1.5 mm) was determined by the nominal machining allowance per side. A typical finishing allowance of 0.5 mm is recommended, which corresponds to a single finishing pass with a depth of cut of 0.5 mm, provided that a low feed rate and efficient heat removal are maintained. Machining can also be performed in two passes – e.g., 0.3 mm roughing + 0.2 mm finishing – but this approach contradicts the principle of minimizing overall machining time. However, considering the need to remove supports and surface defects associated with additive manufacturing, the depth of the defective surface layer, and consequently the machining allowance, may increase up to 2 mm. Therefore, the upper limit of the depth-of-cut range was set at 1.5 mm. Higher depths are not recommended, as further increases would lead to deterioration of surface roughness.

The variation ranges for cutting speed (V) and feed per revolution (S) were selected to ensure the required surface roughness of $R_a \leq 2.5$ μm. The chosen parameter ranges implicitly account for this roughness constraint across the entire domain of factor variation.
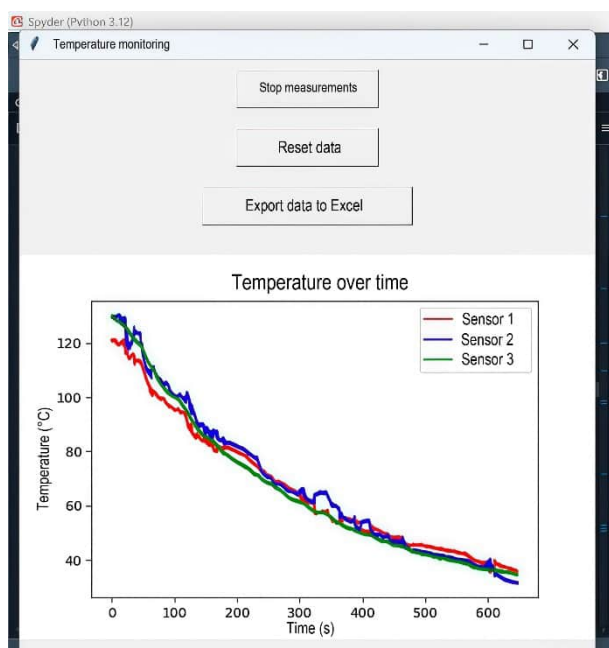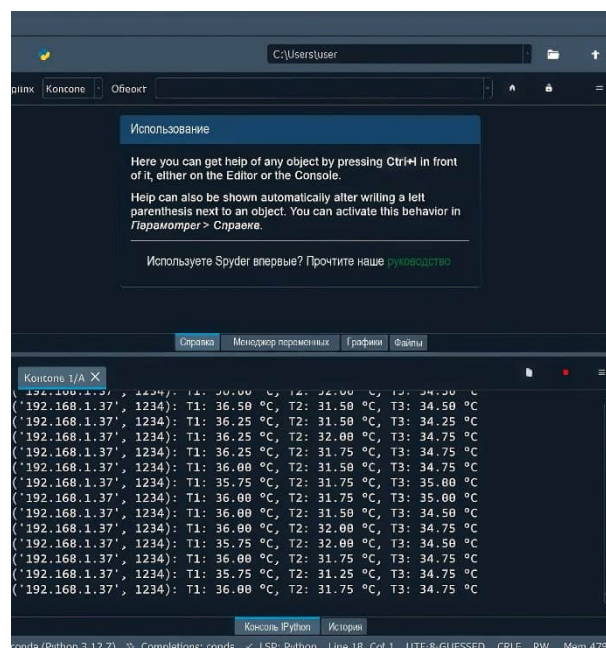
| *a* | *b* |

Fig. 6. (*a*) Dialog box of the Temperature Monitoring program implemented in *Python 3.12* for recording the cutting temperature of the *MCS*; (*b*) System monitor console displaying transmitted temperature data in real time

| *a* | *b* |

Fig. 7. Verification of temperature readings obtained from thermocouples using the
FLUKE Ti400 thermal imager:

(*a*) thermal imager measurement; (*b*) temperature diagram

For each parameter, three variation levels were selected – minimum, maximum, and central – as presented in Table 2.

Table 2

Levels of variation of experimental factors

Factor	*Designation*	−1	0	+1
Feed rate, *S* (mm/rev)	x_1	0.05	0.10	0.15
Cutting speed, *V* (m/min)	x_2	60	90	120
Depth of cut, *t* (mm)	x_3	0.5	1.0	1.5

Table 3 presents the experimental design matrix (full factorial design $2^3 + n_0$). The matrix includes eight factorial points with coded levels (–1, +1) and five central runs (0, 0, 0), which allows for evaluating the curvature of the response surface and verifying the adequacy of the regression model.

T a b l e 3

Levels of variation of experimental factors

No.	x_1, (*S*, mm/rev)	x_2, (*V*, m/min)	x_3, (*t*, mm)	Mode (code)
1	0.5	60	0.05	(–1. –1. –1)
2	0.5	60	0.15	(–1. –1. +1)
3	0.5	120	0.05	(–1. +1. –1)
4	0.5	120	0.15	(–1. +1. +1)
5	0.15	60	0.05	(+1. –1. –1)
6	0.15	60	0.15	(+1. –1. +1)
7	0.15	120	0.05	(+1. +1. –1)
8	0.15	120	0.15	(+1. +1. +1)
9–11	0.10	90	0.10	(0. 0. 0)

As a result of each experimental run, time-dependent datasets of cutting temperature were obtained. For every run, the maximum temperature *T* at the metal-*MPCM* interfacial boundary was recorded using three sensors.

The regression model was constructed using coded variables x_1, x_2, and x_3 [22]. A second-order model with pairwise interaction terms was considered:

$$T = b_0 + b_1 x_1 + b_2 x_2 + b_3 x_3 + b_4 x_1^2 + b_5 x_2^2 + b_6 x_3^2 + b_7 x_1 x_2 + b_8 x_1 x_3 + b_9 x_2 x_3 \qquad (1)$$

The coefficients were estimated using the least squares method. The statistical significance of the coefficients was evaluated using the *t*-test ($\alpha = 0.05$), and the model adequacy was verified using the *F*-test, with calculation of the coefficient of determination (R^2). For engineering visualization [23], response surfaces $T(V, S)$ were constructed at fixed values of *t*.

Results and Discussion

Based on the series of experiments conducted for the *MCS* with a metallic shell thickness of $\delta = 2$ mm, simultaneous temperature measurements were taken using three sensors (T_1, T_2, T_3), resulting in a total of 39 observations (three temperature maxima per experimental run). Fig. 8 shows the temperature plot for the second experimental run.

The summarized maximum temperature values for each experimental run are presented in Table 4.

The experiment showed that the characteristic temperature levels ranged from approximately 27 °C to 190 °C, with peak values up to ~189 °C observed under the most aggressive combination of cutting parameters (Run No. 2). This exceeds the technological heat resistance limit of the *MPCM* for finish machining operations, confirming the critical importance of proper selection of cutting conditions for *MCS* with this metallic shell thickness.

When constructing the model based on experimental data with thermocouples embedded at a depth of 2 mm, only the data obtained from thermocouple No. 3 were used. This model was designated as *2T3*, where '2' denotes the thickness of the metallic shell, and 'T3' refers to the thermocouple from which the valid data were obtained. This decision was made because thermocouples No. 1 and No. 2 produced evidently unreliable readings in certain trials. For example, in Run 8, thermocouple No. 1 recorded a maximum temperature of 27.3 °C, which did not reflect the actual cutting conditions. Similarly, thermocouple No. 2 showed inconsistent readings during Runs 1, 4, 6, and 8.
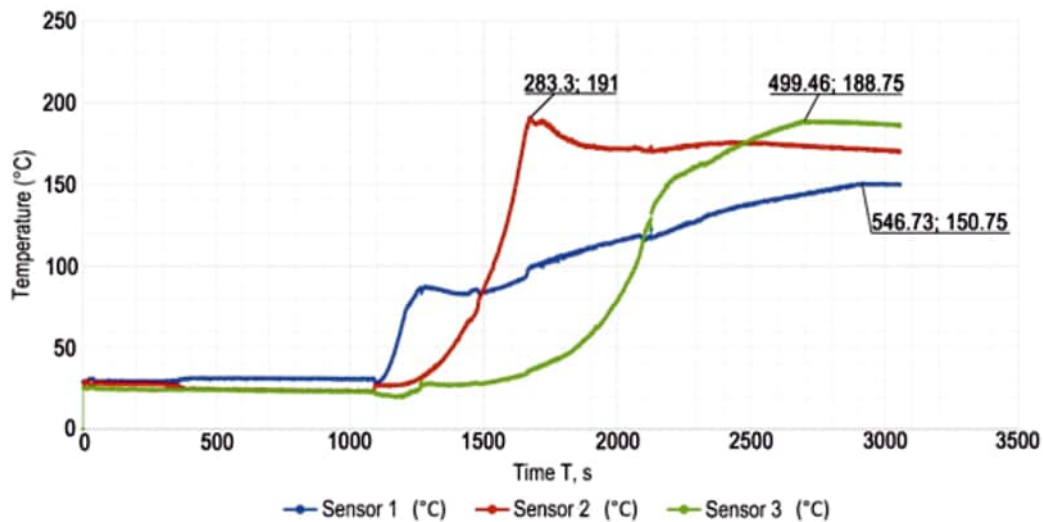
Fig. 8. Graph of temperature change during turning, experiment No. 2 (**δ** = 2 mm)

Table 4

Maximum temperature values from thermocouples for the 2 mm *MCS* metal shell

No.	Thermocouple 1, C	Thermocouple 2, ℃	Thermocouple 3, ℃	Average, ℃
1	96.8	75	155.75	109.2
2	150.8	191	188.75	176.8
3	112.0	113	111.75	112.3
4	153.3	106.25	148.5	136.0
5	108.5	106.5	102.25	105.8
6	100.5	77.5	140.5	106.2
7	96.5	90.25	86.75	91.2
8	27.3	70	97	64.8
9	105.8	112	103	106.9
10	108.5	109.25	104	107.3
11	80.0	68.75	96.25	81.7
12	84.8	73.58	101.1	86.5
13	83.9	72.63	100.1	85.5

Table 5 presents the values of the calculated polynomial coefficients obtained from the physical data. The least squares method was applied, which provides coefficient estimates through statistical procedures that account for effects such as parameter correlations.

For the *2T3* model, the statistical metrics are: $R^2 = 0.98534$, $F = 22.4$, $p = 0.01336$ (< 0.05). The resulting *2T3* regression model has the following form:

$$2T3 = 292.497 - 509.117S - 1.433V - 134.602t - 98.166S^2 + 0.005\,V^2 +$$

$$+96.488t^2 + 2.104SV - 106.205St - 0.202Vt. \tag{2}$$

The interpretation of the estimated coefficients in coded variables shows a consistent physical meaning of the main effects: the linear terms for feed (x_S), cutting speed (x_V), and depth of cut (x_t) are negative (i.e., an increase in *S, V,* and *t* within the investigated ranges leads to a decrease in *T*). Nonlinearity is expressed by the quadratic terms: one of the quadratic coefficients is significantly negative, while the other two are positive. Another quadratic term (V^2) lies at the boundary of statistical significance. The pairwise interaction terms exhibit borderline significance, indicating a moderate but noticeable interdependence of the factors,

T a b l e 5

Evaluation of the significance of the coefficients of the *2T3* mathematical model

Symbol	Coefficient	Standard error SE_i	*t*-statistic	*p*-value	Interpretation
b_0	292.49651	29.17582	10.02530	0.00017	The coefficient is statistically significant ($p < 0,05$)
b_1	−509.11672	144.98610	−3.51149	0.01707	The coefficient is statistically significant ($p < 0,05$)
b_2	−1.43312	0.44609	−3.21259	0.02366	The coefficient is statistically significant ($p < 0,05$)
b_3	−134.60192	16.56281	−8.12676	0.00046	The coefficient is statistically significant ($p < 0,05$)
b_4	−98.16642	28.83137	−3.40485	0.01915	The coefficient is statistically significant ($p < 0,05$)
b_5	0.00460	0.00233	1.97237	0.10560	The coefficient is not statistically significant
b_6	96.48846	6.11772	15.77196	0.00002	The coefficient is statistically significant ($p < 0,05$)
b_7	2.10417	1.34301	1.56676	0.17795	The coefficient has low statistical significance
b_8	−106.25000	80.58035	−1.31856	0.24448	The coefficient is not statistically significant
b_9	−0.20208	0.13430	−1.50471	0.19273	The coefficient is not statistically significant

primarily between cutting speed and depth of cut, and between feed and cutting speed. Taken together, this means that for $\delta = 2$ mm, the temperature is most sensitive to changes in depth of cut, followed by feed, and to a lesser extent cutting speed, which is consistent with the observed heating behavior in the experiments.

The constructed *2T3* model is presented in real physical units for engineering applications. Validation of the model using the full set of experimental observations demonstrated good agreement [24]. The maximum deviation between the calculated and experimental temperatures did not exceed 5 °C, which falls within the established allowable range. Overall, the level of discrepancy was deemed acceptable for predicting the threshold of 170 °C and for constructing temperature distribution maps [25, 26].

Visualization of the response surface $T(V, S)$ at fixed values of t demonstrates a monotonic decrease in temperature T with increasing V and S, as well as a shift of the isotherms toward more restrictive regions with increasing t (Fig. 9).

a

b
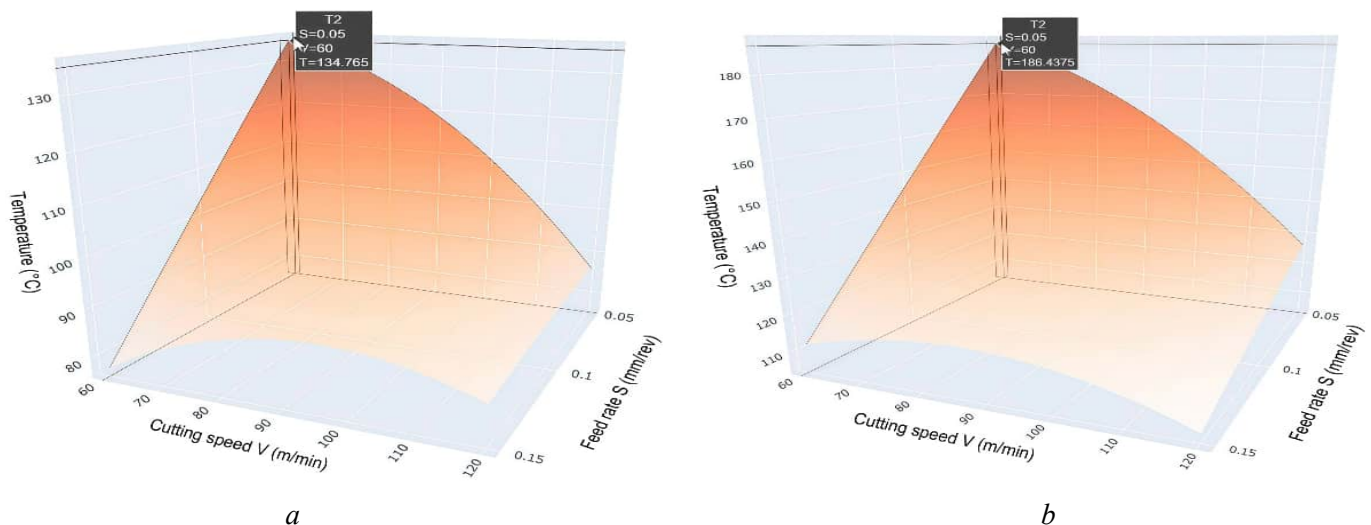
Fig. 9. Temperature surface graphs for model *2T3*:
(*a*) cutting depth of 1 mm; (*b*) cutting depth of 1.5 mm

On the contour map for a cutting depth of $t = 1.5$ mm (Fig. 10), which corresponds to the most thermally loaded condition, an acceptable zone of cutting parameters can be identified, along with regions where the temperature potentially exceeds 170 °C.
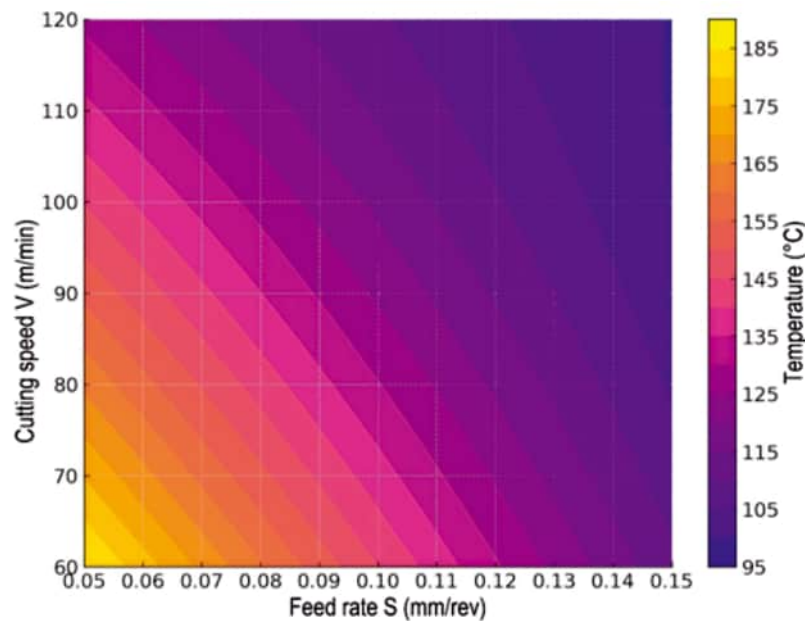
Fig. 10. Temperature contour graph for model *2T3*, with a cutting depth of 1.5 mm

Further research should be aimed at expanding the applicability of the obtained results:

1. Parametric investigation of the influence of shell thickness (δ) on the thermal response during turning;

2. Validation of the developed models on alternative grades of metal-polymer composites with different thermal conductivities and temperature limits, as well as on various structural steels;

3. Coupled analysis of the "temperature-surface roughness-tool wear" relationship, including the recording of cutting forces and vibroacoustic signals to construct integrated maps of permissible cutting conditions;

4. Although the experiment was conducted with the application of coolant and lubrication fluids (*CLF*), it is advisable to investigate the role of advanced cooling and lubrication techniques (such as minimum quantity lubrication (*MQL*) and cryogenic cooling) and their effect on reducing peak temperatures;

5. Identification and monitoring of heat transfer at the interfacial boundary, including the effect of adhesion degradation under cyclic thermomechanical loading;

6. Development of numerical 3D thermomechanical models and digital twins, calibrated using experimental data, to enable rapid prediction of optimal cutting conditions in industrial applications.

The implementation of these directions will allow the proposed approach to evolve into a standardized methodology for determining machining parameters for metal-composite systems (*MCS*) in tool engineering applications.

Conclusion

A hardware–software device has been developed and experimentally validated, accurately simulating a metal-composite system (*MCS*) comprising a thin-walled metallic shell and a metal-polymer composite filler. This setup enabled the direct measurement of the temperature response at the metal-*MPCM* interfacial boundary during the turning process.

The implemented full factorial experimental design $2^3 + n_0$ yielded statistically reliable data, allowing for the identification of the main effects and interactions of the cutting parameters (*V, S, t*) and accounting for nonlinear dependencies through the inclusion of central points.

The constructed second-order regression model for a shell thickness of δ = 2 mm (designated as model *2T3*) adequately describes the temperature at the interface and is consistent with the results of thermal imaging verification.

It was established that, within the investigated parameter ranges, the depth of cut (*t*) has the greatest influence on the temperature rise, the feed rate (*S*) has a moderate effect, and the cutting speed (*V*) has the least effect.

Based on the developed model, response surfaces and contour maps have been constructed. These allow for the identification of acceptable machining parameter regions that satisfy the condition $\mathbf{T} \leq 170$ °C, corresponding to the heat resistance threshold of the metal–polymer composite.

It was demonstrated that maintaining the technological constraint $\boldsymbol{T} \leq 170$ °C is achievable through a rational combination of parameters *V*, *S*, and *t*. This confirms the feasibility of finish turning metal-composite systems without causing thermal damage to the polymer matrix of the filler.

The obtained results provide a scientifically grounded basis for standardizing the machining parameters of tool-engineering components, such as forming dies with conformal cooling channels and composite drill bodies, thereby reducing the risk of defects and improving product quality repeatability.

References

1. Lubimyi N.S., Polshin A.A., Gerasimov M.D., Tikhonov A.A., Antsiferov S.I., Chetverikov B.S., Ryazantsev V.G., Brazhnik J., Ridvanov I. Justification of the use of composite metal-metal-polymer parts for functional structures. *Polymers*, 2022, vol. 14 (2), p. 352. DOI: 10.3390/polym14020352.

2. Zhang K., Cheng G. Three-dimensional high resolution topology optimization considering additive manufacturing constraints. *Additive Manufacturing*, 2020, vol. 35, p. 101224. DOI: 10.1016/j.addma.2020.101224.

3. Lubimyi N.S., Chepchurov M., Polshin A.A., Gerasimov M.D., Chetverikov B.S., Chetverikova A., Tikhonov A.A., Maltsev A. Reducing the cost of 3D metal printing using selective laser melting (SLM) technology in the manufacture of a drill body by reinforcing thin-walled shell forms with metal-polymers. *Journal of Manufacturing and Materials Processing*, 2024, vol. 8 (2), p. 44. DOI: 10.3390/jmmp8020044.

4. Morillas A.V., Alonso J.M., Caballero A.B., Sisamón C.C., Ceruti A. Adaptive variable design algorithm for improving topology optimization in additive manufacturing guided design. *Inventions*, 2024, vol. 9 (70), p. 9040070. DOI: 10.3390/inventions9040070.

5. Sambo A.M., Younas M., Njuguna J. Insights into machining techniques for additively manufactured Ti6Al4V alloy: A comprehensive review. *Applied Sciences*, 2024, vol. 14 (22), p. 10340. DOI: 10.3390/app142210340.

6. Zhu J., Zhou H., Wang C., Zhou L., Yuan S., Zhang W. A review of topology optimization for additive manufacturing: Status and challenges. *Chinese Journal of Aeronautics*, 2021, vol. 65, pp. 91–110. DOI: 10.1016/j.cja.2020.09.020.

7. Lubimyi N., Voronenko V., Polshin A., Gerasimov M., Antsiferov S., Öztürk O.K., Chetverikov B., Tikhonov A., Ryazantsev V., Shumyacher V., Melentiev N. What is the economic feasibility of manufacturing a metal-metal-polymer composite part compared to other technologies? *Australian Journal of Mechanical Engineering*, 2022, vol. 22 (2), pp. 314–325. DOI: 10.1080/14484846.2022.2094533.

8. Malyshev V.F., D'yachenko S.V. *Rezanie trudnoobrabatyvaemykh stalei* [Cutting of hard-to-machine steels]. Moscow, Mashinostroenie Publ., 2010. 248 p.

9. Trent E.M., Wright P.K. *Rezanie metallov* [Metal cutting]. Moscow, Mashinostroenie Publ., 2001. 385 p. (In Russian).

10. Aurich J.C., Zimmermann M., Schindler S., Steinmann P. Effect of the cutting condition and the reinforcement phase on the thermal load of the workpiece when dry turning aluminum metal matrix composites. *The International Journal of Advanced Manufacturing Technology*, 2016, vol. 82, pp. 1317–1334. DOI: 10.1007/s00170-015-7444-0.

11. Liu H., Wang C., Li T., Bo Q., Liu K., Wang Y. Fixturing technology and system for thin-walled parts machining: a review. *Frontiers of Mechanical Engineering*, 2023, vol. 17 (4), p. 55. DOI: 10.1007/s11465-022-0711-5.

12. Park J.-K., Lee C.-M., Kim D.-H. Investigation on the thermal effects of WC-Co turning inserts deposited by additive manufacturing of titanium alloy powder. *Metals*, 2021, vol. 11 (11), p. 1705. DOI: 10.3390/met11111705.

13. Sultana M.N., Dhar N.R., Zaman P.B. A review on different cooling/lubrication techniques in metal cutting. *American Journal of Mechanics and Applications*, 2019, vol. 7, pp. 71–87. DOI: 10.11648/j.ajma.20190704.11.

14. Schiffler M., Maul T., Welzel F., Frank H., Cselle T., Lümkemann A. Machining technology and PVD coatings for milling thin structural parts of Inconel 718. *SSRN Electronic Journal*, 2020, vol. 7, pp. 55–63. DOI: 10.2139/ssrn.3724144.

15. Taufik M., Jain P.K. A study of build edge profile for prediction of surface roughness in fused deposition modeling. *Journal of Manufacturing Science and Engineering*, 2016, vol. 138 (6), p. 061002. DOI: 10.1115/1.4032193.

16. Wang D., Yang Y., Yi Z., Su X. Research on the fabricating quality optimization of the overhanging surface in SLM process. *The International Journal of Advanced Manufacturing Technology*, 2013, vol. 65, pp. 1471–1484. DOI: 10.1007/s00170-012-4271-4.

17. Hoang V.Ch. Prakticheskie voprosy issledovaniya temperatury rezaniya pri tochenii [Practical research cutting of temperature in turning]. *Izvestiya Tul'skogo gosudarstvennogo universiteta. Tekhnicheskie nauki = Izvestiya Tula State University. Technical Sciences*, 2015, no. 7-1, pp. 78–84.

18. CJSC Metal-Polymer Materials LEO. *Tekhnicheskie usloviya TU 2257-002-48460567-00. Metallopolimer «Ferro-khrom»* [Technical conditions TU 2257-002-48460567-00. Metal-Polymer "Ferro-Chrom"]. Moscow, 2009. Available at: http://www.leopolimer.ru (accessed 10.11.2025).

19. Tselikov P.V., Kisel A.G. Issledovanie iznashivaniya rezhushchego instrumenta pri tochenii splava TN1 [Investigation of the dependence of the wear intensity of the cutting tool during turning of TN1 alloy]. *Sistemy. Metody. Tekhnologii = Systems. Methods. Technologies*, 2025, no. 2 (66), pp. 43–49. DOI: 10.18324/2077-5415-2025-2-43-49.

20. Bordachev E.V., Lapshin V.P. Matematicheskoe modelirovanie temperatury v zone kontakta instrumenta i izdeliya pri tokarnoi obrabotke metallov [Mathematical temperature simulation in tool-to-work contact zone during metal turning]. *Vestnik Donskogo gosudarstvennogo tekhnicheskogo universiteta = Vestnik of Don State Technical University*, 2019, vol. 19, no. 2, pp. 130–137. DOI: 10.23947/1992-5980-2019-19-2-130-137.

21. Jones T., Cao Y. Tool wear prediction based on multisensor data fusion and machine learning. *International Journal of Advanced Manufacturing Technology*, 2025, vol. 137, pp. 5213–5225. DOI: 10.1007/s00170-025-15472-4.

22. Zhuang K., Shi Z., Sun Y., Gao Z., Wang L. Digital twin-driven tool wear monitoring and predicting method for the turning process. *Symmetry*, 2021, vol. 13, p. 1438. DOI: 10.3390/sym13081438.

23. Khadiri I.E., Zemzami M., Hmina N., Lagache M., Belhouideg S. Topology optimization methods for additive manufacturing: a review. *International Journal for Simulation and Multidisciplinary Design Optimization*, 2023, vol. 14, p. 12. DOI: 10.1051/smdo/2023015.

24. Zhangabay N., Chepela D., Tursunkululy T., Zhangabay A., Kolesnikov A. Analysis of the effect of porosity on thermal conductivity with consideration of the internal structure of arbolite. *Construction Materials and Products*, 2024, vol. 7 (3), pp. 1–12. DOI: 10.58224/2618-7183-2024-7-3-4.

25. Andreacola F.R., Capasso I., Langella A., Brando G. 3D-printed metals: Process parameters effects on mechanical properties of 17-4 PH stainless steel. *Heliyon*, 2023, vol. 9 (7), p. 17698. DOI: 10.1016/j.heliyon.2023.e17698.

26. Lisyatnikov M.S., Chibrikin D.A., Prusov E.S., Roshchina S.I. Mechanical characteristics of polymer composites based on epoxy resins with silicon carbide. *Construction Materials and Products*, 2024, vol. 7 (5). DOI: 10.58224/2618-7183-2024-7-5-3.

Conflicts of Interest

The authors declare no conflict of interest.

Obrabotka metallov -
Metal Working and Material Science

Journal homepage: http://journals.nstu.ru/obrabotka_metallov

Modern methods of manufacturing of complex-profile electrode-tools for electrical discharge machining: a literature review

Timur Ablyaz [a], Ilya Osinnikov [b], Evgeniy Shlykov [c, *], Karim Muratov [d], Vladimir Blokhin [e]

Perm National Research Polytechnic University, 29 Komsomolsky prospekt, Perm, 614990, Russian Federation

[a] https://orcid.org/0000-0001-6607-4692, lowrider11-13-11@mail.ru; [b] https://orcid.org/0009-0006-4478-3803, ilyuhaosinnikov@bk.ru;
[c] https://orcid.org/0000-0001-8076-0509, Kruspert@mail.ru; [d] https://orcid.org/0000-0001-7612-8025, Karimur_80@mail.ru;
[e] https://orcid.org/0009-0009-2693-6580, warkk98@mail.ru

ARTICLE INFO

ABSTRACT

Introduction. Pilot production plays an important role in modern mechanical engineering. Copy-piercing electrical discharge machining (*CPEDM*) technology has become widespread in machining pilot parts manufactured in flexible production flows. Manufacturing tool-electrodes (*TE*) is one of the main stages of the CPEDM technological cycle. **Purpose of the work.** Review of existing studies of modern methods of manufacturing tool-electrodes for electrical discharge machining. **Research methods.** A literature review of studies in the field of electrical discharge machining devoted to tool-electrodes, carried out mainly over the past 20 years, is presented. Various configurations of structural elements machined using *CPEDM* technology, as well as *TE* configurations for their machining, are described. The dependences of the influence of the geometric parameters of the simplest *TE* configurations on the output parameters of *CPEDM* are shown. The main groups of *TE* manufacturing methods are identified. The limitations, advantages, and disadvantages of alternative methods to traditional ones are described. The main trends in the development of modern *TE* manufacturing methods are revealed. **Results and discussion.** Based on the literature review of modern research in the field of electrical discharge machining, current trends in the development of tool-electrode configurations are presented, and problems in the manufacture of complex-shaped tool-electrodes using traditional methods are identified. It has been established that among the alternative methods for manufacturing tool-electrodes, investment casting, powder metallurgy, and additive methods are of greatest interest to modern scientists. It has been shown that each method has its own advantages and disadvantages, confirmed by a number of studies. The following current areas of development of complex-shaped tool-electrodes and methods for their manufacture are highlighted: topological optimization of tool-electrodes, use of modern high-tech casting methods; expansion of the range of tool-electrodes materials with improved electrical discharge properties; optimization of powder metallurgy modes, *FDM* printing, and selective laser melting; increasing the thickness and quality of tool-electrodes coatings obtained using rapid prototyping technologies.

Introduction

Currently, accelerated scientific and technological progress is affecting all sectors of production. Modern mechanical engineering enterprises are forced to operate in a highly competitive environment [1–2].

To maintain competitiveness, enterprises need to ensure flexible operations and a wide range of manufactured products, as well as the ability to respond quickly to changes in market requirements [3–5].

With intensifying competition and the rapid expansion of production portfolios, minimizing the time required to bring products to market is essential. At the same time, it is essential to maintain high quality

---

* Corresponding author
Shlykov Evgeniy S., Ph.D. (Engineering), Associate Professor
Perm National Research Polytechnic University,
29 Komsomolsky prospekt,
614990, Perm, Russian Federation
Tel.: +7 961 759-88-49, **e-mail:** Kruspert@mail.ru

standards for engineering products throughout their entire life cycle. In pilot production, companies design and develop new products and prepare for their mass production [6]. Customer requirements and product quality are key factors in the creation of a prototype.

During the technical and economic assessment stage of manufacturing technology optimization, considering the specific features and complexities of pilot production, prototype manufacturing methods are analyzed and selected [6]. As a rule, traditional manufacturing methods for mechanical engineering products are not optimally suited for prototype production. The high level of equipment utilization for traditional processing methods, the complexity of the part profile, and the high physical and mechanical properties of the product material all necessitate the use of alternative prototype manufacturing methods [7–9].

When machining complex structural elements (such as hard-to-reach surfaces, curved and narrow grooves, blind holes, and thin-walled structures), as well as complex-profile pilot parts manufactured in flexible production flows, electrical discharge machining (*EDM*) is widely used [10]. This machining method is based on copying the shape of the tool-electrode (*TE*) onto the workpiece-electrode (*WE*) through the action of electrical discharges between the *TE* and *WE* [11–12].

High machining accuracy and the non-contact nature of the process (absence of mechanical force on the *TE*) enable the *EDM* method to be used in machining complex structural elements. This method is often used in the production of various tools, such as casting molds, injection molds, and dies [13–17]. This method is widely used in the machining of blind curved grooves, deep, small-diameter holes, and internal splines and teeth [18].

A volumetric profile electrode tool serves as the tool in *EDM*. In copy-piercing machines, the volumetric profile electrode undergoes translational motion at speed V_z towards the *WE* (Fig. 1) [11].
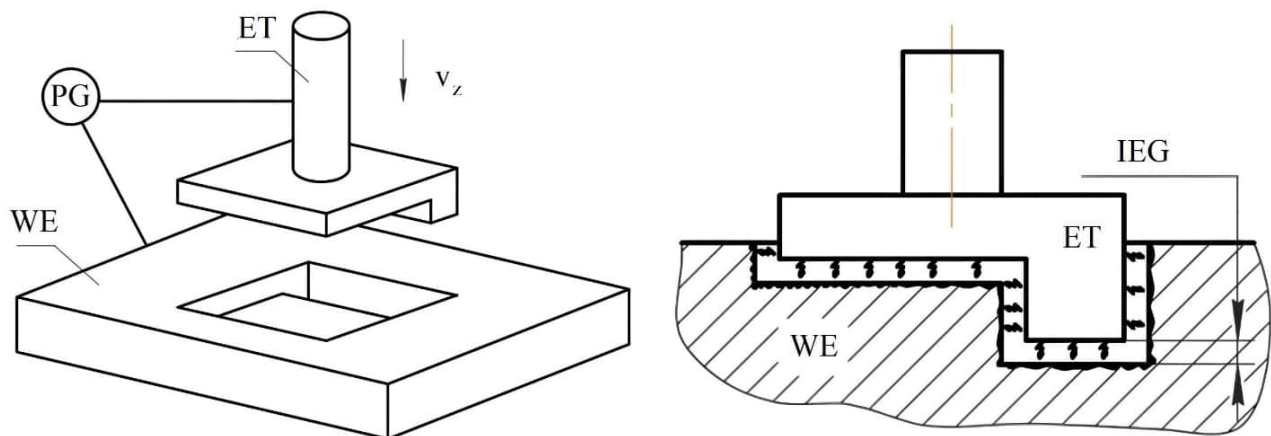
Fig. 1. Schematic of copy-piercing *EDM* process

Due to the ever-increasing complexity of structural components processed using the *EDM* method, the need arises for the use of *TE*s with complex geometries. One of the most time-consuming stages in this process is the manufacture of *TE*s. Machine-building companies are faced with the challenge of choosing a manufacturing method for *TE*s that maximizes economic efficiency by ensuring maximum productivity and minimizing time and material costs.

The problem of manufacturing tool electrodes for electrical discharge machining has been known practically since the advent of electrical discharge machining. Research into these methods remains relevant due to trends in modern mechanical engineering toward ever-more complex geometries, reduced mass and size characteristics, and other improvements to workpieces.

Currently, there are many studies in the field of electrical discharge machining (EDM) devoted to the methods of manufacturing *TE*.

The purpose of this paper is to review existing research on modern methods of manufacturing electrode tools for electrical discharge machining.

The following *tasks* were solved during the research:

– classification of methods for manufacturing *TE*, definition of methods alternative to traditional blade processing;

– determination of the advantages, disadvantages and limitations of modern methods of manufacturing *TE* in comparison with traditional methods;

– determination of development trends of the selected methods.

Research methodology

This paper presents a literature review of electrical discharge machining (*EDM*) research on electrode tools, primarily conducted over the past 20 years. Various configurations of structural components machined using *EDM* technology, as well as the configurations of *WE*s used for their machining, are described. The influence of the geometric parameters of simple *EDM* configurations on the output parameters of *EDM* is demonstrated. Key groups of *EDM* manufacturing methods are identified. The limitations, advantages, and disadvantages of alternative methods to traditional ones are described. Key trends in the development of modern *EDM* manufacturing methods are identified.

Results and Discussion

The configuration of the tool electrodes is determined by the geometric parameters of the structural elements being processed. A wide range of structural elements processed using the *EDM* method is extensively discussed in [19–23]. Fig. 2 shows examples of such structural elements.
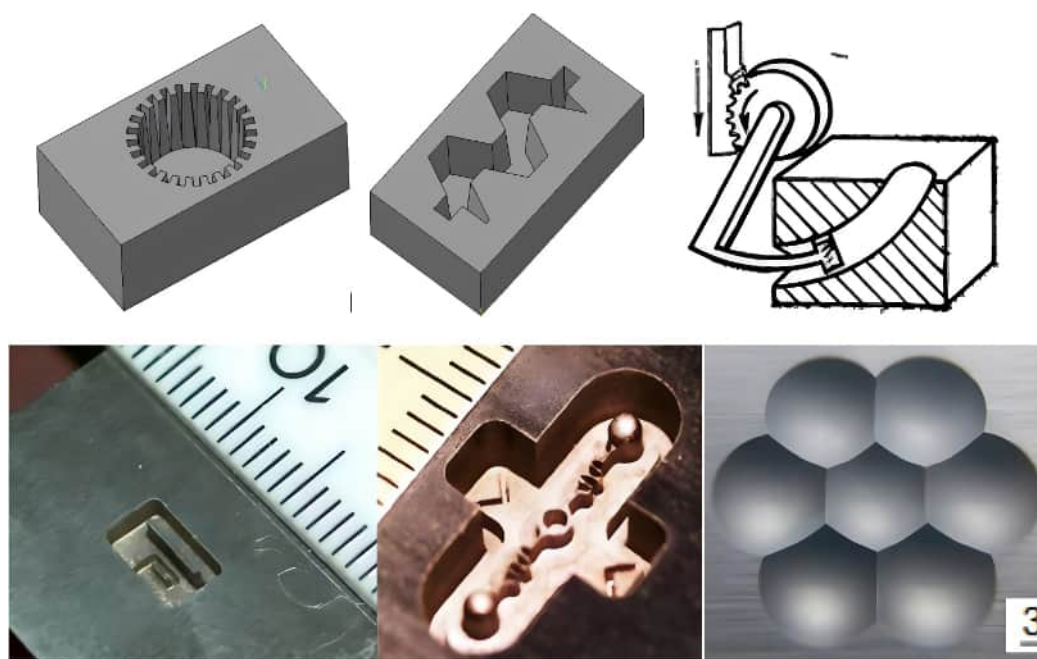
Fig. 2. Examples of structural elements processed by the *CPEDM* method

TE configurations

The design of complex-profile surfaces requires appropriate geometric parameters for the *TE*. Currently, numerous studies describe the design features of the *TE*.

Simple form TEs

In real-world production settings, the simplest *TE* configurations are rarely used, as the structural components processed with them can generally be machined using mechanical methods without any technological difficulties. However, there are a number of studies examining the influence of *TE* geometric parameters on the output parameters of *EDM*. In such cases, *TE*s with round, square, triangular, and other

simple cross-sections are typically used. These *TE*s are manufactured using traditional blade-cutting methods without any difficulties.

The paper [24] presents a study of the performance of *EDM* depending on the configuration of the electrode shape. Simple configurations of TE with round, triangular, square and rhombic cross-sections were investigated. It was found that, with the same cross-sectional area, machining with a round *TE* is characterized by the highest material removal rate and the least wear of the *TE*. *EDM* with a rhombic *TE*, on the contrary, exhibits the greatest wear and the lowest material removal rate. This is due to the fact that rhombic electrodes have the largest peripheral area, which allows for faster heat dissipation into the environment. As a result, less thermal energy is available for material removal compared to other electrodes. However, in the sharp corners of these electrodes, a high heat concentration is observed, which leads to intense melting and evaporation processes of the electrode, which increases its wear. The graphs of the dependence of the material removal rate (*MRR*) and tool electrode wear rate (*EWR*) on its configuration are presented in Fig. 3.
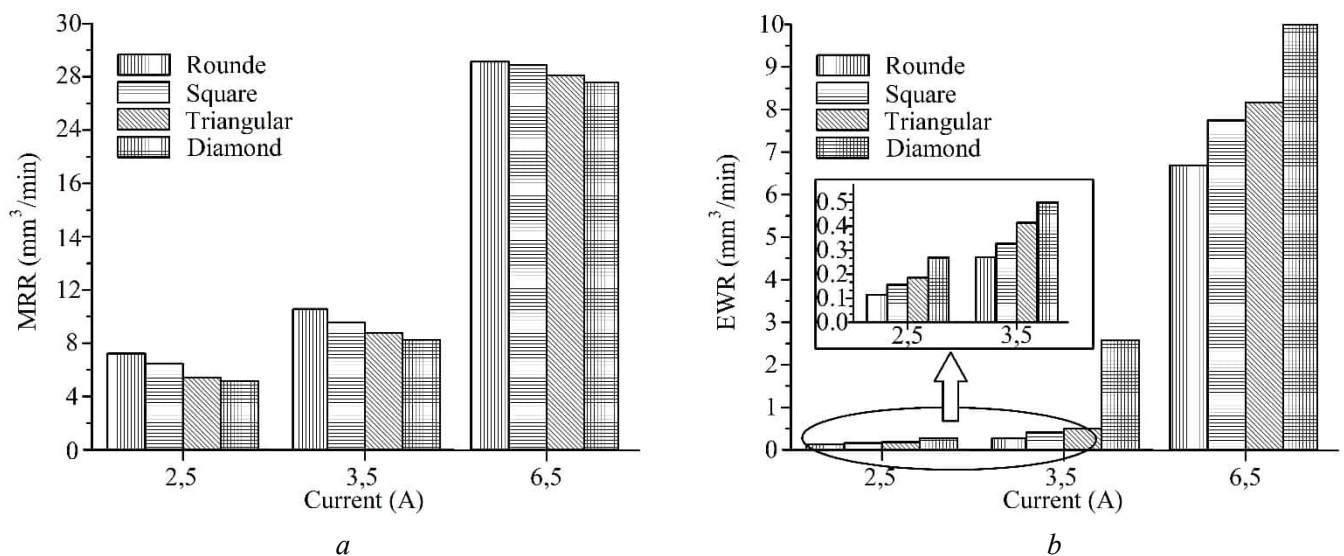
Fig. 3. Influence of *TE* configuration and current intensity on:
a) material removal rate (*MRR*); *b)* tool-electrode wear rate (*EWR*) [24]

The best performance of *TE* with a round cross-section among *TE* with a simple configuration was also confirmed by the authors of the study [25]. In this work, the performance of cylindrical *TE* was compared with electrodes of triangular and rectangular cross-section.

The work [107] also presents a study of the influence of the geometric parameters of rotating *TE* of the simplest configurations on the output parameters of the *EDM*. The study used *TE* of eight configurations, shown in Fig. 4.
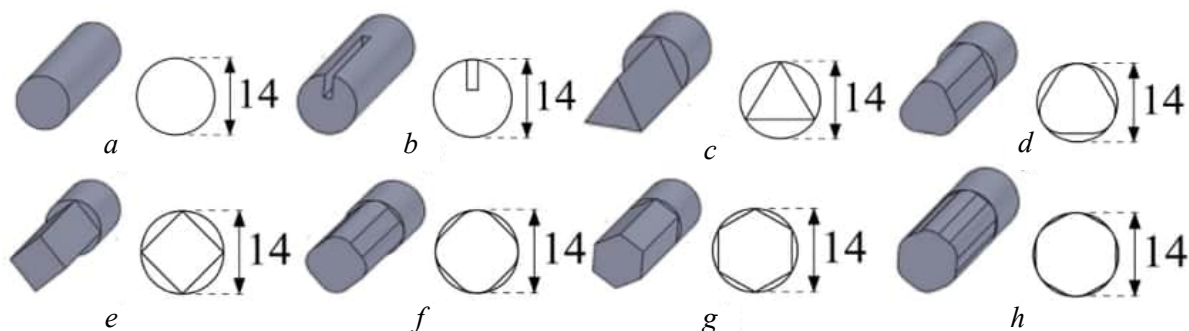
Fig. 4. Configurations of tool-electrodes:

a) cylindrical; *b)* cylindrical with a groove; *c)* triangular; *d)* triangular with rounded corners; *e)* square; *f)* square with rounded corners; *g)* hexagonal; *h)* hexagonal with rounded corners [107]

Of all the possible cross-sections, triangular, square, and hexagonal shapes were chosen because they were the easiest to design and manufacture for *EDM* testing. Electrode cross-sectional profiles were chosen based on the fact that non-cylindrical shapes — triangular, square, and hexagonal – are the easiest to machine. In these cases, cross-sections with sharp and rounded corners were tested. A cylindrical electrode with slots was also analyzed. A cylindrical electrode was also tested for comparison.

In all cases, the rotating outer diameter of the electrode cross-section was 14 mm. Therefore, all electrodes used in these tests had the same effective area. All radii used for electrodes with rounded corners were 4 mm, and for the slotted cylindrical electrode, the slot width was 2 mm and the depth was 5.5 mm. For electrodes with sharp corners, no radius was used. All these electrodes were manufactured on a machining center using a simple milling operation.

According to the results of this study, the use of profiled electrodes yields better results in terms of *MRR*, but not *EWR* and taper angle, compared to the characteristics of a simple cylindrical electrode. Moreover, the more intricate the electrode geometry, the lower the *TWR* and taper angle values can be. *EWR* will increase due to the difference in electrode volume, which depends on the shape of the electrode used. The discrepancy between the obtained data and the results of studies [24] and [25] is due to the rotation of the *ET* during machining.

*TE*s of the simplest configurations are rarely used in production settings, but they have high practical applicability in research and development. Data on the influence of the geometric parameters of ETs of the simplest configurations on the output parameters of the EDM can be used in the design of complex and modular EIs.

TE for deephole machining

Electrical discharge drilling is a technique for hole machining, also known as *EDM* drilling (*EDD*) [26–28]. *EDD* is used with cylindrical electrodes to create holes, especially those with small diameters and large aspect ratios, in difficult-to-machine materials without the expense of expensive cutting tools. However, problems with deephole machining or deep drilling often lead to undesirable surface quality and geometry issues.

The main problem with deephole *EDD* is its low productivity compared to blade machining. This is largely due to the low efficiency of fine material removal from the machining zone. When machining deep holes, fine material removal is difficult. Furthermore, secondary fine material is created, which returns to the *TE* and is re-thrown onto the hole wall, resulting in a rough inner wall [103–104] and a loss of hole shape.

Electrode configuration has a significant impact on the performance of the *EDD*. Insufficient flushing is a major problem, causing clogging of the machining zone with fine material and leading to short circuits [29–30, 62]. Flushing efficiency can be improved by using electrodes with different shapes. Changing the external and internal shape of the electrode can alter the behavior of the dielectric flow in the machining zone, thereby increasing flushing efficiency.

Researchers from the University of Melbourne conducted a major review study [31] in the field of electrical discharge machining. They described the *TE* configurations for *EDD* and their effects on the machining process. The spiral electrode, side-cut electrode, notch electrode, and step electrode can be combined with electrode rotation and vibration to significantly alter the dielectric flow behavior and provide a channel for fine material removal. The hollow electrode is one type of electrode commonly used in the *EDD* process. The dielectric can be delivered to the machining zone through the internal hole of the electrode, which helps in removing fine material [32–34]. The use of a slot electrode provides additional removal of gases and fine material from the machining zone, reduces side sparking and conicity [35–37]. In addition to the step electrode, spiral electrodes can also be used to improve the productivity of the *EDD* process. The spiral grooves provide channels for fine material removal and can reduce the amount of fine material in the machining zone and, as a result, reduce the relative wear rate of the tool [38].

Thus, the use of electrodes of various shapes improves the efficiency of the electrical discharge machining system. Electrodes of a certain shape provide additional channels for the evacuation of electrical erosion products and also help prevent short circuits and arcing.

Modular (composite TEs)

Modular electrodes are also widely discussed in numerous studies. For example, studies [39–41] present modular *TE*s consisting of a set of rods secured to a rotary table. Several small cylindrical copper electrodes are placed on the rotary table, rotating around a vertical axis. A large rotary table with multiple electrodes increases material removal. *EDM* products are easily removed from the gap due to the space between the electrodes. Similar *TE* designs can also be used to machine multiple holes in a single process step [42].

Another area of application for modular *TE*s is the machining of curved holes. Modular *TE*s have now been developed consisting of conductive segments mounted on elastic guides. This design allows for the machining of curved holes that are virtually impossible to process using traditional blade methods and the *EDM* method with electrodes of simple configurations [32, 43–46].

Complex-profile TEs

The diversity of *TE* configurations is dominated by electrodes with unique profiles designed to machine complex structural elements in a single process step [20]. These *TE*s are designed based on the geometric parameters of the elements being machined and are typically dedicated to a single product type. A wide range of products processed by *EDM* and the *TE*s used to machine them are presented in [47–48]. A distinctive feature of this group of *TE*s is the complex profiles of their active surfaces [49].

Topologically optimized TEs

Topologically optimized *TE*s deserve special mention. *TE*s used for machining dies, casting molds, and other complex structural components are often large in size and, therefore, heavy. Machining with such *TE*s places high loads on the machine's guides and drives, and also requires high material consumption during manufacture. Currently, topological optimization is widely used in mechanical engineering to reduce the mass and size characteristics of critical components while maintaining strength [50–53].

Incorporating topology optimization into the initial stage of the *TE* design process can speed it up several times over the traditional approach. This speedup is due to the minimal initial data required for optimization.

In works [54–61], the possibility of using topological optimization methods in the design of *TE*s is noted, and modern methods of their manufacture allow them to be manufactured without structural defects that reduce the strength and rigidity of their design.

Table 1 presents a summary of the characteristics of *TE*s, based on the analysis of studies devoted to *TE* configurations.

T a b l e 1

Tool electrode configurations for *CPEDM*

*TE*s configuration	References	Application	Image
Simple-Form *TE*s	[24], [25]	Processing of structural elements with a simple cross-section (circle, square, etc.)	Fig. 5, *a*
*TE*s for deep hole machining	[26], [27], [28], [29], [30], [31], [32], [33], [34], [35], [36], [37], [38]	Deep hole machining, where the machining depth significantly exceeds the hole diameter	Fig. 5, *b*
Modular (composite) *TE*s	[32], [39], [40], [41], [42], [43], [44], [45], [46]	Processing of an array of holes. Processing of curved holes	Fig. 5, *c–d*
Complex-profile *TE*s	[20], [47], [48], [49]	Processing of complex profile shaped surfaces in one step	Fig. 5, *e–f*
Topologically optimized *TE*s	[54], [55], [56], [57], [58], [59], [60], [61]	Processing of large-sized products	Fig. 5, *g*

Based on an analysis of Table 1 and fig. 5, it can be concluded that the vast majority of *TE*s for *EDM* feature complex-shaped working surfaces. These surfaces make it possible to machine the corresponding structural elements, but the issue of *TE* manufacturing becomes pressing.

a

b

c

d

e

f

g
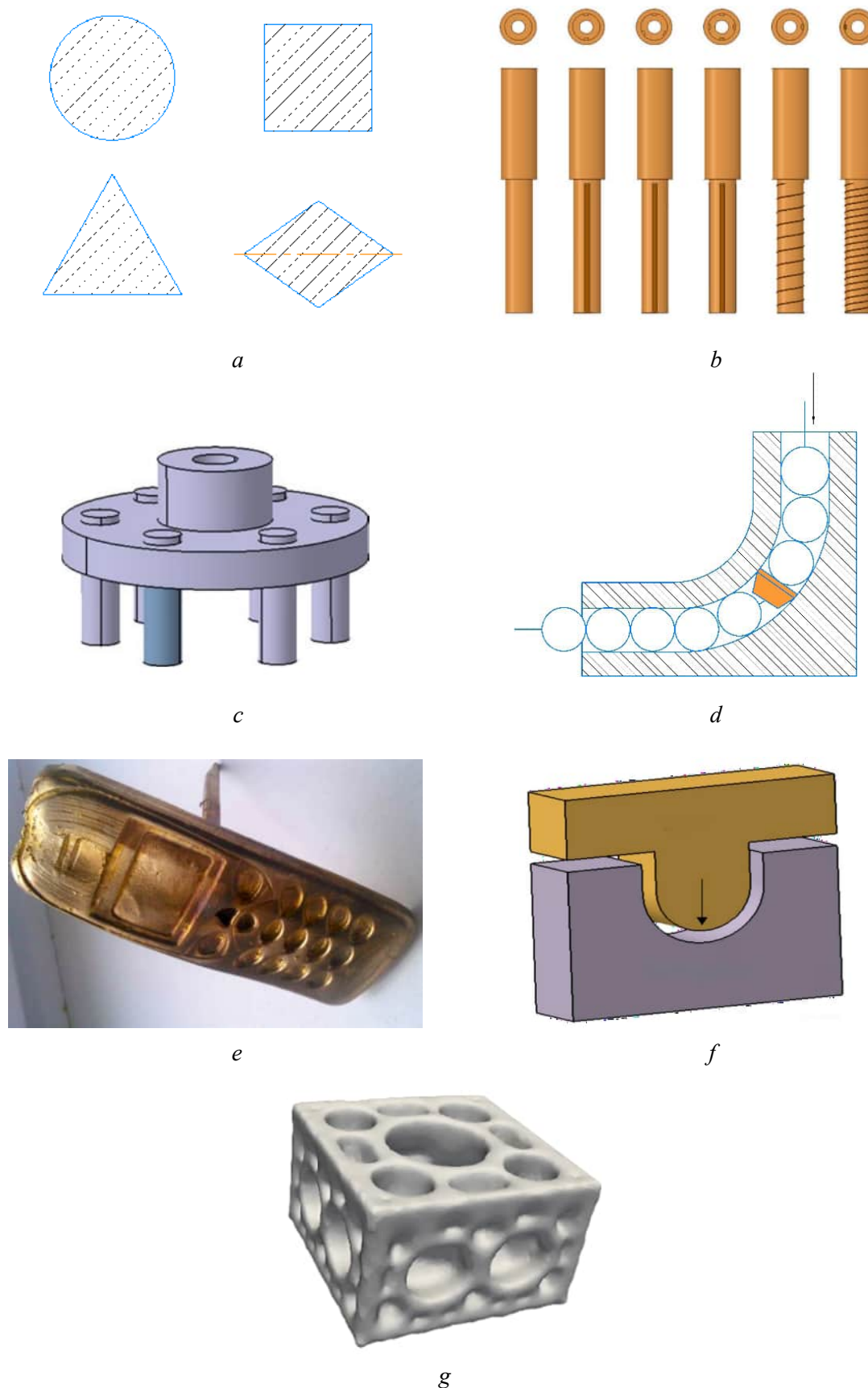
Fig. 5. Tool-electrode configurations for *CPEDM*

Electrode manufacturing is one of the key stages in the technological cycle of *EDM*. In pilot production, electrode manufacturing accounts for more than 50% of the financial and time costs [17]. This is due to the ever-increasing complexity of the profile of the structural elements being processed and the configuration of the electrodes.

An analysis of studies [11, 19] showed that, under conditions of serial production at modern mechanical engineering enterprises, when using electrophysical complex-profile machining technologies, traditional blade machining technologies and the use of press molds are employed for the manufacture of *TE*s. Thus, high-precision *TE*s obtained by high-precision blade machining methods are used for finishing *EDM* [70]. The use of these *TE*s is characterized by the removal of minimal allowances from the machined surfaces of the product during the *EDM* process, while the wear of the *TE*s is insignificant, which makes the use of high-precision blade machining technology in the manufacture of finishing *TE*s cost-effective.

The use of blade technologies in the production of roughing and semi-finishing electrode sets does not provide the required economic benefits. Excessive wear of the electrodes during the *EDM* process, as well as the low material utilization rate during electrode production, significantly impacts the cost-effectiveness of the final component manufacturing process.

Implementing approaches for rapidly adaptable pilot production of components requires new approaches to developing and refining process modes using cost-effective technologies for creating tool electrodes. Difficult-to-machine surfaces and complex geometries of modern components lead to complex tool electrode shapes and a significant increase in their manufacturing costs. This raises the challenge of finding alternative, cost-effective methods for manufacturing tool electrodes for *EDM* of prototypes.

Currently, the most common methods for producing *TE*s are additive manufacturing, casting, electroforming/electrodeposition, and powder metallurgy.

Powder metallurgy

Powder metallurgy (*PM*) technology for electrode fabrication is a simple and controllable method offering advantages over other methods, according to a study [69].

A study by *Garba*, *Abdul-Rani*, *Yunus* et. al. [70] provided a comprehensive review of the research on *TE* manufactured using powder metallurgy. *TE* can influence both macro- and microvariables in electrical discharge machining, and their properties can be significantly controlled by varying the sintering and compaction conditions. Powder metallurgy offers many advantages over traditional manufacturing methods, including better control of electrode properties, improved productivity, and lower costs.

This paper describes numerous studies devoted to the influence of *TE* material on the *EDM* process and the output parameters of the workpiece. A wide range of materials suitable for *TE* manufacturing using the *PM* method is presented. A schematic of *TE* manufacturing using the *PM* method is shown in fig. 6.

Despite its advantages, the *PM* method has a number of limitations. The most significant among these are the difficulty of manufacturing large-sized parts and the limitations of profile curvature. Furthermore, this method is prone to structural defects and inhomogeneity in the properties of the resulting product, which is unacceptable for critical parts or for *EDM* using large-sized *TE*s.

Fig. 6. Schematic of tool-electrode manufacturing by powder metallurgy (*PM*) method [71]

Investment casting/burnt-out casting

Numerous studies show that investment casting (*IC*) offers significant advantages for electrode manufacturing, allowing for the production of complex shapes, shorter production times, and lower production costs [64].

The *IC* method involves producing shell molds using wax or polymer 3D models of the product and a sprue system, removing the models from the mold, and then pouring the melt of the product material into the mold [49].

IC allows the production of *TE* with high surface cleanliness, thin-walled structures and complex geometry [63].

The manufacturing scheme of the finished product using the *TE* obtained by the *IC* method is shown in Fig. 7.
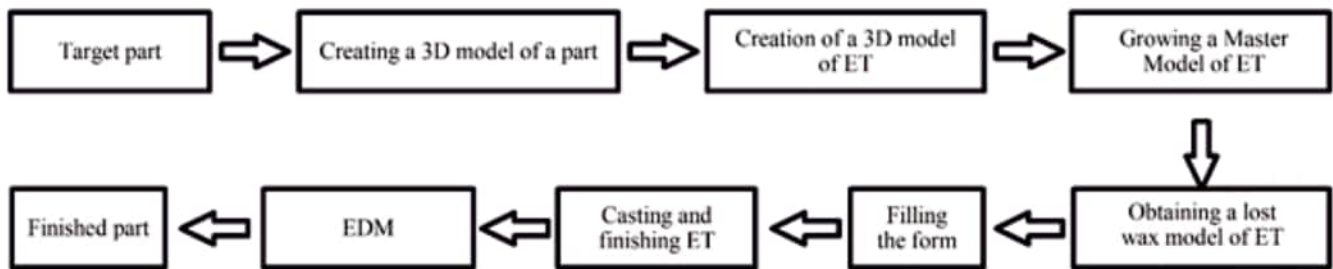
Fig. 7. Schematic of finished product manufacturing using an investment cast tool electrode

The authors of [64] conducted a study of the influence of the *TE* material obtained by the *IC* method on the roughness of the treated surface. Models for obtaining shell molds, as in many other studies [49, 65–67], were made by the stereolithography (*SLA*) method from liquid photopolymers (Fig. 8).
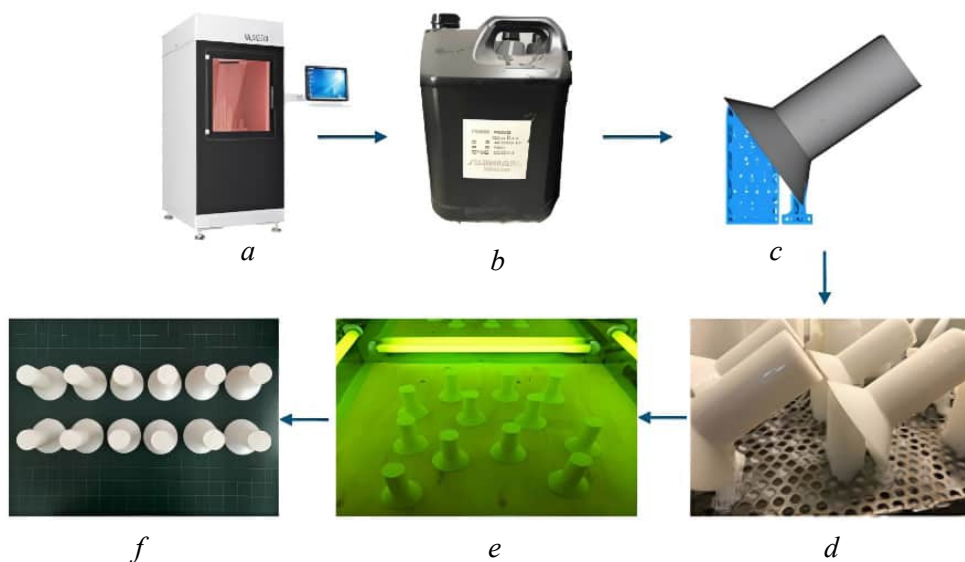
Fig. 8. Prototyping process using *SLA* method [64]:

a) Zongheng SLA-600 3D printer; *b) HONY-01* epoxy resin; *c)* model support design; *d)* model in 3D printing process; *e) UV* curing, *f)* finished models

The resulting *TE*s were found to have a shrinkage of 0.8–1.9% and a surface roughness of ***Ra*** 3.20–6.35 μm, depending on the material. These *TE*s allow for a roughness ***Ra*** of 10 μm on the machined surface.

A significant disadvantage of the *IC* method is the defects characteristic of casting processes and described in [68], such as pores, shrinkage cavities, and cracks. To minimize these defects, it is rational to use modern casting methods, such as injection molding or centrifugal casting [64].

Additive manufacturing methods for electronic components

Currently, there is active development of additive technologies in the creation of complex *TE* for pilot production [72].

In the manufacture of *TE*, traditional manufacturing methods are limited by complex geometry and local integration of channels [106]. A comparison of the process chains of tool manufacturing using additive and traditional manufacturing methods is presented in Fig. 9.
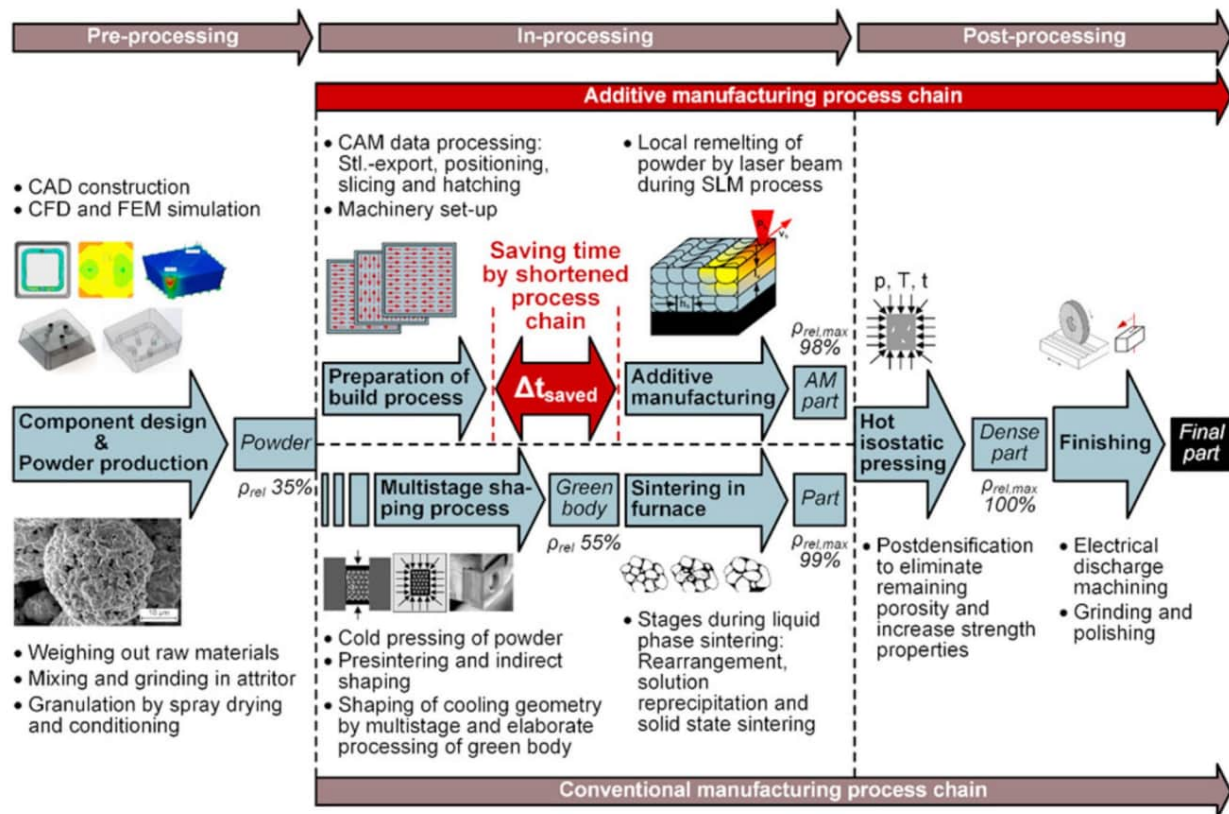
Fig. 9. Comparison of technological chains of additive manufacturing and traditional production of tool electrodes [106]

Modern additive manufacturing methods are characterized as promising production technologies, enabling the production of complex electronic components with high precision, including those with complex geometric shapes and spatial configurations. Additive technologies enable the production of components with complex geometries and spatial configurations in the shortest possible time. This eliminates the need to develop specialized tooling and fixtures or a separate process plan for each component [73–74].

Additive manufacturing methods for *EDM* tools offer a number of advantages:

1) the possibility of using the equipment in both pilot and serial production without retooling;

2) energy efficiency of production;

3) flexible reconfiguration of equipment for the production of *TE* of various configurations for the *EDM* of various products;

4) high level of automation of the technological process;

5) reduction of time costs for technological preparation of production and manufacturing of *TE*;

6) high level of repeatability of the characteristics of the technological process and manufacturing of *TE* and equipment;

7) a wide range of materials used, as well as the possibility of combining them and using them on one piece of equipment;

8) high level of predictability of time and material costs at all stages of production;

9) reduction in the number of personnel for equipment maintenance, low required qualifications of operators;

10) the possibility of varying the physical and mechanical properties of the *TE* material depending on the required output parameters of the *EDM*.

Currently, from the wide range of additive manufacturing methods, the following technologies are most widely used in the production of electronic components:

● *FDM* (fused deposition modeling) is the production of products from thermoplastic materials (for example, ABS or PLA plastic) by layer-by-layer application of material heated to a highly elastic state in the form of a thread;

● *SLS/SLM* (selective laser sintering/selective laser melting, respectively — selective laser sintering/ melting) is production of products from metal powder materials by sintering/melting them with a laser beam;

● *SLA* (stereolithography apparatus) is the layer-by-layer growth of a product through the crystallization of liquid photopolymer materials by a laser beam.

Fused deposition modeling (*FDM*) is a widely used 3D printing method that can be used to produce electrodes for *EDM*. *FDM* involves melting a thermoplastic material (*TPM*) and extruding it through a nozzle to create a 3D object layer by layer. To produce electrodes using *FDM*, the thermoplastic material is mixed with an electrically conductive material (*ECM*) to enhance the electrical conductivity of the finished *TE* [75–80].

The stages of creating *TE* using the *FDM* method are shown in Fig. 10.
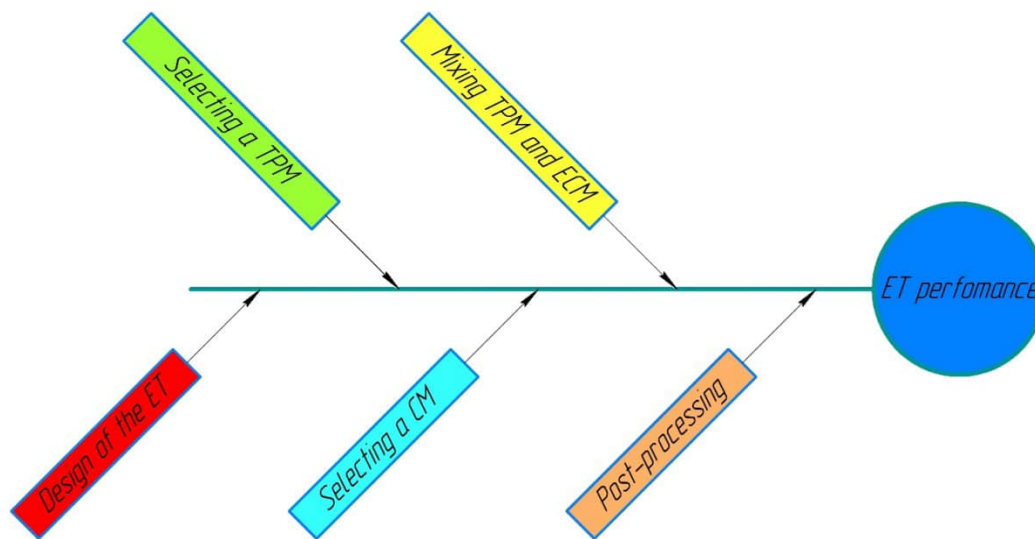
Fig. 10. Schematic of manufacturing tool electrodes by *FDM* method

Research in the field of additive manufacturing methods for *TE*s has shown that the *FDM* method allows for the efficient production of electrodes that meet the technological requirements of *EDM* [75, 76]. However, the question remains regarding the relationship between the electrical discharge properties of *TE*s obtained by this method and those of ETs made from solid material, manufactured using a blade cutting tool or by casting.

The authors of [77] investigated the conductivity of *TE*s based on *PLA* and *ABS* produced by *FDM*. It was found that the conductivity of the materials increased with increasing deposition time, reaching maximum conductivity after 48 hours. However, the results were not confirmed using real-time processing and therefore require further verification.

Fefar and *Karacagikar* [78] compared the electrical discharge properties of metallized *FDM* electrodes with solid copper electrodes in the *EDM* of *EN-19* alloy steel workpieces. The study showed that under identical machining conditions, the performance of the metallized *FDM* electrode was not different from that of the solid copper electrode.

A study [79] confirmed these findings. The experiment showed that the electrode produced using *FDM* performed better than the solid copper electrode.

Danad et al. [80] investigated the feasibility of machining an *ABS* part manufactured using *FDM* that was subsequently coated with copper to provide electrical conductivity. These *TE*s were found to have a lower mass than metal ones with comparable performance values.

The disadvantages of the *FDM* method for manufacturing *TE*s are described in detail in a review study [70]. The most significant ones are the multi-stage production, low processing accuracy, and technological difficulties of metallization.

Selective laser sintering (*SLS*) is an additive manufacturing method that enables the production of three-dimensional, complex-shaped parts directly from their *CAD* models. *SLS* creates parts layer by layer by consolidating successive layers of powder material. Consolidation is achieved by selectively fusing or sintering each layer using thermal energy delivered by a focused laser beam, which, using a mirror deflection system, scans the layers according to the cross-section of a mathematically sliced *CAD* model of the object. The main characteristic of *SLS* is the ability to produce complex-shaped parts without the need for tooling. It helps eliminate labor-intensive pre- and post-processing compared to traditional manufacturing processes [81–83].

The *SLS* method is one of the most widely used alternative methods for manufacturing complex-shaped *TE*s, as it helps reduce the time to final product and processing costs. This is confirmed by numerous studies [84].

An important factor in the *SLS* production of *TE*s is the deposited material. A study [85] described the production of electrodes for electrical discharge tools using the *SLS* method with four materials: copper, a bronze-nickel alloy, a steel alloy, and a combination of copper and a bronze-nickel alloy. Cross-sectional micrographs were used to analyze the porosity and compaction behavior of the electrodes. The steel alloy and the bronze-nickel alloy demonstrated improved compaction behavior and the lowest porosity compared to *Cu* and mixtures of *Cu* and these alloys. It was concluded that the addition of the bronze-nickel alloy to pure copper improved the compaction process.

The authors of [86] conducted an experiment to study *SLS* electrodes made from powdered bronze-nickel alloys, copper-bronze-nickel alloys, pure copper, and steel alloys. The materials were selected based on their electrical discharge properties and the feasibility of fabrication by the *SLS* method. It was concluded that the productivity of *TE*s manufactured by the *SLS* method is significantly lower compared to mechanically processed copper *TE*s. Among *TE*s obtained by the *SLS* method, bronze-nickel *TE*s demonstrated the best performance indicators for *EDM*. It was also found that the use of copper as a material for laser sintering is irrational.

In addition to traditional materials used in *EDM* (copper, graphite, brass), a number of fundamentally new composite materials are currently being used that rival standard materials in terms of *EDM* process output parameters. However, products made from these materials are virtually impossible to produce using subtractive processing methods.

L. Amorim et al. compared copper powder and a new TiB_2–*CuNi* metal matrix composite electrode fabricated by *SLS*. In the *EDM* experiments, it was found that the TiB_2–*CuNi* electrode significantly outperformed the copper powder electrode [87].

In the study [88], three new metal matrix materials were presented: *Mo–CuNi*, TiB_2–*CuNi*, and ZrB_2–*CuNi*. Electrodes were fabricated using the *SLS* method. Experiments were conducted at different discharge energy levels, and the output characteristics of the *EDM* were represented by the material removal rate and tool wear. The results showed that the new composite materials are rational for use as *EDM* electrode materials. Electrodes made from these materials demonstrated excellent stability of the *EDM* process over a range of variable process parameters.

There are a number of studies reflecting the shortcomings of *TE*s obtained by the *SLS* method, among which one can highlight the porosity and discontinuity of the obtained *TE*s, as well as their increased wear.

Dürr et al. [81] investigated *TE*s produced by selective laser sintering (*SLS*) from a powder mixture of bronze and nickel. The porosity of the resulting *TE*s reached 20%. The authors found that the wear of such electrodes was comparable to that of massive copper electrodes; however, the wear was unstable, which negatively affected the shape of the *TE*s and the workpiece. A repeat experiment was conducted in which the *TE*s were impregnated to reduce porosity. The use of such *TE*s resulted in a significant reduction in relative wear.

The authors of [82] also encountered difficulties in the *EDM* of *TE*s produced by the *SLM* method. *TE*s made from powders of pure copper, bronze-nickel alloy, copper-bronze-nickel alloy, and steel alloy were studied. The steel alloy electrode produced by the *SLS* method removed virtually no material from the

workpiece, while the performance of the remaining *TE*s produced by the *SLS* method was lower compared to solid copper electrodes.

As noted earlier, the possibility of using topological optimization methods in the design of electrical discharge components (*TE*s) (Fig. 11) is noted in [54–61]. *SLM* technology is one of the few methods that allows the production of topologically optimized electrical discharge components. During electrical discharge machining, electrical discharge components are subjected to the complex action of thermodynamic, electrophysical, hydromechanical, and other forces. Therefore, it is necessary to ensure the absence of defects in the internal structure of the electrical discharge components, which is achieved by using appropriate growth modes.

Fig. 11. Optimization of tool electrode geometry

It has been established that during the production of *TE*s using *SLS* and *SLM* methods, the appearance of structural defects is observed, which directly depend on the parameters of the growth process. The most significant manufacturing parameters influencing the quality of the final product are laser power, scanning speed, hatching distance, layer thickness, chemical composition of the powder material, and the atmosphere in the growth chamber [82]. The most common and difficult to eliminate defect arising in products manufactured using *SLS* and *SLM* methods is porosity. The formation of pores is determined by many parameters: the physicochemical properties of the powder material, the parameters of the *SLM*/*SLS* equipment, and the sintering/melting process parameters [83].

The deposition modes also directly affect the quantity and size of pores. Due to insufficient power density, the powder layer is not fully melted, spherodization is observed, and interlayer lack of fusion and particle fusion occur [84]. The appearance of lack of fusion and increased porosity can also be caused by insufficient overlap of individual tracks. During the cladding process, areas of lack of fusion form between individual tracks, where the powder particles are not fully exposed to the laser beam [85].

In the opposite case, when the current power density value is too high, voids are also formed due to the evaporation of the material or alloy components with a lower melting point.

The presence of pores and lack of fusion negatively impacts the performance of the *TE*, significantly increasing its wear during the *EDM* process. Furthermore, structural defects that arise during manufacturing reduce the stability of the spark generation process during *EDM* and, consequently, the performance parameters and quality of the finished surface.

Based on the analysis of the research, it can be stated that the *SLS* method is rational to use in the production of complex-shaped *TE*s, however, the use of this method requires additional research to optimize the surfacing modes and minimize structural defects, as well as the selection of materials that simultaneously satisfy the processes of *EDM* and *SLS*.

Another group of current methods for producing complex-profile *TE*s involves the use of rapid prototyping technologies, such as electroforming or *SLA* (layer-by-layer growth of a product by curing a photopolymer with a laser beam) followed by the application of a conductive coating. This combination of methods can be used to simultaneously produce multiple electrodes, offering a cost advantage.

In die and mold manufacturing, the *EDM* cycle can account for 25 to 40% of the tool shop's development time. In today's manufacturing environment, cost reduction is a primary goal, with significant emphasis placed on reducing task completion times. Advances in rapid prototyping have enabled significant time savings in ongoing research.

The use of these non-traditional manufacturing methods is explored in [10], where these methods are compared with traditional methods of producing electroformed electrodes in terms of processing time, material removal rate, tool wear, and surface roughness under several standard machining settings. It was
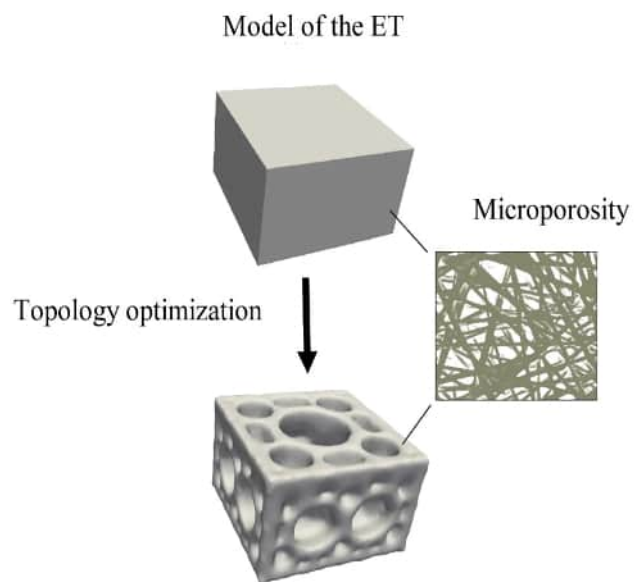
found that traditionally manufactured electrodes perform similarly to non-traditional (electroformed) electrodes. If the electrodes could be manufactured with a much more uniform shell thickness, this could reduce the randomness of defects. Electroformed electrodes perform, on average, comparable to solid electrodes.

Research groups are conducting research in many areas of rapid prototyping of electronic components. This research shows that significant opportunities still exist for potential research to improve manufacturing technologies for complex electronic components.

Harris et al. [89, 90] found that low volume part production could be accomplished in much less time and at a lower cost using additive manufacturing technologies such as additive manufacturing of *TE*s and rapid tooling.

Noguchi and *Nakagawa*, and *Chan* [91–92] showed that the combination of *SLA* and rapid forming metallization processes is a rational method for producing *TE*s.

The studies [93] and [94] showed comparisons between non-traditional electrodes produced by electroforming and conventional machined electrodes. *Jensen* et al. [94] showed a general comparison of non-traditional electrodes with machined electrodes, but did not provide a detailed insight into the performance of the electrodes. The studies of *Leu* et al. [93] show a more detailed comparison of different electrodes in terms of material removal rate as well as the roughness parameter *Ra*, but this work is based on the *EDM* process of *TE*s produced by conventional methods.

A key step in manufacturing *TE*s using rapid prototyping technologies is the metallization of their non-conductive housings. The applied coatings must meet the requirements of conductivity, uniformity, electrical erosion resistance, and adhesion strength. Several coating methods are currently used on components made from non-conductive materials.

Non-conductive materials, partially or completely coated with metal deposited on their surface, possess unique characteristics due to the combination of beneficial properties of conductive and non-conductive materials. These materials are widely used in many branches of mechanical engineering [95–96].

Currently, metallization methods are classified into three main groups: mechanical, physical, and chemical. Each group includes several methods, used individually or in combination. More detailed classifications of metallization methods also exist, based on the type of combined materials and the technological specifics of the metallization process.
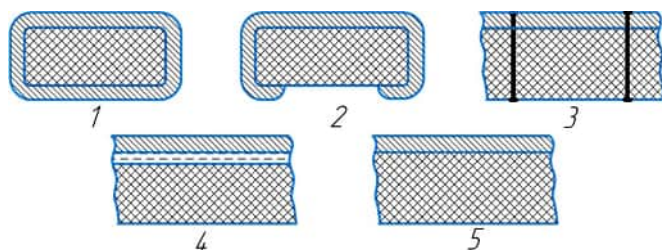
Fig. 12. Mechanical methods of metallization:
1 – wrapping; 2 – bending; 3 – riveting; 4 – gluing; 5 – hot stamping or pouring [97–98]

Traditional and most basic mechanical methods of metallization, when the metal coating is formed in advance and in finished form is attached to the surface of the product, are shown in Fig. 12 [97–98].

Despite the high labor intensity of these mechanical metallization methods, they are widely used in the manufacture of small-sized parts. The main limitation of these methods is the high metal consumption required for the target coating and the large amount of waste generated. Furthermore, coatings obtained by mechanical methods require post-processing, which is typical for metal parts.

Physical methods, which involve melting or evaporating the metal followed by deposition on the target surface (Fig. 13), are characterized by the use of more complex specialized equipment, but are also widely used in modern mechanical engineering enterprises [99].

One of the physical methods widely used for metallization of plastic and fabric products is liquid metal spray metallization. This method allows for the production of coatings from a wide range of metals, such as aluminum, zinc, lead, copper, nickel, tin, and various alloys. The method involves melting the deposited material in a gas torch flame, an electric arc, or a plasma stream, followed by spraying it onto the surface to be metallized using streams of compressed air or gas.

Electrolytic metallization methods (galvanotechnics) are generally used to create a wide range of coatings with various mechanisms of action (e.g., anti-corrosion, protective and decorative, wear-resistant,

anti-friction, reflective), as well as for the production of metal copies of products (electroplating).

These metallization methods require preliminary surface preparation, depending on the coating's intended purpose. Before cadmium or zinc plating, the target surface must be degreased and etched. In the case of chromium or nickel plating, in addition to removing grease and oxides, mechanical surface preparation by grinding and polishing is also necessary. This is because surface defects are revealed during the coating process due to the correlation between current density and surface microrelief.

In the electroplating process, the workpiece serves as the cathode, and plates made of the coating material serve as the anode. When applying an alloy coating, separate anodes are used (e.g., copper and zinc for brass plating).

Fig. 13. Physical methods of metallization:

1 – dipping; 2 – smearing; 3 – spraying; 4 – blasting; 5 – spraying (steaming); 6 – painting [99]

In the work [100] two types of technological schemes for applying galvanic coating are presented:

1) the scheme with full immersion of samples (Fig. 14, *a*) is used to apply a coating to all surfaces of the metallized product and is characterized by a high metallization rate;

2) the gradual immersion process (Fig. 14, *b*) is designed for metallization of complex-shaped parts. It allows for maximum metallization of individual structural elements (grooves, cavities, etc.).

Fig. 14. Schematics of galvanic metallization for non-conductive substrates with pre-applied conductive coatings:

a) complete immersion; *b)* gradual immersion. 1 – sample; 2 – electrodes; 3 – electrolyte bath; 4 – magnetic stirrer [100]

To increase the productivity of the copper metallization process, it is recommended to perform additional rotation of the metallized product during the processing.

The use of methods for applying conductive coatings in the production of *TE* using rapid prototyping methods is presented in the work [70]. It is shown that electrolytic and galvanic methods are mainly used in the production of *TE*.

The technology for fabricating *TE*s using the *SLA* method from non-conductive polymeric materials with subsequent application of a conductive coating is presented in detail in the study [101]. A comparison was made of the output parameters of *EDM* using *TE*s made of photopolymer resin with an applied copper coating and solid copper *TE*s processed mechanically. The stages of *TE* fabrication using the *SLA* method are shown in Fig. 15. Based on the experiments conducted, the authors identified the possibility of using

a *b* *c*

d *e* *f*
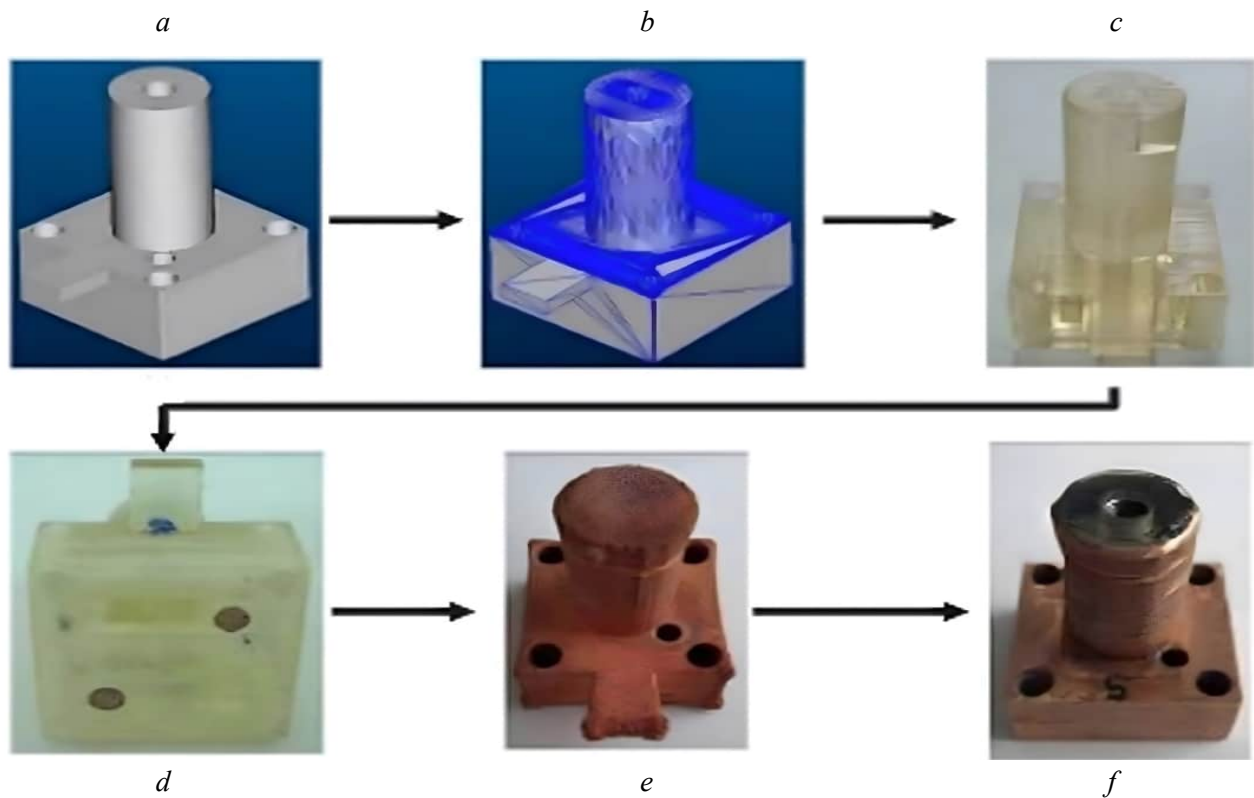
Fig. 15. Stages of tool-electrode creation by *SLA* method and subsequent coating [101]:

a–b) creation and preparation of 3D model; *c–d)* obtaining and preparing tool-electrode for metallization; *e)* coating;
f) post-processing

polymer *TE*s with an applied copper coating. However, these *TE*s were characterized by low durability. This is due to the thinning of the conductive coating.

The widespread use of *TE*s produced by rapid prototyping methods is hampered by a number of shortcomings associated with the applied conductive coatings. The authors of a critical review study [102] clearly presented (Fig. 16) and described the defects of metallic *TE* coatings. It was shown that the majority of *TE* defects arise from uneven heat dissipation and insufficient coating thickness.

Electroforming and *SLA* technologies with subsequent application of a conductive coating are applicable for the production of *TE*s for *EDM*, but further research is needed to improve the thickness and quality of these coatings.

Based on the analysis of research into methods for manufacturing tool electrodes for *EDM*, a summary Table 2 has been compiled.

a *b*
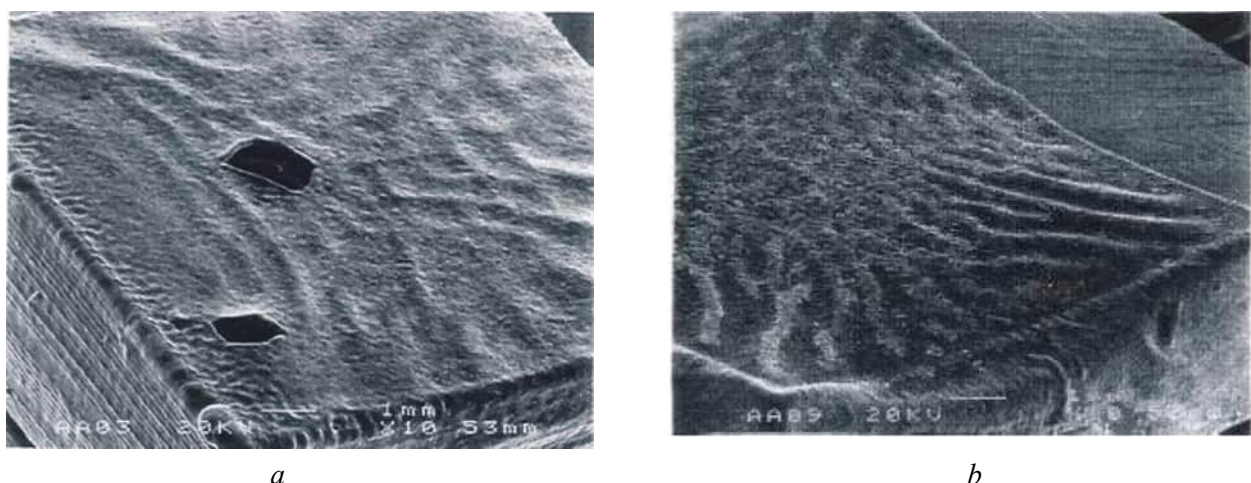
Fig. 16. Defects of conductive coating: *a)* delaminations and ruptures; *b)* deformations [102]

T a b l e 2

Methods for manufacturing tool electrodes

Method	Research	Advantages	Flaws
Traditional blade cutting methods (turning, milling, abrasive machining)	[11], [19], [62]	Wide processing capabilities. A wide range of equipment in mechanical engineering enterprises. Possibility of obtaining *TE*s with high roughness and accuracy indicators for finishing *EDM*	Difficulties in processing complex *TE*s. High costs for cutting tools and equipment. High level of equipment utilization. High wear of cutting tools during the production of TEs from materials with improved physical and mechanical properties
Powder metallurgy	[69], [70]	Wide range of *TE* materials. The ability to control the properties of the electrode by changing the composition of the material and sintering conditions. High performance	Difficulties in manufacturing complex-profile *TE*s. The complexity of manufacturing large-sized parts. Structural defects and inhomogeneity in the properties of the resulting product. High cost of equipment
Investment casting (*IC*)	[49], [63], [64], [65], [66], [67]	Possibility of obtaining complex-profile and thin-walled *TE*s. High level of adaptability of the method in pilot production conditions. Possibility of obtaining *TE*s with high roughness indices. High performance	Limited range of *TE* materials. High cost of equipment. Casting defects (pores, shrinkage cavities, cracks). High cost of equipment
Fused deposition method (*FDM*)	[70], [75], [76], [77], [78], [79], [80]	Possibility of obtaining complex-profile and thin-walled *TE*s. High level of adaptability of the method in pilot production conditions. Reduced mass and dimensional characteristics of the *TE*s. Low cost of equipment	Difficulty in manufacturing large-sized products. Low accuracy and roughness of *TE*s. Technological difficulties in metallization
Selective laser sintering (*SLS*)	[81], [82], [83], [84], [85], [86], [87], [88]	Possibility of obtaining complex-profile and thin-walled *TE*s. High level of adaptability of the method in pilot production conditions. Wide range of *TE* materials	Structural defects and heterogeneity of properties of the resulting product. High cost of equipment. Low accuracy and roughness of *TE*s
Stereolithography (*SLA*), electroforming	[10], [89], [90], [91], [92], [93], [94], [101], [102]	Possibility of obtaining complex-profile and thin-walled *TE*s. High level of adaptability of the method in pilot production conditions. Reduced mass and dimensional characteristics of the *TE*s. Low cost of equipment	Difficulty in manufacturing large-sized products. Technological difficulties in metallization. Low resource of *TE*s. Coating defects

Based on an analysis of research into tool electrode manufacturing methods for *EDM*, it can be concluded that the use of additive and other methods, as alternatives to traditional subtractive machining, will improve the competitiveness of modern mechanical engineering companies utilizing *EDM* technology in their production, by reducing the cost of manufactured products, decreasing *EDM* manufacturing time, and expanding the range of products that can be processed. However, there is a need for more thorough

development of technological processes using alternative manufacturing methods and their implementation in a pilot production environment for *EDM*, taking into account the shortcomings and limitations of these methods.

Conclusions

This paper provides a review of research on methods for manufacturing tool electrodes for wire-cutting electrical discharge machining (*EDM*). Current trends in the development of tool electrode configurations are presented. Challenges in manufacturing complex-shaped tool electrodes using traditional methods are identified. It is established that among alternative methods for manufacturing tool electrodes, investment casting, powder metallurgy, and additive manufacturing are of greatest interest to modern scientists. Each method is shown to have advantages and disadvantages, confirmed by a number of studies. The analysis revealed several relevant areas for research.

Directions for future research

1. Topological optimization of tool electrodes to reduce their mass and dimensional characteristics, while maintaining strength and electrical discharge properties.

2. Investigating modern high-tech casting methods (die casting, centrifugal casting) for the manufacture of tool electrodes.

3. Expansion of the range of new powder materials with improved electrical discharge properties; optimization of processing parameters; and development of specialized equipment for obtaining complex-profile products in the manufacture of tool electrodes using powder metallurgy.

4. Optimization of *FDM* printing parameters for tool electrodes to improve the accuracy and roughness of the resulting tool electrodes.

5. Expansion of the range of *TPM* and *ECM* for *FDM* printing of tool electrodes.

6. Expansion of the range of new powder materials with improved electrical discharge properties to ensure the performance of tool electrodes obtained by the SLS method comparable to tool electrodes obtained by traditional methods.

7. Optimization of *SLS* printing parameters to reduce porosity and, consequently, wear of the tool electrode, as well as to improve the manufacturing accuracy.

8. Increasing the thickness and quality of coatings on tool electrodes obtained using rapid prototyping technologies to increase their service life by stabilizing heat dissipation and increasing strength and electrical discharge characteristics.

References

1. Egorova A.O. Konkurentnye strategii predpriyatii mashinostroeniya: sovremennaya rossiiskaya praktika [Mechanical engineering enterprises' competitive strategies: present-day Russian practice]. *Sovremennye naukoemkie tekhnologii. Regional'noe prilozhenie = Modern High Technologies. Regional Application*, 2013, no. 2 (34), pp. 45–51.

2. Gunina I.A., Savich Y.A. K voprosu o problemakh povysheniya konkurentosposobnosti mashinostroitel'nykh predpriyatii [The questions about the problems of increase of the competitiveness of machine-building enterprise]. *Vestnik Voronezhskogo gosudarstvennogo tekhnicheskogo universiteta = Bulletin of the Voronezh State Technical University*, 2017, vol. 13, no. 2, pp. 136–140.

3. Sergeev A.A. Konkurentosposobnost' mashinostroeniya: real'nost' i perspektivy [Competitiveness of mechanical engineering: reality and prospects]. *Ekonomika. Nalogi. Pravo = Economics, Taxes & Law*, 2014, no. 5, pp. 44–49. (In Russian).

4. Golovikhin S.A., Danilkin V.A. [Formation of demand for high-tech engineering products by ensuring competitive advantages]. *Reformirovanie sistemy upravleniya na sovremennom predpriyatii* [Reforming the management system at a modern enterprise]. Collection of conference materials. Penza, MNITS Publ., 2003, pp. 29–30. (In Russian).

5. Samochkin V.N. Zakonomernost' gibkogo razvitiya mashinostroitel'nogo predpriyatiya kak osnova ego konkurentosposobnosti [Principle of flexible development of machine-building enterprise as a basis for its

competitiveness]. *Izvestiya Tul'skogo gosudarstvennogo universiteta. Ekonomicheskie i yuridicheskie nauki = News of the Tula State University. Economic and Legal Sciences*, 2017, no. 4-1, pp. 236–241.

6. Shiryaeva Yu.S., Oranova M.V. Sovremennyi vzglyad na opytnoe proizvodstvo i mekhanizm upravleniya im na promyshlennom predpriyatii [Modern views of experimental production and the mechanism of its management at an industrial enterprise]. *Vestnik Nizhegorodskogo universiteta im. N.I. Lobachevskogo = Vestnik of Lobachevsky State University of Nizhni Novgorod*, 2007, no. 6, pp. 197–200.

7. Feoktistov A.N., Feoktistov K.A., Masyukov A.A. Innovatsionnye podkhody k tekhnologicheskoi podgotovke proizvodstva v usloviyakh opytnogo proizvodstva samoletov [Innovative approaches to technological preparation of production in the conditions of pilot production of aircraft]. *Nauka, tekhnika i obrazovanie = Science, technology and education*, 2024, no. 4 (96), pp. 16–21.

8. Fokina D.A., Dzhamay E.V., Zinchenko A.S. Gibkie proizvodstvennye sistemy kak osnova innovatsionnogo razvitiya promyshlennykh predpriyatii [Flexible production systems as the basis for innovative development of industrial enterprises]. *Vestnik Gosudarstvennogo universiteta prosveshcheniya. Seriya: Ekonomika = Bulletin of the State University of Education. Series: Economics*, 2024, no. 2, pp. 113–121. DOI: 10.18384/2949-5024-2024-2-113-121.

9. Kuzhanbaev R.T. Osobennosti planirovaniya i upravleniya mul'tiseriinym proizvodstvom [Features of planning and management of multi-series production]. *Vestnik evraziiskoi nauki = The Eurasian Scientific Journal*, 2019, vol. 11, no. 6, p. 73. (In Russian).

10. Blom R.J. *Production and evaluation of rapid tooling for electric discharge machining using electroforming and spray metal deposition techniques*. Master thesis. Queensland, Queensland University of Technology, 2005. 169 p.

11. Kamenskikh A.A., Muratov K.R., Shlykov E.S., Sidhu S.S., Mahajan A., Kuznetsova Y.S., Ablyaz T.R. Recent trends and developments in the electrical discharge machining industry: A review. *Journal of Manufacturing and Materials Processing*, 2023, vol. 7 (6), p. 204. DOI: 10.3390/jmmp7060204.

12. Vijayan V., Saju K.K. A comprehensive review of performance improvement in electrical discharge machining and future research scopes: Enhancing performance through cutting-edge technologies. *Johnson Matthey Technology Review*, 2025, vol. 69 (3), pp. 358–377. DOI: 10.1595/205651325X17309868513523.

13. Mitryushin E.A., Morgunov Yu.A., Saushkin S.B. Unifitsirovannye tekhnologii izgotovleniya shtampov s primeneniem elektrofizicheskikh metodov obrabotki [Unified technologies for manufacturing stamps using electrophysical processing methods]. *Metalloobrabotka = Metalworking*, 2010, no. 2 (56), pp. 42–45. (In Russian).

14. Timoshchenko V.A. Ispol'zovanie elektroerozionnogo legirovaniya v komplekse mer povysheniya iznosostoikosti razdelitel'nykh shtampov [The use of electroerosion alloying in a complex of measures to increase the wear resistance of dividing stamps]. *Elektronnaya obrabotka materialov = Electronic Processing of Materials*, 2000, no. 4, pp. 12–16. (In Russian).

15. Khan M.Y., Rao P.S. Electrical discharge machining: Vital to manufacturing industries. *International Journal of Innovative Technology and Exploring Engineering*, 2019, vol. 8 (11), pp. 1516–1520. DOI: 10.35940/ijitee.K1516.0981119.

16. Das S., Paul S., Doloi B. Feasibility assessment of some alternative dielectric mediums for sustainable electrical discharge machining: a review work. *Journal of the Brazilian Society of Mechanical Sciences and Engineering*, 2020, vol. 42 (148), pp. 1–21. DOI: 10.1007/s40430-020-2238-1.

17. Ablyaz T.R., Shlykov E.S., Muratov K.R., Zhurin A.V. Study of the EDM process of bimetallic materials using a composite electrode tool. *Materials*, 2022, vol. 15 (3). DOI: 10.3390/ma15030750.

18. Schulze V., Ruhs C. On-machine measurement for the micro-EDM-milling process using a confocal white-light sensor. *Proceedings of the 10th International Conference of the European Society for Precision Engineering and Nanotechnology (EUSPEN)*. Delft, 2010, vol. 2, pp. 37–40.

19. Livshits A.L., Rosh A., eds. *Elektroerozionnaya i elektrokhimicheskaya obrabotka: raschet, proektirovanie, izgotovlenie i primenenie elektrodov-instrumentov. V 2 ch. Ch. 1. Elektroerozionnaya obrabotka* [Electroerosive and electrochemical processing: Calculation, design, manufacture and application of electrode-tools. In 2 pt. Pt. 1: Electroerosive processing]. Moscow, 1980. 224 p. (In Russian).

20. Zhang X., Bai X., Yang T., Li L. Interaction of machining parameters on MRR of sintered NdFeB processed by EDM-milling. *Applied Sciences*, 2025, vol. 15 (9). DOI: 10.3390/app15094897.

21. Uhlmann E., Polte M., Yabroudi S. Novel advances in machine tools, tool electrodes and processes for high-performance and high-precision EDM. *Procedia CIRP*, 2022, vol. 113, pp. 611–635. DOI: 10.1016/j.procir.2022.10.080.

22. Zeng K., Wu X., Jiang F., Shen J., Zhu L., Wen Q., Li H. The non-traditional and multi-energy field hybrid machining processes of cemented carbide: a comprehensive review. *The International Journal of Advanced Manufacturing Technology*, 2024, vol. 133, pp. 3561–3592. DOI: 10.1007/s00170-024-13791-6.

23. Priyadarshini M., Pradhan S., Barua A., Behera A., Kanchan S. Experimental analysis of wire-EDM on sub-cooled low-carbon tool steel using hybrid MARCOS method and honey badger algorithm. *Surface Review and Letters*, 2023, vol. 31 (2). DOI: 10.1142/S0218625X24500495.

24. Khan A., Ali M., Haque M.M. A study of electrode shape configuration on the performance of die sinking EDM. *International Journal of Mechanical and Materials Engineering*, 2009, vol. 4 (1), pp. 19–23.

25. Yamaguchi A., Okada A., Miyake T. Development of curved hole drilling method by EDM with suspended ball electrode – optimization of suspending parts structure and possibility of curved hole drilling. *Seimitsu Kogaku Kaishi = Journal of the Japan Society for Precision Engineering*, 2015, vol. 81 (5), pp. 435–440. DOI: 10.2493/jjspe.81.435.

26. Shah J. Optimization of process parameters for AISI 304 using micro-EDM drilling process: A review. *Journal of Mechanical Engineering and Technology*, 2024, vol. 13 (1), pp. 26–37.

27. Kumar D., Pathak V., Singh R., Dikshit M. A comprehensive review on powder mixed electrical discharge machining: advances in dielectric enhancement and machining efficiency. *Discover Applied Sciences*, 2025, vol. 7 (1). DOI: 10.1007/s42452-025-07365-8.

28. Puertas-Arbizu I., Salvide-González U., Luis-Pérez C. Study of spacing surface roughness parameters and proposal of a wear behaviour criterion in die-sinking EDM of cobalt-bonded tungsten carbide. *The International Journal of Advanced Manufacturing Technology*, 2025, vol. 139, pp. 1–13. DOI: 10.1007/s00170-025-16091-9.

29. Paswan K., Sharma S., Li C., Mohammed K., Kumar A., Abbas M., Tag-Eldin E. Unravelling the analysis of electrical discharge machining process parameters, microstructural morphology, surface integrity, recast layer formation, and material properties: A comparative study of aluminum, brass, and Inconel 617 materials. *Journal of Materials Research and Technology*, 2023, vol. 27, pp. 2881–2902. DOI: 10.1016/j.jmrt.2023.11.186.

30. Li C., Zhang B., Li Y., Tong H., Ding S., Wang Z., Zhao L. Self-adjusting EDM/ECM high speed drilling of film cooling holes. *Journal of Materials Processing Technology*, 2018, vol. 262, pp. 95–103. DOI: 10.1016/j.jmatprotec.2018.06.026.

31. Mao X., de Almeida S., Mo J., Ding S. The state of the art of electrical discharge drilling: a review. *The International Journal of Advanced Manufacturing Technology*, 2022, vol. 121 (7–8), pp. 4919–4950. DOI: 10.1007/s00170-022-09549-7.

32. Chuvaree S., Kanlayasiri K. Effects of side flushing and multi-aperture inner flushing on characteristics of electrical discharge machining macro deep holes. *Metals*, 2021, vol. 11 (1). DOI: 10.3390/met11010148.

33. Karim M.A., Jahan M.P. Electrical discharge machining technologies in the aerospace industry. *Modern Manufacturing Processes for Aircraft Materials*. Elsevier, 2024, pp. 171–226. DOI: 10.1016/B978-0-323-95318-4.00007-0.

34. Kumar R., Singh I. Productivity improvement of micro EDM process by improvised tool. *Precision Engineering*, 2018, vol. 51, pp. 529–535. DOI: 10.1016/j.precisioneng.2017.10.008.

35. Uhlmann E., Polte M., Yabroudi S., Gerhard N., Sakharova E., Thißen K., Penske W. Helical electrodes for electro-discharge drilling: experimental and CFD-based analysis of the influence of internal and external flushing geometries on the process characteristics. *Journal of Manufacturing and Materials Processing*, 2023, vol. 7 (6). DOI: 10.3390/jmmp7060217.

36. Jamkamon K., Janmanee P. Improving machining performance for deep hole drilling in the electrical discharge machining process using a step cylindrical electrode. *Applied Sciences*, 2021, vol. 11 (5). DOI: 10.3390/app11052084.

37. Sahoo A., Mishra D. Experimental characteristic evaluation of micro hole EDM drilling of $Ni_{51.58}Ti_{48.34}$ alloy with copper electrode and response optimization using GRG assisted with GA. *Journal of Engineering and Applied Science*, 2024, vol. 71 (1), pp. 1–22. DOI: 10.1186/s44147-024-00447-1.

38. Hu G., Fu F., Zhang S., Gao W., Zhang J., Wang J. High speed short electric arc deep hole drilling experimental study based on tube electrode. *The International Journal of Advanced Manufacturing Technology*, 2025, vol. 139, pp. 1087–1103. DOI: 10.1007/s00170-025-15827-x.

39. Jamkamon K., Kumkoon P., Chuvaree S. Influence of electrical parameters on the machining performance in the small hole drilling by EDM process. *Solid State Phenomena*, 2023, vol. 349, pp. 33–39. DOI: 10.4028/p-CtB8KO.

40. Ji R., Liu Y., Zhang Y., Wang F. Machining performance of silicon carbide ceramic in end electric discharge milling. *International Journal of Refractory Metals and Hard Materials*, 2011, vol. 29 (1), pp. 117–122. DOI: 10.1016/j.ijrmhm.2010.09.001.

41. Ablyaz T.R., Shlykov E.S., Osinnikov I.V., et al. *Ustroistvo dlya elektroerozionnoi proshivki otverstiya elektrod-instrumentom* [Device for electrical discharge piercing of a hole with an electrode-tool]. Patent RF, no. 2802609, 2023. (In Russian).

42. Makireddi D., Puri Y., Ghuge V. Development of crank–connecting rod attachment for electric discharge machining of curved holes. *Advances in Mechanical Engineering*. Singapore, Springer, 2021, pp. 777–783. DOI: 10.1007/978-981-15-3639-7_93.

43. Okada A., Yamaguchi A., Ota K. Improvement of curved hole EDM drilling performance using suspended ball electrode by workpiece vibration. *CIRP Annals*, 2017, vol. 66 (1), pp. 189–192. DOI: 10.1016/j.cirp.2017.04.125.

44. Yamaguchi A., Inaba Y., Shiraga S., Okada A. Development of curved hole drilling method by EDM with suspended ball electrode-improvement in shape accuracy of bending holes using foil supporting guide. *Seimitsu Kogaku Kaishi = Journal of the Japan Society for Precision Engineering*, 2021, vol. 87 (5), pp. 461–466. DOI: 10.2493/jjspe.87.461.

45. Inaba Y., Li S., Yamaguchi A., Okada A. Fundamental study on internal space forming by EDM. *Procedia CIRP*, 2020, vol. 95, pp. 215–219. DOI: 10.1016/j.procir.2020.01.156.

46. Hsue A.W.J., Pan Y.D., Lu L.W. A novel string-bead EDM mechanism for dressing of the conformal cooling channel fabricated by the SLM-additive manufacture. *Journal of Physics: Conference Series*, 2021, vol. 2020 (1). DOI: 10.1088/1742-6596/2020/1/012035.

47. Grzesik W., Ruszaj A. Physical fundamentals of conventional and unconventional machining processes. Grzesik W., Ruszaj A. *Hybrid manufacturing processes*. Cham, Springer, 2021, pp. 35–60. DOI: 10.1007/978-3-030-77107-2_4.

48. Singh K., Singh K., Khan M. Investigation and optimization of process parameters in the electrical discharge machining process for Inconel 660 using response surface methodology. *Future Technology*, 2025, vol. 4, pp. 22–29. DOI: 10.55670/fpll.futech.4.2.3.

49. Ablyaz T.R., Blokhin V.B., Shlykov E.S., Muratov K.R., Osinnikov I.V. Features of the use of tool electrodes manufactured by additive technologies in electrical discharge machining of products. *Obrabotka metallov (tekhnologiya, oborudovanie, instrumenty) = Metal Working and Material Science*, 2024, vol. 26, no. 3, pp. 135–148. DOI: 10.17212/1994-6309-2024-26.3-135-148.

50. Lozhkin D.V., Maksimov P.V. Topological optimization of a part taking into account technological constraints. *IOP Conference Series: Materials Science and Engineering*, 2021, vol. 1100 (1). DOI: 10.1088/1757-899x/1100/1/012036.

51. Dagld'yan A.O., Lozhkin D.V., Maksimov P.V. Metodologiya topologicheskoi optimizatsii izdelii s yacheistymi strukturami [Methodology of topological optimization of products with cellular structures]. *Nauchno-tekhnicheskii vestnik Povolzh'ya = Scientific and Technical Volga region Bulletin*, 2022, no. 12, pp. 41–44.

52. Lozhkin D.V., Maksimov P.V. [Designing lightweight products based on topological optimization methods]. *Matematika i mezhdistsiplinarnye issledovaniya – 2021* [Mathematics and Interdisciplinary Research – 2021]. Proceedings of the All-Russian Scientific and Practical Conference of Young Scientists with International Participation. Perm, 2021, pp. 76–80. (In Russian).

53. Maksimov P.V., Fetisov K.V., Kurchev A.I., Belousov A.S. Ispol'zovanie topologicheskoi optimizatsii i setchatykh mikrostruktur v proektirovanii detalei dlya additivnogo proizvodstva [Topology optimization and lattice microstructures in the design of parts for additive manufacturing]. *STIN = Russian Engineering Research*, 2021, no. 2, pp. 38–44. (In Russian).

54. Ambrosi A., Shi R.R.S., Webster R.D. 3D-printing for electrolytic processes and electrochemical flow systems. *Journal of Materials Chemistry A*, 2020, vol. 8 (42), pp. 21902–21929. DOI: 10.1039/D0TA07939A.

55. Forner-Cuenca A., Brushett F.R. Engineering porous electrodes for next-generation redox flow batteries: recent progress and opportunities. *Current Opinion in Electrochemistry*, 2019, vol. 18, pp. 113–122. DOI: 10.1016/j.coelec.2019.11.002.

56. Haverkort J. A theoretical analysis of the optimal electrode thickness and porosity. *Electrochimica Acta*, 2019, vol. 295, pp. 846–860. DOI: 10.1016/j.electacta.2018.10.065.

57. Roy T., Salazar de Troya M.A., Beck V.A. LLNL/TOPE: topology optimization for porous electrodes. *Zenodo*, 2022. DOI: 10.5281/zenodo.6366849.

58. Roy T., Salazar de Troya M.A., Worsley M.A., Beck V.A. Topology optimization for the design of porous electrodes. *Structural and Multidisciplinary Optimization*, 2022, vol. 65, art. 171. DOI: 10.1007/s00158-022-03249-2.

59. Lu X., Bertei A., Finegan D.P., Tan C., Daemi S.R., Weaving J.S., O'Regan K.B., Heenan T.M.M., Hinds G., Kendrick E., Brett D.J.L., Shearing P.R. 3D microstructure design of lithium-ion battery electrodes assisted by X-ray nano-computed tomography and modelling. *Nature Communications*, 2020, vol. 11. DOI: 10.1038/s41467-020-15811-x.

60. Park S.H., Goodall G., Kim W.S. Perspective on 3D-designed micro-supercapacitors. *Materials & Design*, 2020, vol. 193. DOI: 10.1016/j.matdes.2020.108797.

61. Zheng J., Xing G., Jin L., Lu Y., Qin N., Gao S., Zheng J. Strategies and challenge of thick electrodes for energy storage: A review. *Batteries*, 2023, vol. 9 (3). DOI: 10.3390/batteries9030151.

62. Goiogana M., Elkaseer A. Self-flushing in EDM drilling of Ti6Al4V using rotating shaped electrodes. *Materials*, 2019, vol. 12 (6). DOI: 10.3390/ma12060989.

63. Nguyen T.T., Nguyen V.-T., Tran V.T., Le A.T., Nguyen T.D., Huynh Q.D., Ho M.T., Dang M.P., Le H.G., Nguyen V.T.T. Insight into various casting material selections in rapid investment casting for making EDM electrodes. *Micromachines*, 2025, vol. 16 (5). DOI: 10.3390/mi16050595.

64. Equbal A., Equbal M.I., Badruddin I.A., Algahtani A.A. A critical insight into the use of FDM for production of EDM electrode. *Alexandria Engineering Journal*, 2022, vol. 61 (5), pp. 4057–4066. DOI: 10.1016/j.aej.2021.09.033.

65. Equbal A., Equbal M.I., Sood A.K. An investigation on the feasibility of fused deposition modelling process in EDM electrode manufacturing. *CIRP Journal of Manufacturing Science and Technology*, 2019, vol. 26, pp. 10–25. DOI: 10.1016/j.cirpj.2019.07.001.

66. Khan M., Rao P.S., Pabla B.S. On the use of copper tool developed by Atomic Diffusion Additive Manufacturing (ADAM) process for electrical discharge machining. *E3S Web of Conferences*, 2023, vol. 455. DOI: 10.1051/e3sconf/202345502014.

67. Purwar U., Javed A., Vidya S. A review on research aspects and trends in rapid prototyping and tooling assisted investment casting. *Materials Today: Proceedings*, 2021, vol. 46 (11), pp. 6704–6707. DOI: 10.1016/j.matpr.2021.04.172.

68. Sugavaneswaran M., John R.A., Bhagywani H., Wilson V., Swaminathan J., Selvaraj S. Innovative electrode tool manufacturing methods for electrode discharge machining. *Artificial Intelligence in Material Science*. Boca Raton, CRC Press, 2024, pp. 81–107. DOI: 10.1201/9781003452515-5.

69. Sharma S., Gajević S., Sharma L., Mohan D.G., Sharma Y., Radojković M., Stojanovic B. Significance of the powder metallurgy approach and its processing parameters on the mechanical behavior of magnesium-based materials. *Nanomaterials*, 2025, vol. 15 (2). DOI: 10.3390/nano15020092.

70. Garba E., Abdul-Rani A.M., Yunus N.A., Aliyu A.A.A., Gul I.A., Al-Amin M., Aliyu R.A. A review of electrode manufacturing methods for electrical discharge machining: current status and future perspectives for surface alloying. *Machines*, 2023, vol. 11 (9). DOI: 10.3390/machines11090906.

71. Sundaram C., Sivasubramanian R., Sivakumar M. Development of new metal matrix composite electrodes for electrical discharge machining through powder metallurgy process. *Carbon – Science and Technology*, 2014, vol. 6 (4), pp. 34–40.

72. Ablyaz T.R., Shlykov E.S., Muratov K.R., Blokhin V.B., Osinnikov I.V., Shiryaev V.V. Investigation of controlled microrelief formation on products obtained by selective laser melting using copy-penetrating electro-erosion processing. *Russian Engineering Research*, 2024, vol. 44 (12), pp. 1823–1826. DOI: 10.3103/S1068798X24703076.

73. Equbal A., Equbal M.I., Sood A.K. PCA-based desirability method for dimensional improvement of part extruded by fused deposition modeling technology. *Progress in Additive Manufacturing*, 2019, vol. 4 (3), pp. 269–280. DOI: 10.1007/s40964-018-00072-4.

74. Equbal A., Ahmad S., Badruddin I., Khan Z., Kamangar S., Syed J. Evaluating machining performance of acrylonitrile-butadiene-styrene (ABS) based electrical discharge machining (EDM) electrodes fabricated by fused deposition modelling (FDM) followed by a novel metallization method. *Proceedings of the Institution of Mechanical Engineers, Part B: Journal of Engineering Manufacture*, 2023, vol. 238 (2), pp. 209–222. DOI: 10.1177/09544054221151093.

75. Shirbhate N.J., Vinchurkar S.M., Borade A.B. FDM technology for EDM electrode fabrication: progress, prospects, and perspectives. *International Journal of Mechanical Engineering*, 2024, vol. 11 (9), pp. 11–27. DOI: 10.14445/23488360/IJME-V11I9P102.

76. Wang J., Zhu R., Liu Y., Zhang L. Understanding melt pool characteristics in laser powder bed fusion: An overview of single- and multi-track melt pools for process optimization. *Advanced Powder Materials*, 2023, vol. 2 (4). DOI: 10.1016/j.apmate.2023.100137.

77. Prakash C., Kansal H.K., Pabla B., Puri S., Aggarwal A. Electric discharge machining – A potential choice for surface modification of metallic implants for orthopedic applications: a review. *Proceedings of the Institution of Mechanical Engineers, Part B: Journal of Engineering Manufacture*, 2016, vol. 230 (2), pp. 331–353. DOI: 10.1177/0954405415579113.

78. Fefar S.D., Karajagikar M.J.S. Study and analysis of metallized electrode fabricated with FDM rapid prototyping technique for electro discharge machining (EDM). *Proceedings of the 5th International & 26th All India Manufacturing Technology Design and Research Conference (AIMTDR 2014)*, 2014, pp. 37–42.

79. Sridhar S., Valeti S.V., Koti V., Sathish S., Chand R.R., Sivakumar N.S., Mahesh M., Subbiah R., Veerappan G. Surface modification of strenx 900 steel using electrical discharge alloying process with Cu-10Ni-Cr$_x$ powder metallurgy sintered electrode. *Materials Research*, 2022, vol. 25. DOI: 10.1590/1980-5373-MR-2021-0390.

80. Danade U.A., Londhe S.D., Metkar R.M. Machining performance of 3D-printed ABS electrode coated with copper in EDM. *Rapid Prototyping Journal*, 2019, vol. 25 (7), pp. 1224–1231. DOI: 10.1108/RPJ-11-2018-0297.

81. Dürr H., Pilz R., Eleser N.S. Rapid tooling of EDM electrodes by means of selective laser sintering. *Computers in Industry*, 1999, vol. 39 (1), pp. 35–45. DOI: 10.1016/S0166-3615(98)00123-7.

82. Amorim F.L., Lohrengel A., Müller N., Schäfer G., Czelusniak T. Performance of sinking EDM electrodes made by selective laser sintering technique. *The International Journal of Advanced Manufacturing Technology*, 2013, vol. 65 (9–12), pp. 1423–1428. DOI: 10.1007/s00170-012-4267-0.

83. Sahu A., Mahapatra S., Patterson A., Leite M., Peças P., Singh Y., Sahoo S. Electro-discharge machining using copper-coated additively-manufactured AlSi10Mg electrodes. *Proceedings of the Institution of Mechanical Engineers, Part L: Journal of Materials: Design and Applications*, 2024, vol. 239 (8), pp. 1462–1471. DOI: 10.1177/14644207241293919.

84. Mohije R., Titre H., Gohil V., Meshram D.B. A study in EDM electrode manufacturing using additive manufacturing. *Materials Today: Proceedings*, 2023. DOI: 10.1016/j.matpr.2023.01.044.

85. Amorim F.L., Czelusniak T., Higa C.F. Producing sinking EDM electrodes using selective laser sintering technique. *7th Brazilian Congress on Manufacturing Engineering.* Penedo, Brazil, 2013, pp. 1–10.

86. Torres A., Luis C.J., Puertas I. Analysis of the influence of EDM parameters on surface finish, material removal rate, and electrode wear of an INCONEL 600 alloy. *The International Journal of Advanced Manufacturing Technology*, 2015, vol. 80 (1–4), pp. 123–140. DOI: 10.1007/s00170-015-6974-9.

87. Amorim F.L., Lohrengel A., Schäfer G., Czelusniak T. A study on the SLS manufacturing and experimenting of TiB$_2$-CuNi EDM electrodes. *Rapid Prototyping Journal*, 2013, vol. 19 (6), pp. 418–429. DOI: 10.1108/RPJ-03-2012-0019.

88. Czelusniak T., Amorim F.L., Higa C.F., Lohrengel A. Development and application of new composite materials as EDM electrodes manufactured via selective laser sintering. *International Journal of Advanced Manufacturing Technology*, 2014, vol. 72 (9), pp. 1503–1512. DOI: 10.1007/s00170-014-5765-z.

89. Harris R.A., Hague R.J.M., Dickens P.M. The structure of parts produced by stereolithography injection mould tools and the effect on part shrinkage. *International Journal of Machine Tools and Manufacture*, 2004, vol. 44 (1), pp. 59–64. DOI: 10.1016/j.ijmachtools.2003.08.007.

90. Harris R.A., Newlyn H.A., Dickens P.M. Part shrinkage anomalies from stereolithography injection mould tooling. *International Journal of Machine Tools and Manufacture*, 2003, vol. 43 (9), pp. 879–887. DOI: 10.1016/S0890-6955(03)00080-4.

91. Noguchi H., Nakagawa T. Manufacturing of high precision forming tool transferred from laser stereolithography models by powder casting method. *Computers in Industry*, 1999, vol. 39 (1), pp. 55–60.

92. Chan S.F., Law C.K., Wong T.T. Re-engineering the roto-casting mould making process. *Journal of Materials Processing Technology*, 2003, vol. 139 (1–3), pp. 527–534. DOI: 10.1016/S0924-0136(03)00532-6.

93. Leu M.C., Yang B., Yao W. Feasibility study of EDM tooling using metalized stereolithography models. *Society of Manufacturing Engineers (SME) Engineering Technical Paper*. MR98-180. SME, 1998, pp. 1–6.

94. Jensen K.L., Hovtun R. Making electrodes for EDM with rapid prototyping. *2nd European Conference of Rapid Prototyping*. University of Nottingham, 1993, pp. 221–233.

95. Garba E., Majdi A., Azeez A., Aliyu A.A., Gul I., Aliyu R. A review on additively manufactured electrodes for use in electro-discharge process. *Journal of Electrical Systems*, 2024, vol. 20 (10s), pp. 6919–6930.

96. Sahu A., Mahapatra S., Martin A., Schubert A., Leite M., Peças P. Electrical discharge machining by rapid tools prepared by micro stereo-lithography process with copper metallization. *Scientific Reports*, 2025, vol. 15, art. 22667. DOI: 10.1038/s41598-025-07020-7.

97. Yudhanto A., Li X., Tao R., Melentiev R., Lubineau G. Identifying adhesion characteristics of metal-polymer interfaces: Recent advances in the case of electroplated acrylonitrile butadiene styrene. *Materials Today Communications*, 2023, vol. 35. DOI: 10.1016/j.mtcomm.2023.106218.

98. Mandal P., Chatterjee S., Chakraborty S. Bi-objective optimization of an EDM process with Cu-MWCNT composite tool using single-valued neutrosophic grey relational analysis. *World Journal of Engineering*, 2025, vol. 22 (3), pp. 472–481. DOI: 10.1108/WJE-10-2023-0443.

99. Swain S., Pradhan M., Das S., Rautray T. Constructing antibacterial responsive multi-functionalized agent CSA13 loaded on a hydroxyapatite-TiO_2 nanotube network. *Materials Chemistry and Physics*, 2025, vol. 333. DOI: 10.1016/j.matchemphys.2024.130337.

100. Wang L.-N., Luo J.-L. Preparation of hydroxyapatite coating on CoCrMo implant using an effective electrochemically-assisted deposition pretreatment. *Materials Characterization*, 2011, vol. 62 (11), pp. 1076–1086. DOI: 10.1016/j.matchar.2011.08.002.

101. Anil D., Çoğun C. Performance of copper-coated stereolithographic electrodes with internal cooling channels in electric discharge machining (EDM). *Rapid Prototyping Journal*, 2008, vol. 14, pp. 202–212. DOI: 10.1108/13552540810896157.

102. Equbal A., Sood A.K. Problems and challenges in EDM electrode fabrication using RP: A critical review. *World Applied Sciences Journal*, 2013, vol. 28, pp. 1127–1133. DOI: 10.5829/idosi.wasj.2013.28.08.1461.

103. Reddy G.K., Esanakula J.R. Optimization of operating parameters of wire EDM using design of experiments criteria. *International Conference on Self Sustainable Artificial Intelligence Systems (ICSSAS)*, Erode, India, 2023, pp. 1504–1509. DOI: 10.1109/ICSSAS57918.2023.10331679.

104. Duan X., Saxena K., Wang J., Arshad M.H., Ayesta I., Wang Y., Reynaerts D., Yang X. Residual stress and its modification strategies in the surface/sub-surface layer of components machined by electrical discharge machining: a review. *The International Journal of Advanced Manufacturing Technology*, 2025, vol. 139, pp. 41–58. DOI: 10.1007/s00170-025-15861-9.

105. Mufti N., Rafaqat M., Ahmed N., Saleem M., Hussain A., Al-Ahmari A. Improving the performance of EDM through relief-angled tool designs. *Applied Sciences*, 2020, vol. 10 (7), art. 2432. DOI: 10.3390/app10072432.

106. Selvarajan L., Venkataramanan K., Srinivasa Perumal K.P., Alghanmi S., Paulraj S., Ellappan V., Venkatesh K., Choudhury B., Jayamurugan S., Sakthivel G., Kasthuri N. Review on characterization, impacts and optimization of EDM parameters on composite structure in additive manufacturing. *Progress in Additive Manufacturing*, 2025, vol. 10, pp. 4573–4624. DOI: 10.1007/s40964-024-00907-3.

107. Kumar P., Shekhar A., Yadav S.K.S. Experimental analysis of electrical discharge drilling (EDD) of carbon-carbon composite. *Materials Today: Proceedings*, 2020, vol. 22, pp. 3106–3115. DOI: 10.1016/j.matpr.2020.03.447.

Conflicts of Interest

The authors declare no conflict of interest.

Obrabotka metallov –
Metal Working and Material Science

Investigation of the effect of process parameters on photochemical machining of SS316l for manufacturing vascular stents

Devendra Agrawal [1, a, *], *Sushil Patil* [1, b], *Dinesh Washimkar* [2, c], *Nitin Ambhore* [2, d], *Dhroov Agrawal* [3, e]

[1] Department of Mechanical Engineering, S.V.P.M'S College of Engineering Malegaon (Bk.), Savitribai Phule Pune University, Pune, Maharashtra, 413115, India

[2] Department of Mechanical Engineering, Vishwakarma Institute of Technology, Savitribai Phule Pune University, Pune, Maharashtra, 411037, India

[3] Department of Bachelor of Medicine & Bachelor of Surgery, KD Medical College Mathura, Uttar Pradesh, 281406, India

[a] https://orcid.org/0000-0002-2477-1841, ✉ dpagrawal@engg.svpm.org.in; [b] https://orcid.org/0000-0002-0547-6038, ✉ sspatil@engg.svpm.org.in;
[c] https://orcid.org/0000-0002-1312-2619, ✉ dinesh.washimkar@vit.edu; [d] https://orcid.org/0000-0001-8468-8057, ✉ nitin.ambhore@vit.edu;
[e] https://orcid.org/0009-0000-8547-9484, ✉ dhroovagrawal109@gmail.com

ARTICLE INFO

ABSTRACT

Introduction. Photochemical machining (*PCM*) is a non-traditional machining method capable of developing burr-free and stress-free biomedical components. A stent is a small meshed tube used to remove blockages and open blood passages in arteries and veins. *SS316L* is one of the recommended materials for stents due to its biocompatibility and machinability with photochemical processes. Vascular stents are made from metal mesh, fabric, silicone, or combinations of materials. **The purpose of this work** is to investigate the effect of process parameters on the *PCM* process during the machining of *SS316L* and to manufacture an *SS316L* stent as a substrate using photochemical machining. The manufactured stent is used in larger arteries, such as the aorta, to provide a stable channel for blood flow. **Methods of investigation.** The process parameters for the photochemical machining process were optimized using the *Taguchi* method with an L_9 experimental array (*DoE*). The effect of process parameters on responses was investigated using ***F***-values. An *ANN* was employed as a predictive tool for observing deviations in the responses. **Results and discussion.** The optimum set of machining parameters was obtained and utilized for manufacturing the vascular stent. A phototool with the required stent strut size was developed using CAD software. Controlled etching with ferric chloride generated the mesh, and laser seam welding was performed to develop the tubular stent for placement in blockages. The dimensions of the developed stent were measured with *SEM*, and the stent strut size was found to vary from 312 µm to 900 µm.

Introduction

One of the significant risks to human health is vascular disease. Cerebrovascular stents are primarily of two types: self-expanding and balloon-expandable. However, both have been associated with issues such as stent migration, vascular injury, and complications related to sudden expansion and contraction within the vessel. While balloon-expandable stents offer precise placement, ease of use, and high radial force, their flexibility in navigating tortuous arteries is limited. There is a clinical need to establish a permanent blood flow pathway in branch vessels through the placement of a permanent vascular stent. The stent implantation procedure involves deploying a mesh-like device into the diseased or occluded segment of the blood vessel. Once positioned at the target lesion, the stent restores and maintains patency by providing mechanical support to the narrowed or blocked lumen, ensuring sustained blood flow.

---

* Corresponding author
Agrawal Devendra Prabhudayal, Ph.D. (Engineering), Associate Professor
S.V.P.M'S College of Engineering Malegaon (Bk.),
Savitribai Phule Pune University, Pune,
Maharashtra, 413115, India.
Tel.: +91-9421054282, **e-mail**: dpagrawal@engg.evpm.org.in

Because human vasculature varies significantly among individuals, a standard stent often does not conform precisely to a patient's specific vascular anatomy. The conventional tubular mesh may require customized sizing. Although self-expanding stents offer flexibility and good wall apposition, their complex deployment procedure can lead to prolonged operation times and an increased risk of embolic stroke. Vascular stents can be fabricated from metals, polymers, or composites and typically feature uniform unit-cell designs, sizes, and shapes. *Alizera* et al. designed and developed three innovative hybrid auxetic stents and analyzed their behavior under quasi-static loading. The stents were fabricated using the fused deposition modeling (*FDM*) additive manufacturing technique. A comparison between experimental and finite element simulation results showed good agreement [1].

Canic et al. developed a novel mathematical and computational framework for geometrically optimized mesh-like stents. These stents are modeled as a network of one-dimensional curved rods, approximated by piecewise straight rods to simplify computation [2]. *Ebrahimi* et al. explored the tailoring of metamaterial stents for biomedical applications. These findings hold considerable potential for advancing stent technology, ultimately benefiting patients with conditions such as arterial stenosis [3]. *Pang* et al. established a micro-milling process route for magnesium alloy cardiovascular stents and evaluated the machined stents' mechanical properties and quality [4].

Li et al. investigated the fabrication of vascular stents using various *AM* techniques and materials, including cost-effective bio-inert metals, bioresorbable polymers, and bioresorbable metals. The study highlighted the potential of *AM* to produce patient-specific stents with unique unit-cell designs, leading to improved conformability and crimping-expansion performance [5]. *Yan* et al. developed stents for curved arteries and performed multi-objective optimization of process parameters to enhance overall stent performance [6].

Roxanne et al. investigated the influence of *FDM* process parameters – such as line width, print speed, and travel speed – on stent quality. By controlling these parameters, stents could be produced in close compliance with the original *CAD* designs. The study concluded that *FDM's* ability to process medical-grade materials offers promising prospects for 3D-printed stents [7]. *Demir* et al. provided an overview of metallic stent manufacturing using laser-based processes, including additive laser powder bed fusion and subtractive laser cutting. The authors emphasized the potential for enhanced collaboration between engineers and clinicians in the biomedical implant industry [8].

Antonio et al. studied the effect of the dip-coating process on the properties of *PCL/PLA* composite tubes for stent fabrication. Dynamic mechanical analysis and degradation studies revealed the limitations of pure *PCL* and *PLA*, while the composite tube exhibited behavior more aligned with stent require-ments [9].

Despite these advances, the aforementioned methods present certain constraints, including high cost, multi-stage processing, residual stress formation, specialized environment and operator skill requirements, material limitations, and the need for post-processing. To address these challenges, photochemical machining (*PCM*) – a non-traditional microfabrication technique–has been employed for the development of vascular stents. *PCM* has emerged as an efficient alternative to conventional machining for producing thin components with complex geometries [10]. The process involves selective etching of a substrate using a photoresist and etchant [11]. *Fadaei* et al. reported improved surface quality and material removal rate during *PCM* of stainless steel 304 using triethanolamine (*TEA*) as an etchant [12]. *Allen* et al. established performance criteria and metrics for industrial etchants [13]. *Cakir* investigated the parametric effects of etching aluminum with ferric chloride (*FeCl₃*) etchant [14]. *Agrawal* et al. optimized *PCM* parameters for machining *SS304* with *FeCl₃* etchant, identifying ideal conditions for fabricating microfluidic channels and micromolds with features down to 100 μm [15].

The literature indicates that *PCM* offers several advantages: it is burr-free and stress-free, eliminating the need for post-machining treatment. It is a unique method for machining thin, complex profiles at low cost. The process can be controlled by optimizing parameters, and it leaves the metallurgical properties of the material unaffected. To explore *PCM's* capabilities, the authors have applied it to vascular stent fabrication.

In the present study, the authors attempt to manufacture a vascular stent using the photochemical machining process. All steps – including centrifugal photoresist coating, drying, controlled etching, and *UV* exposure – were conducted in the laboratory. A phototool with stent strut dimensions was designed using *CAD* software and printed using a high-*DPI* precision printer. Ferric chloride etchant was used with parameters optimized via *Taguchi* analysis to produce a mesh with specified dimensions. An artificial neural network (*ANN*) model was developed to predict output parameters, and prediction errors were estimated. Laser seam welding was employed to join the mesh edges into a tubular structure. Stent dimensions were measured using scanning electron microscopy (*SEM*), revealing strut sizes ranging from 312 μm to 900 μm. The manufactured stent is intended for use in larger arteries, such as the aorta, to provide a stable conduit for blood flow.

Methods

SS316L is a widely recommended material for biomedical implants due to its excellent corrosion resistance, biocompatibility, favorable mechanical properties, and broad applicability. It is also well-suited for the photochemical machining (*PCM*) process. The chemical composition of *SS316L* includes: *Mo* (2–3 %), *Si* (≤0.75 %), *N* (0.10%), *P* (≤0.045 %), *C* (≤0.03%), *Ni* (10–14%), *Cr* (16–18 %), with the balance being *Fe*. The *PCM* process involves several steps: material selection, phototool and specimen preparation, photoresist coating (masking), drying, controlled etching, stripping, and inspection, all conducted in a darkroom and laboratory environment. For this study, *SS316L* sheets with dimensions of 30 mm × 30 mm and a thickness of 0.08 mm were used. The phototool consisted of a black circular pattern with a diameter of 10 mm. The artwork was designed using *CAD* software and printed with a high-*DPI* printer. The key process parameters for evaluation were etching time (min), etchant temperature (°C), and etchant concentration (g/L) [16].

Preliminary experiments were conducted using a **one-factor-at-a-time approach** to determine appropriate parameter levels for the design of experiments (*DoE*), with three replicates for each condition [17]. The resulting parameter levels are shown in Table 1. Measurements from the *DoE* are presented in Table 2.

Table 1

Process parameters and their levels

Parameters	Level 1	Level 2	Level 3
Concentration (g/L)	300	400	500
Time (min)	2	3	4
Temperature (°C)	50	55	60

Table 2

Experimental design matrix

Sr. No.	Conc. (g/L)	Time (min)	Temp. (°C)	*MRR* (mm^2/min)	Undercut (mm)	Depth of cut (mm)	Etch Factor
1	300	2	50	2.88	0.018	0.0366	2.0333
2	300	3	55	3.12	0.058	0.0396	0.6843
3	300	4	60	3.88	0.098	0.0493	0.5037
4	400	2	55	4.91	0.031	0.0623	2.0045
5	400	3	60	5.12	0.033	0.0651	1.9860
6	400	4	50	5.28	0.039	0.0671	1.7223
7	500	2	60	5.15	0.033	0.0655	2.0037
8	500	3	50	5.78	0.035	0.0732	2.0857
9	500	4	55	6.12	0.038	0.0823	2.1466

Undercut (Uc)

Undercut is an undesirable machining artifact in *PCM*, resulting from isotropic etching beneath the photoresist mask. As illustrated in Fig. 1, while etching is intended for area *A*, the process extends laterally under the mask, effectively machining area *B*. This excess removal is termed undercut (*Uc*) and is quantified using Equation. U_c was measured using a video measuring machine (*VMM*) (Fig. 2). The *VMM* image (Fig. 3) clearly shows two concentric circles: the inner circle corresponds to the phototool dimensions, while the outer circle represents the undesired material removal due to undercut.

$$Uc = 1/2(B-A)$$

PCM for stent manufacturing

An optimal set of parameters – namely, an etchant temperature of 50 °C, a concentration of 500 g/L, and an etching time of 2 minutes – was used to achieve the best results. To maintain a uniform etchant concentration throughout the tank, compressed air was bubbled through the solution from the bottom.

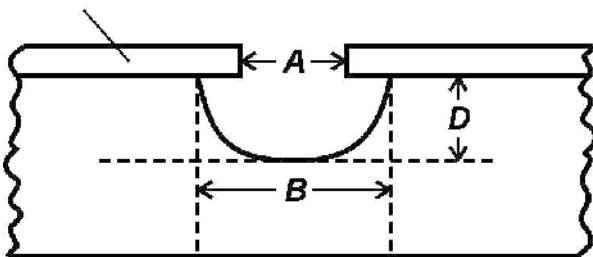*Fig. 1*. Definition of undercut (*Uc*), where:

A is the area for machining; *B* is the actual machined area

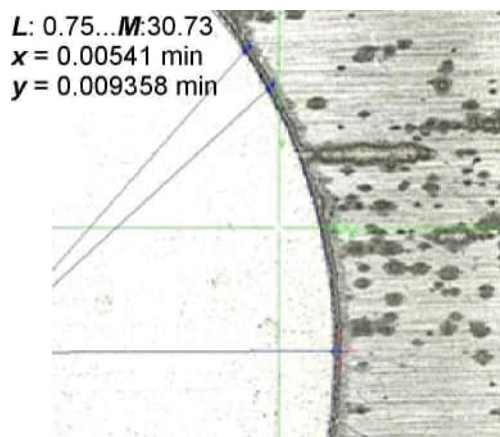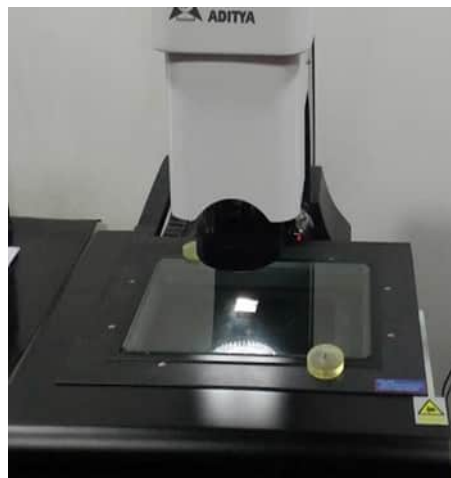*Fig. 2*. Specimen under *VMM*

Fig. 3. Specimen showing the inner circle (phototool size) and the outer circle (extra machining)

During etching, the specimen was held in a polymer mesh bag. All necessary safety precautions were observed during the drying, *UV* exposure, and controlled etching stages. Gentle rinsing was employed to remove the etchant and the exposed photoresist. A mesh pattern (stent strut) matching the dimensions specified in the phototool was etched onto the specimen. Any remaining photoresist was removed via soft cleaning with water. A view of the phototool used for stent fabrication is shown in Fig. 4.
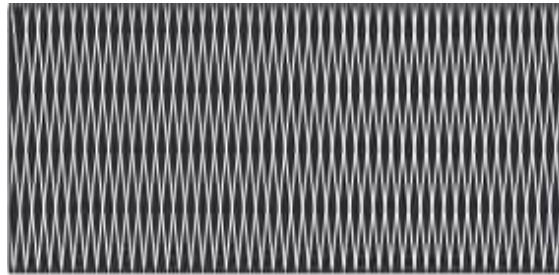
Fig. 4. Phototool used for stent manufacturing

To form a tubular structure, the flat, etched mesh specimen was wrapped around a cylindrical mandrel with a diameter corresponding to the desired stent diameter (ranging from 100 μm to 1,000 μm). The edges of the mesh were aligned and overlapped. A continuous, micro-seam weld was then created along the joint line using laser welding technology. This laser-welded tube ensures a seamless joint. Upon expansion, the stent provides a stable conduit, allowing blood to flow through the stent lumen and its struts within the vessel.

Results and Discussion

The parameter effects and *ANOVA* analysis for undercut are shown in Tables 3 and 4. The *ANOVA* results indicate that etching time is the most significant parameter affecting undercut, followed by etchant concentration. The rate of interaction between the solute (active species in the etchant) and the solvent (substrate) increases with time. The dissolution of material along grain boundaries in the heterogeneous substrate is more pronounced over longer durations. Material removal proceeds more rapidly in the lateral direction (beneath the photoresist mask) than in the vertical direction. Consequently, undercut increases with etching time.

Table 3

Undercut parameters and their levels

Parameters	Level 1	Level 2	Level 3
Concentration (g/L)	0.0580	0.0343	0.0353
Temp. (°C)	0.0306	0.0424	0.0545
Time (min)	0.0272	0.0419	0.0584

Table 4

***ANOVA* table for undercut**

Factor	*D.F.*	*S.S.*	*M.S.*	*F*	*P*
Concentration (g/L)	2	0.00107	0.00053	1.14	0.467
Temp. (°C)	2	0.00145	0.00072	1.54	0.394
Time (min)	2	0.00084	0.00042	0.90	0.526
Error	2	0.00094	0.00047		
Total	8	0.00432			

The parameter effects and *ANOVA* analysis for *MRR* are presented in Tables 5 and 6. It is observed that etchant concentration is the most significant process parameter for *MRR*, followed by etching time [18]. The density of active ferric ions increases with higher etchant concentration. A greater quantity of these ions accelerates the reaction rate. As the frequency of collisions between active ions and the metallic substrate rises, the diffusion of active atoms is enhanced. This directly influences the *MRR* as a key response characteristic. Therefore, as the concentration gradient of the etchant increases, the *MRR* exhibits an upward trend.

Table 5

MRR parameters and their levels

Parameters	Level 1	Level 2	Level 3
Concentration (g/L)	2.368	4.712	4.716
Temp. (°C)	4.310	4.673	5.093
Time (min)	3.293	5.102	5.681

Table 6

ANOVA table for MRR

Factor	D.F.	S.S.	M.S.	F	P
Concentration (g/L)	2	9.3246	4.6623	53.53	0.018
Temp. (°C)	2	0.9144	0.4572	5.25	0.160
Time (min)	2	0.0098	0.0049	0.06	0.947
Error	2	0.1742	0.0871		
Total	8	10.423			

The parameter effects and *ANOVA* analysis for the etch factor are shown in Tables 7 and 8. Etchant concentration is identified as the most significant parameter for the etch factor. The etch factor is defined as the ratio of depth of cut to undercut. Since the increase in depth of cut with rising concentration is more pronounced than the corresponding increase in undercut, the etch factor shows an increasing trend with higher etchant concentration. Based on the *ANOVA* analysis, the optimum machining parameters for *SS316L* using ferric chloride etchant are determined as: etching time of 2 minutes, etchant temperature of 50 °C, and etchant concentration of 500 g/L.

Table 7

Etch factor parameters and their levels

Parameters	Level 1	Level 2	Level 3
Concentration (g/L)	1.0737	1.9042	2.0786
Temp. (°C)	1.9471	1.6117	1.4977
Time (min)	2.0138	1.5853	1.4574

Table 8

ANOVA table for etch factor

Factor	D.F.	S.S.	M.S.	F	P
Concentration (g/L)	2	1.7300	0.8650	2.79	0.264
Temp. (°C)	2	0.5094	0.2547	0.82	0.549
Time (min)	2	0.3273	0.1636	0.53	0.655
Error	2	0.6208	0.4908		
Total	8	3.1875			

Regression and artificial neural network (*ANN*) models were developed to predict process performance. The percentage error between experimental and predicted values was found to be satisfactory for all response parameters (as shown in Fig. 5) [19]. The error between experimental and predicted results was less than 15 % (as illustrated in Figs. 6, 7, and 8). The maximum error values were 1.781, 0.001, and 0.170, and the minimum error values were 0 for *MRR*, undercut (*Uc*), and etch factor, respectively (as detailed in Tables 9, 10, and 11).
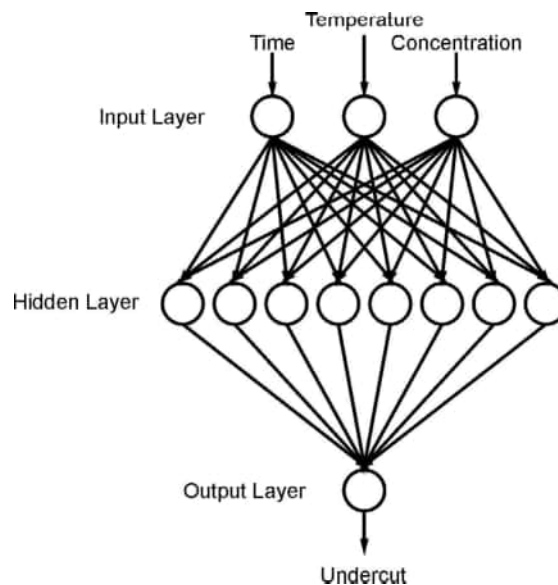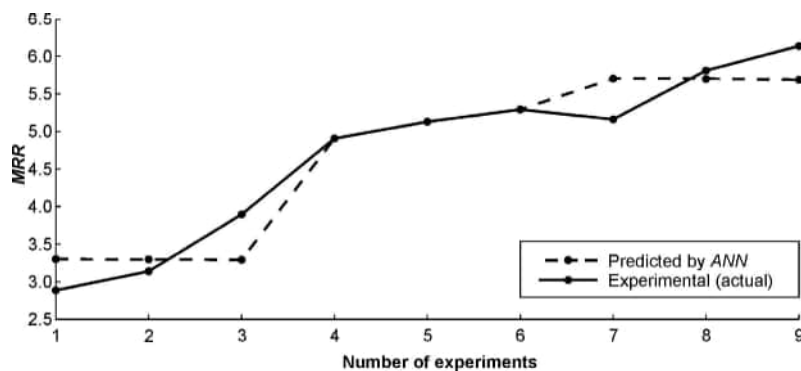

Fig. 5. *ANN* Architecture for undercut

Fig. 6. Implementation of the *ANN* model for prediction
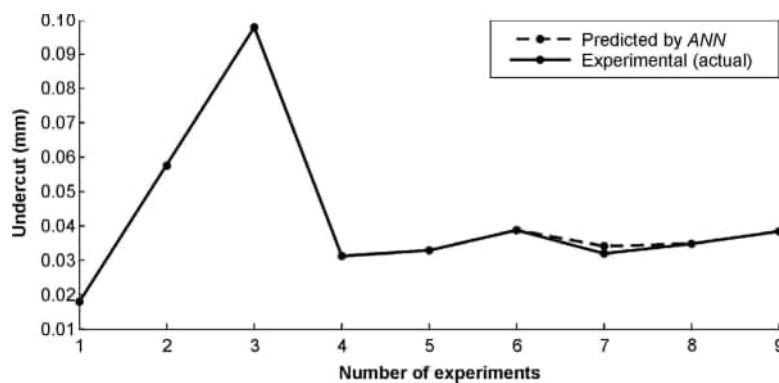of *MRR* (mm³/min)

Fig. 7. Implementation of the *ANN* model for prediction
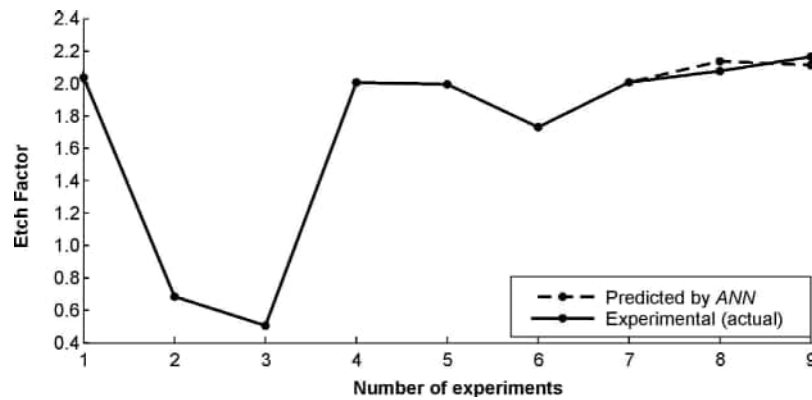of undercut (***Uc***) (mm)

Fig. 8. Implementation of the *ANN* model for prediction
of Etch Factor (*EF*)

Table 9

Comparison of actual and predicted *MRR* values and calculated errors

Actual (*MRR*)	2.88	3.12	3.88	4.91	5.12	5.28	5.15	5.78	6.12
Predicted (*MRR*)	3.29	3.29	3.29	4.91	5.12	5.28	5.68	5.68	5.68
Error	1.25	0.52	1.781	0	0	0	0.93	0.17	0.76

Table 10

Comparison of actual and predicted undercut (*Uc*) values and calculated errors

Actual (*Uc*)	0.01	0.05	0.09	0.03	0.03	0.03	0.03	0.03	0.03
Predicted (*Uc*)	0.01	0.05	0.09	0.03	0.03	0.03	0.031	0.03	0.03
Error	0	0	0	0	0	0	0.001	0.001	0

Table 11

Comparison of actual and predicted etch factor (*EF*) values and calculated errors

Actual (*EF*)	2.033	0.684	0.503	2.003	1.986	1.722	2.003	2.098	2.146
Predicted (*EF*)	2.033	0.684	0.503	2.003	1.986	1.722	2.003	2.122	2.146
Error	0	0	0	0	0	0	0	0.170	0

A stent in tubular form was manufactured in the laboratory using photochemical machining. Various measurements were performed using scanning electron microscopy (*SEM*)**,** and the stent observations were recorded. A stent strut is a part of the stent designed to open a narrowed or occluded artery. The strut's shape and thickness are crucial for the stent's durability and influence the risk of restenosis. It was observed that the etching process produces a mesh with vertical and horizontal gaps, which is capable of withstanding blood pressure and providing a conduit for blood flow. The undercut generated during etching contributes to weight reduction without compromising the stent's strength. Vessel wall injury is also reduced due to the decreased contact area between the stent and the vein wall. Stent expansion is maintained owing to the work hardening/strain hardening effect induced during the transformation of the flat specimen into a tube. The flat ends provide a suitable surface for laser seam welding.

In Fig. 9, the stent mesh structure – comprising vertical and horizontal struts and the gaps between them – is observed under scanning electron microscopy. Measurements indicate a maximum horizontal strut width of 994.1 μm and a vertical mesh gap of 361.1 μm. The etched specimen shown in Fig. 9 was subsequently formed into a tubular shape.

As shown in Fig. 10, the dimensions of a reference (commercial) stent are measured as 340 μm and 1.1 mm. The dimensions of the *PCM*-manufactured stent closely resemble those of stents produced by conventional methods. Fig. 11 (*SEM* image) reveals that in the tubular (deployed) form, the stent struts align accurately with each other, ensuring unimpeded blood flow through all sections of the stent. The strut width measured across the side edge is 352.8 μm. Due to symmetric double-sided exposure and etching, the mesh pattern is consistent and matches perfectly along the stent's edge. Fig. 12 illustrates the elliptical cross-section of a vertical stent strut, with a major (vertical) axis dimension of 1.137 mm and a minor (horizontal) axis dimension of 318 μm. For comparison, the dimensions of a standard stent strut are provided in Fig. 10.
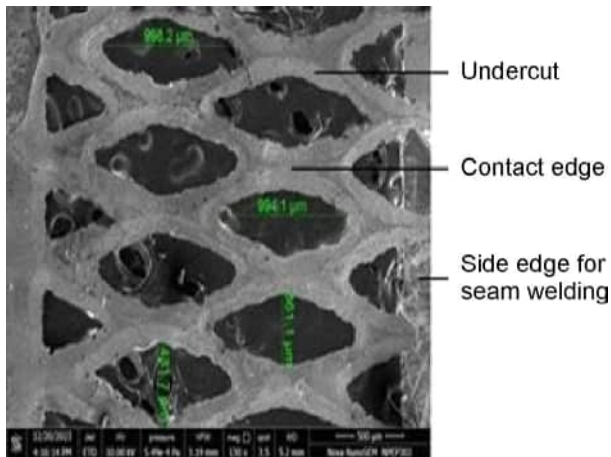
Fig. 9. Observation of vertical and longitudinal stent struts in tubular mesh
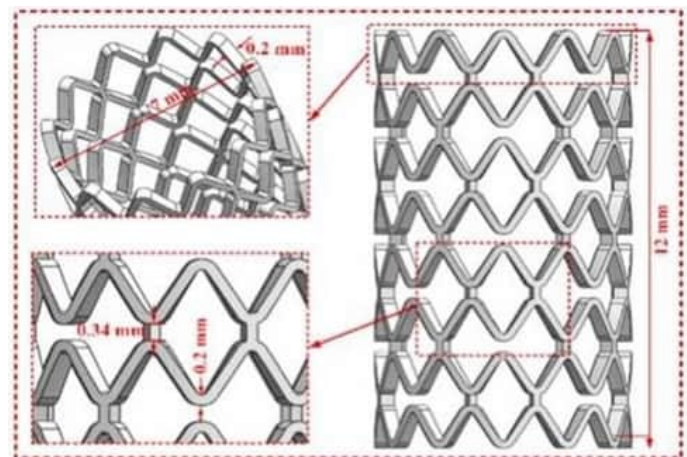
Fig. 10. Standard-sized stent used in vein blockages. (Courtesy of [20])
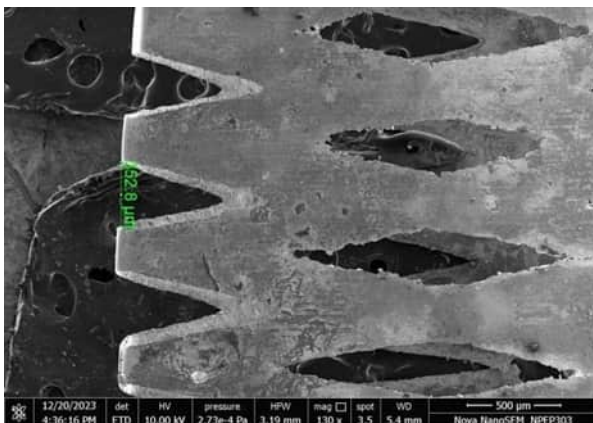
Fig. 11. Observation of longitudinal stent strut
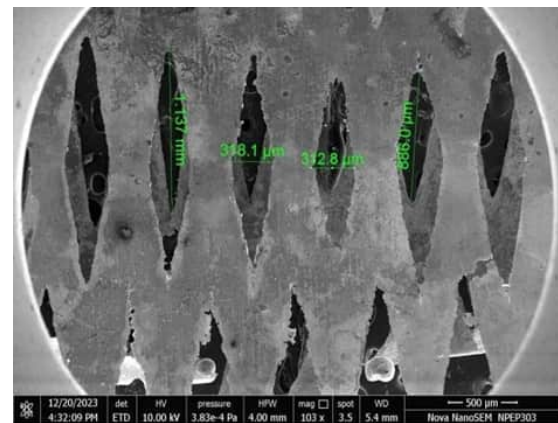
Fig. 12. Observation of vertical stent strut

Conclusion

The key finding of this study is that photochemical machining (*PCM*) can be successfully applied to biomedical applications, such as stent manufacturing. The optimal set of machining parameters for *SS316L* steel was determined to be an etchant temperature of 50 °C, an etchant concentration of 500 g/L, and an etching time of 2 minutes. Through precise phototool fabrication, *UV* exposure, and controlled etching on biocompatible material, a tubular mesh structure (stent struts) was produced, designed to fit within arterial blood vessels to restore or maintain blood flow through blocked veins. The authors achieved a stent strut width of up to 994.1 μm in the vertical direction and a mesh gap of 361.1 μm in the horizontal direction.

For future work, formal medical certification of the stent will be required, adhering to stringent manufacturing and quality control standards. This approach holds significant promise for patients, as the *PCM*

process offers high cost-effectiveness in mass production. Consequently, stent costs could be substantially reduced, improving affordability and accessibility. The application of *PCM* in stent development marks a significant milestone in the advancement of non-traditional machining techniques for medical device fabrication.

References

1. Zamani M.M.A., Etamadi E., Bodaghi M., Hu H. Conceptual design and analysis of novel hybrid auxetic stents with superior expansion. *Mechanics of Materials*, 2023, vol. 187, pp. 1–16. DOI: 10.1016/j.mechmat.2023.104813.

2. Čanić S., Grubišić L., Ljulj M., Maretić M., Tambača J. Geometric optimization of vascular stents modeled as networks of 1D rods. *Journal of Computational Physics*, 2023, vol. 494, pp. 1–32. DOI: 10.1016/j.jcp.2023.112497.

3. Ebrahimi M.S., Noruzi M., Hamzehei R., Etemadi E., Hashemi R. Revolutionary auxetic intravascular medical stents for angioplasty applications. *Materials & Design*, 2023, vol. 235, pp. 1–17. DOI: 10.1016/j.matdes.2023.112393.

4. Pang S., Zhao W., Qiu T., Liu W., Jiao L., Wang X. Study on surface quality and mechanical properties of micro-milling WE43 magnesium alloy cardiovascular stent. *Journal of Manufacturing Processes*, 2023, vol. 101, pp. 1080–1090. DOI: 10.1016/j.jmapro.2023.06.061.

5. Li Y., Shi Y., Lu Y., Li X., Zhou J., Zadpoor A.A., Wang L. Additive manufacturing of vascular stents. *Acta Biomaterialia*, 2023, vol. 167, pp. 16–37. DOI: 10.1016/j.actbio.2023.06.014.

6. Wang Y., Yan C., Mei D., Li Y., Sheng K., Wang J., Wang L., Zhu S., Guan S. Optimized structure design of asymmetrical Mg alloy cerebrovascular stent with high flexibility. *Smart Materials in Manufacturing*, 2024, vol. 2, p. 100040. DOI: 10.1016/j.smmf.2023.100040.

7. Khalaj R., Tabriz A.G., Junqueira L.A., Okereke M.I., Douroumis D. 3D printed stents using fused deposition method. *Journal of Drug Delivery Science and Technology*, 2024, vol. 97, p. 105724. DOI: 10.1016/j.jddst.2024.105724.

8. Demir A.G., Previtali B. Lasers in the manufacturing of cardiovascular metallic stents: Subtractive and additive processes with a digital tool. *Procedia Computer Science*, 2023, vol. 217, pp. 604–613. DOI: 10.1016/j.procs.2022.12.256.

9. Guerra A.J., San J., Ciurana J. Fabrication of PCL/PLA composite tube for stent manufacturing. *Procedia CIRP*, 2017, vol. 65, pp. 231–235. DOI: 10.1016/j.procir.2017.03.339.

10. Chanmanwar R.M., Balasubramaniam R., Wankhade L.N. Application of manufacturing of microfluidic devices: review. *International Journal of Modern Engineering Research*, 2013, vol. 3 (2), pp. 849–856.

11. Çakır O. Etchants for chemical machining of aluminium and its alloys. *Acta Physica Polonica A*, 2019, vol. 135 (4), pp. 586–587. DOI: 10.12693/APhysPolA.135.586.

12. Tehrani F.A., Imanian E. A new etchant for the chemical machining of St304. *Journal of Materials Processing Technology*, 2004, vol. 149 (1–3), pp. 404–408. DOI: 10.1016/j.jmatprotec.2004.02.055.

13. Allen D., Almond H. Characterisation of aqueous ferric chloride etchants used in industrial photochemical machining. *Journal of Materials Processing Technology*, 2004, vol. 149 (1–3), pp. 238–245. DOI: 10.1016/j.jmatprotec.2004.02.044.

14. Cakir O. Chemical etching of aluminum. *Journal of Materials Processing Technology*, 2008, vol. 199 (1–3), pp. 337–340. DOI: 10.1016/j.jmatprotec.2007.08.012.

15. Agrawal D., Kamble D. Optimization of photochemical machining process parameters for manufacturing microfluidic channel. *Materials and Manufacturing Processes*, 2019, vol. 34 (1), pp. 1–7. DOI: 10.1080/10426914.2018.1512115.

16. Wangikar S.S., Patowari P.K., Misra R.D. Effect of process parameters and optimization for photochemical machining of brass and German silver. *Materials and Manufacturing Processes*, 2016, vol. 32 (15), pp. 1747–1755. DOI: 10.1080/10426914.2016.1244848.

17. Jadhav P.K., Sahai R.S.N., Solanke S., Gawande S.H. Multi-objective optimization of EN19 steel milling parameters using Taguchi, ANOVA, and TOPSIS approach. *Journal of Alloys and Metallurgical Systems*, 2024, vol. 7, p. 100102. DOI: 10.1016/j.jalmes.2024.100102.

18. Jatti V.S., Singarajan V., Saiyathibrahim A., Jatti V.S., Krishnan M.R., Jatti S.V. Enhancement of EDM performance for NiTi, NiCu, and BeCu alloys using a multi-criteria approach based on utility function. *Obrabotka metallov (tekhnologiya, oborudovanie, instrumenty) = Metal Working and Material Science*, 2025, vol. 27, no. 2, pp. 57–88. DOI: 10.17212/1994-6309-2025-27.2-57-88. (In Russian).

19. Anita J., Das R., Pradhan M.K. Multi-objective optimization of electrical discharge machining processes using artificial neural network. *Jordan Journal of Mechanical and Industrial Engineering*, 2016, vol. 10 (1), pp. 11–18.

20. Ji H., Zhang W., Li Z., Chai M., Wang Y. Experimental study of NiTi alloy cardiovascular stent formed via SLM. *Materials Today Communications*, 2024, vol. 41, p. 110426. DOI: 10.1016/j.mtcomm.2024.110426.

Conflicts of Interest

The authors declare no conflict of interest.

Obrabotka metallov –
Metal Working and Material Science

Journal homepage: http://journals.nstu.ru/obrabotka_metallov

Prediction of tool wear intensity during machining of titanium nickelide TN-1

Anton Kisel' [1, 2, a, *], *Nikolaj Bobrovskij* [1, 3, b], *Dmitrij Podashev* [2, c], *Pavel Tselikov* [2, d], *Renat Kamenov* [1, 3, e]

[1] National Research University of Electronic Technology (MIET), 1 Shokin Square, Moscow, Zelenograd, 124498, Russian Federation

[2] Kaliningrad State Technical University, 1 Sovetsky Prospekt, Kaliningrad, 236022, Russian Federation

[3] Togliatti State University, 14 Belorusskaya st., Togliatti, 445020, Russian Federation

[a] https://orcid.org/0000-0002-8014-0550, ✉ kisel1988@mail.ru; [b] https://orcid.org/0000-0002-9299-2822, ✉ bobrnm@yandex.ru;
[c] https://orcid.org/0000-0001-9112-9253, ✉ dbp90@mail.ru; [d] https://orcid.org/0009-0008-6040-0600, ✉ patersort@list.ru;
[e] https://orcid.org/0000-0001-9181-5704, ✉ renatkamenov@mail.ru

ARTICLE INFO

ABSTRACT

Introduction. One of the crucial criteria for evaluating the effectiveness of the chosen strategy for machining blanks is the tool wear intensity. Reducing the intensity of tool wear leads to a reduction in production costs related to cutting tool expenditures and an improvement in overall productivity. **The purpose of this** work is to reduce tool wear intensity during the machining of a blank manufactured from the shape memory alloy titanium nickelide *TN-1*. **Methods.** As part of this research, a complete three-factor turning experiment was conducted on the alloy blank to determine the cutting insert wear intensity over a wide range of cutting conditions. During the tests, the geometric parameters of the resulting chips, specifically thickness and width, were measured. By constructing graphs representing the dependencies of the chip parameters, approximating these dependencies, and assessing the reliability of each approximation, a key parameter was identified for developing a methodology to predict tool wear intensity. **Results and discussion.** The study demonstrates that for predicting the cutting insert wear intensity when turning a titanium nickelide *TN-1* blank, it is advisable to use the dependency on the resulting chip thickness. The established mathematical dependency is described by a system of equations that allows for the determination of the cutting insert wear intensity and the calculation error. The probability of accurately predicting the true value of tool wear intensity within the specified range is at least 87.5% at a 95% confidence level, which indicates sufficient practical accuracy. The essence of the methodology developed within this study for predicting the cutting insert wear magnitude lies in performing a test cut to obtain a chip whose thickness is then used to calculate the wear intensity magnitude and the most probable absolute error based on the established dependencies. Additionally, the study establishes that the wear intensity dependency exhibits a minimum point. This circumstance allowed for the establishment of the minimal possible wear intensity during *TN-1* alloy machining, as well as the associated calculation error: $\delta_{Vmin} = (0.432 \pm 0.096) \cdot 10^{-3}$ mm^{-2}. For an optimal chip thickness of $a = 0.34$ mm, the closest tested mode yielding a comparable wear intensity of $0.475 \cdot 10^{-3}$ mm^{-2} is: cutting speed 5 m/min, feed rate 0.2 mm/rev, depth of cut 0.3 mm. The chip thickness for this mode was 0.4 mm.

Introduction

The intensity of tool wear during manufacturing processes in mechanical engineering plays a crucial role in evaluating the efficiency of selected machining strategies. Low wear intensity indicates that the machining conditions are rationally chosen in terms of tool life. A decrease in tool wear intensity reduces production costs related to tool expenses and increases overall productivity [1].

Therefore, manufacturers strive to minimize tool wear through various methods:

– using rational cutting parameters [2, 3, 4];

– applying tools made from wear-resistant materials with optimized geometry and coatings [2, 5–8];

– lowering the temperature in the cutting zone [9, 10–13];

– physical and chemical treatment of tools or workpieces to alter their properties prior to or during machining [14–18].

However, tool wear intensity depends on numerous factors, making it variable even under constant machining conditions. Despite its unpredictability, research efforts have been directed towards forecasting it. Possible approaches include:

– empirical relationships derived from preliminary experimental studies [20–22];

– artificial intelligence and machine learning applications [23, 24];

– experimental identification of dependencies between controlled factors and wear intensity for specific machining scenarios [25–27].

The first approach suffers from low accuracy due to random influences such as material composition, coating quality, equipment performance, and coolant characteristics. The second option is costly. Thus, the third approach was adopted in this study as the most reasonable.

As an example of the processed material, titanium nickelide (nitinol) grade **TN-1** was selected because of its limited research coverage and importance in industries requiring shape memory alloys, particularly aerospace. Dry turning was used to eliminate external influences and align with industrial practices.

In view of the above considerations, ***the purpose of this study*** was to reduce tool wear intensity during the machining of titanium nickelide *TN-1*. To achieve this goal, the several following ***tasks*** were addressed:

– Conduct experimental investigations of tool wear intensity under different machining conditions.

– Select a parameter for analyzing process behavior and identifying its correlation with tool wear intensity.

– Establish a dependency between tool wear intensity and the chosen parameter.

– Develop a methodology for predicting tool wear intensity and provide recommendations for selecting efficient machining settings.

Methods

The chemical composition and properties of the material used for the research are presented in Tables 1 and 2 respectively [28–30].

An example of an aerospace product where the *TN-1* alloy is applied is a single-use valve shown in Fig. 1 [31]. The operating principle of this valve is based on restoring the original shape of a pre-deformed (compressed) pusher 5 when heated, causing the tailpiece 8 to rupture at its groove. As a result, the working medium (gas or liquid) flows through the resulting gap towards the nipple 4.

From Fig. 1, it can be seen that the pushers 5 are bodies of rotation. Therefore, their manufacture involves turning operations.

Table 1

Chemical composition of the *TN-1* alloy, under *TU 1-809-394-84* (% by weight)

Ni	Ti	Impurities (not more than)							Sum of other impurities (not more than)
		C	Co	Fe	Si	N	O	H	
53.5-56.5	Bal.	0.1	0.2	0.3	0.15	0.05	0.2	0.013	0.3

Table 2

Mechanical properties of the *TN-1* alloy

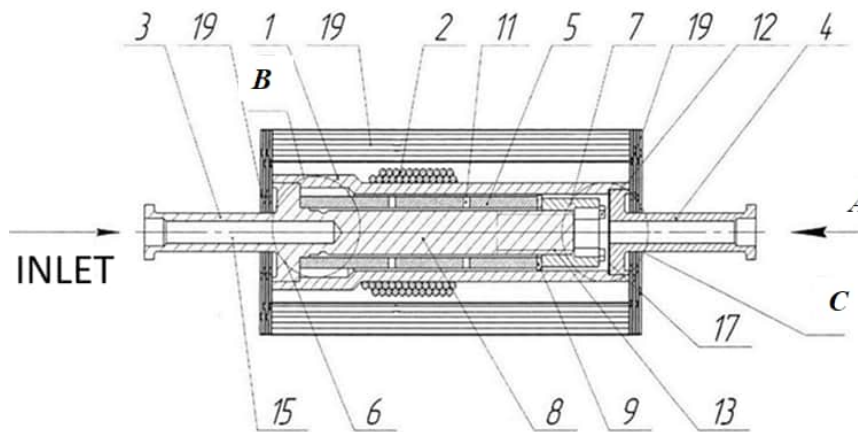| ρ, kg/m³	σ_v, MPa	$\sigma_{0.2}$, MPa	δ, %	E, GPa	HV	T_{mel}, °C	λ, W/(m·K)	c, J/(kg·K)
6,450–6,500	588	294	>10	33	331±42	1,250-1,310	8.6-18	456

Fig. 1. Single-acting valve

The evaluation of wear intensity was carried out on a *UTS6* bench-type lathe with a computerized *CNC* system. Turning was chosen as the most common method for manufacturing products from the *TN-1* alloy. A cutting tool with indexable cemented carbide inserts *CCMT09T308-EM* with a multilayer *PVD* coating of total thickness of 4 μm based on *AlTiN* (aluminum titanium nitride) (*ZCC Cutting Tools*, China) was used. The substrate material of these inserts is an ultrafine-grained cemented carbide *YBG205* consisting of cobalt, tungsten carbides, and titanium carbides. The percentage content of each component is a trade secret of the manufacturer. These cutting inserts are intended for machining the following groups of materials up to 55 *HRC* hardness: carbon steels, alloy steels, corrosion-resistant steels, titanium alloys, and heat-resistant alloys.

The geometric parameters of the tool were as follows: $\gamma = 0°$, $\alpha = 7°$, $\varphi = 90°$, $\varepsilon = 80°$, $r = 0.4$ mm. The diameter of the workpiece was 10 mm.

Cutting conditions during testing were selected based on those commonly employed in finishing and semi-finishing operations in production, specifically:
– cutting speed: from 5 to 30 m/min;
– feed rate: from 0.03 to 0.2 mm/rev;
– depth of cut: from 0.1 to 0.3 mm.

It should be noted that since determining the direct relationship between cutting parameter settings and the wear intensity of the insert was not part of the study objectives, it was decided to limit the number of experiments by using only the extreme levels of factor variation. However, different combinations of selected factors provided varying cutting conditions, leading to different values of the characteristic parameter describing the process. This allowed for constructing a graph showing the dependence of tool wear intensity on the chosen parameter.

Thus, a full three-factor experiment was conducted. During the tests, the controlled parameter was the wear of the cutting insert on the rear face, which was measured using a calibrated digital microscope. The limiting value of wear was set at 0.3 mm, corresponding to the average criterion for wear under finishing and semi-finishing conditions. Since the adopted limiting wear value significantly exceeds the thickness of the coating on the cutting insert, durability assessment was performed for the entire tool assembly without considering the influence of the coating layer. Subsequently, the results obtained were used to determine the wear intensity δ_V of the cutting insert relative to the volume of material removed from the workpiece:

$$\delta_V = \frac{h_\mathrm{r}}{V_{rem}},\qquad(1)$$

where h_r is the tool wear on the rear face, mm; V_{rem} is the volume of removed stock material, mm^3.

However, conducting durability tests is labor-intensive and resource-consuming, so it is reasonable to derive a mathematical dependency that allows predicting wear intensity based on a parameter that is easily measurable during processing and does not require expensive equipment for its measurement.

One such factor characterizing the cutting process is the generated chip. Its main parameters – thickness (**a**) or width (**b**) – in this study were measured using a calibrated digital microscope.

During the investigations, a specific machining mode was established. After completing a tool pass, the cutting insert was removed from the tool holder, and the wear on the rear face was measured. For the chip produced, its thickness and width were also measured. The recorded values were entered into a table, after which the insert was reinstalled into the holder, and another pass was executed. Testing continued until the maximum permissible wear level was reached, after which another machining mode was set.

To enhance the reliability of the experimental findings, each test was repeated five times, followed by calculating the arithmetic mean values of wear intensity and chip parameters, which were then recorded in the table.

Results and Discussion

The test results, including values of insert wear intensity and measurements of chip thickness (*a*, mm) and width (*b*, mm), are summarized in Table 3.

Based on provided data, graphs representing the dependencies $\delta_v = f(a)$ and $\delta_v = f(b)$ were constructed, as depicted in Fig. 2.

Table 3

Test results

Experiment number	V, m/min	S, mm/rev	t, mm	δ_V, 10^{-3} mm^{-2}	a, mm	b, mm
1	5	0.03	0.1	0.594	0.260	0.685
2	30	0.03	0.1	3.271	0.092	0.541
3	5	0.2	0.1	1.435	0.167	0.514
4	30	0.2	0.1	3.723	0.129	0.455
5	5	0.03	0.3	1.45	0.471	0.892
6	30	0.03	0.3	3.444	0.111	0.628
7	5	0.2	0.3	0.475	0.400	0.863
8	30	0.2	0.3	1.377	0.237	0.879
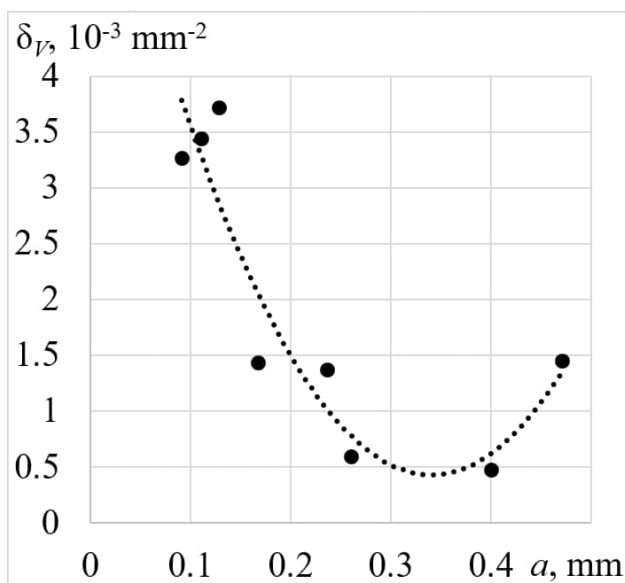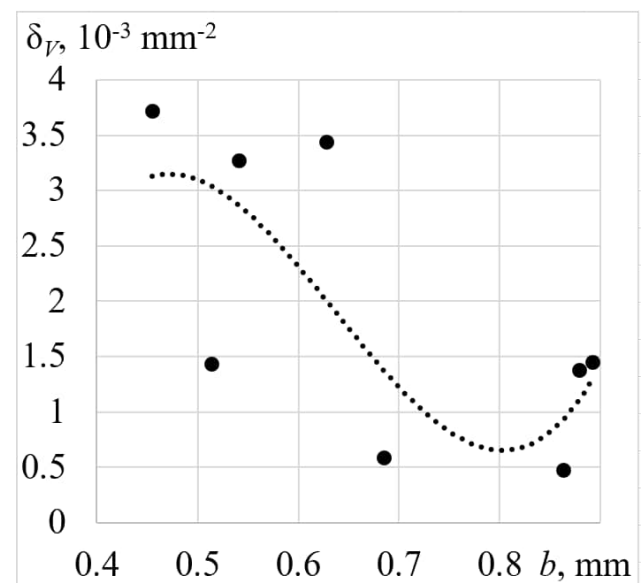
Fig. 2. Dependence graphs $\delta_V = f(a)$ (*a*) and $\delta_V = f(b)$ (*b*)

Evaluation of these dependencies using *MS Excel* tools yielded the coefficient of determination (R^2), which amounted to:
– for the graph $\delta_v = f(a) - R^2 = 0.8653$;
– for the graph $\delta_v = f(b) - R^2 = 0.4943$.

Therefore, for forecasting wear intensity, it is advisable to use the first dependency – $\delta_v = f(a)$ – since it provides greater calculation accuracy. The established dependency is described by the empirical formula:

$$\delta_v = 54.0785a^2 - 36.8231a + 6.7004. \tag{2}$$

To estimate the error, previously measured chip thicknesses were substituted into Equation (2); wear intensity was calculated, and the relative error ε compared to experimental data was determined. The obtained data are presented in Table 4.

Table 4

The results of calculations of the wear intensity

Experiment number	a, mm	δ_V(experimental), 10^{-3} mm^{-2}	δ_V(calculated), 10^{-3} mm^{-2}	ε, %
1	0.260	0.594	0.782	31.67
2	0.092	3.271	3.784	15.68
3	0.167	1.435	2.059	43.49
4	0.129	3.723	2.862	−23.14
5	0.471	1.45	1.354	−6.65
6	0.111	3.444	3.292	−4.42
7	0.400	0.475	0.621	30.63
8	0.237	1.377	1.016	−26.18

Evaluation of the calculation results indicates that determining specific wear intensity values using the derived dependency yields significant errors ranging from 4.42 to 43.49 %. This discrepancy arises from the relatively small dimensions of the measured chips, low values of wear intensity, and heterogeneity of both tool and workpiece materials, influencing their properties. Consequently, it is essential not only to establish the dependency of wear intensity but also to assess the error associated with its calculation using the derived formula. To achieve this objective, absolute errors $\Delta\delta_V$ were computed, and a graph illustrating their dependency on the thickness of the formed chips was plotted, as displayed in Fig. 3. Points exhibiting significant deviations from the constructed dependency were discarded and excluded from further analysis as erroneous outliers.

Fig. 3. Dependency graph $\Delta\delta_V = f(a)$

The evaluation of the obtained dependence showed that its coefficient of determination is $R^2 = 0.9697$. The graph presented in the figure is described by the formula:

$$\Delta\delta_V = 11.179a^2 - 8.7612a + 1.7833. \tag{3}$$

Thus, the final dependency for predicting tool wear intensity when machining a titanium nickelide *TN-1* workpiece can be described by the following system of equations:

$$\begin{cases} \delta_V = 54.0785a^2 - 36.8231a + 6.7004, \\ \Delta\delta_V = 11.179a^2 - 8.7612a + 1.7833. \end{cases} \tag{4}$$

Graphically, the established system of equations can be represented as curves bounding the scatter of values of cutting insert wear intensity during turning of a titanium nickelide **TN-1** workpiece (Fig. 4).
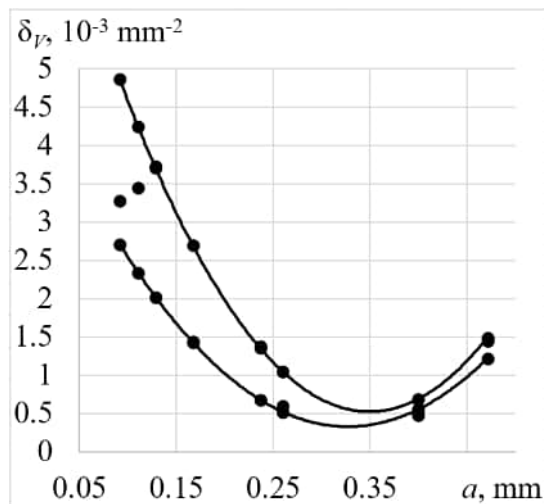
Fig. 4. Variation in tool wear intensity during turning of titanium nickelide *TN-1*

Evaluation of this figure through comparison with experimental results has shown that the probability of an actual value of tool wear intensity falling within the given area is no less than 87.5% at a confidence level of 95 %. This indicates sufficient accuracy for practical use.

Furthermore, it **is** evident that the wear intensity dependence exhibits a minimum point. This suggests the possibility of determining an optimal or range of optimal values for wear intensity if the maximum permissible value is known.

To determine the optimal wear intensity value, Equation (2) was differentiated with respect to chip thickness *a* and set equal to zero. Solving the resulting equation allowed for establishing the minimal wear intensity value for the case under consideration, along with the calculation error according to expression (3):

$$\delta_{V\min} = (0.432 \pm 0.096) \cdot 10^{-3} \text{ mm}^{-2}.$$

The optimal chip thickness value is *a* = 0.34 mm.

Among the tested modes, the one providing comparable wear intensity of the cutting insert (0.475×10^{-3} mm^{-2}) was found to be: cutting speed of 5 m/min, feed rate of 0.2 mm/rev, depth of cut of 0.3 mm, leading to a chip thickness of 0.4 mm.

In summary, the methodology for forecasting tool wear intensity during machining of titanium nickelide *TN-1* or similar alloys is as follows. Prediction involves performing a trial pass of the tool to obtain chips whose thickness will allow calculating both the magnitude of wear intensity and the most probable absolute error using the dependencies provided above (Equation 4). Performing such operations significantly reduces testing time and expenses on cutting tools.

It should also be noted that the identified dependencies of tool wear intensity under dry machining conditions without the application of coolant-lubricants correlate well with modern trends toward environmentally safe mechanical processing technologies (dry machining, minimum quantity lubrication – *MQL*). These findings may not only assist in selecting rational cutting parameters but also contribute to forming the methodological foundations for modeling surface plastic deformation processes, particularly burnishing. This opens up possibilities for integrating the proposed approach into tasks related to the prediction of surface layer properties, including roughness and wear resistance.

Conclusions

The conducted research achieved the following results:

– Experimental determination of tool wear intensity values for various turning regimes of titanium nickelide *TN-1* workpieces;

– selection of chip thickness as the parameter characterizing the process due to its significant impact on the precision of tool wear intensity calculations;

– establishment of an empirical relationship between tool wear intensity and chip thickness. The dependence is parabolic in nature, allowing identification of the minimum point and the corresponding minimum possible tool wear intensity;

– development of a method for predicting tool wear intensity based on chip thickness when machining titanium nickelide *TN-1*. The recommended machining regime is: cutting speed of 5 m/min, feed rate of 0.2 mm per revolution, depth of cut of 0.3 mm.

These results enable extrapolation of established cutting regimes to other types of cutting machining methods applicable to titanium nickelide and its analogs, subject to certain assumptions. Additionally, the

morphology and characteristics of chips serve as diagnostic indicators reflecting the mechanical properties of the material, such as strength and ductility. The established correlations suggest the potential utilization of these parameters for predictive analysis in surface plastic deformation (*SPD*) processes. Consequently, they could act as criteria for choosing rational *SPD* regimes aimed at achieving desired surface-layer properties. Considering also the influence of the surface condition after machining on subsequent *SPD* operations [32], the presented outcomes might be integrated into reverse-modeling systems focused on geometrical product specification (*GPS*) characteristics optimization during burnishing. Such integration ensures continuity and systematicity in ongoing investigations.

References

1. Zhang G., Wang J. Tool wear mechanism and suppression in machining ferrous materials. *Material-oriented cutting processes in precision machining. Springer Tracts in Mechanical Engineering*. Singapore, Springer, 2025, pp. 109–145. DOI: 10.1007/978-981-96-2504-8_5.

2. Pham H.T., Tchigirinskiy Yu.L., Polyanchikov Yu.N. Metody snizheniya intensivnosti iznashivaniya tverdosplavnogo instrumenta [Methods of intensity decreasing of hard alloy tool wear]. *Fundamental'nye issledovaniya = Fundamental Research*, 2017, no. 12-1, pp. 132–137. (In Russian).

3. Unyanin A.N., Finageev P.R. Issledovanie effektivnosti metodiki korrektsii rezhima protsessa mekhanicheskoi obrabotki s izmenyayushchimisya vo vremeni parametrami v usloviyakh neopredelennosti tekhnologicheskoi informatsii [Study of the technique performance for the correction of the mode of the machining process with time-varying parameters in the conditions of technological information uncertainty]. *Naukoemkie tekhnologii v mashinostroenii = Science Intensive Technologies in Mechanical Engineering*, 2023, no. 12 (150), pp. 23–29. DOI: 10.30987/2223-4608-2023-23-29.

4. Kusyi Y., Kuk A., Hryniv N., Danylo Y. Optimization of cutting modes during machining of difficult-to-cut materials. *New Technologies, Development and Application VIII (NT 2025). Lecture Notes in Networks and Systems*. Cham, Switzerland, Springer, 2025, vol. 1482, pp. 451–458. DOI: 10.1007/978-3-031-95194-7_46.

5. Chigirinskii Yu.L., Pham H.T. Osobennosti mekhanicheskoi obrabotki dupleksnykh korrozionnostoikikh stalei [Features of mechanical processing of duplex corrosion-resistant steels]. *Izvestiya Volgogradskogo gosudarstvennogo tekhnicheskogo universiteta = Izvestia Volgograd State Technical University*, 2016, no. 5 (184), pp. 51–54.

6. Gadalov V.N., Abashkin R.E., Boldyrev Yu.V., Balabaeva E.F., Lytkin A.I. Cutting-tool wear and hardening of high-speed steel by local electrospark coating application. *Russian Engineering Research*, 2009, vol. 29 (4), pp. 419–422. DOI: 10.3103/S1068798X09040200.

7. Fominov E.V., Aliev M.M., Torop Yu.A., Mironenko A.E., Fomenko A.V., Marchenko A.A. Vliyanie mnogosloinykh pokrytii na osnove tsirkoniya i titana na iznosostoikost' tverdosplavnogo instrumenta pri tochenii nerzhaveyushchei stali [Effect of multilayer coatings based on zirconium and titanium on wear resistance of carbide tools during turning of stainless steel]. *Uprochnyayushchie tekhnologii i pokrytiya = Strengthening Technologies and Coatings*, 2022, vol. 18, no. 11 (215), pp. 494–496. DOI: 10.36652/1813-1336-2022-18-11-494-496.

8. Babaev A.S., Kozlov V.N., Semenov A.R., Shevchuk A.S., Ovcharenko V.A. Study of the effect of microgeometry parameters of the cutting edge on cutting force, wear, and machinability during milling. *Russian Engineering Research*, 2024, vol. 44 (12), pp. 1756–1766. DOI: 10.3103/S1068798X24703271.

9. Dubrov D.Yu. Snizhenie intensivnosti razmernogo iznosa rezhushchikh instrumentov [Reducing the intensity of dimensional wear of cutting tools]. *Vestnik Evraziiskoi nauki = The Eurasian Scientific Journal*, 2018, vol. 10, no. 5, art. 73.

10. Kireinov A.V., Esov V.B. Vliyanie polusinteticheskoi SOZh s metalloorganicheskimi prisadkami na iznos tverdosplavnogo instrumenta pri tochenii korrozionnostoikoi stali 12Kh18N10T [The influence of semi-synthetic cutting fluid with organometallic additives on tool wear in turning of stainless steel 12H18N10T]. *Fundamental'nye i prikladnye problemy tekhniki i tekhnologii = Fundamental and Applied Problems of Engineering and Technology*, 2018, no. 5 (331), pp. 70–73.

11. Dos Santos R.G., De Paiva J.M.F., Torres R.D., Amorim F.L. Performance of cutting fluids with nanoparticles in the Ti5553 alloy turning process using high-speed cutting. *The International Journal of Advanced Manufacturing Technology*, 2025, vol. 136 (10), pp. 4623–4645. DOI: 10.1007/s00170-025-15126-5.

12. Nelson N., Nair A.R. The coupling of heat transfer between tool–chip–workpiece interfaces and the wear rate while applying nanofluids as cutting fluids in MQCL-assisted machining: a comprehensive review. *Journal of Thermal Analysis and Calorimetry*, 2025, vol. 150, pp. 9743–9774. DOI: 10.1007/s10973-025-14400-8.

13. Jing Ch., Zheng G., Cheng X., Cui Yu., Liu H., Zhang H. Cutting performance and machining economy of the hard cutting tools in clean cutting of hardened H13 steel. *The International Journal of Advanced Manufacturing Technology*, 2024, vol. 130 (11–12), pp. 5165–5179. DOI: 10.1007/s00170-024-13012-0.

14. Kovalevskyy S.V., Kovalevska O.S., Koshovii A.O. Vysokovol'tnyi razryad kak faktor povysheniya rezhushchikh svoistv neperetachivaemykh plastin [High-voltage discharge as a factor of increasing the cutting properties of disposable inserts]. *Obrabotka metallov (tekhnologiya, oborudovanie, instrumenty) = Metal Working and Material Science*, 2018, vol. 20, no. 3, pp. 6–17. DOI: 10.17212/1994-6309-2018-20.3-6-17. (In Russian).

15. Sin'ko A.N., Nikonova T.Yu., Yurchenko V.V., Mateshov A.K., Marchenko I.A. Matematicheskaya model' protsessa tocheniya s ispol'zovaniem vibratsionnogo vozdeistviya na rezhushchii instrument [Mathematical model of the turning process using vibration impact on the cutting tool]. *Morskie intellektual'nye tekhnologi = Marine Intellectual Technologies*, 2020, no. 2-1 (48), pp. 216–222. DOI: 10.37220/MIT.2020.48.2.045.

16. Bondarev A.A., Otenii Ya.N., Polyanchikov Yu.N., Krainev D.V. Snizhenie temperaturno-silovoi napryazhennosti protsessa rezaniya pri ispol'zovanii operezhayushchego plasticheskogo deformirovaniya [Reducing the temperature-force stress of the cutting process using advanced plastic deformation]. *Naukoemkie tekhnologii v mashinostroenii = Science Intensive Technologies in Mechanical Engineering*, 2016, no. 3 (57), pp. 40–44.

17. Ambrosimov S.K. Snizhenie sil rezaniya pri operezhayushchem plasticheskom deformirovanii metallov [Cutting force decrease at leading metal plastic deformation]. *Vestnik Bryanskogo gosudarstvennogo tekhnicheskogo universiteta = Bulletin of Bryansk State Technical University*, 2018, no. 7 (68), pp. 13–18. DOI: 10.30987/article_5 ba8a1865b1200.15607548.

18. Kupczyk M.J. The use of the addition of Cr_3C_2 in nanocrystalline sintered carbides to create a composite tool material with better operational properties. *Materials Design And Applications V. Advanced Structured Materials*. Cham, Switzerland, Springer, 2024, vol. 212, pp. 3–14. DOI: 10.1007/978-3-031-73906-4_1.

19. Khadka S., Rahman Rashid R.A., Stephens G., Papageorgiou A., Navarro-Devia J., Hägglund S., Palanisamy S. Predicting cutting tool life: models, modelling, and monitoring. *The International Journal of Advanced Manufacturing Technology*, 2025, vol. 136 (7–8), pp. 3037–3076. DOI: 10.1007/s00170-024-14961-2.

20. Thakur R., Sahu N.K., Shukla R.K. Parametric optimization of dry turning for improved machining of duplex stainless steel (DSS2205) using response surface methodology (RSM) and design of experiments (DOE). *Sadhana*, 2025, vol. 50 (1), p. 2. DOI: 10.1007/s12046-024-02649-y.

21. Vagaská A., Gombár M., Panda A. Application of mathematical programming methods in optimization of cutting conditions in machining processes. *Optimization Methods in Mathematical Modeling of Technological Processes. Mathematical Engineering*. Cham, Switzerland, Springer, 2023, pp. 95–127. DOI: 10.1007/978-3-031-35339-0_6.

22. Kolocheva V.V., Boridko N.V. Methodology for assessing the competitiveness of metal-cutting tools. *Ecological Footprint of the Modern Economy and the Ways to Reduce It. Advances in Science, Technology & Innovation*. Cham, Switzerland, Springer, 2024, pp. 251–256. DOI: 10.1007/978-3-031-49711-7_42.

23. Airao J., Gupta A., Nirala Ch.K., Hsue A.W.J. Bayesian neural networks modeling for tool wear prediction in milling Al 6061 T6 under MQL conditions. *The International Journal of Advanced Manufacturing Technology*, 2024, vol. 135 (5–6), pp. 2777–2788. DOI: 10.1007/s00170-024-14678-2.

24. Lapshin V.P., Turkin I.A., Dudinov I.O. Compilation of a set of informative features for neural network-based determination of minimum vibration of cutting tools. *Russian Engineering Research*, 2024, vol. 44 (9), pp. 1356–1362. DOI: 10.3103/S1068798X24702101.

25. Mokriskij B.Y., Morozova A.V. Controlling the parameters of the cutting technological system by the dissipative structures state. *Proceedings of the 8th International Conference on Industrial Engineering. ICIE 2022. Lecture Notes in Mechanical Engineering*. Cham, Switzerland, Springer, 2023. DOI: 10.1007/978-3-031-14125-6_91.

26. Babouri M.Kh., Ouelaa N., Djamaa M.Ch., Ouelaa Z., Chaabi L., Djebala A. Experimental Investigation of tool lifespan evolution during turning operation based on the new spectral indicator OL_{mod}. *Journal of Vibration Engineering and Technologies*, 2024, vol. 12, pp. 5455–5473. DOI: 10.1007/s42417-023-01175-1.

27. Kusyi Y., Kostiuk O., Kuk A., Attanasio A., Cocca P. Optimization of cutting modes during sustainable machining of products based on economic criteria. *Advanced Manufacturing Processes V (InterPartner 2023). Lecture Notes in Mechanical Engineering*. Cham, Switzerland, Springer, 2024, pp. 167–181. DOI: 10.1007/978-3-031-42778-7_16.

28. Volod'ko S.S. *Razrabotka tekhnologii polucheniya kompaktnykh zagotovok iz poroshkovykh intermetallidov TiNi i (Ti,Hf)Ni na osnove gidridno-kal'tsievogo sinteza*. Diss. kand. tekhn. nauk [Development of a technology for producing compact blanks from powdered intermetallic compounds TiNi and (Ti,Hf)Ni based on calcium hydride synthesis. PhD eng. sci. diss.]. Moscow, 2022. 110 p.

29. Karelin R.D. *Formirovanie struktury i funktsional'nykh svoistv nikelida titana na osnove kvazinepreryvnoi intensivnoi plasticheskoi deformatsii v tsikle R.K.U.P. i rotatsionnoi kovki*. Diss. kand. tekhn. nauk [Formation of the structure and functional properties of titanium nickelide based on quasi-continuous intense plastic deformation in the R.K.U.P. cycle and rotational forging. PhD eng. sci. diss.]. Moscow, 2021. 129 p.

30. Andronov I.N., Bogdanov N.P., Severova N.A., Tarsin A.V. Metod kolichestvennogo opisaniya zavisimosti modulya Yunga nikelida titana ot temperatury [Method of quantitative description of temperature dependence of NiTi Young's modulus]. *Izvestiya Komi nauchnogo tsentra UrO RAN = Proceedings of the Komi Science Centre Ural Branch Russian Academy of Sciences*, 2013, no. 3 (15), pp. 87–90.

31. Vertakov N.M., Grechushnikov V.A., Katashov A.V., Panfilov V.A. *Klapan odnokratnogo deistviya vysokogo davleniya* [Single-action high-pressure valve]. Patent RF, no. 2821357, 2024.

32. Makhalov M.S., Blumenstein V.Yu. The residual stress modeling in surface plastic deformation machining processes with the metal hardening effect consideration. *Solid State Phenomena*, 2022, vol. 328, pp. 27–37. DOI: 10.4028/p-z92o0e.

Conflicts of Interest

The authors declare no conflict of interest.

Obrabotka metallov –
Metal Working and Material Science

Anisotropy of properties in metal materials fabricated by wire arc additive manufacturing (WAAM)

Andrey Kirichek [1, a], Dmitry Solovyev [2, b, *], Alexander Yashin [2, c], Sergey Silantyev [2, d],
Artemy Aborkin [2, e], Maxim Novikov [1, f]

[1] Bryansk State Technical University, 7 50 Let Oktyabrya Bul., Bryansk, 241035, Russian Federation

[2] Vladimir State University named after Alexander and Nikolay Stoletovs, 87 Gorkogo str., Vladimir, 600000, Russian Federation

[a] https://orcid.org/0000-0002-3823-0501, avkbgtu@gmail.com; [b] https://orcid.org/0000-0002-4475-319X, murstin@yandex.ru;
[c] https://orcid.org/0000-0002-3186-1300, yashin2102@yandex.ru; [d] https://orcid.org/0000-0002-3524-385X, ppdsio@yandex.ru;
[e] https://orcid.org/0000-0003-4979-7164, aborkin@vlsu.ru; [f] https://orcid.org/0009-0000-7552-312X, novikovmax14@yandex.ru

ARTICLE INFO

ABSTRACT

Introduction. Additive manufacturing (*AM*) technologies, particularly wire arc additive manufacturing (*WAAM*), offer a rapid and cost-effective approach for producing complex metal components. However, *WAAM* can induce anisotropy in the resulting material's physical and mechanical properties. This anisotropy must be considered in design and application to ensure reliable performance in service. **The purpose of the work.** This study aims to quantitatively assess the anisotropy of mechanical properties in materials produced by *WAAM* to enhance the reliability of components used in critical applications. **Research methodology.** Samples were fabricated from low-carbon alloyed steel (0.08 *C*-2 *Mn*-1 *Si*), stainless steel (0.04 *C*-19 *Cr*-9 *Ni*), and aluminum alloy (97 *Al*-3 *Mg*) using the *WAAM* process. These samples were then subjected to mechanical testing to determine their tensile and impact toughness and hardness. Results were compared to those of the materials in the initial state to determine the relative anisotropy of each property. **Results and discussion.** For 0.08 *C*-2 *Mn*-1 *Si* steel, the tensile strength of *WAAM*-fabricated samples exhibited minimal variation across different orientations, indicating relatively high isotropy (relative anisotropy of 1.3 %). A relative anisotropy of 33 % was observed for elongation, 21 % for impact toughness, and 16 % for hardness. The 0.04 *C*-19 *Cr*-9 *Ni* stainless steel exhibited a relative anisotropy of 15.1 % for tensile strength, 244 % for elongation, 33 % for impact toughness, and 4% for hardness. The 97 *Al*-3 *Mg* aluminum alloy showed a significant relative anisotropy in tensile strength (83.6 %) and relative elongation (513 %) due to differences in the "vertical" direction. Impact toughness exhibited only slight variations (28 %) depending on sample orientation, while hardness can be considered isotropic. In general, hardness demonstrated the lowest relative anisotropy, while elongation exhibited the highest.

***** Corresponding author**
Solovyev Dmitry L., D.Sc. (Engineering), Professor
Vladimir State University named after Alexander and Nikolay Stoletovs,
87 Gorky str.,
600000, Vladimir, Russian Federation
Tel: +7 920 900-46-42, **e-mail:** murstin@yandex.ru

Introduction

Currently, additive technologies (*AT*) open up new possibilities for manufacturing complex metal products. Wire arc additive manufacturing (*WAAM*) combines the advantages of welding technologies and additive manufacturing. The *WAAM* method uses a standard welding arc and filler wire [1]. In the *WAAM* process, an electric arc melts the wire, which then deposits layer by layer, forming the desired part or component. The advantages of using the *WAAM* method are high deposition speed, the ability to manufacture large-sized parts, and relative cost-effectiveness [2]. However, like many AT based on layer-by-layer deposition of material, *WAAM* technology leads to the formation of anisotropy of the physical and mechanical properties of the synthesized materials [3, 4]. This is crucial for the practical application of such a technology in the creation of critical, complexly loaded components.

Anisotropy in materials obtained by the *WAAM* method is a consequence of the specific thermodynamic conditions of the process. One of these conditions is directional heat input, namely, when the arc successively melts the wire, creating local volumes of melt (weld pools) that quickly solidify. This leads to the formation of a pronounced columnar-dendritic microstructure [5], usually oriented upward from the substrate or previous layer, and radially from the center of the bead [6]. Another condition is the inherent characteristics of the layer-by-layer deposition process, which creates a layered macrostructure with boundaries between beads and layers. These boundaries can be zones with altered chemical composition, grain size, defect density, and residual stresses. Along the boundaries of beads or layers, the resulting defects (pores and lack of fusion) can have an elongated shape and a preferred orientation [7]. Also, during deposition, the synthesized material experiences complex thermal cycles, since each newly deposited layer subjects the underlying layers to multiple heating and cooling, which leads to recrystallization, grain growth, phase transformations in previously deposited layers, as well as the development of significant residual stresses due to uneven heating and cooling [8].

Studies have shown that when using *WAAM* technology for various alloys, the mechanical properties of the resulting materials, such as tensile strength and relative elongation, often depend on the manufacturing direction. As a rule, these characteristics are higher in the horizontal direction compared to the vertical one [9]; the difference varies depending on the material and can reach significant values [10–12]. However, there are technological modes that allow for relatively isotropic behavior [13]. In addition, for some alloys, such as magnesium *AZ31*, the opposite tendency is observed – the best mechanical properties are revealed in the vertical direction [14], which also indicates a pronounced anisotropy of the structure and properties of products obtained by the *WAAM* method.

The ability to direct the properties of a material in the desired direction allows us to optimize the product and enhance its operational performance.

To control the anisotropy of the synthesized material properties by the *WAAM* method, a whole range of measures is used, for example:

– selection of modes with reduced heat input [15];

– use of pulsed or *CMT* (cold metal transfer) modes to reduce the volume of the weld pool and thermal effects [16];

– application of strategies that change the deposition direction to disrupt the columnar structure [17];

– preliminary and concomitant heating of the substrate [18];

– heat treatment to relieve stress, homogenize the structure, and achieve the required set of properties [19];

– application of surface plastic deformation after (shot blasting) or during synthesis (ultrasonic treatment, rolling, impact forging, wave strain hardening) of each or several layers to refine the grain and break down the columnar structure, reduce porosity, and create compressive residual stresses on the surface [20].

The purpose of this work is to quantitatively evaluate the anisotropy of mechanical properties of materials synthesized by wire arc additive manufacturing (*WAAM*). To achieve this purpose, the following ***tasks*** were addressed during the study:

– synthesis of first-order samples from three materials commonly used in mechanical engineering, exhibiting significantly different technological and mechanical properties: low-carbon alloy steel 0.08 *C*-2 *Mn*-1 *Si*, stainless steel 0.04 *C*-19 *Cr*-9 *Ni*, and aluminum alloy 97 *Al*-3 *Mg*, using *WAAM*;

– cutting out second-order samples from the synthesized first-order samples, with specific orientations relative to the direction of both feedstock feed and *WAAM* synthesis, to assess the mechanical properties;

– characterization of the mechanical properties of the synthesized material in several directions, including tensile strength, relative elongation, impact toughness, and hardness;

– comparison of the mechanical properties of the synthesized material with those of the original material (rolled product), determination of the relative anisotropy for each property parameter, and analysis of the relationship between the level of anisotropy and the material grade, synthesis direction, and feedstock supply.

Methods

To predict the reliability and optimize the process of achieving isotropic or controlled-anisotropic properties, it is essential to study the anisotropy of the mechanical properties of materials obtained by the *WAAM* method. For this purpose, the following properties were analyzed: tensile strength, tensile relative elongation, impact toughness, and hardness of various materials with significantly different technological and mechanical properties that are commonly used in *AT*: low-carbon steels, stainless steels, and aluminum alloys. Specific samples from each category were selected for the analysis: low-carbon alloy steel 0.08 *C*-2 *Mn*-1 *Si*, stainless steel 0.04 *C*-19 *Cr*-9 *Ni*, and aluminum alloy 97 *Al*-3 *Mg*.

The concept of 'relative anisotropy' is proposed, which enables a quantitative assessment of not only the variation of properties in different directions within the material synthesized by the *WAAM* method (classical anisotropy), but also the deviation of these properties in characteristic directions from the known values reported in the reference literature for rolled products of the same material grade – the 'original material'. This approach allows for the following:

– to evaluate the influence of the *WAAM* synthesis direction and feedstock movement direction on the homogeneity of the material properties in the volume of the synthesized product and on the deviation of the material properties of the synthesized sample from the properties of rolled products of the same material grade, as well as the heterogeneity of these deviations depending on the characteristic direction within the synthesized volume;

– to identify critical directions where the deviation of properties from the original material is the most significant;

– to provide an integral assessment of the suitability of the material and technology for critical applications; for instance, a high (especially negative) value of relative anisotropy in any direction for a key property signals a potential weakness of the structure in that direction.

The relative anisotropy of the ultimate strength of the synthesized samples compared to the ultimate strength of the material in its initial state was estimated as:

$$\Delta\sigma_u = \frac{\sigma_{u0} - \sigma_u}{\sigma_u} \cdot 100\,\%,$$

where σ_{u0} and σ_u are the ultimate strength values, with σ_{u0} representing the ultimate strength of the material in its initial state and σ_u representing that measured in the synthesized samples, in MPa.

The relative anisotropy of the tensile relative elongation of the synthesized samples compared to the tensile relative elongation of the material in its initial state was estimated as:

$$\Delta\varepsilon = \frac{\varepsilon_0 - \varepsilon}{\varepsilon} \cdot 100\,\%,$$

where where ε_0 and ε are the tensile relative elongation values, with ε_0 representing the tensile relative elongation of the material in its initial state and ε representing that measured in the synthesized samples, in %.

The relative anisotropy of the impact toughness of the synthesized samples compared to the impact toughness of the material in its initial state was estimated as:

$$\Delta KCU = \frac{KCU_0 - KCU}{KCU} \cdot 100\,\%,$$

where KCU_0 and KCU are the impact toughness values, with KCU_0 representing the impact toughness of the material in its initial state and KCU representing that measured in the synthesized samples, in J/cm² (or equivalent unit), with the calculated anisotropy expressed as a percentage.

The relative anisotropy of the hardness of the synthesized samples compared to the hardness of the material in its initial state was estimated as:

$$\Delta HV = \frac{HV_0 - HV}{HV} \cdot 100\,\%$$

where HV_0 and HV are the hardness values, with HV_0 representing the hardness of the material in its initial state and HV representing that measured in the synthesized samples, in HV.

If $\Delta\sigma_u$, $\Delta\varepsilon$, ΔKCU, ΔHV are positive, then the corresponding characteristics (σ_u, ε, KCU, HV) of the material synthesized by the *WAAM* method are inferior to those of the original material. If the values are negative, then the characteristics of the *WAAM* material are superior. The total relative anisotropy for the first-order samples was calculated as the difference between the maximum and minimum values of the relative anisotropy values obtained from the second-order samples.

To conduct the research, first-order samples in prism form were synthesized using the *WAAM* method, from which second-order samples were cot out for tensile strength tests according to *GOST 1497-84*, impact toughness tests according to *GOST 9454-78*, and for Vickers hardness measurements. To conduct strength and impact toughness tests, the samples were positioned within the synthesized prisms as shown in Figs. 1 and 2.
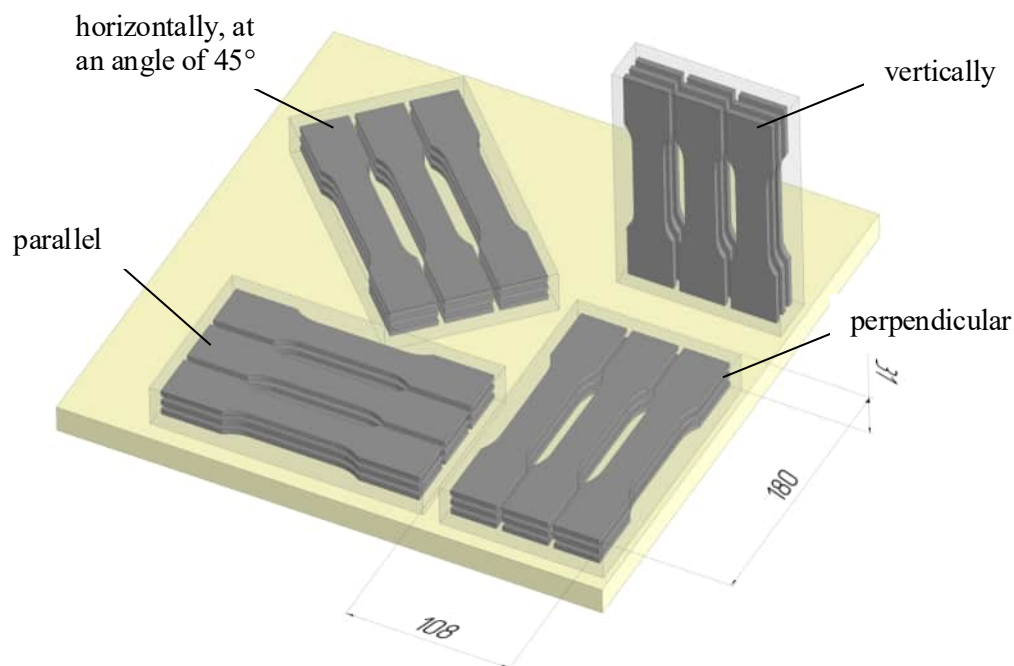
Fig. 1. Schematic representation of synthesized samples arrangement on the substrate
(welding torch direction consistent for all samples)

The second-order samples were manufactured in the vertical direction (the synthesis direction) and three horizontal orientations: parallel to the feedstock feed direction, perpendicular to it, and at an angle of 45°. Hardness measurements were performed in three planes: vertical, parallel, and perpendicular to the feedstock feed direction (Fig. 3).

Hardness measurements were performed with a step of 0.3 mm over a 10 mm base. In each direction, at least three parallel series of such measurements were conducted. For each level (consisting of at least three measurement points), the average hardness value was calculated. The height of each synthesized layer for 0.08 *C*-2 *Mn*-1 *Si* and 0.04 *C*-19 *Cr*-9 *Ni* steels was 2.2 mm; for the 97 *Al*-3 *Mg* aluminum alloy, it was 2.5 mm.
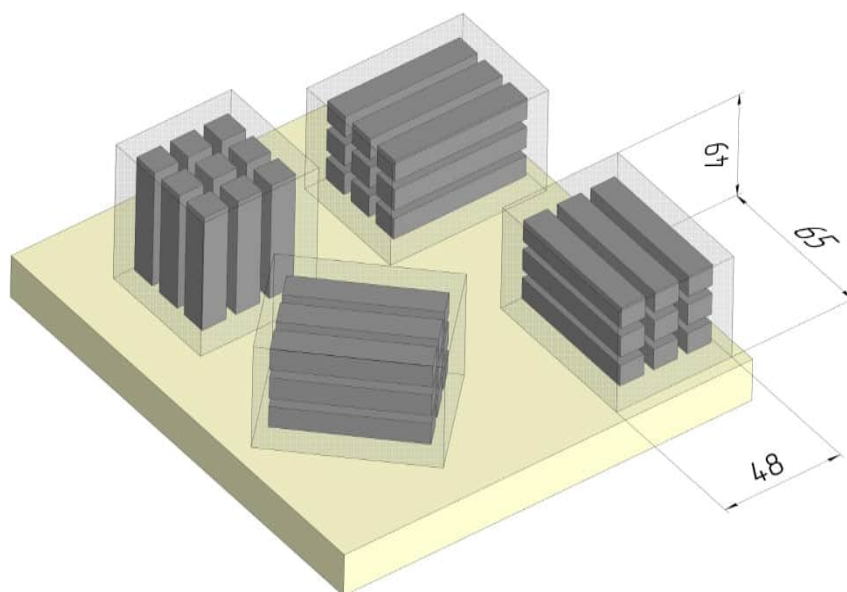
Fig. 2. Schematic representation of synthesized sample arrangement for impact toughness testing on the substrate (welding torch direction consistent for all samples)
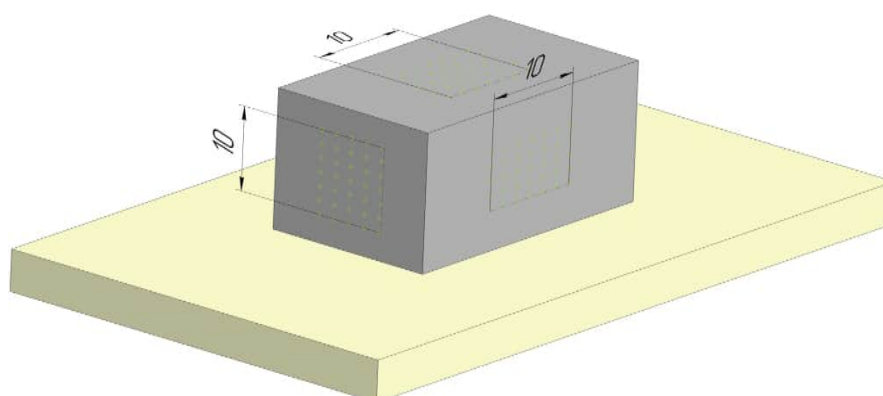
Fig. 3. Hardness measurement scheme for synthesized samples

The synthesis modes were selected based on the conditions for obtaining high-quality samples with a minimum number of pores (Table 1) [21].

Table 1

Synthesis parameters

Parameter	Material		
	0.08 *C*-2 *Mn*-1 *Si*	0.04 *C*-19 *Cr*-9 *Ni*	97 *Al*-3*Mg*
Current, A	175	170	125
Voltage, V	19.6	18.3	18.7
Wire feed rate, m/min	5.64	6.37	7.3
Feedstock feed rate, mm/min	1,000	1,000	1,000
Wire diameter, mm	1.2	1.2	1.2

Results and Discussion

It was found that for 0.08 *C*-2 *Mn*-1 *Si* steel, the ultimate strength of samples obtained by the *WAAM* method is practically the same in all directions of orientation, measuring 486–492 MPa (Table 2), and is practically not inferior to the ultimate strength of rolled products in the delivered condition (490–510 MPa). The ultimate strength relative anisotropy was 1.3% (Fig. 4, *a*). Based on this parameter, the synthesized material can be considered isotropic. The relative elongation of the "vertically" positioned sample is slightly lower compared to the horizontally positioned sample, at 12% and 13%, respectively, and is significantly inferior to the relative elongation values of rolled products made from this material in the delivered condition (20–30%). The relative elongation relative anisotropy was 33% (Fig. 4, *b*).

The maximum impact toughness value of 192 J/cm² was recorded on samples with the "horizontal, at an angle of 45°" cutting direction, while the minimum (154 J/cm²) was observed for samples with the "perpendicular" cutting direction (Table 2). This exceeds the impact toughness of rolled products made of this material in the delivered condition (130–162 J/cm²). The impact toughness relative anisotropy was no more than 21% (Fig. 4, *c*).

T a b l e 2

Mechanical properties of synthesized materials

| Material	Property	Second-order sample position within the prism	Sample cutoff direction relative to feedstock feed direction	Source material (rolled stock)	*WAAM*-fabricated material	Relative anisotropy, %
0.08 *C*-2 *Mn*-1 *Si*	σ_u, MPa	vertically	–	500	486	2.9
		horizontally	at a 45-degree angle		490	2.0
			perpendicular		492	1.6
			parallel		487	2.7
	ε, %	vertically	–	25	10.8	131
		horizontally	at a 45-degree angle		12.6	98
			perpendicular		12.6	98
			parallel		12.6	98
	KCU, J/cm^2	vertically	–	146	166	−12
		horizontally	at a 45-degree angle		192	−24
			perpendicular		154	−5
			parallel		168	−13
	HV, kgf/mm^2	vertically	–	190	212	−10
		horizontally	perpendicular		179	6
			parallel		202	−6
0.04 *C*-19 *Cr*-9 *Ni*	σ_u, MPa	vertically	–	620	534	16.1
		horizontally	at a 45-degree angle		614	1.0
			perpendicular		537	15.5
			parallel		562	10.3
	ε, %	vertically	–	35	22	56
		horizontally	at a 45-degree angle		16.7	110
			perpendicular		9	300
			parallel		20.1	74
	KCU, J/cm^2	vertically	–	120	177	−32
		horizontally	at a 45-degree angle		125	−4
			perpendicular		119	1
			parallel		141	−15
	HV, kgf/mm^2	vertically	–	190	355	−47
		horizontally	perpendicular		318	−40
			parallel		336	−43

The End Table 2

Material	Property	Second-order sample position within the prism	Sample cutoff direction relative to feedstock feed direction	Source material (rolled stock)	WAAM-fabricated material	Relative anisotropy, %
97 Al-3 Mg	σ_u, MPa	vertically	–	230	129	78.3
		horizontally	at a 45-degree angle		230	0
			perpendicular		243	−5.3
			parallel		220	4.5
	ε, %	vertically	–	13	2	550
		horizontally	at a 45-degree angle		8.55	52
			perpendicular		9.03	44
			parallel		9.47	37
	KCU, J/cm^2	vertically	–	40	17	134
		horizontally	at a 45-degree angle		16	145
			perpendicular		18	117
			parallel		18	128
	HV, kgf/mm^2	vertically	–	45	74	−39
		horizontally	perpendicular		74	−39
			parallel		73	−39
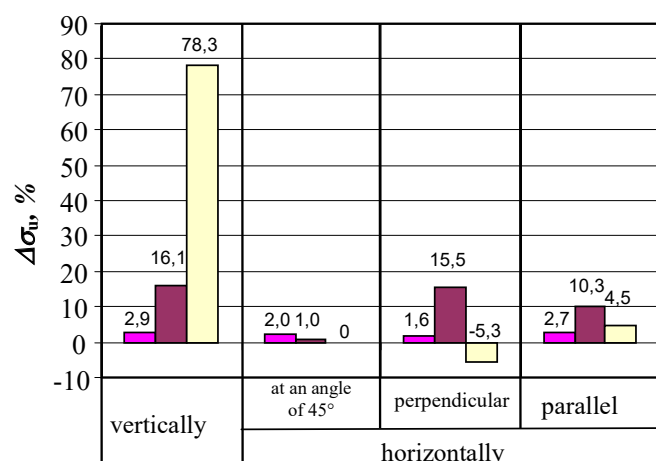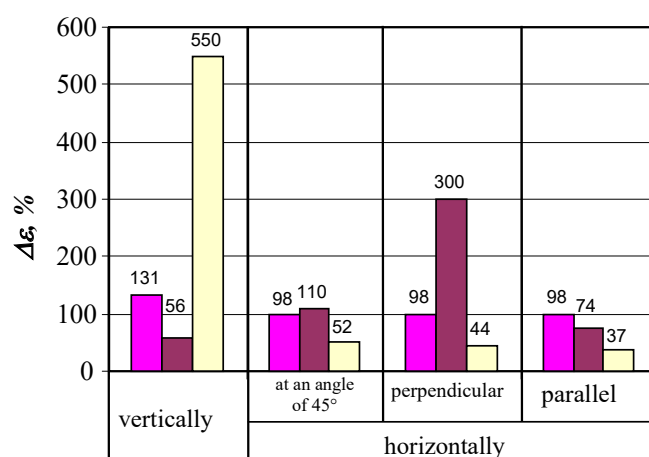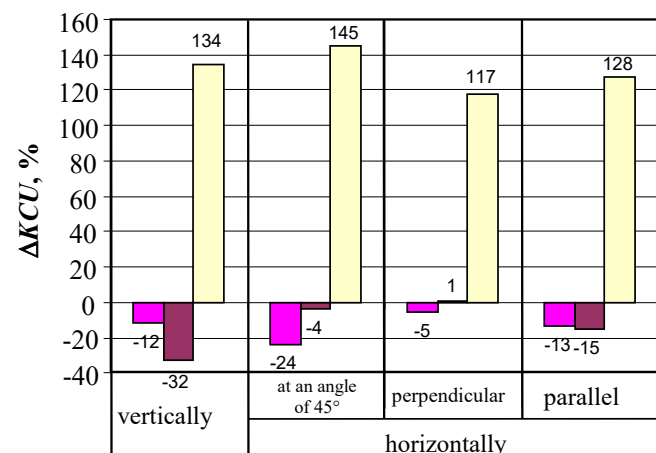
Fig. 4. Relative anisotropy of synthesized samples measured in different directions: tensile strength (*a*), relative elongation (*b*), impact toughness (*c*), and hardness (*d*)

The maximum average hardness value of 212 HV was recorded in the "vertical" direction, the minimum – in the "perpendicular" direction (179 HV), and the average hardness value in the "parallel" direction was 202 HV (Table 2). Therefore, the hardness measured in the "perpendicular" direction is notably lower than in the "parallel" and "vertical" directions (Fig. 5, *a*). The obtained hardness of the synthesized sample is comparable to the hardness of rolled products made from this material in the delivered condition (180–200 HV). The relative hardness anisotropy was 16% (Fig. 4, *d*).

Fig. 5. Hardness of synthesized samples measured in different directions:
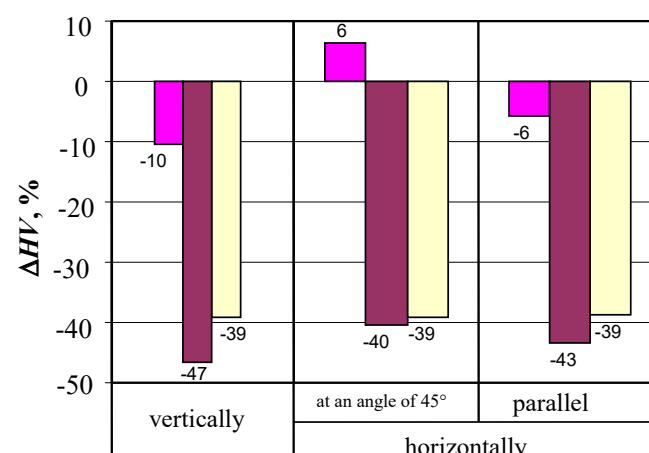0.08 *C*-2 *Mn*-1 *Si* steel (*a*), 0.04 *C*-19 *Cr*-9 *Ni* steel (*b*), 97 AL-3 *Mg* aluminum alloy (*c*)

Analysis of the obtained data on the hardness of all synthesized materials showed that the spread of values in each of the three measurement directions is comparable to that observed when measuring the hardness of alloys produced by casting or rolling.

For steel 0.04 *C*-19 *Cr*-9 *Ni*, the maximum tensile strength of 614 MPa (Table 2) was obtained with the "perpendicular" arrangement of the sample, and the minimum of 534 MPa with the "parallel" one. The obtained values are somewhat inferior to the tensile strength of rolled products made from this material in the delivered condition (610–620 MPa). The tensile strength relative anisotropy was 15.1% (Fig. 4, *a*). The maximum relative elongation of 22% was recorded for the sample with the "parallel" arrangement, and the minimum value of 9% was recorded for the sample with the "horizontal, at an angle of 45°" arrangement. This is significantly inferior to the relative elongation values of rolled products made of this material in the delivered condition (33–36%). The relative anisotropy of the relative elongation was 244% (Fig. 4, *b*).

The maximum impact toughness value was recorded for samples with the "vertical" cutting direction at 177 J/cm² (Table 2), and the minimum – with the "perpendicular" cutting direction (119 J/cm²). This value corresponds to or exceeds the impact toughness of rolled products made from this material in the delivered condition (120 J/cm²). The impact toughness relative anisotropy was 33% (Fig. 4, *c*).

For stainless steel 0.04 *C*-19 *Cr*-9 *Ni*, as well as for steel 0.08 *C*-2 *Mn*-1 *Si*, the highest average hardness value of 355 HV (Table 2) was recorded in the "vertical" direction, the lowest – in the "perpendicular" direction (318 HV), and the average hardness value in the "parallel" direction was 336 HV. Therefore, the hardness measured in the "perpendicular" direction is lower than in the "parallel" direction, and approximately as much lower than in the "vertical" direction (Fig. 5, *b*). The synthesized sample's obtained hardness in all directions significantly exceeds the hardness of rolled products made from this material in the delivered condition (160–180 kgf/mm²). The relative hardness anisotropy was 4% (Fig. 4, *d*).
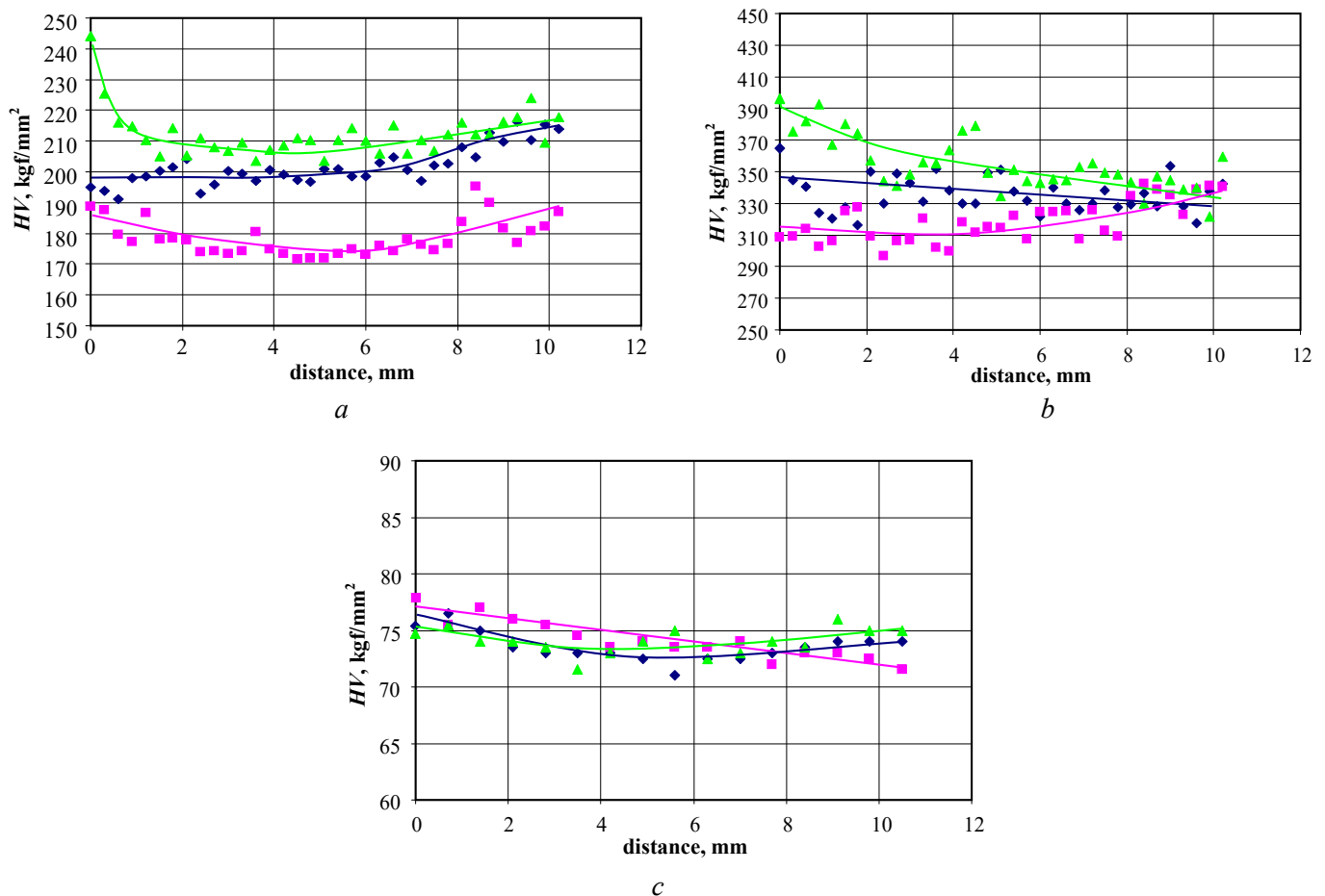
For the aluminum alloy 97 *Al*-3 *Mg*, the maximum tensile strength of 243 MPa (Table 2) was obtained with the "perpendicular" arrangement of the sample, and the minimum one of 129 MPa – with the "vertical" arrangement. The tensile strength of the samples cut in all horizontal directions, in contrast to the sample cut "vertically", is not inferior to the tensile strength of rolled products made of this material in the delivered condition (200–230 MPa). Specifically due to the "vertical" direction, the tensile strength relative anisotropy was 83.6% (Fig. 4, *a*). The relative elongation with the sample positioned "vertically" is almost 4.5 times lower than that of the samples cut in horizontal directions (2% vs. 8.6–9.4%, respectively). The values of relative elongation in all directions are inferior to the relative elongation of rolled products made from this material in the delivered condition (13%). The relative anisotropy of the relative elongation was 513% (Fig. 4, *b*).

The maximum impact toughness value of 18 J/cm² (Table 2) was recorded for samples with the "perpendicular" cutting direction, the minimum one – with the "horizontal, at an angle of 45°" cutting direction (16 J/cm²). Impact toughness changes insignificantly depending on the location from which the samples are cut out; the relative anisotropy was 28% (Fig. 4, *c*), but is significantly inferior to the impact toughness of rolled products made from this material in the delivered condition (40 J/cm²).

The average hardness value in all directions of measurement was consistent, amounting to 74 HV (Fig. 5, *c*), which exceeds the hardness of rolled products made from this material in the delivered condition by 1.6 times (45 HV). In terms of hardness, the synthesized material can be considered isotropic (Fig. 4, *d*).

The relative anisotropy values of the studied materials in terms of tensile strength, relative elongation, impact toughness, and hardness are presented in Table 3.

Table 3

Relative anisotropy values of the studied materials

Material grade	Relative anisotropy, %			
	of the ultimate tensile strength	of the relative elongation	of the impact toughness	of the hardness
0.08 *C*-2 *Mn*-1 *Si*	1,3	33	21	16
0.04 *C*-19 *Cr*-9 *Ni*	15,1	244	33	4
97 *Al*-3 *Mg*	83,6	513	21	0

It was found that during the synthesis of the studied metallic materials using the *WAAM* method, hardness exhibits the smallest relative anisotropy, while relative elongation shows the largest. The low-carbon steel 0.08 *C*-2 *Mn*-1 *Si* is the most isotropic with respect to all the studied properties. In contrast, the aluminum alloy 97 *Al*-3 *Mg* is the most anisotropic (due to samples cut in the vertical direction). The anisotropy of steel 0.04 *C*-19 *Cr*-9 *Ni* is associated with the low relative elongation values obtained from samples cut in the horizontal plane perpendicular to the torch feed during deposition.

Conclusion

Synthesis of three base materials was carried out using the *WAAM* method: low-carbon alloy steel 0.08 *C*-2 *Mn*-1 *Si*, stainless steel 0.04 *C*-19 *Cr*-9 *Ni*, and aluminum alloy 97 *Al*-3 *Mg*, in order to cover materials with significantly different mechanical properties. Synthesis modes that make it possible to obtain samples

with a tensile strength comparable to the tensile strength of rolled products made of the above materials were identified.

The concept of relative anisotropy was introduced as a percentage deviation of the synthesized material properties from the values for the original material (rolled product). This concept is proposed to evaluate both the change in mechanical properties in different directions within the synthesized material and the deviation of these properties from the rolled product.

It was established that for steel 0.08 *C*-2 *Mn*-1 *Si*, the smallest relative anisotropy was observed in ultimate strength (1.3%), and the largest was in relative elongation (33%). Therefore, the material can be considered practically isotropic in terms of strength. The strength of the synthesized steel 0.08 *C*-2 *Mn*-1 *Si* practically corresponds to the strength of rolled steel, but the relative elongation is 2–2.3 times lower.

For 0.04 *C*-19 *Cr*-9 *Ni* steel, the relative anisotropy minimum level was determined by hardness, which was 4%, and the maximum by relative elongation, which was 244%. This allows us to consider the material to be practically isotropic in hardness. At the same time, the hardness of the synthesized steel 0.04 *C*-19 *Cr*-9 *Ni* is close to the hardness of rolled products, and the relative elongation is reduced by 1.5–4 times.

Due to the "vertical" direction, the aluminum alloy 97 *Al*-3 *Mg* demonstrates the greatest anisotropy in tensile strength (83.6%) and in relative elongation (513%). However, anisotropy is absent in hardness, so the obtained material can be considered isotropic in this parameter. Comparison with the initial material shows that hardness is similar to that of rolled products. The tensile strength in the vertical direction is reduced by 1.8 times (in other directions, it is comparable to rolled products), and relative elongation is reduced by 1.4–6.5 times relative to rolled products.

In general, the minimum relative anisotropy is observed in hardness for all materials, which makes hardness the most stable parameter in *WAAM* synthesis. The most significant directions are vertical and horizontal (parallel and perpendicular to the feedstock feed direction during deposition).

References

1. Tomar B., Shiva S., Nath T. A review on wire arc additive manufacturing: Processing parameters, defects, quality improvement and recent advances. *Materials Today Communications*, 2022, vol. 31, p. 103739. DOI: 10.1016/j.mtcomm.2022.103739.

2. Cunningham C.R., Flynn J.M., Shokrani A., Dhokia V., Newman S.T. Invited review article: Strategies and processes for high quality wire arc additive manufacturing. *Additive Manufacturing*, 2018, vol. 22, pp. 672–686. DOI: 10.1016/j.addma.2018.06.020.

3. Hadjipantelis N., Weber B., Buchanan C., Gardner L. Description of anisotropic material response of wire and arc additively manufactured thin-walled stainless steel elements. *Thin-Walled Structures*, 2022, vol. 171, p. 108634. DOI: 10.1016/j.tws.2021.108634.

4. Palmeira Belotti L., van Nuland T.F.W., Geers M.G.D., Hoefnagels J.P.M., van Dommelen J.A.W. On the anisotropy of thick-walled wire arc additively manufactured stainless steel parts. *Materials Science and Engineering: A*, 2023, vol. 863, p. 144538. DOI: 10.1016/j.msea.2022.144538.

5. Williams S.W., Martina F., Addison A.C., Ding J., Pardal G., Colegrove P. Wire + Arc additive manufacturing. *Materials Science and Technology*, 2016, vol. 32 (7), pp. 641–647. DOI: 10.1179/1743284715Y.0000000073.

6. Siddiqui N.A., Muzamil M., Jamil T., Hussain G. Heat sources in wire arc additive manufacturing and their impact on macro-microstructural characteristics and mechanical properties – An overview. *Smart Materials in Manufacturing*, 2025, vol. 3, p. 100059. DOI: 10.1016/j.smmf.2024.100059.

7. Albannai A.I. A brief review on the common defects in wire arc additive manufacturing. *International Journal of Current Science Research and Review*, 2022, vol. 5 (12), pp. 4556–4576. DOI: 10.47191/ijcsrr/V5-i12-19.

8. Sun J., Hensel J., Köhler M., Dilger K. Residual stress in wire and arc additively manufactured aluminum components. *Journal of Manufacturing Processes*, 2021, vol. 65, pp. 97–111. DOI: 10.1016/j.jmapro.2021.02.021.

9. Le V.Th., Mai D.S. Microstructural and mechanical characteristics of 308L stainless steel manufactured by gas metal arc welding-based additive manufacturing. *Materials Letters*, 2020, vol. 271, p. 127791. DOI: 10.1016/j.matlet.2020.127791.

10. Lu X., Zhou Y.F., Xing X.L., Shao L.Y., Yang Q.X., Gao S.Y. Open-source wire and arc additive manufacturing system: Formability, microstructures, and mechanical properties. *The International Journal of Advanced Manufacturing Technology*, 2017, vol. 93 (5–8), pp. 2145–2154. DOI: 10.1007/s00170-017-0636-z.

11. Wahg Y., Chen X., Su Ch. Microstructure and mechanical properties of Inconel 625 fabricated by wire-arc additive manufacturing. *Surface and Coatings Technology*, 2019, vol. 374, pp. 116–123. DOI: 10.1016/j.surfcoat.2019.05.079.

12. Vlasov I.V., Gordienko A.I., Kuznetsova A.E., Semenchuk V.M. Structure and mechanical properties anisotropy of a steel product manufactured by layer-by-layer electric arc wire 3D printing. *Izvestiya. Ferrous Metallurgy*, 2023, vol. 66 (6), pp. 709–717. DOI: 10.17073/0368-0797-2023-6-709-717.

13. Nagasai B., Malarvizhi S., Balasubramanian V. Mechanical properties of wire arc additive manufactured carbon steel cylindrical component made by gas metal arc welding process. *Journal of the Mechanical Behavior of Materials*, 2021, vol. 30 (1), pp. 188–198. DOI: 10.1515/jmbm-2021-0019.

14. Yang X., Liu J., Wang Zh., Lin X., Liu F., Huang W., Liang E. Microstructure and mechanical properties of wire and arc additive manufactured AZ31 magnesium alloy using cold metal transfer process. *Materials Science and Engineering: A*, 2020, vol. 774, p. 138942. DOI: 10.1016/j.msea.2020.138942.

15. Rosli N.A., Alkahari M.R., Abdollah M.F. bin, Maidin Sh., Ramli F.R., Herawan S.G. Review on effect of heat input for wire arc additive manufacturing process. *Journal of Materials Research and Technology*, 2021, vol. 11, pp. 2127–2145. DOI: 10.1016/j.jmrt.2021.02.002.

16. Selvi S., Vishvaksenan A., Rajasekar E. Cold metal transfer (CMT) technology – An overview. *Defence Technology*, 2018, vol. 14 (1), pp. 28–44. DOI: 10.1016/j.dt.2017.08.002.

17. Nguyen Q.L. *Tool path planning for wire-arc additive manufacturing processes*. Thesis for: Doctoral. BTU Cottbus – Senftenberg, 2022. DOI: 10.26127/BTUOpen-5982.

18. Rajput G.S., Gor M., Soni H., Badheka V., Sahlot P. Effect of deposition strategies on mechanical strength of wire arc additively manufactured Inconel 625. *Materials Today: Proceedings*, 2022, vol. 62 (13), pp. 7324–7328. DOI: 10.1016/j.matpr.2022.05.164.

19. Andreacola F.R., Capasso I., Langella A., Brando G. 3D-printed metals: Process parameters effects on mechanical properties of 17-4 P H stainless steel. *Heliyon*, 2023, vol. 9 (7), p. e17698. DOI: 10.1016/j.heliyon.2023.e17698.

20. Kirichek A.V., Fedonin O.N., Khandozhko A.V., Zhirkov A.A., Soloviyov D.L., Barinov S.V. Gibridnye tekhnologii i oborudovanie additivnogo sinteza izdelii [Hybrid technologies and technical equipment for additive synthesis of products]. *Naukoemkie tekhnologii v mashinostroenii = Science Intensive Technologies in Mechanical Engineering*, 2022, no. 8 (134), pp. 31–38. DOI: 10.30987/2223-4608-2022-8-31-38.

21. Li S., Lin Z., Kirichek A.V., Nagorkin M.N., Novikov M.A. Vliyanie tekhnologicheskikh faktorov na protsessy formirovaniya parametrov kachestva izdelii, izgotavlivaemykh WAAM-metodom na osnove dugovoi svarki v zashchitnykh gazakh [Technology factors effect on the quality parameters of products manufactured by the WAAM-technique based on GMAW (gas-metal-arc-welding)]. *Naukoemkie tekhnologii v mashinostroenii = Science Intensive Technologies in Mechanical Engineering*, 2025, no. 5 (167), pp. 3–14. DOI: 10.30987/2223-4608-2025-5-3-14.

Conflicts of Interest

The authors declare no conflict of interest.

Obrabotka metallov –
# Metal Working and Material Science

Journal homepage: http://journals.nstu.ru/obrabotka_metallov

Study of tribological properties of silicon bronze in different structural states

Andrey Filippov [a, *], *Nikolay Shamarin* [b], *Sergei Tarasov* [c]

Institute of Strength Physics and Materials Sciences SB RAS, 2/4 per. Academicheskii, Tomsk, 634055, Russian Federation

[a] https://orcid.org/0000-0003-0487-8382, avf@ispms.ru; [b] https://orcid.org/0000-0002-4649-6465, shnn@ispms.ru;
[c] https://orcid.org/0000-0003-0702-7639, tsy@ispms.ru

ARTICLE INFO

ABSTRACT

Introduction. Silicon bronzes are widely used in critical friction units due to their combination of corrosion resistance, machinability, electrical conductivity, and satisfactory mechanical properties. Electron beam additive manufacturing (*EBAM*) is promising for the production of complex parts, but it forms a large columnar grain structure, leading to anisotropy of properties and limiting their practical application. Methods of severe plastic deformation (*SPD*), such as multi-axis forging and rolling, are effective for refining the structure, eliminating anisotropy, and increasing strength. However, their effect on the overall properties of silicon bronzes has not been sufficiently studied. **Purpose of the work.** The purpose of this study is a comparative analysis of the effect of the structural state of silicon bronze on its mechanical characteristics and tribological properties under dry sliding friction. **Research methods.** Samples in five structural states were obtained by electron-beam additive manufacturing (1), hot rolling (2), multi-axis forging (3), rolling at room temperature (4), and low-temperature annealing after rolling (5). The structure of the samples was investigated by optical metallography and transmission electron microscopy. Mechanical tests were carried out by tensile testing of double-sided dog-bone samples and Vickers microhardness testing. Tribological tests for dry sliding friction against 52100 steel were carried out with a constant load and speed. During friction, the friction coefficient (*FC*), vibrations in the normal and tangential directions, and acoustic emission (*AE*) were recorded. A detailed analysis of the surface and subsurface layer of friction tracks was performed using confocal laser scanning microscopy, as well as scanning electron microscopy with energy-dispersive X-ray spectroscopy (*EDS*). **Results and discussion.** The microstructure of the samples after *EBAM* exhibits large columnar grains, while after hot rolling it shows large equiaxed grains with twins. Multi-axial forging results in the formation of subgrains (lamellae) (<100 nm) with a high dislocation density. Rolling leads to further refinement of the original grains and the formation of elongated submicron grains. Low-temperature annealing forms more equiaxed submicron grains (100–200 nm) with a reduced dislocation density and high-angle boundaries. Samples with a coarse-grained structure have low strength and hardness. After *SPD*, the strength and hardness increase significantly, and the relative elongation decreases compared to the original material. Low-temperature annealing provides maximum strength with partial restoration of ductility and a decrease in hardness. The smallest and most stable friction coefficient, as well as minimum vibration amplitudes (especially in the tangential direction), were recorded for samples after *SPD*. The greatest wear occurred for the sample in the as-received condition (hot rolling). *SPD* reduces wear by 2.1–2.2 times compared to the hot-rolled and *EBAM* samples. Low-temperature annealing increases wear by 10% relative to the sample after rolling. The predominant wear mechanisms were determined to be: mixed (adhesive-oxidative) for bronze after *EBAM*; adhesive for hot rolled; and oxidative for samples after *SPD*. Based on metallographic studies, it was found that the depth of subsurface deformation is maximum for coarse-grained samples (145–155 μm) and decreases by 3.3–4.7 times after *SPD*. **Conclusion**. A comprehensive study has revealed a decisive influence of the structural state of 96% *Cu*-3% *Si*-1% *Mn* bronze on its key properties. The use of *SPD* methods (multi-axial forging and rolling) has proven to be highly effective in dramatically improving the mechanical and tribological properties of silicon bronze, regardless of the original production method (hot-rolled steel or electron beam additive manufacturing).

Introduction

Silicon bronzes, a class of copper-based alloys containing 1–4 wt.% silicon, are widely used in various industries due to their unique combination of high corrosion resistance, good machinability, excellent electrical and thermal conductivity, and satisfactory mechanical and antifriction properties. These alloys are commonly employed in the manufacture of plain bearings, bushings, gears, valves for aggressive media, and electrical components [1]. Conventionally, silicon bronze products are produced via casting followed by thermomechanical processing (e.g., rolling, forging, pressing) or through powder metallurgy routes.

---

* Corresponding author
Filippov Andrey V., Ph.D. (Engineering), Head of Laboratory
Institute of Strength Physics and Materials Sciences SB RAS,
2/4 per. Academicheskii,
634055, Tomsk, Russian Federation
Tel.: +7 999 178-13-40, **e-mail:** avf@ispms.ru

Binary *Cu-Si* alloys with silicon contents below 5 wt.% consist of a single-phase face-centered cubic (*FCC*) α-*Cu* solid solution [2]. The addition of manganese refines the dendritic grain structure without altering the phase composition, as demonstrated in cast *Cu-3Si* alloy [3, 4]. This grain refinement is accompanied by improvements in ductility, tensile strength, and hardness. It has been established that significant alterations in solid-phase reactions can be achieved by modifying the processing scale, temperature, or initial microstructure [5]. While heat treatment can influence the microstructure and phase composition of silicon bronzes [6], the low-silicon α-*Cu* solid solution is not susceptible to phase transformations [7].

Recently, wire and electron beam additive manufacturing (*WEBAM*) has garnered significant interest for fabricating silicon bronze components. This highly productive technique enables the creation of complex, custom geometries with minimal machining allowances. However, an inherent characteristic of additively manufactured metals, including those produced by *WEBAM*, is epitaxial solidification, which leads to the formation of coarse columnar grains [8]. This microstructure results in pronounced anisotropy of mechanical properties and can adversely affect tribological characteristics, thereby limiting the application of these materials in highly-loaded friction units that require isotropic behavior.

Severe plastic deformation (*SPD*) techniques, such as equal-channel angular pressing (*ECAP*), multi-axis forging, and rolling, are highly effective for mitigating these drawbacks and enhancing the mechanical properties of alloys, including silicon bronze. *SPD* methods can significantly refine the coarse, columnar grain structure, transforming it into an ultrafine-grained (*UFG*) or nanocrystalline (*NC*) state with equiaxed grains, thereby eliminating anisotropy. The resultant grain boundary strengthening leads to substantial improvements in strength and hardness. A subsequent short-term, low-temperature annealing step is often employed to partially relieve internal stresses and improve ductility without sacrificing a significant portion of the strength gained from strain hardening. This balance is critical for tribological applications requiring a combination of high strength and wear resistance.

Previous research has demonstrated the efficacy of *SPD*; for instance, hydrostatic extrusion of *C65500* bronze (an analog of *96% Cu-3% Si-1% Mn*) increased its tensile strength and yield strength by 45% and 130%, respectively, compared to the commercial counterpart [8]. Similarly, the transformation of a columnar grain structure into an equiaxed, twinned one was achieved in a *96% Cu-3% Si-1% Mn* alloy through drawing followed by softening annealing [9]. These findings confirm that *SPD* is a viable strategy for microstructural refinement and property enhancement in silicon bronzes. However, a review of the literature indicates that the potential of specific *SPD* methods, particularly multi-axis forging and rolling, for processing silicon bronzes remains insufficiently explored.

Therefore, ***the purpose of this work*** is to conduct a comparative study of the mechanical and tribological properties of a silicon bronze in different structural states. The following ***tasks*** were defined to achieve this purpose:

1. Perform microstructural characterization.
2. Conduct mechanical testing.
3. Perform tribological tests under dry sliding friction conditions.
4. Analyze the friction surface and subsurface deformation layers after sliding.

Methods

Silicon bronze samples were produced using a wire-feed electron beam additive manufacturing (*WEBAM*) machine to fabricate layer-by-layer deposits from a *96% Cu-3% Si-1% Mn* wire onto steel substrates. The printing parameters for these block-shaped samples were implemented in accordance with modes detailed in reference [11]. These samples correspond to the first structural state, characterized by large columnar grains, and are designated herein as Sample 1.

The second structural state comprises a material with large equiaxed grains and annealing twins, characteristic of the microstructure found in commercial hot-rolled bar stock. Samples in this condition are designated as Sample 2.

The third structural state features a subgrain structure consisting of submicron lamellae, formed by subjecting the *WEBAM*-fabricated samples (Sample 1) to severe plastic deformation via multi-axial forging

at room temperature. The process was conducted at a constant crosshead speed of 10 mm/s until a degree of deformation of ε = 0.5 was achieved along each of the three geometric axes of the sample. These samples are designated as Sample 3.

The fourth structural state is a material with submicron grains, produced by further processing Sample 3 through multiple passes of room-temperature rolling to a total strain of ε = 0.75. These samples are designated as Sample 4.

The fifth structural state comprises a material with near-equiaxed submicron grains, produced by subjecting Sample 4 to a low-temperature annealing at 200 °C for 30 minutes. The heat treatment was conducted in a laboratory muffle furnace, followed by rapid quenching in a large volume of water. These samples are designated as Sample 5.

The mechanical properties of the samples were determined by tensile testing standard double-sided blade specimens on a *Testsystems UTS-110M* universal testing machine at a crosshead speed of 1 mm/min. Vickers microhardness was measured using a *Tochline-TBM* hardness tester by indenting the samples with a diamond pyramid under a load of 100 N (HV10).

Metallographic analysis of samples in the rolled and as-printed conditions was performed using an *Olympus LEXT 4100* laser scanning confocal microscope. The fine microstructure of samples after severe plastic deformation was characterized by transmission electron microscopy (*TEM*) using a *JEOL JEM-2100* microscope.

For tribological testing, plate-shaped samples were prepared for sliding contact against 6 mm diameter balls made of *ShKh15* (*AISI 52100* equivalent) bearing steel. Tests were conducted under dry sliding conditions at a velocity of 100 mm/s under a normal load of 20 N. During friction, acoustic emission signals and vibration amplitudes were recorded. Vibration accelerations were measured in both the normal (parallel to the applied load) and tangential (parallel to the friction force) directions. The morphology of the resulting wear tracks was examined using scanning electron microscopy (*Thermo Fisher Scientific Apreo S LoVac*) and laser scanning microscopy (*Olympus LEXT 4100*).

Results and Discussion

Wire and electron beam additive manufacturing (Sample 1) results in the formation of a large columnar grain structure (Fig. 1, *a*). The grain width ranges from 150 to 600 μm, with lengths often significantly exceeding 1 mm. This microstructure results from directional solidification under the pronounced thermal gradient of the melt pool during layer-by-layer deposition. Samples in the as-received hot-rolled condition (Sample 2) exhibit a microstructure of nearly equiaxed grains with annealing twins (Fig. 1, *b*), with grain size ranging from 200 to 500 μm.

Multi-axial forging (Sample 3) produces a highly deformed substructure characterized by significant azimuthal misorientation, arising from strain-induced grain subdivision and refinement. The subgrain structure consists of curved, submicron lamellae with thicknesses below 100 nm, formed during non-uniform deformation in the forging process. This state is also characterized by a high dislocation density. Subsequent rolling (Sample 4) further refines the structure into elongated submicron grains (Fig. 1, *d*). The selected area electron diffraction (*SAED*) pattern exhibits a substantial increase in azimuthal misorientation, with reflections degenerating into nearly continuous rings, indicating extreme grain refinement. This grain formation likely results from recovery and dynamic recrystallization processes during severe plastic deformation [12].

Low-temperature annealing (Sample 5) after rolling reduces the dislocation density and promotes the formation of nearly equiaxed submicron grains, ranging from 100 to 200 nm in size (Fig. 1, *e*).

Tensile testing revealed that the different structural states exhibit distinct combinations of strength and ductility (Fig. 2, *a–c*). The *WEBAM*-fabricated and as-received hot-rolled samples (Sample 1 and Sample 2) demonstrated the lowest strength but highest ductility. Their ultimate tensile strength (*UTS*) was nearly identical, at 340–346 MPa. However, their yield strength differed significantly, by approximately a factor of two, with the *WEBAM* sample exhibiting a characteristically low yield stress, a known trait of structures formed by electron beam printing [13].
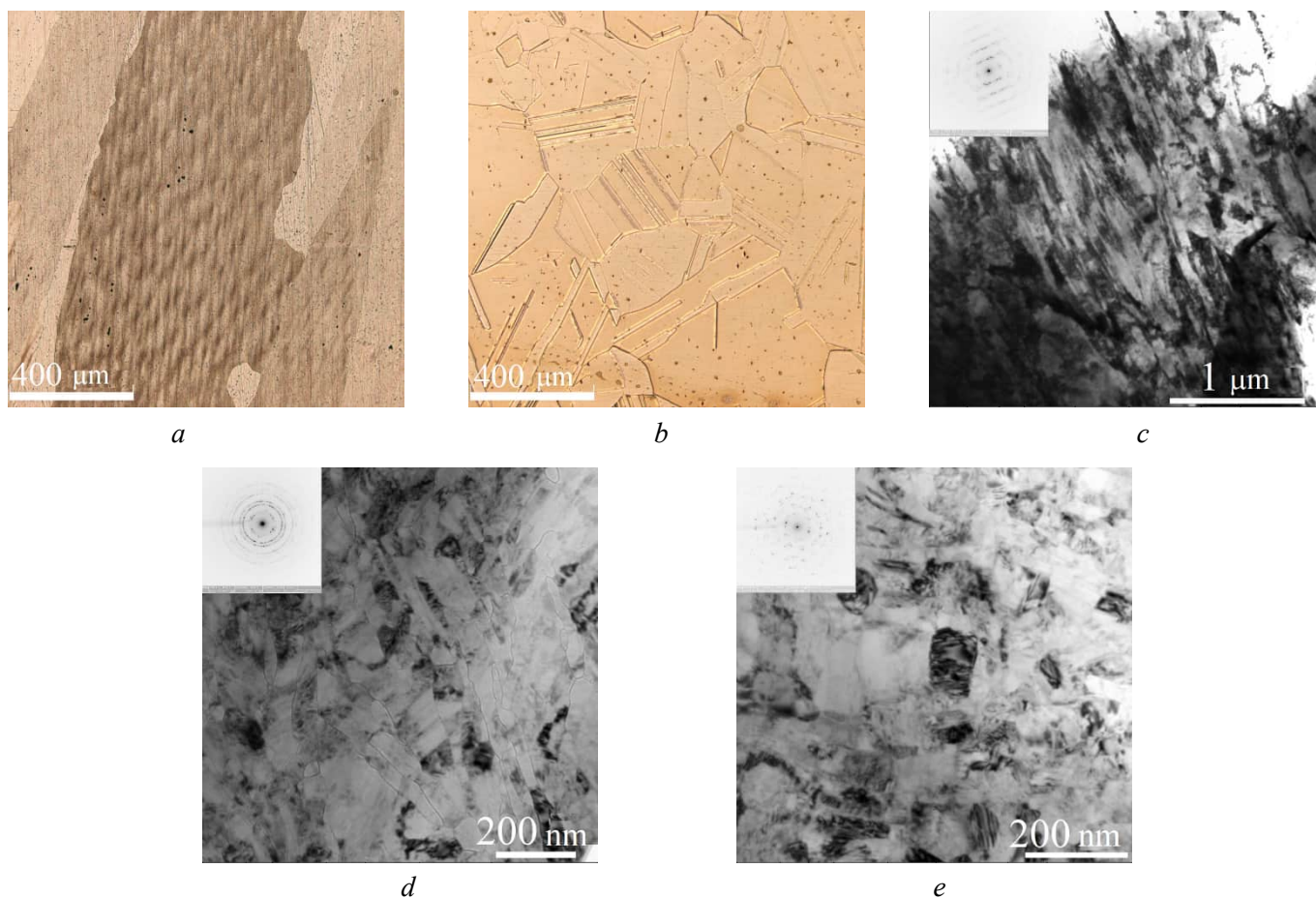
Fig. 1. Images of typical structure of 96% *Cu*-3% *Si*-1% *Mn* bronze samples.
Samples 1 (*a*), **2** (*b*), **3** (*c*), **4** (*d*) and **5** (*e*)

Severe plastic deformation via multi-axial forging (Sample 3) and the associated microstructural changes resulted in a significant increase in both ultimate tensile strength (Fig. 2, *a*) and yield strength (Fig. 2, *b*) compared to the as-received hot-rolled and *WEBAM*-fabricated materials. This enhancement is a consequence of strain hardening according to the *Hall-Petch* relationship [14]. The UTS increased to 525 MPa and 519 MPa and the yield strength to 403 MPa and 298 MPa, while the relative elongation decreased from 70–100% to 18.1% (Fig. 2, *c*). Subsequent rolling (Sample 4) after forging further increased the *UTS* by 88 MPa and the yield strength by 376 MPa (Fig. 2, *a*, *b*), but reduced the relative elongation from 18.1% to 9.2%, compared with multi-axial forging (Fig. 2, *c*).

Low-temperature annealing (Sample 5) after rolling resulted in the highest strength values among all samples, with a *UTS* of 1022 MPa and a yield strength of 1,008 MPa (Fig. 2, *a*, *b*). Furthermore, this annealing improved the material's ductility, increasing the relative elongation from 8.2% to 12.2%.

Hardness represents a mechanical characteristic equally as important as strength and ductility (Fig. 2, *e*). The *WEBAM*-fabricated (Sample 1) and as-received hot-rolled (Sample 2) samples exhibit the lowest microhardness values of 0.86 GPa and 0.96 GPa, respectively (Fig. 2, *d*), which can be attributed to their coarse-grained microstructures [15, 16]. Severe plastic deformation via multi-axial forging (Sample 3) resulted in a threefold increase in microhardness compared to the coarse-grained Sample 1 and Sample 2. This enhancement stems primarily from grain refinement and the development of a high dislocation density. At the microstructural level, these changes produce strengthening through dislocation interactions and a substantial increase in dislocation density during deformation, directly reflected in the measured microhardness. A higher degree of deformation achieved through subsequent rolling (Sample 4) after multi-axial forging resulted in the maximum microhardness of 3.34 GPa among all investigated samples – 18% greater than after forging alone.
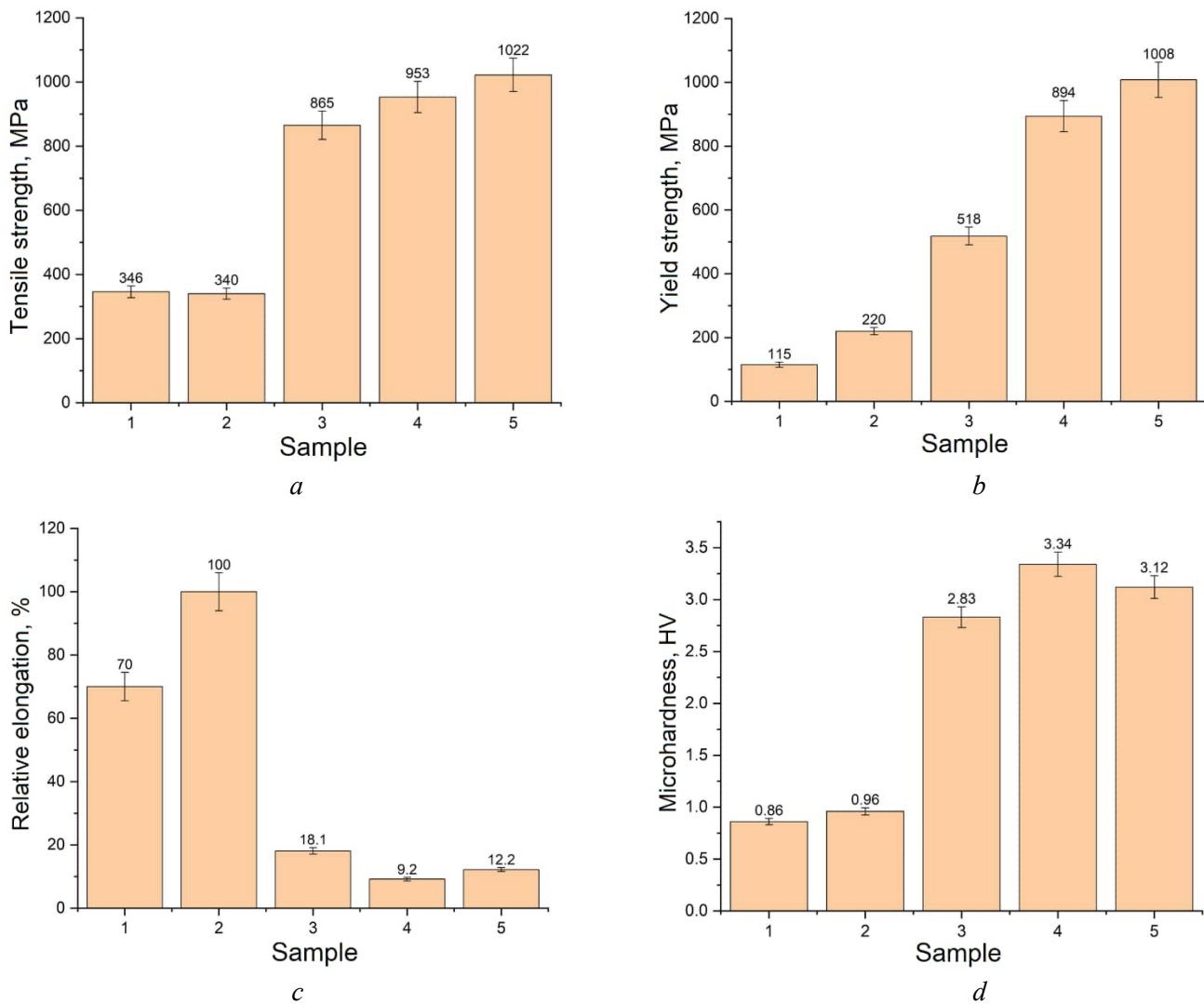
Fig. 2. Mechanical properties of 96% *Cu*-3% *Si*-1% *Mn* bronze samples

Low-temperature annealing (Sample 5) reduced the microhardness by approximately 7% relative to Sample 4, due to dislocation density reduction through recovery and polygonization processes.

During sliding friction, the coefficient of friction (*CoF*) undergoes significant evolution (Fig. 3, *a*). Initially, all bronze samples exhibited a high *CoF*, attributable to running-in processes within the steel-bronze tribological pair. During this initial stage, pre-existing oxide films are removed, forming a clean bronze surface. The interaction with this nascent surface results in significantly increased adhesion due to the enhanced molecular component of the friction force [17]. Subsequently, as the surface layer wears and sliding conditions evolve, the *CoF* may either increase or decrease, depending on the dominant wear mechanism and the specific characteristics of wear track formation.

The recorded friction coefficient data show that the *CoF* decreased over the first 15–25 minutes. For Sample 1 (*WEBAM*), this running-in stage transitioned into a period of steady-state sliding friction. The as-received hot-rolled sample (Sample 2) exhibited a sinusoidal *CoF* dynamic with a period of approximately 25 minutes, indicating a cyclical process of friction layer formation and degradation. A similar pattern was observed for the multi-axially forged sample (Sample 3), though with a longer period of about 30 minutes. Both Sample 2 and Sample 3 were characterized by a relatively monotonic increase and decrease in *CoF* within these intervals. In contrast, sliding for Sample 4 (forged + rolled) featured more frequent but lower amplitude *CoF* fluctuations, with a period of roughly 13 minutes. Sample 5 (forged + rolled + annealed) demonstrated oscillatory *CoF* behavior without a clearly defined periodicity.

The average *CoF* values, derived from the experimental data, are presented in Fig. 3, *b*. The results indicate that the highest average *CoF* is characteristic of the electron beam printed Sample 1. Sample 2
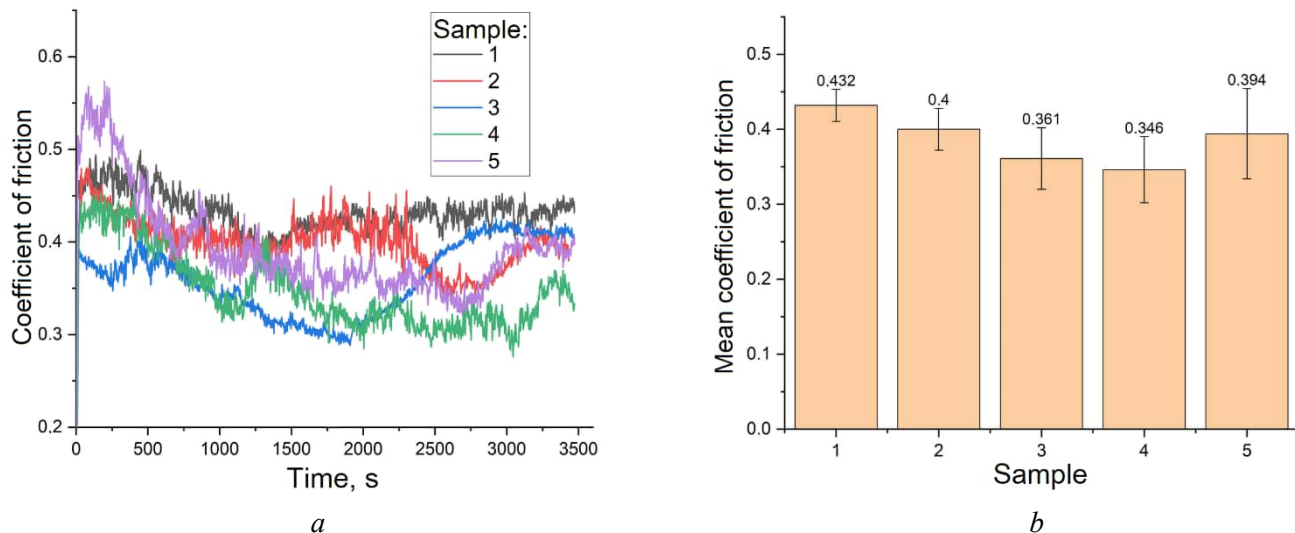
Fig. 3. Coefficients of friction vs. time during sliding tests (*a*) and their average values (*b*)

(hot-rolled) and Sample 5 (forged + rolled + annealed) exhibited slightly lower values. Severe plastic deformation via multi-axial forging and subsequent rolling (Sample 3 and Sample 4) led to a significant reduction in the average *CoF* – by 9% to 25% – compared to the coarse-grained (Sample 1 and Sample 2) and heat-treated (Sample 5) conditions.

Vibration acceleration signals were recorded from two accelerometers during tribological tests. The accelerometers were mounted to record signals in the direction of normal pressure and friction forces, enabling detailed monitoring of the tribosystem's dynamic behavior.

During friction of the printed bronze (Sample 1), vibration accelerations in the normal (Fig. 4, *a*) and tangential (Fig. 4, *b*) directions reached values of ~4.4 m/s² and ~5.8 m/s², respectively. In the normal direction, vibrations occurred uniformly from the test onset, while fluctuations in the tangential direction showed no pronounced periodicity.

The as-received Sample 2 exhibited vibration accelerations of ~6.7 m/s² in the normal direction and ~9.7 m/s² in the tangential direction. In this case, significant fluctuations in acceleration amplitude were observed only in the tangential direction, substantially exceeding those recorded for other samples.

Sliding of bronze deformed by multi-axial forging (Sample 3) showed vibration accelerations of ~3.1 m/s² in the normal direction and ~3.6 m/s² in the tangential direction, with sufficiently uniform vibration acceleration amplitude and no significant fluctuations.

During friction of bronze deformed by rolling (Sample 4), vibration accelerations measured ~3 m/s² in the normal direction and ~3.2 m/s² in the tangential direction were the lowest levels among all samples investigated. Unlike other samples, amplitude fluctuations in the normal direction exceeded those in the tangential direction.

The heat-treated bronze Sample 5 displayed vibration acceleration amplitudes of ~3.5 m/s² in the normal direction and ~4.7 m/s² in the tangential direction. Annealing after severe plastic deformation by rolling resulted in increased vibration amplitude during sliding in both normal and tangential directions.

The difference in vibration acceleration amplitude between tangential and normal directions (D_v, Fig. 4, *c–e*) reflects changes in sliding friction conditions. Values closer to zero indicate more stable sliding friction. Higher tangential vibration amplitude suggests intense adhesive bonding (sticking) between the steel ball and bronze disk. When this bonding ruptures, the stick phase transitions to slip (stick-slip mode), causing sharp increases in tangential vibration acceleration. Normal direction vibrations likely result from wear particle formation and surface deterioration.

The data indicate that the most stable sliding occurs with Sample 4 (*SPD* by rolling) and Sample 3 (multi-axial forging). Conversely, Sample 1 (*WEBAM*) and Sample 2 (as-received) exhibit high-amplitude vibration accelerations during sliding with significant directional differences, suggesting strong adhesive
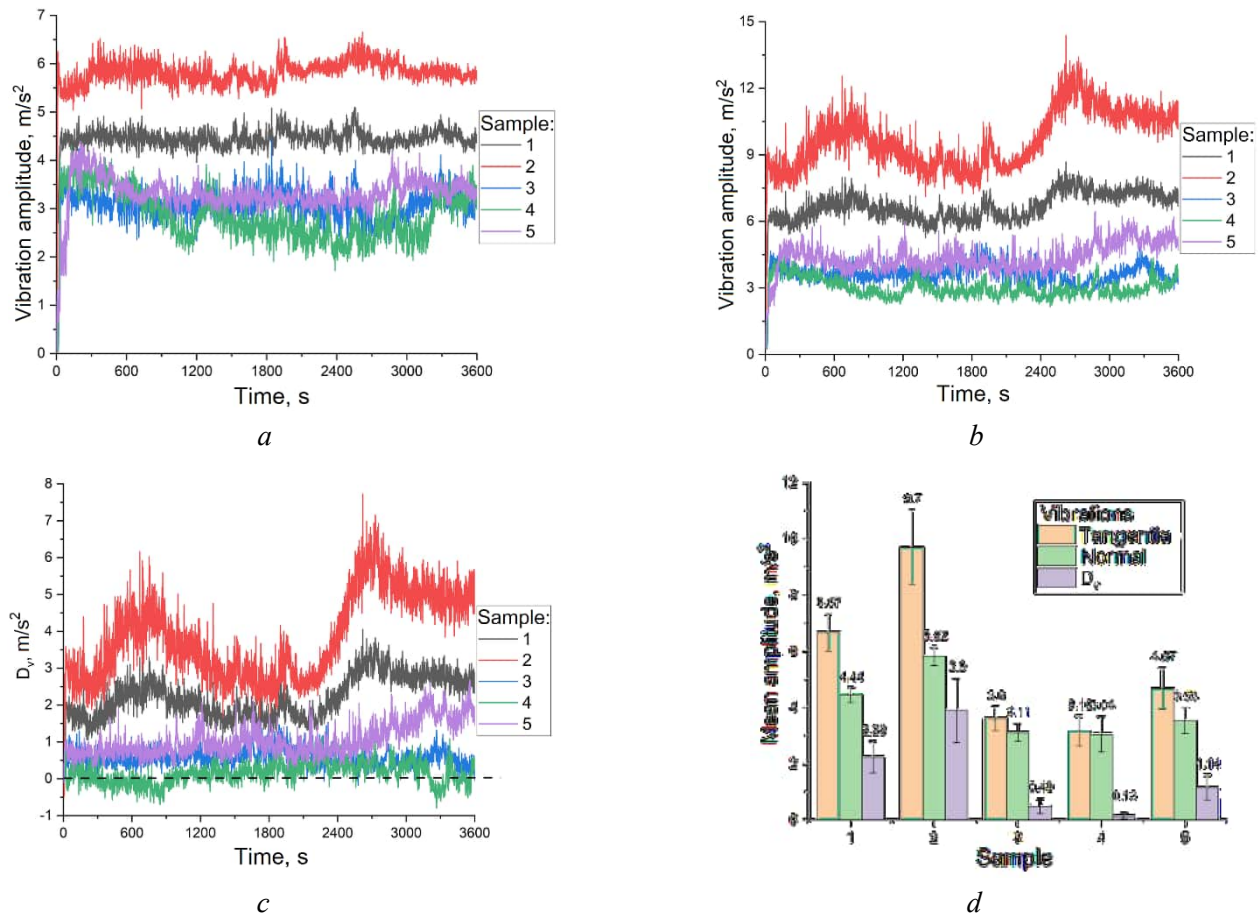
Fig. 4. Change in vibration acceleration amplitude during sliding friction in the normal (*a*) and tangential (*b*) directions, their difference (*c*), and average value (*d*)

interaction in the sliding pair. Low-temperature annealing (Sample 5) increased the D_v value, indicating enhanced adhesion during testing.

Previous studies [18] have established that the energy and median frequency (*MF*) of acoustic emission (*AE*) signals can characterize sliding friction modes. In this work, acoustic emission was detected and recorded using a sensor mounted on the sample during sliding friction. The *AE* signal waveforms were analyzed to determine the average values of energy (Fig. 5, *a*) and median frequency (Fig. 5, *b*).
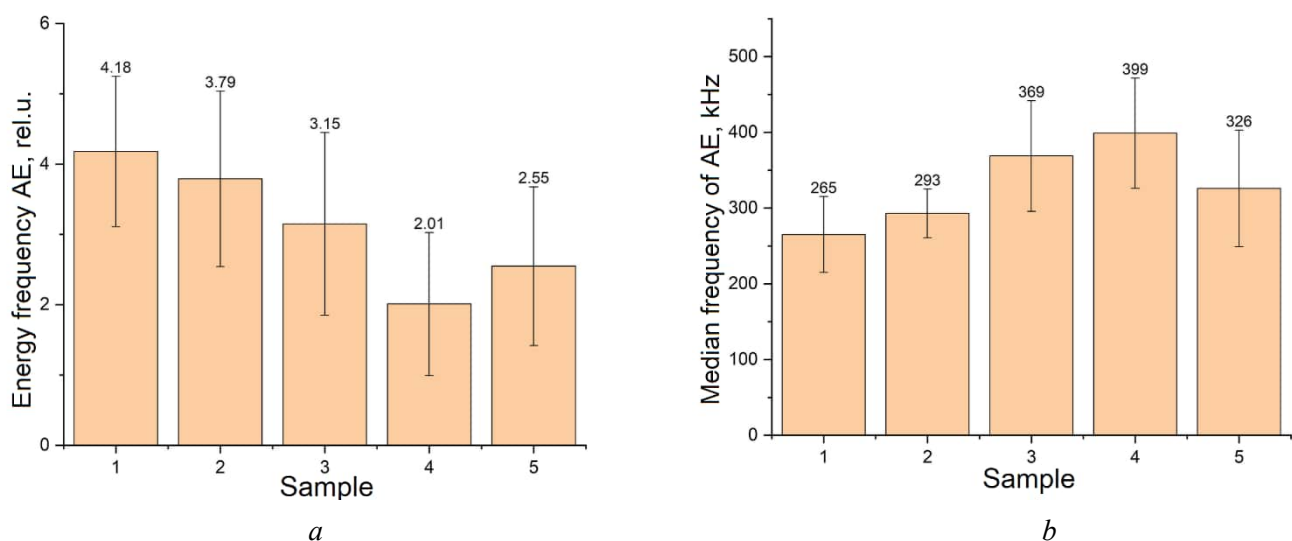
Fig. 5. Average energy (*a*) and median frequency (*b*) of acoustic emission (*AE*)

The results show a successive reduction in *AE* energy during sliding from coarse-grained Sample 1 to Sample 3, accompanied by a corresponding increase in *MF*. Sample 4 (rolled and heat-treated) exhibited the absolute minimum *AE* energy and maximum *MF*. Conversely, Sample 5 showed increased *AE* energy and reduced *MF* compared to Sample 4.

Comparison between vibrometry and acoustic emission data reveals a consistent pattern: *AE* energy increases in sliding modes characterized by high vibration acceleration amplitudes. This correlation occurs because significant stick-slip vibrations generate repeated impacts between contact asperities. The rupture of adhesive bonds and associated impacts excite powerful elastic waves in the material, consequently increasing *AE* energy. Conversely, these conditions reduce the median frequency, primarily due to adhesive bond rupture. Previous research [18] demonstrated that viscous crack formation in materials causes short-term *MF* drops. Additionally, changes in sliding friction conditions – such as wear particle formation, development of thick abrasion-resistant oxide layers, and surface layer deterioration – also affect the frequency characteristics of *AE* signals [19–21].

The current study confirms variations in friction and wear conditions across bronzes with different structural states, consistent with vibrometry data, friction coefficient measurements, and examination of worn surfaces.

Analysis of the wear track surfaces revealed characteristic wear features of silicon bronze in different structural states (Fig. 6). Sliding of Sample 1 produced a rough worn surface characterized by: light areas with relatively large wear grooves, smoother dark tribo-oxidized regions, and material displaced to the track periphery through plowing (Fig. 6, *a*). These features indicate the combined action of at least two wear mechanisms, specifically adhesive-oxidative wear.

The worn surface of the as-received Sample 2 (Fig. 6, *b*) exhibits curved wear grooves and plowing, with no oxidation traces, along with deformed material buildups resulting from adhesion-mediated transfer. In this process, plasticized bronze initially adheres to the steel counterface, then detaches and re-adheres to the disk's wear track surface. The absence of oxidation suggests a predominantly adhesive wear mechanism.

Sliding of Sample 3 (multi-axial forged) yields a wear track surface almost entirely covered by a uniform black layer of oxidized material (Fig. 6, *c*). The adhesive wear areas are small (250–500 μm) and contain oxide inclusions. The absence of plowing indicates insignificant plastic deformation of the material, which
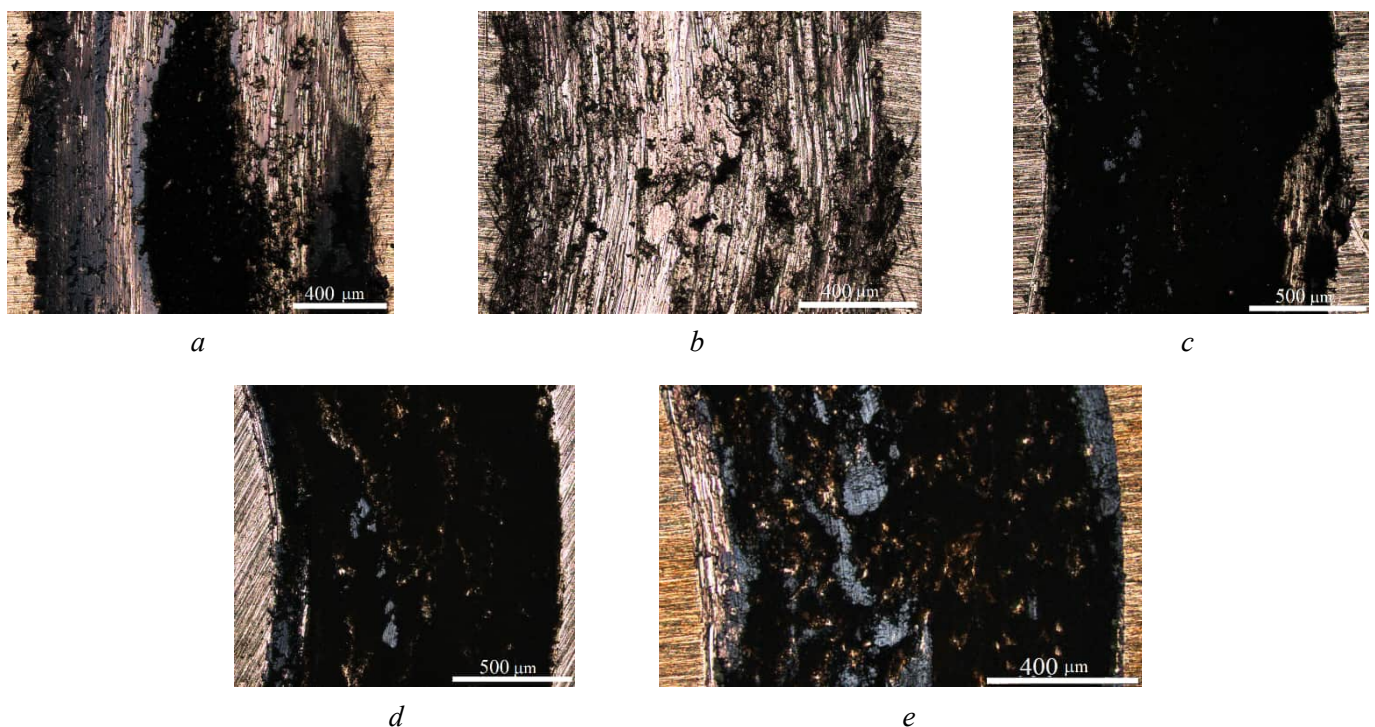

a	*b*	*c*

d	*e*

Fig. 6. Optical images of the wear track surfaces of 96% *Cu*-3% *Si*-1% *Mn* bronze samples.
Samples 1 (*a*), 2 (*b*), 3 (*c*), 4 (*d*) and 5 (*e*)

is expected since Sample 3 underwent severe plastic deformation, acquiring higher hardness and lower ductility through work hardening.

The friction track surface of Sample 4 resembles that of Sample 3 (Fig. 6, *d*), indicating the predominance of oxidative wear. Apparently, from the sliding onset, an oxidized layer forms through adhesive transfer and compaction of wear particles. This layer exhibits resistance to mechanical impact and remains adherent to the bronze substrate, unlike more ductile samples that are susceptible to plastic deformation and cannot provide stable support for surface oxide layers.

Low-temperature annealing of Sample 5 after rolling resulted in the formation of slightly more extensive adhesive wear areas (Fig. 6, *e*) compared to Samples 3 and Samples 4. This phenomenon results from increased material plasticity and reduced load-bearing capacity, consequently enhancing adhesive wear components.

The worn surfaces of the ball bearing steel counterparts (balls) were examined to validate the findings obtained from the bronze samples (Fig. 7). The observed wear patterns confirm the previously identified differences in wear mechanisms across bronze structural states.

In cases of predominantly adhesive wear, a bronze transfer layer formed on the ball surface (Fig. 7, *b*). This layer consists of material transferred through adhesive wear from the ductile as-received bronze (Sample 2).

Under predominant oxidative wear, a black oxide layer formed on the ball surface (Fig. 7, *c*). These oxides accumulated in micro-depressions and represent detached surface layers from the work-hardened bronzes manufactured via multi-axial forging (Sample 3) and rolling (Sample 4).

Significant oxidation of the low-temperature annealed sample (Sample 5) resulted in oxide layer formation covering substantial portions of the wear track, which correspondingly contributed to oxide deposition on the ball surface.

Under mixed adhesive-oxidative wear conditions, cyclic formation and removal of the surface layer occurred within the wear track. Consequently, neither plastic bronze transfer nor stable oxide layers became established on the ball surface (Fig. 7, *a*).

The worn surfaces of the bronze samples were further characterized using scanning electron microscopy (*SEM*) equipped with energy-dispersive X-ray spectroscopy (*EDS*), as shown in Figs. 8 and 9. The backscattered electron (*BSE*) images in Figs. 8, *a*–*e* reveal the worn surfaces of all bronze samples, displaying distinct bright and dark regions. The *BSE* image contrast is governed by the local elemental composition, wherein elements with lower atomic numbers appear darker. Consequently, darker areas correspond to more heavily oxidized regions.

In this context, Sample 1 exhibits a worn surface with predominantly gray and bright areas, indicating limited oxidation (Fig. 8, *a*). The grayscale intensity further reveals that although oxides are present on the worn surface of the as-received Sample 2 (Fig. 8, *b*), they are confined to small, isolated areas of material adhered during the wear process. In contrast, Sample 3, Sample 4, and Sample 5 display extensively

| *a* | *b* | *c* |
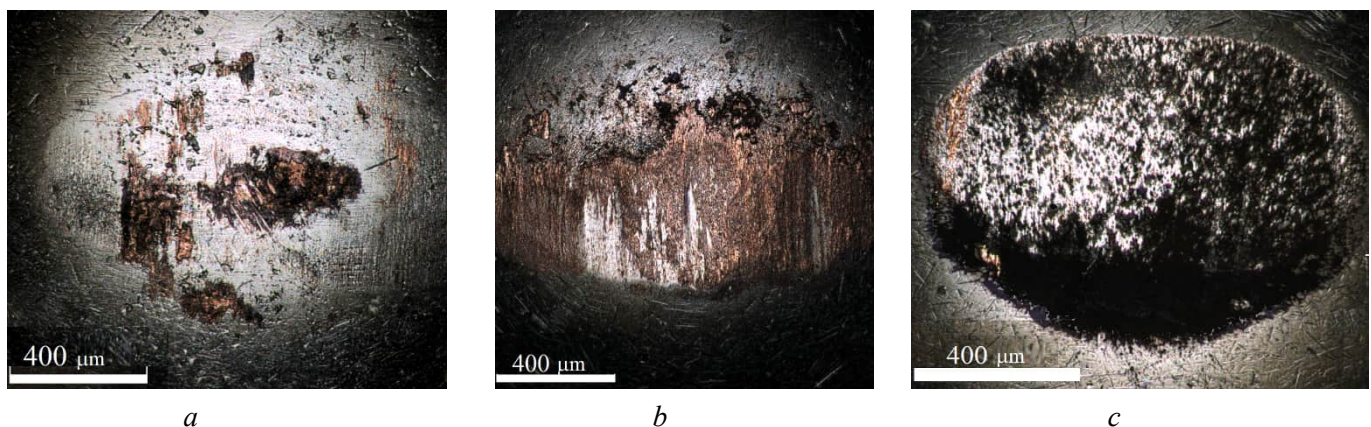
Fig. 7. Typical optical images of the ball surface after sliding against Sample 1 (*a*), Sample 2 (*b*), Samples 3–5 (*c*)

a

b

c

d

e
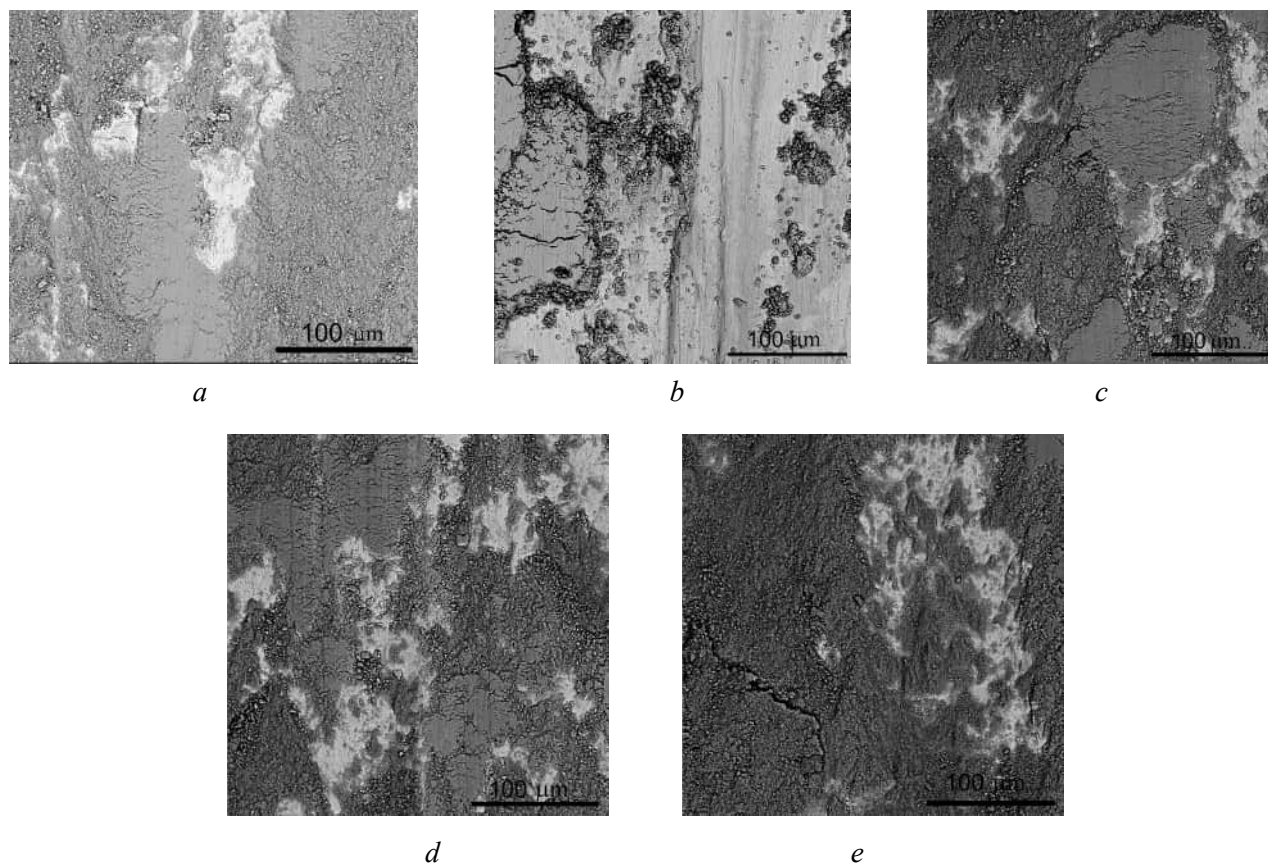
Fig. 8. SEM BSE images of the wear track surfaces of 96% *Cu*-3% *Si*-1% *Mn* bronze. Sample 1 (*a*), Sample 2 (*b*), Sample 3 (*c*), Sample 4 (*d*) and Sample 5 (*e*)

a

b

c

d

e
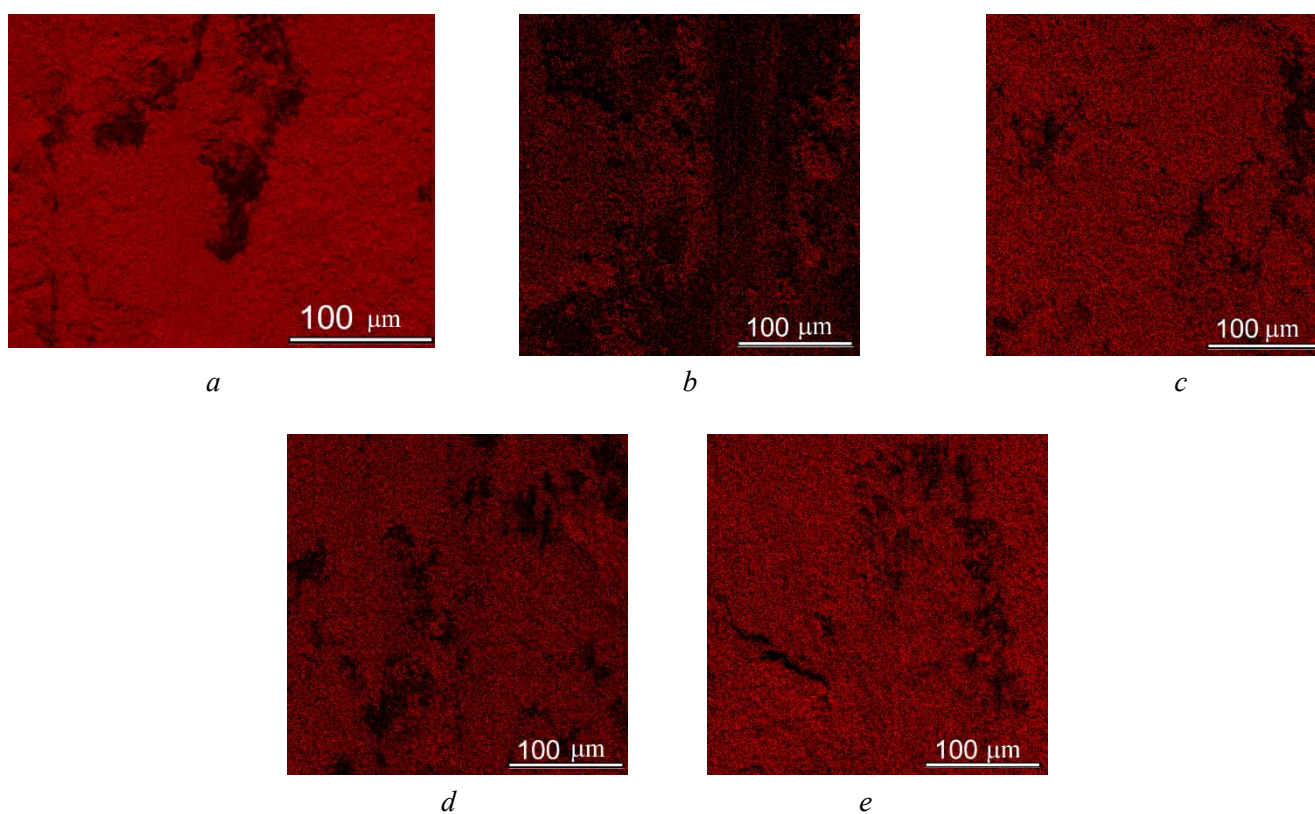
Fig. 9. EDS oxygen maps on the wear track surfaces of 96% *Cu*-3% *Si*-1% *Mn* bronze. Sample 1 (*a*), Sample 2 (*b*), Sample 3 (*c*), Sample 4 (*d*) and Sample 5 (*e*)

oxidized worn surfaces resulting from sliding on the severely plastically deformed (*SPD*) and strengthened materials (Figs. 8, *c–e*). The *EDS* elemental maps presented in Figs. 9, *a–e* confirm the presence of oxygen across these worn surfaces.

Fig. 10 presents the wear track profiles and corresponding cross-sectional area data. The obtained profiles (Fig. 10, *a*) reveal that sliding against Sample 1 and Sample 2 produced wear tracks with pronounced edge pile-ups. These pile-ups result from plastic deformation (ploughing) of the coarse-grained bronzes by the steel counter-body. In contrast, the *SPD*-strengthened Samples 3–5 exhibit no such pile-ups.

a   *b*

Fig. 10. Cross-sectional profiles of wear tracks (*a*) of 96% *Cu*-3% *Si*-1% *Mn* bronze and their areas (*b*)

Measurements of the wear track cross-sectional areas (Fig. 10, *b*) indicate that the most severe wear occurred during sliding against Sample 2 (as-received condition). The wear volumes for Sample 1, Sample 3, and Sample 4 were lower than that of Sample 2 by factors of 1.6, 2.1, and 2.2, respectively. Wear was minimal during friction against the rolled bronze (Sample 4), being 2.2 times a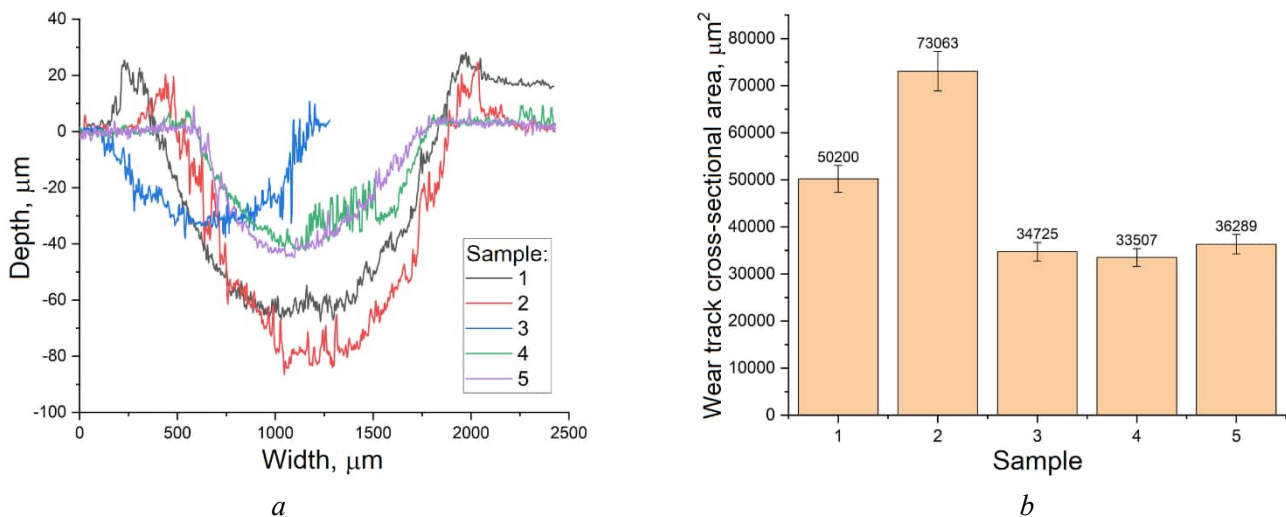nd 1.5 times lower than that of the hot-rolled and *WEBAM*-fabricated samples, respectively. The application of low-temperature annealing after rolling (Sample 5) increased wear by 10% compared to the condition obtained by rolling alone (Sample 4).

To analyze the effect of structural state on the subsurface deformation of silicon bronze induced by sliding friction, the regions beneath the worn surfaces were examined (Fig. 11). In coarse-grained Sample 1 and Sample 2 (Figs. 11, *a*, *b*), deformation bands are unevenly distributed across grains with different orientations relative to the loading axis. This is evidenced by developed systems of shear bands oriented at various angles to the sliding plane. The deformation zone extends to a depth of up to 50 μm below the worn surface in Sample 2, resulting from strong adhesive bonding within the friction pair. This adhesion causes the bronze material to stretch in the direction of the friction force, with the effect being most pronounced near the contact surface. Adhesive interaction is less intensive during sliding of Sample 2, consequently resulting in shallower plastic deformation penetration.

The *SPD*-processed samples (Figs. 11, *c–d*) consist of refined grains with high dislocation densities, making the identification of distinct deformation bands challenging. Instead, these samples exhibit curved shear bands and distorted grains. A thin tribological layer is visible immediately beneath the worn surfaces in these samples.

For quantitative assessment of subsurface deformation, the maximum penetration depth was measured. The results demonstrate that both the depth of plastic deformation penetration in the bronze (Fig. 12) and the wear behavior (Fig. 10) are governed by the material's mechanical characteristics (Fig. 2), which are in turn determined by its structural state.
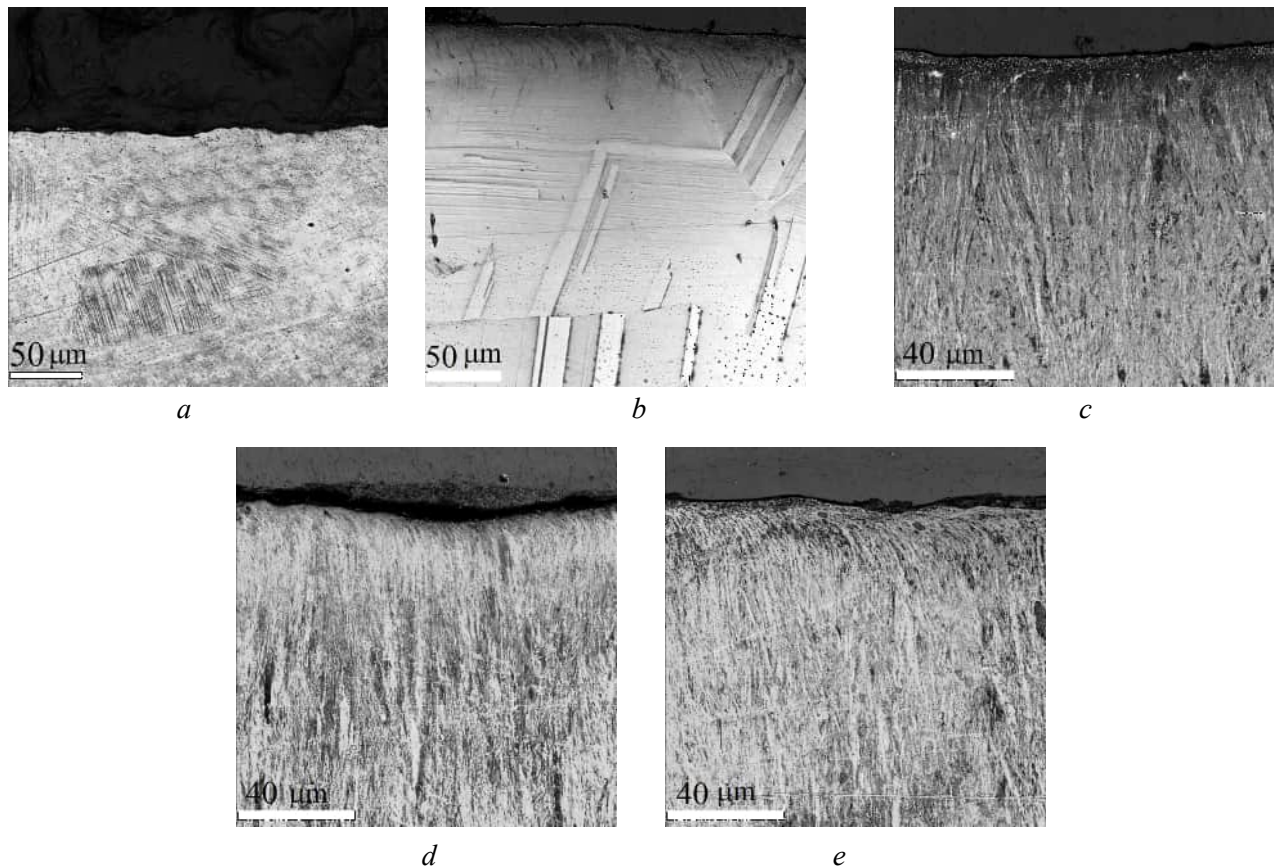
Fig. 11. Metallographic images of bronze 96% *Cu*-3% *Si*-1% *Mn* below the worn surfaces. Sample 1 (*a*),
Sample 2 (*b*), Sample 3 (*c*), Sample 4 (*d*) and Sample 5 (*e*)
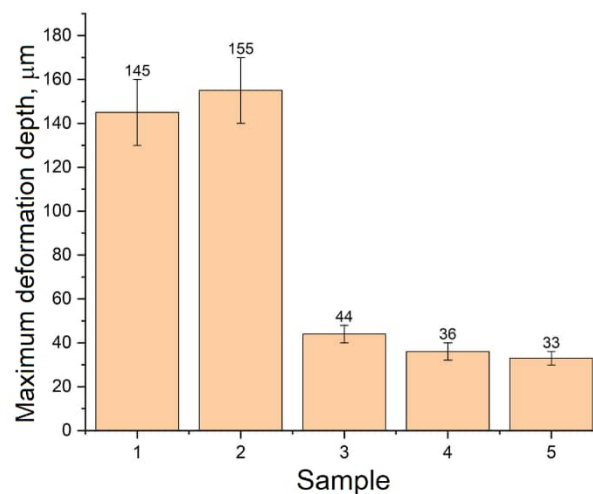
Fig. 12. Depth of penetration of plastic
deformation below the worn surface

Conclusions

Experimental studies of the mechanical, tribological, and structural characteristics of a silicon bronze in different structural states – ranging from coarse-grained (produced by electron-beam additive manufacturing and hot rolling) to submicron-grained (resulting from severe plastic deformation via multi-axial forging and rolling) – yield the following conclusions:

1. The manufacturing method significantly influences the structural state of silicon bronze. Wire and electron-beam additive manufacturing (*WEBAM*) and hot rolling produce very large grains (150–600 μm

or more). Multi-axial forging produces nano-sized subgrains (lamellae under 100 nm) with high dislocation density. Subsequent rolling after forging further refines the structure, creating subgrains elongated along the rolling direction. Low-temperature annealing after rolling yields more equiaxed submicron grains (100–200 nm) with reduced dislocation density.

2. The structural state directly determines the mechanical properties. In the coarse-grained condition, the alloy exhibits low strength ($\sigma_u \approx$ 340–346 MPa) and hardness ($HV \approx$ 0.86–0.96 GPa) but high ductility ($\delta \approx$ 70–100%). The refined structures produced by *SPD* methods show a sharp increase in strength (σ_u up to 3 times higher) and hardness (HV up to 3.9 times higher), accompanied by a drop in ductility (δ decreasing from 100% to a minimum of 9.2%). Low-temperature annealing after rolling maintains high strength while slightly improving the ductility of the deformed material.

3. The structural state also governs the tribological characteristics. The lowest coefficient of friction was observed in samples subjected to severe plastic deformation. Furthermore, sliding friction for these samples was more stable, as evidenced by the lowest recorded amplitudes of vibration acceleration.

4. The structural state and mechanical properties significantly influence the wear mechanisms. The hot-rolled sample wears primarily by an adhesive mechanism. In high-strength samples processed by multi-axial forging and rolling, oxidative wear predominates. A mixed adhesive-oxidative mechanism was observed in the *WEBAM*-fabricated sample. The depth of plastic deformation penetration beneath the worn surface correlates strongly with the material's strength and hardness, reaching 145–155 μm in Sample 1 and Sample 2, but decreasing by a factor of 3.3–4.7 in the *SPD*-processed Samples 3–5.

5. Severe plastic deformation by multi-axial forging and rolling reduces the wear of silicon bronze by a factor of 2.1–2.2 compared to the as-received hot-rolled condition. Low-temperature annealing increases wear by 10% compared to the cold-worked Sample 4.

6. From a practical perspective, the results recommend the sequential application of multi-axial forging followed by rolling to achieve maximum wear resistance and sliding stability. This processing route yields high hardness (3.34 GPa), minimal wear (2.2 times lower than the hot-rolled condition), and the lowest and most stable coefficient of friction and vibration acceleration amplitude. Material with these properties is suitable for critical friction pairs operating under dry or boundary lubrication conditions where wear and vibration control are paramount.

7. To achieve maximum strength with acceptable ductility, low-temperature annealing after severe plastic deformation is recommended. This processing provides maximum strength with partial restoration of ductility. Material in this structural state is advisable for highly loaded structural components subjected to static and moderate dynamic loads, where strength is critical and wear resistance is of secondary importance.

References

1. Osintsev O.E., Fedorov V.N. *Med' i mednye splavy. Otechestvennye i zarubezhnye marki* [Copper and copper alloys. Domestic and foreign brands]. 2nd ed., rev. and enl. Moscow, Innovatsionnoe mashinostroenie Publ., 2016. 360 p. ISBN 978-5-9907638-3-8.

2. Kroupa A., Zobac O., Zemanova A., Richter K.W. CALPHAD-type reassessment of Cu-Si and full assessment of the Al-Cu-Si systems. *Journal of Phase Equilibria and Diffusion*, 2024, vol. 45, pp. 1206–1243. DOI: 10.1007/s11669-024-01160-5.

3. Shee S.K., Pal H., Pradhan S.K., De M. Correlation of microstructure with mechanical property of Cu-Si-Mn alloys. *Materials Engineering*, 1996, vol. 7 (4), pp. 431–442.

4. Nnakwo K.C., Mbah C.N., Daniel-Mkpume C.C. Investigation of the structural sensitive behavior of Cu-3Si-xMn ternary alloys. *Journal of King Saud University – Science*, 2019, vol. 31, pp. 1056–1063. DOI: 10.1016/j.jksus.2019.01.001.

5. Chromik R.R., Neils W.K., Cotts E.J. Thermodynamic and kinetic study of solid state reactions in the Cu–Si system. *Journal of Applied Physics*, 1999, vol. 86, pp. 4273–4281. DOI: 10.1063/1.371357.

6. Ezeobi U.E., Nwambu C.N., Nnuka E.E., Bosan B.M. Effect of solutionizing heat treatment on the structure and mechanical properties of silicon bronze (Cu-10wt%Si-2wt%Ni). *Archive of Biomedical Science and Engineering*, 2024, vol. 10, pp. 017–022. DOI: 10.17352/abse.000033.

7. Mattern N., Seyrich R., Wilde L., Baehtz C., Knapp M., Acker J. Phase formation of rapidly quenched Cu–Si alloys. *Journal of Alloys and Compounds*, 2007, vol. 429, pp. 211–215. DOI: 10.1016/j.jallcom.2006.04.046.

8. Kolubaev E.A., Rubtsov V.E., Chumaevsky A.V., Astafurova E.G. Micro-, meso- and macrostructural design of bulk metallic and polymetallic materials by wire-feed electron-beam additive manufacturing. *Physical Mesomechanics*, 2022, vol. 25 (6), pp. 479–491. DOI: 10.1134/S1029959922060017.

9. Kulczyk M., Skiba J., Przybysz S., Pachla W., Bazarnik P., Lewandowska M. High strength silicon bronze (C65500) obtained by hydrostatic extrusion. *Archives of Metallurgy and Materials*, 2012, vol. 57 (3), pp. 859–862. DOI: 10.2478/v10172-012-0094-4.

10. Tavolzhanskii S.A., Vedenkin E.D., Plisetskaya I.V., Nikitina A.A. Study of properties and structure of silicon bronze CuSi3Mn1 (C65500) wire at various stages of its production by continuous casting and subsequent drawing. *Metallurgist*, 2022, vol. 66, pp. 962–969. DOI: 10.1007/s11015-022-01408-w.

11. Filippov A., Shamarin N., Moskvichev E., Savchenko N., Kolubaev E., Khoroshko E., Tarasov S. The effect of heat input, annealing, and deformation treatment on structure and mechanical properties of electron beam additive manufactured (EBAM) silicon bronze. *Materials*, 2022, vol. 15, p. 3209. DOI: 10.3390/ma15093209.

12. Huang K., Logé R.E. A review of dynamic recrystallization phenomena in metallic materials. *Materials & Design*, 2016, vol. 111, pp. 548–574. DOI: 10.1016/j.matdes.2016.09.012.

13. Vorontsov A., Gurianov D., Zykova A., Nikonov S., Chumaevskii A., Kolubaev E. Phase formation and morphological characteristics of aluminum bronze and nickel alloy composites produced by the additive manufacturing process. *Scripta Materialia*, 2024, vol. 239, p. 115811. DOI: 10.1016/j.scriptamat.2023.115811.

14. Hansen N. Hall–Petch relation and boundary strengthening. *Scripta Materialia*, 2004, vol. 51, pp. 801–806. DOI: 10.1016/j.scriptamat.2004.06.002.

15. Yang B., Vehoff H. Dependence of nanohardness upon indentation size and grain size – A local examination of the interaction between dislocations and grain boundaries. *Acta Materialia*, 2007, vol. 55, pp. 849–856. DOI: 10.1016/j.actamat.2006.09.005.

16. Liu G., Ni S., Song M. Effect of indentation size and grain/sub-grain size on microhardness of high purity tungsten. *Transactions of Nonferrous Metals Society of China*, 2015, vol. 25, pp. 3240–3246. DOI: 10.1016/S1003-6326(15)63958-9.

17. Popov V.L., Heß M., Willert E. *Handbook of plane contact mechanics*. Berlin, Heidelberg, Springer, 2025. 260 p. DOI: 10.1007/978-3-662-70173-7.

18. Filippov A.V., Rubtsov V.E., Tarasov S.Yu. Acoustic emission study of surface deterioration in tribocontacting. *Applied Acoustics*, 2017, vol. 117, pp. 106–112. DOI: 10.1016/j.apacoust.2016.11.007.

19. Hase A., Sato Y., Shinohara K., Arai K. Identification of the wear process of a silver-plating layer by dual acoustic emission sensing. *Coatings*, 2021, vol. 11, p. 737. DOI: 10.3390/coatings11060737.

20. Morita M., Tachiyama S., Onodera K., Hase A. Study on reaction mechanism of sulfur and phosphorus type additives using an acoustic emission technique. *Tribology Online*, 2022, vol. 17, pp. 78–85. DOI: 10.2474/trol.17.7.

21. Mishina H., Hase A. Effect of the adhesion force on the equation of adhesive wear and the generation process of wear elements in adhesive wear of metals. *Wear*, 2019, vol. 432–433, p. 202936. DOI: 10.1016/j.wear.2019.202936.

Conflicts of Interest

The authors declare no conflict of interest.

Obrabotka metallov –
Metal Working and Material Science

Effect of heat treatment on the structure and properties of magnesium alloy MA20 subjected to severe plastic deformation

Nikita Luginin [1, 2, a], Anna Eroshenko [1, b, *], Konstantin Prosolov [1, c], Margarita Khimich [1, d], Ivan Glukhov [1, e], Alexander Panfilov [1, f], Alexey Tolmachev [1, g], Pavel Uvarkin [1, h], Alexander Kashin [1, i], Yurii Sharkeev [1, 2, j]

[1] Institute of Strength Physics and Materials Sciences SB RAS, 2/4 per. Academicheskii, Tomsk, 634055, Russian Federation
[2] National Research Tomsk Polytechnic University, Lenin Ave., 30, Tomsk, 634050, Russian Federation

[a] https://orcid.org/0000-0001-6504-8193, ✉ nikishek90@ispms.ru; [b] https://orcid.org/0000-0001-8812-9287, ✉ eroshenko@ispms.ru;
[c] https://orcid.org/0000-0003-2176-8636, ✉ konstprosolov@ispms.ru; [d] https://orcid.org/0000-0001-5859-7418, ✉ khimich@ispms.ru;
[e] https://orcid.org/0000-0001-5557-5950, ✉ gia@ispms.ru; [f] https://orcid.org/0000-0001-8648-0743, ✉ alexpl@ispms.ru;
[g] https://orcid.org/0000-0003-4669-8478, ✉ tolmach@ispms.ru; [h] https://orcid.org/0000-0003-1169-3765, ✉ uvarkin@ispms.ru;
[i] https://orcid.org/0000-0003-1860-3654, ✉ kash@ispms.ru; [j] https://orcid.org/0000-0001-5037-245X, ✉ sharkeev@ispms.ru

ARTICLE INFO

ABSTRACT

Introduction. One of the most promising fields for the application of magnesium alloys is medicine. Their key advantages are bioresorbability and a low elastic modulus, comparable to that of human cortical bone (up to 30 GPa). Biocompatible *Mg-Zn-Zr-Ce* (*MA20*) system alloys are among the most promising for medical applications. Due to their relatively low mechanical properties, the development of severe plastic deformation (*SPD*) techniques for forming an ultrafine-grained (*UFG*) state in bulk billets of the *Mg-Zn-Zr-Ce* alloy to achieve optimal functional properties requires further research. Analyzing the conditions for forming a high-strength *UFG* state necessitates considering various strengthening mechanisms, including well-known ones related to the effect of *UFG* structures. Identifying the deformation and strain hardening mechanisms in magnesium alloys subjected to *SPD* is also highly relevant. The **purpose of this work** is to establish the mechanisms of strain hardening and to investigate the influence of heat treatment on the structure and properties of the *MA20* magnesium alloy after combined *SPD*. **Research methods.** The study object was the *MA20* alloy in a *UFG* state (wt. %: *Mg* – 98.0; *Zn* – 1.3; *Ce* – 0.1; *Zr* – 0.1; *O* – 0.5). The *UFG* state was achieved via a combined *SPD* process involving *ABC*-pressing followed by multi-pass rolling in grooved rolls. To study the effect of annealing on the microstructure and mechanical tensile properties, samples were annealed in air at temperatures of 200, 250, 300, and 500 °C for 24 hours. The microstructure and phase composition of the samples were investigated using optical and transmission electron microscopy. **Results and discussion.** It was established that applying a combined *SPD* method (*ABC*-pressing and multi-pass rolling) to the *MA20* alloy results in the formation of an ultrafine-grained structure with an average grain size of about 1 μm. This leads to a significant increase in yield strength ($\sigma_{0.2}$) to 250 MPa and ultimate tensile strength (σ_u) to 270 MPa, while simultaneously reducing ductility to 3%. Annealing at 200 °C was found to preserve the *UFG* state in the *MA20* alloy and to lead to a 100% increase in ductility, with an 8% decrease in $\sigma_{0.2}$ and a 4% decrease in σ_u compared to the initial *UFG* state (non-annealed). ***Conclusions.*** It was revealed that the grain boundary ($\sigma_{grain} = 202$ MPa) and dislocation ($\sigma_{dis} = 69$ MPa) strengthening contributions provide the most significant increase in the strength of the *UFG MA20* magnesium alloy. For the magnesium alloy in the *UFG* and fine-grained (*FG*) states, a critical grain size interval of (1–7) μm was identified, corresponding to a sharp increase in the intensity of change for the calculated contributions of dislocation ($d\sigma_{dis}/dd$), grain boundary ($d\sigma_{grain}/dd$), overall strengthening ($d\sigma_{total}/dd$), and dislocation density ($d\rho/dd$). For the coarse-grained (*CG*) state of the alloy in the grain size range (7–40) μm, these parameters stabilize.

* Corresponding author
Eroshenko Anna Yu., Ph.D. (Engineering), Senior Researcher
Institute of Strength Physics and Materials Science SB RAS,
2/4 per. Academicheskii,
634055, Tomsk, Russian Federation
Tel.: +7 3822 286 911, **e-mail**: eroshenko@ispms.ru

Introduction

One of the most promising areas for the use of magnesium alloys is considered to be medicine [1]. Their key advantages are bioresorbability and a relatively low elastic modulus, comparable to that of human cortical bone (up to 30 GPa). The matching of the elastic moduli of bone tissue and the magnesium alloy eliminates high stresses at the bone-implant interface [2]. Magnesium and its alloys have the ability to undergo bioresorption, making them useful for certain types of orthopedic and vascular surgeries. The resorption of a magnesium implant and its replacement by bone tissue in the body during treatment avoids the need for repeated surgical intervention. The disadvantages of magnesium alloys include low corrosion resistance and the release of hydrogen during metal corrosion [3]. Furthermore, for some implants subjected to load-bearing applications, the level of strength properties does not meet the necessary requirements. Alloying magnesium with specific elements can reduce the resorption rate of the implanted device, thereby increasing corrosion resistance, as well as enhance mechanical strength while maintaining satisfactory ultimate plasticity.

Elements considered favorable for medical applications include Ca, Mn, Zn, Sn, Sr, and Ce [4]. The most promising for medical applications are alloys based on the Mg-Zn-Zr system. The addition of Ce up to 0.3 wt. % to the Mg-Zn-Zr system improves plasticity [5]. Microalloying with Ce leads to the formation of finer and more spherical intermetallic compounds, which promote the nucleation of crystallization sites and refine the average grain size [6].

In magnesium alloys, an enhancement of mechanical properties can be achieved by refining the grain structure using methods of severe plastic deformation (SPD) [7]. This approach allows for a 2 to 2.5-fold increase in strength properties without the introduction of additional alloying elements, due to the formation of an ultrafine-grained (UFG) structure.

To date, there are publications presenting research results on the structure [5] and mechanical properties [8] of Mg-Zn-Zr system alloys with additions of Ce and Ca in various structural states [9]. However, despite a number of publications [1,3,4,10-12] dedicated to achieving an ultrafine-grained (UFG) state in magnesium alloys via SPD methods, the problem of obtaining an average grain size of less than 1 μm still remains. Furthermore, there is a need to identify regimes for the subsequent thermal treatment of magnesium alloy products to relieve residual internal stresses and enhance plasticity while simultaneously preserving the UFG structure of the alloy. UFG and fine-grained (FG) states in magnesium alloys are characterized by relatively low plasticity and limited fatigue endurance. This is associated with the peculiarities of their hexagonal close-packed (HCP) lattice, in which deformation occurs primarily through slip on basal planes, significantly reducing the workability of products and semi-finished workpieces made from such alloys.

At room temperature, two main deformation mechanisms are realized in magnesium alloys: basal slip and twinning [13]. An increase in temperature during deformation leads to the activation of several slip planes: basal {0001}, prismatic {1010}, pyramidal {1122}, and twinning {1012}, and consequently, to an increase in the plasticity of magnesium after deformation processing [14]. Therefore, the pressure treatment of magnesium and its alloys is conducted at temperatures of 250-430 °C, which allows for the activation of prismatic and pyramidal slip systems [15], as well as secondary twinning [16]. A study of the deformation behavior of magnesium and its alloys in [17] showed that at temperatures below 225 °C, the primary deformation mechanism is twinning, which usually leads to a sharp drop in plasticity.

It is known that the UFG structure formed by SPD methods in metals and alloys has its own specific features associated with the small grain size, high lattice curvature, extensive non-equilibrium grain boundaries, etc., which leads to a significant increase in the strength of materials [18]. Furthermore, the use of SPD methods promotes the segregation of alloying elements at grain boundaries and the formation of fine dispersoids of secondary phases [19]. In combination with the ultrafine-grained structure, this provides an additional contribution to the enhancement of the strength characteristics of metals. In this regard, research aimed at analyzing the influence of various strengthening mechanisms on strength properties, including UFG alloys, is of particular relevance.

For magnesium alloys, strengthening mechanisms have been studied in works [12,20]. Study [12] established that in the Mg-1Zn-0.2Ca alloy, microalloying with Zn and Ca promotes the realization of the

grain boundary strengthening mechanism by refining the structure to an FG state during multi-directional isothermal forging. This made it possible to significantly increase the mechanical properties in tensile tests, raising the yield strength to 210 MPa, the ultimate tensile strength to 260 MPa, and the elongation to failure to 20 %.

The authors of [21] investigated the effect of extrusion on the microstructure of an Mg-Y-Gd-Zr alloy, which was additionally alloyed with Sm and Gd. It was found that the reduction in grain size is related to the magnitude of accumulated strain. The study also investigated the influence of the Sm addition on the kinetics of the decomposition of the magnesium solid solution in the Mg-Y-Gd-Zr alloy in the deformed state. It was shown that after deformation, the Mg-Y-Gd-Zr and Mg-Y-Gd-Sm-Zr alloys were additionally strengthened by the solid solution mechanism.

In work [20], a significant contribution of strain hardening to the overall strength of an alloy from the Mg-Zn-Ca system was identified. It is shown that the application of a combined SPD method allows for a reduction of the average grain size from 220 to 20 μm, thereby increasing the ultimate strength of the alloy from 144 to 233 MPa.

To analyze the conditions for the formation of a high-strength state in UFG alloys, it is necessary to account for various strengthening mechanisms, including well-known ones associated with the influence of UFG structures. Therefore, the issues of identifying the deformation and strain hardening mechanisms of magnesium alloys formed under severe deformation conditions require further investigation.

The aim of this work was to establish the mechanisms of strain hardening in MA20 alloy subjected to combined SPD and to determine the influence of heat treatment on its structure and properties. To achieve this aim, the following ***research tasks*** were set:

1. To evaluate the grain size in MA20 alloy after the application of the SPD method.

2. To perform mechanical testing of alloy samples in various states to assess the strength and plasticity of the alloy.

3. To evaluate the contributions of various strengthening mechanisms (grain boundary, dislocation, etc.) to the yield strength of the alloy under different thermal treatments.

4. To determine the grain size interval at which a change in the strain hardening mechanisms of MA20 magnesium alloy occurs.

Research methodology

The object of the study was the commercial magnesium alloy (MA20) of the Mg-Zn-Zr-Ce system, developed at the All-Russian Scientific Research Institute of Aviation Materials (Moscow, Russia). The magnesium alloy billet was produced by remelting at the All-Russian Institute of Light Alloys (Moscow, Russia, JSC VILS) followed by hot rolling to a plate thickness of 30 mm. The alloy had the following composition (wt. %): Mg – 98.0; Zn – 1.3; Ce – 0.1; Zr – 0.1; O – 0.5.

The UFG state in MA20 magnesium alloy was achieved using a combined SPD method, consisting of 3abc pressing and multi-pass rolling [22]. At the 3abc pressing stage, the billet was pressed in a die at a temperature of 250 °C, being rotated by 90° after each pressing cycle. The total logarithmic strain for all pressing stages amounted to 1.1. Rolling of the samples, preheated to 250 °C, was carried out at room temperature to a total logarithmic strain of 1.5.

To investigate the influence of the final heat treatment temperature on the mechanical properties of the magnesium alloy, samples in the UFG state were annealed at temperatures of 200, 250, and 300 °C for 24 hours in a SNOL 10/11 muffle furnace and cooled in air. The selected temperature-time regimes of thermal treatment ensured a low rate of diffusion processes in the magnesium alloys [23]. For the complete relaxation of stresses, the initial alloy was annealed at a temperature of 500 °C for 8 hours in a SNOL 10/11 muffle furnace followed by cooling in air.

The microstructure of the obtained billets was studied using an optical microscope (Altami MET 1 MT, St. Petersburg, Russia) and a transmission electron microscope (TEM) (JEOL JEM 2100 electron microscope, Tokyo Boeki Ltd., Tokyo, Japan) equipped with an energy-dispersive X-ray spectroscopy
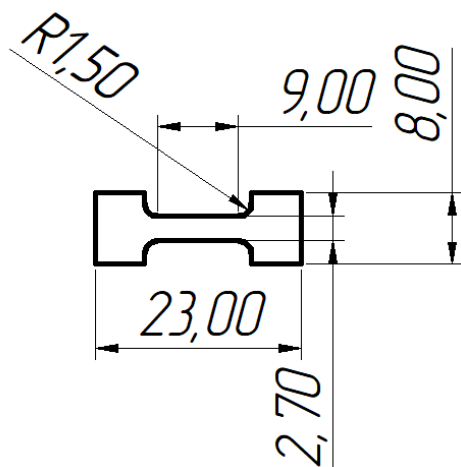
Fig. 1. Schematic representation of specimens for mechanical tensile testing

(EDS) attachment. The elemental composition of the samples prior to deformation was determined using a Niton XL3t X-ray fluorescence analyzer (Thermo Scientific, Massachusetts, USA).

Microhardness measurements were conducted using the Vickers method on a Duramin-5 tester (Struers, Ballerup, Denmark). The yield strength, ultimate tensile strength, and maximum elongation were determined during tensile tests using a UTS-110M-100 testing machine (Test-Sistemy, Ivanovo, Russia). For these tests, flat "dog-bone" shaped specimens with the following working dimensions were used: thickness – 3.0 mm, width – 2.7 mm, length – 9.0 mm. A diagram of the specimens for mechanical testing is presented in Figure 1. The specimens were manufactured using the wire electrical discharge machining (EDM) method.

Sample preparation for transmission electron microscopy (TEM) was performed by cutting the billets into 0.3 mm thick plates using electrical discharge machining (EDM), which were then mechanically thinned to a thickness of 0.1 mm on P2500 grit sandpaper. Further sample preparation was carried out by ion milling using an ion mill (JEOL Ion Slicer EM-09100IS, Tokyo Boeki Ltd., Tokyo, Japan). Interplanar spacing data were calculated from microdiffraction patterns using the Crystallography Open Database (COD) as of 21.01.2025. The average size (of grains, subgrains, fragments) was determined by the linear intercept method. The scalar dislocation density was determined by the linear intercept method using bright-field TEM images and the following formula [24]:

$$< \rho > = \frac{1}{t} \cdot \left(\frac{N_1}{L_1} + \frac{N_2}{L_2} \right), \tag{1}$$

where $t = 150$ nm is the foil thickness; N_1 and N_2 are the total numbers of intersections of dislocations with the horizontal and vertical lines, respectively, drawn on the bright-field TEM image; L_1 and L_2 are the total lengths of all horizontal and vertical lines, respectively, drawn on the bright-field TEM image, nm.

Additionally, the types of dislocation substructures were determined based on the corresponding values of scalar dislocation density and electron microscopy images of the regions of the studied samples. The assessment of the contributions of various mechanisms to the strain hardening of the alloy for the investigated structural states was performed according to the methodology presented in [19].

Subsequently, dependencies of dislocation density and the contributions of strengthening mechanisms on the average grain size were plotted. The obtained dependencies were differentiated, and the derivatives were plotted, characterizing the intensity of change in the contributions of the strengthening mechanisms, the total stress, and the dislocation density with respect to the grain size.

Results and Discussion

Figure 2a shows an optical image of the microstructure of MA20 magnesium alloy in the initial coarse-grained (CG) state. The alloy's microstructure consists of equiaxed grains based on an α-solid solution of alloying elements in magnesium. The average grain size, determined by the linear intercept method, was 25.0 ± 10.0 μm. A large number of predominantly spherical particles and regions of particle accumulation are observed inside the grains, which are uniformly distributed within the grains.

According to literature data, in alloys of the Mg-Zn-Zr-Ce system, these particles are identified as nanoscale intermetallic compounds $MgZn_2$, $CeZn_3$, and Ce_3Zn_{11} [25]. Furthermore, the alloys contain larger particles ranging from 2 to 10 μm, which are zirconium and cerium hydrides (ZrH_2 and Ce_2H_5) [22].

During deformation, hydride particles can acquire additional mobility, which, in turn, leads to their further agglomeration in the process of deformation, affecting the level of mechanical properties. Thus, the authors of [26] established the role of the influence of hydrides and dissolved hydrogen in the magnesium
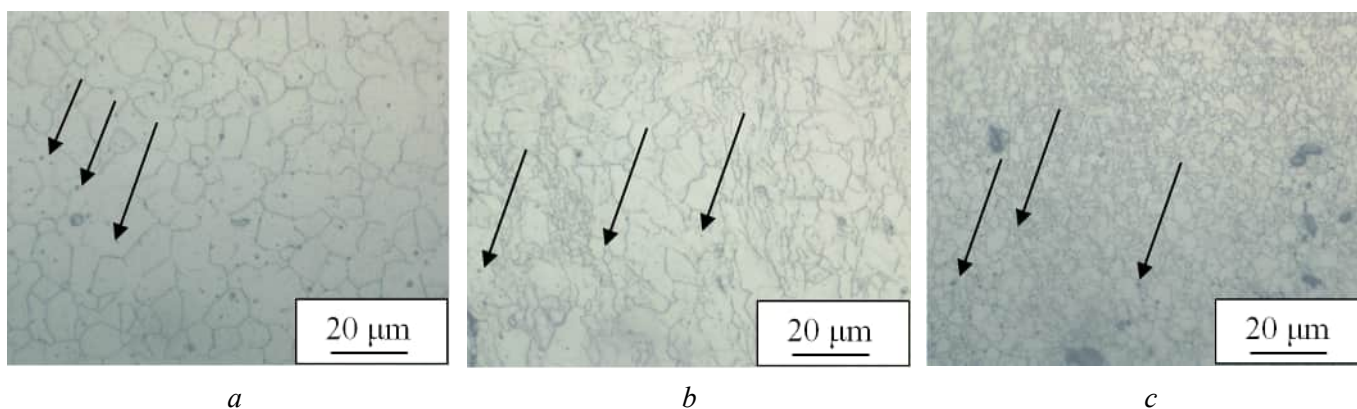
a   *b*   *c*

Fig. 2. Optical images of the microstructure of the *MA20* alloy in different states:
a – CG; b – FG; c – UFG. Particles of hydrides and intermetallics are indicated by arrows

matrix on the mechanical properties of Mg-Al, Mg-Zn, Mg-Ca, and Mg-RE alloy systems. It was shown that hydrides reduce the mechanical properties of magnesium alloys because they act as sinks for dislocations, leading to crack formation. Hydrides also agglomerate during deformation. This reduces the material's plasticity and is a significant drawback that limits the practical application of magnesium alloys [27]. A more detailed description of the microstructure of the MA20 alloy was provided by the authors of this study in work [22].

The average grain size decreases after deformation by 3abc pressing. After 3abc pressing, a fine-grained (FG) state is formed with an average grain size of 3.0 ± 1.5 μm (Figure 2b). The fraction of hydride and intermetallic particles remains unchanged after the deformation processing. Most grains are non-equiaxed and have an irregular shape. Subsequent deformation by rolling promoted additional refinement of the primary phase microstructure to 1.0 ± 0.7 μm (Figure 2c), which corresponds to an ultrafine-grained (UFG) state. According to optical metallography data (Figure 2), deformation by rolling leads to the agglomeration of particles and hydrides, which may indicate their high mobility during SPD [28].

The results of TEM studies of the alloy's microstructure in the CG state are presented in Figure 3. Bright-field TEM images show equiaxed grains of the primary phase based on an α-solid solution of alloying elements in magnesium (HCP lattice) and particle inclusions (Figure 3a, d). As a result of microdiffraction analysis, the intermetallic compounds $MgZn_2$, $CeZn_3$, and Ce_3Zn_{11} were identified in the CG alloy (Figure 3b, e). Figure 3a, c, d, e present dark-field and bright-field images of $MgZn_2$, $CeZn_3$, and Ce_3Zn_{11} particles.

Additionally, EDS analysis was performed, which showed that in $MgZn_2$ particles, the ratio of magnesium to zinc (at. %) is 1.5:2, which corresponds to the stoichiometric composition of the intermetallic compound, since magnesium is the primary phase in the alloy. For the $CeZn_3$ and Ce_3Zn_{11} intermetallics, the element ratios (at. %) are 1:3.5 and 1:4, respectively, which are close to the stoichiometric compositions of the particles.

According to the Mg-Zn [29] and Zn-Ce [30] phase diagrams, the indicated intermetallic compounds are stable and exist at room temperature. It should be noted that intermetallic compounds can significantly influence deformation processes by inhibiting grain boundary motion [19].

After *abc*-pressing, subgrains form inside the matrix grains (Figure 4a). A network dislocation substructure forms inside the subgrains (Figure 4b, c) with a scalar dislocation density of $5 \cdot 10^9$ cm^{-2}. The phase composition of the alloy in the FG state corresponds to that of the alloy in the CG state. The alloy contains intermetallic compounds $MgZn_2$, $CeZn_3$, and Ce_3Zn_{11}, as well as a certain amount of zirconium hydride ZrH_2 and cerium hydride Ce_2H_5, which was confirmed by SEM studies and X-ray phase analysis by the authors in a previous work [22].

Combined SPD (*abc*-pressing + rolling) leads to the formation of a UFG structure with an average grain size of 1.0 ± 0.7 μm. TEM images reveal a cellular-network dislocation substructure (Figure 5b, c) with a scalar dislocation density of $2 \cdot 10^{10}$ cm^{-2}. The phase composition of the alloy did not change qualitatively after the combined SPD.
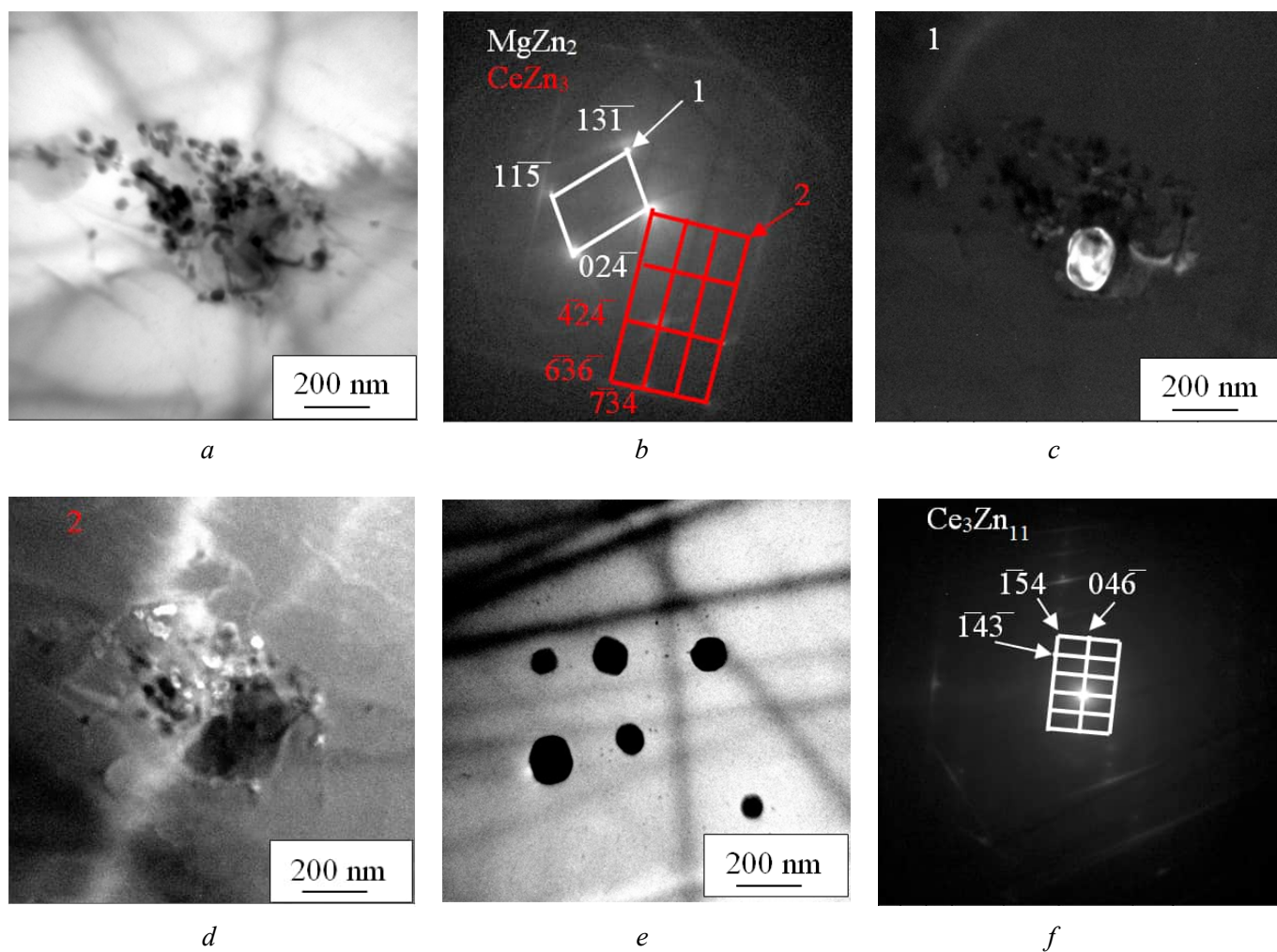
Fig. 3. TEM images of the microstructure of the magnesium alloy in the *CG* state:

a, e – bright-field image of particles *MgZn₂*, *CeZn₃* and *Ce₃Zn₁₁*; *b, f* – microdiffraction pattern from intermetallic compounds *MgZn₂*, *CeZn₃* and *Ce₃Zn₁₁*; *c, d* – dark-field image of particles *MgZn₂* and *CeZn₃*

Fig. 4. TEM images of *MA20* alloy in the *FG* state:

a – bright-field image of the alloy grain structure; *b, c* – bright-field image of the dislocation substructure. Network dislocation structure is indicated by arrows

Fig. 5. Bright-field *TEM* images of *MA20* alloy in the *UFG* state:

a – subgrain structure; *b*, *c* – cellular-network dislocation substructure. Arrows indicate the dislocation substructure

At the next stage, microstructural studies were conducted for the UFG alloy samples after annealing for 24 hours at temperatures of 200, 250, and 300 °C. Optical images of the microstructure of the UFG alloy subjected to heat treatment at various temperatures are presented in Figure 6.

Based on the results of optical microscopy, it was established that annealing the magnesium alloy in the UFG state at a temperature of 200 °C preserves the UFG state of the alloy. Annealing at 250 and 300 °C increases the average grain size to 1.5 ± 0.8 μm and 7.0 ± 5.0 μm, respectively, transitioning the alloy into the FG state.

TEM images of the alloy's microstructure after thermal treatment are presented in Figure 7. The results of TEM studies confirm the optical microscopy data. Annealing at 200 °C leads to a decrease in dislocation density in the alloy from $2 \cdot 10^{10}$ to $9 \cdot 10^{9}$ cm^{-2}; however, the dislocation substructure remains largely unchanged – cellular-network (Figure 7a). An increase in the annealing temperature to 250 °C leads to an increase in grain size and a further decrease in the scalar dislocation density to $6 \cdot 10^{9}$ cm$^{-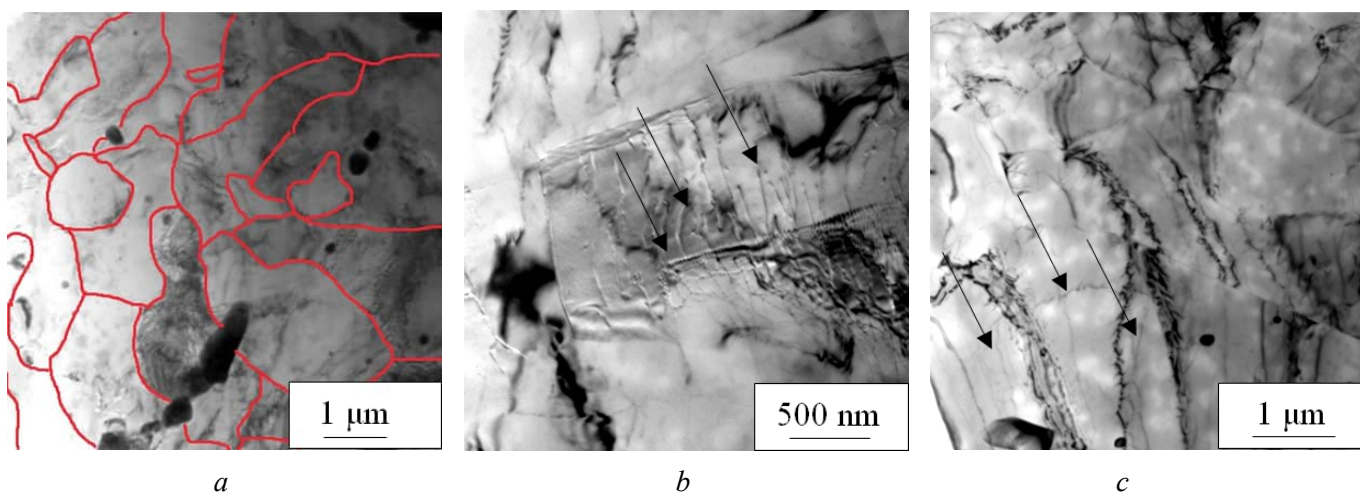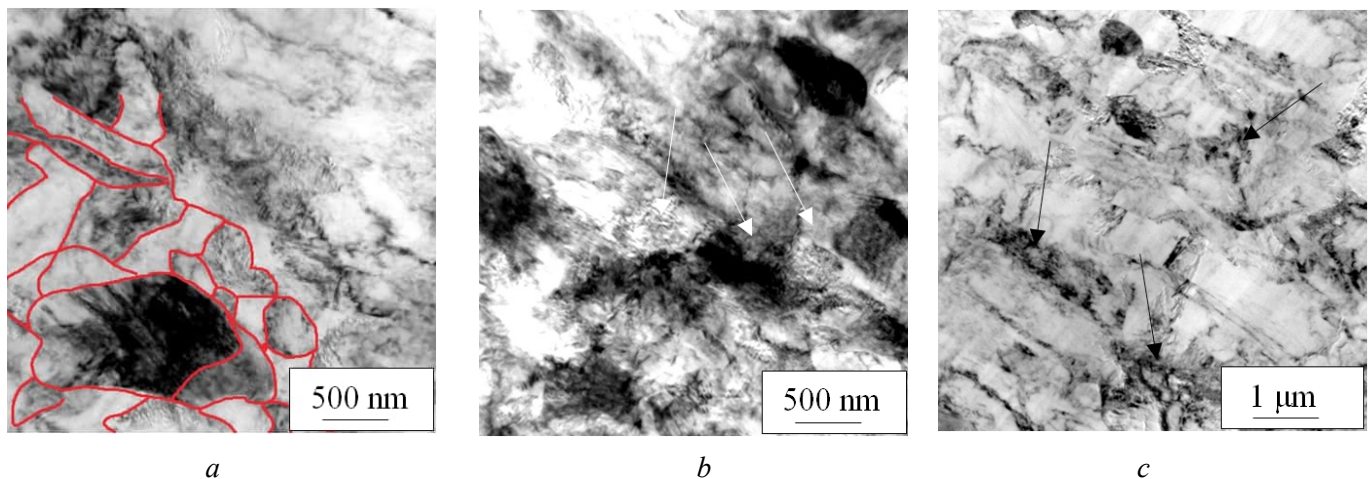2}$; the dislocation structure becomes a network with a chaotic distribution of dislocations within it (Figure 7b). The TEM images show that the alloy's structure becomes more homogeneous throughout the volume, which indicates the onset of recrystallization processes. A further increase in the annealing temperature to 300 °C leads to more intense recrystallization processes in the alloy and a substantial increase in grain size. The network dislocation structure transforms into individual dislocation clusters. The dislocation density decreases to $4 \cdot 10^{9}$ cm^{-2} (Figure 7c).

After annealing at 200 °C, the dislocation density was found to be 9×10^{9} cm^{-2}, which is lower than that of the UFG state ($2 \cdot 10^{10}$ cm^{-2}). An increase in the annealing temperature to 250 and 300 °C reduces the
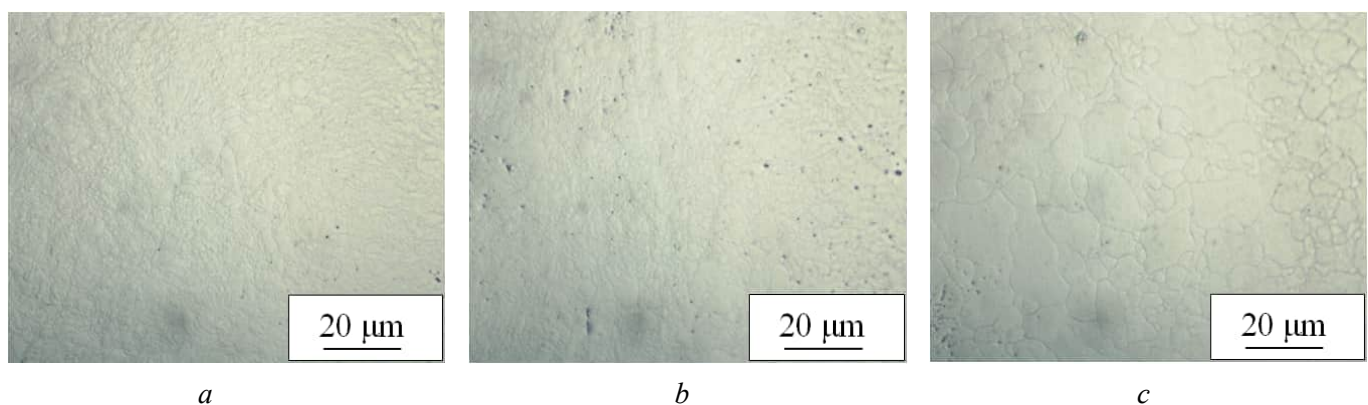
Fig. 6. Optical images of the structure of the *UFG* alloy after heat treatment:

a – 200 °C; *b* – 250 °C; *c* – 300 °C
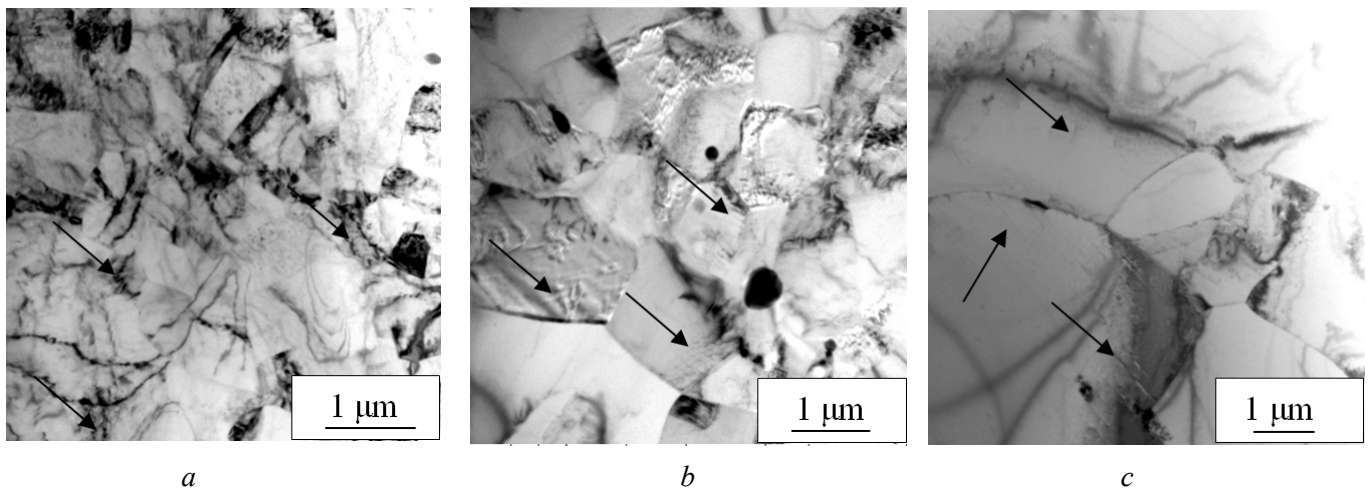
Fig. 7. Bright-field *TEM* images of the microstructure of the *UFG* alloy after heat treatment:

a – 200 °C, cellular-network dislocation structure; *b* – 250 °C, network dislocation structure; *c* – 300 °C, dislocation clusters and tangles. Arrows indicate the dislocation substructure

scalar dislocation density to $6 \cdot 10^9$ cm^{-2} (annealing at 250 °C) and further to $4 \cdot 10^9$ cm^{-2} (annealing at 300 °C), respectively, due to the activation of the recovery process [31].

Figure 8 shows the microstructure of the coarse-grained (initial) alloy after annealing at 500 °C. In this state, the structure has a distinct granular character and consists of equiaxed α-grains based on a magnesium solid solution (Figure 8a). The average grain size was 40.0 ± 15.0 μm. Furthermore, a small number of intermetallic particles of secondary phases, which did not dissolve during the annealing process, are observed along the grain boundaries.

Figure 9a presents the tensile stress-strain curves of the alloy samples. Mechanical testing showed that the UFG sample has the maximum values of yield strength and ultimate tensile strength ($\sigma_{0.2} = 250$ MPa and $\sigma_{UTS} = 270$ MPa) compared to the FG ($\sigma_{0.2} = 40$ MPa and $\sigma_{UTS} = 220$ MPa) and CG ($\sigma_{0.2} = 250$ MPa and $\sigma_{UTS} = 190$ MPa) states. The ultimate plasticity of the alloy for the UFG, FG, and CG states was 3%, 9%, and 13%, respectively.

Heat treatment of the alloy in the UFG state leads to a decrease in strength properties and an increase in the plasticity of the alloy (Figure 9b). Annealing at a temperature of 200 °C results in a 100% increase in plasticity and the achievement of high strength without changing the grain size. In this case, $\sigma_{0.2}$ and σ_{UTS} decrease slightly – by 8% and 4%, respectively – compared to the UFG state (without annealing). Fur-
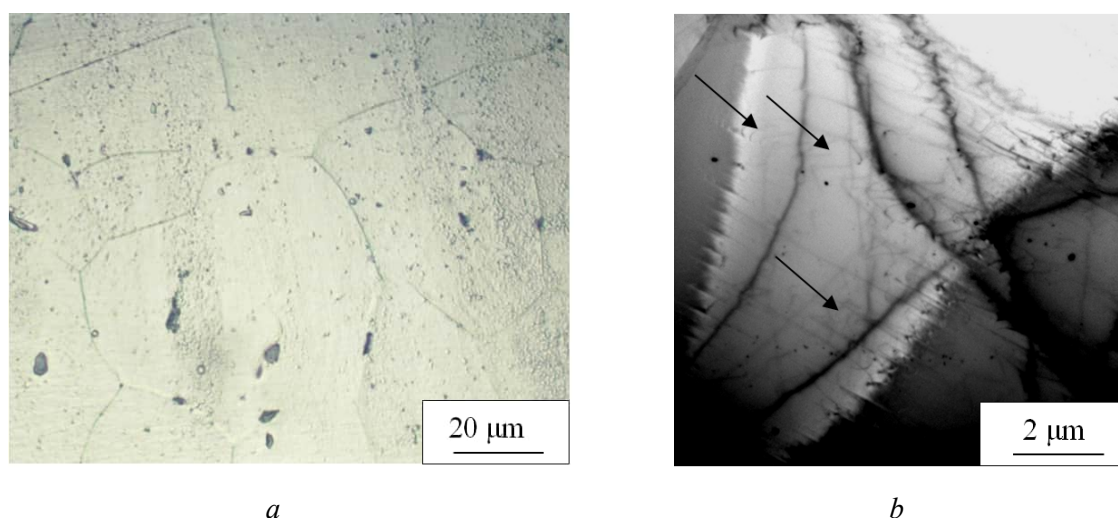
Fig. 8. Optical (*a*) and bright-field *TEM* (*b*) images of the alloy microstructure after annealing at 500 °C. Arrows indicate the dislocation substructure
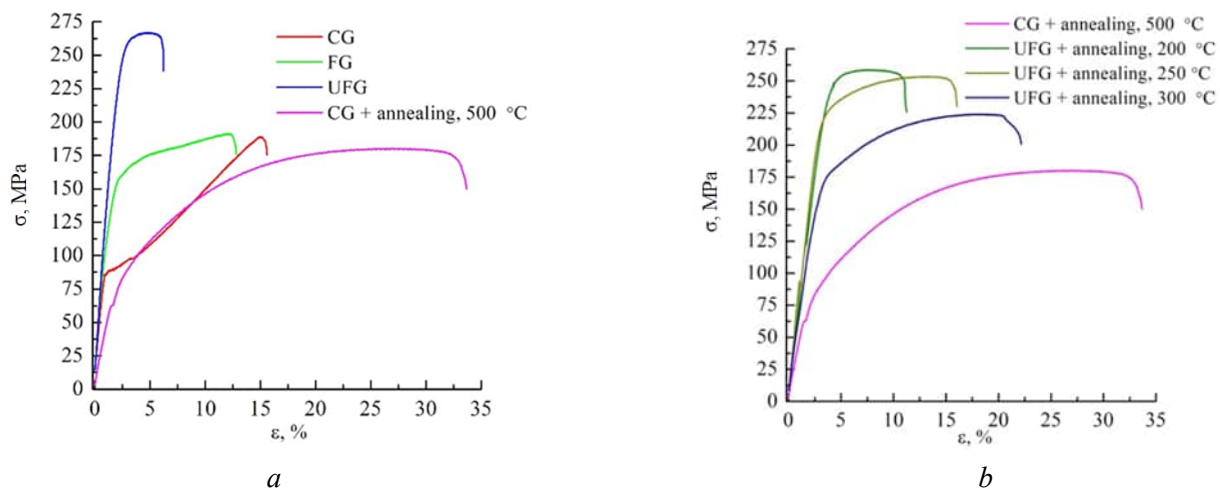
Fig. 9. Stress-strain curves in different structural states (*a*) and after annealing at 500, 300, 250 and 200 °C (*b*)

ther annealing of the alloy at 250 °C leads to an increase in ultimate plasticity and a decrease in the yield strength. Subsequently, annealing at 300 °C also results in a decrease in strength properties and an increase in ultimate plasticity due to a reduction in defect density and recrystallization.

High-temperature annealing (500 °C) of the alloy in the CG state, which was applied for the complete relaxation of internal stresDses, is characterized by active recrystallization, which leads to a sharp decrease in strength and the achievement of the highest plasticity.

Table 1 presents data on the influence of grain size on the mechanical properties of the alloy. To identify the main strengthening mechanisms in the magnesium alloy, an assessment of the contributions of the active

T a b l e 1

Mechanical and structural properties of MA20 alloy

Number	Alloy state	Average grain size, μm	$\sigma_{0,2}$, MPa	σ_{UTS}, MPa	δ, %	Scalar dislocation density, $\langle\rho\rangle$, cm^{-2} Dislocation substructure type
1	CG + annealing, 500 °C	40,0±15,0	60	180	25	$8\cdot10^{8}$ Individual dislocations and dislocation clusters
2	CG	25,0±10,0	90	190	13	$4\cdot10^{9}$ Dislocation clusters
3	UFG + annealing, 300 °C	7,0±5,0	150	220	17	$4\cdot10^{9}$ Dislocation clusters and tangles
4	FG	3,0±2,0	140	220	9	$5\cdot10^{9}$ Network dislocation substructure
5	UFG + annealing, 250°C	1,5±0,8	210	250	11	$6\cdot10^{9}$ Network dislocation substructure and dislocation clusters
6	UFG + annealing, 200 °C	1,0±0,7	230	260	6	$9\cdot10^{9}$ Network dislocation substructure
7	UFG	1,0±0,7	250	270	3	$2\cdot10^{10}$ Cellular-network dislocation substructure

Note: $\sigma_{0,2}$ – yield strength, σ_{UTS} – ultimate tensile strength, δ – elongation to failure.

strengthening mechanisms to the yield strength of the magnesium alloy was carried out [19,32]. This work involved the calculation of the additive contributions of strengthening mechanisms, such as the lattice friction stress, dislocation strengthening, and grain boundary strengthening, to the yield strength of the alloy:

$$\sigma_{total} = \sigma_0 + \sigma_{dis} + \sigma_{gb}, \tag{2}$$

where σ_{total} is the calculated yield strength of the alloy; σ_0 is the stress due to dislocation slip in a single crystal, as well as solid solution and dispersion strengthening; σ_{dis} is dislocation strengthening; σ_{gb} is grain boundary strengthening.

It is known that the primary strengthening mechanism in UFG metals and alloys is grain boundary strengthening, described by the Hall-Petch equation [18,19,33]. The mechanisms of strain hardening in magnesium alloys also include dislocation slip and twinning [34]. Study [35] demonstrated that the primary strengthening mechanism in samples of extruded AZ31 alloy under cyclic deformation according to a "compression-tension" scheme is twinning. Typically, active twinning in magnesium alloys promotes effective grain refinement even at low strains. Study [36] investigated a ZK60 alloy in the FG state (average grain size – 3 µm), produced by extrusion. It was established that the alloy deforms through twinning and basal slip at high strain rates ($\varepsilon = 10^3$ s^{-1}); however, at lower rates ($\varepsilon = 10^1$ s^{-1}), the twinning mechanism is suppressed, leading to a sharp decrease in the plasticity of the magnesium alloy.

In study [37], grain boundary strengthening for the magnesium alloy was determined using the Hall-Petch relationship:

$$\sigma_{gb} = Kd^{-1/2}, \tag{3}$$

where K is the Hall-Petch constant; d is the average grain size of the primary phase. Based on the obtained experimental data (Table 1), the dependence of the yield strength $\sigma_{0.2}$ on $d^{-1/2}$ was plotted (Figure 10). In the grain size interval of (1-40) µm, the dependence of $\sigma_{0.2}$ on $d^{-1/2}$ is linear (K = 202 MPa·µm$^{1/2}$). In accordance with the Hall-Petch relationship, for the studied alloy, the value of σ_{gb} is 40 MPa.

The contribution of the dislocation structure to the material's strengthening was calculated using the Taylor equation [38]:

$$\sigma_{dis} = b \cdot \div \cdot G \cdot \sqrt{<\rho>}, \tag{4}$$

where $\chi = 0.9$ is a constant characterizing the interaction between dislocations [38]; b = 0.321 nm is the magnitude of the Burgers vector for the most probable slip plane (the basal plane {0001} was considered as the most probable in this work); G = 17 GPa is the shear modulus for magnesium [39]; and $<\rho>$ is the scalar dislocation density. The dislocation density values for magnesium in various structural states are presented in Table 1.

The value of the friction stress σ_0 in a single crystal was taken as $\sigma_0 = 14$ MPa, assuming that this value corresponds to the σ_0 for the equilibrium state of the CG alloy (annealed at 500 °C). The value of σ_0 for the CG state of the alloy was estimated as: $\sigma_0 = \sigma_{0.2} - \sigma_{dis} - \sigma_{gb}$, where $\sigma_{0.2} = 60$ MPa (experimental data); $\sigma_{dis} = 14$ MPa and $\sigma_{gb} = 32$ MPa (calculated data, Table 2).

The calculated values of σ_{gb} and σ_{dis} are presented in Table 2. For the CG alloy, the contribution from grain boundary strengthening was

Fig. 10. Dependence of the yield strength $\sigma_{0.2}$ on the $d^{-1/2}$

<div align="right">T a b l e 2</div>

Contributions of different strain hardening mechanisms in *MA20* alloy in various structural states

Alloy state	σ_{dis}, MPa	σ_{gb}, MPa	σ_0, MPa	σ_{total}, MPa	$\sigma_{0,2}$, MPa
CG	16	40	14	96	90
FG	35	117	14	166	140
UFG	69	202	14	286	250
UFG + annealing at 200 °C	47	202	14	263	230
UFG + annealing at 250 °C	38	165	14	217	210
UFG + annealing at 300 °C	31	76	14	122	140
CG + annealing at 500 °C*	14	32	14	60	60

* Note: CG + annealing at 500 °C – annealing of the initial coarse-grained state of the alloy at 500 °C for 8 hours to achieve a large grain size and relaxation of internal stresses.

≈40 MPa. The transition of the alloy to the FG state is accompanied by a substantial increase in σ_{gb} – to 117 MPa, due to the significant refinement of the grain structure. The application of the combined SPD method, including abc press forging followed by rolling, forms a structure with a minimal grain size, which increases the value of grain boundary strengthening to 202 MPa. Annealing of the UFG alloy at 200 °C does not affect the value of σ_{gb} compared to the UFG state without annealing, while maintaining an average grain size of 1 μm. Annealing at 250 and 300 °C promotes grain growth to 1.5 and 7 μm, respectively, and thereby reduces the grain boundary strengthening of the alloy to 165 and 76 MPa.

Annealing the CG (initial) alloy at 500 °C leads to the formation of a coarse-grained structure, whereby the contribution of grain boundary strengthening decreases to 32 MPa.

For the alloy in the CG state, the contribution of the dislocation strengthening mechanism was 16 MPa. In the FG state, the dislocation density increases, and the contribution of dislocation strengthening reaches 35 MPa. The UFG state is characterized by a high dislocation density and the maximum contribution of dislocation strengthening – 69 MPa. Annealing at 200 °C causes microstructural relaxation, a significant reduction in dislocation density, and, consequently, a decrease in σ_{dis} to 47 MPa. Subsequent annealing at 250 and 300 °C leads to a reduction in σ_{dis} to 38 and 31 MPa, which can be attributed to the activation of recovery processes and a decrease in the scalar dislocation density in the magnesium alloy samples. These results are consistent with the TEM data, which show a reduction in scalar dislocation density accompanied by a decrease in the contribution of dislocation strengthening. Simultaneously, annealing increases the average grain size, which reduces strength due to the decrease in both dislocation and grain boundary strengthening. During recrystallization annealing of the CG alloy at 500 °C, the dislocation density is minimal, and the calculated contribution of dislocation strengthening decreases to 14 MPa. The calculated values of σ_{total} are in good agreement with the experimental data for $\sigma_{0.2}$ obtained from tensile mechanical tests.

Thus, the greatest contribution to the increase in strength of the magnesium alloy during combined SPD is made by the grain boundary strengthening mechanism, whose contribution due to grain refinement to 1 μm is σ_{gb} = 202 MPa, and the dislocation strengthening mechanism with a contribution of σ_{dis} = 69 MPa.

The presented calculated data are estimates but allow for the identification of the most significant contributions to the overall strengthening, and thereby, the primary strengthening mechanisms of the magnesium alloy. The dependencies of dislocation density and the calculated strengthening contributions on the average grain size for alloy MA20 are presented in Figure 11.

On the presented dependencies, a range with grain sizes from 1 to 7 μm can be identified, where a decrease in grain size is accompanied by a decrease in the values of σ_{dis}, σ_{gb}, σ_{total} и <ρ>. This specified grain size range corresponds to the following alloy states: UFG, UFG (annealed at 200, 250, 300 °C), and FG.

Figure 12 presents graphs of the change in the intensity of the contributions to the flow stress.

On the specified dependencies, two regions with different intensities of change in σ_{dis}, σ_{gb}, σ_{total}, and <ρ> can be indentified. In Region I, (1–7) μm, a sharp change in the contributions and dislocation density occurs
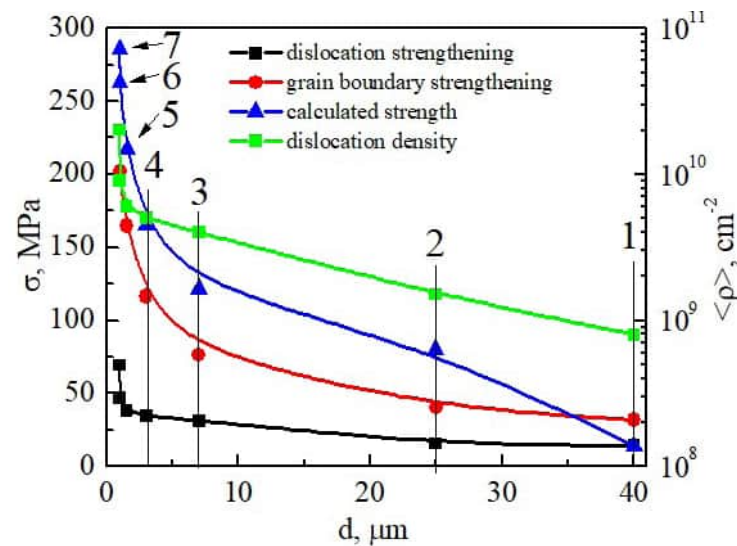
Fig. 11. Dependences of the contributions: σ_{dis}, σ_{grain}, σ_{total}, and dislocation density on the grain size (sample numbers are presented in Table 1)
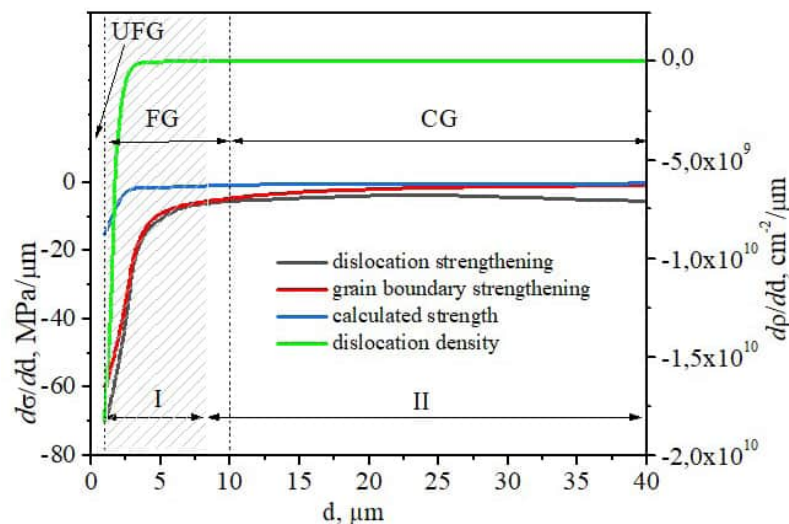
Fig. 12. Dependences of changes in the intensity of $d\sigma_{dis}/dd$, $d\sigma_{grain}/dd$, $d\sigma_{total}/dd$, $d\rho/dd$ on the grain size

for the UFG and FG states of the alloy. Region II can be characterized by a small change in the values $d\sigma_{dis}/dd$, $d\sigma_{gb}/dd$, $d\sigma_{total}/dd$, $d\rho/dd$, which corresponds to the CG state.

The change in the character of the dependencies is associated with the structural relaxation of the alloy during the transition from the UFG to the FG state due to recovery and defect annihilation processes, transformations of the structure inside grains and at grain boundaries, and the reorganization of the dislocation substructure during annealing. It is assumed that non-equilibrium grain boundaries, unlike equilibrium ones, form long-range stress fields that remain significant even over considerable distances and are capable of influencing the motion of intragranular dislocations. The low intensity of change in the contributions $d\sigma_{dis}/dd$, $d\sigma_{gb}/dd$, $d\sigma_{total}/dd$, and the density $d\rho/dd$ for the CG state of the alloy suggests the formation of an equilibrium "sub-lattice" of grain boundary defects [19].

Conclusion

1. The application of a combined SPD method, involving sequential abc press forging and multi-pass rolling of MA20 magnesium alloy, leads to the refinement of the grain structure to a UFG state (average

grain size: 1 μm), a substantial increase in yield and ultimate tensile strength ($\sigma_{0,2}$ = 250 MPa, σ_{UTS} = 270 MPa) and a reduction in plasticity to 3%.

2. An assessment of the contributions from strain hardening mechanisms to the total yield strength σ_{total} during combined SPD was conducted. It was shown that the greatest contribution to the strengthening of the UFG MA20 magnesium alloy is made by the grain boundary (σ_{gb} = 202 MPa) and dislocation (σ_{dis} = 69 MPa) strengthening mechanisms.

3. Annealing at 200 °C preserves the UFG state in the MA20 magnesium alloy but, compared to the initial UFG state, promotes partial structural relaxation, a significant reduction in dislocation density, a 31% decrease in the σ_{dis} contribution, an 8% decrease in $\sigma_{0.2}$, a 4% decrease in σ_{UTS}, and a 100% increase in plasticity.

4. For the studied alloy in the UFG and FG states, an interval of grain sizes equal to (1–7) μm was identified, corresponding to an abrupt change in the intensities of the dislocation density derivative ($d\rho/d$d), the contributions of the dislocation and grain boundary mechanisms to strain hardening ($d\sigma_{dis}/d$d, $d\sigma_{gb}/d$d), and the value of the total strengthening derivative $d\sigma_{total}/d$d.

References

1. Yuan Y., Ma A., Gou X., Jiang J., Arhin G., Song D., Liu H. Effect of heat treatment and deformation temperature on the mechanical properties of ECAP processed ZK60 magnesium alloy. *Materials Science and Engineering: A*, 2016, vol. 677, pp. 125–132. DOI: 10.1016/j.msea.2016.09.037.

2. Chen S., Tseng K.-K., Tong Y., Li W., Tsai C.-W., Yeh J.-W., Liaw P.K. Grain growth and Hall-Petch relationship in a refractory HfNbTaZrTi high-entropy alloy. *Journal of Alloys and Compounds*, 2019, vol. 795, pp. 19–26. DOI: 10.1016/j.jallcom.2019.04.291.

3. Pan H., Yang C., Yang Y., Dai Y., Zhou D., Chai L., Huang Q., Yang Q., Liu S., Ren Y., Qin G. Ultra-fine grain size and exceptionally high strength in dilute Mg–Ca alloys achieved by conventional one-step extrusion. *Materials Letters*, 2019, vol. 237, pp. 65–68. DOI: 10.1016/j.matlet.2018.11.080.

4. Tong L.B., Chu J.H., Jiang Z.H., Kamado S., Zheng M.Y. Ultrafine-grained Mg-Zn-Ca-Mn alloy with simultaneously improved strength and ductility processed by equal channel angular pressing. *Journal of Alloys and Compounds*, 2019, vol. 785, pp. 410–421. DOI: 10.1016/j.jallcom.2019.01.181.

5. Xu C., Wang Z., Zhou L., Wang F., Wei Z., Mao P. Effect of element Ce on the strain rate sensitivity of Mg-Zn-Zr alloy. *Journal of Magnesium and Alloys*, 2025, vol. 13 (8), pp. 4005–4019. DOI: 10.1016/j.jma.2025.04.017.

6. Zhou Y.-L., Li Y., Luo D.-M., Ding Y., Hodgson P. Microstructures, mechanical and corrosion properties and biocompatibility of as extruded Mg–Mn–Zn–Nd alloys for biomedical applications. *Materials Science and Engineering: C*, 2015, vol. 49, pp. 93–100. DOI: 10.1016/j.msec.2014.12.057.

7. Yu K., Li W., Zhao J., Ma Z., Wang R. Plastic deformation behaviors of a Mg–Ce–Zn–Zr alloy. *Scripta Materialia*, 2003, vol. 48 (9), pp. 1319–1323. DOI: 10.1016/S1359-6462(03)00046-0.

8. Shunmugasamy V.C., AbdelGawad M., Sohail M.U., Ibrahim T., Khan T., Seers T.D., Mansoor B. In vitro and in vivo study on fine-grained Mg–Zn–RE–Zr alloy as a biodegradeable orthopedic implant produced by friction stir processing. *Bioactive Materials*, 2023, vol. 28, pp. 448–466. DOI: 10.1016/j.bioactmat.2023.06.010.

9. Volkova E.F. Some regular features of formation of phase composition in a magnesium alloy of the Mg – Zn – Zr – Y system. *Metal Science and Heat Treatment*, 2014, vol. 55 (9–10), pp. 477–482. DOI: 10.1007/s11041-014-9657-5.

10. Dobatkin S.V., Rokhlin L.L., Lukyanova E.A., Murashkin M.Y., Dobatkina T.V., Tabachkova N.Y. Structure and mechanical properties of the Mg-Y-Gd-Zr alloy after high pressure torsion. *Materials Science and Engineering: A*, 2016, vol. 667, pp. 217–223. DOI: 10.1016/j.msea.2016.05.003.

11. Minárik P., Král R., Pešička J., Chmelík F. Evolution of mechanical properties of LAE442 magnesium alloy processed by extrusion and ECAP. *Journal of Materials Research and Technology*, 2015, vol. 4 (1), pp. 75–78. DOI: 10.1016/j.jmrt.2014.10.012.

12. Merson D., Brilevsky A., Myagkikh P., Markushev M., Vinogradov A. Effect of deformation processing of the dilute Mg-1Zn-0.2Ca alloy on the mechanical properties and corrosion rate in a simulated body fluid. *Letters on Materials*, 2020, vol. 10 (2), pp. 217–222. DOI: 10.22226/2410-3535-2020-2-217-222.

13. Jin Z.-Z., Zha M., Wang S.-Q., Wang S.-C., Wang C., Jia H.-L., Wang H.-Y. Alloying design and microstructural control strategies towards developing Mg alloys with enhanced ductility. *Journal of Magnesium and Alloys*, 2022, vol. 10 (5), pp. 1191–1206. DOI: 10.1016/j.jma.2022.04.002.

14. Nie J.-F. Precipitation and hardening in magnesium alloys. *Metallurgical and Materials Transactions A*, 2012, vol. 43 (11), pp. 3891–3939. DOI: 10.1007/s11661-012-1217-2.

15. Shabana M.A., Bhattacharyya J.J., Niewczas M., Agnew S.R. Thermally activated nature of basal and prismatic slip in mg and its alloys. *Magnesium Technology 2021*. Cham, Springer, 2021, pp. 53–60. DOI: 10.1007/978-3-030-65528-0_9.

16. Yue Y., Wang J., Nie J.-F. Twin-solute, twin-dislocation and twin-twin interactions in magnesium. *Journal of Magnesium and Alloys*, 2023, vol. 11 (10), pp. 3427–3462. DOI: 10.1016/j.jma.2023.07.015.

17. Li L., Liu W., Qi F., Wu D., Zhang Z. Effects of deformation twins on microstructure evolution, mechanical properties and corrosion behaviors in magnesium alloys – A review. *Journal of Magnesium and Alloys*, 2022, vol. 10 (9), pp. 2334–2353. DOI: 10.1016/j.jma.2022.09.003.

18. Valiev R.Z., Islamgaliev R.K., Alexandrov I.V. Bulk nanostructured materials from severe plastic deformation. *Progress in Materials Science*, 2000, vol. 45 (2), pp. 103–189. DOI: 10.1016/S0079-6425(99)00007-9.

19. Glezer A.M., Kozlov E.V., Koneva N.A., Popova N.A., Kurzina I.A. *Plastic deformation of nanostructured materials*. CRC Press, 2017. ISBN 9781315111964.

20. Botkin A.V., Valiev R.Z., Volkova E.P., Khudododova G.D., Ebrahimi R. Effect of preliminary deformation on the formation of ultrafine-grained structure during equal channel angular pressing of magnesium alloys. *Fizicheskaya mezomekhanika = Physical Mesomechanics*, 2024, vol. 27, no. 4, pp. 63–72. DOI: 10.55652/1683-805X_2024_27_4_63-72. (In Russian).

21. Lukyanova E., Tarytina I., Tabachkova N., Dobatkina T., Martynenko N., Rybalchenko O., Rybalchenko G., Temralieva D., Andreev V., Ovchinnikova O., Andreeva N., Dobatkin S. The effect of rotary swaging on the structure and mechanical properties of Mg-Y-Gd-Zr alloys additionally alloyed with samarium. *Materials Today Communications*, 2025, vol. 43, p. 111857. DOI: 10.1016/j.mtcomm.2025.111857.

22. Luginin N., Eroshenko A., Khimich M., Prosolov K., Kashin A., Uvarkin P., Tolmachev A., Glukhov I., Panfilov A., Sharkeev Y. Severe plastic deformation of Mg–Zn–Zr–Ce alloys: advancing corrosion resistance and mechanical strength for medical applications. *Metals*, 2023, vol. 13 (11), p. 1847. DOI: 10.3390/met13111847.

23. Pekguleryuz M., Celikin M. Creep resistance in magnesium alloys. *International Materials Reviews*, 2010, vol. 55 (4), pp. 197–217. DOI: 10.1179/095066010X12646898728327.

24. Hirsch P.B., Howie A., Nicholson R.B., Pashley D.W., Whelan M.J., Marton L. Electron microscopy of thin crystals. *Physics Today*, 1966, vol. 19 (10), pp. 93–95. DOI: 10.1063/1.3047787.

25. Sun L., Wang Z., Zhou L., Wang F., Zhang W., Wei Z., Mao P. Effect of Ce on microstructure and corrosion behavior of as cast ZK60 alloy. *Materials Today Communications*, 2025, vol. 42, p. 111345. DOI: 10.1016/j.mtcomm.2024.111345.

26. Fruchart D., Skryabina N., de Rango P., Fouladvind M., Aptukov V. Severe plastic deformation by fast forging to easy produce hydride from bulk Mg-based alloys. *Materials Transactions*, 2023, vol. 64 (8), pp. 1886–1893. DOI: 10.2320/matertrans.MT-MF2022049.

27. Kappes M., Iannuzzi M., Carranza R.M. Hydrogen embrittlement of magnesium and magnesium alloys: a review. *Journal of the Electrochemical Society*, 2013, vol. 160 (4), pp. C168–C178. DOI: 10.1149/2.023304jes.

28. Zhang J., Yan S., Qu H. Stress/strain effects on thermodynamic properties of magnesium hydride: A brief review. *International Journal of Hydrogen Energy*, 2017, vol. 42 (26), pp. 16603–16610. DOI: 10.1016/j.ijhydene.2017.05.174.

29. Mezbahul-Islam M., Mostafa A.O., Medraj M. Essential magnesium alloys binary phase diagrams and their thermochemical data. *Journal of Materials*, 2014, vol. 2014, pp. 1–33. DOI: 10.1155/2014/704283.

30. Aljarrah M., Alnahas J., Alhartomi M. Thermodynamic modeling and mechanical properties of Mg-Zn-{Y, Ce} alloys: Review. *Crystals*, 2021, vol. 11 (12), p. 1592. DOI: 10.3390/cryst11121592.

31. Sharkeev Yu.P., Kozlov E.V. The long-range effect in ion implanted metallic materials: dislocation structures, properties, stresses, mechanisms. *Surface and Coatings Technology*, 2002, vol. 158–159, pp. 219–224. DOI: 10.1016/S0257-8972(02)00212-8.

32. Goldstein M.I., Litvinov V.S., Bronfin M.B. *Metallofizika vysokoprochnykh splavov* [Metal physics of high-strength alloys]. Moscow, Metallurgiya Publ., 1986. 312 p. (In Russian).

33. Gleiter H. Nanostructured materials: basic concepts and microstructure. *Acta Materialia*, 2000, vol. 48 (1), pp. 1–29. DOI: 10.1016/S1359-6454(99)00285-2.

34. Raynor G.V. *The physical metallurgy of magnesium and its alloys*. New York, Pergamon Press, 1959. 531 p.

35. Gong W., Zheng R., Harjo S., Kawasaki T., Aizawa K., Tsuji N. In-situ observation of twinning and detwinning in AZ31 alloy. *Journal of Magnesium and Alloys*, 2022, vol. 10 (12), pp. 3418–3432. DOI: 10.1016/j.jma.2022.02.002.

36. Prasad N.S., Naveen Kumar N., Narasimhan R., Suwas S. Fracture behavior of magnesium alloys – Role of tensile twinning. *Acta Materialia*, 2015, vol. 94, pp. 281–293. DOI: 10.1016/j.actamat.2015.04.054.

37. Balog M., Krížik P., Školáková A., Švec P., Kubásek J., Pinc J., de Castro M.M., Figueiredo R. Hall-Petch strengthening in ultrafine-grained Zn with stabilized boundaries. *Journal of Materials Research and Technology*, 2024, vol. 33, pp. 7458–7468. DOI: 10.1016/j.jmrt.2024.11.132.

38. Oppedal A.L., El Kadiri H., Tomé C.N., Kaschner G.C., Vogel S.C., Baird J.C., Horstemeyer M.F. Effect of dislocation transmutation on modeling hardening mechanisms by twinning in magnesium. *International Journal of Plasticity*, 2012, vol. 30–31, pp. 41–61. DOI: 10.1016/j.ijplas.2011.09.002.

39. Ganeshan S., Shang S.L., Wang Y., Liu Z.-K. Effect of alloying elements on the elastic properties of Mg from first-principles calculations. *Acta Materialia*, 2009, vol. 57 (13), pp. 3876–3884. DOI: 10.1016/j.actamat.2009.04.038.

Conflicts of Interest

The authors declare no conflict of interest.

Obrabotka metallov –
Metal Working and Material Science

Effect of laser radiation wavelength on the structure and functional properties of TiNi alloy during UV laser treatment

Tatyana Sablina [a, *], Marina Kandaurova [b], Ilya Zyatikov [c], Yurii Panchenko [d]

Institute of High Current Electronics of the Siberian Branch of the Russian Academy of Sciences, 2/3 Akademichesky Avenue, Tomsk, 634055, Russian Federation

[a] https://orcid.org/0000-0002-5941-5732, ✉ sabltat@mail.ru; [b] https://orcid.org/0000-0003-0236-2227, ✉ panchenko.marina4@gmail.com;
[c] https://orcid.org/0000-0003-3219-9299, ✉ zyatikov@lgl.hcei.tsc.ru; [d] https://orcid.org/0000-0001-8017-7268, ✉ yu.n.panchenko@mail.ru

ARTICLE INFO

ABSTRACT

Introduction. The widespread use of *TiNi*-based functional alloys in medicine requires targeted management of their surface properties, such as wettability and biocompatibility. One of the promising methods for surface modification is laser treatment, especially in the *UV* range of the spectrum. The efficiency of *UV* laser treatment is due to the high photon energy, strong absorption by metals, and the shallow depth of the thermal effect zone. **The purpose of this work** is to investigate the effect of *UV* laser radiation wavelength (266 and 355 nm) on the structural and phase state, chemical composition, and wettability of the *TiNi* alloy surface, with the goal of subsequently controlling the material's functional properties. **Materials and research methods.** *TiNi* surface modification was performed using a pulsed *Nd:YAG* laser operating at wavelengths of 266 and 355 nm in ambient air. The modified surfaces were analyzed by scanning electron microscopy with energy-dispersive spectroscopy (*SEM-EDS*). Microstructure, elemental composition, and phase composition were analyzed by X-ray diffraction (*XRD*). Wettability was estimated using the sessile drop method. The free surface energy, along with its dispersive and polar components, was then calculated from the contact angle data using the *OWRK* method. **Results and discussion.** *UV* laser treatment, varying parameters such as laser radiation wavelength and scanning speed, was found to induce changes in the morphology, elemental composition, phase composition of the surface layer of *TiNi* alloy samples, and their surface properties. Following *UV* laser treatment at wavelengths of 266 and 355 nm and low scanning speeds (V = 200 and 500 μm/s), single microcracks or microcrack networks resulting from thermal exposure were observed on the specimen surfaces. The oxygen content on the *TiNi* surface increased by a factor of 5 to 18 compared to the initial state after *UV* laser treatment. Furthermore, the phase composition of the *TiNi* alloy underwent noticeable changes, with titanium oxide phases being detected on the surface after laser exposure. The higher-energy photons (λ = 266 nm) resulted in a more pronounced change in the surface morphology and properties of *TiNi* compared to the 355 nm radiation under identical treating conditions. *UV* laser treatment significantly increased the surface hydrophilicity: the contact angle decreased from ≈75° in the initial state to ≈25° and ≈11° after treatment with 355 and 266 nm radiation wavelength, respectively. Additionally, an increase in the free surface energy of the *TiNi* specimens was observed, primarily due to a significant increase in the polar component.

Introduction

Alloys based on titanium nickelide (*TiNi*) occupy an important place among functional materials due to their unique properties, such as the shape memory effect and superelasticity, which makes them attractive for use in medicine (implants, stents), the aerospace industry, and microelectronics [1–3]. However, the successful application of *TiNi* largely depends on its surface properties, including wettability, which affects

* Corresponding author
Sablina Tatyana Yu., Ph.D. (Engineering), Scientific associate
Institute of High Current Electronics
of the Siberian Branch of the Russian Academy of Sciences,
2/3 Akademichesky Avenue,
634055, Tomsk, Russian Federation
Tel.: +7 913 843-21-78, **e-mail:** sabltat@mail.ru

the alloy's biocompatibility and corrosion resistance [4]. Therefore, researchers' attention is focused on finding effective surface treatment methods for these alloys to improve their biofunctional properties.

Modern strategies for surface modification of functional materials include a wide range of methods, such as ion implantation [5], high-energy techniques (laser, electron beam, plasma) [6, 7], thermal and chemical treatments [8], deposition of functional coatings [9], etc. Among high-energy methods, laser treatment holds a special place due to its precision, non-contact nature, environmental friendliness, and high processing speed [6, 10]. A key advantage of laser surface modification technologies is the ability to precisely control changes in microstructure, chemical composition, and surface topography, which opens prospects for targeted control of its functional properties.

Numerous studies confirm the positive effect of laser treatment on the corrosion resistance and biocompatibility of *TiNi*-based alloys, particularly by reducing the migration of nickel ions into the physiological environment [11–15]. It was shown in [11] that treatment with an *Nd*:*YAG* laser ($\lambda = 1,064$ nm) improves corrosion resistance due to the formation of a protective oxide layer, although excessive melting can locally enhance nickel ion release from the *TiNi* surface. In turn, *Q. Zhang* et al. [12] demonstrated that ultrashort laser pulses not only control wettability but also create wettability gradients, which improves anti-adhesion properties and reduces the hemolytic activity of *TiNi*. Study [13] showed that texturing with femtosecond laser pulses ($\lambda = 1,028$ nm) creates hierarchical structures on the *TiNi* alloy surface, significantly improving wettability and promoting endothelialization. Other work [14] indicates that laser-induced changes in the oxide layer impart antibacterial properties to the surface, reducing *Staphylococcus aureus* adhesion. Additionally, it was found in [15] that controlling the parameters of femtosecond laser ($\lambda = 1,035$ nm) microtreatment enables achieving low surface roughness in *TiNi* powder samples, which improves biocompatibility and resistance to biocorrosion.

Nevertheless, systematic studies on the influence of laser treatment on the wettability and biocompatibility of titanium nickelide-based alloys remain limited. Despite these achievements, the task of controlling the wettability of the *TiNi* surface by laser methods is far from complete and requires in-depth research, especially for industrial implementation. At the same time, the application of ultraviolet (*UV*) laser radiation to modify the surface of TiNi alloy is a little-studied area. Laser radiation in the *UV* range ($\lambda = 100$–400 nm) has higher photon energy and stronger absorption in metals, which leads to lower penetration depth and a reduced size of the thermal effect zone compared to radiation in the visible and infrared ranges [10, 16]. In [17] we found that local exposure to *UV* laser radiation ($\lambda = 266$ nm) on stainless steel and *TiNi* alloy leads to a significant increase in surface hydrophilicity due to oxidation and an increase in the polar component of the surface free energy. Y. Wang and co-authors [18] have shown that exposure to nanosecond *UV* laser radiation ($\lambda = 355$ nm) makes it possible to create a controlled texture with a roughness of ≈5 μm on the surface of a titanium alloy, ensuring high cellular adhesion and proliferation. In [19] it was found that nanostructuring of the surface using a laser with a wavelength of $\lambda = 355$ nm improves the adhesion and proliferation of osteoblasts on the *TiNi* alloy. Thus, despite the proven effectiveness of *UV* laser treatment, there is no data in the literature on a comprehensive study of the influence of its parameters on the surface characteristics and wettability of metallic materials. Most existing works use a fixed wavelength (often 266 or 355 nm), and systematic studies varying the wavelength under controlled conditions are lacking.

The purpose of this work is to study the influence of the wavelength of *UV* laser radiation (266 and 355 nm) on the structural and phase state, chemical composition, and wettability of the *TiNi* alloy surface for subsequent control of the material's functional properties.

The objectives of the study are:

– conducting a comparative analysis of the morphology, chemical, and phase composition of the surface of *TiNi* specimens before and after *UV* laser treatment with various parameters (wavelength, scanning speed);

– estimation of the hydrophilicity degree of the surface by measuring the contact wetting angles and calculating the free surface energy with determination of dispersion and polar components of the studied *TiNi* specimens subjected to *UV* laser treatments according to different modes;

– investigating the influence of wavelength (266 and 355 nm) radiation during *UV* laser treatment on the structural and phase state and functional properties of the modified *TiNi* alloy surface.

Materials and methods of research

The specimens for investigation were 10 mm × 10 mm × 3 mm plates made of a *TiNi* alloy, grade *TN-10* (chemical composition: 50.0–51.5% *Ni*, 0.5–1.5% *Mo*, ≤0.5% *Fe*, bal. *Ti*, at. %), hereafter referred to as *TiNi*. To ensure a consistent initial surface topography for all specimens, standard surface preparation procedures were employed. All specimens were mechanically ground and subsequently subjected to final polishing using diamond pastes (*ASM* and *ASN* grades, with abrasive particle sizes ranging from 3/2 to 1/0 μm) to achieve a smooth, mirror-like surface. For final contamination removal, the specimens were ultrasonically cleaned in ethanol for 10 minutes.

The prepared surfaces of the specimens were irradiated with a pulsed *Nd:YAG* laser (*Model LS2137U*, *Lotis TII*, Belarus) in the ultraviolet (*UV*) range. The third (355 nm) and fourth (266 nm) harmonic wavelengths of the laser radiation were used for the treatment. The laser treatment was conducted in ambient air at atmospheric pressure and room temperature (22 ± 3 °C). The main parameters of the *UV* laser treatment are summarized in Table. A schematic of the *UV* laser treatment setup and the laser scanning strategy are presented in Fig. 1.

UV laser treatment parameters

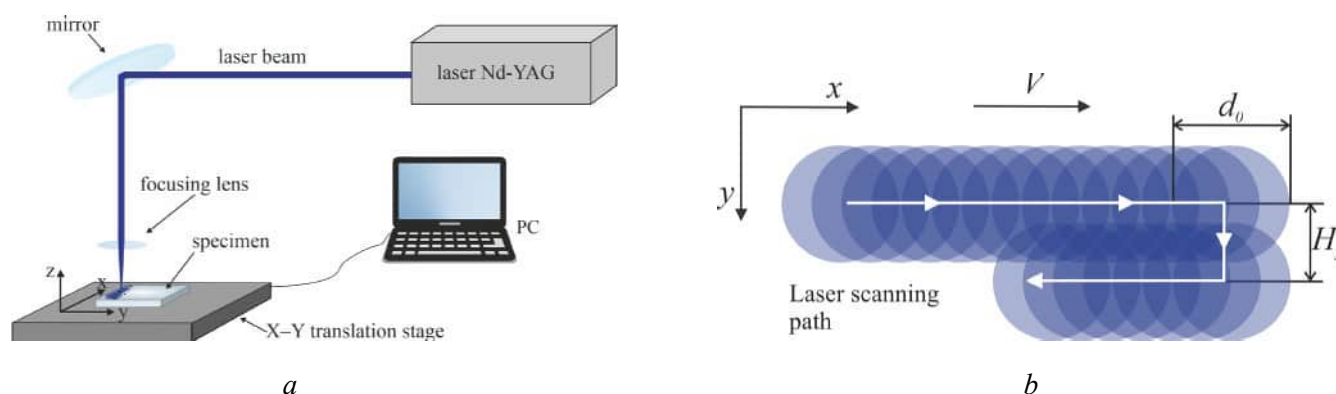| Wavelength, nm (λ)	Pulse duration, ns	Pulse repetition rate, Hz	Laser spot diameter, mm (d_0)	Fluence, J/cm² (j)	Scanning speed, μm/s (V)
266	7	10	3.5	0.22	200–5,000
355	7	10	3.5	0.22	200–5,000

Fig. 1. Schematic of the experimental setup for *UV* laser surface treatment (*a*) and the scanning strategy employed (*b*). Diagram (*b*) illustrates the laser spot diameter (d_0), hatch distance (H_y), and scanning speed (*V*)

X-ray diffraction (*XRD*) analysis was employed to investigate the changes in the structure and phase composition of the *TiNi* alloy resulting from the *UV* laser treatment under different regimes. Diffraction patterns were acquired using a *DRON "Burevestnik"* diffractometer (Russia). A copper anode (*CuKα* radiation, λ = 1.5418 Å) was used as the X-ray source, and the measurements were performed over a 2Θ range from 30° to 100°. The lattice parameter (*a*) was determined by extrapolating the values of a_{hkl}, calculated for each diffraction peak with indices (*hkl*), against the function $0.5(\cos^2\theta/\sin\theta + \cos^2\theta/\theta)$.

Scanning Electron Microscopy (*SEM*) was used to investigate the microstructure and elemental composition of the specimen surfaces before and after *UV* laser treatment. The studies were conducted using a *TESCAN VEGA 3* microscope (Czech Republic) equipped with an Energy Dispersive X-ray Spectrometer (*EDS*). For a statistical evaluation of the elemental composition, *EDS* analysis was performed on at least ten randomly selected areas for each specimen.

The wettability of the surfaces before and after *UV* laser treatment was assessed using the sessile drop method with liquids of known surface tension. Droplets with a volume of 3 μL were dispensed onto the specimen surfaces using an automatic micropipette. After deposition, the droplets were allowed to stabilize for 60 seconds, after which their images were captured using a *Levenhuk Discovery Artisan 1024* digital

microscope. The contact angle values were averaged from at least five independent measurements. To quantitatively evaluate the changes in the surface properties induced by the *UV* laser treatment, the free surface energy (γ_{total}) and its components were determined. The calculations were performed according to the *Owens-Wendt-Rabel-Kaelble* (*OWRK*) method [20, 21], which allows for the separate evaluation of the dispersive (γ_d) and polar (γ_p) components of the total surface energy.

Results and Discussion

Fig. 2, *a* shows an *SEM* image of the microstructure and the elemental composition of the initial *TiNi* alloy specimen. It can be seen that the structure of the *TiNi* alloy is predominantly homogeneous. The matrix (light area in Fig. 2, *a*) contains a small fraction (≤5%) of secondary phase inclusions (dark particles in Fig. 2, *a*). The *EDS* results presented in Fig. 2, *a* indicate that, in addition to the main matrix components *Ti* and *Ni*, small amounts of the *TN-10* alloying elements, such as *Fe* and *Mo*, as well as minor concentrations of *C* and *O*, were detected. The dark inclusions consist primarily of *Ti* and *C*, with a small amount of *Ni*. The presence of *Ni* in the spectra is likely attributable to the matrix surrounding these particles. Based on the elemental analysis, the light matrix corresponds to titanium nickelide (*TiNi*), while the dark inclusions are titanium carbide (*TiC*). This is further corroborated by the *XRD* data. The diffraction peaks in the *XRD* pattern obtained from the surface of the initial specimen, presented in Fig. 2, *b*, are identified as belonging to the *B2*-phase of *TiNi*. A peak attributed to *TiC* is also registered in the low-angle region. The lattice parameter of the *B2*-phase in the initial state was determined to be $a = 0.3018 \pm 0.0004$ nm.
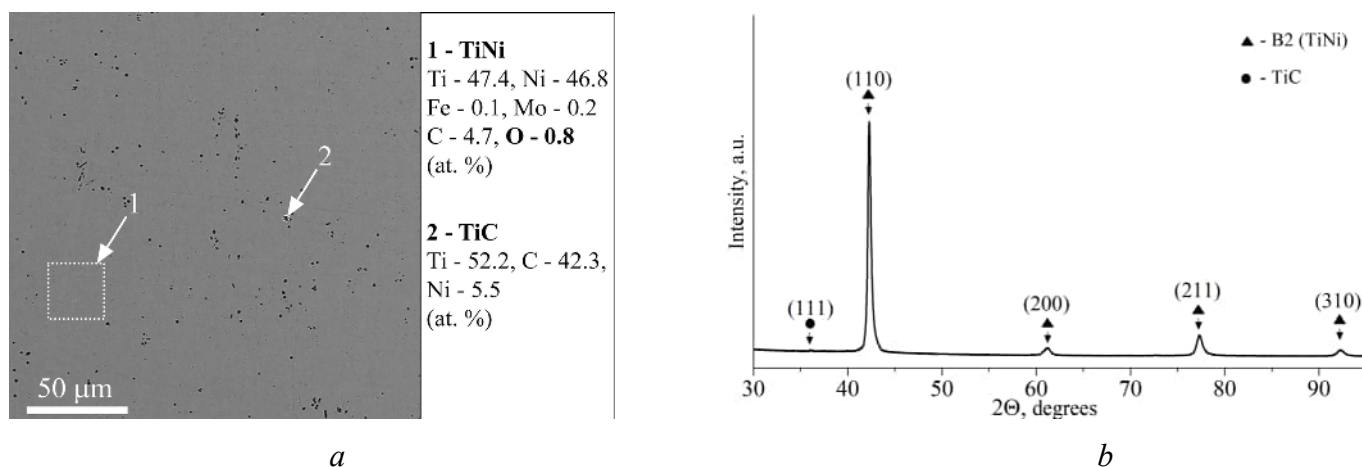

a

b

Fig. 2. Microstructural and compositional characterization of the untreated *TiNi* specimen surface:
(*a*) *SEM* micrograph with corresponding *EDS* elemental mapping; (*b*) X-ray diffraction pattern

The investigation of the structure, elemental, and phase composition of the *TiNi* alloy after *UV* laser treatment revealed that variations in laser processing parameters, such as wavelength and scanning speed, induce significant changes in the morphology, elemental, and phase composition of the surface layer.

Fig. 3 presents *SEM* images and the corresponding elemental composition of the *TiNi* alloy surface following *UV* laser treatment at wavelengths of 355 nm (Fig. 3, *a*, *c*) and 266 nm (Fig. 3, *b*, *d*), with laser scanning speeds of 500 μm/s (Fig. 3, *a*, *b*) and 200 μm/s (Fig. 3, *c*, *d*), respectively.

Fig. 3 reveals that after *UV* laser treatment at wavelengths of 355 nm and 266 nm with a scanning speed of 500 μm/s, the surface morphology of the material remains largely unchanged (Fig. 3, *a*, *b*). However, isolated microcracks are observed on the *TiNi* surface after treatment with the 266 nm wavelength, as indicated by the yellow arrows in Fig. 3, *b*. While the elemental composition of the *TiNi* surface remains the same after these treatment regimes, the quantitative ratios of the elements change. A comparison of the oxygen content on the initial and laser-modified surfaces showed that the amount of oxygen increases by 5–8 times after *UV* laser irradiation. Furthermore, the oxygen content on the *TiNi* surface is approximately 1.5 times higher after treatment with the shorter wavelength (266 nm) compared to the 355 nm wavelength.
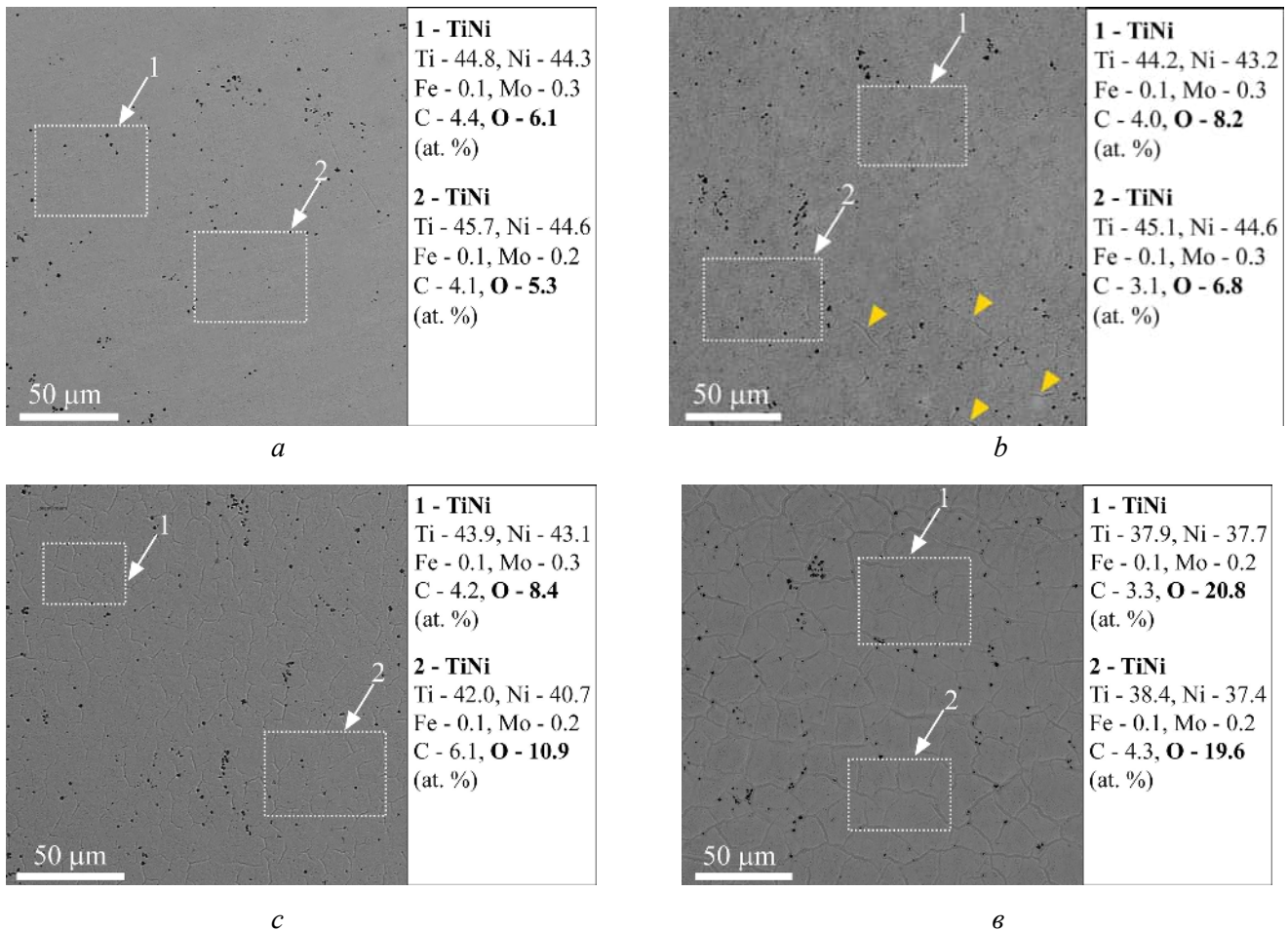
1 - TiNi
Ti - 44.8, Ni - 44.3
Fe - 0.1, Mo - 0.3
C - 4.4, **O - 6.1**
(at. %)

2 - TiNi
Ti - 45.7, Ni - 44.6
Fe - 0.1, Mo - 0.2
C - 4.1, **O - 5.3**
(at. %)

50 μm

a

1 - TiNi
Ti - 44.2, Ni - 43.2
Fe - 0.1, Mo - 0.3
C - 4.0, **O - 8.2**
(at. %)

2 - TiNi
Ti - 45.1, Ni - 44.6
Fe - 0.1, Mo - 0.3
C - 3.1, **O - 6.8**
(at. %)

50 μm

b

1 - TiNi
Ti - 43.9, Ni - 43.1
Fe - 0.1, Mo - 0.3
C - 4.2, **O - 8.4**
(at. %)

2 - TiNi
Ti - 42.0, Ni - 40.7
Fe - 0.1, Mo - 0.2
C - 6.1, **O - 10.9**
(at. %)

50 μm

c

1 - TiNi
Ti - 37.9, Ni - 37.7
Fe - 0.1, Mo - 0.2
C - 3.3, **O - 20.8**
(at. %)

2 - TiNi
Ti - 38.4, Ni - 37.4
Fe - 0.1, Mo - 0.2
C - 4.3, **O - 19.6**
(at. %)

50 μm

в

Fig. 3. SEM images of the *TiNi* alloy surface after *UV* laser treatment with different parameters and corresponding *EDS* analysis results:

(*a*) λ = 355 nm, *V* = 500 μm/s; (*б*) λ = 266 nm, *V* = 500 μm/s; (*в*) λ = 355 nm, *V* = 200 μm/s; (*г*) λ = 266 nm, *V* = 200 μm/s. (λ is a wavelength, *V* is a scanning speed)

As seen in Figs. 3, *c* and *d*, at the minimum scanning speed of 200 μm/s, a uniform network of microcracks is formed on the *TiNi* alloy surface under *UV* laser irradiation, regardless of the wavelength. The microcracking is more pronounced on the surface of specimens treated with the 266 nm wavelength at 200 μm/s. The formation of individual microcracks and the enhanced microcracking of the thin surface layer after UV laser treatment are attributed to several primary reasons related to the physical and chemical interaction of the laser radiation with the material.

The high energy of *UV* laser radiation causes rapid and localized surface heating, leading to abrupt thermal expansion and the subsequent development of significant thermal stresses within the material surface. The ultraviolet wavelength (100–400 nm) has a lower penetration depth into the material compared to *IR* or visible laser radiation. This concentrates the energy within a thin surface layer and increases the temperature gradient between the surface and the bulk material. Such a gradient amplifies internal stresses and promotes microcrack formation. The difference in the coefficients of linear thermal expansion between the underlying *TiNi* material and the metal oxides formed on the alloy surface during laser treatment may also contribute to microcracking [17, 22].

The scanning speed also influences the cracking process: a lower speed results in more intensive, prolonged exposure to a local area, which enhances the thermal load and the risk of crack formation. According to *EDS* data (Fig. 3), a significant increase in oxygen concentration, up to a depth of 3 μm, occurs under *UV* laser irradiation, depending on the wavelength. Whereas the initial (untreated) *TiNi* surface exhibited a minor oxygen content not exceeding 1 at.%, the surfaces treated with a 355 nm wavelength showed oxygen contents of 5.7 ± 0.4 at.% at a scanning speed of *V* = 500 μm/s and 9.7 ± 1.3 at.% at

V = 200 μm/s. For specimens treated with a 266 nm wavelength, an even more substantial increase in oxygen was observed: 7.5 ± 0.7 at.% at 500 μm/s and 18.7 ± 2.1 at.% at 200 μm/s. The increased oxygen concentration on the *TiNi* alloy surface after laser treatment is likely caused by the intense interaction of *Ti* with atmospheric oxygen, leading to the formation of titanium oxides. The local thermal impact on the surface during laser treatment can result in the formation of oxide phases such as *TiO*, *TiO₂*, *Ti₂O₃*, and *Ti₂Ni₄Oₓ*. These phases not only enhance surface hardness and corrosion resistance but also improve surface hydrophilicity and bioactivity [17, 23, 24].

Fig. 4 presents the *XRD* patterns of *TiNi* specimens after *UV* laser treatment at a scanning speed of 200 μm/s. The *XRD* pattern obtained after *UV* laser treatment with a wavelength of 266 nm and a scanning speed of 200 μm/s reveals, in addition to the primary *B2-TiNi* phase and traces of the secondary phase *TiC*, distinct peaks corresponding to titanium dioxide (*TiO₂*, rutile) and the complex oxide *Ni₂Ti₄Oₓ*. Therefore, the *XRD* data provide clear evidence of the formation of an oxide film on the *TiNi* alloy surface following *UV* laser treatment with a wavelength of 266 nm. In contrast, the *XRD* patterns of *TiNi* specimens irradiated with a 355 nm wavelength, even at the lowest scanning speed of 200 μm/s, show only peaks belonging to the *B2-TiNi* phase and the *TiC* impurity phase. The absence of diffraction peaks from oxide phases on the *XRD* patterns obtained after irradiation with the 355 nm wavelength could be attributed to either a very thin oxide film, a low concentration of oxides (less than 3%) below the detection limit of the *XRD* technique, or the potential quasi-amorphous nature of the oxide phases. This quasi-amorphous state could prevent the identification of oxides on the laser-modified surface under these specific *UV* laser treatment parameters using the *XRD* method. The lattice parameter of the *B2*-phase in the *TiNi* specimens subjected to *UV* laser treatment decreased compared to the initial state: to $a = 0.3016 \pm 0.0002$ nm for $\lambda = 355$ nm ($V = 200$ μm/s) and to $a = 0.3014 \pm 0.0001$ nm for $\lambda = 266$ nm. This reduction in the lattice parameter may qualitatively indicate a depletion of titanium in the *B2-TiNi* matrix and an associated change in the phase composition of the specimens.

The changes in the morphology, elemental, and phase composition of the *TiNi* alloy surface induced by pulsed *UV* laser treatment significantly affect its surface properties, such as wettability and free surface energy.

The wettability of titanium nickelide (*TiNi*) plays a crucial role in the material's biocompatibility, influencing cell proliferation on its surface. As shown in [25], a moderately hydrophilic surface on *TiNi* implants, with a water contact angle of less than 60°, ensures good wetting by biological fluids and enhanced
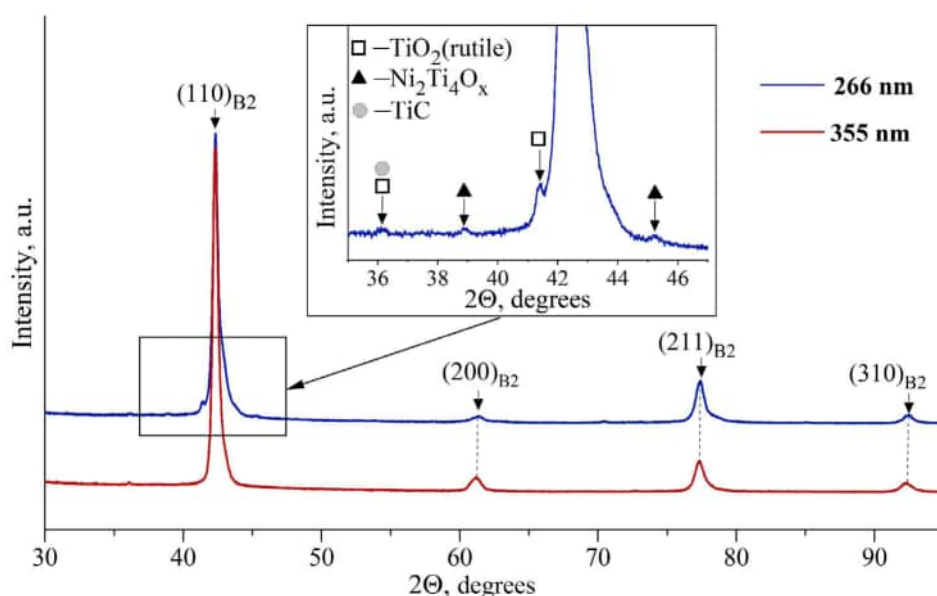

Fig. 4. X-ray diffraction (*XRD*) patterns obtained from *TiNi* specimens after *UV* laser treatment at wavelengths of $\lambda = 266$ nm and $\lambda = 355$ nm, using a scanning speed of 200 μm/s

cell adhesion, thereby stimulating the proliferation of endothelial and smooth muscle cells. Increased hydrophilicity promotes more active cell adhesion, spreading, and multiplication, which is particularly important for medical implants. The degree of hydrophilicity, characterized by the material surface's ability to attract and hold water, is determined by the water contact angle.

UV laser treatment of the *TiNi* alloy surface alters its hydrophilicity. The average water contact angle for the initial *TiNi* specimens was 75.1° ± 3.8°. After *UV* laser treatment, the hydrophilicity increases substantially. The plots of the water contact angle versus scanning speed for the *TiNi* alloy surface treated with *UV* laser radiation at wavelengths of 266 nm and 355 nm are presented in Fig. 5. Representative images of water droplets on the *UV* laser-treated surfaces are provided in the insets of Fig. 5. A decrease in the laser wavelength and a reduction in the scanning speed during *UV* laser treatment lead to a decrease in the contact angle. As shown by the data presented in Fig. 5, when the material is laser treated with a 355 nm wavelength at the maximum scanning speed of 5,000 µm/s, the contact angle decreases by 10% compared to the initial state. When the scanning speed is reduced to 200 µm/s, the contact angle decreases threefold to 24.7° ± 1.5°. The most pronounced increase in hydrophilicity is observed after *UV* laser treatment with a wavelength of 266 nm. Even at the maximum scanning speed (5,000 µm/s), the contact angle is reduced by more than threefold compared to the initial state. It should be noted that reducing the scanning speed from 5,000 µm/s to 200 µm/s has only a minor effect on surface hydrophilicity at this wavelength, with the contact angle varying within the range of 11–20°.
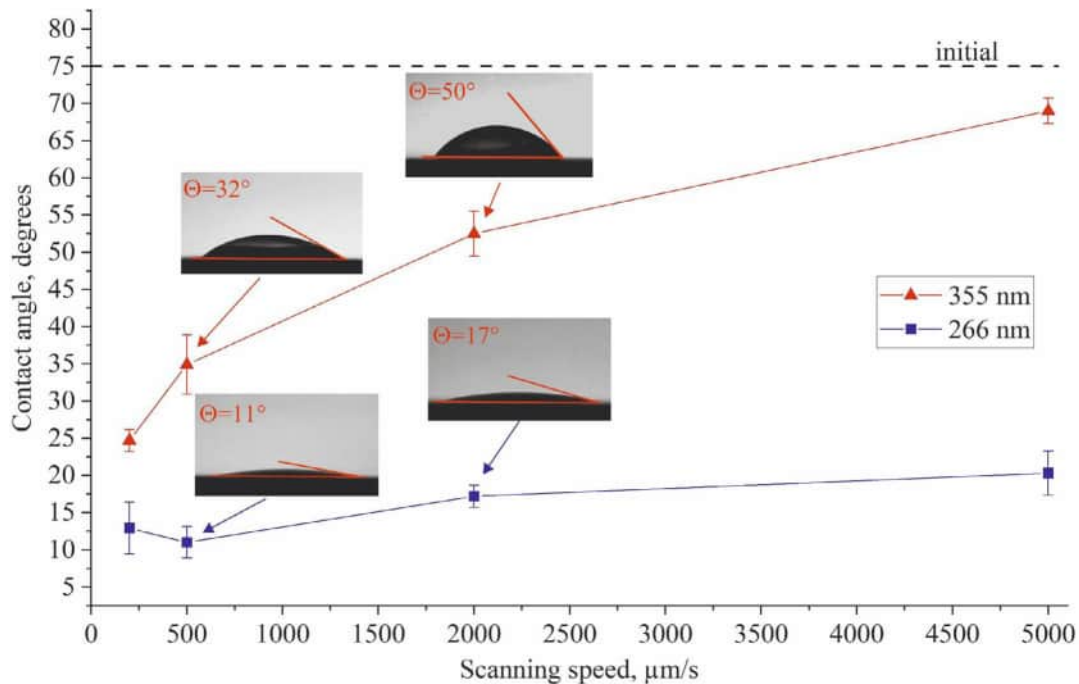

Fig. 5. Effect of laser wavelength on the dependence of the water contact angle on the scanning speed during *UV* laser treatment

Surface hydrophilicity is directly related to the magnitude of the free surface energy. An increase in free surface energy, achieved through surface modification techniques such as UV laser treatment or the application of hydrophilic coatings, leads to enhanced wettability. This, in turn, improves functional characteristics such as adhesion, biocompatibility, and cell proliferation [26, 27]. Fig. 6 shows the dependencies of the free surface energy and its components on the wavelength of *UV* laser radiation and the scanning speed during surface treatment of *TiNi* specimens.

Following *UV* laser treatment, the ratio between the dispersive (γ_d) and polar (γ_p) components of the surface energy changes. A more than two-fold decrease in the dispersive component and a significant increase in the polar component are observed.

When the scanning speed is reduced during *UV* laser treatment, the value of the dispersive component remains almost unchanged and does not exceed 10 mJ/m², while the polar component increases by 5 to 7
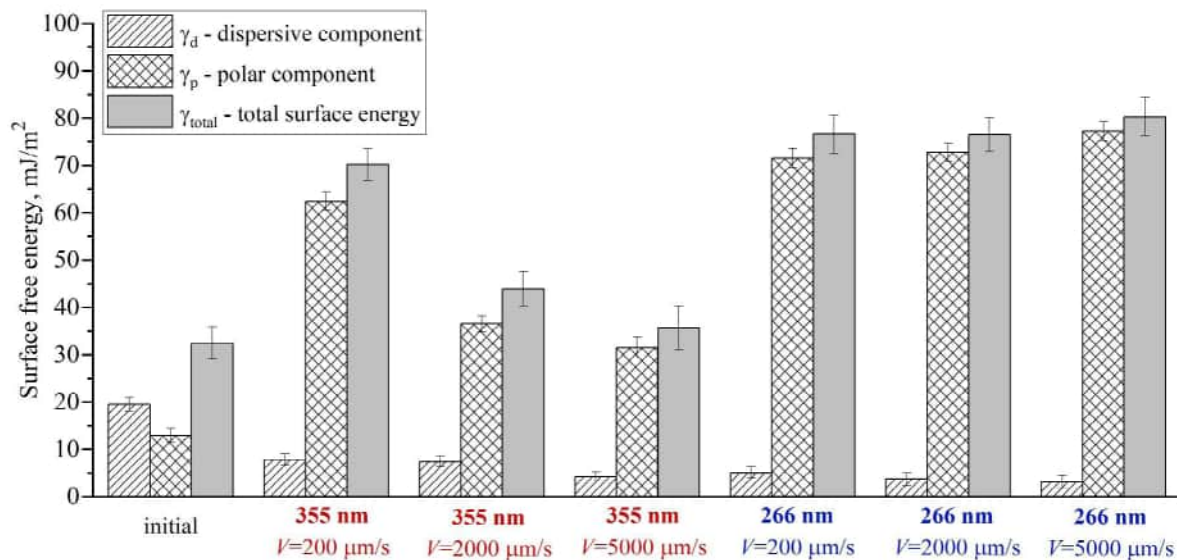
Fig. 6. Surface free energy (γ_{total}) and its components (polar γ_p and dispersive γ_d) of *TiNi* specimens before and after *UV* laser treatment with different parameters

times. This effect is primarily attributed to the oxidation of the *TiNi* surface during laser treatment, which increases the oxygen content and leads to the formation of polar oxide groups. These groups enhance the polar component of the surface energy, thereby increasing the material's hydrophilicity. In addition, it can be assumed that during *UV* laser treatment, the surface electric potential of *TiNi* specimens shifts to the positive region. As a result, surfactant molecules from the environment adsorb onto the modified surface in such a way that their hydrophilic polar groups, which carry a positive charge, are oriented away from the surface, while the hydrocarbon radicals, which exhibit hydrophobic properties, are directed towards the metal. It is this reorientation of the adsorbed layer that can explain the sharp increase in the polar component of the surface energy [28].

A comparative analysis of the laser treatment modes revealed distinct differences in the effects of *UV* laser radiation at 266 nm and 355 nm wavelengths on the *TiNi* specimens. For the 355 nm wavelength, the free surface energy exhibits a dependence on the scanning speed: as the speed decreases, the surface energy increases. In contrast, the surface treated with the 266 nm wavelength demonstrates different behavior. Even at the maximum scanning speed ($V = 5000$ μm/s), the surface energy increases approximately 2 times compared to the initial state. A further reduction in the scanning speed results in only minor changes to the free surface energy and its components (γ_d and γ_p). These results are consistent with the water contact angle measurements presented in Fig. 5.

The different effects of 266 nm and 355 nm *UV* laser surface treatment on the water contact angle of *TiNi* specimens are caused by the distinct changes in the free surface energy, which depends on both the microrelief and the structural-chemical characteristics of the surface formed after *UV* laser treatment. Key governing parameters that determine surface modification during laser treatment include wavelength, pulse energy, pulse repetition rate, pulse duration, and the spatial beam profile. In the present case, the wavelength was the variable parameter. Therefore, the observed difference in the structure and properties of the surface after modification with 266 nm and 355 nm radiation is specifically related to the distinct influence of the laser wavelength.

The difference in the characteristics of the *TiNi* specimen surfaces modified by ultraviolet laser radiation with wavelengths of 266 nm and 355 nm is primarily due to the distinct degree of interaction between the radiation and the material. This is related to the differences in reflectivity and the material's absorption coefficient at these wavelengths. *UV* laser radiation with a wavelength of 266 nm possesses higher photon energy and exhibits significantly greater energy absorption within the surface layer of the material. This leads to more intense local heating and surface oxidation. In turn, *UV* laser radiation with a wavelength of 355 nm is characterized by a greater penetration depth, resulting in a different energy distribution and

the formation of a distinct surface microstructure. The experimentally determined values of the reflection coefficient R, measured using a *Gentec QE50LP-H-MB-D0* energy meter, were $R \approx 20\%$ for the 266 nm wavelength and $R \approx 30\%$ for 355 nm. These data are in good agreement with the results obtained for the *Ti6Al4V* alloy [16], where it was established that the reflectivity of the alloy increases with the wavelength of the incident laser radiation in the range of 266 to 1064 nm. The lower value of the reflection coefficient for *UV* laser radiation with a wavelength of 266 nm indicates significantly greater energy absorption in the near-surface layer, which is explained by the higher photon energy. Consequently, these differences affect the changes in morphology, chemical composition, phase state of the surface, as well as the free surface energy and hydrophilicity of the material after *UV* laser treatment. Therefore, *UV* laser radiation with a wavelength of 266 nm is characterized by a lower penetration depth and a more intense effect on the surface layers, which determines the differences in the resulting microstructure and chemical composition of the *TiNi* specimens after *UV* laser treatment.

Conclusion

1. It was established that at scanning speeds above 500 µm/s, the original surface morphology of the *TiNi* alloy is preserved upon exposure to *UV* laser radiation at wavelengths of 266 and 355 nm. The formation of isolated microcracks is observed on the *TiNi* alloy surface subjected to *UV* laser radiation at a scanning speed of $V = 500$ µm/s only with the 266 nm wavelength. At the lowest scanning speed of $V = 200$ µm/s, exposure to *UV* laser radiation for both wavelengths (266 and 355 nm) leads to the formation of localized structural damage on the *TiNi* alloy surface in the form of a microcrack network. The individual microcracks and the overall microcracking of the *TiNi* surface after *UV* treatment are caused by local thermal stresses arising from rapid heating and subsequent quenching of the surface during the *UV* laser treatment.

2. It was demonstrated that during *UV* laser treatment of the *TiNi* alloy surface, a decrease in the radiation wavelength from 355 to 266 nm and a reduction in scanning speed from 5,000 to 200 µm/s lead to an increase in oxygen content in the near-surface layer of *TiNi* up to ≈ 20 at.% ($\lambda = 266$ nm, $V = 200$ µm/s) and ≈ 10 at.% ($\lambda = 355$ nm, $V = 200$ µm/s), with the formation of titanium oxides.

3. *UV* laser treatment results in a significant increase in the wettability of the *TiNi* surface. The maximum reduction in the water contact angle to $\approx 11°$ was achieved using radiation with a wavelength of 266 nm, whereas treatment with 355 nm laser radiation reduced the angle to $\approx 25°$ ($V = 200$ µm/s). It was determined that the observed significant increase in the hydrophilicity of the *TiNi* specimens is due to the enrichment of the near-surface layer with oxygen, the formation of oxide phases, and, consequently, a substantial increase in the free surface energy driven by a sharp rise in its polar component.

Thus, *UV* laser treatment with a wavelength of 266 nm induces more significant changes in the morphology and properties of the *TiNi* alloy surface compared to 355 nm radiation under identical processing regimes. This is manifested in more intense surface oxidation with the formation of oxide phases, more pronounced development of microcracks at low scanning speeds (200 and 500 µm/s), and a substantial enhancement of hydrophilicity. The observed effects are associated with the higher photon energy and the lower surface reflection coefficient ($R \approx 20\%$ for 266 nm radiation versus $R \approx 30\%$ for 355 nm radiation) of the *TiNi* specimens. This ensures efficient energy absorption in the near-surface layer and promotes changes in morphology and topography, as well as oxidation processes on the surface of the *TiNi* specimens.

References

1. Jani J.M., Leary M., Subic A., Gibson M.A. A review of shape memory alloy research, applications and opportunities. *Materials & Design*, 2014, vol. 56, pp. 1078–1113. DOI: 10.1016/j.matdes.2013.11.084.

2. Elahinia M., Moghaddam N.S., Andani M.T., Amerinatanzi A., Bimber B.A., Hamilton R.F. Fabrication of NiTi through additive manufacturing: A review. *Progress in Materials Science*, 2016, vol. 83, pp. 630–663. DOI: 10.1016/j.pmatsci.2016.08.001.

3. Ryhänen J., Kallioinen M., Tuukkanen J., Junila J., Niemelä E., Sandvik P., Serlo W. In vivo biocompatibility evaluation of nickel-titanium shape memory metal alloy: Muscle and perineural tissue responses and encapsule

membrane thickness. *Journal of Biomedical Materials Research*, 1998, vol. 41 (3), pp. 481–488. DOI: 10.1002/(sici)1097-4636(19980905)41:3<481::aid-jbm19>3.0.co;2-l.

4. Liu K., Yao X., Jiang L. Recent developments in bio-inspired special wettability. *Chemical Society Reviews*, 2010, vol. 39 (8), pp. 3240–3255. DOI: 10.1039/b917112f.

5. Poon R.W.Y., Ho J.P.Y., Liu X., Chung C.Y., Chu P.K., Yeung K.W.K., Lu W.W., Cheung K.M.C. Improvements of anti-corrosion and mechanical properties of NiTi orthopedic materials by acetylene, nitrogen and oxygen plasma immersion ion implantation. *Nuclear Instruments and Methods in Physics Research, Section B: Beam Interactions with Materials and Atoms*, 2005, vol. 237 (1–2), pp. 411–416. DOI: 10.1016/j.nimb.2005.05.030.

6. Slobodyan M.S., Markov A.B. Laser and electron-beam surface processing on TiNi shape memory alloys: a review. *Russian Physics Journal*, 2024, vol. 67 (5), pp. 565–615. DOI: 10.1007/s11182-024-03158-5.

7. Meisner L.L., Markov A.B., Rotshtein V.P., Ozur G.E., Meisner S.N., Yakovlev E.V., Semin V.O., Mironov Yu.P., Poletika T.M., Girsova S.L., Shepel D.A. Microstructural characterization of Ti-Ta-based surface alloy fabricated on TiNi SMA by additive pulsed electron-beam melting of film/substrate system. *Journal of Alloys and Compounds*, 2018, vol. 730, pp. 376–385. DOI: 10.1016/j.jallcom.2017.09.238.

8. Firstov G.S., Vitchev R.G., Kumar H., Blanpain B., Van Humbeeck J. Surface oxidation of NiTi shape memory alloy. *Biomaterials*, 2002, vol. 23 (24), pp. 4863–4871. DOI: 10.1016/S0142-9612(02)00244-2.

9. Marchenko E., Yasenchuk Yu., Baigonakova G., Gunther S., Yuzhakov M., Zenkin S., Potekaev A., Dubovikov K. Phase formation during air annealing of Ti-Ni-Ti laminate. *Surface and Coatings Technology*, 2020, vol. 388, p. 125543. DOI: 10.1016/j.surfcoat.2020.125543.

10. Khan M.A., Halil A.M., Abidin M.S.Z., Hassan M.H., Rahman A.A.A. Influence of laser surface texturing on the surface morphology and wettability of metals and non-metals: A review. *Materials Today Chemistry*, 2024, vol. 41, p. 102316. DOI: 10.1016/j.mtchem.2024.102316.

11. Pequegnat A., Michael A., Wang J., Lian K., Zhou Y., Khan M.I. Surface characterizations of laser modified biomedical grade NiTi shape memory alloys. *Materials Science and Engineering: C*, 2015, vol. 50, pp. 367–378. DOI: 10.1016/j.msec.2015.01.085.

12. Zhang Q., Dong J., Peng M., Yang Z., Wan Y., Yao F., Zhou J., Ouyang C., Deng X., Luo H. Laser-induced wettability gradient surface on NiTi alloy for improved hemocompatibility and flow resistance. *Materials Science and Engineering: C*, 2020, vol. 111, p. 110847. DOI: 10.1016/j.msec.2020.110847.

13. Biffi C.A., Fiocchi J., Rancan M., Gambaro S., Cirisano F., Armelao L., Tuissi A. Ultrashort laser texturing of superelastic NiTi: Effect of laser power and scanning speed on surface morphology, composition and wettability. *Metals*, 2023, vol. 13 (2), p. 381. DOI: 10.3390/met13020381.

14. Chan C.-W., Carson L., Smith G.C. Fibre laser treatment of martensitic NiTi alloys for load-bearing implant applications: Effects of surface chemistry on inhibiting Staphylococcus aureus biofilm formation. *Surface and Coatings Technology*, 2018, vol. 349, pp. 488–502. DOI: 10.1016/j.surfcoat.2018.06.015.

15. Chenrayan V., Vaishnav V., Shahapurkar K., Dhanabal P., Kalayarasan M., Raghunath S., Mano M. The effect of fs-laser micromachining parameters on surface roughness, bio-corrosion and biocompatibility of nitinol. *Optics & Laser Technology*, 2024, vol. 170, p. 110200. DOI: 10.1016/j.optlastec.2023.110200.

16. Milovanović D.S., Radak B.B., Gaković B.M., Batani D., Momčilović M.D., Trtica M.S. Surface morphology modifications of titanium based implant induced by 40 picosecond laser pulses at 266 nm. *Journal of Alloys and Compounds*, 2010, vol. 501 (1), pp. 89–92. DOI: 10.1016/j.jallcom.2010.04.047.

17. Sablina T.Y., Panchenko M.Yu., Zyatikov I.A., Puchikin A.V., Konovalov I.N., Panchenko Yu.N. Study of surface hydrophilicity of metallic materials modified by ultraviolet laser radiation. *Obrabotka metallov (tekhnologiya, oborudovanie, instrumenty) = Metal Working and Material Science*, 2024, vol. 26, no. 4, pp. 218–233. DOI: 10.17212/1994-6309-2024-26.4-218-233. (In Russian).

18. Wang Y., Zhang M., Li K., Hu J. Study on the surface properties and biocompatibility of nanosecond laser patterned titanium alloy. *Optics & Laser Technology*, 2021, vol. 139, p. 106987. DOI: 10.1016/j.optlastec.2021.106987.

19. Li S., Cui Z., Zhang W., Li Y., Li L., Gong D. Biocompatibility of micro/nanostructures nitinol surface via nanosecond laser circularly scanning. *Materials Letters*, 2019, vol. 255, p. 126591. DOI: 10.1016/j.matlet.2019.126591.

20. Hebbar R.S., Isloor A.M., Ismail A.F. Contact angle measurements. *Membrane Characterization*. Ed. by N. Hilal, A.F. Ismail, T. Matsuura, D. Oatley-Radcliffe. Elsevier, 2017, pp. 219–255. DOI: 10.1016/B978-0-444-63776-5.00012-7.

21. Owens D.K., Wendt R.C. Estimation of the surface free energy of polymers. *Journal of Applied Polymer Science*, 1969, vol. 13 (8), pp. 1741–1747. DOI: 10.1002/app.1969.070130815.

22. Razi S., Mollabashi M., Madanipour K. Laser processing of metallic biomaterials: An approach for surface patterning and wettability control. *The European Physical Journal Plus*, 2015, vol. 130, p. 247. DOI: 10.1140/epjp/i2015-15247-5.

23. Min J., Wan H., Carlson B.E., Lin J., Sun C. Application of laser ablation in adhesive bonding of metallic materials: A review. *Optics & Laser Technology*, 2020, vol. 128, p. 106188. DOI: 10.1016/j.optlastec.2020.106188.

24. Choi H., Na M., Jun I., Lee M.-H., Jung H.-D., Lee H., Han J., Lee K., Park C.-H., Kim H.-E., Song J., Koh Y.-H., Kim S. Repetitive nanosecond laser-induced oxidation and phase transformation in NiTi alloy. *Metals and Materials International*, 2024, vol. 30, pp. 1200–1208. DOI: 10.1007/s12540-023-01581-w.

25. Yasenchuk Yu.F., Gunther S.V., Kokorev O.V., Marchenko E.S., Gunther V., Baigonakova G.A., Dubovikov K.M. The influence of surface treatment on wettability of TiNi-based alloy. *Russian Physics Journal*, 2019, vol. 62 (2), pp. 333–338. DOI: 10.1007/s11182-019-01716-w.

26. Villapun Puzas V.M., Carter L.N., Schröder C., Colavita P.E., Hoey D.A., Webber M.A., Addison O., Shepherd D.E.T., Attallah M.M., Grover L.M., Cox S.C. Surface free energy dominates the biological interactions of postprocessed additively manufactured Ti-6Al-4V. *ACS Biomaterials Science & Engineering*, 2022, vol. 8 (10), pp. 4311–4326. DOI: 10.1021/acsbiomaterials.2c00298.

27. Peethan A., Unnikrishnan V.K., Chidangil S., George S.D. Laser-assisted tailoring of surface wettability – Fundamentals and applications: A critical review. *Progress in Adhesion and Adhesives*. Vol. 5. *Surface modification of polymers: methods and applications*. Ed. by K.L. Mittal, S.D. George. Scrivener Publishing LLC, 2020, pp. 331–265. ISBN 9781119748069. DOI: 10.1002/9781119749882.ch11.

28. Ryzhenkov A.V., Volkov A.V., Trushin E.S., Cherepanov S.P. Change of wettability of stainless steel surface based on laser texturing of relief. *Global'naya energiya = Global Energy*, 2022, vol. 28, no. 4, pp. 136–146. DOI: 10.18721/JEST.28409. (In Russian).

Conflicts of Interest

The authors declare no conflict of interest.

Obrabotka metallov –
Metal Working and Material Science

Effect of Zr, Sc, and Hf additions on the microstructure formation of cast ALTEK alloys

Alina Levagina [1, a, *], *Evgenii Aryshenskii* [1, b], *Sergey Konovalov* [1, c], *Dmitry Rasposienko* [2, d]

[1] Siberian State Industrial University, 42 Kirova str., Novokuznetsk, 654007, Russian Federation

[2] M.N. Miheev Institute of Metal Physics of Ural Branch of Russian Academy of Sciences, 18 S. Kovalevskoy st., Yekaterinburg, 620990, Russian Federation

[a] https://orcid.org/0000-0002-7270-6008, levagina_aa@sibsiu.ru; [b] https://orcid.org/0000-0003-3875-7749, arishenskiy_ev@sibsiu.ru;
[c] https://orcid.org/0000-0003-4809-8660, konovalov@sibsiu.ru; [d] https://orcid.org/0000-0002-7670-9054, dmitrijrasp@gmail.com

ARTICLE INFO

ABSTRACT

Introduction. Aluminum alloys of the *Al-Cu-Mn* system, alloyed with 23% copper and 1–2% manganese (*ALTEK*), are distinguished by heat resistance and high mechanical properties due to the formation of nano-dispersed particles of the $Al_{20}Cu_2Mn_3$ phase. When exposed to high temperatures (up to 400°C), the particles block the processes of polygonization and recovery, hindering the movement of grain boundaries. A promising direction for improving these alloys is the modification of the cast structure with transition metals (*TMs*). An insufficient content of *TMs* does not provide a modifying effect, while an excessive amount leads to a reduction in strength due to the formation of a large number of coarse intermetallic particles. **The subject** of this work a *ALTEK* alloys alloyed with *Mg*, *Zr*, *Sc*, and *Hf*. **The purpose** of the work is to determine the optimal concentrations of scandium, hafnium, and zirconium required for effective modification of the cast structure of *ALTEK* alloys during complex alloying. The effect of complex additions of transition metals (*Zr*, *Sc*, *Hf*) on the formation of the cast structure of *Base0.15Zr0.05Sc0.05Hf*, *Base0.1Zr0.14Sc0.16Hf*, *Base0.1Zr0.2Sc0.16Hf, and Base0.1Zr0.25Sc0.16Hf* alloys is investigated in comparison to the base alloy. **The research methods** were optical and scanning electron microscopy, and X-ray diffraction analysis. **Results and discussion.** Modification of the grain structure in alloys with a scandium content of less than 0.20% is not observed, and the average grain structure size is 350 μm. The addition of scandium in the amount of 0.20% and 0.25% leads to a decrease in the average grain diameter to 41.8 μm and 29.7 μm, respectively. Scanning electron microscopy showed that particles of the Al_6Mn and Al_2CuMg phases are present in all the alloys studied. Particles of the $Al_3(Sc,Hf,Zr)$ phase are found in the *Base0.1Zr0.2Sc0.16Hf* and *Base0.1Zr0.25Sc0.16Hf* compositions. X-ray diffraction analysis revealed the $Al_{20}Cu_2Mn_3$ phase and small amounts of Al_6Mn and Al_2CuMg in the base alloy and in the *Base0.1Zr0.25Sc0.16Hf* alloy. The structural modification is explained by the precipitation of primary $Al_3(Sc, Zr, Hf)$ particles. **Application of the results.** The obtained results are promising for the development of new materials for the manufacture of aerospace products. **Conclusions.** The addition of 0.20–0.25% scandium with a zirconium content of 0.1% and hafnium of 0.16% is the most effective.

Introduction

The combination of low density and high corrosion resistance makes aluminum a high-demand material. Its alloys, modified with alloying elements and thermomechanical treatment, provide excellent mechanical and performance characteristics, making them indispensable in the aerospace, automotive, and power generation industries [1, 2].

ALTEK alloys of the *Al-Cu-Mn* system, which possess above-average thermal stability, are of particular scientific and practical interest. Such alloys are characterized by a low copper content (1–3 %) compared

_____
* Corresponding author
Levagina Alina A., junior researcher
Siberian State Industrial University,
42 Kirova str.,
654007, Novokuznetsk, Russian Federation
Tel.: +7 900 321-55-05, **e-mail:** levagina_aa@sibsiu.ru

to industrial alloys, and the manganese content varies within the 1–2 % range. A two-phase structure, consisting of an aluminum solid solution and a thermally stable $Al_{20}Cu_2Mn_3$ phase, is formed in these alloys [3–5]. Nanosized $Al_{20}Cu_2Mn_3$ particles effectively suppress recrystallization and recovery processes at temperatures up to 400 °C during prolonged exposure (at least 3 hours) [6–8]. One method for improving the structural and functional properties of *ALTEK* alloys is to modify their as-cast microstructure.

Fine-grained structures exhibit enhanced plasticity and strength and are less prone to low-temperature brittleness. In contrast, coarse-grained structures degrade the performance and service properties of rolled sheets due to non-uniform deformation and increase the rejection rate [9]. Fine-grain structure formation is facilitated by high cooling rates, physical effects (e.g., ultrasound), the introduction of modifying additives, and thermomechanical treatment parameters. However, crystallization at high cooling rates and the application of physical effects are not always feasible in production. Therefore, the use of modifying agents is the most practical method for grain refinement during casting [10].

Transition metals (*TMs*) are the most commonly used modifying agents [11–17]. Scandium (*Sc*), as the most effective modifying agent, forms primary Al_3Sc particles that act as crystallization nuclei. However, the high cost of *Sc* necessitates alternative solutions. It has been experimentally established that the combined addition of *Zr* and *Hf* allows for a reduction in *Sc* content while enhancing the modifying effect [11]. The aspect of combined *Zr*, *Sc*, and *Hf* addition has been insufficiently studied for *ALTEK* system alloys. Existing studies have addressed the effects of *Zr* [6, 18] and *Zr* and *Sc* (with *Cr* addition) [7]; however, the effect of *Hf* addition has not been investigated.

Studies [6, 19, 20] mention the effect of zirconium addition on the properties of *ALTEK* alloys. Typically, zirconium content varies within the 0.22–0.59 *Zr* range (compositions: *1.97% Cu-1.92% Mn-0.22% Zr; 1.48% Cu-1.53% Mn-0.41% Zr; 1.11% Cu-0.95% Mn-0.59% Zr* [6, 19]; *1.6% Cu-1.37% Mn-0.5% Zr* [18]). However, unlike the base compositions, zirconium had a negligible effect on the as-cast structure in the above alloys, as it was fully dissolved in the aluminum solid solution in the as-cast state. Study [21] examined an alloy with *Sc* addition (*1.74% Cu-1.57% Mn-0.25% Zr-0.1% 1Sc*). This alloy exhibits an as-cast structure similar to that of ternary *Al-Cu-Mn* alloys. Al_7Cr particles were identified in [7] for an *Al-Cu-Mn-(Sc, Cr)* alloy (*1.6% Cu–1.8% Mn–0.4% Zr–0.15% Cr*). The grain structure consists of two zones: columnar and equiaxed crystals, which may also be associated with crystallization in a small-diameter (40 mm) graphite mold. It should be noted that in all the studied compositions, the selection of rare earth metals was aimed at preventing the formation of primary intermetallic compounds; therefore, the TMs did not significantly affect the as-cast structure. Primary Al_3Sc- and Al_3Zr-type intermetallic compounds, in turn, have a dual function: on one hand, they act as modifying agents, refining the grain structure and thereby improving strength properties according to the *Hall-Petch* relationship [22]; on the other hand, such intermetallic compounds act as stress concentrators, often leading to a reduction in plasticity in the alloys containing them. For this reason, in practical applications, efforts are made to select transition element concentrations that, on one hand, ensure as-cast structure refinement and, on the other hand, do not cause the formation of large amounts of primary intermetallic compounds. However, such studies have not been conducted for *ALTEK* alloys.

Thus, ***the objective of this study*** is to determine the optimal *Sc*, *Hf*, and *Zr* concentrations required for effective as-cast structure modification during complex alloying of *ALTEK* alloys. The following ***tasks*** will be addressed to achieve this objective:

1. Comparative analysis of grain structures.

2. Identification of intermetallic compounds formed in the studied *ALTEK* alloys using scanning electron microscopy and X-ray diffraction analysis.

Methods

It is known that for effective grain structure modification of aluminum alloys, the combined amount of *Sc* and *Zr* should not exceed 0.11–0.15 % [16], and *Hf* addition is effective if its maximum content is 0.2 % [11]. These guidelines were observed to select the transition metal contents.

The phase composition was analyzed using computational methods with the *Thermo-Calc* software and the *TTAL5* database. The alloy phase composition was simulated at temperatures of 200 and 400 °C.

Casting

Five alloys with the chemical compositions listed in Table 1 were cast in a steel chill mold to investigate the effect of the *TM* complex.

Table 1

Chemical composition of model alloys

No.	Content, %					
	Cu	*Mn*	*Mg*	*Zr*	*Sc*	*Hf*
1	2	2	1.5	–	–	–
2	2	2	1.5	0.15	0.05	0.05
3	2	2	1.5	0.1	0.14	0.16
4	2	2	1.5	0.1	0.20	0.16
5	2	2	1.5	0.1	0.25	0.16

The following designations were introduced for convenience:
- **Base** – base alloy **2% Cu-2% Mn-1.5% Mg**
- **Base0.15Zr0.05Sc0.05Hf**
- **Base0.1Zr0.14Sc0.16Hf**
- **Base0.1Zr0.2Sc0.16Hf**
- **Base0.1Zr0.25Sc0.16Hf**

The numbers preceding the chemical symbols indicate their concentration in weight percent (wt.%).

The ingots were produced by melting in an induction furnace and casting into a steel chill mold. The melting procedure was performed as described in a previous study [14]. The following materials were used as charge: *A85* grade aluminum, *Mg90* magnesium, *M1* copper, *Al-Sc2, Al-Zr5, Al-Hf2* master alloys, and *Mn90Al10* alloying pellets.

The chemical composition of the produced alloys was determined according to [15]. The sampling for analysis was performed at 730 °C.

Microstructure examination

Optical microscopy was used to assess the efficiency of the selected ratio and concentration of the modifying agents. The microstructure was examined on a smooth, cleaned surface. For metallographic preparation, the samples were mounted in epoxy resin, and the surfaces were ground using a *Forcipol 2* dual-disk grinder/polisher with abrasive papers of varying grit sizes (*P400*, *P600*, *P800*, *P1000*, *P1500*, and *P2000*). Final polishing was achieved using a felt cloth and *Goya* paste. The grain structure was revealed by etching in a 15% *NaOH* solution and subsequently treated with a special reagent for visualization. The reagent composition was as follows: 400 ml hydrochloric acid, 220 ml nitric acid, 50 g copper filings, and 300 ml water. For each sample, two images were captured at magnifications of ×50 and ×200 (or lower, if necessary). The average grain size was measured using the linear intercept method according to *GOST 21073.2*. Microstructure images were obtained using an *OLYMPUS GX-51* optical microscope.

For the examination of Al_6Mn, Al_2CuMg, and $Al_3(Sc,Zr,Hf)$ particles, the sample surfaces were prepared by grinding and polishing after mounting in epoxy resin. The samples were then removed from the resin for further examination using a scanning electron microscope. The particles were examined using a *KYKY EM6900* scanning electron microscope, with 10 images captured per sample. For particle identification, *EDS* analysis data were compared with published data [9, 17, 24–27].

X-ray diffraction analysis

X-ray diffraction analysis was performed using a *BRUKER D8 ADVANCE* diffractometer with *CuKα* radiation ($\lambda = 0.15418$ nm) over a 2θ angular range of 20° to 60°, with an exposure time of 10 seconds per point. The data were processed using *DIFFRAC.EVA 4.0* and *DIFFRAC.TOPAS 5.0* software [23].

The phase composition of the samples was determined via X-ray phase analysis. Interplanar distances, calculated from the diffraction peak positions, were compared with the *PDF-2/1202* database.

Transmission electron microscopy (TEM)

The **Base0.1Zr0.2Sc0.16Hf** alloy was used for $Al_{20}Cu_2Mn_3$ phase identification via *TEM*. The samples were prepared by mechanical thinning followed by electrolytic thinning. 3 mm diameter disks were punched using an *Ultratonic Disk Cutter*. Electropolishing was performed in an *A2* electrolyte using a *Struers Tenupol* unit. A *PIPS II* ion polishing system was used to remove carbon contamination. Grain structure and phase analyses were performed using standard techniques, including bright-field (*BF*) and dark-field (*DF*) imaging and electron microdiffraction. Phases were identified by correlating their interplanar distances with reference data from the *JCPDS-ICDD* database, followed by chemical analysis. The interplanar distances were calculated based on additional reflections in the electron diffraction patterns.

Results and Discussion

Based on optical microscopy data (Fig. 1), the alloy without *TM* additions exhibits a dendritic grain structure with a grain size of approximately 350 µm. No significant grain refinement was observed in the **Base0.15Zr0.05Sc0.05Hf** alloy with a low TM content. The average grain diameter was 239 µm. An initial modifying effect was observed in the **Base0.1Zr0.14Sc0.16Hf** alloy, where individual fine grains (up to 35 µm in diameter) appeared against a predominantly coarse-grained as-cast structure, reducing the average grain size to 118 µm.
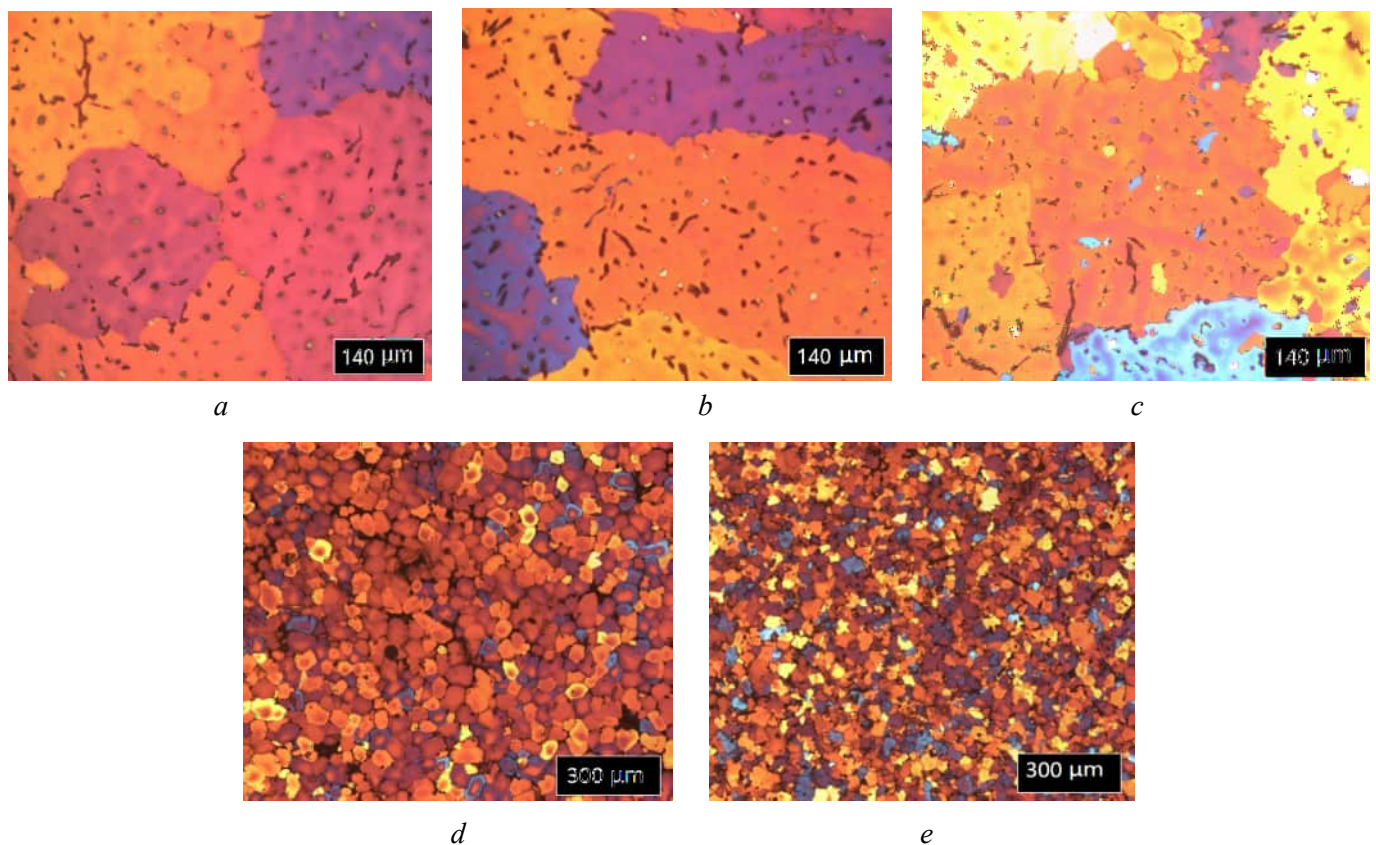

a   *b*   *c*

d   *e*

Fig. 1. Microstructure of *Al-Cu-Mn-Mg* (*Zr, Sc, Hf*) alloys:

Base (a), Base0.15Zr0.05Sc0.05Hf (b), Base0.1Zr0.14Sc0.16Hf (c), Base0.1Zr0.2Sc0.16Hf (d), Base0.1Zr0.25Sc0.16Hf (e)

Qualitative changes in the microstructure occurred in the **Base0.1Zr0.2Sc0.16Hf** and **Base0.1Zr0.25Sc0.16Hf** alloys, where effective grain refinement and the formation of an equiaxed grain structure were achieved, likely due to the precipitation of primary *Al₃(Zr,Sc,Hf)* particles. An increase in scandium content from 0.14 to 0.25 % led to a gradual reduction in grain size from 41.8 μm (0.2% *Sc* alloy) to 29.7 μm (0.25% *Sc* alloy).

According to scanning electron microscopy (*SEM*) data, the *Al₆Mn* phase was present in all studied alloys (Figs. 2 and 3). A typical *EDS* spectrum from such an inclusion is shown in Fig. 3, *a*. However, the inclusions exhibited significantly different sizes: their length in the base alloy does not exceed 15 μm (Fig. 2, *a*), while the largest inclusions, with lengths exceeding 45 μm, were identified in the **Base0.15Zr0.05Sc0.05Hf** alloy (Fig. 2, *b*). Inclusion sizes in the **Base0.1Zr0.14Sc0.16Hf** (Fig. 2, *c*) and **Base0.1Zr0.25Sc0.16Hf** (Fig. 2, *f*) alloys are comparable and do not exceed 20–25 μm. Individual large particles up to 40 μm in length were detected in the **Base0.1Zr0.2Sc0.16Hf** alloy (Fig. 2, *d*). The presence of the *Al₆Mn* phase in the **Base** and **Base0.1Zr0.2Sc0.16Hf** alloys was also confirmed by X-ray diffraction analysis (Figs. 4, 5).

All alloys contained *Al₂CuMg* inclusions, with a typical *EDS* spectrum shown in Fig. 3, *b*. Particularly large inclusions, up to 45–60 μm in length, were found in the **Base0.15Zr0.05Sc0.05Hf** (Fig. 2, *b*) and **Base0.1Zr0.2Sc0.16Hf** (Fig. 2, *e*) alloys. In the **Base0.1Zr0.25Sc0.16Hf** alloy, these phase inclusions were smaller, up to 20 μm (Fig. 2, *f, g*). In the **Base** (Fig. 2, *a*) and **Base0.1Zr0.2Sc0.16Hf** (Fig. 2, *e*) alloys, the
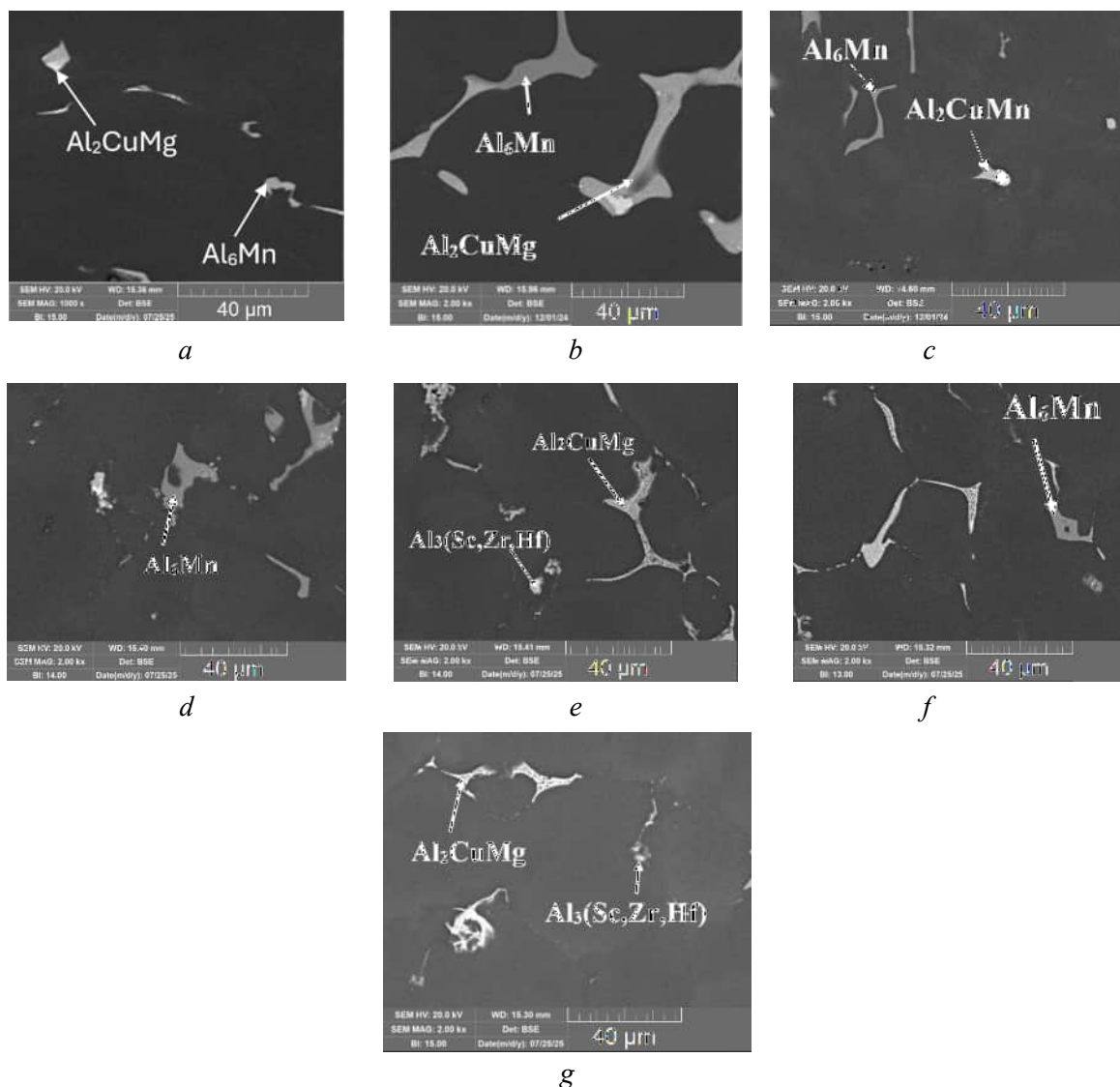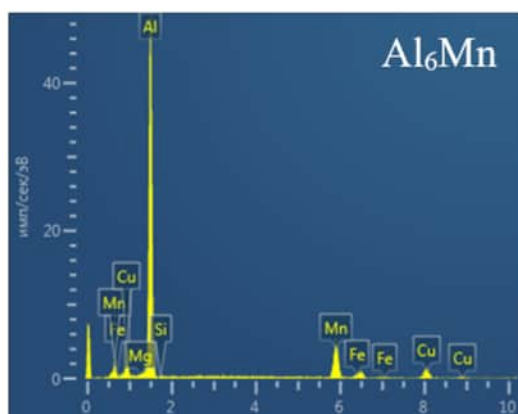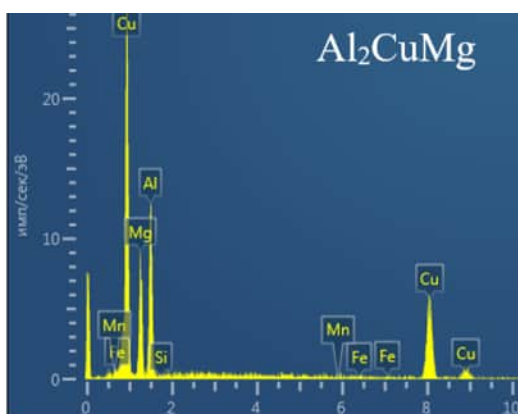

Fig. 2. Microstructure of alloys (*SEM* data):

Base (a); Base0.15Zr0.05Sc0.05Hf (b); Base0.1Zr0.14Sc0.16Hf (c); Base0.1Zr0.2Sc0.16Hf (d, e);
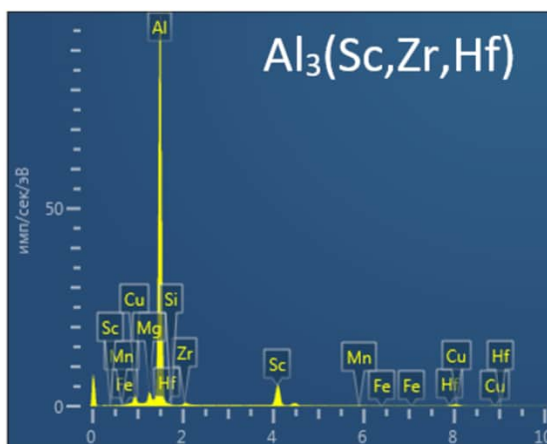*Base0.1Zr0.25Sc0.16Hf (f, g)*

Элемент	Атом. %
Al	78,53
Mn	13,67
Cu	6,39
Si	0,42
Fe	0,88
Mg	0,11

a

Элемент	Атом. %
Al	37,31
Cu	32,60
Mg	29,36
Si	0,28
Mn	0,23
Fe	0,21

b

Элемент	Атом. %
Al	86,10
Sc	7,96
Mg	2,44
Cu	1,79
Zr	0,91
Hf	0,38
Si	0,29

c

*Fig. 3*. Spectrograms of particles in alloys (*EDS* analysis):
Al_6Mn (*a*), Al_2CuMg (*b*), $Al_3(Sc, Zr, Hf)$ (*c*)

inclusion size did not exceed 5–10 μm. The presence of these phases was confirmed by *XRD* analysis of the studied alloys (Figs. 4, 5).

Primary intermetallic compounds $Al_3(Sc,Zr,Hf)$, with a near-equiaxed shape and diameters up to 4 μm (Fig. 2, *e*, *g*), were observed in alloys containing 0.2–0.25% *Sc*. A typical *EDS* spectrum from such an inclusion is presented in Fig. 3, *c*. It can be assumed that grain structure refinement is initiated precisely by these primary particles.

According to *XRD* results (Figs. 4, 5), the (*Al*) matrix and $Al_{20}Cu_2Mn_3$ phase are predominant in the **Base** and **Base0.1Zr0.2Sc0.16Hf** alloys. Minor amounts of the Al_2CuMg and Al_6Mn phases were also detected.

The results of phase composition modeling are presented in Fig. 6 and Table 2.
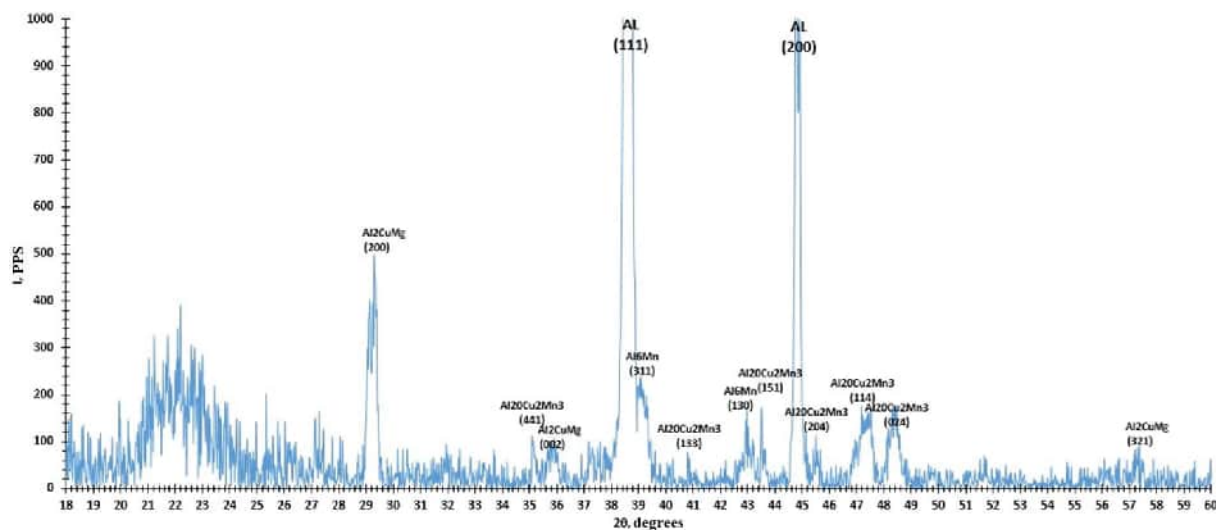
Fig. 4. Section of diffraction pattern of *Base* composition
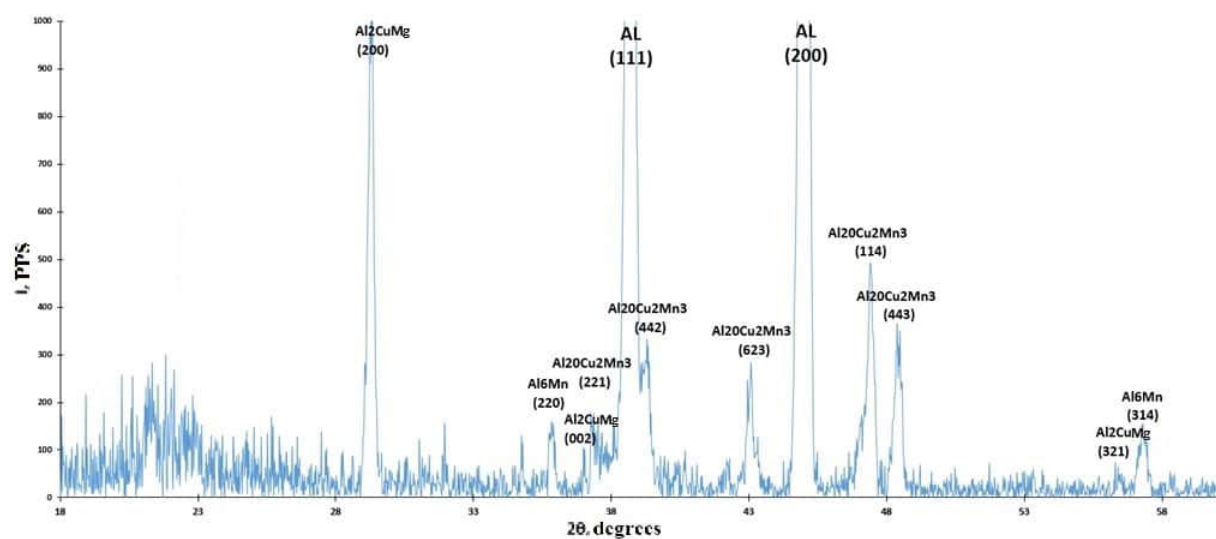
Fig. 5. Section of diffraction pattern of composition *Base0.1Zr0.2Sc0.16Hf*
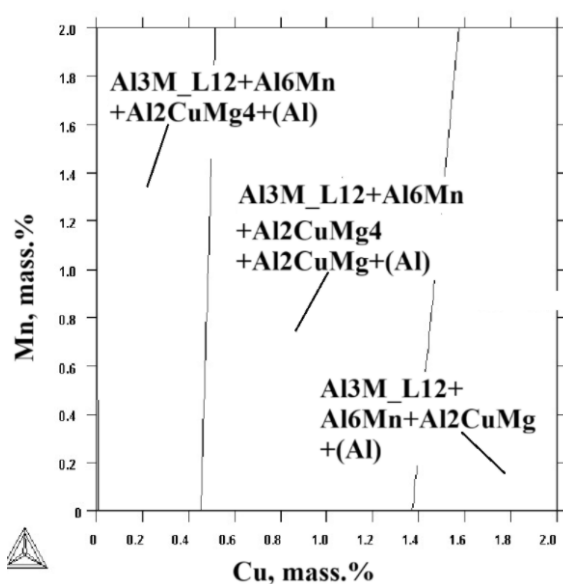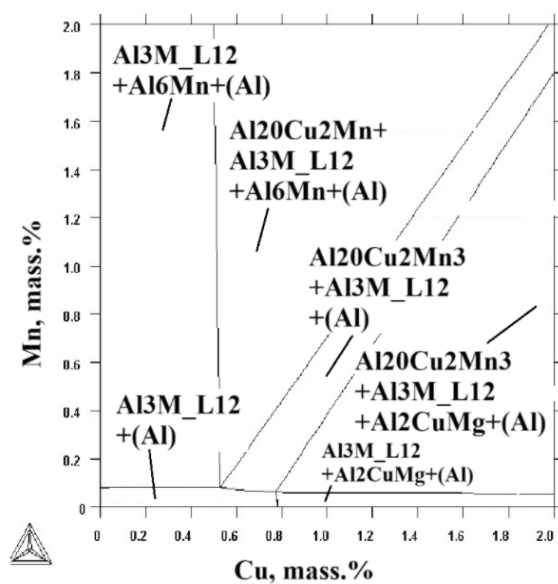
Fig. 6. Isothermal sections of the *Base0.1Zr0.14Sc0.16Hf alloy*:
at 200°C (*a*), at 400°C (*b*)

Table 2

Chemical composition of the alloys (*Thermo-Calc*)

No	Chemical composition	Phase composition		
		at 20°C	at 200°C	at 400°C
1	*2% Cu-2% Mn*	$Al_{20}Cu_2Mn_3+Al_2Cu+(Al)$	$Al_{20}Cu_2Mn_3+Al_2Cu+(Al)$	$Al_{20}Cu_2Mn_3+(Al)$
2	*Base*	$Al_{20}Cu_2Mn_3+Al_6Mn+$ $+Al_2CuMg+(Al)$	$Al_{20}Cu_2Mn_3+Al_6Mn+$ $+Al_2CuMg+(Al)$	$Al_{20}Cu_2Mn_3+(Al)$
3	*Base0.15Zr0.05Sc0.05Hf*	$Al_{20}Cu_2Mn_3+Al_6Mn+$ $+Al_2CuMg\,Al_3M\_L1_2+(Al)$	$Al_{20}Cu_2Mn_3+Al_2CuMg+$ $+Al_6Mn+Al_3M\_L1_2+(Al)$	$Al_{20}Cu_2Mn_3+$ $+Al_3M\_L1_2+(Al)$
4	*Base0.1Zr0.14Sc0.16Hf*	$Al_{20}Cu_2Mn_3+Al_6Mn+$ $+Al_2CuMg+Al_3M\_L1_2+(Al)$	$Al_{20}Cu_2Mn_3+Al_2CuMg+$ $+Al_6Mn+Al_3M\_L1_2+(Al)$	$Al_{20}Cu_2Mn_3+$ $+Al_3M\_L1_2+(Al)$

Modeling demonstrated that ingots of the base alloy have a phase composition consisting of an aluminum solid solution (*Al*), as well as $Al_{20}Cu_2Mn_3$, Al_2CuMg, and Al_6Mn phases. Ingots produced from alloys with *TM* additions (**Base0.15Zr0.05Sc0.05Hf, Base0.1Zr0.14Sc0.16Hf**) contained the Al_3M_L12 phase (where $M = Sc$, Zr, Hf). Thus, the addition of *Mg* to the *2% Cu–2% Mn* alloy leads to the formation of Al_2CuMg and Al_6Mn phases, while the addition of transition metals (*TM*) leads to the formation of a phase with an $L1_2$ (Al_3M_L12) crystal lattice.

Table 3 lists the particles identified in the model alloys and the methods used for their identification. The letter '***M***' indicates that the phase presence was verified by modeling using the *Thermo-Calc* software.

The addition of Mg reduced the grain size. This effect is related to the ability of *Mg* to reduce the interfacial tension in the liquid phase, thereby contributing to an increase in the density of crystallization

Table 3

Particles in the model alloys and methods of their identification

Alloys	Identified particles	Methods
Base	Al_6Mn Al_2CuMg $Al_{20}Cu_2Mn_3$	*SEM*, X-ray diffraction analysis, *M* *SEM*, X-ray diffraction analysis, *M* X-ray diffraction analysis, *M*
Base0.15Zr0.05Sc0.05Hf	Al_6Mn Al_2CuMg $Al_{20}Cu_2Mn_3$	SEM, M
Base0.1Zr0.14Sc0.16Hf	Al_6Mn Al_2CuMg $Al_{20}Cu_2Mn_3$	SEM
Base0.1Zr0.2Sc0.16Hf	Al_6Mn Al_2CuMg $Al_{20}Cu_2Mn_3$ $Al_3(Sc,Zr,Hf)$	*SEM*
Base0.1Zr0.25Sc0.16Hf	Al_6Mn Al_2CuMg $Al_{20}Cu_2Mn_3$ $Al_3(Sc,Zr,Hf)$	*SEM*, X-ray diffraction analysis, *M* *SEM, M* *X-ray* diffraction analysis, *M* *SEM, M*

nuclei. Consequently, the average grain size decreased from 3 mm (in *2% Cu–2% Mn*) to 350 μm (in *2% Cu–2% Mn–1.5% Mg*), confirming the influence of Mg on the crystallization process.

As noted above, a small *TM* addition (**Base0.15Zr0.05Sc0.05Hf**) has an insignificant effect on grain morphology, and the average grain diameter decreases only to 239 μm, while the grains retain an irregular, elongated shape. The **Base0.1Zr0.14Sc0.16Hf** composition was characterized by a preserved dendritic structure with an average grain diameter of 118 μm. A transition to a modified, refined structure occurs in alloys with *Sc* contents of 0.20–0.25%, with average grain sizes of 41.8 and 29.7 μm, respectively.

The addition of magnesium in this study led to the formation of *Al₂CuMg* and *Al₆Mn* inclusions (e.g., in the **Base0.15Zr0.05Sc0.05Hf** composition): magnesium, dissolved in the solid solution, displaces manganese, facilitating the formation of *Al₆Mn* particles. *Al₂₀Cu₂Mn₃* phase particles were not detected by *SEM*, likely due to their small size. *TEM* analysis was employed for their identification in the **Base0.1Zr0.2Sc0.16Hf** alloy (Fig. 7). The identified particles had an elongated, axis-symmetric shape and a length of approximately 200 nm.
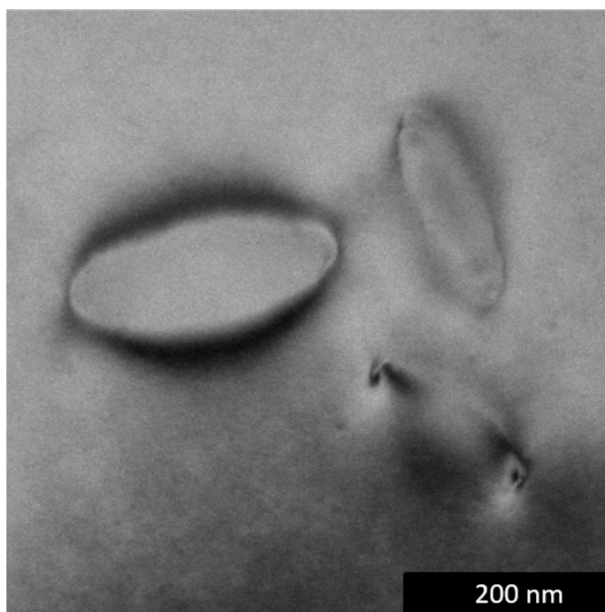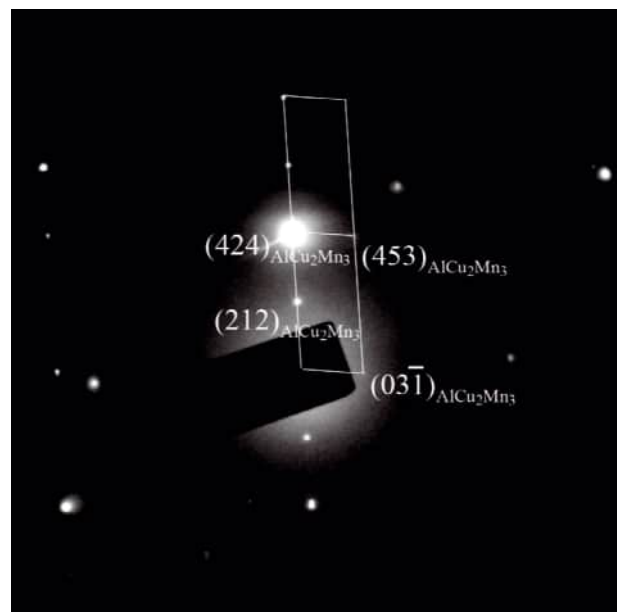
a   *b*

Fig. 7. $Al_{20}Cu_2Mn_3$ particle:
particle image (*TEM*) (*a*), electron diffraction pattern (zone axis [7–2–6]) (*b*)

It should be noted that in the *ALTEK* alloys, phases other than the *Al₂₀Cu₂Mn₃* type are present in insignificant amounts. The diffraction peak intensities of the *Al₂CuMg* and *Al₆Mn* phases are comparable to the background, indicating their low concentration. However, the combined application of *EDS* analysis and *Thermo-Calc* computations confirmed the presence of these phases in all studied alloys; therefore, they are marked on the diffraction patterns (Figs. 4, 5).

Al₃(Sc,Zr,Hf) particles were not detected by *XRD* analysis, which is explained by the extremely low *Sc* content, making their detection and identification particularly difficult.

Conclusion

1. The effect of complex transition metal (*TM*) additions was investigated for the following alloys: *2% Cu-2% Mn-1.5% Mg* (**Base**), **Base0.15Zr0.05Sc0.05Hf**, **Base0.1Zr0.14Sc0.16Hf**, **Base0.1Zr0.2Sc0.16Hf**, and **Base0.1Zr0.25Sc0.16Hf**. It was established that significant grain refinement does not occur at *Sc* contents of 0.05–0.14 %. In alloys containing 0.20 and 0.25 % *Sc*, an equiaxed grain structure was formed with average grain diameters of 41.8 μm and 29.7 μm, respectively.

2. Al_6Mn and Al_2CuMg phase inclusions were identified by scanning electron microscopy (*SEM*) in all studied alloys. Furthermore, this method enabled the detection of primary $Al_3(Sc,Zr,Hf)$ particles in alloys containing 0.20–0.25 % *Sc*, which were not resolvable by X-ray diffraction (*XRD*) analysis due to their low concentration and volume fraction.

References

1. Sizyakov V., Bazhin V., Vlasov A. Status and prospects for growth of the aluminum industry. *Metallurgist*, 2010, vol. 54, pp. 409–414. DOI: 10.1007/s11015-010-9316-z.

2. Belov N.A., Naumova E.A., Akopyan T.K. *Evtekticheskie splavy na osnove alyuminiya: novye sistemy legirovaniya* [Eutectic alloys based on aluminum: new alloying systems]. Moscow, Ruda i metally Publ., 2016. 256 p. ISBN 978-5-98191-083-8.

3. Dar S.M., Liao H. Creep behavior of heat resistant Al–Cu–Mn alloys strengthened by fine (θ′) and coarse (Al$_{20}$Cu$_2$Mn$_3$) second phase particles. *Materials Science and Engineering: A*, 2019, vol. 763, p. 138062. DOI: 10.1016/j.msea.2019.138062.

4. Feng Z.Q., Yang Y.Q., Huang B., Li M., Chen Y.X., Ru J.G. Crystal substructures of the rotation-twinned T (Al$_{20}$Cu$_2$Mn$_3$) phase in 2024 aluminum alloy. *Journal of Alloys and Compounds*, 2014, vol. 583, pp. 445–451. DOI: 10.1016/j.jallcom.2013.08.200.

5. Li X., Chen X., Feng Y., Chen B. Characterization and theoretical calculations of the T (Al20Cu2Mn3)/Al interface in 2024 alloys: TEM and DFT studies. *Vacuum*, 2023, vol. 210, pp. 111884. DOI: 10.1016/j.vacuum.2023.111884.

6. Belov N.A. [Substantiation of the composition and structure of deformable alloys based on the Al–Cu–Mn (Zr) system that do not require homogenization and hardening]. *Innovatsionnye tekhnologii, oborudovanie i material'nye zagotovki v mashinostroenii* [Innovative technologies, equipment and materials for blanking productions in mechanical engineering]. International Conference. Collection of works. Moscow, 2022, pp. 10–13. (In Russian).

7. Petrova A.N., Rasposienko D.Yu., Astafyev V.V., Yakovleva A.O. Structure and strength of Al-Mn-Cu-Zr-Cr-Fe ALTEC alloy after radial-shear rolling. *Letters on Materials*, 2023, vol. 13 (2), pp. 177–182. DOI: 10.22226/2410-3535-2023-2-177-182.

8. Fridlyander I.N., Berstenev V.V., Tkachenko E.A., Goloviznina G.M., Latushkina L.V., Lantsova L.P. Effect of heat treatment and deformation on the grain size and mechanical properties of duralumin-type alloys. *Metal Science and Heat Treatment*, 2003, vol. 45, pp. 239–245. DOI: 10.1023/A:1027316015223.

9. Belov N.A., Korotkova N.O., Akopyan T.K., Pesin A.M. Phase composition and mechanical properties of Al–1.5%Cu–1.5%Mn–0.35%Zr(Fe, Si) wire alloy. *Journal of Alloys and Compounds*, 2019, vol. 782, pp. 735–746. DOI: 10.1016/j.jallcom.2018.12.240.

10. Napalkov V.I., Frolov V.F., Baranov V.N., Belyaev S.V., Bezrukikh A.I. *Plavlenie i lit'e alyuminievykh splavov* [Melting and casting of aluminum alloys]. Krasnoyarsk, Siberian Federal University Publ., 2020. 716 p. ISBN 978-5-7638-4269-2.

11. Elagin V.I. *Legirovanie deformiruemykh alyuminievykh splavov perekhodnymi metallami* [Alloying of wrought aluminum alloys with transition metals]. Moscow, Metallurgiya Publ., 1975. 248 p.

12. Nokhrin A.V., Gryaznov M.Yu., Shotin S.V., Nagicheva G., Chegurov M.K., Bobrov A.A., Kopylov V.I., Chuvildeev V.N. Effect of Sc, Hf, and Yb additions on superplasticity of a fine-grained Al-0.4%Zr alloy. *Metals*, 2023, vol. 13, p. 133. DOI: 10.3390/met13010133.

13. Davydov V.G., Elagin V.I., Zakharov V.V., Rostova D. Alloying aluminum alloys with scandium and zirconium additives. *Metal Science and Heat Treatment*, 1996, vol. 38, pp. 347–352. DOI: 10.1007/bf01395323.

14. Drits A.M., Aryshenskii E.V., Kudryavtsev E.A., Zorin I.A., Konovalov S.V. Issledovanie raspada peresyshchennogo tverdogo rastvora v vysokomagnievykh alyuminievykh splavakh so skandiem, legirovannykh gafniem [The study of supersaturated solid solution decomposition in magnesium-rich aluminum alloys with scandium and hafnium additions]. *Frontier Materials & Technologies*, 2011, no. 4, pp. 38–48. DOI: 10.18323/2782-4039-2022-4-38-48.

15. Zorin I.A., Aryshenskii E.V., Kudryavtsev E.A., Drits A.M., Konovalov S.V. Vliyanie gafniya na vysokomagnievye splavy, legirovannye perekhodnymi metallami, pri termicheskoi obrabotke [The influence of hafnium on high-magnesium alloys doped with transition metals during heat treatment]. *Frontier Materials & Technologies*, 2024, no. 1, pp. 29–36. DOI: 10.18323/2782-4039-2024-1-67-3.

16. Zakharov V.V., Filatov Yu.A. Ekonomnolegirovannye skandiem alyuminievye splavy [Aluminum alloys sparingly alloyed with scandium]. *Tekhnologiya legkikh splavov = Technology of Light Alloys*, 2025, vol. 28, no. 4. DOI: 10.24412/0321-4664-2021-4-31-37.

17. Ragazin A.A., Aryshenskii E.V., Zorin I.A., Kudryavtsev E.A., Drits A.M., Konovalov S.V. Effect of hafnium on the microstructure formation during high-temperature treatment of high-magnesium aluminum alloys microalloyed with scandium and zirconium. *Physical Mesomechanics*, 2025, vol. 28, pp. 535–546. DOI: 10.1134/S1029959924601702.

18. Toleuova A.R., Belov N.A., Chervyakova V.V., Alabin A.N. Quantitative analysis of the Al–Cu–Mn–Zr phase diagram as a base for deformable refractory aluminum alloys. *Metal Science and Heat Treatment*, 2012, vol. 54 (7), pp. 402–406. DOI: 10.1007/s11041-012-9521-4.

19. Belov N.A., Alabin A.N. Energy efficient technology for Al–Cu–Mn–Zr sheet alloys. *Materials Science Forum*, 2013, vol. 765, pp. 13–17. DOI: 10.4028/www.scientific.net/MSF.765.13.

20. Belov N., Alabin A., Aleshchenko A., Mann V., Tsydenov K. Simultaneous increase of electrical conductivity and hardness of Al–1.5 wt.% Mn alloy by addition of 1.5 wt.% Cu and 0.5 wt.% Zr. *Metals*, 2019, vol. 9 (12), p. 1246. DOI: 10.3390/met9121246.

21. Belov N.A., Alabin A.N., Matveeva I.A. Optimization of phase composition of Al–Cu–Mn–Zr–Sc alloys for rolled products without requirement for solution treatment and quenching. *Journal of Alloys and Compounds*, 2014, vol. 583, pp. 206–213. DOI: 10.1016/j.jallcom.2013.08.202.

22. Malygin G.A. Prochnost' i plastichnost' nanokristallicheskikh materialov i nanorazmernykh kristallov [Strength and plasticity of nanocrystalline materials and nanosized crystals]. *Uspekhi fizicheskikh nauk = Physics-Uspekhi*, 2011, vol. 181, no. 11, pp. 1129–1156. DOI: 10.3367/UFNr.0181.201111a.1129. (In Russian).

23. Petrova A.N., Klenov A.I., Brodova I.G., Rasposienko D.Yu., Pil'shchikov A.A., Orlova N.Yu. Vliyanie tekhnologicheskikh faktorov na strukturu i svoistva Al–Cu–Mg–Si-splava, poluchennogo selektivnym lazernym splavleniem [Influence of technological factors on the structure and properties of Al–Cu–Mg–Si alloy obtained by selective laser melting]. *Fizika metallov i metallovedenie = Physics of Metals and Metallography*, 2023, vol. 124, no. 10, pp. 961–970. DOI: 10.31857/S0015323023600922.

24. Mondal C., Mukhopadhyay A.K. On the nature of $T(Al_2Mg_3Zn_3)$ and $S(Al_2CuMg)$ phases present in as-cast and annealed 7055 aluminum alloy. *Materials Science and Engineering: A*, 2005, vol. 391 (1–2), pp. 367–376. DOI: 10.1016/j.msea.2004.09.013.

25. Chen Z., Li Z., Zhao K., Zhang H., Nagaumi H. Dendrite morphology evolution of Al_6Mn phase in suction casting Al–Mn alloys. *Materials*, 2020, vol. 13 (10), p. 2388. DOI: 10.3390/ma13102388.

26. Kang H., Li X., Su Ya., Liu D., Guo J., Fu H. 3-D morphology and growth mechanism of primary Al_6Mn intermetallic compound in directionally solidified Al-3at.%Mn alloy. *Intermetallics*, 2020, vol. 23, pp. 32–38. DOI: 10.1016/j.intermet.2011.12.015.

27. Lombardi A., Mu W., Ravindran C., Dogan N., Barati M. Influence of Al_2Cu morphology on the incipient melting characteristics in B206 Al alloy. *Journal of Alloys and Compounds*, 2018, vol. 747, pp. 131–139. DOI: 10.1016/j.jallcom.2018.02.329.

Conflicts of Interest

The authors declare no conflict of interest.

Obrabotka metallov –
Metal Working and Material Science

Journal homepage: http://journals.nstu.ru/obrabotka_metallov

Study of abrasive wear resistance of flux-cored wires during surfacing on high-manganese Hadfield steel

Yulia Karlina [1, a, *], Vladimir Konyukhov [2, 3, b], Tatiana Oparina [2, c]

[1] National Research Moscow State University of Civil Engineering, 26 Yaroslavskoe Shosse, Moscow, 129337, Russian Federation
[2] Irkutsk National Research Technical University, 83 Lermontova str., Irkutsk, 664074, Russian Federation
[3] Cherepovets State University, 5 Lunacharsky pr., Cherepovets, 162600, Russian Federation

[a] https://orcid.org/0000-0001-6519-561X, jul.karlina@gmail.com; [b] https://orcid.org/0000-0001-9137-9404, konyukhov_vyu@mail.ru;
[c] https://orcid.org/0000-0002-9062-6554, martusina2@yandex.ru

ARTICLE INFO

ABSTRACT

Introduction. Austenitic high-manganese steel is commonly used in various railway and mining components, such as crusher plates, where high impact and abrasive resistance and sliding wear resistance are required, as it exhibits a unique combination of high toughness and high work-hardening ability. Therefore, it is important to understand the behavior of wear-resistant materials such as austenitic high-manganese steel under impact and sliding wear. However, this steel has a limitation: it develops its high work-hardening ability only under high impact loads and high-stress conditions. Alternatively, various hardening methods, surfacing, or replacement with low-carbon, high-alloy steels and high-chromium cast irons are used. **The purpose** of this study is to evaluate the abrasive wear resistance of flux-cored wires during surfacing on high-manganese *Hadfield* steel. **Methods and materials.** This study examines surfacing wires whose main alloying elements are chromium, vanadium, and tungsten. The chemical composition of the surfaced samples was determined using a *BRUKER S1 TITAN* portable X-ray fluorescence analyzer for metals and alloys. A *Duramin-40 AC3* hardness tester (*STRUERS APS*, Ballerup, Denmark) was used to measure Rockwell hardness. *1.1% C-13% Mn* steel demonstrated an initial bulk hardness of $HRc = 23 \pm 3$. Specimens for microstructural study were selected from cast and surfaced samples. The microstructures were examined by optical microscopy after etching in 2.5% nitric acid solutions, rinsing in methanol, and immersion in 15% HCl solution. Impact abrasive wear tests were conducted on a *DUCOM* (*TR-56-M3*) impact abrasive wear testing machine (made in India**). Results and discussion.** An analysis of a cross-section of a *1.1% C-13% Mn* steel specimen after abrasive wear testing revealed crack propagation beneath the surface of the part, with no visible connection to the surface, indicating that cracks initiated both at and below the surface. The microstructure of the surfaced layers, rich in finely dispersed boron carbides dispersed in the martensitic matrix, combined with a lamellar molybdenum boride phase, suggests that the material surfaced on *Hadfield* steel may possess higher hardness and wear resistance than the base material. Industrial tests of surfaced beaters revealed that the dominant wear mechanisms are micro-cutting, pitting, and micro-fracture (chipping and micro-indentation). Based on the results of the studies of surfacing materials, it can be concluded that wires with chromium content in the range of 3–6% have the characteristics for applications requiring high abrasive wear resistance in the mining industry.

Introduction

Coal mills are essential components of thermal power plants, used to prepare solid fuels such as peat, lignite, bituminous coal, and anthracite. These mills consist of drills fixed around the perimeter of the disk or mounted on a shaft. The material is ground into dust, which is blown into the combustion chamber of the boiler. Mill shafts are typically manufactured from wear-resistant cast iron or *Hadfield* steel [1–3].

* Corresponding author
Karlina Yulia I., Ph.D. (Engineering), Research Associate
National Research Moscow State Construction University,
26 Yaroslavskoe shosse,
129337, Moscow, Russian Federation
Tel.: +7 914 879-85-05, **e-mail:** jul.karlina@gmail.com

In the mining industry, components made from *Hadfield* steel are subjected to severe impact and abrasion, creating a significant impetus for a deeper understanding of wear, deformation, and work hardening in various high-manganese steels under high-stress conditions.

The deformation and wear mechanisms in rock crushers and mills can be classified into two primary categories [4–15]: (1) surface deformation under high stress and high strain rates, similar to impact deformation occurring when rock strikes and fragments against the surface, and (2) high-stress abrasive wear caused by the sliding of large and fragmented rock particles across the surface. Materials must endure repeated cycles of these high loads – causing scratching, indentation, impact, and mineral fracture – without premature failure or critically shortened service life. High-strength steels can offer extended service life due to their durability compared to most low-carbon steels or coated structures under such conditions. To this end, various technologies for modification, heat treatment, and surfacing are employed.

Hadfield austenitic high-manganese steel (typically ~1.2% C and ~12% Mn) holds a special place among wear-resistant high-carbon manganese alloys [1–7]. Owing to its high toughness and wear resistance, *Hadfield* steel is widely used in various industrial applications, including components of stone-crushing machinery, railway crossings, excavator bucket teeth, and tracked vehicle components [5–10].

Literature reports indicate that as-cast *Hadfield* austenitic manganese steel contains *(Fe, Mn)₃C* carbides[1, 2, 7–18]. It is standard industrial practice to dissolve these carbides prior to service through a solution heat treatment, transforming the structure into a fully single-phase austenite. The traditional heat treatment for cast *110G13L* steel blanks, used by most metallurgical companies, involves solution annealing at approximately 1,050 °C for several hours, followed by water quenching.

Analysis of the literature [1, 2, 5–17] reveals a practical challenge in the application of high-manganese steel machine parts: low wear resistance due to insufficient work-hardening capacity under "mild" operating conditions (i.e., low or absent impact loads) [11, 12]. Given this disadvantage, many researchers have explored modifying the manganese content and optimizing heat treatment to improve the in-service hardening properties. Studies on medium-manganese steels (8–12 wt.% Mn) have shown relatively low abrasive wear resistance [13–16]. Mechanical properties and wear resistance can be enhanced by adding alloying elements such as *Ti*, *Cr*, *Mo*, and *V*, which contribute to solid solution and dispersion strengthening [17–22]. The alloying, heat treatment, hardening behavior, and wear resistance of medium-manganese steels have been systematically studied [23–27]. Results indicate that deformation-induced martensitic transformation in medium-manganese steels provides a self-hardening effect under moderate or low applied loads, leading to better wear resistance compared to high-manganese, bainitic, and martensitic steels [23–27].

The effect of aging on the mechanical properties and wear resistance of medium-manganese steel reinforced with *Ti(C, N)* particles has been investigated [23–25]. These studies analyzed the influence of precipitate morphology, distribution, and volume fraction on microstructure and mechanical properties, described the relationship between mechanical properties and wear mechanisms, and explained the effects of work-hardening mechanisms.

Alloying significantly influences the deformation mechanisms in steel, promoting slip, twinning, or austenite transformation into α′- and/or ε-martensite, depending on the alloy's stacking fault energy (*SFE*) [1, 2]. However, as noted by several authors [6–12], under high strain rate conditions (e.g., strain rates of 10^3–10^5 s^{-1}), the mechanical properties and wear resistance of high-manganese steels can change substantially during operation. This must be considered when designing components for applications such as mining machinery. The addition of carbide-forming elements likely increases the abrasion resistance of high-manganese steels but may also reduce their toughness due to grain boundary carbide precipitation. Therefore, many researchers emphasize the need for continued study of the mechanical properties and wear resistance of high-manganese steels to better understand their performance and enable further development [10–24].

In particular, it has been shown that only a surface layer with a depth of 0.2–0.8 mm is exposed to aggressive media in parts operating under wear conditions [10–12]. In such cases, applying an additional wear-resistant coating to the surface of *110G13L* steel parts can be an effective solution.

In recent years, surfacing and additive manufacturing (*AM*) technologies have been increasingly used to enhance performance by surfacing heterogeneous materials onto the surfaces of metal parts. *Fe-C-Mo-V-B* surfacing compositions are known, developed specifically for rapidly wearing components of various ore-crushing equipment. These are recommended by manufacturers due to their excellent performance compared to *Ni-WC* compositions and lower cost in applications where corrosion resistance is not a primary requirement [15–28].

According to many researchers, the high wear resistance of *Fe-C-Mo-V-B* compositions stems from the high volume fraction of carbides and borides within a martensitic matrix. Strength and crack resistance are attributed to the fine lamellar structure of molybdenum borides and the spherical morphology of vanadium carbides [20–29].

There are known compositions from both domestic and international manufacturers of surfacing wires based on the *Fe–Cr* system, where additional elements such as *W*, *Nb*, *B*, *Si*, etc., are introduced to enhance the abrasive resistance of machine parts in mining equipment [10–20]. However, systematic analyses of the wear resistance of these wires specifically for mining equipment applications are scarcely available in the public domain.

It is known that wear resistance under abrasive and impact-abrasive conditions depends on the microstructure and mass fraction of carbide phases. A coarser microstructure and lower mass fraction of carbides generally lead to greater weight loss [18]. However, controlling the size and distribution of carbides is a significant challenge for *Fe-Cr-C* surfacing alloys due to the brittleness of large primary chromium carbides. In *Fe-Cr-C* system surfacing, primary carbides often form in the surfaced layer, which can impair the interfacial bonding between the carbides and the matrix [19]. Thus, the wear resistance of a surfaced alloy depends on multiple factors, including the type, shape, and distribution of hard phases, as well as the toughness and work-hardening capacity of the matrix [9]. Consequently, it is necessary to investigate the compatibility between carbides and the matrix to establish the relationship between microstructure and wear based on their distribution and morphology.

Borides and carbides are common hard phases in surfaced alloys [20]. It is well-established that borides formed with transition metals have high potential for extreme applications due to their high hardness and excellent resistance to wear, friction, and corrosion [21]. Literature indicates that boron promotes the formation of primary hard phases, such as borides or carbides, and increases their volume fraction [20–27]. Studies have shown that boron directly influences not only carbide formation but also bulk hardness and wear resistance [22]. Surfacing wires with high boride content are widely used for surfacing in various industrial applications via welding or thermal spraying [24].

Currently, a new field known as remanufacturing is developing — the process of restoring end-of-life and used components to a reusable condition [27–35]. Remanufacturing is becoming increasingly important as a key element for achieving resource efficiency in industry and building a circular economy. Additive manufacturing has emerged as a technology enabling the automated repair and restoration of worn, high-value parts to new condition for their next life cycle.

This paper investigates options for surfacing *110G13L* steel with various commercially available surfacing wires recommended by manufacturers to increase abrasive wear resistance. The studied surfaced materials are based on the *Fe-Cr-C* system, with additional elements such as *W*, *Nb*, *B*, *Mo*, *V*, and *Si* introduced to mitigate excessive wear on *Hadfield* steel drill bits used in coal mills. The study analyzes the chemical composition of the surfaced compositions, conducts macro- and microscopic structural examinations, hardness testing, and wear resistance evaluation.

The purpose of this work is to evaluate the abrasive wear resistance of various commercially available surfacing wires when used for surfacing on *Hadfield* high-manganese steel, specifically for real-world operation in coal mills. To achieve this aim, the following ***tasks*** were addressed:

– Determining the degree of dilution between the surfaced and base metals.

– Conducting metallographic studies of the microstructure of the surfaced samples.

– Assessing the hardness distribution through the depth of the surfaced layer.

– Performing abrasive wear tests on experimental samples surfaced with wires from different manufacturers and conducting industrial trials on surfaced *Hadfield* steel components.

Materials and methods of research

Product information: hammer mill beaters made of 110G13L steel for a tangential hammer mill (Fig. 1). The chemical composition was determined by optical emission spectrometry using an *ARL 3460* spectrometer and is presented in Table 1.

Fig. 1. Original beater component for surfacing

The main alloying elements in the surfaced metal layer of the samples were determined using a *BRUKER S1 TITAN* portable X-ray fluorescence (*XRF*) analyzer for metals and alloys.

A *Duramin-40 AC3* hardness tester (*STRUERS*, Denmark) was used to measure Rockwell hardness and microhardness at loads ranging from 0.025 to 0.1 kgf. The *110G13L* steel substrate exhibited an initial bulk hardness of HRC = 23 ± 2.

Samples for microstructural examination were extracted from both the cast substrate and the surfaced specimens. The samples were sectioned using a wire electrical discharge machining (*EDM*) unit to prevent cracking or phase transformations due to heat input during conventional machining. Subsequently, they underwent standard metallographic preparation: mounting, planar grinding, and polishing. The microstructures were examined by optical microscopy using a *Neophot-21* microscope equipped with a digital camera (*Carl Zeiss*, Germany).

Impact-abrasive wear tests were conducted on a *DUCOM TR-56-M3* impact-abrasive wear testing machine (India).

Table 1

Chemical composition of the *1.1% C-13% Mn* steel beater according to *GOST 977-88*

C	Si	Mn	Cr	Ni	Cu	S	P
			no more				
0.90–1.50	0.30–1.00	11.50–15.00	1.00	1.00	0.30	0.05	0.120
1.12 (actual)	0.98	12.34	0.6	0.1	0.2	0.055	0.134

The technical documentation governing the repair of *110G13L* steel plates specifies the following conditions for restoring a worn surface: *T-590* and *T-620* grade electrodes were used, with a maximum of 1-2 layers. *UONI 13/45* electrodes were used for the buffer layer formation.

This study examined several types of surfacing wires (diameter 1.2–1.6 mm) available on the Russian market:

1. **ASM 57-OA**, Russian Federation.
2. **TD-600**, Italy, manufacturer *Italfil*.
3. **TD-RC3**, Italy, manufacturer *Italfil*.
4. **CARBO AF D600**, Germany, manufacturer *CarboWeld*.
5. **K-600NT**, *Kiswel*, South Korea.
6. **K-700NT**, *Kiswel*, South Korea.
7. **OK Tubrodur 58 O/GM**, *ESAB*, manufactured in Poland.

SV-08Kh18N10T (0.08% *C*-18% *Cr*-10% *Ni*-1% *Ti*) welding wire (Russian Federation) was used as a buffer layer, which was pre- surfaced onto the *110G13L* steel surface prior to surfacing.

The chemical compositions of the aforementioned surfacing wires are presented in Table 2. The surfacing parameters for the samples are detailed in Fig. 2 and Table 3.

Sample No. 1 was surfaced using *ASM 57-OA* wire (ø 1.6 mm). According to Table 2, this wire contains 0.80% *C*, up to 18% *Cr*, and up to 2% *B*, which increases the susceptibility of the surfaced metal to cracking. To minimize cracking, preheating to 180 °C was applied, and the interpass temperature was maintained

Chemical composition of the investigated surfacing wire grades

Chemical element	Wire grade						
	ACM 57-OA	*TD-600*	*TD-RC3*	*CARBO AF D600*	*K-700HT*	*K-600HT*	*OK Tubrodur 58 O/GM ESAB*
C	0.8	0.15	0.37	0.5	0.3	0.25	0.42
Si	1	3	0.4	2.7	2.4	2.18	0.31
Mn	2	0.1	1.1	0.5	0.5	0.36	1.22
Cr	18	9.3	7	9.5	7	6.5	4.89
B	2.6						
P		<0.025	<0.03				
S		<0.020	<0.020				
Cu		<0.25	<0.25				
Ni		<0.15	<0.20				
V		<0.030					
Al		<0.030					0.6
Mo			2.2			0.5	1.14
Ti			0.3				
W					0.7		

Fig. 2. Wire surfaced samples

Surfacing parameters

Surfacing material	Current, A	Voltage, V	Wire feed speed mm/sec
ACM 57–OA	258	29.5	9.1
TD-RC3	258	23.2	9.6
TD-600	258	27.0	5.5
CARBO AF D600	260	28.5	5.6
K-700HT	260	28.0	5.6
K-600HT	260	28.0	5.6

in the range of 250–270 °C. Temperature was monitored with an *ADA TemPro 900 A00225* non-contact thermometer with a measurement error of ±15 °C.

Sample No. 2 was surfaced using *TD-RC3* wire (ø 1.6 mm).
Sample No. 3 was surfaced using *TD-600* wire (ø 1.6 mm).
Sample No. 4 was surfaced using *T-590* electrodes (ø 4.0 mm).

Sample No. 5 was surfaced using *CARBO AF D600* wire (ø 1.6 mm). To minimize cracking, preheating to 180 °C was applied, and the interpass temperature was maintained at 250–270 °C. Temperature was monitored with the same ADA thermometer.

Sample No. 6 was surfaced using *K-600NT* wire (ø 1.6 mm).

Sample No. 7 was surfaced using *K-700NT* wire (ø 1.6 mm).

Surfacing was performed using *LORCH P5500 MIG/MAG* welding equipment: an industrial semi-automatic welding system *P 5500 Speed XT*, a compact power source with water cooling, integrated wire feeder and control panel, an *SB 550W* liquid-cooled welding torch (550A for CO_2 / 500A for Ar/CO_2, 100% duty cycle, for 1.2–1.6 mm wire), equipped with an ergonomic handle and Euro connector.

Research results

Prior to surfacing on the experimental batch of hammers (beat), incoming inspection of the cast products was performed:
- Items were numbered and documented with photographs (Figs. 3–5);
- Surfaces were cleaned using mechanical tools on three sides;
- Weighing was conducted.

Visual and penetrant testing of the seven received products revealed the defects listed in Table 4.

A milling operation of the working surface was performed to a depth of 10 mm. Extensive through-hole defects were identified on two hammers (No. 1 and 3). Subsequently, new hammer samples were selected for surfacing, which successfully passed visual and capillary control.

Preliminary studies were conducted on witness (test) samples to determine the microstructure in the surfaced layer, measure hardness, and evaluate wear resistance.

Fig. 3. Visual inspection of the beater surface after removal of metallurgical slag

Fig. 4. Penetrant testing

Fig. 5. Extended through-thickness defects on the
beater, numbered 1, 3 (see Fig. 3)

T a b l e 4

Defects identified by visual and liquid penetrant testing

Product number	Identified defects
1	Pores and a shrinkage cavity in the working section of the component
2	Pores and micro-cracks on the surface
3	Pores and cracks extending to the surface. After sectioning 7 mm deep, a shrinkage void was observed in the functional area of the part
4	Pores and cracks extending to the surface
5	Pores extending to the surface
6	Pores extending to the surface
7	Pores extending to the surface

Metallographic Studies

Fig. 6 shows the microstructure of cast *110G13L* steel, where non-metallic inclusions and carbides along grain boundaries are clearly visible. Examination of the heat-affected zone (*HAZ*) revealed a fully austenitic microstructure with a high density of deformation slip bands and twinning within the grains, indicating
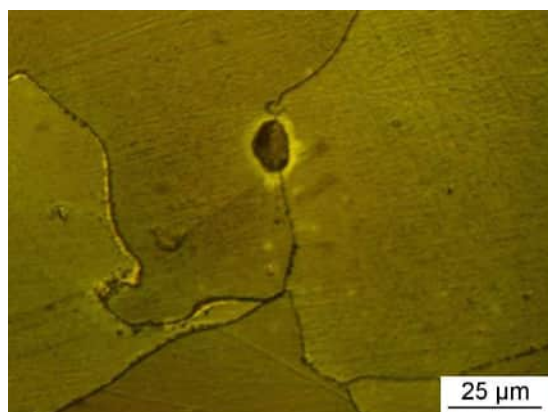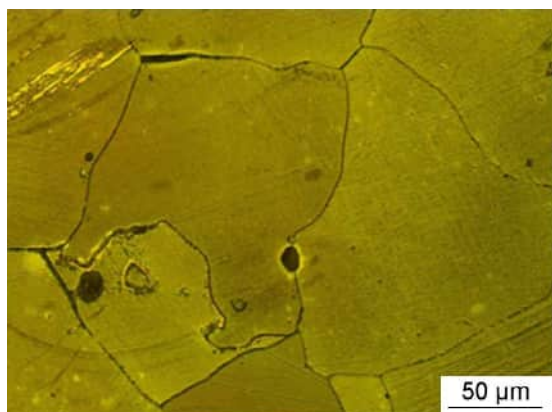

Fig. 6. Carbides at austenite grain boundaries and non-metallic inclusions

significant work hardening. Additionally, cracks propagating along some austenitic grain boundaries were observed in several sections, while other grain boundaries remained intact.

The microstructure of the surfaced layers is shown in Figs. 7–8. The structure of the surfaced metal contains boron carbides (Figs. 8, *a*, *b*) and chromium carbides (Figs. 8, *c*, *d*).

The chemical composition of the surfaced layers, determined using the *Bruker S1 TITAN* fluorescence spectrometer, is presented in Tables 5–10. The main alloying elements are chromium, molybdenum, manganese, and vanadium. Titanium (declared by the manufacturer for *CARBO AF D600* wire) and tungsten (declared for *K-700NT*) were not detected in the surfaced metal.
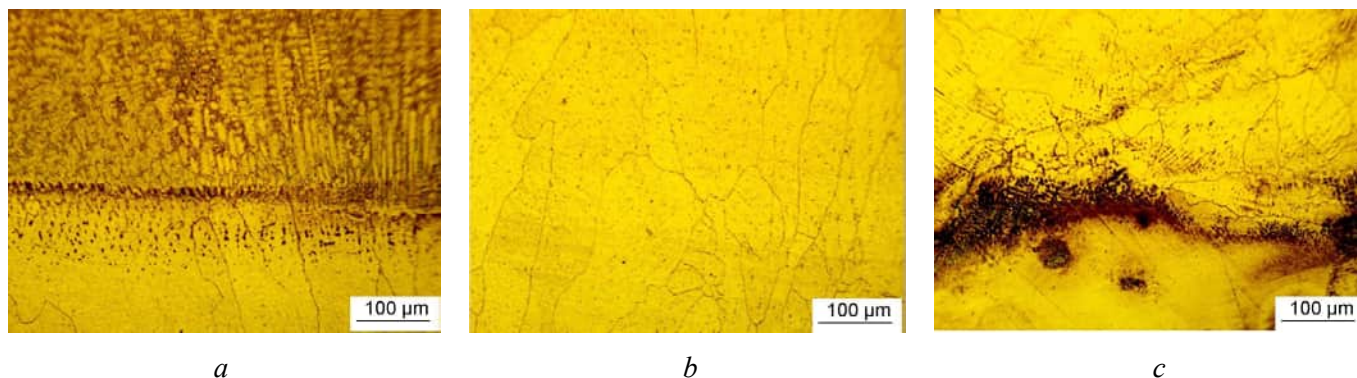

a   *b*   *c*

Fig. 7. Microstructure of the surfaced layer with a buffer layer:

a – surfaced layer at the boundary with the buffer layer; *b* – buffer layer; *c* – transition layer between the buffer layer and *1.1% C-13% Mn* steel
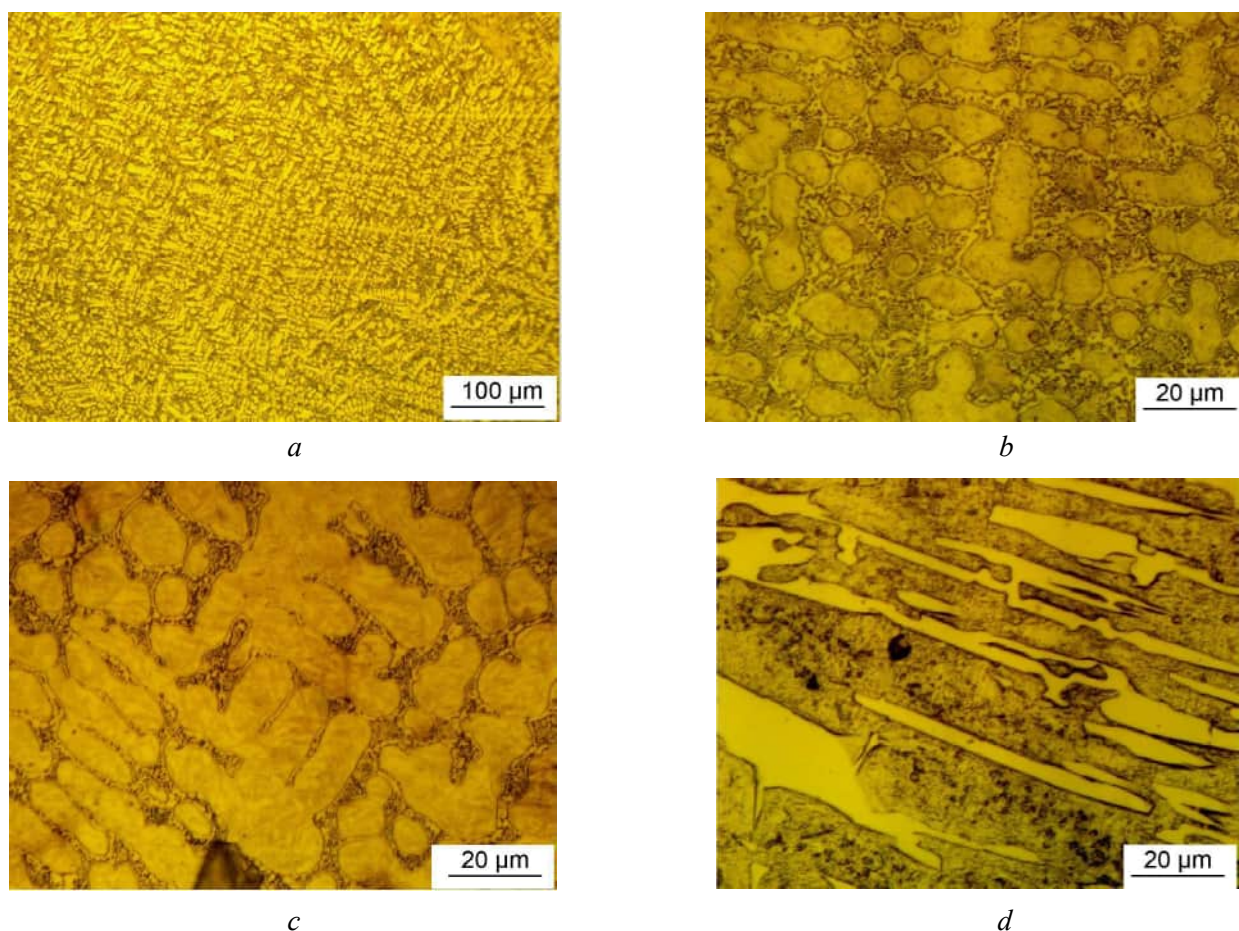

a   *b*

c   *d*

Fig. 8. Microstructure of surfaced layers:

a – surfaced layer with *ASM 57 – OA* wire; *b* – surfaced layer with *CARBO AF D600* wire; *c* – surfaced layer with *TD-RC3* wire; *d* – surfaced layer with *TD-600* wire

Chemical composition of the layer surfaced with *T-590* wire. %

Mn	Cr	Si	Cu	Ni	Mo
6.23	4.29	2.0	0.07	0.06	0.02

Chemical composition of the layer surfaced with *ASM 57 – OA* wire

Mn	Cr	Si	Ni	B	Cu
6.00	8.32	0.43	0.07	0.16	0.05

Chemical composition of the layer surfaced with *TD-RC3* wire

Cr	Mn	Mo	Si	Cu	S	Ni
5.32	2.94	1.61	0.51	0.36	0.24	0.22

Chemical composition of the layer surfaced with *TD-600* wire

Cr	Mn	Si	Cu	Ni	Mo
7.18	2.93	2.36	0.29	0.12	0.02

Chemical composition of the layer surfaced with *CARBO AF D600* wire

Cr	Mn	Si	Cu	Ni
8.18	0.53	0.36	0.29	0.12

Chemical composition of the layer surfaced with *K-700NT* wire

Mn	Cr	Si	Cu	Ni
4.23	6.29	2.0	0.07	0.06

All wires demonstrate chromium as the primary alloying element, differing only in its concentration in the surfaced metal (see Tables 5–10). Notably, the manufacturer's certificate for *ASM 57-OA* wire stated a chromium content of 18%, whereas the actual chromium content in the surfaced metal was 2.2 times lower (Table 6).

The results of macrohardness measurements on the surface of the surfaced samples are shown in Table 11. Three measurements were taken at different points on the surfaced surface, showing that hardness is uniformly distributed across the surfaced metal.

Fig. 9 graphically presents the results of microhardness distribution measurements across the depth of the surfaced layer.

The results of the abrasion resistance test are shown in Fig. 10. Initially, it can be confirmed that all surfacing materials used for surfacing exhibited lower mass loss during testing compared to samples of the base *Hadfield* steel. In terms of mass loss, wires designated in Fig. 10 as **No. 7** – *K-600NT* and **No. 8** – *K-700NT* demonstrated the lowest values.
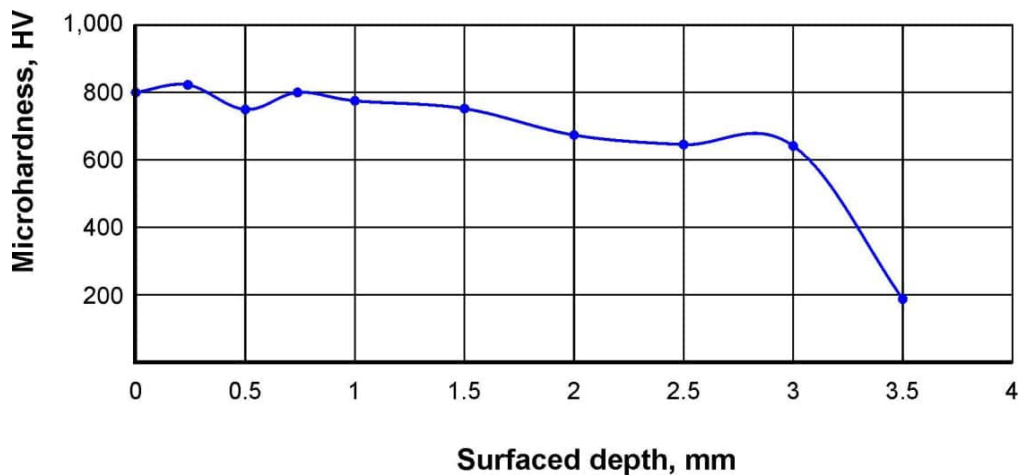
T a b l e 1 1

Rockwell hardness of the surfaced layer of samples, HRC

Sample name	Hardness 1	Hardness 2	Hardness 3	Average value
ACM 57 – OA	48.5	50	51	49.83
TD-RC3	45.5	46.0	48	46.5
TD-600	50	51	51	50.66
CARBO AF D600	55	54	58	56.5
K-600HT	58	55	59	57.5
K-700HT	61	61.5	61	61
T-590	40	42	44	42
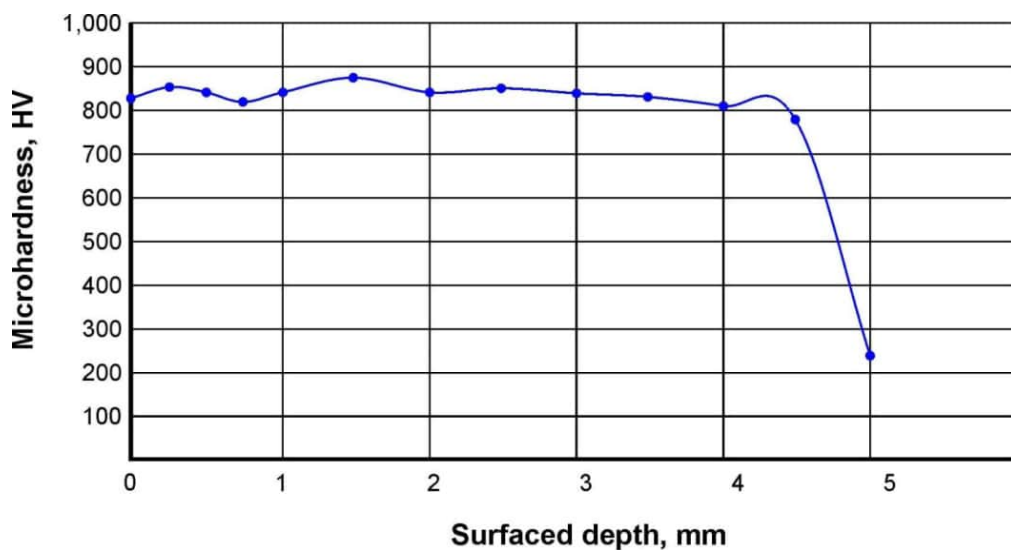
a

b

Fig. 9. Microhardness profiles across the surfaced depth:

a – K-700NT wire; *b – TD-600* wire

Subsequently, a batch of 12 hammers (Fig. 11), surfaced with *K-700NT* wire, was installed on the *MMT-1A* mill. The remaining rows were fitted with standard, non-surfaced *110G13L* steel hammers in the quantity of 114 pieces (Fig. 12). After 466 hours of testing, an inspection was conducted (Fig. 13). Following this inspection, testing was continued until the hammers were completely worn out.

Fig. 10. Abrasive wear test results (mass loss of surfacing wires):

1 – *Hadfield* steel; 2 – *ASM 57 – OA*; 3 – *T590*; 4 – *TD-RC3*; 5 – *CARBO AF D600*; 6 – *TD-600*; 7 – *K-600NT*; 8 – *K-700NT*
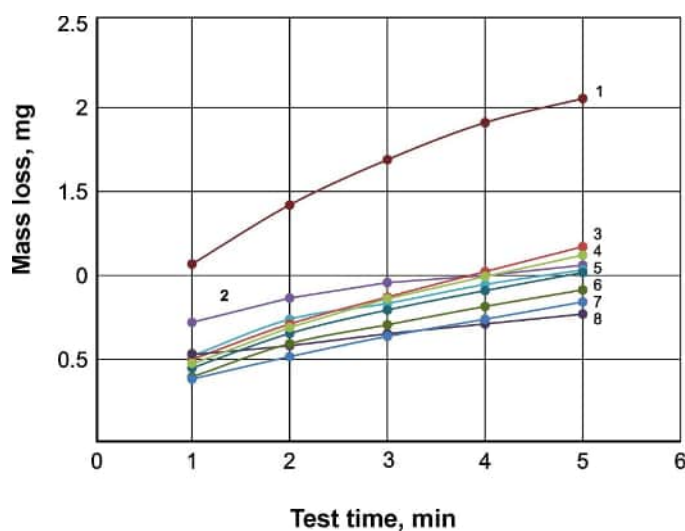

Fig. 11. Surfaced beaters for mill mounting

Fig. 12. Placement of beaters in the mill

Discussion of the results

Studies have shown that the microstructure of the surfaced metal is based on martensite and carbides of the M_3C, M_7C_3, and $M_{23}C_6$ types. Borides are observed in the microstructure of the deposit from *ASM 57-OA* wire (Fig. 8, *a*). The high carbon content in the wires *ASM 57-OA*, *TD-RC3*, *CARBO AF D600*, and K-600NT promotes the formation of a martensitic matrix with inclusions of y (Fig. 8, *d*). The martensitic microstructure is often chosen for its excellent abrasion resistance and satisfactory impact toughness.

Analyzing the average hardness and microhardness values measured along the cross-section of the surfaced beads, it can be noted that hardness values were in the range of 720–900 HV, except for the sample surfaced with *TD-RC3* wire, which had a hardness of approximately 46.5 HRC (equivalent to ~460 HV).
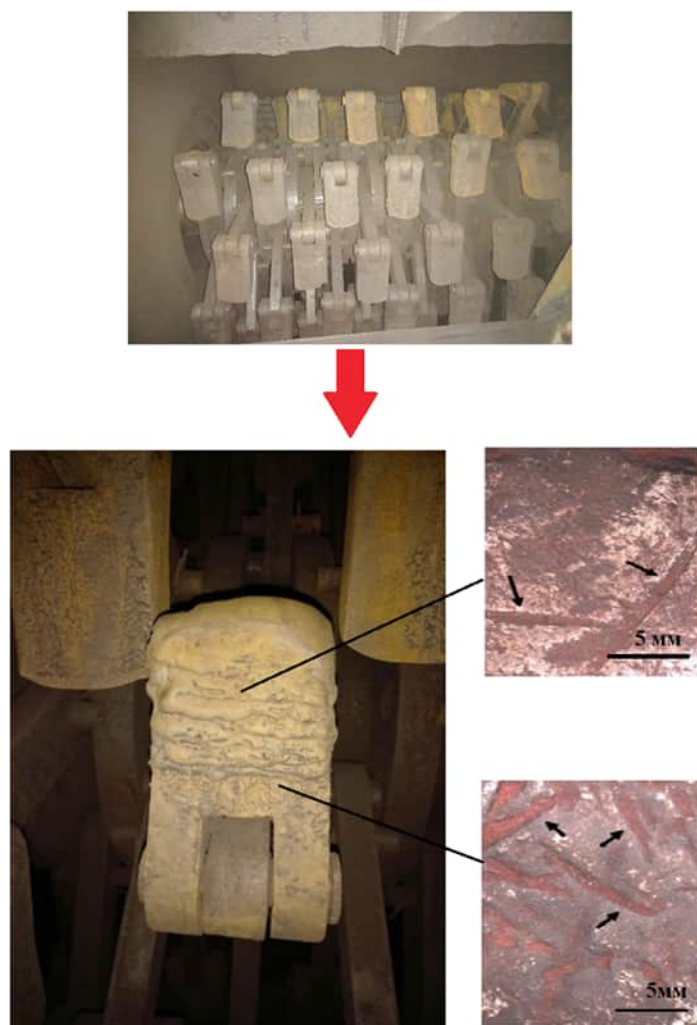
Fig. 13. Inspection of welded beaters after 466 hours
of testing

These values are significantly higher than those of the Hadfield steel substrate, which measured 258 HV. The microhardness profile measured through the depth of the coating is shown in Fig. 9. The depth of the surfaced layers is 3–4 mm. The hardness in the middle of the coating averaged 750 HV, while the highest hardness values were recorded in the top layer of the coating. Figure 9 shows a peak microhardness of 900 HV for two samples. The higher hardness of the coating is attributed to the formation of a large number of primary M_7C_3 carbides and may also be associated with the martensitic phase. In the case of the *TD-RC3* wire (Fig. 10, *b*), the hardness is lower, which correlates with a relatively lower concentration of elements such as Cr and C in the surfaced metal. Thus, it can be inferred that the type, size, shape, and distribution of carbides, as well as the matrix structure, strongly influence the hardness of the surfaced layer.

It should be noted that, regardless of the surfacing material used, the thermal conditions during deposition did not alter the microstructure to an extent that would significantly change the hardness of the surfaced beads. Furthermore, the hardness of the surfaced beads is approximately twice as high as that of the *110G13L* steel substrate, suggesting greater wear resistance compared to the substrate. The increase in hardness relative to the substrate can be explained by the volume fraction of carbides distributed in the matrix phase [12, 36–37]. The ratio of carbide to matrix volume plays an important role in wear resistance. A coating with a higher volume fraction of carbides exhibits greater wear resistance, which also correlates with higher hardness [20–24, 38–40].

In our studies of standard *110G13L* steel plates surfaced with various wires exhibiting different chemical compositions and high hardness, some explanation of the obtained results is required. It is known that the hardness of both the matrix and the carbide phase determines the overall hardness of the surfaced layer. The

hardness of alloy steels can generally serve as an indicator of abrasive wear resistance [24, 41–42]. Wear resistance typically increases with hardness [25]. The authors of [26] reported that the wear resistance of Ni_3Al-M_7C_3 carbide coatings improved significantly due to the presence of hard phases in a ductile matrix.

In our case, carbides are embedded in a hard (martensitic) matrix. According to the results of our hardness measurements and abrasive wear tests, a correlation exists between hardness and wear resistance, as surfaced samples with hardness ranging from 500 to 1,000 HV showed 30–50% higher resistance to abrasion compared to 110G13L steel samples (Fig. 10). Since mass loss was low for all surfaced samples, the sensitivity of the test must also be considered; thus, it can be stated that all samples performed similarly, as observed in other studies [19–24, 43–45]. Carbides protruding above the surface can temporarily protect it from further wear by preventing direct contact between the sample surface and the abrasive. Protruding carbides can also serve as sites for the accumulation and compaction of wear debris, contributing to the formation of a stable protective tribolayer [19–20].

Analysis of the cross-section of a *110G13L* steel sample after industrial abrasive wear testing by coal particles revealed subsurface cracks with no visible connection to the surface. The authors of [20] conducted a systematic analysis of the significance of carbide inclusions for assessing the impact toughness of three steel types: manganese steel (Grade B3), high-carbon steel (Grade B4), and chromium steel (Grade C). They reported that the degree of embrittlement in austenitic manganese steels depends on the extent of grain boundary coverage by brittle phases. Thin carbides (thickness < 0.2 μm) and thick carbides (thickness ~0.5–1.5 μm) were classified, with the latter being more detrimental, especially in large weld deposits [20].

In the present study, many cracks were found in areas with carbides larger than 0.2 μm, and others propagated where carbide inclusions were smaller than 0.2 μm. This suggests that under the combined impact and abrasion conditions in which the *110G13L* steel component operates, merely having carbide inclusions smaller than 0.2 μm is insufficient; it is necessary to prevent or eliminate carbide precipitation at grain boundaries. This finding motivates our further research into heat treatment to meet the impact and abrasion resistance requirements for coal mill hammer components.

Fig. 13 shows the worn surface of a crusher segment (upper part) examined using a stereo microscope. Deformation marks are clearly visible during macroscopic examination. These marks resemble wear patterns resulting from significant particle impacts on the surface. The authors of [22] classified wear caused by repeated solid particle impact as impact wear. However, the synergistic effect between impact and abrasion, referred to in the literature as impact-abrasion, has been described by several authors [12–20]. The observed damage mechanisms on worn hammers operating on coal ash led us to conclude that impact damage mechanisms, synergistically interacting with abrasion mechanisms, create resultant wear rates exceeding the sum of individual components, consistent with the results of other work [16–23]. It is important to emphasize that the observed wear features (see Fig. 12) exceed the material's grain size, suggesting that the material removal process occurs on a millimeter scale. Therefore, given the nature of this phenomenon involving the grinding of abrasive coal fragments and impact between metal bodies, the term "impact-abrasive wear" better describes the mechanism considered in this study.

To compare the wear resistance of surfacing materials with various microstructures, including some in different deformed states, the wear rate can be expressed as wear per unit of impact energy [23]. It should be noted that during impact, energy is also dissipated in other processes (e.g., friction). In [23], energies dissipated during impact were calculated individually from high-speed images of each test. According to the authors, representing wear rates based on dissipated energy and the mass of erosive particles can provide a more accurate assessment of wear test results.

In conclusion, industrial tests of surfaced hammers have demonstrated a significant increase in service life compared to non-surfaced hammers. Evaluation of the abrasive wear resistance of the investigated welding wires from various manufacturers shows similar results. All investigated wires possess characteristics that allow their use for surfacing coatings on components made of *110G13L* steel in mining equipment or other applications requiring high wear resistance.

Conclusions

1. Analysis of the cross-sections for all investigated welding wires revealed that dilution between the surfaced layer and the substrate is minimal. Higher heat input from the welding arc typically results in the formation of higher and wider weld beads, whereas lower heat input values can lead to incomplete fusion or bead detachment. The presence of cracks was noted in some samples, with their propagation arrested within the buffer (buttering) layer.

2. Microstructural analysis demonstrated that the surfaced layer consists of carbide inclusions (chromium, iron, and boron-based) embedded within a martensitic matrix. During the surfacing process, grains in regions closer to the substrate interface were finer than those on the surface. This is attributed to a higher cooling rate near the interface, which suppresses grain growth.

3. The microhardness of all studied surfacing wires ranged from 550 to 900 HV, which is 2–3 times higher than the microhardness of the base *110G13L* steel (approximately 250 HV). This high hardness is attributed to the significant volume fraction of chromium carbides within the surfaced metal.

4. Abrasive wear resistance tests indicated that all samples, with chromium content in the surfaced metal ranging from 4.3 to 8.4 wt.%, exhibited comparable wear resistance. Industrial field trials of surfaced hammers (beaters) under actual coal grinding conditions at a thermal power plant demonstrated a 40–50% increase in service life compared to standard, non-surfaced *110G13L* steel beaters.

References

1. Tweedale G., Paton W.D.M. Sir Robert Abbott Hadfield F.R.S (1858–1940) and the discovery of manganese steel. *Notes and Records of the Royal Society of London*, 1985, vol. 40 (1), pp. 63–74.

2. Gauzzi F., Rossi M., Verdini B. Cold-working induced martensitic transformation in 12 percent Mn austenitic steel (Hadfield steel). *Metallurgia Italiana*, 1971, vol. 63 (11), p. 555.

3. Dastur Y.N., Leslie W.C. Mechanism of work hardening in Hadfield manganese steel. *Metallurgical Transactions A*, 1981, vol. 12 (5), pp. 749–759. DOI: 10.1007/BF02648339.

4. Bhattacharyya S. A friction and wear study of Hadfield manganese steel. *Wear*, 1966, vol. 9 (6), pp. 451–461. DOI: 10.1016/0043-1648(66)90136-0.

5. Lindroos M., Apostol M., Heino V., Valtonen K., Laukkanen A., Holmberg K., Kuokkala V.T. The deformation, strain hardening, and wear behavior of chromium-alloyed Hadfield steel in abrasive and impact conditions. *Tribology Letters*, 2015, vol. 57 (3), p. 24. DOI: 10.1007/s11249-015-0477-6.

6. Ten E.B., Bazlova T.A., Likholobov E.Yu. Vliyanie vnepechnoi obrabotki na strukturu i mekhanicheskie svoistva stali 110G13L [Effect of out-of-furnace treatment on the structure and mechanical properties of steel 110G13L]. *Metallovedenie i termicheskaya obrabotka metallov = Metal Science and Heat Treatment*, 2015, no. 3, pp. 26–28. (In Russian).

7. Bolobov V.I., Bochkov V.S., Qinyan X. Iznosostoikost' stali Gadfil'da pri bol'shikh udel'nykh nagruzkakh [The influence of high specific loads to wear resistance of Hadfield steel]. *Gornoe oborudovanie i elektromekhanika = Mining Equipment and Electromechanics*, 2012, no. 10, pp. 12–14.

8. Kolokoltsev V.M., Vdovin K.N., Chernov V.P., Feoktistov N.A., Gorlenko D.A., Dubrovin V.K. Issledovanie mekhanizmov abrazivnogo i udarno-abrazivnogo iznashivaniya vysokomargantsevoi stali [Study of abrasive and impact and abrasive wear mechanisms of high manganese steel]. *Vestnik Magnitogorskogo gosudarstvennogo tekhnicheskogo universiteta im. G.I. Nosova = Vestnik of Nosov Magnitogorsk State Technical University*, 2017, no. 2, pp. 54–62. DOI: 10.18503/1995-2732-2017-15-2-54-62.

9. Chorshanbiev Sh.M., Karimov K.A., Adilova Sh.R., Turakhodjaev N.J., Erkinjonov A., Mirmuhamedov M.M., Sharipov J.H., Obidov Z.R., Komolov Kh. Development of wear-resistant parts of high-manganese modified 110G13L brand steel. *Zhurnal Sibirskogo federal'nogo universiteta. Tekhnika i tekhnologii = Journal of Siberian Federal University. Engineering & Technologies*, 2024, vol. 17 (2), pp. 175–185.

10. Bolobov V.I., Chupin S.A. Vliyanie vida uprochnyayushchei obrabotki na iznosostoikost' materialov gornogo oborudovaniya [Influence of the type of hardening treatment on the wear resistance of mining equipment materials]. *Zapiski Gornogo instituta = Journal of the Mining institute*, 2015, vol. 216, pp. 44–48.

11. Bolobov V.I., Batalov A.P., Bochkov V.S., Chupin S.A. Iznosostoikost' stali 110G13L v razlichnykh abrazivnykh sredakh [Wear resistance of 110G13L steel in various abrasive environments]. *Zapiski Gornogo instituta = Journal of the Mining institute*, 2014, vol. 209, pp. 17–22.

12. Balanovsky A.E., Shtayger M.G., Grechneva M.V., Kondrat'ev V.V., Karlina A.I. Comparative metallographic analysis of the structure of St3 steel after being exposed to different ways of work-hardening. *IOP Conference Series: Materials Science and Engineering*, 2018, vol. 411 (1), p. 012012. DOI: 10.1088/1757-899X/411/1/012012.

13. Teplukhin V.G., Popov A.I., Kudryavtsev V.N., Fomin D.S., Radkevich M.M. Features of investigation of steels with a metastable austenitic structure. *Advances in Mechanical Engineering: Selected contributions from the conference "Modern engineering: Science and education"*, Saint Petersburg, Russia, June 2022. Cham, Springer Nature Switzerland, 2023, pp. 164–171. DOI: 10.1007/978-3-031-30027-1_18.

14. Filippov M.A., Shveikin V.P., Sharapova V.A., Nikiforova S.M., Khadyev M.S. Formation of a dissipative structure of metastable austenite for raising the wear resistance of carbon steels. *Metal Science and Heat Treatment*, 2023, vol. 64 (9), pp. 509–515. DOI: 10.1007/s11041-023-00854-w.

15. Vdovin K., Pesin A., Feoktistov N., Gorlenko D. Surface wear in Hadfield steel castings DOPED with nitrided vanadium. *Metals*, 2018, vol. 8 (10), p. 845. DOI: 10.3390/met8100845.

16. Kondrat'ev V.V., Gorovoy V.O., Kolosov A.D., Kononenko R.V., Konyukhov V.Y. Description of the complex of technical means of an automated control system for the technological process of thermal vortex enrichment. *Journal of Physics Conference Series*, 2020, vol. 1661 (1), p. 012101. DOI: 10.1088/1742-6596/1661/1/012101.

17. Kozyrev N., Usoltsev A., Kryukov R., Gusev A., Osetkovskiy I. Operational factors of new flux cored wires of the Fe–C–Si–Mn–Cr–Ni–Mo system for surfacing of protective plates of shearer cutting drums. *IOP Conference Series: Earth and Environmental Science*, 2019, vol. 377, p. 012022. DOI: 10.1088/1755-1315/377/1/012022.

18. Kozyrev N., Usol'tsev A., Kryukov R., Gusev A., Osetkovskii I. Ekspluatatsionnye pokazateli novykh poroshkovykh provolok sistemy Fe-C-Si-Mn-Cr-Ni-Mo [Operation indices of the new cored wire of Fe-C-Si-Mn-Cr-Ni-Mo system]. *Chernaya metallurgiya. Byulleten' nauchno-tekhnicheskoi i ekonomicheskoi informatsii = Ferrous Metallurgy. Bulletin of Scientific, Technical and Economic Information*, 2019, vol. 75, no. 7, pp. 860–869.

19. Gusev A.I., Kibko N.V., Popova M.V., Kozyrev N.A., Osetkovskii I.V. Naplavka poroshkovymi provolokami sistem C–Si–Mn–Mo–V–V i C–Si–Mn–Cr–Mo–V detalei gornorudnogo oborudovaniya [Surfacing of details of mining equipment by powder wires of C–Si–Mn–Mo–V–B and C–Si–Mn–Cr–Mo–V systems]. *Izvestiya vysshikh uchebnykh zavedenii. Chernaya Metallurgiya = Izvestiya. Ferrous Metallurgy*, 2017, vol. 60, no. 4, pp. 318–323. DOI: 10.17073/0368-0797-2017-4-318-323.

20. Shlyakhova G.V., Danilov V.I. Issledovanie vliyaniya elektrodugovoi naplavki na strukturu i svoistva pokrytii [Effect of electric arc surfacing on the structure and properties of coatings]. *Izvestiya vysshikh uchebnykh zavedenii. Chernaya Metallurgiya = Izvestiya. Ferrous Metallurgy*, 2024, vol. 67, no. 4, pp. 433–439. DOI: 10.17073/0368-0797-2024-4-433-439.

21. Metlitskii V.A. Flux-cored wires for arc welding and surfacing of cast iron. *Welding International*, 2008, vol. 22 (11), pp. 796–800. DOI: 10.1080/09507110802593646.

22. Mutașcu D., Karancsi O., Mitelea I., Crăciunescu C.M., Buzdugan D., Uțu I.D. Pulsed TIG cladding of a highly carbon-, chromium-, molybdenum-, niobium-, tungsten- and vanadium-alloyed flux-cored wire electrode on duplex stainless steel X2CrNiMoN 22-5-3. *Materials*, 2023, vol. 16 (13), p. 4557. DOI: 10.3390/ma16134557.

23. Świerczyńska A., Varbai V., Pandey Ch., Fydrych D. Exploring the trends in flux-cored arc welding: scientometric analysis approach. *The International Journal of Advanced Manufacturing Technology*, 2024, vol. 130 (1), pp. 87–110. DOI: 10.1007/s00170-023-12682-6.

24. Golyakevich A.A., Orlov L.N., Maksimov S.Yu. Peculiarities of welding process using metal cored wire of TMV5-MK grade. *The Paton Welding Journal*, 2019, vol. 6, pp. 50–53. DOI: 10.15407/tpwj2019.06.10.

25. Sabzi M., Obeydavi A., Mousavi Anijdan S.H. The effect of joint shape geometry on the microstructural evolution, fracture toughness, and corrosion behavior of the welded joints of a Hadfield steel. *Mechanics of Advanced Materials and Structures*, 2018, vol. 26 (12), pp. 1053–1063. DOI: 10.1080/15376494.2018.1430268.

26. Eremin E.N., Losev A.S. A flux-core wire for hardfacing sealing surfaces of stop valves. *Welding International*, 2016, vol. 30 (3), pp. 216–219. DOI: 10.1080/09507116.2015.1044268.

27. Kanishka K., Acherjee B. A systematic review of additive manufacturing-based remanufacturing techniques for component repair and restoration. *Journal of Manufacturing Processes*, 2023, vol. 89, pp. 220–283. DOI: 10.1016/j.jmapro.2023.01.034.

28. Lee C.M., Woo W.S., Roh Y.H. Remanufacturing: Trends and issues. *International Journal of Precision Engineering and Manufacturing-Green Technology*, 2017, vol. 4 (1), pp. 113–125. DOI: 10.1007/s40684-017-0015-0.

29. Konstantinova M.V., Balanovskiy A.E., Gozbenko V.E., Kargapoltsev S.K., Karlina A.I., Shtayger M.G., Guseva E.A., Kuznetsov B.O. Application of plasma surface quenching to reduce rail side wear. *IOP Conference Series: Materials Science and Engineering*, 2019, vol. 560 (1), p. 012146. DOI: 10.1088/1757-899X/560/1/012146.

30. Yelemessov K., Baskanbayeva D., Martyushev N.V., Skeeba V.Y., Gozbenko V.E., Karlina A.I. Change in the properties of rail steels during operation and reutilization of rails. *Metals*, 2023, vol. 13 (6), p. 1043. DOI: 10.3390/met13061043.

31. Shtayger M.G., Balanovskiy A.E., Kargapoltsev S.K., Gozbenko V.E., Karlina A.I., Karlina Yu.I., Govorkov A.S., Kuznetsov B.O. Investigation of macro and micro structures of compounds of high-strength rails implemented by contact butt welding using burning-off. *IOP Conference Series: Materials Science and Engineering*, 2019, vol. 560 (1), p. 012190. DOI: 10.1088/1757-899X/560/1/012190.

32. Balanovskiy A.E., Shtayger M.G., Karlina A.I., Kargapoltsev S.K., Gozbenko V.E., Karlina Yu.I., Govorkov A.S., Kuznetsov B.O. Surface hardening of structural steel by cathode spot of welding arc. *IOP Conference Series: Materials Science and Engineering*, 2019, vol. 560 (1), p. 012138. DOI: 10.1088/1757-899X/560/1/012138.

33. Skeeba V.Yu., Ivancivsky V.V., Kutyshkin A.V., Parts K.A. Hybrid processing: the impact of mechanical and surface thermal treatment integration onto the machine parts quality. *IOP Conference Series: Materials Science and Engineering*, 2016, vol. 126 (1), p. 012016. DOI: 10.1088/1757-899x/126/1/012016.

34. Efremenkov E.A., Martyushev N.V., Skeeba V.Yu., Grechneva M.V., Olisov A.V., Ens A.D. Research on the possibility of lowering the manufacturing accuracy of cycloid transmission wheels with intermediate rolling elements and a free cage. *Applied Sciences*, 2022, vol. 12 (1), p. 5. DOI: 10.3390/app12010005.

35. Martyushev N.V., Skeeba V.Yu. The method of quantitative automatic metallographic analysis. *Journal of Physics: Conference Series*, 2017, vol. 803 (1), p. 012094. DOI: 10.1088/1742-6596/803/1/012094.

36. Skeeba V.Yu., Ivancivsky V.V. Reliability of quality forecast for hybrid metal-working machinery. *IOP Conference Series: Earth and Environmental Science*, 2018, vol. 194 (2), p. 022037. DOI: 10.1088/1755-1315/194/2/022037.

37. Zverev E.A., Skeeba V.Yu., Skeeba P.Y., Khlebova I.V. Defining efficient modes range for plasma spraying coatings. *IOP Conference Series: Earth and Environmental Science*, 2017, vol. 87 (8), p. 082061. DOI: 10.1088/1755-1315/87/8/082061.

38. Mamadaliev R.A., Bakhmatov P.V., Martyushev N.V., Skeeba V.Yu., Karlina A.I. Influence of welding regimes on structure and properties of steel 12KH18N10T weld metal in different spatial positions. *Metallurgist*, 2022, vol. 65 (11–12), pp. 1255–1264. DOI: 10.1007/s11015-022-01271-9.

39. Balanovsky A.E., Shtayger M.G., Kondrat'ev V.V., Huy V. Van, Karlina A.I. Plasma-arc surface modification of metals in a liquid medium. *IOP Conference Series: Materials Science and Engineering*, 2018, vol. 411 (1), p. 012013. DOI: 10.1088/1757-899X/411/1/012013.

40. Karlina A.I., Karlina Y.I., Gladkikh V.A. Studying the microstructure, phase composition, and wear resistance of alloyed layers after laser surface melting of low-carbon steel 20. *Metallurgist*, 2024, vol. 68 (5), pp. 757–766. DOI: 10.1007/s11015-024-01782-7.

41. Karlina A.I., Karlina Y.I., Kondratiev V.V., Kononenko R.V., Breki A.D. Study of wear of an alloyed layer with chromium carbide particles after plasma melting. *Crystals*, 2023, vol. 13 (12), p. 1696. DOI: 10.3390/cryst13121696.

42. Balanovsky A.E., Shtayger M.G., Kondrat'ev V.V., Nebogin S.A., Karlina A.I. Complex metallographic researches of 110G13L steel after heat treatment. *IOP Conference Series: Materials Science and Engineering*, 2018, vol. 411 (1), p. 012014. DOI: 10.1088/1757-899X/411/1/012014.

43. Karlina A.I., Balanovskiy A.E., Kondratiev V.V., Romanova V.V., Batukhtin A.G., Karlina Y.I. An investigation into the behavior of cathode and anode spots in a welding discharge. *Applied Sciences Switzerland*, 2024, vol. 14 (21), p. 9774. DOI: 10.3390/app14219774.

Conflicts of Interest

The authors declare no conflict of interest.

Obrabotka metallov – Metal Working and Material Science

Development of an assessment method for pickup formation on furnace rolls

Kirill Bersenev [1, a, *], Mikhail Puzanov [2, b], Aleksey Chernov [1, c], Yury Korobov [1, d],
Larisa Karenina [2, e], Yulia Khudorozhkova [3, f], Aleksey Makarov [1, g],
Denis Davydov [1, h], Galiya Kinzhebaeva [1, i]

[1] M. N. Mikheev Institute of Metal Physics, RAS (Ural Branch), 18 S. Kovalevskaya st., Ekaterinburg, 620108, Russian Federation
[2] NLMK Group, VIZ-Steel, 28 Kirova st., Ekaterinburg, 620108, Russian Federation
[3] Institute of Engineering Science, RAS (Ural Branch), 34 Komsomolskaya st., Ekaterinburg, 620049, Russian Federation

[a] https://orcid.org/0009-0004-5505-3000, ✉ bersenev@imp.uran.ru; [b] https://orcid.org/0009-0009-9457-4008, ✉ puzanov_mp@nlmk.com;
[c] https://orcid.org/0009-0006-3478-6277, ✉ chernov_aa@imp.uran.ru; [d] https://orcid.org/0000-0003-0553-918X, ✉ yukorobov@imp.uran.ru;
[e] https://orcid.org/0009-0001-5439-2711, ✉ karenina_ls@nlmk.com; [f] https://orcid.org/0000-0003-3832-1419, ✉ khjv@mail.ru;
[g] https://orcid.org/0000-0002-2228-0643, ✉ avm@imp.uran.ru; [h] https://orcid.org/0000-0003-1381-0929, ✉ davidov@imp.uran.ru;
[i] https://orcid.org/0009-0004-1243-6765, ✉ galikinz@outlook.com

ARTICLE INFO

ABSTRACT

Introduction. During the recrystallization annealing of cold-rolled electrical and automotive steels, the formation of pickups on the surface of furnace rolls presents a significant issue, as they lead to surface damage of the steel strip in the form of indentations. **The focus of the present study** is the evaluation of this defect. **Methods.** To this end, a laboratory-based methodology was developed to assess the tendency of furnace rolls to form pickups. The method replicates the contact interaction between the furnace roll and the steel strip under real annealing conditions, taking into account the applied contact pressure, a temperature range of 700–900 °C, the (H_2–N_2) furnace atmosphere, and a humidity level arising from the presence of oxygen adsorbed on the steel strip. To validate the method's reliability, a comparative analysis was conducted between pickups formed on the roll surface after industrial operation and those generated under laboratory conditions in the contact zone between steel samples made of roll and strip materials. The analysis employed optical microscopy, X-ray diffraction, and scanning electron microscopy. **Results and discussion.** The study confirmed that the developed methodology produces pickups on the specimen surfaces with morphology, chemical composition, and phase structure closely resembling those observed on the furnace rolls. A comparative assessment of the pickup formation rate between a typical furnace roll material (*EI 283* steel) and a *NiCrAlY* coating applied by plasma spraying revealed that the pickup formation rate for the *EI 283* steel was an order of magnitude higher. The validated methodology can thus be used to evaluate the effectiveness of strategies aimed at mitigating pickup formation on furnace rolls under long-term high-temperature contact conditions.

---

* Corresponding author
Bersenev Kirill A., Post-graduate Student, Research assistant
M. N. Mikheev Institute of Metal Physics, RAS (Ural Branch),
18, S. Kovalevskaya st.,
620108, Ekaterinburg, Russian Federation
Tel.: +7 982 326-70-30, **e-mail:** bersenev@imp.uran.ru

Introduction

To achieve the required operational properties in steel strip for electrical (transformer) steel [1, 2] and automotive steel [3, 4] with a thickness of 0.3–1.0 mm, recrystallization annealing is performed after cold rolling. This process is conducted in furnaces at 700–900 °C under reducing atmospheres. A significant operational issue is the formation of pickups on the surface of the furnace rolls that transport the strip. Subsequent contact between the steel strip and these rolls damages its surface layer, resulting in dents or the transfer of pickup material onto the strip surface as indentations. For electrical steel, this also degrades magnetic properties by disrupting the deformation (*Goss*) texture [1].

The appearance of pickup defects on furnace rolls and corresponding indentations on the processed strip is illustrated in Fig. 1. Pickups on rolls transporting automotive sheet (Fig. 1, *a* [5]) and electrical steel (Fig. 1, *b*, author's data) show minor visual differences, attributable to the distinct chemical compositions of the metals and variations in transport loading conditions. Contact between a roll with pickups and the strip leads to dent and indentation formation on the strip surface (Fig. 1, *c* [1]), a consequence of material transfer from the pickups. Micro-X-ray spectral analysis confirms that the chemical composition of indentations on the strip matches that of the pickups on the rolls [1].
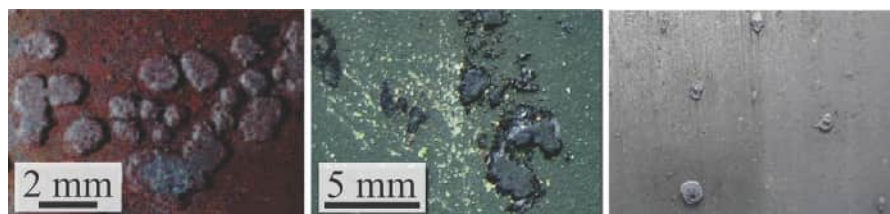

Fig. 1. Defects resulting from recrystallization annealing
(see explanations in the text)

The formation mechanism of pickups on furnace rolls in contact with the strip is as follows. Upon heating to ~500 °C in a nitrogen-hydrogen atmosphere, the surface of a silicon steel strip oxidizes due to the higher oxygen affinity of silicon, iron, and other alloying elements compared to hydrogen. This process forms a thin oxide film containing iron, silicon, and aluminum oxides. The composition of the oxide film varies with depth: the layer adjacent to the metal is rich in silicon and manganese oxides, while upper layers contain increasing amounts of iron oxides [6].

As temperature rises, the reducing power of hydrogen and (diffusing) carbon increases. Above ~650 °C, simultaneous reduction of iron oxides occurs – directly from the oxide film by hydrogen and beneath it by carbon diffusing to the metal-oxide interface. This weakens the adhesion between the oxide film and the annealed strip surface.

Silicon plays a key role in oxide film spalling. The formed fayalite (Fe_2SiO_4) creates a eutectic with wüstite ($Fe_{1-X}O$) that melts at only 1,177 °C. Manganese oxides form solid solutions with the main scale components (wüstite, fayalite). Aluminum promotes the formation of a ternary eutectic ($FeAl_2O_4 - Fe_2SiO_4 - Fe_{1-X}O$) with an even lower melting point (1,148 °C). Chromium oxides may also be present in the spalled scale, with silicon and chromium not forming mixed compounds but existing in close proximity [2].

Following spalling, individual microparticles of reduced iron are pressed into the roll surface. This process intensifies, leading to the growth of pickup particles that can reach 2–3 mm in height. The typical chemical composition of pickups is 94.8–95.3 wt.% *Fe*, 2.0–3.2 wt.% *Si*, 0.3–0.4 wt.% *Mn*, and 0–0.3 wt.% *Al*. Their structure is featureless, resembling reduced iron with residues of ferrous oxide [1].

Although continuous annealing lines operate at elevated temperatures, moisture is present on the strip surface. Potential sources include water condensation on the metal before furnace entry or from the furnace atmosphere gases (**H_2, N_2**) when their temperature falls below the **dew point**. Condensation forms droplets or oxide films. For a given hydrogen content, the partial pressure of water vapor in the atmosphere is determined in accordance with equation [7]:

$$\lg P_{H_2O} = 9.8 T_{DP}/(273.8 + T_{DP}) - 2.22,$$

where P_{H_2O} is the partial pressure of water vapor; T_{DP} is the dew point temperature.

In turn, the thermodynamic stability of the oxides forming the pickups is a function of the partial pressure of oxygen in the furnace atmosphere. The oxidation potential (P_{H_2O}/P_{H_2}) **of** the furnace atmosphere is one of the main technological parameters of recrystallization annealing.

The typical dew point in an industrially employed annealing atmosphere is –30 °C (380 ppm H_2O, corresponding to P_{O_2} = 3.16·10^{-22} atm). According to the *Richardson-Ellingham-Jeffes* diagram [8], decreasing the dew point to –58 °C (≈14 ppm H_2O, $\boldsymbol{P_{O_2}} \approx 7.6 \cdot 10^{-25}$ atm) leads to a reduction in the driving force for oxidation. Although the annealing conditions are reducing for iron, selective oxidation of alloying elements with high oxygen affinity (*Si*, *Mn*, etc.) may nevertheless occur, depending on the oxidizing potential of the atmosphere. Studies of various classes of steels have shown that an increase in the water vapor content of the incoming gas, i.e., an increase in the oxidizing potential of the annealing furnace atmosphere, leads to an increase in the thickness of the oxide film on the metal surface and a change in its structure [3, 9–12]. Thus, variations in atmospheric humidity alter the rate of pickup growth owing to changes in the oxidizing potential of the working atmosphere. In the furnace atmosphere, the concentrations of H_2O and H_2 are monitored using standard furnace instruments, such as a thermohygrometer, which measures the temperature and dew point [13].

In addition to chemical processes, mechanical stresses also influence the formation of pickups on the furnace roll and the corresponding indentations on the steel strip. The pressure exerted by the strip on the roll is low and is determined by the mass of the strip between two consecutive rolls in the vertical section of the annealing unit. An estimation indicates that for a strip with a thickness of 0.7 mm and a width of 1,000 mm, and a vertical distance between the axes of consecutive rolls of 8,000 mm, its mass suspended between the rolls will be approximately 40 kg. Under these parameters, the maximum pressure in the contact zone between the smooth surface of the roll (with a diameter of 600 mm) and the strip will be 0.5 MPa; however, at point contacts over the pickups, the pressure increases by an order of magnitude or more. Furthermore, the mismatch in linear velocities between the strip and the roll surface accelerates pickup growth [14]. However, in the production process, the velocity mismatch can be controlled and maintained at a level of ~0.3%, under which conditions pickups on the roll form after several months of continuous operation. This led to the conclusion that the role of chemical reactions between elements is significantly greater than the role of the mismatch in linear velocities between the roll and the strip [10].

Various methods are used to reduce the tendency for pickup formation: changing the chemical composition of the steel strip and the furnace roll [15], applying protective coatings [5, 14, 16], or installing intermediate components, e.g., carbon sleeves [13, 17]. Determining the effectiveness of these methods requires the development of a method for assessing the resistance of metallic surfaces to pickup formation.

The most reliable assessment, based on full-scale roll tests, is characterized by excessive duration and substantial cost, since the time between maintenance cycles of the annealing furnace spans 4–9 months [1].

To reduce the duration of testing, a method for assessing resistance to pickup formation was proposed, in which a sandwich assembly, consisting of two metal plates with a steel strip placed between them, is heated in a laboratory furnace at 800–950 °C under a nitrogen-hydrogen atmosphere with a typical composition of 97% N_2 + 3% H_2. Following this exposure, pickups form on the surface of the steel strip via the mechanism described above. The material of the metal plate serves as an analog for the annealing furnace roll, while the steel strip simulates the processed sheet. After holding the assembly in the laboratory furnace for up to 200 hours, the resistance of the plates to pickup formation is evaluated based on the number (density) of pickups per unit area [6]. Although this method enables the formation of pickups, it does not account for the humidity of the furnace atmosphere, and does not allow for the evaluation of humidity variations, which reduces the reliability of the results.

The purpose of this work was to develop a methodology for evaluating the propensity of metallic surfaces to form pickups during contact under elevated temperature conditions in an H_2-N_2 atmosphere with controlled humidity.

Methods

To assess the resistance of furnace rolls to the typical operational defect of pickup formation, a methodology was developed involving the heating of a sandwich assembly under simultaneous exposure to pressure (**P**), temperature (**T**), controlled environmental humidity (**Hum**), and a gas atmosphere (**H₂–N₂**). The assembly, designated "Plate 1 – Strip 2 – Plate 1" (Fig. 2), consists of two plates of **EI 283 steel** (according to *GOST 5632–2014*), which is the standard material for furnace rolls, and a central strip of **Fe–3% Si electrical steel** (*GOST 21427.1–83*), simulating the processed strip. The chemical compositions of these steels are provided in Table 1.
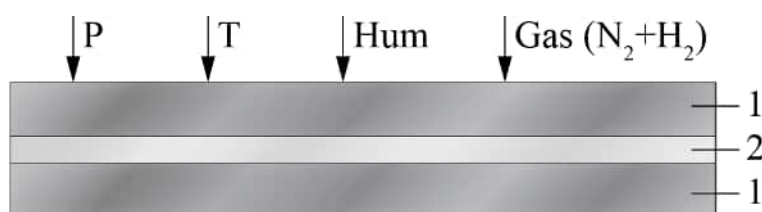

Fig. 2. Scheme of the method for assessing the resistance of furnace rolls to pickup formation (see explanations in the text)

Table 1

Standard chemical composition of steels *EI283* and *Fe-3 Si*, wt.%

Element	Steel *EI283*	Steel *Fe-3 Si*
C	0.003–0.04	0.003–0.04
P	< 0.03	< 0.03
S	< 0.03	≤ 0.03
Si	2.9–3.5	2.9–3.5
Cr	22–25	≤ 0.3
Ni	17–20	≤ 0.3
Mn	< 2	–
Al	–	0.004–0.03
Cu	–	0.01–0.6
N	–	0.001–0.013
Ti	–	≤ 0.006
Fe	Bal.	Bal.

Fig. 3, *a* presents a schematic of the laboratory setup for pickup formation. The sandwich assembly comprises two metal plates (**1**) with dimensions of $50 \times 20 \times 4$ mm and a steel strip (**2**) of $50 \times 20 \times 0.7$ mm placed between them. This assembly is mounted inside a quartz tube (**3**), the working part of which is inserted into a *SUOL-0.4.4/12-M2-U4.2* muffle furnace (*AB "Umega"*, Lithuania) capable of maintaining a set temperature of 850 ± 1 °C (with a maximum capability of 1,250 °C). The quartz tube is connected to a vacuum pump (**5**) for initial air evacuation and to a gas mixer (**6**) for supplying a gas mixture from cylinders with a composition of (95–97% N_2 + 3–5% H_2) by volume. A humidity adjustment unit (**7**) regulates the moisture content of the incoming gas. This is achieved by diverting the gas flow through tubes (**9**) and (**10**), which are integrated into a flask containing distilled water sealed with a hermetic stopper (**8**). The gas mixture is bubbled through the water via tube (**9**) and exits via tube (**10**) before re-entering the main gas line to the quartz tube. The gas flow is controlled by valves. The water vapor content in the gas mixture is measured at the inlet of tube (**10**) using a hygrometer and is correlated with the dew point of the surrounding

atmosphere. This correlation allows the water vapor content inside the quartz tube (**3**) to be equated to the humidity of the ambient atmosphere. By controlling the ambient temperature, the humidity level inside the quartz tube can be adjusted. This capability enables the assessment of the impact of humidity on the oxidation rate of the strip surface, which serves as an analogue for the annealed sheet under actual humidity conditions in the high-temperature zone of an industrial annealing furnace.

The implemented setup for evaluating pickup formation (Fig. 3, *b*) includes the following key components: the muffle furnace with the inserted quartz tube containing the samples; the gas mixer for supplying the gas mixture from cylinders; the vacuum pump for evacuating air from the working zone prior to gas supply, equipped with a control unit and a pressure gauge; and the humidity adjustment unit. The duration of the continuous laboratory tests was set at 96 hours, which is approximately 40 times shorter than the typical duration required for full-scale industrial trials.
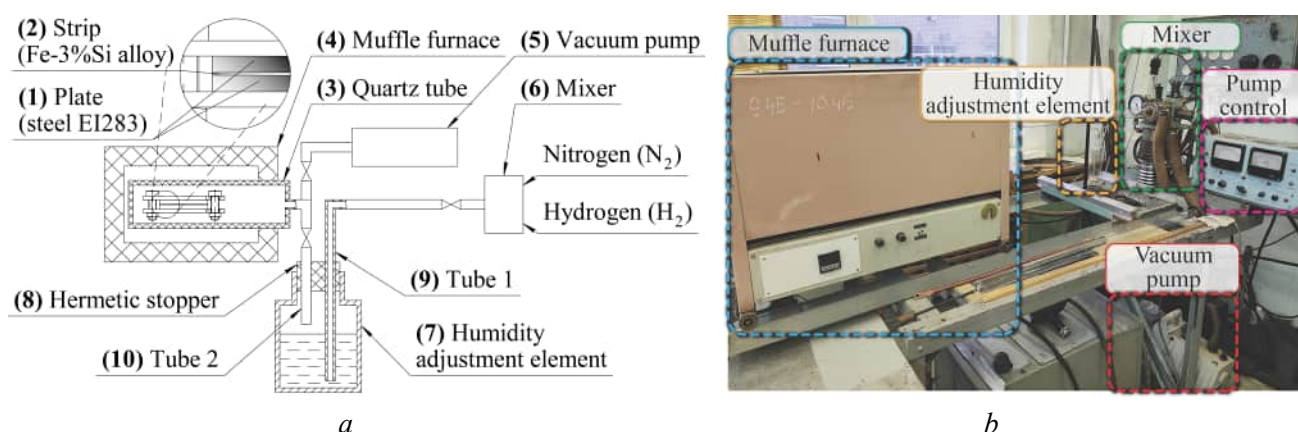

a   *b*

Fig. 3. Installation for assessing the pickup formation:

a – diagram; *b* – view (see explanations in the text)

During the laboratory experiments, a series of pickups were generated and subsequently compared with pickups retrieved from a furnace roll after full-scale industrial operation. The microstructure and elemental distribution on the investigated surfaces were analyzed using scanning electron microscopy (*SEM*). A *Carl Zeiss EVO 40* microscope (Germany) operating at an accelerating voltage of 20 kV with a tungsten cathode and a *TESCAN VEGA II XMU* microscope (Czech Republic) equipped with an *INCA ENERGY 450* energy-dispersive X-ray spectroscopy (*EDS*) system (*Oxford Instruments*, UK) were employed. X-ray diffraction (*XRD*) analysis was performed using a *Shimadzu XRD 7000 Maxima* diffractometer (Japan) with a graphite monochromator and *CuKα* radiation. Diffraction patterns were recorded in the angular range of **2θ** = 10–80° with a step size of **Δθ** = 0.02° and an accumulation time of 2 seconds per step. Full-profile analysis was conducted using the International Centre for Diffraction Data (*ICDD*) *PDF-4* database.

Results and Discussion

Pickups formed on the furnace roll

Fig. 4, *a* shows the surface of the furnace roll with formed pickups after six months of continuous operation. Fig. 5 and Table 2 present scanning electron microscopy (*SEM*) images of an individual pickup and the chemical composition from the investigated areas *A* and *B* (Figs. 4, *b-d*) in the form of spectra. The pickups shown in Fig. 4, *b* have average dimensions of 11×4 mm.

The chemical composition of the pickup surface (Table 2) includes the metals *Cr*, *Al*, *Fe*, *Mn*, *Ni*, and *Si*, which diffuse from both the strip and the roll. The high oxygen content (20–25 wt.% O) indicates the presence of oxides.

X-ray phase analysis was conducted on the sample depicted in Fig. 4, *b*. The determination error is 2%, which is attributable to the error in measuring the intensity of superimposed diffraction lines. The data are presented in Fig. 5 and Table 3.
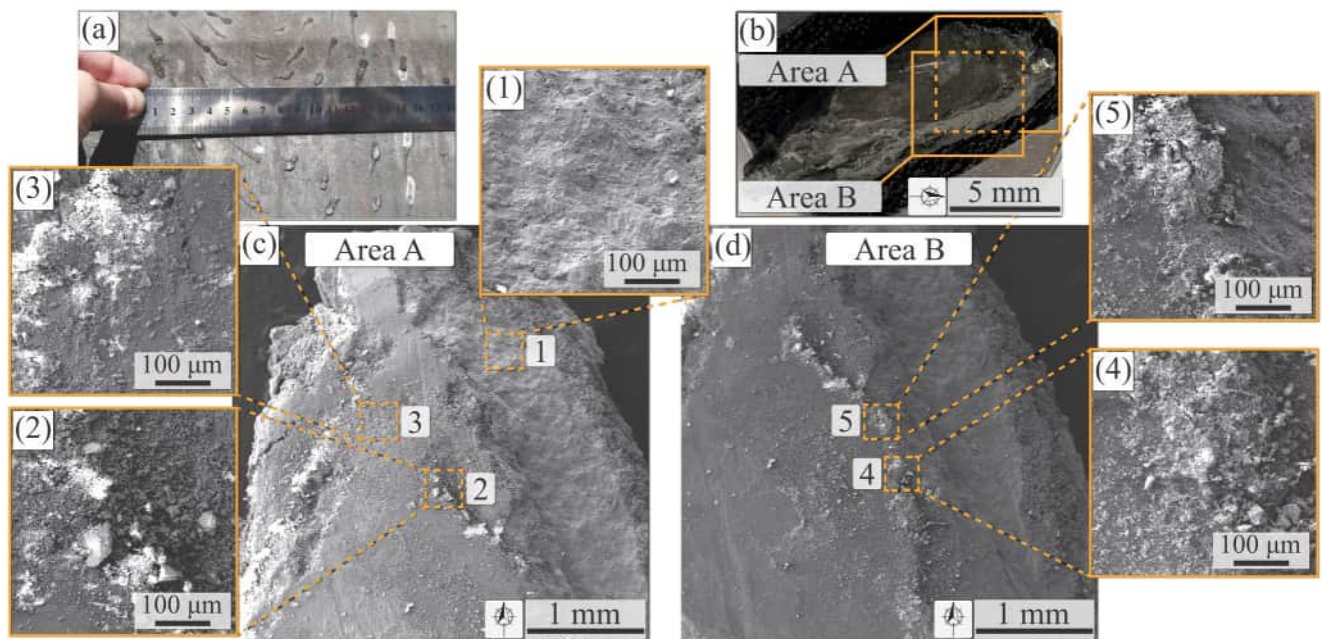
Fig. 4. Photographs of pickups on the surface of the furnace roll (*a*) and a single pickup (*b*) with details of its areas (*c, d*); *SEM* images of areas "*A*" (1–3) and "*B*" (4–5)

T a b l e 2

Chemical composition of the pickup surface, sections 1–5 in Fig. 4, *c-d*, wt.%

Spectrum	O ($\delta < 1.24$ %)	Al	Cr	Ni	Fe	Mn	Si
1	22.66	0.27	–	–	74.61	2.23	0.24
2	20.62	1.46	1.4	–	71.84	1.79	2.89
3	24.73	1.8	2.44	0.17	64.47	2.54	3.84
4	21.07	1.68	1.46	0.17	70.5	2.42	2.71
5	22.36	1.44	1.03	0.14	70.19	2.01	2.82

* The accuracy of micro-elemental analysis with this instrument is ±5% of the measured value. To ensure the total elemental content sums to 100%, values are presented with higher precision, which is due to the algorithms embedded in the instrument's software.
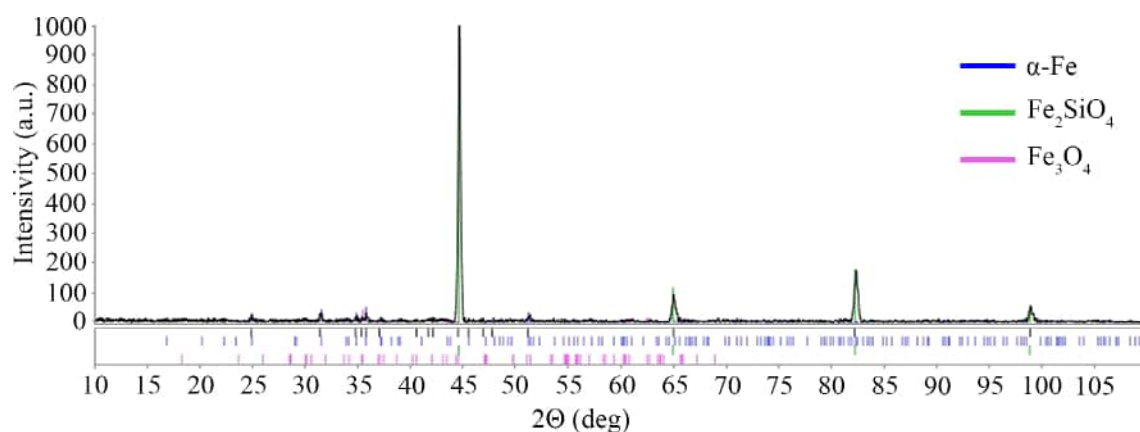

Fig. 5. X-ray diffraction patterns of the pickup removed from the roll

Table 3

Phase composition of the pickup removed from the roll, at.%

Phase	PDF-4	ат. % / at. %
α-*Fe* (iron)	01-080-3816	89
Fe_2SiO_4 (fayalite)	01-079-1208	5
Fe_3O_4 (magnetite)	01-084-9337	4

The higher iron content and lower content of the other elements, as determined by X-ray diffraction analysis compared to chemical analysis, may be attributable to the partial dissolution of these elements in iron, whereas the positions of the iron peaks in the diffraction pattern remain unchanged.

Laboratory formed pickups

Surface analysis

Visual inspection of the samples (Figs. 6, *a-b*) revealed that the pickups on the plate and the indentations on the strip have an appearance comparable to the formations on the actual furnace roll and transformer steel strip shown in Fig. 1. Dark areas corresponding to the color of the metal are observed along the edges of the plate, where the least pressing force was applied, and lighter areas are observed around the pickups and indentations.

The microstructure of the formed pickup surface in areas *A* and *B* is presented in Figs. 6, *c-d*. The corresponding chemical composition of these areas, as determined by *SEM* analysis, is given in Table 4. These areas were detailed in the figure as "area *A*" (regions 1–2 in Fig. 6, *c*) and "area *B*" (regions 3–10 in Fig. 6, *e*), as well as region 11 at the boundary between the pickup and the area without pickups, and region 12, where no pickups were visually observed (Fig. 6, *d*).

The oxygen and metal contents in the surface layer of the pickup on the plate (Table 4) are similar to the values obtained for the pickup surfaces on the roll according to the author's data (Table 2). The observed variation in iron content (in the range of 2.47–97.46 wt.% *Fe*) may be associated with the extraction of the
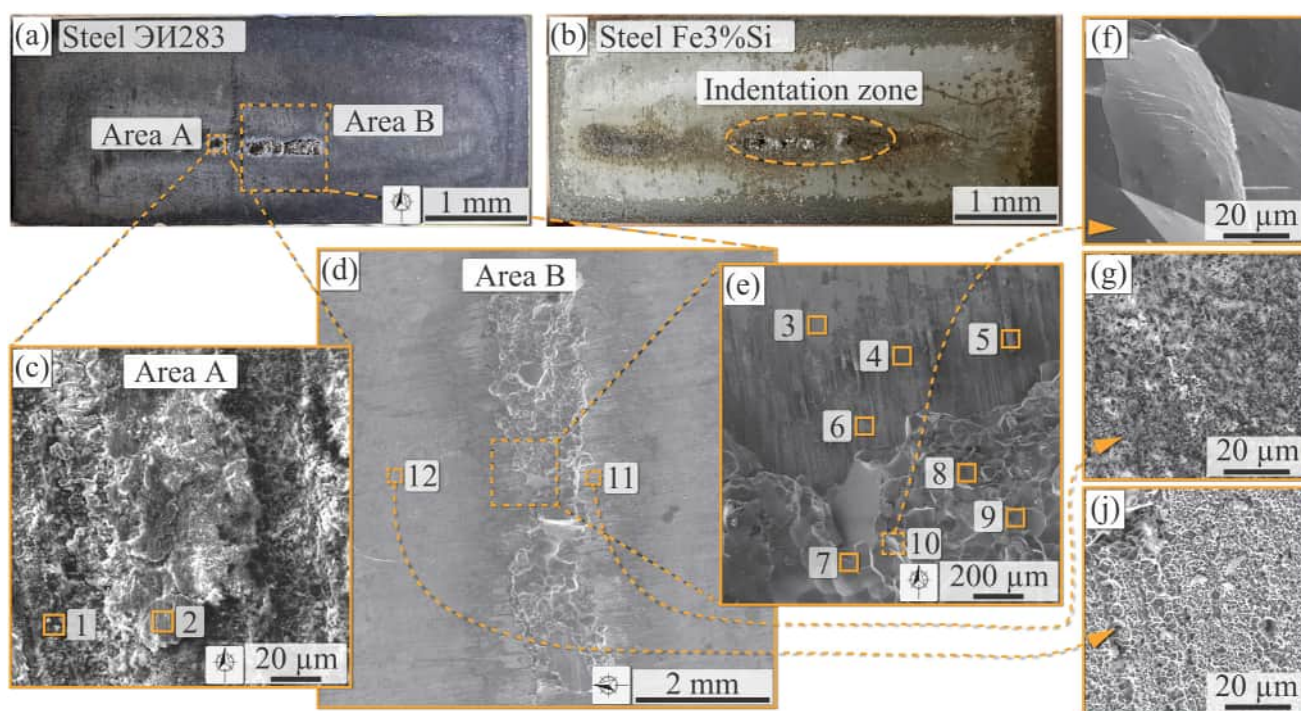

Fig. 6. View of plates with pickups (*a*) and strips of transformer steel (*b*) after testing according to the developed method, 96 hours; images of the surface of the pickups in areas "*A*" (*c*) and "*B*" (*d-j*)

Chemical composition of the plate surface areas according to Fig. 6, *a*, wt.%

Spectrum	O	Al	Cr	Ni	Fe	Mn	Si
1	3.25	–	4.26	–	87.78	0.96	3.76
2	24.74	0.24	31.3	1.39	25.01	10.72	6.61
3	25.99	0.12	47.69	0.89	6.73	18.27	0.31
4	19.23	0.48	27.95	3.44	30.26	16.22	2.43
5	30.32	0.46	21.89	–	2.47	35.3	9.55
6	5.52	1.51	2.85	1.44	82.66	0.47	5.55
7	7.83	–	–	–	89.2	0.55	2.43
8	2.01	–	–	–	94.22	0.4	3.38
9	1.01	–	–	–	97.46	0.44	1.1
10	0.74	0.08	0.06	0.05	95.37	0.43	3.26
11	23.38	–	43.49	0.69	6.29	25.32	0.83
12	2.67	1.69	3.45	1.5	86.36	1.2	3.14

internal material volume from the strip due to intense diffusional adhesion. The high oxygen content (up to 30.32 wt.% *O*) in the chemical composition of the pickup (Table 4) indicates the presence of metal oxides on its surface, primarily *Fe* (82–98 wt.% in spectra 1, 6–10, and 12). The presence of aluminum (up to 1.69 wt.% *Al*), nickel (up to 3.44 wt.% *Ni*), manganese (up to 35.3 wt.% *Mn*), and silicon (0.31–9.55 wt.% *Si*) indicates the presence of oxides of these elements. The elevated *Mn* concentration can be explained by its high affinity for oxygen and the transfer of corresponding atoms from the furnace roll material to its surface in the contact zone with transformer steel. During the annealing process of high-strength manganese steels, the presence of *Mn* oxides in the pickups is more pronounced than in the electrical steel examined in this study [6, 13]. In all other respects, the data from other researchers on the chemical composition of pickups on rolls during annealing are similar.

Laboratory-formed pickups

Cross-section analysis

For the pickup in area ***B*** (Fig. 6, *a*), a cross-sectional analysis was performed, the general view of which is presented in Fig. 7, *a*. *SEM* and elemental mapping were conducted for characteristic sections of the "pickup–plate metal" interface boundary: in the middle of the pickup (Figs. 7, *b-c*) and at its edge (Figs. 7, *d-f*). The chemical composition of the cross-section of the pickup on the plate, as determined after spectrum processing, is given in Table 5 for sections located within the pickup (**1**), at the interface boundary (**2**, **3**), and in the near-surface layer of the plate (**4**).

As evident from Table 5, the oxygen content is several orders of magnitude higher than its solubility limit in iron [18]; thus, it is present in the form of oxides. Meanwhile, in the cross-section, the oxygen content is 20–100 times lower than on the surface (Table 4), which is qualitatively corroborated by the elemental mapping of characteristic sections of the pickup (Fig. 7).

The obtained data are consistent with the results of chemical analysis (Table 2) and X-ray phase analysis (Fig. 5) of the pickup surface removed from the roll, as well as with data from other studies on the elemental content within the volume of pickups during recrystallization annealing of steel [1–3, 9, 13]. This attests to the reliability of the laboratory method developed for assessing pickup formation on the surface of furnace rolls.
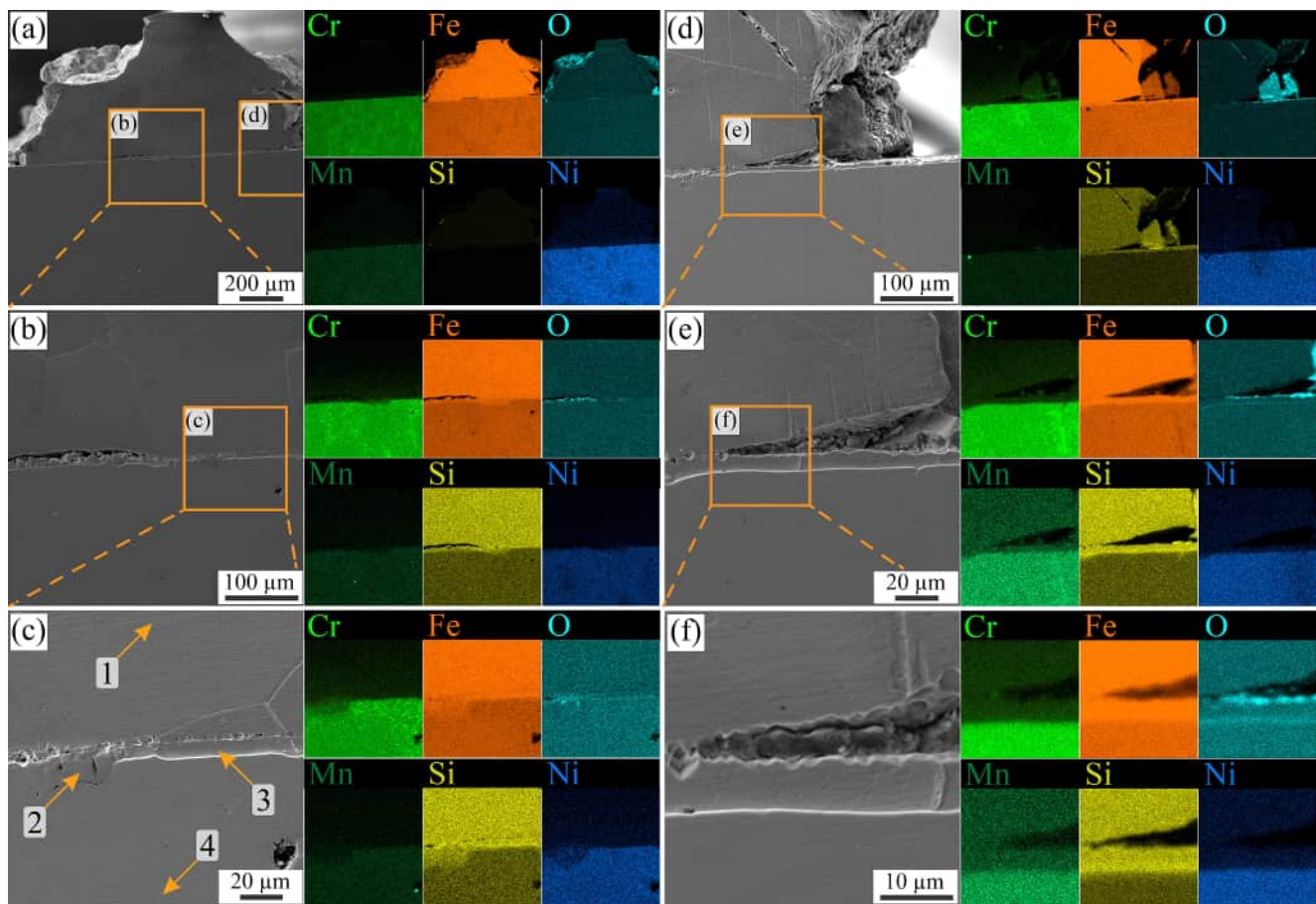
Fig. 7. SEM images and elemental mapping (EDM) of the cross-section of the EI283 steel plate with the pickup

Table 5

Chemical composition of the cross-sectional areas of the pickups on the plate, shown in Fig. 7, wt.%

Spectrum	O	Cr	Ni	Fe	Mn	Si
1	0.22	1.75	0.98	94.06	–	3.2
2	–	9.26	5.57	81.92	1.01	2.23
3	0.04	3.72	1.53	90.98	0.64	3.13
4	0.21	16.77	9.53	71.49	1.51	0.7

Laboratory test of NiCrAlY-based coating on plates

One approach to reducing the propensity for pickup formation involves the application of thermal spray coatings to the surface of furnace rolls. In particular, *MCrAlY*-type coatings (*M – Co, Ni*) are promising, as they enable the formation of protective oxide scales based on Al_2O_3 and Cr_2O_3 at elevated temperatures. The formation mechanism of these scales is detailed in monographs [19, 20]. Such coatings have demonstrated high durability in gaseous environments such as *Ar*-20% O_2 and *Ar*-4% H_2–2% H_2O. They are employed to extend the service life of gas turbine blades [21], as well as technological rolls in metallurgy [5, 22], and components of tribological pairs operating under boundary lubrication or dry friction conditions, with elevated loads and temperature fluctuations (in engine building, metallurgical equipment, aviation, and space technology) [23].

In accordance with the methodology described above, the propensity for pickup formation was evaluated on plates made of *AISI 310S* steel (analog of *EI 283* steel), onto which coatings were applied via plasma spraying using powders of (*NiCrAlY* (70–20–9–0.38) + n·Y_2O_3), where n = 0, 5, and 10 wt.% [24].

Visual inspection after testing revealed differences in the surface condition of the plates (Figure 8). The surfaces of the coated plates exhibited no traces of adhesion with the strip material, in contrast to the uncoated *AISI 310S* steel plate.

Further investigation of the contact zones included determination of microhardness, roughness parameters, and topography, as well as energy-dispersive X-ray spectroscopy (*EDS*) on the surface and on characteristic cross-sections before and after testing.
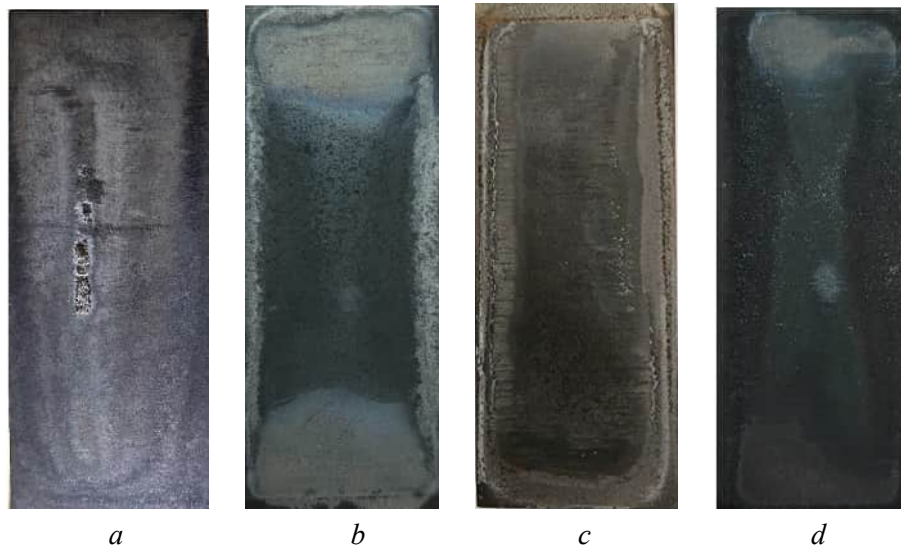

a   *b*   *c*   *d*

Fig. 8. A view of plates with *NiCrAlY* coating after testing:

a – without coating, *b-d* – with coating ($NiCrAlY + n \cdot Y_2O_3$), $n = 0, 5, 10$ wt. % for *b*, *c*, *d*, respectively

It has been demonstrated, in particular, that spinels of the (*Al*, *Cr*, *Y*)*Ox* type formed in the cross-sections of $NiCrAlY + (5–10$ wt.% Y_2O_3) coatings after spraying, with the Y fraction increasing from approximately 18 to 45 wt.% as the Y_2O_3 content in the initial powder increased (Fig. 9). Post-test examination revealed an insufficient quantity of Fe and Si in the contact zone to enable adhesion of the electrical steel strip to the coating. Furthermore, the addition of Y_2O_3 was found to exert opposing effects. On one hand, increasing its content leads to enhanced hardness, which is beneficial for improving the coating's wear resistance. Additionally, during wear, the oxides within the layer will impede adhesion. On the other hand, the addition of Y_2O_3 facilitates Si diffusion from both the strip and the substrate sides, thereby increasing the propensity for pickup formation. To determine which of these processes will exert the predominant influence on the coating's performance, full-scale industrial testing is required.
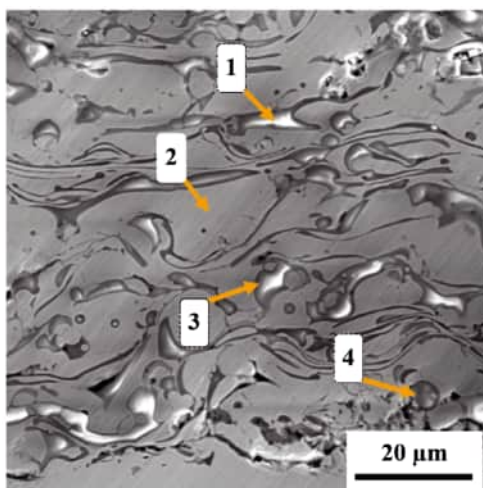
Microchemical analysis of coating cross-section areas 1–4

	1	2	3	4
O	33.84	–	15.13	27.08
Al	35.45	9.90	9.45	27.55
Cr	3.43	18.72	19.63	13.38
Ni	3.71	71.38	55.79	18.93
Y	23.56	–	–	13.07

Fig. 9. Microstructure of a cross-section of a sprayed coating ($NiCrAlY + 5$ % Y_2O_3) with microanalysis regions

Conclusion

The experiments demonstrated that the developed methodology, which entails the forced application of pressure on the contact surface of steel samples during prolonged heating at 850 °C for 96 hours in an atmosphere of (95–97% N_2 + 3–5% H_2) with controlled humidity, results in the formation of pickups on the plate surfaces. These pickups exhibit a morphology (shape and chemical composition) analogous to that observed during the operation of furnace rolls in continuous annealing lines. Optical microscopy, X-ray diffraction, and scanning electron microscopy revealed that the chemical and phase compositions of the pickups under laboratory and full-scale conditions were comparable. The study results confirm the reliability of assessing pickup formation on the surface of furnace rolls using the developed laboratory method.

The application of the developed method is illustrated through the assessment of the comparative propensity for pickup formation on *AISI 310S* steel and on plasma-sprayed coatings based on *NiCrAlY* with additions of up to 10 wt.% Y_2O_3. The results indicate that laboratory testing enables the selection of a coating material with the required properties to enhance resistance to pickup formation on metallic surfaces.

References

1. Mindlin B.I., Nastich V.P., Cheglov A.E. *Izotropnaya elektrotekhnicheskaya stal'* [Isotropic electrical steel]. Moscow, Intermet Inzhiniring Publ., 2006. 240 p. ISBN 5-89594-130-3.

2. Mikl G., Höfler T., Gierl-Mayer C., Danninger H., Linder B., Angeli G. Scaling behaviour of Si-alloyed steel slabs under reheating. *Conditions Journal of Casting & Materials Engineering*, 2021, vol. 5 (4), pp. 71–74. DOI: 10.7494/jcme.2021.5.4.71.

3. Grabke H.J., Leroy V., Viefhaus H. Segregation on the surface of steels in heat treatment and oxidation. *ISIJ International*, 1995, vol. 35 (2), pp. 95–113. DOI: 10.2355/isijinternational.35.95.

4. Kuklík V., Kudláček J. *Hot-dip galvanizing of steel structures*. Oxford, Butterworth-Heinemann, 2016. 234 p. ISBN 9780081007532. DOI: 10.1016/C2014-0-03512-5.

5. Fukubayashi H.H., Brennan M.S. Present furnace and pot roll coatings and future development. *ITSC 2004 – Conference Proceedings*, Osaka, Japan, May 2004. ASM, 2004, pp. 125–131. DOI: 10.31399/asm.cp.itsc2004p0125.

6. Huang T.S. Effect of Mn on the formation of oxide buildups upon HVOF-sprayed MCrAlY-ceramic-type cermet coatings. *Journal of Thermal Spray Technology*, 2011, vol. 20 (3), pp. 447–455. DOI: 10.1007/s11666-010-9531-y.

7. Kim Y., Lee J., Shin K., Jeon S., Chin K. Effect of dew point on the formation of surface oxides of twinning-induced plasticity steel. *Materials Characterization*, 2014, vol. 89, pp. 138–145. DOI: 10.1016/j.matchar.2014.01.012.

8. Devereux O.F. *Problemy metallurgicheskoi termodinamiki* [Topics in metallurgical thermodynamics]. Moscow, Metallurgiya Publ., 1986. 424 p. (In Russian).

9. Zhang X., Corrêa da Silva C., Liu C., Prabhakar M., Rohwerder M. Selective oxidation of ternary Fe-Mn-Si alloys during annealing process. *Corrosion Science*, 2020, vol. 174, p. 108859. DOI: 10.1016/j.corsci.2020.108859.

10. Zheng X., Kang Y., Zhou J. Influence of coating and dew point on hearth roll pickup. *Journal of Iron and Steel Research International*, 2019, vol. 26 (6), pp. 647–652. DOI: 10.1007/s42243-019-00231-z.

11. Wang H., Jin X., Hu G., He Y. Changing oxide layer structures with respect to the dew point prior to hot-dip galvanizing of δ-TRIP steel. *Surface and Coatings Technology*, 2018, vol. 337, pp. 260–269. DOI: 10.1016/j.surfcoat.2017.12.046.

12. Maderthaner M., Jarosik A., Angeli G., Haubner R. Effect of dew point on the selective oxidation of advanced high strength steels. *Materials Science Forum*, 2017, vol. 891, pp. 292–297. DOI: 10.4028/www.scientific.net/MSF.891.292.

13. He M., Peng S., Xue G., Ouyang Y., Zhang J., Chen H., Liu B. Cause analysis on buildup formation of carbon sleeve in continuous annealing furnace for non-oriented silicon steel produced by CSP process. *Characterization of Minerals, Metals, and Materials 2015*. Cham, Springer International Publishing, 2016, pp. 587–593. DOI: 10.1007/978-3-319-48191-3_73.

14. Singh S., Berndt C.C., Singh Raman R.K., Singh H., Ang A.S.M. Applications and developments of thermal spray coatings for the Iron and Steel Industry. *Materials*, 2023, vol. 16 (2), p. 516. DOI: 10.3390/ma16020516.

15. Sukhov A.I., Korotchenkova A.V. Osobennosti proizvodstva elektrotekhnicheskikh izotropnykh stalei s osobo nizkimi udel'nymi magnitnymi poteryami [Features of the production of isotropic electrical steel with very low specific magnetic losses]. *Sovremennye materialy, tekhnika i tekhnologii*, 2019, no. 4 (26), pp. 172–180. (In Russian).

16. Midorikawa S., Yamada T., Nakazato K. Development of surface-modifying technologies by thermal spraying of process rolls in steel production process. *Kawasaki Steel Technical Report*, 2001, no. 45, pp. 57–63. Available at: https://www.jfe-steel.co.jp/archives/en/ksc_giho/no.45/tobira057.html (accessed 20.11.2025).

17. He M., Wang X., Zhou W., Gong X., Zhang J., Xu J. Effect of microstructure on resistance to buildups formation of carbon sleeves in continuous annealing furnace for silicon steel production. *Characterization of Minerals, Metals, and Materials. Minerals, Metals and Materials Series*. Springer, 2019, pp. 351–359. DOI: 10.1007/978-3-030-05749-7_35.

18. Turkdogan E.T. *Fundamentals of steelmaking*. Maney Publishing, 2010. 345 p. ISBN 1906540977.

19. Sims C.T., Stoloff N.S., Hagel W.C., eds. Superalloys II: *High-temperature materials for aerospace and industrial power*. New York, Willey, 1987. 640 p. ISBN 0471011479.

20. Gol'dshtein M.I., Grachev S.V., Veksler Yu.G. *Spetsial'nye stali* [Special steels]. Moscow, Metallurgiya Publ., 1985. 408 p.

21. Dorfman M.R., Sporer D., Meyer P. Thermal spray technology growth in gas turbine applications. *ASM Handbook. Vol. 5A. Thermal Spray Technology*. ASM International, 2013, pp. 280–286. DOI: 10.31399/asm.hb.v05a.a0005737.

22. Matthews S., James B. Review of thermal spray coating applications in the steel industry: Part 1 – Hardware in steel making to the continuous annealing process. *Journal of Thermal Spray Technology*, 2010, vol. 19 (6), pp. 1267–276. DOI: 10.1007/s11666-010-9518-8.

23. Panteleenko F.I., Okovity V.A., Devoino O.G., Volodko A.S., Sidorov V.A., Okovity V.V., Astashinskii V.M. Sovremennoe primenenie metallokeramicheskikh pokrytii na osnove sistem metall-khrom-alyuminii-ittrii [Modern application of cermet coatings based on metal-chromium-aluminum-yttrium systems]. *Progressivnye tekhnologii i sistemy mashinostroeniya = Progressive Technologies and Systems of Mechanical Engineering*, 2021, no. 3 (74), pp. 72–81.

24. Chernov A.A., Bersenev K.A., Puzanov M.P., Korobov Yu.S., Karenina L.S., Khudorozhkova Yu.V., Makarov A.V., Davydov D.I. Vliyanie Y2O3 na stoikost' NiCrAlY plazmennykh pokrytii protiv obrazovaniya narostov na pechnykh rolikakh [The influence of Y2O3 on the durability of NiCrAlY plasma coatings against the formation of deposits on furnace rollers]. *Stal' = Steel in Translation*, 2025, no. 5, pp. 24–30. (In Russian).

Conflicts of Interest

The authors declare no conflict of interest.

Obrabotka metallov –
Metal Working and Material Science

Journal homepage: http://journals.nstu.ru/obrabotka_metallov

Structure and properties of coatings based on refractory elements obtained by non-vacuum electron beam surfacing

Evdokia Bushueva [1, a, *], Artem Nastavshev [1, b], Ksenia Skorokhod [2, c], Evgeniy Domarov [3, d], Ivan Mishin [4, e]

[1] Novosibirsk State Technical University, 20 Prospekt K. Marksa, Novosibirsk, 630073, Russian Federation
[2] Khristianovich Institute of Theoretical and Applied Mechanics SB RAS, 4/1 Institutskaya str., Novosibirsk, 630090, Russian Federation
[3] Budker Institute of Nuclear Physics of Siberian Branch Russian Academy of Sciences, 11 Acad. Lavrentieva Pr., Novosibirsk, 630090, Russian Federation
[4] Institute of Strength Physics and Materials Science of the Siberian Branch of the RAS, 2/4 pr. Akademicheskii, Tomsk, 634055, Russian Federation

[a] https://orcid.org/0000-0001-7608-734X, bushueva@corp.nstu.ru; [b] https://orcid.org/0009-0002-1082-2086, artem.nastavshev@yandex.ru;
[c] https://orcid.org/0000-0003-0210-8405, k.skorokhod@itam.nsc.ru; [d] https://orcid.org/0000-0003-2422-1513, domarov88@mail.ru;
[e] https://orcid.org/0000-0001-8294-7238, mip@ispms.ru

ARTICLE INFO

ABSTRACT

Introduction. The development of modern industry requires materials capable of withstanding high temperatures and loads while maintaining functionality and performance. Traditional materials, such as *0.4 C-Cr* structural steel, are widely used in mechanical engineering and are inexpensive. However, ordinary and low-alloy steels are subject to intense oxidation when exposed to temperatures above 400°C. To improve the performance of structural steels under high-temperature conditions, the development of effective methods for modifying their surfaces is an an urgent task. **The purpose of this work** is to develop a technology for creating high-temperature oxidation resistant surface layers on *0.4 C-Cr* structural steel. For this purpose, the non-vacuum electron beam surfacing method was used, employing powder materials based on refractory elements: niobium, molybdenum, and boron. **Materials and methods.** In this study, modified layers were formed on *0.4 C-Cr* steel using non-vacuum electron beam surfacing of *Nb-Mo-B* powder composites. The following research methods were used: optical microscopy, scanning electron microscopy, X-ray diffraction analysis, microhardness testing, high-temperature oxidation testing, and oxidation reaction kinetics determination. **Results and discussion.** The modified layers, which were 2.0–2.3 mm thick, exhibited a gradient structure consisting of molybdenum-doped niobium carbide present as dendrites and irregularly shaped crystals, as well as eutectic colonies based on the same carbide and α-*Fe* and α-(*Mo,Fe*) solid solutions. X-ray phase analysis identified the following phases in the modified layers: (*Nb,Mo*)*C* carbide and α-*Fe* and α-(*Mo,Fe*)-based solid solutions. The surfacing with *Nb*, *Mo*, and *B* resulted in the formation of layers on the surface of *0.4 C-Cr* carbon steel that are 2.9 times harder and 3.9 times more temperature oxidation resistant than those of the unmodified steel.

Introduction

Industries such as power engineering, chemical engineering, aircraft manufacturing, and mechanical engineering require products capable of operating under high loads, at elevated temperatures, and in aggressive corrosive environments. To ensure these performance characteristics, components are manufactured from structural materials with enhanced strength and corrosion-resistant properties. However, the widespread use of such materials is limited by their high cost. Surface modification and protective coating methods,

* Corresponding author
Bushueva Evdokia G., Ph.D. (Engineering), Associate Professor
Novosibirsk State Technical University,
20 Prospekt K. Marksa,
630073, Novosibirsk, Russian Federation
Тел.: +7 383 346-06-12, **e-mail:** bushueva@corp.nstu.ru

including surfacing, are considered to be cost-effective alternatives [1, 2]. Surface treatment methods include plasma, laser, electron beam, and other technologies [3, 4]. These technologies make it possible to form protective layers on the surface of components made from inexpensive and widely used materials. These methods can also be used to restore a damaged component surface instead of replacing it, which reduces the cost of expensive materials and shortens the repair time. A promising area in materials science is the forming coatings based on refractory elements (niobium, molybdenum, vanadium, tungsten, etc.) [5–7], since, depending on the chemical composition and production technology, they are capable of providing strength at elevated temperatures, high hardness and wear resistance [8], as well as increased high temperature oxidation resistance above 500 °C and under normal conditions [9]. Recently, it has been proposed to use compounds of refractory elements with non-metals, such as borides and carbides [10, 11, 12]. In particular, works [11, 12] consider the prospects of using compounds of niobium and molybdenum with boron and carbon [13-15]. The presence of these compounds in the structure of the material increases the heat resistance, hardness and wear resistance of the coating [16]. It should be noted that niobium, molybdenum and boron are used as alloying components individually or sometimes in combination of only two components, for example, boron-niobium [17, 18, 19]. However, the production of coatings by surfacing on structural medium-carbon steel with simultaneous alloying with niobium, molybdenum and boron has not been considered in the literature. An important point is that the creation of coatings based on refractory elements requires high energy costs [20]. The use of a beam of relativistic electrons released into the air atmosphere, due to its high efficiency, makes it possible to easily remelt powder mixtures of refractory elements and their compounds. Thus, it is possible to form a modified layer up to 3 mm thick, based on refractory compounds, possessing a set of properties: wear resistance, corrosion resistance, heat resistance, and high hardness [21]. Coatings obtained by this technology have high adhesion to steel and low defectivity. Part of the electron beam energy is dissipated in the powder layer, causing its heating and melting, and part of the energy is used to heat the substrate. This method allows for the melting of even refractory elements and compounds while exerting minimal thermal impact on the substrate [22]. In the present study, modified layers based on *Nb*, *Mo*, and *B*, their microhardness, and high temperature oxidation resistance were investigated for the first time. The layers were obtained by non-vacuum electron beam surfacing of *Nb-Mo-B* powders, with the simultaneous introduction of these three components into the melt pool.

The purpose of this study was to modify the surface layers of *0.40% C-1% Cr* structural steel using non-vacuum electron beam surfacing of powder composites consisting of niobium, molybdenum, and boron to form layers with increased high temperature oxidation resistance and hardness. To achieve this goal, the following ***objectives*** were addressed:

– to form modified layers containing refractory elements such as niobium, molybdenum, and boron on *0.40% C-1% Cr* steel blanks using surfacing;
– to analyze the structure and phase composition of the modified layers;
– to evaluate the microhardness of the resulting materials;
– to analyze the high temperature oxidation resistance of the layers.

Materials and methods

Structural steel *0.40% C-1% Cr* was chosen as a model material for forming a heat-resistant coating [23]. This steel is widely used in the manufacturing products and mechanisms; however, it does not have high-temperature oxidation resistance. Therefore, this work considers the prospects of forming protective coatings based on refractory elements on inexpensive structural materials. In this regard, powder mixtures of niobium, molybdenum, and boron were surfaced onto the steel surface (Table 1). In order to minimize oxidation processes during electron beam processing, a fluxing additive – magnesium fluoride (*MgF₂*) – was added to the charge mixture to ensure the creation of a protective environment. An *ELV-6* industrial electron accelerator was used as a source of concentrated energy during surfacing; the work was carried out on an experimental setup of the *G.I. Budker Institute of Nuclear Physics SB RAS* (Novosibirsk). The surfacing modes are listed in Table 2.

Powder mixtures compositions

Composition designation	Powder mixtures compositions, wt.%			
	Nb	*Mo*	*B*	*MgF₂*
Composition 1 (*Nb20-Mo10*)	20	10	10	60
Composition 2 (*Nb10-Mo20*)	10	20	10	60

T a b l e 2

Non-vacuum electron beam surfacing modes

Parameter	Value
Electron beam current, *I*	23 mA
Electron beam energy, *E*	1.4 MeV
Powder mass per unit area, *m*	0.45 g/cm²
Sample movement speed, *V*	10 mm/s

The structure of the surfaced layers was analyzed using a *Carl Zeiss Axio Observer Alm* metallographic microscope and a *Carl Zeiss EVO50 XVP* scanning electron microscope in secondary electron mode. Particle sizes and their volume fraction in the surfaced layer were estimated using the ImageJ software package based on five images of the structure from different areas of the coating. Energy-dispersive spectroscopy was used to determine the elemental composition of the microstructure. Microhardness was measured using the Vickers method in accordance with *GOST 6507-1-2007* on a *Wolpert Group 402MVD* microhardness tester at a load of 0.98 N in the direction from the surface of the surfaced layer to the steel substrate [24]. For each surfacing mode, the hardness was estimated using five samples. X-ray phase analysis of the materials was performed on a *Thermo Scientific ARL X'TRA* diffractometer. The high-temperature oxidation resistance of 40Kh steel and the resulting layers was assessed in accordance with *GOST 6130-71* [25]. The high-temperature oxidation resistance test parameters were as follows: samples were maintained at 850°C for 48 hours in air. Every 4 hours, the samples were weighed on a Gosmetr-124 analytical balance with a measurement accuracy of 0.1 mg. The base material, *0.40% C-1% Cr* steel, was used as the reference for all measurements.

To calculate the rate constant of the oxidation reaction, the following Equation was used:

$$(\Delta W)^n = k_p t , \tag{1}$$

where ΔW is the mass gain per unit area; n is the exponential constant; t is the oxidation time; k_p is the oxidation rate constant.

Equation (1) can be reduced to a linear equation using logarithms:

$$n \ln \Delta W = \ln k_p + \ln t . \tag{2}$$

A linear regression approximation of the graph in coordinates **ln ΔW− ln t** was carried out.

Results and Discussion

Fig. 1 shows the images of the microstructure and the schematic diagram of the structure of the formed layers. For materials with **composition 1** (*Nb20-Mo10*) and **composition 2** (*Nb10-Mo20*), a similar structure is formed during surfacing. The microstructure consists of finely dispersed particles (having an average size of 8 ± 2 μm and 18 ± 5 μm for the modified layers obtained by surfacing **compositions 1** and **2**, respectively), which are presumably molybdenum-alloyed niobium carbides, distributed uniformly throughout the volume of the surfaced layer. The morphology of the carbide particles varies from crystals with irregular
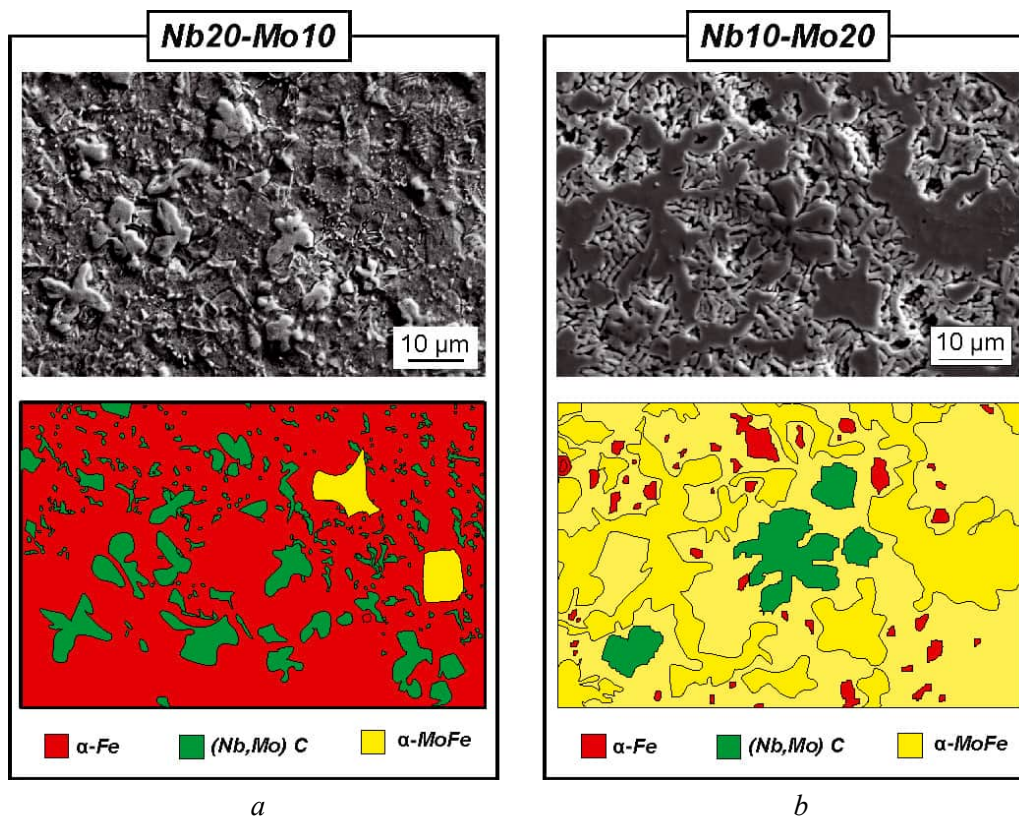
Fig. 1. Microstructure of modified layers formed during surfacing of powder mixtures:

a – Nb20-Mo10; *b – Nb10-Mo20*

geometry to a petal-shaped form. According to the literature, irregularly shaped niobium carbide crystals are formed first. The primary formation of niobium carbides is due to their crystallization temperature and a stronger affinity for carbon in niobium than in molybdenum and iron [26]. Next, niobium carbide crystals grow, acquiring a petal-shaped form. Simultaneously with the preceding process, partial replacement of niobium atoms in the carbide with molybdenum atoms occurs. This is how molybdenum-alloyed niobium carbides are formed. Furthermore, it should be noted that a decrease in niobium concentration in the melt is a key factor influencing the morphology of the forming phases. A niobium deficiency limits the growth of petal-shaped carbide crystals, leading to the formation of finely dispersed, irregularly shaped particles. The final stage of the crystallization process is the precipitation of an iron-molybdenum matrix, which fills the spaces between the molybdenum-alloyed niobium carbides.

The volume fraction of hardening particles (carbides) in the coating of **composition 1** – *Nb20-Mo10* – is approximately 17.5 %. For the **composition 2** – *Nb10-Mo20* – a decrease in the volume fraction of hardening particles to 12.5% was recorded (Fig. 1).

The elemental mapping results presented in Fig. 2, *a*, *b* for coatings obtained by surfacing powder **compositions 1** and **2**, respectively, allow for a qualitative analysis of the element distribution among the structural components. The maps demonstrate that the petal-shaped and irregular crystals are enriched in niobium, molybdenum, and carbon, which supports their identification as the carbide phase *(Nb,Mo)C*. The intercrystalline space, in turn, is characterized by a predominant content of iron and molybdenum, indicating the formation of a ductile matrix based on an **α**-iron solid solution (**α**-*Fe*) and a molybdenum-based solution (**α**-*(Mo,Fe)*).

The analysis of the diffraction patterns (Fig. 3) showed that the phase composition of the surfaced layer includes a carbide phase of the *(Nb,Mo)C* type and two main metallic phases – solid solutions based on **α**-*Fe* and **α**-*(Mo,Fe)*.

According to the literature, boron has low solubility in *Nb* (~0.15 wt.%), *Mo* (~0.1 wt.%), and **α**-*Fe* (~0.002 wt.%). However, it easily forms niobium borides [26]. Despite this, no chemical compounds with
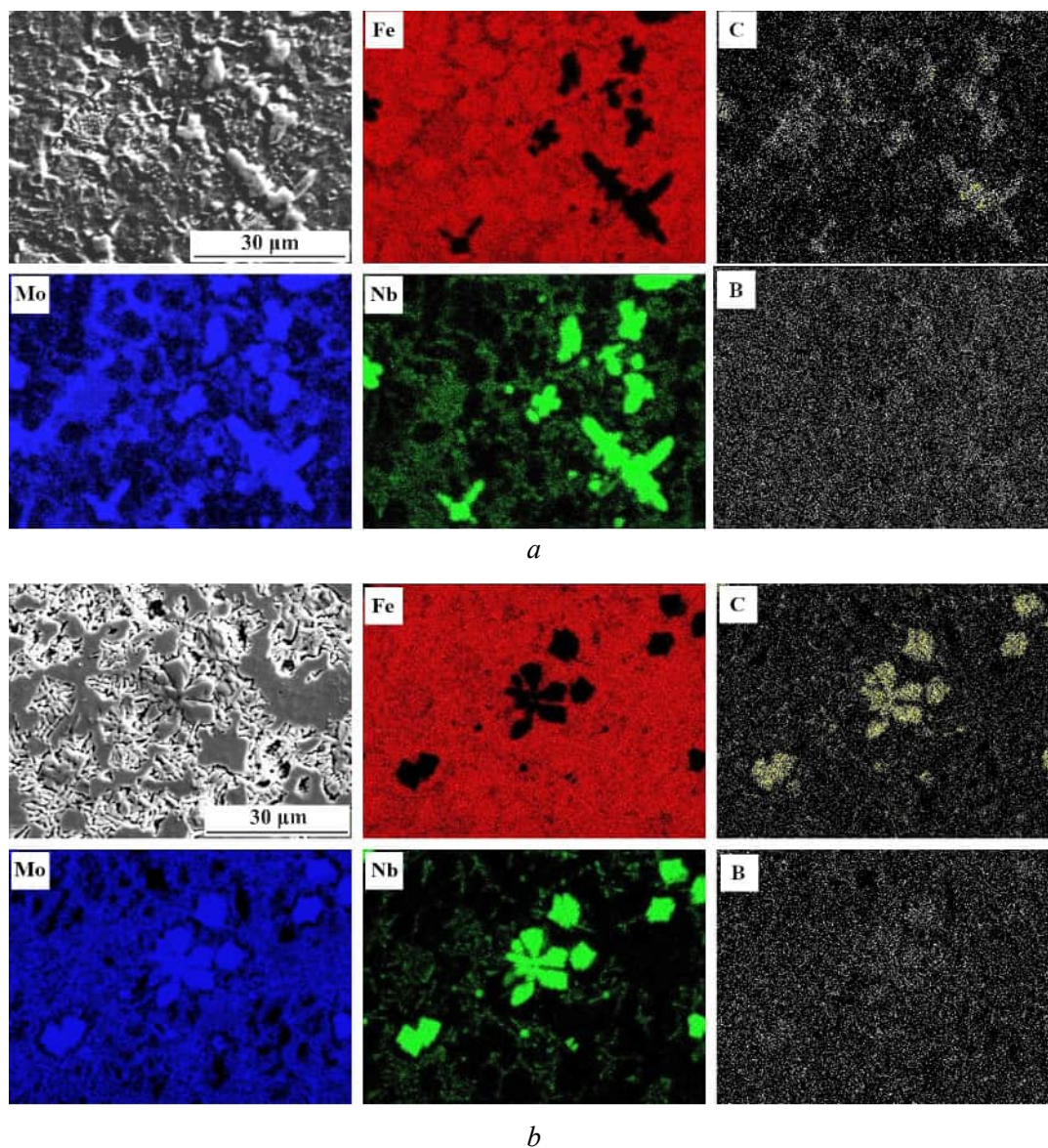
a

b

Fig. 2. Energy-dispersive spectroscopy of modified layers: composition of the powder mixture:
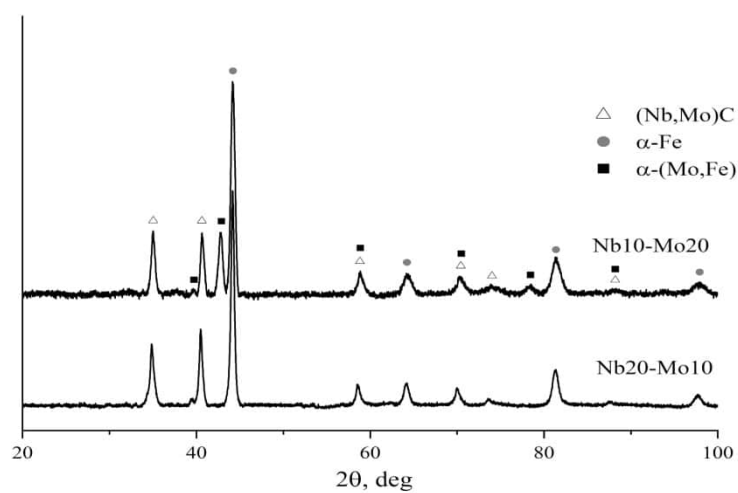
a – Nb20-Mo10; b – Nb10-Mo20

Fig. 3. X-ray diffraction patterns of modified layers

boron were recorded. This is explained by the oxidation of most of the boron during the surfacing process with the formation of boron anhydride B_2O_3. This oxide melts at 450 °C and mixes with slag [27]. The remaining small portion of boron dissolved in the plastic matrix based on **α**-phase solutions of molybdenum and iron and did not have time to separate as individual compounds due to the suppression of diffusion processes caused by high cooling rates. The results of energy-dispersive spectroscopy confirm the distribution of boron throughout the volume of the material (Fig. 2).

The results of structural and phase studies also indicate that the layers surfaced with powder mixtures of **compositions 1** and **2** have different proportions of iron-molybdenum-based solid solutions. *Nb10-Mo20* materials contain a higher amount of the **α**-(*Mo,Fe*) phase than *Nb20-Mo10*. This is confirmed by scanning electron microscopy images (Figs. 1 and 2) and X-ray phase analysis, as evidenced by the increased intensity of reflections from this phase (Fig. 3). This feature is associated with the increased molybdenum content in the powder coating.

The results of microhardness tests (Fig. 4) demonstrate the formation of modified layers with significantly higher hardness values compared to the original steel matrix. The layers formed by surfacing with mixture **composition 1** exhibit the greatest increase in microhardness values — 2.9 times. This is explained by the presence of a large amount of (*Nb,Mo*)*C* carbides in the structure of these layers, which have a high hardness of approximately 20 GPa [28].
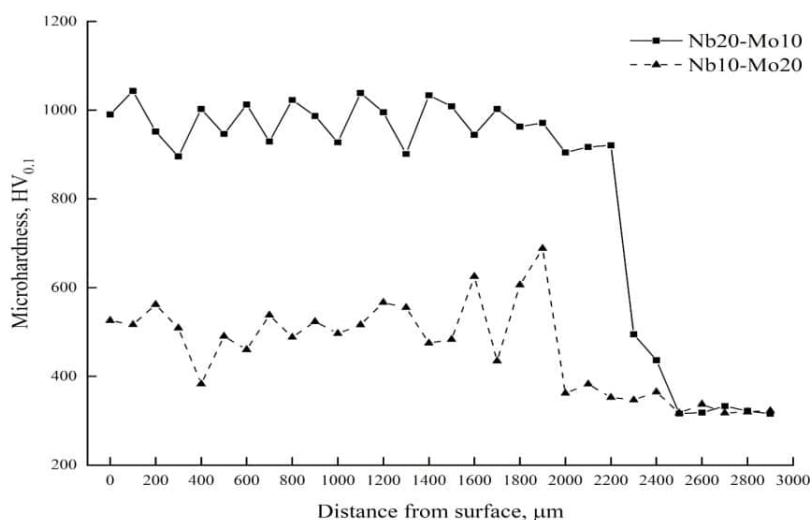

Fig. 4. Microhardness testing results

This study focuses on improving the high-temperature oxidation resistance of structural steel. To this end, high-temperature oxidation resistance tests were conducted on samples, followed by an analysis of the reaction kinetics and morphology of the oxidation products.

Fig. 5 shows the dependences of the change in sample weight on the holding time in the furnace, obtained from the results of high-temperature oxidation resistance tests. The plot shows that *0.40% C-1% Cr* steel is characterized by a linear relationship between the increase in weight and the holding time. This means that the oxidation rate does not change over time and the steel does not possess high-temperature oxidation resistance. A nonlinear relationship is characteristic of the modified *Nb20-Mo10* and *Nb10-Mo20* layers. It is also evident from the dependences that the increase in weight after oxidation does not reach the saturation level, which is typical for the cessation of the oxidation process and surface passivation. This is likely due to intense oxidation processes along the interfaces of the carbide phases and the solid solution [29]. Fig. 6 shows a diagram of the relative high-temperature oxidation resistance of the studied materials.

As a result of the calculation, the oxidation reaction rate constant k_p for the *Nb20-Mo10* coating was 2.3×10^{-3} mg^2/(cm$^4 \cdot$h) for the *Nb10-Mo20* coating it was 0.84×10^{-3} mg^2/(cm$^4 \cdot$h). For *0.40% C-1% Cr* steel, the reaction rate constant was 16.1×10^{-3} mg^2/(cm$^4 \cdot$h). A lower constant value indicates better high-temperature oxidation resistance. The exponent for the **surfaced** compositions was approximately equal to
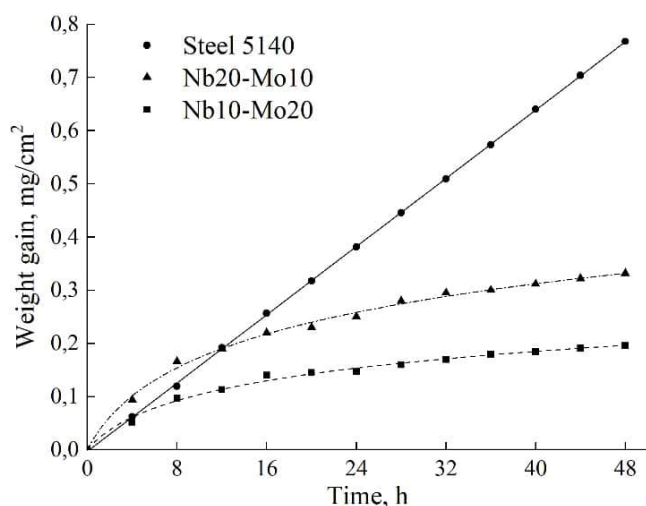
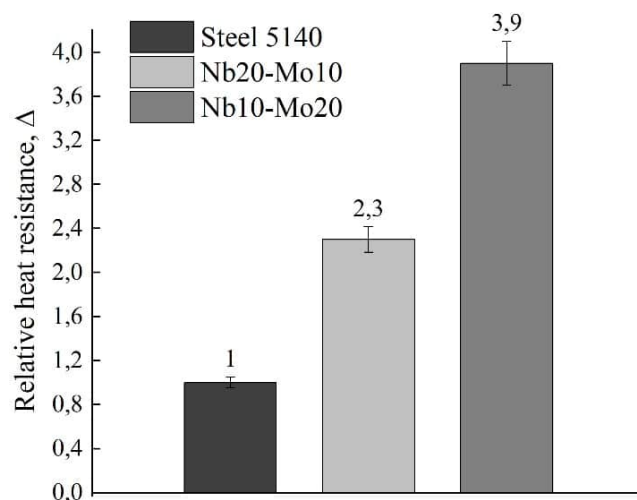Fig. 5. Dependence of the mass change on the test time

Fig. 6. Relative high-temperature oxidation resistance of surfaced layers

2, which indicates a parabolic law of oxide film growth. The exponent for *0.40% C-1% Cr* steel is 1, which confirms the linear law of film growth. The linear law corresponds to a steady-state oxidation mode; in this case, the oxidation process is determined by the rate of oxygen diffusion through the formed oxide layer.

Fig.7 shows the morphology of the oxide films formed on the samples after high-temperature oxidation resistance testing. The film structure on the *Nb20-Mo10* samples developed in the form of columnar structures (Fig. 7, *a*, *b*). They consist of plate-shaped crystals with rounded edges, quite tightly bonded to
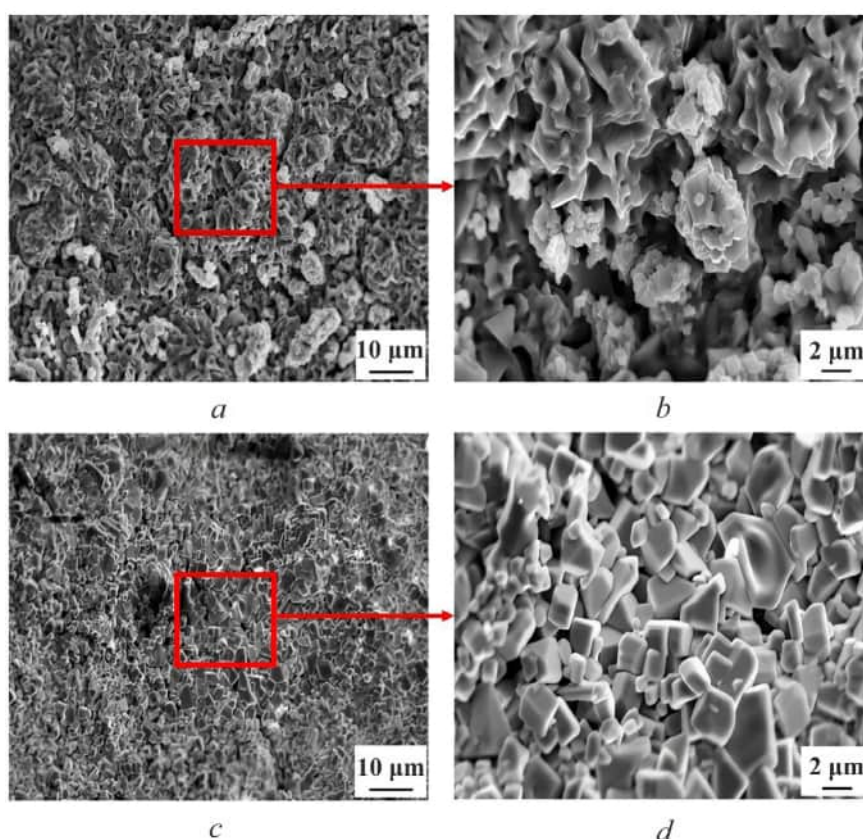

Fig. 7. Oxide layers formed on the surface of samples after high-temperature exposure:

a, b – Nb20-Mo10; *c, d – Nb10-Mo20*. The red square and arrow highlight the areas shown at a higher resolution on the right

one another. The oxide layer on the surface of the *Nb10-Mo20* samples is dense, without cracks or pores (Fig. 7, *c*, *d*). The oxidation products are uniformly distributed polyhedral oxide crystals with sizes of 1–5 μm.

According to experimental data, the coating obtained by surfacing the powder mixture of **composition 2** has better high-temperature oxidation resistance compared to the *Nb20-Mo10* coating. This difference is due to the fact that *Nb10-Mo20* coatings form a denser, continuous**,** and uniform oxide film, presumably of the composition MoO_2 [30]. The proportion of molybdenum introduced into the powder mixture of **composition 2** (*Nb10 + Mo20*) is greater than in **composition 1** (*Nb20 + Mo10*). This led to a greater enrichment of the modified layer with molybdenum and increased its high-temperature oxidation resistance, which is consistent with the literature data [31].

Conclusion

1. The study demonstrated that non-vacuum electron beam surfacing of powder mixtures based on niobium (*Nb*), molybdenum (*Mo*), and boron (*B*) enables the creation of modified layers on the surface of *0.40% C-1% Cr* medium-carbon structural steel up to 2,400 μm thick. The structure of these layers consists of molybdenum-alloyed niobium carbides distributed in a ductile matrix consisting of solid solutions of iron and molybdenum.

2. The analysis revealed that, at any of the studied niobium and molybdenum ratios (20% *Nb* + 10% *Mo* or 10% *Nb* + 20% *Mo*), the following phases are formed in the structure of the surfaced layer: alloyed niobium carbide (*Nb,Mo*)*C*, an **α**-solid solution of iron, and an **α**-solid solution of molybdenum alloyed with iron. Despite the introduction of 10% boron, there are no signs of the formation of *Nb* or *Mo* borides, which indicates its transition to a solid solution based on iron and molybdenum. In addition, it was found that in the modified layer, when using the *Nb20 + Mo10* powder surfacing mixture, alloyed niobium carbides with a size of 8 ± 2 μm are formed in an amount of 17.5%; when using the *Nb10 + Mo20* powder surfacing mixture, alloyed niobium carbides with a size of 18 ± 5 μm are formed in an amount of 12.5%.

3. The formation of modified layers alloyed with niobium, molybdenum, and boron significantly increases the microhardness of the surface layer of *0.40% C-1% Cr* steel (the microhardness of unmodified steel is 330 HV). The average microhardness value (~970 HV) was obtained for the modified layer of the *Nb20 + Mo10* composition, while for the *Nb10 + Mo20* composition this value was ~522 HV. The high *Nb* content (20%) enhances the formation of niobium carbides alloyed with molybdenum, which increases the hardness.

4. Alloying the surface of *0.40% C-1% Cr* steel with niobium and molybdenum significantly improves the material's high-temperature oxidation resistance. Quantitative analysis showed that the addition of molybdenum (20%) and niobium (10%) increases high-temperature oxidation resistance by 3.9 times, while alloying with niobium (20%) and molybdenum (10%) increases this indicator by 2.3 times. Increasing the proportion of *Mo* (20%) facilitates the production of molybdenum-based solid solutions, which improve high-temperature oxidation resistance.

References

1. Sun S., Wu Z., Pang M., Chang J., Xuan Y., Qi H., Yang R., Wu Y. Microstructure and corrosion behavior of chromium-rich stainless steel coatings deposited by different laser cladding processes. *Journal of Materials Research and Technology*, 2024, vol. 29, pp. 3879–3890. DOI: 10.1016/j.jmrt.2024.02.044.

2. Ssenteza V., Eklund J., Hanif I., Liske J., Jonsson T. High temperature corrosion resistance of FeCr(Ni, Al) alloys as bulk/overlay weld coatings in the presence of KCl at 600 °C. *Corrosion Science*, 2023, vol. 213, p. 110896. DOI: 10.1016/j.corsci.2022.110896.

3. Lakkannavar V., Yogesha K.B., Prasad C.D., Phanden R.K., Srinivasa G., Prasad S.C. Thermal spray coatings on high-temperature oxidation and corrosion applications – A comprehensive review. *Results in Surfaces and Interfaces*, 2024, vol. 16, p. 100250. DOI: 10.1016/j.rsurfi.2024.100250.

4. Matts O.E., Tarasov S.Yu., Domenichini B., Lazurenko D.V., Filippov A.V., Bataev V.A., Rashkovets M.V., Chakin I.K., Emurlaev K.I. Tribo-oxidation of Ti-Al-Fe and Ti-Al-Mn cladding layers obtained by non-vacuum electron beam treatment. *Surface and Coatings Technology*, 2021, vol. 421, p. 127442. DOI: 10.1016/j.surfcoat.2021.127442.

5. Ospennikova O.G., Podjyachev V.N., Stolyankov Yu.V. Tugoplavkie splavy dlya novoi tekhniki [Refractory alloys for innovative equipment]. *Trudy VIAM = Proceedings of VIAM*, 2016, no. 10 (46), pp. 55–63. DOI: 10.18577/2307-6046-2016-0-10-5-5. Available at: http://www.viam-works.ru (accessed 21.11.2025).

6. Shestakov A.V., Karashaev M.M., Dmitriev N.S. Tekhnologicheskie puti sozdaniya kompozitsionnykh materialov na osnove zharoprochnykh tugoplavkikh soedinenii (obzor) [Technological ways to create composite materials based on heat-resistant refractory compounds (review)]. *Trudy VIAM = Proceedings of VIAM*, 2021, no. 8 (102), pp. 12–20. DOI: 10.18577/2307-6046-2021-0-8-12-20. Available at: http://viam-works.ru/ru/articles?art_id=1732 (accessed 21.11.2025).

7. Chen B., Zhuo L. Latest progress on refractory high entropy alloys: Composition, fabrication, post processing, performance, simulation and prospect. *International Journal of Refractory Metals and Hard Materials*, 2023, vol. 110, p. 105993. DOI: 10.1016/j.ijrmhm.2022.105993.

8. Rymer L.-M., Lindner T., Lampke T. Enhanced high-temperature wear behavior of high-speed laser metal deposited $Al_{0.3}CrFeCoNi$ coatings alloyed with Nb and Mo. *Surface and Coatings Technology*, 2023, vol. 470, p. 129832p. DOI: 10.1016/j.surfcoat.2023.129832.

9. Xiao Z., Liu J., Jiang Z., Luo L. Corrosion behavior of refractory metals in liquid lead at 1000 °C for 1000 h. *Nuclear Engineering and Technology*, 2022, vol. 54 (6), pp. 1954–1961. DOI: 10.1016/j.net.2021.12.014.

10. Teplykh A., Golkovskiy M., Bataev A., Drobyaz E., Veselov S.V., Golovin E., Bataev I.A., Nikulina A. Boride coatings structure and properties, produced by atmospheric electron-beam cladding. *Advanced Materials Research*, 2011, vol. 287–290, pp. 26–31. DOI: 10.4028/www.scientific.net/AMR.287-290.26.

11. Graboś A., Rutkowski P., Huebner J., Kozień D., Zhang S., Kuo Y.-L., Kata D., Hayashi S. Oxidation performance of spark plasma sintered Inconel 625-NbC metal matrix composites. *Corrosion Science*, 2022, vol. 205, p. 110453. DOI: 10.1016/j.corsci.2022.110453.

12. Wieczerzak K., Stygar M., Brylewski T., Chulist R., Bała P., Michler J. Kinetics and mechanisms of high-temperature oxidation in BCC and FCC high-alloy Fe-based alloys with high volume fraction of carbides. *Materials & Design*, 2024, vol. 244, p. 113163. DOI: 10.1016/j.matdes.2024.113163.

13. Santana D.A., Koga G.Y., Wolf W., Bataev I.A., Ruktuev A.A., Bolfarini C., Kiminami C.S., Botta W.J., Jorge Jr A.M. Wear-resistant boride reinforced steel coatings produced by non-vacuum electron beam cladding. *Surface & Coatings Technology*, 2020, vol. 386, p. 125466. DOI: 10.1016/j.surfcoat.2020.125466.

14. Xia T., Wang R., Bi Z., Wang R., Zhang P., Sun G., Zhang J. Microstructure and mechanical properties of carbides reinforced nickel matrix alloy prepared by selective laser melting. *Materials*, 2021, vol. 14, p. 4792. DOI: 10.3390/ma14174792.

15. Liu Y., Liu Y., Zhao Z., Chen Y., Tang H. Effect of addition of metal carbide on the oxidation behaviors of titanium matrix composites. *Journal of Alloys and Compounds*, 2014, vol. 599, pp. 188–194. DOI: 10.1016/j.jallcom.2014.02.056.

16. Zhang G., Zhang Z., Xuan J., Chen B., Jiang D., Song X. The elevated temperature oxidation and wear behavior of $Fe_{20}Co_{20}Ni_{20}Cr_8Mo_{12}B_{10}Si_{10}$ high-entropy alloy coating by laser cladding. *Journal of Materials Research and Technology*, 2024, vol. 29, pp. 4216–4231. DOI: 10.1016/j.jmrt.2024.02.135.

17. Feng M., Lin T., Lian G., Chen C., Huang X. Effects of Nb content on the microstructure and properties of CoCrFeMnNiNbx high-entropy alloy coatings by laser cladding. *Journal of Materials Research and Technology*, 2024, vol. 28, pp. 3835–3848. DOI: 10.1016/j.jmrt.2024.01.002.

18. Moreno M., Andersson J.M., Johansson-Jöesaar M.P., Friedrich B.E., Boyd R., Schramm I.C., Johnson L.J.S., Odén M., Rogström L. Wear of Mo- and W-alloyed TiAlN coatings during high-speed turning of stainless steel. *Surface and Coatings Technology*, 2022, vol. 446, p. 128786. DOI: 10.1016/j.surfcoat.2022.128786.

19. Li Z., Ren J., Ma J., Zhang C., Wang W., Li Y., Dong N., Han P. B and Ce composite microalloying for improving high-temperature oxidation resistance of 254SMO super-austenite stainless steel. *Intermetallics*, 2024, vol. 174, p. 108457. DOI: 10.1016/j.intermet.2024.108457.

20. Komarov D.V., Konovalov S.V., Zhukov D.V., Vinogradov I.S., Panchenko I.A. Analiz sovremennoi situatsii v oblasti primeneniya elektronno-puchkovoi obrabotki razlichnykh splavov. Ch. 1 [Analysis of the current situation in the field of application of electron-beam processing of various alloys. Part 1]. *Polzunovskiy vestnik*, 2021, no. 4, pp. 129–139. DOI: 10.25712/ASTU.2072-8921.2021.04.017. (In Russian).

21. Bataev I.A., Bataev A.A., Golkovsky M.G., Teplykh A.Yu., Burov V.G., Veselov S.V. Non-vacuum electronbeam boriding of low-carbon steel. *Surface and Coatings Technology*, 2012, vol. 207, pp. 245–253. DOI: 10.1016/j. surfcoat.2012.06.081.

22. Hassel T., Murray N., Klimov G., Beniyash A. Cutting and welding of high-strength steels using non-vacuum electron beam as a universal tool for material processing. *World Journal of Engineering and Technology*, 2016, vol. 4, pp. 598–607. DOI: 10.4236/wjet.2016.44056.

23. Zubchenko A.S., ed. *Marochnik stalei i splavov* [Brand book of steels and alloys]. Moscow, Mashinostroenie Publ., 2003. 784 p. ISBN 978-5-94275-582-9.

24. GOST R ISO 6507-1–2007. *Metally i splavy. Izmerenie tverdosti po Vikkersu*. Ch. 1. *Metod izmereniya* [State standard R ISO 6507-1–2007. Metals and alloys. Vickers hardness test. Part 1. Test method]. Moscow, Standartinform publ., 2008. 16 p.

25. GOST 6130–71. *Metally. Metody opredeleniya zharostoikosti* [State standard 6130–71. Metals. Methods of determining heat resistance]. Moscow, Standards Publ., 1990. 14 p.

26. Rogl P., Korniyenko K., Velikanova T. Boron – Carbon – Niobium. *Refractory Metal Systems*. Springer, 2009, pp. 474–498. DOI: 10.1007/978-3-540-88053-0_20.

27. Gur G.E., Montgomety P.W., Knutson C.D., Gorres B.T. The crystal structure of trigonal diboron trioxide. *Acta Crystallographica*, 1970, vol. 26 (7), pp. 906–915. DOI: 10.1107/S0567740870003369.

28. Mesquita R.A., Schuh C.A. Tool steel coatings based on niobium carbide and carbonitride compounds. *Surface and Coatings Technology*, 2012, vol. 207, pp. 472–479. DOI: 10.1016/j.surfcoat.2012.07.052.

29. Uhlig H.H., Revie R.W. *Corrosion and corrosion control: An introduction to corrosion science and engineering*. Wiley, 1985. 512 p. ISBN 0-471-07818-2 (Russ. ed.: Ulig G.G., Revi R.U. *Korroziya i bor'ba s nei: vvedenie v korrozionnuyu nauku i tekhniku*. Leningrad, Khimiya Publ., 1989. 456 p. ISBN 5-7245-0355-7).

30. Mao X., Meng Q., Wang S., Huang S., Yuan M., Qiu Y. Oxidation mechanism and high-temperature strength of Mo–B–C-coated diamonds in the 700°C–1200 °C temperature range. *Journal of Materials Research and Technology*, 2024, vol. 33, pp. 7829–7841. DOI: 10.1016/j.jmrt.2024.10.249.

31. Wu T., Yu L., Chen G., Wang R., Xue Y., Lu Y., Luan B. Effects of Mo and Nb on the microstructure and high temperature oxidation behaviors of CoCrFeNi-based high entropy alloys. *Journal of Materials Research and Technology*, 2023, vol. 27, pp. 1537–1549. DOI: 10.1016/j.jmrt.2023.10.058.

Conflicts of Interest

The authors declare no conflict of interest.

«Обработка металлов (технология • оборудование • инструменты)» – рецензируемый научно-технический и производственный журнал, издающийся с 1999 года с периодичностью 4 раза в год.

В журнале публикуются в основном результаты оригинальных фундаментальных, прикладных и поисковых научных исследований и аспирантских работ. Значительное внимание уделяется публикациям обзорных, проблемных и дискуссионных работ по актуальным вопросам машиностроения, материаловедения и современной металлургии. Научно-технические статьи, направленные в адрес журнала, проходят рецензирование и редактирование. *Публикация статей бесплатная.*

Журнал предназначен для профессорско-преподавательского состава и научных работников высших учебных заведений и научно-исследовательских институтов, инженерно-технических работников производственных предприятий и проектных организаций.

Присутствуют разделы: **«Технология»**, **«Оборудование»**, **«Инструменты»**, **«Материаловедение»**, **«Научно-техническая информация»** и др.

Журнал «Обработка металлов (технология • оборудование • инструменты)» индексируется в крупнейших в мире реферативно-библиографических и наукометрических базах данных *Web of Science* и *Scopus*.

Полный текст журнала «Обработка металлов (технология • оборудование • инструменты)» можно найти в базах данных компании EBSCO Publishing на платформе EBSCOhost. EBSCO Publishing является ведущим мировым агрегатором научных и популярных изданий, а также электронных и аудиокниг.

Журнал входит в «Перечень ведущих рецензируемых научных журналов и изданий, в которых должны быть опубликованы основные научные результаты диссертаций на соискание ученых степеней доктора и кандидата наук».

ОБРАБОТКА МЕТАЛЛОВ

ТЕХНОЛОГИЯ
ОБОРУДОВАНИЕ
ИНСТРУМЕНТЫ

НОВОСИБИРСК